INTEGRATED ELECTRONICS ON ALUMINUM NITRIDE : MATERIALS AND DEVICES

A Dissertation

Presented to the Faculty of the Graduate School

of Cornell University

in Partial Fulfillment of the Requirements for the Degree of

Doctor of Philosophy

by

Reet Tapaskumar Chaudhuri

December 2021

INTEGRATED ELECTRONICS ON ALUMINUM NITRIDE :

MATERIALS AND DEVICES

Reet Tapaskumar Chaudhuri, Ph.D.

Cornell University 2021

The ultra-wide bandgap (UWBG) semiconductor aluminum nitride (AlN) has conventionally been used in optoelectronics, and as piezoelectric layers in radio-frequency (RF) micro electro-mechanical systems (MEMS). AlN, as an electronics platform, is now positioned as a strong candidate to meet the demands of next-generation high-frequency communication. This is thanks to its unique capability of integrating RF active devices, such as transistors and passive RF devices, such as filters, antennas and waveguides, onto a single chip.

This dissertation represents a significant step towards realizing the vision of integrated RF electronics on the AlN-platform. Conductive channels are realized on this otherwise electrical insulator, by employing careful polarization physics, heterostructure design and epitaxial growth, which are then used to fabricate record-performance complementary n- and p-channel transistors.

First, the discovery of the long-missing undoped III-nitride 2D hole gas (2DHG) in GaN/AlN heterostructures is presented. The suppression of impurities from the substrate using carefully engineered blocking layers is found to be crucial in achieving repeatable, large-area growths of these 2DHGs. These 2DHGs overcome the limitations of acceptor doping of GaN to exhibit record high p-type conductivity. Combined with the best-in-class low-resistance Mg-InGaN ohmic contacts, these 2DHGs are then used to enable the first nitride p-channel transistors that break the GHz-speed barrier.

Next, by adding a thin AlN layer on top of the GaN/AlN heterostructure, a parallel 2D electron gas (2DEG) is induced. Electroluminescence from this structure proves the presence of first-of-its-kind polarization-induced 2DEG-2DHG bilayer. The high-density 2DEG in the AlN/GaN/AlN heterostructure is then studied in detail for use as a channel in AlN high electron mobility transistor (HEMT)-based mm-wave power amplifiers (PAs). This 2DEG provides access to GaN conduction band electron states higher than previously possible in magnetotransport measurements, through which electron effective mass of $0.3.m_0$ is extracted at densities of 2-3×10^{13} cm^{-2}. The state-of-art scaled AlN HEMTs demonstrate output powers of ~2 W/mm at operating frequencies upto 94 GHz. A path to higher output powers is provided through a unique *in-situ* AlN passivation technique which drastically reduces the RF-DC dispersion from the surface states in AlN HEMTs. By scaling the GaN channel layer down to 3 nm, enhancement-mode operation is achieved for the first time in AlN metal-oxide-semiconductor (MOS)-HEMTs for use in complementary logic and RF circuits.

The dissertation then details the integration of these active RF devices on the AlN-platform. Combined with the recent demonstrations of passive RF components like epitaxial-AlN bulk acoustic waveguide (BAW) filters and SiC substrate integrated waveguides (SIW) on the same materials as the active devices, this work should unlock new high-efficiency and low cost applications spaces for RF and complementary integrated UWBG electronics on the AlN-platform.

BIOGRAPHICAL SKETCH

A Bengali by birth, Reet Chaudhuri, grew up in the small town of Anand in the Indian state of Gujarat. Coming from an academic family, his father was instrumental in developing his interest in physics during his Anandalaya school days. He studied Electronics at NIT Trichy for his undergraduate degree, and then spent a couple of years as a circuit designer at Nvidia, Bangalore. His interest in fundamental device physics brought him to the beautiful hills of Ithaca as a Masters student in Applied Physics. He continued at Cornell University for his doctoral research under Prof Debdeep Jena.

He works at the intersection of material science, solid-state physics and electronics engineering. His research interests include designing novel III-nitride semiconductor electronic devices through epitaxial growth of high-quality materials, understanding the underlying physics of carrier transport and semiconductor devices.

Outside the laboratory, Reet is actively involved in sports, leading the Jena-Xing group intramural soccer team "Nitriders", and captaining the Cornell Cricket Team. He is an Indian classical music enthusiast, an avid quizzer, collector of random trivia, and a loyal Madridista. He is also (in)famous for his pun-ditry which generates a lot of (mostly hidden) laughter and entertainment for people around once it has groan on them.

Education

Ph.D., Electrical Engineering   (2021)

minor in Applied Physics, Materials Engineering

Cornell University, Ithaca, NY

M.S., Electrical Engineering   2019

Cornell University, Ithaca, NY

M.S., Applied Physics   2016

Cornell University, Ithaca, NY

B.Tech., Electronics and Communication Engineering   2012

National Institute of Technology (NIT) Tiruchirappalli, India

Professional Experience

1. Soctera Inc., *Co-founder*, 2020

2. School of Electrical and Computer Engineering, *Research Assistant*, 2016-2021

3. Nvidia, *ASIC Design Engineer*, 2012-2014

Publications

Links available at https://www.reetchaudhuri.com/publications

22. *in-situ* crystalline AlN Passivation for Reduced RF Dispersion in strained-channel AlN/GaN/AlN HEMTs

    Reet Chaudhuri, Austin Hickman, Jashan Singhal, Joseph Casamento, Huili Grace Xing, and Debdeep Jena

    in review

21. High conductivity Polarization-induced 2D hole gases in Undoped GaN/AlN Heterojunctions enabled by Impurity Blocking Layers

    Reet Chaudhuri, Zhen Chen, David A Muller, Huili Grace Xing, and Debdeep Jena

    Journal of Applied Physics, 2021

20. Electric Fields and Surface Fermi Level in Undoped GaN/AlN Two-Dimensional Hole Gas Heterostructures

    Łukasz Janicki[1], **Reet Chaudhuri**[1], Samuel Bader, Huili Grace Xing, Debdeep Jena and Robert Kudrawiec

    physica status solidi Rapid Research Letters, 2021

19. Molecular Beam Epitaxy Growth of Large-Area GaN/AlN 2D Hole Gas Heterostructures.

    Reet Chaudhuri, Samuel Bader, Zhen Chen, David A Muller, Huili Grace Xing, and Debdeep Jena

    physica status solidi (B), 2020

18. A Polarization-induced 2D Hole Gas in Undoped Gallium Nitride Quantum Wells.

    Reet Chaudhuri, Samuel Bader, Zhen Chen, David A Muller, Huili Grace Xing, and Debdeep Jena

    Science, 2019

17. 2.2 W/mm at 94 GHz in AlN/GaN/AlN HEMTs on SiC

    Austin Lee Hickman, **Reet Chaudhuri**, Lei Li, Kazuki Nomoto, Neil Moser, Micheal Elliot, Matthew Guidry, James Hwang, Huili Grace Xing, Debdeep Jena

    submitted, 2021

---

[1]equal contribution

16. Next generation electronics on the ultrawide-bandgap aluminum nitride platform

    Austin Lee Hickman, **Reet Chaudhuri**, Samuel James Bader, Kazuki Nomoto, Lei Li, James Hwang, Huili Grace Xing, Debdeep Jena

    Semiconductor Science and Technology, 2021

15. Large Signal Response of AlN/GaN/AlN HEMTs at 30 GHz

    Austin Lee Hickman, **Reet Chaudhuri**, Neil Moser, Michael Elliott Kazuki Nomoto, Lei Li, James C. M. Hwang, Huili Grace Xing, Debdeep Jena

    Device Research Conference 2021

14. GaN/AlN p-channel HFETs with I_{max} >420 mA/mm and 20 GHz f_T / f_{MAX}

    K Nomoto, **R Chaudhuri**, SJ Bader, L Li, A Hickman, S Huang, H Lee, T Maeda, HW Then, M Radosavljevic, P Fischer, A Molnar, JCM Hwang, HG Xing, D Jena

    IEEE International Electron Devices Meeting (IEDM), 2020

13. First RF Power Operation of AlN/GaN/AlN HEMTs With > 3 A/mm and 3 W/mm at 10 GHz

    Austin Hickman, **Reet Chaudhuri**, Lei Li, Kazuki Nomoto, Samuel James Bader, James CM Hwang, Huili Grace Xing, Debdeep Jena

    IEEE Journal of the Electron Devices Society, 2020

12. GaN/AlN Schottky-gate p-channel HFETs with InGaN contacts and 100 mA/mm on-current

    SJ Bader, **R Chaudhuri**, A Hickman, K Nomoto, S Bharadwaj, HW Then, HG Xing, D Jena

    IEEE International Electron Devices Meeting (IEDM), 2019

11. Wurtzite phonons and the mobility of a GaN/AlN 2D hole gas, Samuel James Bader, **Reet Chaudhuri**, Martin Schubert, Han Wui Then, Huili

Grace Xing, Debdeep Jena

Applied Physics Letters, 2019

10. High breakdown voltage in RF AlN/GaN/AlN quantum well HEMTs

    Austin Hickman, **Reet Chaudhuri**, Samuel James Bader, Kazuki Nomoto, Kevin Lee, Huili Grace Xing, Debdeep Jena

    IEEE Electron Device Letters, 2019

9. Gate-recessed E-mode p-channel HFET with high on-current based on GaN/AlN 2D hole gas

    Samuel James Bader, **Reet Chaudhuri**, Kazuki Nomoto, Austin Hickman, Zhen Chen, Han Wui Then, David A Muller, Huili Grace Xing, Debdeep Jena

    IEEE Electron Device Letters, 2018

8. Polarization-induced 2D hole gases in pseudomorphic undoped GaN/AlN heterostructures on single-crystal AlN substrates

    Zexuan Zhang, Jimy Encomendero, Reet Chaudhuri, YongJin Cho, Vladimir Protasenko, Kazuki Nomoto, Kevin Lee, Masato Toita, Huili Xing, Debdeep Jena

    in review

7. Prospects for wide bandgap and ultrawide bandgap CMOS devices

    Samuel James Bader, Hyunjea Lee, **Reet Chaudhuri**, Shimin Huang, Austin Hickman, Alyosha Molnar, Huili Grace Xing, Debdeep Jena, Han Wui Then, Nadim Chowdhury, Tomas Palacios

    IEEE Transactions on Electron Devices, 2020

6. Molecular beam epitaxial growth of scandium nitride on hexagonal SiC, GaN, and AlN

Joseph Casamento, John Wright, **Reet Chaudhuri**, Huili Grace Xing, Debdeep Jena

Applied Physics Letters, 2019

5. <u>Overcoming Acoustoelectric Material Limits of Piezoelectric Resonators using Epitaxial Aluminum Nitride</u>

Wenwen Zhao, Mohammad Asadi, Lei Li, **Reet Chaudhuri**, Kazuki Nomoto, Huili Grace Xing, James Hwang, Debdeep Jena

American Physical Society, 2021

4. <u>High-Mobility Two-Dimentional Electron Gases at AlxGa1-xN/GaN Heterostructures Grown by Plasma-assisted Molecular Beam Epitaxy</u>

Yuxing Ren, Yongjin Cho, Austin Hickman, **Reet Chaudhuri**, Phillip Dang, Menyoung Lee, Wenwen Zhao, Zexuan Zhang, Huili Xing, Debdeep Jena

American Physical Society, 2020

3. <u>GaN-based multi-channel transistors with lateral gate for linear and efficient millimeter-wave power amplifiers</u>

Keisuke Shinohara, Casey King, Eric Regan, MP Gomez, Joshua Bergman, Andrew Carter, Andrea Arias, Miguel Urteaga, Berinder Brar, Ryan Page, **Reet Chaudhuri**, Moudud Islam, Huili Grace Xing, Debdeep Jena

IEEE MTT-S International Microwave Symposium (IMS), 2019

2. <u>GaN-based multiple 2DEG channel BRIDGE (buried dual gate) HEMT technology for high power and linearity</u>

Keisuke Shinohara, Casey King, Eric Regan, MP Gomez, Joshua Bergman, Andrew Carter, Andrea Arias, Miguel Urteaga, Berinder Brar, Ryan Page, **Reet Chaudhuri**, Moudud Islam, Huili Grace Xing, Debdeep Jena

ECS Transactions, 2019

1. Terahertz spectroscopy of an electron-hole bilayer system in AlN/GaN/AlN quantum wells

   Hugo Condori Quispe, SM Islam, Samuel J. Bader, A Chanana, K Lee, **R Chaudhuri**, A Nahata, HG Xing, D Jena, B Sensale-Rodriguez

   Applied Physics Letters, 2017

Selected Conference Presentations

Full list at https://www.reetchaudhuri.com/talks

8. GHz-speed GaN/AlN p-channel MIS-HFETs with Imax of 0.5 A/mm

   Reet Chaudhuri[2], Kazuki Nomoto[2], Austin Hickman, Lei Li, James C. Hwang, Huili Grace Xing, Debdeep Jena

   Device Research Conference, 2021

7. E-Mode AlN/GaN/AlN MOS-HFETs with 3 nm GaN Quantum Well Channels

   Reet Chaudhuri, Austin Hickman, Jimy Encomendero, Jashan Singhal, Huili Grace Xing, Debdeep Jena

   Device Research Conference, 2021

6. AlN/GaN/AlN HEMTs with in-situ crystalline AlN Passivation for Reduced RF Dispersion

   Reet Chaudhuri, Austin Hickman, Jashan Singhal, Huili Grace Xing, Debdeep Jena

   Compound Semiconductor Week, 2021

5. Electron-Hole Gas Bilayers in Undoped AlN/GaN/AlN Heterostructures

   Reet Chaudhuri, Jeffery Miller, Samuel James Bader, Huili Grace Xing,

---
[2]equal contribution

ix

Debdeep Jena

International Conference on Nitride Semiconductors, 2019

4. Polarization-induced 2D Hole Gas in undoped GaN/AlN Heterostructures

   Reet Chaudhuri, Samuel James Bader, Zhen Chen, David Muller, Huili Grace Xing, Debdeep Jena

   International Workshop on Nitride Semiconductors, 2018

3. 2D Hole Gas in GaN/AlN Heterostructures

   Reet Chaudhuri, Samuel James Bader, Zhen Chen, David Muller, Huili Grace Xing, Debdeep Jena

   Electronics Materials Conference, 2018

2. Molecular Beam Epitaxy of High Mobility AlN/GaN/AlN Quantum Well FET Structures on 6H-SiC

   Reet Chaudhuri, SM Islam, Samuel James Bader, Austin Hickman, Huili Grace Xing, Debdeep Jena

   Internationl Workshop on Physics of Semiconductor Devices, 2017

1. GaN/AlN Quantum Well FETs on AlN/SiC Platform Using High Temperature MBE Growth

   Reet Chaudhuri, SM Islam, Samuel James Bader, Austin Hickman, Huili Grace Xing, Debdeep Jena

   Electronics Materials Conference, 2017

Patents

4. Polarization-induced 2D Hole Gases for high-voltage p-channel transistors
   Reet Chaudhuri, Samuel James Bader, Huili Grace Xing, Debdeep Jena
   Published Application: WO2020018895A1, January 23 2021

3. A high-voltage p-channel FET based on III-nitride heterostructures
   Samuel James Bader, **Reet Chaudhuri**, Samuel James Bader, Huili Grace Xing, Debdeep Jena
   Published Application: US20200144407A1, May 7 2020

2. Integrated electronics on the aluminum nitride platform
   Austin Hickman, **Reet Chaudhuri**, James C. M. Hwang, Huili Grace Xing, Debdeep Jena
   Provisional application : 16/676083, filed December 19 2020

1. RF high-electron-mobility transistors including group III-N stress neutral barrier layers with high breakdown voltages
   Austin Hickman, **Reet Chaudhuri**, Samuel James Bader, Huili Grace Xing, Debdeep Jena
   Published Application: US2020/0388701, December 10 2020

Invited Talks

5. A wHole new World : Devices and Physics enabled by the undoped GaN/AlN 2D Hole Gases
   Device Component Research
   Intel Corporation, Oregon, PO, 2019

4. Wide-bandgap Complementary Nitride FET

   Condensed Matter Physics and Material Science (CMPMS) Seminar

   TIFR Bombay, India, 2019

3. GaN-on-AlN for Complementary Logic on III-Nitrides

   IEEE AP/EDS Bombay Chapter Seminar

   IIT Bombay India, 2019

2. Complementary Logic on III-Nitrides : Is AlN the answer?

   Electronic Devices Society (EDS) Seminar

   Cornell University, Ithaca NY, 2018

1. III-Nitride semiconductors for power electronics

   Dept. of Applied Physics Guest Lecture Series

   National Institute of Technology Surat, India, 2017

Awards

1. Jacobs Scholar Fellowship

   School of Electrical and Computer Engineering, Cornell University, 2016-2017

2. Aruna Lal Scholarship

   Physical Research Laboratory (PRL), Ahmedabad India, 2005

Dedicated to the Chaudhuri family,

whose legacy of academic excellence is what I strive to continue,

and what inspires me to push forward;

and Shilpa.

Somewhere, something incredible is waiting to be known.

- Carl Sagan

ACKNOWLEDGEMENTS

The work in this dissertation was possible due to the support of countless mentors, colleagues, friends and family members - I am honored to be able to thank them here. Apologies in advance in case I miss or under-represent the contribution of anyone here.

I would like to extend my deepest gratitude to my advisor and mentor, Prof. Debdeep Jena (DJ), who patiently guided me throughout my research journey culminating in this dissertation. My first interaction with him was in his short course on semiconductor device physics back in summer 2015, and his pure excitement about the subject I loved is what pulled me in to work with him for my doctoral research. Since then, over the years, I have experienced the same contagious excitement in every discussion, every informal conversation over beers, every group outing, every Nitriders soccer game, and this excitement is what keeps me going through the rigors of scientific research. He also taught me the importance of taking a step back and looking at the bigger picture to get a good perspective of where we are and how far we have come, and to acknowledge the giants on whose shoulders we are standing.

I am extremely grateful to the other pillar of the Jena-Xing research group, Prof. Huili Xing (Grace), who has provided ample encouragement and re-sources - both technical and otherwise - to keep us focused on our scientific endeavours. She has also taught me how to handle problems and face difficul-ties, lessons which have helped me in life outside the academics as well. I will forever be thankful for her support during the time I was stuck in India due to my visa processing, and the post-PhD transition period. I also appreciate that DJ and Grace have encouraged activities outside the lab such as group outings, happy hours, soccer games etc, which are crucial in breaking the monotony of

the PhD life.

I am also thankful to Prof. David Muller and Prof. Alyssa Apsel, who served as my PhD committee members and collaborators in some of the studies in this work. Helpful discussions with them have helped me gain a different perspective of my interdisciplinary work. I am especially thankful to Prof. Muller, who has been a mentor since my days as a Masters student in Applied Physics, and taught me very valuable lessons, including the importance of effective science communication, which have made me a better scientist.

I am deeply indebted to my parents, without whom this dissertation would not have been possible. Whatever I have achieved so far in my academic life has been due my effort to emulate my dad, Prof. T.K. Chaudhuri, at every step. I consider myself very fortunate to be able to discuss my research with him, and get valuable guidance when necessary in spite of our space-time separation. He has also kept reminding me of the importance of scientific pursuit - a lesson passed down from his father, Prof. P.C. Chaudhuri. My mom, has always been my biggest cheerleader, my pillar of unrelenting support and non-stop encouragement in my best and worst times. My brother Tito has fulfilled a younger sibling's responsibility of being a perpetual punching bag, at the same time inspiring me with his discipline, perseverance and growth.

I would also like to thank the Chaudhuri family's the US branch - Jethu (Tapan Chaudhuri), Jethima, Trina and Chirag, who have supported me emotionally and financially, and without whose help and encouragement I would not have been able to come so far from home and do what I am doing. I am also thankful to Mamu, Maima, Ishita and Brinda for providing Shilpa and I with an invaluable support system.

I have been immensely fortunate work closely with with Dr. Austin Hick-

man and Dr. Samuel Bader - JXHFET dream team - over the course of my PhD research. I could not have asked for a better team to work with. They, along with Nomoto-sensei, were instrumental in fabricating the amazing devices which truly helped demonstrate the potential of my epitaxial materials. I will cherish our fruitful scientific discussions which were filled with non-stop puns and funs through the highs (ICNS Seattle) and lows of this journey. Our trips to Japan, Seattle, Portland and Santa Barbara were some of the best and most memorable times in the past 5 years. I am happy that I get to continue to work with Dr. Hickman as part of our new venture, Soctera.

I must thank Dr. Kevin Lee for the insightful discussions about MBE growth while taking care of the ever-temperamental Veeco Gen10. I am also grateful to Jashan Singhal, who over the past year has helped me sharpen my fundamentals by asking some of the most insightful questions during our many discussions.

I am especially indebted to the senior members of the Jena-Xing research group, Dr. Vladamir Potasenko, Dr. SM Moudud, Dr. Henryk Turski, Dr. Kazuki Nomoto and Dr. YongJin Cho who had a lasting impact on my professional development. I very much appreciate Vlad's help through these years. He has always answered my calls and patiently solved any problems with lab equipment what can only be described as *magic*.

Over the past 5 years, I am really fortunate to have shared time with the an immensely talented, smart and super fun group of lab-mates in the Jena-Xing reasearch group - Dr. Shyam Bharadwaj, Nick Tanen, Ryan Page, Joseph Casamento, Xiang Lee, Hyunjea Lee, Jon McCandless, Jeff Miller, Vasanth Balakrishnan, John Wright, Dr. Alex Chaney, Phillip Dang, Zexuan Zhang, Dr. Jimy Encomendero, Yuxing Ren, Lei Li, Xiaopeng Wang, Dr. Mohammad Asadi, Wen-

wen Zhao, Len van Deurzen, Dr. Wenshen Li, Dr. Amit Verma. I have learnt something from each and every one of them, and hope to cross paths with them down the road as well. In addition, I have been fortunate to be able to guide some of the smartest undergraduate students - Sophia Handley, Nima Leclerc, Sidarth Giddu, Connor Gerlach - during my PhD career.

I would also like to give a shout-out to the Jena-Xing group soccer team Nitriders who are undisputedly the best soccer team in the III-nitride community in the Fingerlakes region, evidenced by their legendary unbeaten run in intramural soccer which continues till this day at the time of writing.

I cannot begin to express my thanks to all the friends I have made in Ithaca over the past 7 years - Rohil, Eshan, Soubhagaya, Vishakha, Nikita, Vighnesh, Swathi, Akshay, Deepika, Manit, Amandeep, Prateek, Pooja, Ajay, Chaitanya, Avik, Steve, Alejandro, Joel, Mingtong, Ravi, Prashanth, Pragya, Arzoo, Neeraj, Shraddha, Vidya, Aravind, Kunal, Pankaj, Ritika, Bhatia, Borkar and many, many more. An exhaustive list will need a dissertation of its own. All the game nights, home-cooked meals, festival celebrations, trips, parties have been integral part of this journey, and have helped me stay sane during the most gruelling parts of it. I am also thankful to my friends from college - Sanjana, Deep, Pallavi, Aruniya, Irene, Rachana, Ketan, Khanjan, Himanshu, Sagar, Anurag, Arpit, K.K. - who have graciously put up with my PhD life and forgiven me for not being in touch regularly, yet cheered and celebrated my every little accomplishment. I am forever grateful for your patience and understanding and I hope to have time now to reconnect with each of you.

Special thanks to the Cornell Cricket Club, SPICMACAY Cornell chapter, Team Nitriders and the Cornell India Association, who let me to pursue my hobbies and interests outside the lab, helped me meet new people and go on

new adventures.

Following Real Madrid's games every weekend was a source of excitement through the past 6 years and I'm glad the historic record-breaking run of 4 Champions League titles in 5 years coincided with my graduate life - Hala Madrid!

I very much appreciate the help of the Cornell ECE department staff members Kimberly Budd, Barbara Walpole, Jessie Hilliker, who have patiently taken care of all the reimbursements, payment orders and paperwork for me, and allowed me to completely focus on doing the science.

And last, but not the least, I would like to thank, and dedicate this work to, my wife Dr. Shilpa Sahoo. We met and started our life together during our PhDs at Cornell, and her unwavering love and support is something I will forever be grateful for. Through all the ups and downs, she has been my one constant, the $\hbar$ of my quantum world, the Hobbes to my Calvin. Thank you.

TABLE OF CONTENTS

LIST OF TABLES

LIST OF FIGURES

CHAPTER 1

INTRODUCTION

1.1 Brief History of Semiconductors in Communication

This dissertation advances the material growth and electronic device performance on the ultra-wide bandgap aluminum nitride (AlN) platform. It presents record p-type and n-type high-speed transistors, enabled by discovery of polarization-induced high-conductivity 2D holes and electrons and material innovations such as low-resistance ohmic contacts. These transistors, together with the recently demonstrated epitaxial AlN passive RF devices, represent a significant advancement in electronics on AlN platform. The high-power, high-frequency integrated electronics on AlN is now just a step away, which shall fulfill the demands of faster wireless communication networks for next-generation technologies such as internet of things (IoT), cloud computing etc.

Interestingly, this human need for faster and better communication has always been a key driver for semiconductor technology innovations throughout its ~ 150 year history. Humans are social animals. By their very nature they have an inherent need to communicate, be it among themselves or with extraterrestrial intelligence [67]. Therefore, before getting into the technical details of this work, it is worth taking a tour of the rich history of semiconductors in communication to learn valuable lessons and to place the results of this work in the larger context. It is especially intriguing to note how paradigm shifts in the communication sector creates new demands, which are more often than not met by new semiconductor materials. These transitions, right from PbS in 1900s to GaAs and GaN in 2000s, took place when the new semiconductor material of-

fered some new capability which the incumbents did not, and therby solved the burning issue of that era.

As it not possible to comprehensively document the vast advancements of this rich field in the few pages of this chapter, interested readers are encouraged to read The Idea Factory [68], Fire in the Belly [69], and books by John Orton [70, 71] for more detailed discussion on the fascinating history of semiconductors.

Every communication system, be it a conversation between two people or 5G cellphone networks, can be broken down to 3 basic elements [72]:

- The Transmitter; that takes the information from the source and transmits it through the channel as an information-carrying "signal".

- The Channel; that carries the signal from the transmitter to the receiver. The channel has some characteristic loss and introduces noise into the signal. Minimizing both is desired.

- The Receiver; that receives the signal from the channel, interprets it by discarding the noise and recovering the loss, and the relays it to the destination.

Back in the 1800s, Samuel Morse's electrical telegraphy dominated communication [73], in which single wires served as the channel carrying the information in the form of electrical signals. Due to the inherent loss of electrical energy from the wires, sending signals over large distances (for example, US coast to coast) was infeasible as the signal would "leak" during travel and not reach the receiver. Added to it, was the challenges in physically laying and maintaining cables across the two points, especially when they are separated by an ocean (US to Europe). By late 1800s, alternative forms of communication were being

explored. The then-recently discovered (1888) Hertzian or electromagnetic radio waves offered the possibility of wireless communication, where the air itself acted the channel. Radio waves could be generated using sparks from a Leyden jar (early form of electrical charge storage device, or capacitor). However the practical applications of this wireless communication were limited by the lack of a suitable detector on the receiver side.

A solution was offered by the Indian scientist Sir Jagdish Chandra Bose [74] at the turn of the century. His invention, the tejometer (*tej* means radiation in Sanskrit) used a galena crystal in contact with a metal as a signal detector. Galena or naturally occurring **lead sulphide (PbS)** crystal, is a semiconductor with bandgap of 0.4 eV. The tejometer is believed to be the first semiconductor device ever patented. When a voltage is applied across a relatively-unstable junction of galena and a thin tungsten wire ("cat's whisker"), a non-linear asymmetric current-voltage (IV) characteristic is observed. This property was very unlike that seen in metals, and was first reported by Karl Braun back in 1874 [75] in what can be considered the first paper on semiconductors. However Bose identified the true technological potential of this scientific discovery and used it as a rectifier to detect radio waves [74]. This marked the beginning of the age of wireless telegraphy, making it possible to beam messages across the seas without physical cables.

To explain the asymmetric IV characteristic in the metal-semiconductor junction in the cat whisker detector, Boris Davydov, Nevill Mott, and Walter Schottky independently proposed the theory of rectification in 1929. Their theories still affect our daily lives through the eponymous Schottky diodes used in high-efficiency power supplies in electric vehicles, trains, microprocessors of DSPs

etc. Thus, technological need of communication led to the invention of a semiconductor device, and the study of the underlying physical phenomena in this devices in turn led to discovery of new physics, which in turn improved the society in ways beyond originally intended. This cycle is a key feature which can be seen throughout the history, and is supported by the sheer number of Nobel Prizes awarded to studies related to, or enabled by, semiconductor devices.

Back to the crystal rectifiers/detectors, the unreliability of a thin metal wire contact to a crystal meant it needed regular adjustment to be usable. Because of this unreliability, radio communication (operating at signal frequencies of 30-300 MHz) moved to thermionic valve or vacuum-tube based diodes for both for detection and transmission of signals during the 1920s. However solid-state semiconductor devices made a comeback with the advent of the World War II. In the wake of the Pearl Harbor attack, the development of RADARs for early detection of the enemies was deemed high priority by the US government. In a RADAR, higher frequency signals translate to higher resolutions. Therefore, the need for detectors which operated at frequencies (300 MHz - 3 GHz) higher than radio communication frequencies (3-300 MHz) arose. Vacuum tubes were fundamentally unsuitable for high frequency operation because of the limit of electron transit time across a cm-scale length. This is solved by a semiconductor-based rectifier, where the electron can transit faster across a micron-scale junction. Therefore renewed research efforts driven by the wartime government funding, both in the US and UK, went into realizing a more stable, field-deployable semiconductor-based detector. Soon, it was found that purified **germanium (Ge)** crystal based detectors performed better and more reliably than galena. This was partly due to the higher purity of the material compared to a naturally occurring crystal, and party due to a larger

energy bandgap of 0.7 eV. This enabled comparatively robust rectification performance at microwave frequencies and served a critical role in the allied power victory in the World War II [76].

It is worth mentioning that the wartime research efforts in the mid-1940s not only renewed interest in solid-state semiconductor devices but more significantly, it laid the foundation for US government funding into fundamental scientific research. This was thanks to pioneering vision of Vannevar Bush. His 1945 influential report "Science, The Endless Frontier" [77] (a must-read for any budding engineer or scientist) was instrumental in the estabilishment of the National Science Foundation, which funds cutting-edge fundamental research to this day (including this work). Additionally, the wartime efforts was the first time that the importance of materials research was identified by the scientific community - (1) for meeting new demands using new semiconductor materials with desired properties, and (2) to improve these properties by enhancing the material purity. The significance of semiconductor material purity is obvious to any device scientist at the current day and age, but it took experimental efforts of teams led by Russel Ohl at Bell Laboratories and Prof Karl Lark-Horovitz at Purdue University [78] to realize that the higher chemical purity germanium crystal is what led to more reliable crystal detectors over naturally-occurring impure galena. Since then, research and development of semiconductor device physics research has always gone hand-in-hand with materials research, with the achievements in the former always being enabled by a key breakthrough in the latter. This is applicable even to the work presented in this dissertation - where the discovery of the long-missing undoped 2D hole gas in GaN and record performance p-channel transistors were possible due to chemically-purer epitaxial crystals [8].

Building on the momentum from the wartime activities, the post-war decade of 1950s-1960s would prove to be a golden-era for semiconductor research. The Bell Laboratories [68] served as one of the key centers for the developments in the field. The "holy-grail" driving the research in the Bell Labs, and the field in general, was the solid-state semiconductor amplifier. The amplifier, located on the transmitter side, is a component that amplifies or intensifies the information carrying signal so that it can travel farther. A robust amplifier was therefore critical to realize the vision of cross-continental telephone networks, by acting as repeaters along long-distance telephone lines to counter the loss in the channel. The crystal-rectifier and p-n junction diodes are passive devices that cannot amplify signals, and the vacuum tube amplifiers were fragile and difficult to deploy. Even though the concept of a semiconductor based solid-state amplifier had been proposed back in 1925 by Lilienfeld [79], experimental realization was proving to be tougher than expected. The search of the field for a solid-state "active device" that could provide power gain culminated in the discovery of the transistor by William Shockley, Walter Brittain and John Bardeen in 1947 [80, 81]. The working transistor realization was an p-n-p point contact transistor made on germanium. Two closely spaced contacts, made by a sliced gold foil wrapped on a spring loaded triangular plastic, were placed on the surface of the germanium crystal. They found that, on application of a voltage to the base of the germanium crystal, a small change in current in the first contact led to a large change in current in the second contact - thus amplification was achieved! The invention of this new device, called a "transistor" by combining 'transconductance' or 'transfer' and 'varistor', was a momentous culmination of many person-decades of research. The transistor is rightfully believed to be the single most important semiconductor device invention - one which was motivated

by, and ultimately instrumental in satisfying, the need of faster communication over greater distances (through the telephone network).

For a layperson in the 21st century, semiconductor is almost synonymous with **silicon** because of its ubiquity in our daily lives. Therefore, it is actually surprising that most of the foundational developments in the field till 1950s, including the discovery of the transistor, were on germanium. It is worth looking into why it was so, and what subsequently motivated the field's transition from germanium to silicon and the silicon dominance.

Silicon as a semiconductor material for devices was known in the 1940s, when the growth of germanium and silicon crystals were both investigated internally at Bell Labs. However, germanium was preferred for device investigations primarily because it was easier to purify. The purification of a crystal requires melting it, removing the impurities and then re-crystallizating it. Germanium has a lower melting point than silicon (~900°C vs ~1400°C) making it easier to purify. In fact, the serendipitous discovery of the p-n junction by Russel Ohl in the 1940s was a result of his investigations into the growth of pure silicon. Phosphorous and boron atoms had inadvertently collected into two parts of a cracked silicon crystal, forming a p-n junction. Even though accidental, this was first demonstration of chemical doping of a semiconductor. He used the p-n junction to patent the silicon solar cell in 1946. However, till the early 1950s, the different types of transistors studied such as point-contact, alloy-junction were all on germanium because of its higher electron mobility than silicon.

The move from germanium to silicon for transistors in the late 1950s was originally motivated by higher thermal stability of operation in silicon. Because of its narrow bandgap, the leakage current in germanium transistors increases

exponentially with temperature to high thermal generation of intrinsic carriers, making it difficult to turn off. The higher bandgap of silicon (1.12 eV) offers higher stability of operation compared to germanium due to lower density of intrinsic carriers. Additionally, by the 1950s, the growth of silicon crystals (Czochralski method, still used today!) was well understood along with controlled doping, thanks to efforts of Morris Tenenbaum and Gordon Kidd Teal at Bell Laboratories. Teal later moved to Texas Instruments and led the effort to demonstrate the first silicon transistor in 1954, again critically enabled by the know-how of silicon crystal growth he brought from his days at Bell Labs.

However, the real reason of the success of silicon in electronics is because of its stable native oxide - the silicon dioxide (SiO_2). Silicon dioxide is easily grown by oxidizing the silicon surface (a serendipitous discovery [82]) and results in a low density of interface states. It was initially developed by Jean Hoerni as an insulating layer to protect (passivate) the key interfaces in silicon transistors and to improve their reliability. However its real power was unleashed when used as a masking layer for device fabrication processes. Because of this property, the silicon dioxide is key to now ubiquitous processes such as planar technology [83], photolithography [84], integrated circuits [85, 86], metal-oxide-semiconductor (MOS) FETs [87], complementary MOS [88]. In retrospect, it is fascinating that all these technologies, which are still very much in use today, were developed over a short period of 1955-1963 at Fairchild, TI, Bell Labs, Intel. Analogous to the impact of assembly lines during the industrial revolution, these processes increased the manufacturing through-puts and drastically reduced the costs of circuit components. This kick-started the Electronics age, and truly established the dominance of silicon in the industry from there on.

Over the next 30 years or so, silicon dominated the electronic communication devices. It was soon realized that speed of a planar transistor, characterized by its operating frequency, can be increased by scaling down the dimensions of the transistor [89]. This increase however comes at the expense of the decreased power handling capability. This fundamental trade-off in operating frequency vs output power is a disadvantage for an amplifier where both are desired to be high. However, it was realized that, if the transistor used as a high-frequency switch instead of an amplifier at *low* operating powers or voltages, it could be used to perform Boolean logic calculations for computation!

Thus began the era of computing in the 1970s. Computers which were room size machines run by vacuum tubes, started getting smaller, eventually fitting on our desks. Push for increase in calculation speed, led to further scaling down of the transistor from centimeter scale to 100s of nanometer scale, governed by Moore's Law [90]. Billions of transistors could now be fit into the same area, increasing the computing speed, and decreasing the computer sizes. Personal desktop computers entered homes in 1990s and in 2000s, portable laptops and cellphones, which were more powerful than supercomputers from few decades back, became mainstream.

After decades of scaling, in the early 2000s, the physical limit was hit when the silicon transistor became < 50 nm small [91]. Scaling beyond this limit with the existing CMOS technology would lead to deviation from expected behavior and unreliable performance. Novel materials (high-K dielectric at 45 nm node) and device architectures (finFETs at 32 nm node) were introduced to circumvent this physical limit. In-spite of these innovations speed of silicon transistors have slowed down and hit a wall [92] in 2010s. The industry is finding ways

to get around this on a higher level of abstraction by exploring new computing paradigms and machine learning which use parallel, high-performance computing. These computing hardware have a much larger footprint and are no longer personal to the user. Instead, the "computer" is hosted in large data centers and remote servers farms, physically separated from the user, sometimes even located halfway around the globe. New applications such as cloud gaming, cloud computing, cloud storage are moving to this model to maintain progress. Because the computation is done remotely, the size is no longer a restriction and hence can be scaled up dynamically as per requirements. The performance bottleneck is therefore no longer the speed of the computation, but instead, it is the speed of the data communication link between the user and remote computer. For example, in cloud gaming, console-level gaming performance is now possible on a mid-level cellphone if the internet connection speed is high enough. Therefore, in the 2020s, faster wireless communication systems are needed more than ever because even computation relies on it.

Going back, how did the semiconductor communication systems evolve from the 1960s, during the silicon computing revolution? In the 1970s, optoelectronic devices such as Lasers and LEDs were seeing rising demand from applications such as compact disk (CD) readers and fibre optic communication. For all its advantages in electronics, silicon is not suitable for optoelectronic applications because of the 1.12 eV bandgap (below visible range) and indirect bandgap. Hence the industry turned to III-V compound semiconductors - **gallium arsenide (GaAs)** and family with a direct bandgap of 1.42 eV. As always, the new semiconductor material also brought with it innovations in crystal growth. Initially, GaAs crystals were grown in a method similar to silicon, by pulling from molten GaAs to form ingots. In the mid 1960s and 1970s *epitax-*

ial growth of GaAs using vapour phase epitaxy (VPE) and liquid phase epitaxy (LPE) was developed in RCA Corporation to reduce the background impurities. However for optoelectronic device heterostructures, accurate control of the doping and layer thicknesses (down to nanometers) was desired. This need led to the invention of epitaxial growth techniques of Metal-organic VPE (MOVPE) in 1968 [93] and molecular beam epitaxy (MBE) in 1969 [94]. These techniques had slow growth rates (~ μm/hr), accurate thickness control, repeatable growths. This proved crucial not only for success of electronic and optoelectronic devices but also supported scientific study of 2D confined carrier physics in nanostructures, which resulted in discovery of interesting physical phenomena such as fractional quantum Hall effect. The initial rewards of these new purer, epitaxial materials were reaped by LEDs and Laser Diodes in the 1970s and 1980s. But soon the real strength of the GaAs material family in electronics was realized on in high speed, high-power signal amplification for wireless communication. GaAs based power amplifiers (PAs) performed better than silicon PAs thanks to their higher electron velocity. In 1960s, state-of-art silicon, germanium transistor speeds were sub-1 GHz, while RADAR and satellite was already starting to move to 1-10 GHz bands. Subsequently in the 1970s, GaAs n-type MESFETs operating at 20-30 GHz were reported for the first time. The speeds kept increasing by scaling the transistor. In 1976 the first microwave integrated circuit (MMIC) was demonstrated on GaAs, which integrated the transistor with other high-frequency circuit components such as waveguides, capacitors, inductors.

A major advancement in heterostructure growth was the invention of modulation doping in 1978 by Ray Dingle, Horst Störmer and team at Bell labs. In this setup, the electrons provided by chemical dopant atoms were confined at a sharp interface between two semiconductors with different bandgaps. The elec-

trons were free to move in the plane (2D) and were hence called a 2D electron gas (2DEG). These 2DEGs were used to make high electron mobility transistors (HEMTs) in GaAs, which were first introduced in the 1980s as GaAs HEMTs and soon replicated in other III-V semiconductors like InP. Initial applications of the HEMT in the 1980s were pretty niche, mainly as low-noise amplifiers (LNAs) on the receiver side of television sets, satellites (SATCOM) and military RADARs. Operating frequencies of upto 200 GHz are reported in GaAs HEMTs, and upto 1 THz in InP HEMT today.

The GaAs HEMTs found renewed commercial, mainstream interest in the 1990s when it became clear that the mobile communication would be the technology of the future. High profit margins of the consumer market injected resources and drove research and development for optimizing the HEMT. The application focus shifted from LNAs to PAs for use in the cellular base stations. PAs are characterized by their frequency and output powers. The former dictates the speed of communication and latter the range of the signal. Hence, PAs with high output powers at high frequencies were the critical to the success of the cellular communication network. GaAs HEMTs provided high speeds thanks to relatively high electron velocity. Additionally, the wider bandgap of GaAs gave it advantage of higher breakdown voltages over silicon and silicon-germanium high-frequency PAs introduced in 1980s. GaAs amplifiers exhibited output powers of $\sim$ 10 W at upto 10 GHz (compared to < 0.01 W for silicon at same frequencies), which was able to meet the demands of sub-2 GHz 1G and 2G cellular networks. GaAs soon became the semiconductor material of choice for radio frequency (RF) power amplifiers the during years rise of mobile communication in the 1990s, taking over from silicon in this application space.

Survival in the uber competitive commercial space of the mobile network market needs rapid progress [95]. The demand for faster data transfer rates and larger bandwidths can be met by using higher frequencies signals to carry the information. Every successive generation (G) of cellular networks therefore operated higher frequency bands - 1.8 GHz (2G) in 1990s to the 2-8 GHz (4G) in 2010s. This drove the RF power amplifier research at systems, circuits, devices level. Soon, the GaAs semiconductor material itself posed a fundamental limit to the output powers of an amplifier at high frequencies [96, 97].

Efforts to identify semiconductor material with desired properties renewed thanks to this immense rise in demand. **Gallium nitride** or GaN slowly gained adoption in the late 1990s and 2000s for RF power amplification. Its main advantage over GaAs is wider bandgap of 3.4 eV, which leads to higher power handling capability, and the higher electron velocity which translates to higher operation frequencies. The III-nitride semiconductors, GaN, AlN, InN and their alloys, were already being studied for optoelectronic applications to access blue emission in LEDs [98]. Therefore, even though GaN was a new material in the RF space, it brought with it years of research results into the epitaxial growth, doping control and device fabrication. In fact, GaN's shift from optoelectronics to RF electronics space in the 2000s mirrors GaAs's journey 20 years back!

GaN-based high electron mobility transistors (HEMTs) were first demonstrated in the laboratory mid-1990s [99]. Interestingly it was found that, unlike the GaAs HEMTs, the 2D electron gas in GaN HEMTs could be generated *without* chamical dopants. The theory of polarization in GaN was proposed [100] to explain this unique observation. Thanks to heavy investment from defense in the 2000s and 2010s into GaN research, it now finds use both in commercial

high-power RF amplifiers [101] and high-voltage switches [102]. State-of-art GaN amplifiers show output powers of 10 W at upto 40 GHz [103] and 3 W at upto 100 GHz [104, 105]. In addition, its mechanical robustness and high temperature operation meant the initial applications were in defense radars and SATCOM, and recently entered the communication space in 4G-LTE base stations [106, 107].

Into the 2020s, with millimeter(mm)-wave (>30 GHz) 5G cellular networks gaining widespread adoption [108] and 6G around the corner [109, 110], wireless communication soon to enter the 100+ GHz territory on the electromagnetic spectrum. This will be critical to support the high-speed, low latency data transfer demands of cloud computing. Current GaN PA technology, with output powers of <1 W at 100+ GHz, is not sufficient to meet these demands. The poor thermal performance of the GaN transistors, which results in the heating up and degradation of the transistor during high-power operation of performance, has been identified as the key bottleneck for GaN PA power outputs [111].

Therefore, with the advent of 6G, the search for new semiconductor materials for high-power amplifiers at these high frequencies has begun. Similar to how the choice of semiconductor evolved from Ge to Si to GaAs to GaN to meet the demands of communication, it is now time for the next semiconductor technology to take over. Massive multi-center academic research with pooled resources from across the industry [112] is being performed to support a top-to-bottom redesign of the communication setups to meet the new demands - right from the semiconductor atoms to the antenna systems and software.

What are the desired characteristics of this new semiconductor technology for PAs? Apart from the fundamental requirements of a PA of a high power

handling capability (wider bandgap) and speed (high electron velocity), it needs to outperform GaN thermally (higher thermal conductivity) [111]. Ultra-wide bandgap semiconductor materials (UWBG) such as aluminum gallium nitride (AlGaN), aluminum nitride (AlN), gallium oxide (Ga_2O_3) and diamond are the main players in the arena vying for the top spot as the new semiconductor technology for the future of communications. However, only one of these meets *all* the key requirements - aluminum nitride (AlN).

AlN, lying right above GaN in the periodic table, has a bandgap of 6.2 eV ($2\times$ that of GaN) resulting much higher breakdown fields to access higher powers. More critically, AlN has a thermal conductivity of 340 W/mK, almost 30% higher than that of GaN (260 W/m.K) at room temperature. This makes it potential platform of high-power RF electronics with never-seen-before opportunities for integration with existing RF technologies.

As opposed to Ga_2O_3 and diamond, AlN not a "new" material in semiconductor research. It has been used to make UV-C LEDs in the 2010s. More interestingly, thanks to its high piezoelectric property [113], AlN has been a huge player in high-frequency circuits in RF passive devices right from 1980s and 1990s. Poly-crystalline AlN has been used in resonators, filters and duplexers. In fact all cellphones in the market at present have multiple AlN-based filters to discern the signal information among the noise. This filter sits right next to the GaN-, GaAs-, InP- or Si-based amplifier in an RF front-end circuit (circuit which is right next to the antenna which connects to the outer world) which handles communication link with the cell phone tower.

Therefore, not only is AlN a promising material for high-power, high-frequency amplifiers, but also for high-frequency filters. This offers a new pos-

sibility of integration which is not possible on any other semiconductor technology! Currently each passive components (filter, duplexers) and active devices (power amplifiers, LNAs) in an RF front end are made from different semiconductor materials, forcing each component to be discrete and integrated at the chip packaging level. If both actives and passives are realized on AlN, then the full RF front end circuit can be integrated onto a single crystal of AlN, drastically reducing the cost and size of the circuits (no chip level wire bonds required), and increasing the speed of operation (lower parasitic delays). This concept of the AlN integrated platform for high-frequency application space is analogous to silicon integrated circuit (IC) technology, which brought a paradigm-shift in low-voltage circuits.

Since AlN as a material has been in use commercially for past 30 years and clearly holds advantage over other semiconductors in RF applications, the question arises - why has it not been adopted for RF electronics already?

There are two main challenges. The first is the structural and chemical purity of material. The AlN films used in RF filters are polycrystalline. They have a high tolerance for chemical impurities as the AlN films are used for its mechanical properties. However, for electronic applications like transistors, AlN with high chemical and structural purity is desired. The second challenge is that AlN is inherently an electrical insulator. The difficulty in making AlN conduct electricity stems from its fundamental property of wide energy bandgap. Introducing chemical dopants, like how it is done in silicon or GaAs, does not produce the desired density of carriers (electrons or holes) at room temperature to date. A highly conductive carrier channel is necessary to make transistors. These two fundamental scientific challenges need to be addressed before the

realizing the vision of AlN integrated platform.

Over the next 4 chapters, this dissertation addresses and solves these challenges. High-quality electronic-grade AlN growth is achieved through molecular bem epitaxy (MBE). Instead of making the AlN bulk crystal itself conduct, record high-conductivity hole (p-type) and electron (n-type) channels are achieved by growing a very thin GaN layer on top of an AlN crystal, without any chemical dopants. This configuration of high-conductivity channels on an electrically insulating but thermally conductive base is highly advantageous for a transistor.

As has been the case historically, purer material enables better device performance. The same is seen here, where the p-channel and n-channel AlN transistors reap the rewards of the material advancements. They show record performance in terms of high currents, high speeds and high output powers compared to GaN-based transistors - a remarkable feat for semiconductor devices within 5-6 years of their conception. Apart from these active devices, individual passive devices such as filters, waveguides and antennas are also realized, thus bringing us to the cusp of realizing integrated high-frequency electronics on the AlN platform.

Before moving on to the technical results, it is worth highlighting that Cornell University has always been at the forefront of the communication advancements over the past century. In fact, the very founding of the university was possible thanks to Ezra Cornell's fruitful partnership with Samuel Morse to spread the telegraph's reach across the country [73]. The department of Electrical Engineering at Cornell, established in 1885, was one of the first ones in the world, and was setup to train engineers for the telegraph revolution. In the later half

of the 20th century, under the leadership of Prof Lester Eastman, the first high speed operation of a GaAs HEMT was demonstrated in the 1980s [114], laying down the route to commercial use of GaAs in high-frequency power amplifiers in the 1990s to usher in the mobile communication era. Meanwhile in 1990s, Cornell was the center of GaN research [100], and was instrumental in understanding this then new and fascinating material [115]. Thanks to their pioneering work, GaN has now found commercial adoption in cellular base stations and is pushing the wireless communication limits. Hence, it is very symbolic that the aluminum nitride (AlN) platform, believed to be key to next-generation communication, is also conceptualized and realized here at the Electrical Engineering department in Cornell. This dissertation adds many more "firsts" to the illustrious list - the first undoped 2DHG in GaN [3], the first GHz-speed AlN pFETs [39], the first high-power AlN HEMTs [54] - continuing the rich legacy of this institution in pushing the boundary of communication technology.

1.2   Layout of this Dissertation

The discovery of the undoped 2DHG in GaN/AlN heterostructures [3], and its chemical and transport properties are presented in **Chapter 2**. This p-type analog to the AlN/GaN 2DEG ends the long search of the field of high-conductivity p-type layers without chemical doping. The key innovation comes by first identifying the role of the Si, O impurities at the GaN/AlN interface which act as compensating dopants and scattering centers, and then blocking them by using AlGaN impurity block layers (IBLs) in the AlN buffer layers [8]. This results in record high conductivity p-type GaN layers and the highest hole mobility recorded in GaN.

The high-conductivity GaN 2DHG is used as a channel to make record p-channel GaN transistors, which are presented in **Chapter 3**. These are enabled by best-in-the-class low-resistance p-type ohmic contacts to the 2DHG ($R_c < 5$ Ω.mm) using Mg-InGaN epitaxial layers [38]. Thanks to these material innovations, scaled p-channel FETs exhibit record high on-currents of upto 0.5 A/mm [39], which are orders of magnitude higher than those in previously reported GaN pFETs. Furthermore, these p-FETs, both Schottky gated and with gate dielectric, break the GHz-speed barrier for the first time in GaN pFETs ($f_t/f_{max} \sim$ 23/40 GHz), and marks the entry of GaN p-channel FETs into the RF application domain which has so far been dominated by GaN n-channel HEMTs.

Chapter 4 moves the discussion to the n-side, by adding a AlN barrier layer on top of the GaN/AlN structure. An undoped 2DEG-2DHG bilayer is observed for the first time in these AlN/GaN/AlN heterostructures. When a bias is applied, these 2DEG-2DHGs recombine and emit light around the GaN band-edge in a unique quasi-lateral LED configuration. The focus is then shifted to the transport of high-density 2DEGs specifically for application as a transistor channel for AlN-based RF HEMTs. Low-temperature magnetotransport studies have been performed, and Shubnikov-de Haas oscillations have been observed for the first time in these AlN/GaN/AlN heterostructures with very high density 2DEGs.

Chapter 5 presents the device applications of these AlN/GaN/AlN 2DEGs, specifically in AlN HEMTs for mm-wave power amplifiers (PAs). A new in-situ crystalline AlN passivation technique is proposed, and demonstrated which provides a path to higher output powers in next generation AlN HEMTs by

suppressing the DC-RF dispersion from the surface states. Enhancement-mode AlN HEMTs are demonstrated by scaling down the GaN channel layer to 3 nm. These transistors show operation similar to a silicon-on-insulator (SOI) n-MOSFET where a 2DEG channel is induced by applying a positive bias in a structure which has an as-grown 2DHG.

The possible strategies to integrate these n- and p-type devices on the AlN-platform are discussed in **Chapter 6**. The in-situ sublimation selective etch of GaN, believed to be one of the key steps for this integration effort, is demonstrated and studied. A short discussion of the ongoing work on passive RF components such as filters, waveguides, antennas on the MBE AlN on SiC is presented.

The future research directions and open scientific questions are presented at the end of each chapter to provide a better context for the reader. **Appendix A** contains the detailed plasma-assisted molecular beam epitaixal (PA-MBE) growth recipes of the GaN/AlN and AlN/GaN/AlN heterostructures studied in this work for reference, including investigations into the in-situ cleaning of 6H-SiC substrates, nucleation of high-quality AlN on SiC and full wafer growths. **Appendix B** briefly discusses the potential performance advantages for the AlN-platform devices on recently available single-crystal AlN substrates to motivate future work.

With the large repertoire of RF passives and active devices now available on materials enabled by this work, the vision of integrated RF electronics on the AlN platform is very close to being realized, and will hopefully prove to be greater than the sum of its parts.

CHAPTER 2

POLARIZATION-INDUCED 2D HOLE GASES IN UNDOPED

(IN)GAN/ALN HETEROSTRUCTURES

2.1 Introduction

The discovery of efficient p-type impurity doping of the wide-bandgap semi-conductor gallium nitride (GaN) around 1990 changed the field of semiconductor physics [98]. It ended a decades long search [116] and enabled the immediate realization of bright blue light emitting diodes and lasers, and started the solid-state lighting revolution, which today has transformed the lives of a large fraction of the population of the planet [117, 118]. To make energy-efficient visible lighting successful, it is necessary to inject both electrons and holes from supply layers in GaN into InGaN quantum wells, where they recombine and produce photons of desired wavelengths. This requires the complementary n-type doping of GaN too, which was fortunately available for several decades before the discovery of p-type impurity doping. While holes are generated by substitution of Ga atoms in the GaN crystal by Mg acceptor atoms, n-type doping is achieved by replacing Ga by Si or Ge donor atoms.

In the mid 1990s, high conductivity quantum-confined 2D electron gases were discovered at the heterointerface of AlGaN/GaN structures [99]. These 2D electron gases (2DEGs) remarkably did not require the presence of dopants. A few years later, the reason for the formation of the 2DEG was tracked down to the existence of broken inversion symmetry in the GaN crystal, combined with the very high polarity of the metal-nitrogen bond in GaN and AlN [100, 1]. These properties lead to the existence of spontaneous and piezoelectric elec-

tronic polarization fields along the [0001] axis of the wurtzite nitride semiconductor crystal. The resulting polarization-induced 2DEG at Al(Ga)N/GaN heterojunctions has, in the last two decades, enabled high-voltage and ultra-high speed transistors that are being adopted in power electronics, and high-speed cellular communications in the radio and millimeter-wave frequencies [101]. The transport of these 2DEG and its applications for RF/mm-wave frequencies electronics is discussed in chapter 4 and 5.

The p-type analog of the undoped polarization-induced 2DEGs - the undoped 2D hole gas (2DHG), however had remained elusive until recently. Although low density 2D hole gases have been previously inferred in nitride heterojunctions in several reports [12, 13, 14, 15, 16, 17, 18, 19], they have been either modulation Mg-doped heterostructures, or structures in which both electrons and holes are present. The missing dual piece of the undoped 2D hole gas has held back the widespread use of GaN for complementary logic electronics for digital applications till today, just like the absence of bulk p-doping had held back high efficiency photonic devices till the 1990s. Significant advances in energy-efficient electronics can be enabled by GaN based high-voltage complementary low loss switches exploiting the large bandgap of the semiconductor, if a high conductivity undoped 2D hole gas can be found.

In this chapter, after a primer on the origin of polarization induced charges in III-nitride semiconductor heterostructures, the recent discovery of the high-conductivity, high-density ($\sim 5 \times 10^{13}$ cm^{-2}) undoped GaN/AlN 2DHG is presented. Then we delve deeper into how the discovery was achieved via careful epitaxial growth techniques to block detrimental impurities from the substrate away from the 2DHG interface. Analysis of the room temperature transport

of this 2DHG answers the question of why it took so long for the undoped 2DHG to be discovered. Finally, by introducing some In in the thin GaN layer, very high density 2DHGs ($> 10^{14}$ cm^{-2}) are obtained in undoped, pseudomorphic InGaN/AlN heterostructures. These (In)GaN/AlN 2DHGs represent the highest conductivity single channel p-type GaN layers reported so far in III-nitride semiconductors, and have had high scientific [5, 8] and technological impact [38] on the scientific community's understanding and use of holes in wide bandgap semiconductors.

2.2 Polarization Charges in III-nitride Heterostructures

This section provides a very brief discussion on origin of the polarization-induced carriers at III-nitride semiconductor interfaces on relaxed GaN and AlN buffer layers. More comprehensive analyses can be found in [100, 119, 1] and references therein.

GaN, InN, AlN and their alloys demonstrate broken inversion symmetry along the [0001] axis or the c-direction of their wurtzite crystal structure, leading to the existence of spontaneous polarization P_{sp} [1]. The magnitude of the spontaneous polarizations in the III-nitride semiconductors is given in **table 2.1**. The presence of this spontaneous polarization leads to fixed charge separation on the crystal surfaces which is on the order of 10^{13} cm^{-2}, that results in large intrinsic electric fields of 1-5 MV/cm along the c-axis. These intrinsic fields are one of the unique properties of III-nitride semiconductors as the electronic band profile bends without the application of external bias (steady state) - which is different from other non-polar semiconductors. Manipulating these

polarizations at epitaxially-controlled discontinuities in the crystal determines the charge distribution. More uniquely, these result in generation of mobile carriers even without the introduction of chemical donor/acceptor atoms.

The direction of P_{sp} in the III-nitride wurtzite crystal implies the existence of two distinct crystal polarities - metal-polar and nitrogen-polar depending on the direction of P_{sp} in the epitaxially grown crystal. This dissertation focuses on metal-polar heterostructures unless otherwise specified.

Table 2.1: Spontaneous and piezoelectric polarization constants for III-nitride semiconductors AlN, GaN and InN [1, 2] used in this work.

	AlN	GaN	InN
P_{sp} (C/m^2)	-0.90	-0.029	-0.032
e_{31} (C/m^2)	-0.60	-0.49	-0.57
e_{33} (C/m^2)	1.46	0.73	0.97
C_{13} (GPa)	108	106	92
C_{33} (GPa)	373	398	224
a_0 (Å)	3.112	3.189	3.545
c_0 (Å)	4.982	5.185	5.703

In addition to the spontaneous polarization, III-nitride semiconductors also exhibit piezoelectric polarization P_{pz} in response to a stress/strain in the crystal. P_{pz} in GaN, InN, AlN and their alloys are order of magnitude higher than those in other III-V semiconductors such as GaAs, InP, InSb etc [119]. In fact, because of this property, AlN has found widespread commercial use for its piezoelectric properties in microelectromechanical systems (MEMS) devices such as acoustic resonators and filters [113], long before its recent foray into mm-wave electronics.

In III-nitride heterostructures, the piezoelectric polarization arises when a layer with a relaxed lattice constant a_0 is epitaxially grown on top of a relaxed buffer layer with different lattice constant a_0', and is thus strained. The resultant

in-plane strain in the top layer ϵ_{xx} determines the piezoelectric polarization P_{pz} through the relation :

$$
\begin{aligned}
P_{pz} &= 2\epsilon_{xx}\left(e_{31} - e_{33}\frac{C_{13}}{C_{33}}\right) \\
&= 2\,\frac{a(r) - a_0}{a_0}\left(e_{31} - e_{33}\frac{C_{13}}{C_{33}}\right),
\end{aligned}
\tag{2.1}
$$

where $e_{31/33}$ are the piezoelectric coefficients and $C_{13/33}$ are the elastic constants of the top layer. The values of these coefficients and the lattice constants for the III-nitride semiconductors are listed in **table 2.1** for reference. $a(r)$ is the *strained* lattice constant of the top layer with a relaxation r. $r = 0$ means the layer is fully or pseudomorphically strained to the bottom layer so that $a(r = 0) = a_0'$. If the top layer is fully relaxed ($r = 1$), then $a(r = 1) = a_0$.
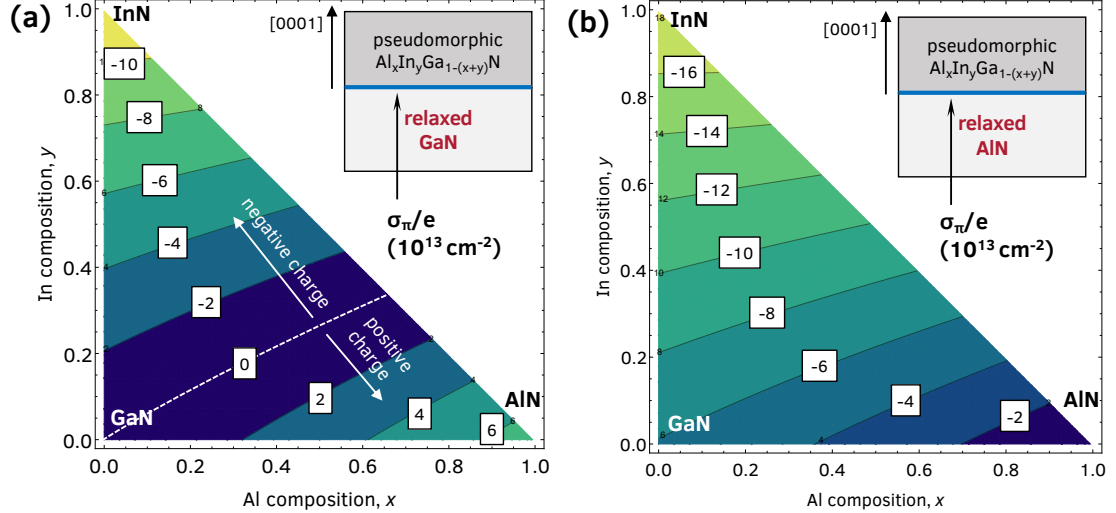
Figure 2.1: Polarization-induced fixed charge densities at the interfaces of (a) pseudomorphic AlInGaN on relaxed GaN and (b) pseudomorphic AlInGaN on relaxed AlN, as a function of the indium and aluminum compositions in the layer. The sign indicates the polarity of the charge.

Now consider a metal-polar heterostructure consisting of a pseudomorphic ternary alloy $Al_xIn_yGa_{1-x-y}N$ grown on relaxed GaN, x and y being the atomic

compositions of Al and In respectively. All layers are undoped. This is illustrated in the inset of **figure 2.1 (a)**. Then due to the polarization difference at the heterointerface, a fixed (not mobile) sheet charge σ_π is expected, given by :

$$
\begin{aligned}
\sigma_\pi(x, y) &= P_{tot}^{top}(x, y) - P_{tot}^{GaN} \\
&= (P_{sp}^{AlInGaN}(x, y) + P_{pz}^{AlInGaN}(x, y)) - P_{sp}^{GaN} \\
&= \Delta P_{sp}(x, y) - 2\,\frac{a_0^{GaN} - a_0(x, y)}{a_0(x, y)}\left(e_{31}(x, y) - e_{33}(x, y)\frac{C_{13}(x, y)}{C_{33}(x, y)}\right), \quad (2.2)
\end{aligned}
$$

where $a_0(x, y)$ is the relaxed in-plane lattice constant of the $Al_x In_y Ga_{1-x-y}N$ layer. The physical constants for $Al_x In_y Ga_{1-x-y}N$ are calculated by linear interpolation (Vegard's Law) of the corresponding values for GaN, InN and AlN from **table 2.1**. The sign of σ_π indicates the type of charge generated.

The interface polarization sheet charge density is plotted as a function of x and y in **figure 2.1 (a)**. It ranges from around $+7 \times 10^{13}$ cm^{-2} in AlN/GaN to -10×10^{13} cm^{-2} in InN/GaN, and changes sign when the polarization cancels each other out across the heterointerface. Importantly, these charges are *fixed* at the interface, i.e. they can not contribute to any current transport.

However, if the top AlInGaN layer is grown thicker than a certain critical thickness d_0, then the polarization dipole is neutralized by carriers of opposite sign from the donor or acceptor states at the surface of AlInGaN [120, 121]. A positive σ_π is compensated by electrons and negative σ_π by holes, which are then electrostatically confined by the conduction or valence band offsets between the two layers to form a 2D electron gas (2DEG) or a 2D hole gas (2DHG) respectively. The salient features of these 2D carrier gases are as follows :

- Polarization-induced :
  No chemical impurity dopants is needed to be introduced in the crystal for

the generation of these 2DEGs. This is in contrast to 2DEGs generated in GaAs by modulation doping using impurities [122], or inversion channels in silicon MOSFETs [28] by applying an external bias. Consequently, no effect of temperature is expected in the polarization-induced carrier density because the carriers are not thermally generated.

- Highly mobile :

  As opposed to the polarization-induced fixed charges, these 2DEGs/2DHGs are mobile in 2 dimensions, while being confined in the third. Since there are no impurity atoms present in the crystal, the mobility of these 2D carriers are ideally are limited by intrinsic scattering by phonons at room temperatures. This leads to higher carrier mobilities compared to bulk, impurity doped layers.

- Tunable:

  The 2DEG/2DHG densities are tunable through heterostructure design and epitaxial growth [100]. The thickness and composition of the top layer electrostatically determines the densities. Since these are compensating the fixed charges, σ_π represents the *maximum* 2D mobile carrier density possible at the interface.

Conventional GaN electronics have been developed on thick, relaxed GaN buffer layers. This is because the initial growth efforts in GaN were motivated by the realization of blue LEDs, which require InGaN quantum wells in thick GaN layers [98]. According to **figure 2.1 (a)**, the AlGaN/GaN structure results in $\sigma_\pi > 0$, which generates a 2DEG of densities in the range of low-10^{12} to mid-10^{13} cm^{-2} at the interface. This 2DEG was discovered back in 1992 [99] and has been the workhorse of the GaN electronics ever since. Because of the high 2DEG

mobilities and densities, AlGaN/GaN 2DEGs form high conductivity channels of high electron mobility transistors, or HEMTs, which are used for both high-power switching and high-frequency signal amplification. Lattice-matched In-AlN [123] and binary AlN barriers [124] have been used in place of AlGaN to reduce the barrier thickness and increase the operation speeds of GaN HEMTs. More details about HEMTs and RF signal amplification are discussed in chapter 4 and 5 of this dissertation.

On the other hand, if a pseudomorphic In(Al)GaN layer is grown on GaN with high indium composition, a 2DHG is expected as $\sigma_\pi < 0$, according to **figure 2.1 (a)**. Similar to the AlGaN/GaN 2DEG, the generation of this 2DHG also should not need any impurity doping. However, the undoped 2DHG has not been observed so far. This, added with the difficulty in efficient p-type chemical doping of GaN using magnesium, means the conductivity of p-type GaN layers to be 2-3 orders of magnitude lower than typical n-type of same thickness. Only a couple of reports exist so far of metal-polar In(Al)GaN/GaN 2DHGs [125, 15] with very high resistance using Mg. Other groups have reported low-density, low-mobility 2DHGs by growing a GaN layer on top of an AlGaN/GaN 2DEG structure [12, 13, 14, 16, 17, 126, 60] - but also needed the magnesium doping in the heterostructure to generate the holes. No undoped 2DHG has been observed or measured so far in the field.

Are there other III-nitride heterostructures which are expected to generate a 2DHG? Instead of a conventional GaN buffer layer, consider a relaxed AlN layer on which the $Al_xIn_yGa_{1-x-y}N$ layer is grown. This is illustrated in the in-set of **figure 2.1 (b)**. The fixed polarization charge at the interface is calculated by equation (2.2) by replacing a_0^{GaN} by a_0^{AlN}. The calculated σ_π is plotted in **fig-**

ure 2.1 (b) as a function of indium and aluminum compositions. Since AlN has the larger P_{sp} than both InN and GaN, the ternary alloy $Al_xIn_yGa_{1-x-y}N$ leads to a negative polarization difference when grown on AlN for all x and y (except $x = 1$, i.e. AlN on AlN). The magnitude of σ_π ranges from very high $\sim 1.6 \times 10^{14}$ cm^{-2} for InN/AlN to $\sim 5.3 \times 10^{13}$ cm^{-2} for GaN/AlN to $< 1 \times 10^{13}$ cm^{-2} in $Al_{0.9}Ga_{0.1}N$/AlN. If the top AlInGaN layer is thick enough, while maintaining pseudomorphic strain state, a 2DHG with density $\leq \sigma_\pi$ is thus expected to be induced. This AlInGaN/AlN heterostructure theoretically offers a large tunability of the 2DHG density over two orders of magnitude.

The explorations into conducting III-nitride layers on AlN has been very limited so far. There has only been one previous report [46] of a 2DHG grown on AlN, using a thin, strained Mg-doped GaN layer. Even though the 2DHG density was as expected of $\sim 6 \times 10^{13}$ cm^{-2}, the hole mobility was very low at ~ 6 cm^2/Vs. Furthermore, the growth was found to be not as robust as the AlGaN/GaN 2DEGs, and were not repeatable across samples and growth runs. Magnesium doping of the GaN layer was found to be necessary to obtain the 2DHG. The undoped GaN/AlN 2DHG has remained elusive so far, almost 3 decades after the discovery of p-type chemical doping of GaN and the undoped 2DEG.

2.3 The Undoped GaN/AlN 2DHGs

From **figure 2.1**, GaN/AlN is simplest structure for generating a 2DHG and is the p-type analog of the AlGaN/GaN 2DEG. If a thin layer of metal-polar GaN is grown on a relaxed AlN substrate, the net interface polarization difference,

$[(P_{sp}^{GaN} + P_{pz}^{GaN}) - P_{sp}^{AlN}] \cdot \hat{n} = \sigma_\pi$ is negative in sign, and should induce holes. The valence band offset of AlN and GaN confines the 2DHG as schematically shown in the energy band diagram of figure 2.2(a), a self-consistent solution of a multiband $k.p$, and Poisson equations [55]. A mobile 2D hole gas of sheet density roughly equal to the fixed interface polarization charge $\sigma_\pi \sim 5 \times 10^{13}$ cm^{-2} is expected to form at the heterojunction, depending on the thickness of the GaN layer. The holes are formed due to the field-ionization (or quantum tunneling) of electrons out of the valence band states into empty, localized surface states.

Figure 2.2 (b) shows the layer structures that were grown for this study. A metal-polar AlN surface on a c-plane sapphire crystal was used as the substrate. An GaN/AlN layer was grown on it by molecular beam epitaxy (MBE). The details of the growth are provided in appendix A. **Figure 2.2 (c,d)** shows a zoomed in lattice image of the crystal heterointerface. A sharp heterojunction is observed, across which GaN and AlN are in the wurtzite crystal structure, and the GaN layer is coherently strained to the AlN layer. The atomic resolution image confirms that the structure is indeed metal polar. Further structural and chemical details of the heterojunction are shown in **figure 2.3**. **Figure 2.3 (a)** shows a smooth surface morphology of the as-grown surface, with rms roughness less than 1 nm in a 10 μm $\times$ 10 μm scan area, and clearly resolved atomic steps. **Figure 2.3(b)** shows the X-ray diffraction spectrum of the heterojunction. The fringes and multiple peaks indicate a smooth, uniform heterostructure over the entire mm-size beam scale. This is further corroborated by the large width TEM images in **figure 2.4**. **Figure 2.3 (c)** is the reciprocal-space X-ray map, which proves that the GaN epitaxial layer is coherently strained to the underlying AlN layer, with an extracted biaxial compressive strain of 2.4 %. The strain state determines the net piezoelectric polarization charge in the heterostructure, which

is this case is $\sim 2 \times 10^{13}$ cm^{-2}. **Figures 2.2, 2.3 and 2.4** thus collectively show that the heterostructure is structurally and chemically in a form that should exhibit the undoped polarization-induced 2D hole gas, and the transport studies discussed next indicate indeed this is the case.

Figure 2.5 (a) shows the layer structure of two GaN/AlN 2DHG samples: Sample A is an undoped ~13 nm GaN layer on AlN. Sample B is identical to A, except the top 10 nm of GaN are doped with Mg to lock the surface potential. The doping screens any mobile carriers that may form at the buried heterojunction quantum well from the variations of the surface condition. The effect of the Mg-doped GaN top layer on the quality of ohmic contacts is discussed in section 3.3. For comparison of these 2DHGs with conventional chemical doping, a thick Mg-doped GaN (sample C), which is expected to have thermal ionization of holes [127], is measured as a control sample. The doping density is [Mg] $\sim 1 \times 10^{19}$ cm^{-3}. Corner ohmic contacts were made to the three samples by using soldered Indium in a van der Pauw geometry. Temperature-dependent Hall-effect transport properties of the three samples were measured from 300 K - 10 K.

Figures 2.5 (b, c, d) show the measured data for the three samples. The Hall data for a fourth Mg-GaN sample labelled "Horita 2017" is also included, which represents the highest reported [4] hole mobility in Mg-doped GaN. The Hall-effect sign was observed to be positive for all samples, ensuring we are studying and comparing only holes in this study, and the interpretation is not clouded by parallel electron conduction. From **figure 2.5 (b)** it is seen that the resistivity of the Mg:GaN doped bulk control sample (Sample C) increases sharply with the lowering of temperature, from ~40 kΩ/sq at 300K to 2000 kΩ/sq at ~180 K.
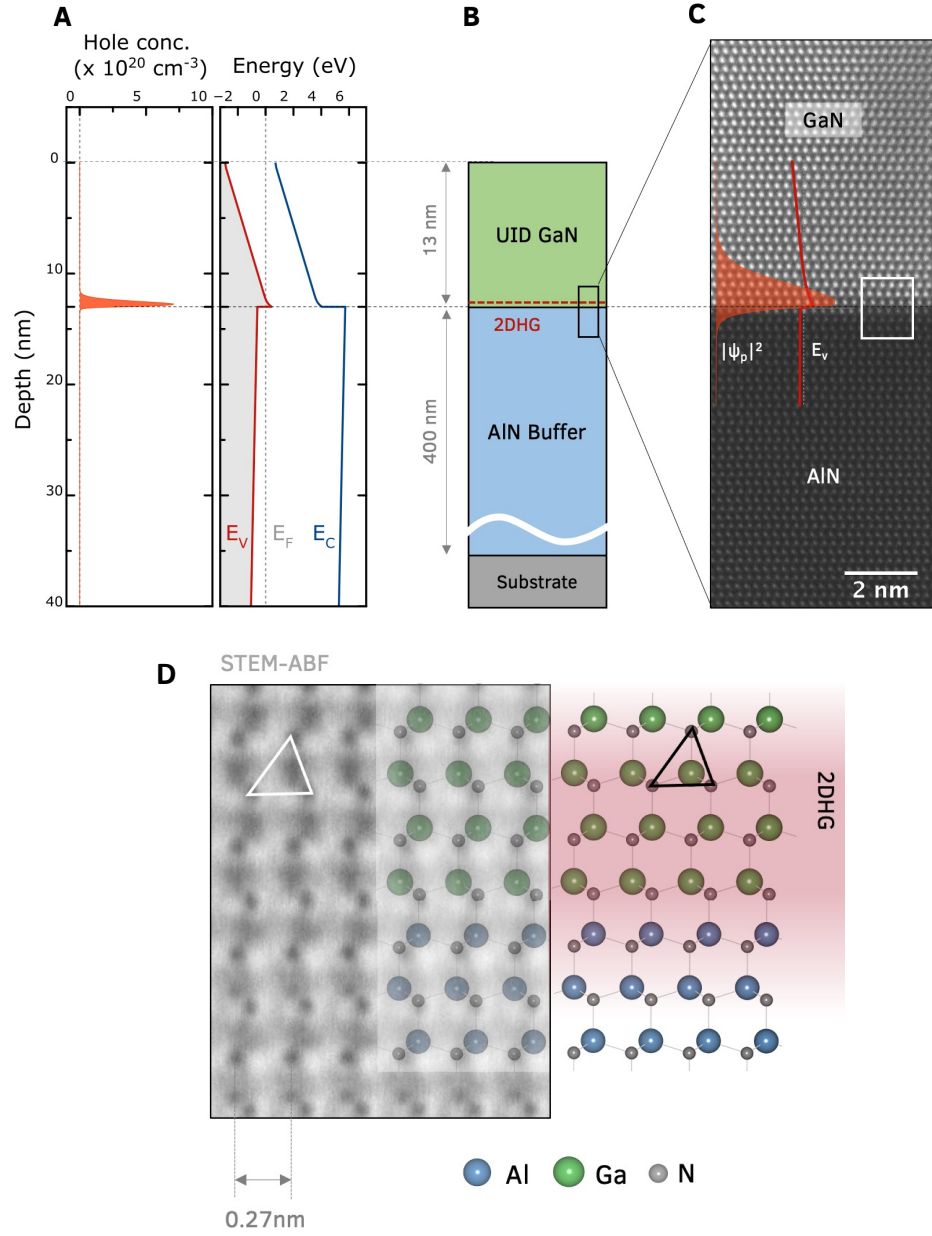
Figure 2.2: Epitaxially grown GaN/AlN heterostructures. (A) Energy-band diagram of a 13 nm undoped GaN on AlN heterostructure, showing the formation of quantum well in the valence band, and the high-density of confined holes accumulated at the GaN/AlN interface. (B) Schematic of the epitaxially grown layer structure. (C) High resolution scanning transmission electron microscopy (STEM) image showing the metal-polar wurtzite crystalline lattice of the heterointerface, as in (D). The valence band edge, and probability density of the holes from (A) are overlaid on the interface. *Figure modified from Chaudhuri et al.* *[3]*
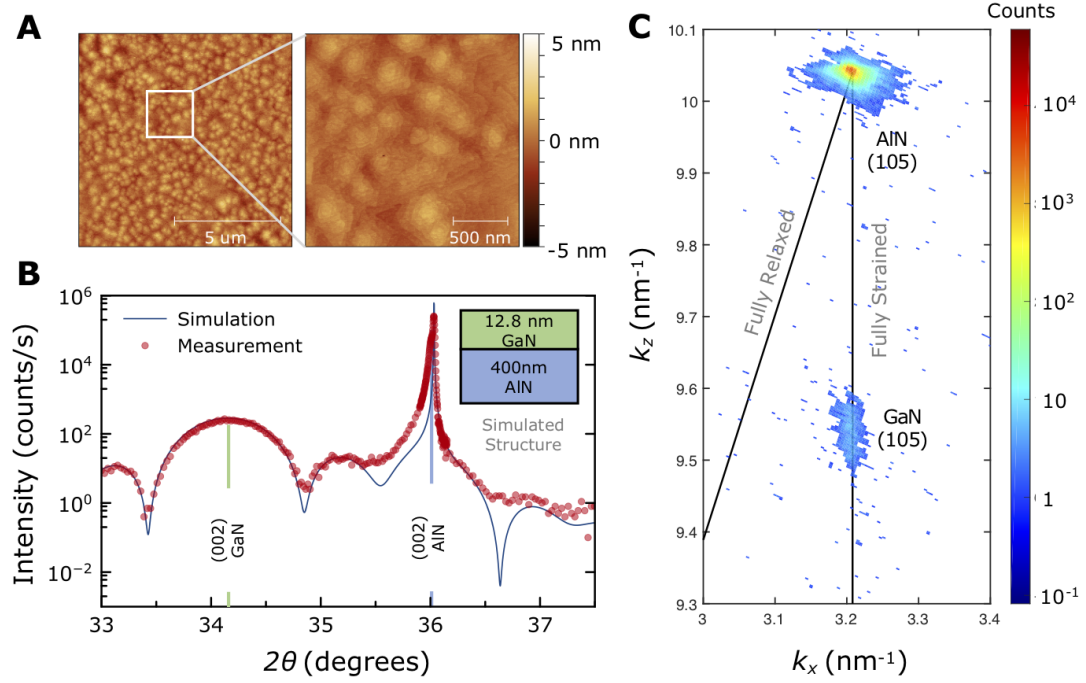
Figure 2.3: Structural properties of the MBE-grown GaN/AlN heterostructures. (A) Atomic Force Microscopy (AFM) scans of the as-grown surface. The rms roughnesses are ~0.69 nm and ~0.46 nm for the 10 μm and 2 μm scans respectively (B) X-ray diffraction (XRD) 2θ scan across the symmetric (002) reflection and the simulated data (19), confirming the targeted thicknesses and sharp interfaces. (C) Reciprocal space map (RSM) scan of the asymmetric (105) reflections of GaN and AlN shows the 13 nm GaN layer is fully strained to the AlN layer. *Figure from Chaudhuri et al. [3]*

Figure 2.5 (b) shows that this increase in resistivity in the control sample C is almost entirely due the decrease of the mobile hole density, which freezes from $\sim 1.5 \times 10^{13}$ cm^{-2} (bulk density of $\sim 4.1 \times 10^{17}$ cm^{-3}) at 300 K to $\sim 2 \times 10^{11}$ cm^{-2} (bulk density of $\sim 5.5 \times 10^{15}$ cm^{-3}) at ~ 180 K. Thus, the thermally ionized holes freeze out with temperature T as $e^{(-E_A/k_bT)}$ with activation energy $E_A \sim 170$ meV, making the sample too resistive to measure below ~ 180 K. The hole mobility of sample C increases very nominally from ~ 10 cm^2/Vs at 300 K to ~15 cm^2/Vs at 180 K. On the other hand, a dramatically different behavior is seen for the undoped heterostructure sample A, and the same heterostructure with the Mg-
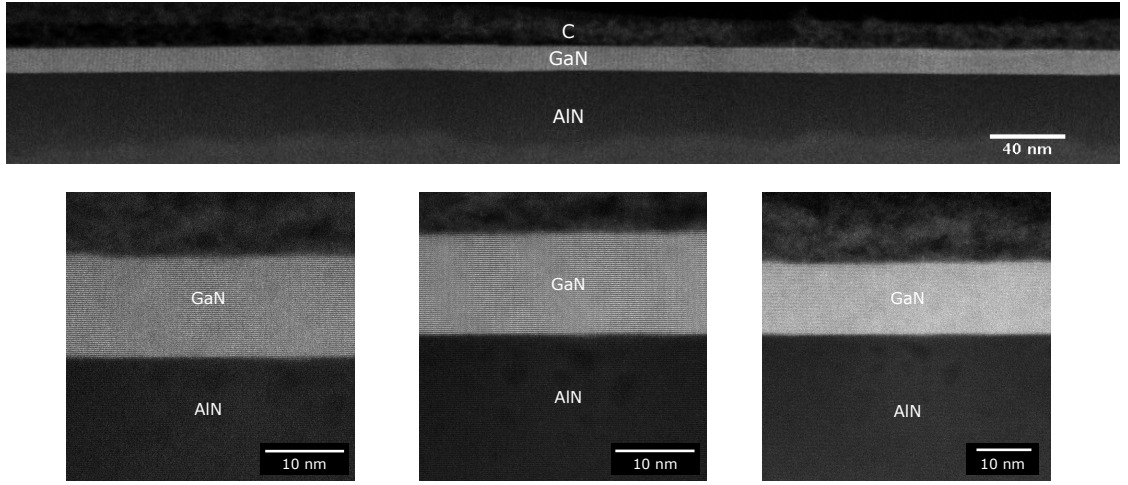
Figure 2.4: STEM annular dark field (ADF) images of the cross-section of the GaN/AlN heterostructure along [-110] zone-axis. The wide-area image and the zoomed-in regions clearly show the coherently sharp interface between the GaN and AlN (~1-2 ML) is maintained over large areas of the wafer, which is essential for a high mobility and high uniformity of the polarization-induced 2D hole gas over the entire wafer. *Figure from Chaudhuri et al. [3]*

doped cap layer Sample B. They are metallic, with the resistivity decreasing with temperature, showing the tell-tale signatures of a 2D hole gas.

Figure 2.5 (b) shows that the resistivity of the undoped GaN/AlN heterostructure Sample A decreases from ~11 kΩ/sq at 300 K to ~4 kΩ/sq at 20 K. The resistivity of the doped heterostructure Sample B decreases from ~8 kΩ/sq to ~2 kΩ/sq over the same temperature range. **Figures 2.5 (b,c)** show that unlike the doped sample, the temperature dependencies are flipped: the hole density in samples A and B are nearly independent of temperature, and all the change in the resistivity is due an increase in the hole mobility as the temperature is lowered. The hole sheet densities measured are nearly identical for the doped and undoped heterostructures in samples A and B. This would be impossible
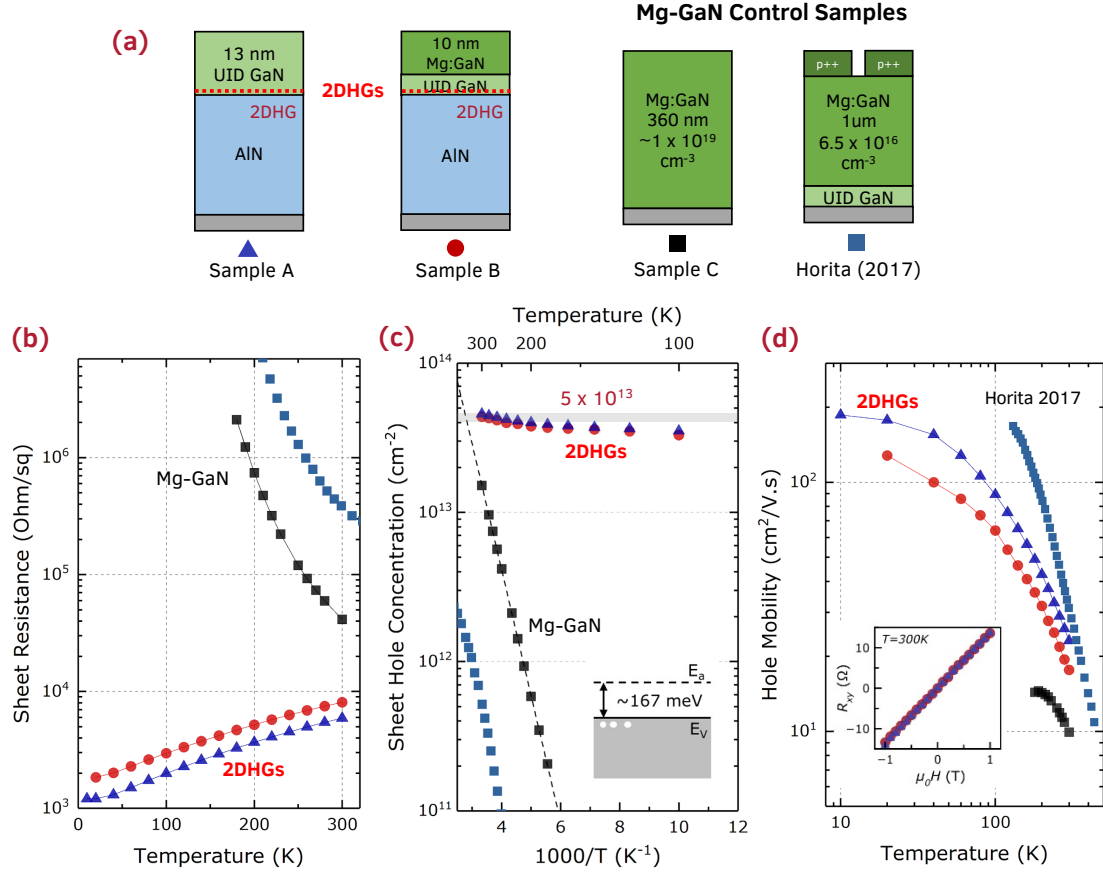
Figure 2.5: Temperature-dependent Hall-effect measurement data from 300 K to 10 K at 1 T magnetic field of 2DHG samples A and B, along with Mg-doped GaN control sample C. Also included for comparison is the Hall data of the highest hole mobility reported [4] in Mg-doped GaN, labelled Horita (2017). (A) The 2DHG samples A and B exhibit a metallic behavior of decreasing sheet resistance with decreasing temperature, whereas the Mg-doped GaN samples are insulating in behavior, becoming too resistive below ~180-200 K for measurement. (B) The measured mobile hole concentrations show freeze-out of holes in the Mg-doped GaN (sample C) holes below 180 K. The density in the 2DHG of Samples A and B show almost no change in the hole concentration down to cryogenic temperatures. (C) The measured hole mobilities in samples A, B, C and Horita (2017) for a range of temperatures. The 2DHG in Samples A and B show significantly higher mobilities than C. Even though Horita (2017) shows a higher mobilities than 2DHG samples A and B (due to low charge concentrations), the 2DHGs survive till much lower temperature. Sample A at 10 K represents the highest hole mobilities ever reported in GaN. (Inset) Hall resistance versus magnetic field measured at room temperature indicates a positive Hall coefficient (holes) in both samples A and B. *Figure from Chaudhuri et al. [3]*

35

without the polarization charge at the interface because the integrated acceptor sheet density in sample B is only $\sim 5 \times 10^{11}$ cm^{-2}, orders of magnitude lower than the measured mobile hole gas density. This measurement constitutes the first unambiguous proof of the presence of a high-density polarization-induced 2D hole gas in undoped nitride heterojunctions. In these heterostructures, there simply are no other carriers such as parallel electrons channels or parallel 3D hole channels that can mask the direct and unambiguous measurement of the properties of the 2D hole gas. Although the Mg-doped cap layer offers very little mobile holes to the 2D hole gas, it can enable low-resistance tunneling p-type contacts to the 2D hole gas because of the high electric field it generates near the surface.

Figure 2.5 (d) shows that the mobility of the 2D hole gas in undoped Sample A and doped Sample B increases substantially, by ~6-9X from 300 K to 20 K. The mobility of the doped GaN/AlN heterostructure 2D hole gas increases from ~20 cm^2/Vs at 300 K to ~120 cm^2/Vs at 20 K, and from ~23 cm^2/Vs to ~190 cm^2/Vs for the undoped GaN/AlN heterostructure. Also plotted in **figure 2.5 (c)** is the highest hole mobility reported in Mg-doped GaN [4]. This was achieved by suppressing the dislocation and impurity scattering by using an ultra-low doping density of 6.5×10^{16} cm^{-3} and low dislocation density (4×10^6 cm^{-2}) substrates. However, the low carrier density resulted a very high sheet resistance at room temperature of 3×10^5 Ω/sq, which sharply rose to $> 5 \times 10^6$ Ω/sq at 180 K due to the freezing-out of the thermally-generated carriers. In comparison, the undoped GaN/AlN 2DHG (sample A) shows a higher hole mobility at 10 K of ~190 cm^2/Vs, which is a new record for hole mobility in GaN at any temperature. But more importantly, it does so while maintaining the high charge density of $> 10^{13}$ cm^{-2} down to cryogenic temperatures - which offers never before pos-

sible access to the valence band of GaN via low temperature magneto-transport experiments.
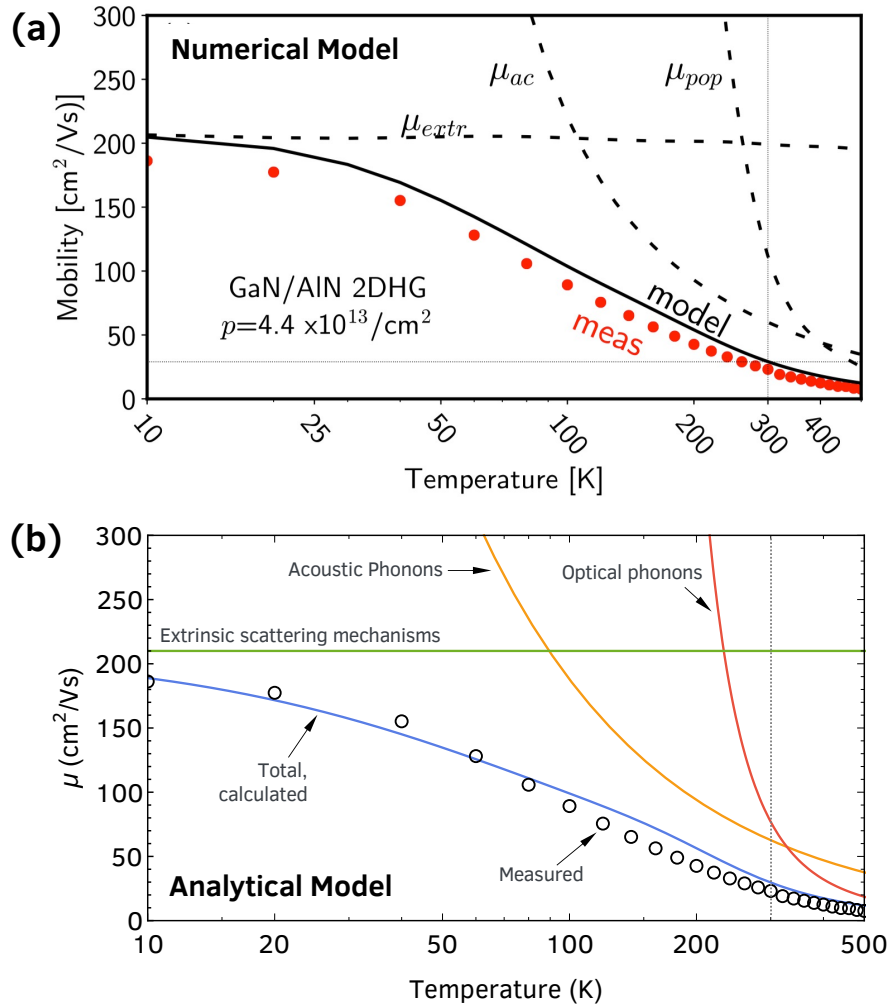
Figure 2.6: (a) Numerical [5] and (b) analytical model of the GaN/AlN 2DHG mobility over a wide range of temperature (10 K - 500 K). Both models show reasonable agreement with the experimental data, and concur that the room-temperature mobility is acoustic phonon scattering limited. *Figure (a) from Bader et al. [5]*

What limits the mobility of this undoped GaN/AlN 2DHG? The room temperature mobility of the chemically-pure undoped GaN/AlN 2DHG has been shown to be limited by the strong acoustic phonon (AP) scattering [5, 128]. **Figure 2.6 (a)** shows the *numerically* calculated GaN/AlN 2DHG mobility using

multi-band $k \cdot p$ models [5]. This includes intrinsic scattering from acoustic phonons (AP), polar optical phonons (POP). The extrinsic scattering mechanism includes the effect of crystal non-idealities like disclocation, interface roughness etc, and is assumed to be constant with temperature. The numerically calculated value [5] shows good agreement to the experimental data in the range 10 - 500 K. This confims that the room temperature mobilities are intrinsically limited by AP scattering to ~ 60 cm^2/Vs. This in contrast to the case of GaN 2DEGs where POP scattering limits the room-temperature mobility at room temperature (see figure 4.10).

Analytically, the AP-limited hole mobility of a 2DHG with density p_s in a single parabolic valence band at temperature T is given by [129, 8] :

$$\mu_{\text{AP}} \approx \frac{16e \, \rho \, v_s^2 \, \hbar^3}{3k_B T \, D^2 \, m_{\text{eff}}^2 \, b(p_s)}, \tag{2.3}$$

where k_B is the Boltzmann constant, $\hbar$ is the reduced Planck's constant, e is the electron charge and ϵ_0 is the vacuum permittivity. $\epsilon_s = 8.9$ is the low frequency dielectric constant of the GaN channel. This expression considers a simplified single parabolic valence band (VB) with hole effective mass [130] $m_{\text{eff}} = 2.0 \, m_0$. $b(p_s) = \left[\left(33 m_{\text{eff}} e^2 \, p_s \right) / \left(8\hbar^2 \epsilon_0 \epsilon_s \right) \right]^{1/3}$ is the variational Fang-Howard wavefunction parameter that quantifies the spatial spread of the 2DHG. Because the 2DHG is located in the GaN layer, the properties of GaN mass density $\rho = 6.15 \times 10^3$ kg/m^3 and sound velocity $v_s = 7963$ m/s are used with a scalar equivalent valence band deformation potential of magnitude $D = 6.2$ eV considered as a simplification of the deformation potential matrix for a single parabolic valence band approximation. This D value also concurs with the sets of GaN VB deformation potentials reported in the literature [21, 131].

Under the same assumption of a single parabolic valence band, the POP-

limited hole mobility of for a 2DHG at temperature T is [132, 30] :

$$\mu_{POP} \approx \frac{\kappa^* \epsilon_0 \, k_0 \, \hbar^2}{2\pi \, \omega_0 \, m_{eff} \, N \, G(k_0)} \left(1 + \frac{1 - e^{-y}}{y} \right), \tag{2.4}$$

where $\hbar\omega_0$ = 92 meV is the optical phonon energy in GaN, k_0 = $\sqrt{2m_{eff}\omega_0/\hbar}$ is the hole wave vector corresponding to the phonon energy, $N(T)$ = $(exp(\hbar\omega_0/k_B T) - 1)^{-1}$ is the Bose-Einstien distribution function and $G(k_0) = b(8b^2 + 9k_0 b + 3k_0^2)/8(k_0 + b)^3$ is the Fang-Howard waveform form-factor. $y = \pi\hbar^2 p_s/m_{eff}k_B T$ depends on the 2DHG density.

The calculated analytical AP- and POP-limited mobilities for the GaN/AlN 2DHG are plotted in **figure 2.6 (b)**. A value of ~ 200 cm^2/Vs is used to represent the effects of the other extrinsic scattering mechanisms. The total mobility, calculated using Mattheisen's rule, is also plotted in **figure 2.6 (b)**. The model agrees reasonably well with the experimental data over the wide range of temperature. It also captures the salient feature of the AP-limited room temperature hole mobility. Slight discrepancy from the full-blown numerical simulation is mainly due to the ignorance of the second light hole valence band. The analytical expressions are useful for quick evaluation and comparison of other extrinsic scattering mechanisms such as impurity scattering and alloy disorder scattering, as will be seen in the upcoming sections.

Sample B from **figure 2.5** was sent to collaborators at Air Force Research Laboratories (AFRL) for a Hall effect measurement across a wider temperature range. Corner Ni/Au contacts were put down via photolithography/evaporation, and used for Hall-effect measurements in the range $\sim 5 - 800$ K. The results are shown in **figure 2.7**. Also plotted is the temperature depen-
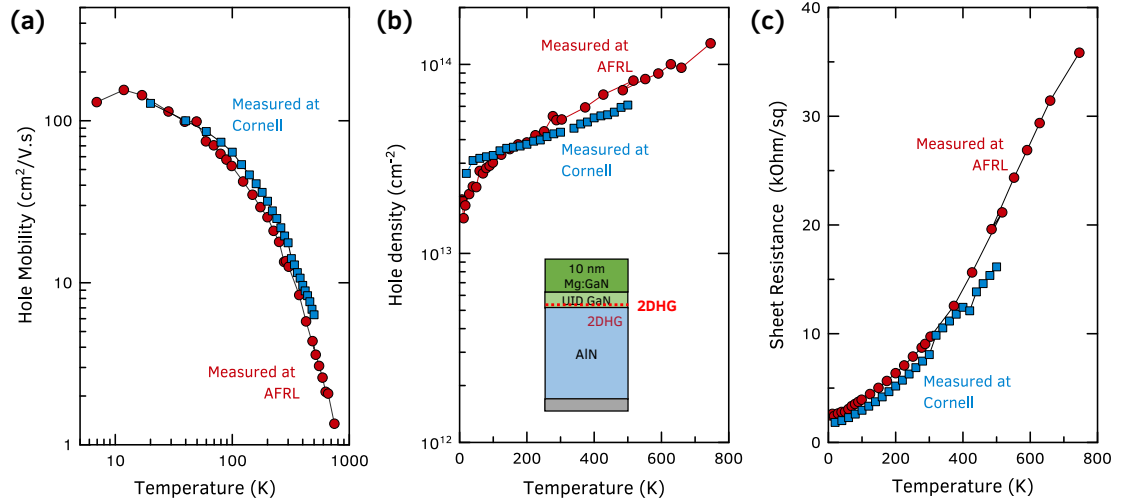
Figure 2.7: Comparison of temperature-dependent Hall effect measurements performed at Air force research labs (AFRL) and Cornell on a GaN/AlN 2DHG sample as shown in inset of (b). Corner soldered indium were used at Cornell and alloyed Ni/Au contacts were used for ohmic contacts to the 2DHG for Hall measurement. The close agreement of the results serves as a independent confirmation of the discovery of the 2DHG. Additionally, the AFRL measurements also provide valuable data points above room temperature, showing that the 2DHG not only survives upto ~ 800 K, but also the hole concentration increases slightly. This makes it suitable for high-temperature circuit applications. *Measurements at AFRL were performed by Dr. Adam Neil.*

dent Hall measurement data taken at Cornell using corner Indium contacts. A good agreement is observed between the two sets of data, providing an independent confirmation of the discovery of the GaN/AlN 2DHG.

At temperatures above 300 K, the 2DHG mobility decreases with increase in temperature and reaches ~ 1 cm^2/Vs at 750 K. This is expected as the number of phonon increases at higher temperatures (more lattice vibrations) and hence the 2DHG undergoes stronger scattering. More interestingly, the 2DHG density rises with increase in temperature, and almost doubles from its 300 K value to > 10^{14} cm^{-2} at ~ 750 K. Even if all Mg donors are thermally ionized, it will result in ~ 1 × 10^{13} cm^{-2} holes, which does not explain the 2× rise in the 2DHG density. This trend in the 2DHG Hall density is also seen in a purely
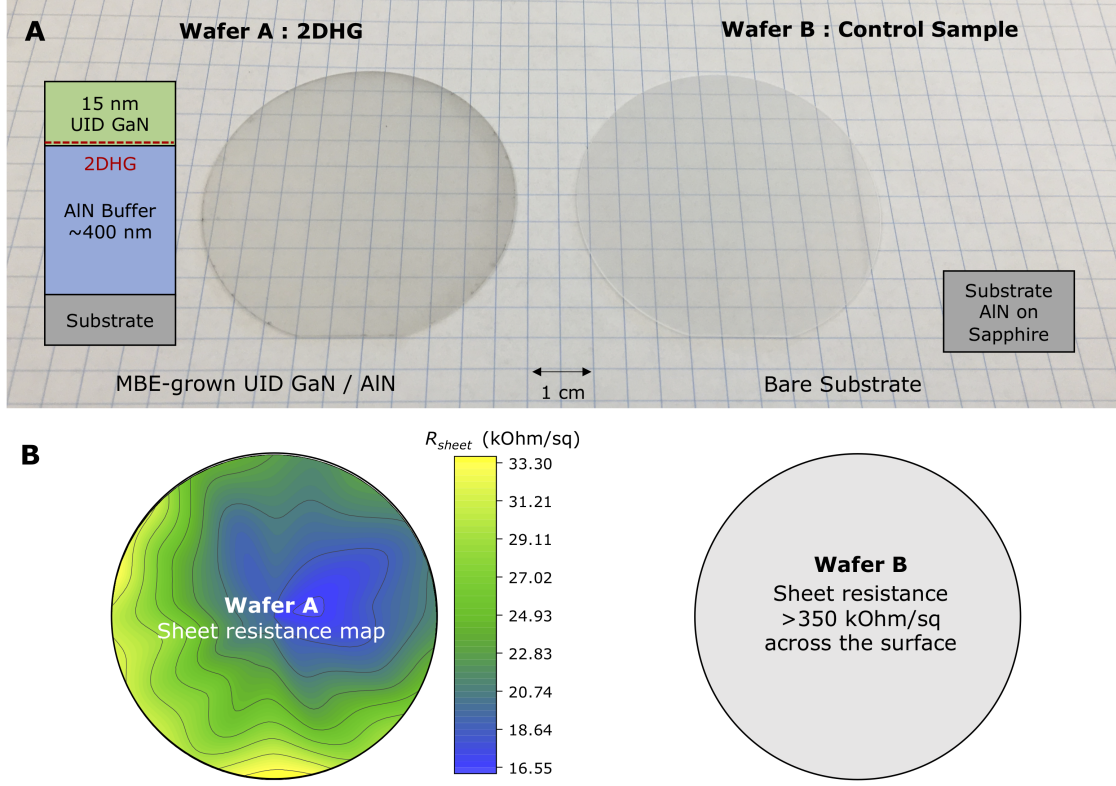
Figure 2.8: Contactless sheet resistance measurements of an undoped GaN/AlN 2DHG wafer performed Teledyne Technologies. (A) 2-inch MBE-grown GaN/AlN heterostructure wafer with the corresponding layer structure shown, along with a bare substrate wafer used as a control sample (B) Sheet resistance map for wafer A shows sheet resistances in the range of ~ 16 − 33 kΩ/sq across the surface, whereas wafer B is highly resistive (> 350 kΩ/sq). These results provide an independent confirmation of the presence of a polarization-induced 2D hole gas as a conductive channel in the undoped heterostructure on wafer A. *Figure from Chaudhuri et al. [3]*

polarization-induced undoped GaN/AlN 2DHG, which varies from ~ 3×10^{13} cm^{-2} at 10 K, to ~ 5×10^{13} cm^{-2} at 300 K to ~ 8×10^{13} cm^{-2} at 500 K. This trend is not observed in polarization-induced III-nitride 2DEGs, and neither in other (Mg-doped) GaN/AlGaN/GaN 2DHGs [133]. These observations point to be some fundamental origin of this variation of 2DHG density related to the GaN/AlN structure or the nature of the 2DHG, and is under further investigation (see section 2.7). However, the high density of holes ~ 10^{14} cm^2/Vs at high

temperatures is attractive for scientific and technological applications.

Contact-less sheet resistance measurement using a Lehighton setup was per-formed on the GaN/AlN structure by collaborators at Teledyne Corporation. The results are shown in **figure 2.8**. Since the instrument can handle only full wafers, a heterostructure with ~15 nm undoped GaN on AlN was grown on a 2-inch substrate wafer (wafer A). A bare substrate wafer without any grown layers was used as a control sample for the measurement (Wafer B). Wafer A showed a sheet resistance in the range of ~16-33 kΩ/sq across the wafer sur-face. The higher sheet resistance compared to the samples in **figure 2.5**, and the non-uniformity across the surface can be attributed to the growth not be-ing optimized for large area substrates at that point in time. Since the bare AlN on Sapphire substrate wafer was highly resistive (sheet resistance >350 $k\Omega$/sq), we conclude that the conductive 2DHG channel is present in the un-doped GaN/AlN heterostructure wafer A. Subsequent Hall-effect measurement results on a diced 8 mm × 8 mm piece from the wafer with corner Indium con-tacts corroborate the measured sheet resistance by the contactless method. The presence of the 2D hole gas detected by a contactless measurement is further confirmation of the fact that the holes are polarization-induced, and are not supplied by the metal contacts in a Hall-effect measurement. Additionally, op-timized large area MBE-growths of GaN/AlN heterostructures [63] since then have achieved low sheet resistance ~ 10 kΩ/sq across a 2-inch wafer (see ap-pendix A).

The results of the transport measurements of the GaN/AlN 2DHG at Tele-dyne Corporation and Air Force Research Laboratories (AFRL) serve as inde-pendent confirmation of the discovery of the undoped GaN/AlN 2DHG.
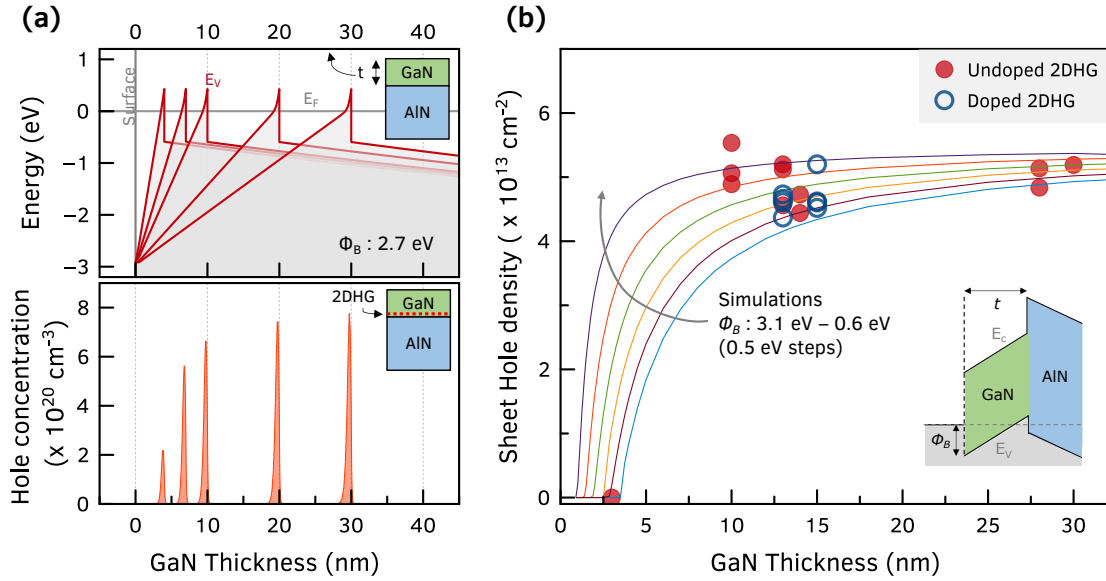
Figure 2.9: Dependence of the properties of the polarization-induced 2D hole gas on the thickness of the undoped strained GaN layer grown on AlN. (A) shows the valence band edge and the spatial hole density distribution as a function of the GaN layer thickness. The triangular quantum well at the heterojunction is clearly visible, with the large valence band offset to confine the 2D holes to a width of ~1 nm in the vertical direction. The 2D hole gas density increases and saturates for GaN layer thicknesses above ~30 nm. (B) shows the measured 2D hole gas densities in various undoped (solid circles) and Mg-doped (hollow circles) GaN/AlN samples with varying GaN thicknesses. The numerical simulations for the variation of the hole gas density with the thickness of the GaN cap layer, for various surface barrier heights is also shown for reference. There clearly exists a critical minimum thickness of GaN for the existence of mobile holes at the GaN/AlN interface - a characteristic of the polarization-induced nature of the 2D hole gas. *Figure from Chaudhuri et al. [3]*

As further evidence for the polarization-induced origin of the 2DHG, **figure 2.9** shows the variation of the density of the 2D hole gas with the thickness of the GaN layer, marking a well-defined critical thickness. **Figure 2.9** (a) shows the expected change in the 2D hole gas density with thickness in the energy band diagram of the valence band, and the mobile hole concentration with depth, as simulated using a self-consistent multiband *k.p* Schrodinger-Poisson solver [55]. A typical bare-GaN surface valence band edge barrier height of 2.9 eV was used for the simulations in **figure 2.9 (a)**. The solid lines in **figure 2.9 (b)** show the ex-

pected variation of the polarization-induced hole density versus GaN thickness for various surface *hole* barrier heights. For example, for a surface barrier height of ~3 eV, the solid lines indicate a critical thickness of ~4 nm below which the 2DHG is depleted from the surface potential, a sharp rise in the 2DHG density from ~5 - 20 nm, beyond which the hole density saturates to the interface polarization sheet density. The critical thickness is lower for a smaller surface barrier height, reaching ~1 nm for a barrier height of 0.6 eV. The measured 2D hole gas densities should follow this trend. To test this, undoped and doped GaN on AlN samples of various thicknesses were grown and their sheet hole densities were measured by Hall-effect at 300 K in a Lakeshore Hall measurement system at a magnetic field of 1 T. The measured 2DHG densities are plotted in **figure 2.9 (b)** alongside the solid lines predicted from the polarization discontinuity for various surface barrier heights. We observe a critical GaN thickness of ~3 nm, below which no hole gas is measured. The measured 2DHG densities variation with the GaN layer thickness indicates that the surface barrier height may not be fixed, but is likely dependent on the thickness of the GaN layer, as has previously been observed in 2D electron gases [134, 135]. Although the qualitative agreement to the simulated model is a further proof that the 2D hole gas is indeed polarization-induced, it is difficult with the available Hall data to conclusively claim values of the surface barrier height for the doped or undoped samples due to its dependence on variations in epitaxial growth conditions, chemical surface modification due to exposure to atmosphere, etc.

Contactless electroreflectance (CER) spectroscopy was performed [7] on the GaN/AlN structures to probe the built-in electric fields in the GaN/AlN heterostructures. In a modulation spectroscopy technique such as CER, a modulating field signal is applied to the heterostructure which varies the complex
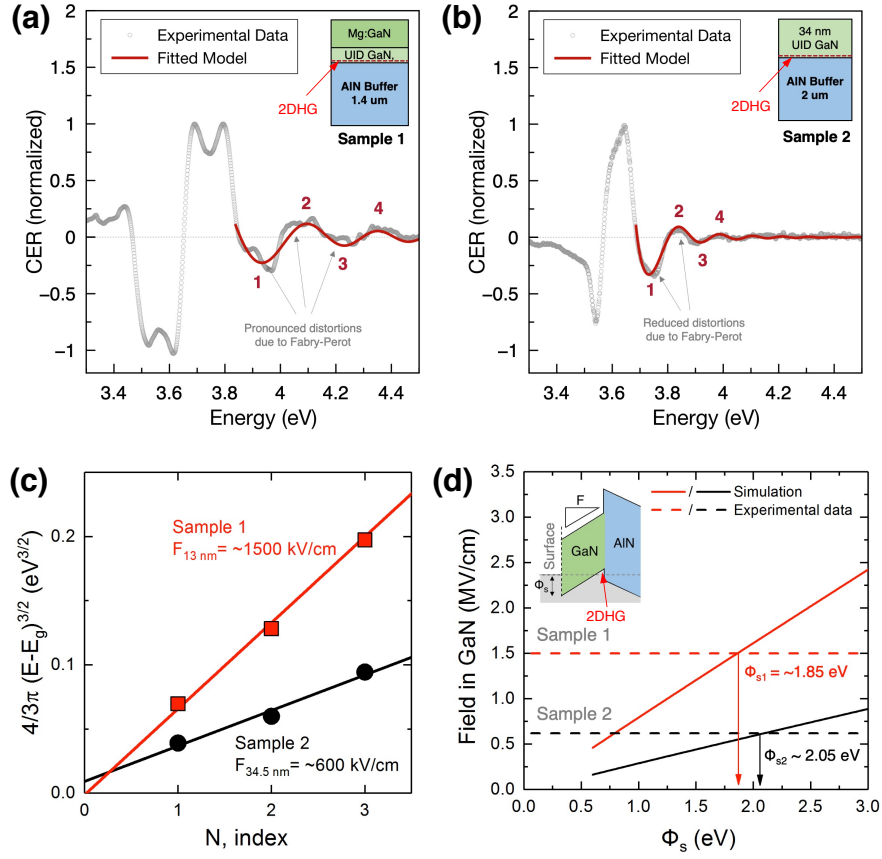
Figure 2.10: Results of contactless electroreflectance (CER) to probe the electric fields in the GaN layer in a GaN/AlN 2DHG sample. (a), (b) show the CER spectra measured from samples 1 and 2 respectively. The layer structures are shown in the insets. Oscillations are observed in both the spectra due to the Franz-Keldysh effect [6]. (c) The extrema from the spectra are then fitted to extract the electric fields of 1.5 MV/cm and 0.6 MV/cm in the top GaN layer of samples 1 and 2 respectively. (d) Extracted surface Fermi level in the samples by comparing to 1-D Schrodinger-Poisson simulation results is ~ 1.9 eV above the valence band in both the samples. *Figures from Janicki, Chaudhuri et al. [7]*

dielectric constant of the film thereby giving rise to a change in the reflectance of an incident light beam [136]. The resulting spectra contain Franz–Keldysh (FK) oscillations that are dependent on the built-in electric field.

Figures 2.10 (a,b) show the CER spectra (normalized change in reflectance signal) from two GaN/AlN 2DHG samples 1 and 2 with and without Mg-doping in the top layer. Signature FK oscillations are visible in both spectra,

which is due to the electric field in the top GaN layer. The FKO extrema in sample 1 and 2, labelled in **figures 2.10 (a,b)**, are of the form [6] :

$$n\pi = \frac{4}{3}\left(\frac{E_n - E_g}{\hbar\theta}\right)^{3/2} + \phi \qquad (2.5)$$

where E_n is the energy of nth extremum, E_g is the GaN bandgap energy, and ϕ is a phase angle. $\hbar\theta$ is the electro-optic energy given by $(\hbar\theta)^3 = (q_e\hbar^2 F^2)/2\mu$, where F is the built-in electric field in the GaN layer being probed, and μ is the electron–hole-reduced mass of GaN. The slope of the fitted line through the plot of $4/(3\pi)(E - E_g)^{3/2}$ versus n is proportional to F. From **figure 2.10 (c)**, the extracted electric field values in the GaN layers are ~1.5 and ~0.6 MV/cm for Sample 1 and 2, respectively. The obtained values of electric fields scale inversely with GaN channel thickness (1500/600 ≈ 34/13). This indicates the Fermi levels are at similar energies on the surface of both these structures as on the other end the energy band is pinned to the valence band at bottom of the GaN layer. The surface Fermi levels are extracted by comparing the experimentally obtained value of the fields to a 1D Schrodinger-Poisson simulation of field vs surface barrier height in GaN. The extracted barrier heights of samples 1 and 2 of 1.9 and 2.0 eV are shown in **figure 2.10 (d)**. These barrier heights for the air exposed surface of GaN in these structures are in reasonable agreement to the Hall measurements shown in figure 2.9.

Further work is necessary to elucidate the "true" surface Fermi level (uncontaminated by air exposure) and its pinning - by either passivating the sample surface in-situ after epitaxy, or by directly measuring the electrical properties of a processed metal-semiconductor Schottky barrier, in both cases ensuring the GaN surface is buried and protected.

2.4 Impurity Blocking Layers in the AlN Buffer Layer

Following the discovery of the 2DHG in undoped GaN/AlN structures, the natural question arises as to why did it remain elusive nearly 2 decades after its prediction and the experimental discovery and subsequent technological impact of its n-type dual, the Al(Ga)N/GaN 2DEG. As has been the case in semiconductor physics [70], the control of impurities during material growth plays a decisive role in all semiconductors, and especially in wide-bandgap semiconductors. For example, the presence of Hydrogen limited the conductivity of MOCVD grown Mg-doped GaN for decades, before its effect was discovered, understood and solved [98]. Driven by the commercialization of GaN RF HEMTs, the growth of GaN buffer layers has been studied and optimized on various substrates for high-quality Al(Ga)N/GaN 2DEGs. Taking advantage of this established platform, most of the earlier 2DHGs reported have been on GaN buffer layers, in metal-polar AlInGaN/GaN [16], InGaN/GaN [15], GaN/AlGaN/GaN [12] structures.

Only in 2010s has the availability of AlN as a photonic and electronic device platform led to the exploration of AlN as a buffer layer for growing 2DEGs [42, 134] and 2DHGs. In 2013, the first 2DHG in a GaN/AlN heterostructure with Mg-doped GaN layer was reported [19]. However, they were not as robust as their n-type analog, the undoped AlGaN/GaN 2D electron gases (2DEGs). In structurally similar GaN/AlN samples, mobile 2DHGs were either absent altogether, or if present, had widely varying sheet densities and mobilities. Mg doping in the top GaN layer [19] was found to stabilize the 2DHG and demonstrate p-channel FETs using such 2DHGs. Only recently were these variations solved to demonstrate the high-conductivity 2DHGs in undoped GaN/AlN

structures [3]. In this section we identify the reason for the earlier variations, and demonstrate a method to obtain these repeatable high-conductivity 2DHGs with a tighter control over densities and transport properties.

Using such GaN/AlN 2DHGs as the channel, scaled GaN p-channel heterostructure field effect transistors (p-HFETs) with record high on-currents exceeding 500 mA/mm were reported in this work recently [39] which, for the first time, broke the GHz speed barrier with cut-off frequencies in the 40 GHz regime. With key p-channel FET device parameters making a climb towards that of GaN n-channel HEMTs, this result represents a significant step towards enabling high-voltage RF wide-bandgap complementary device platforms [137]. The high polarization-induced 2DHG densities are crucial for achieving low contact and access resistances and the resulting high on-currents in these p-HFETs. Variation in 2DHG density directly translates to variations in the transistor threshold voltage and drive current that are undesirable. Repeatable growth of these 2DHGs with tight control on the density and high conductivity is therefore critical.

We find that silicon (Si) and oxygen (O) impurities originate from the starting substrate and float up and incorporate in the GaN layer at the GaN/AlN heterojunction. Because both are donors in GaN, they partially compensate the 2DHG and act as scatterers of mobile holes, resulting in inconsistent densities, lower mobilities and higher sheet resistances. We present a new approach of impurity blocking layers (IBLs) buried in the underlying AlN. The IBLs effectively prevent the impurities from reaching the GaN/AlN interface where the holes are located, significantly enhancing the repeatability and control over the densities, mobilities, and conductivity of the undoped 2DHGs.

Table 2.2: Summary of the samples under study and their Hall-effect measurement results. Samples A, B and C were conductive at 300 K and 77 K with a positive Hall coefficient and increased mobility at low temperatures. The control sample with only AlN buffer layer was highly resistive. Therefore the measured conduction in samples A, B and C are expected to arise from the polarization-induced 2DHG at the GaN/AlN interface.

ID	Structure	Technique Used in AlN Buffer Layer	300K p_s (10^{13} cm^{-2})	300K R$_{sheet}$ Ω/sq	μ_{300K} (cm^2/Vs)	μ_{77K} (cm^2/Vs)
Sample A	15 nm GaN/420 nm AlN	N-rich nucleation layer (NL)	5.48	22.4×10^3	5.11	19.1
Sample B	15 nm GaN/430 nm AlN	Impurity Blocking Layers (IBLs)	4.86	8.67×10^3	14.8	54.2
Sample C	15 nm GaN/440 nm AlN	N-rich NL + IBLs	5.24	11.78×10^3	10.1	48
IBLs only	440 nm AlN	N-rich NL + IBLs	-	> 2 × 10^6	-	-

The heterostructures studied here were grown by plasma-assisted molecular beam epitaxy (MBE). The active nitrogen (N) species is supplied from a RF plasma source. Gallium (Ga) and aluminum (Al) metal fluxes were supplied from effusion cells. The starting substrate surface contains chemical impurities such as Si, O, H, C from exposure to atmosphere. For layer-by-layer epitaxial growth of AlN or GaN, films are grown under metal-rich condition [138, 139], i.e. the incident metal to nitrogen flux ratio is > 1. When AlN is nucleated on a substrate in Al-rich conditions, the Si impurities present on the surface are thermodynamically inhibited from incorporating into the crystal. The relative thermodynamic formation energies of the resultant species during growth [140] dictates that the preference of incorporation of competing cation species into the crystal is Al > Si > Ga > In. Thus, the Si atoms must either desorb, or float up on the Al metal adlayer while the AlN layer is grown. Typical MBE growth temperatures of 800°C-1000°C necessary for smooth epitaxy is insufficient to desorb Si from the AlN surface, implying the Si must float on the Al adlayer.

When a GaN layer is grown on top of the AlN layer, it now becomes thermodynamically favorable for the Si which floated up to incorporate [141, 142]. For GaN/AlN heterostructures where the mobile holes are expected at the interface, this Si incorporation poses a significant problem. In GaN RF HEMTs

grown on SiC substrates, the initial AlN nucleation layers are typically grown in the nitrogen-rich (N-rich) condition (Al:N flux ratio < 1) to suppress Si out-diffusion from a SiC nucleation interface. This forces the Si to incorporate into the N-rich AlN nucleation layer (NL) [141, 142]. However N-rich MBE growth condition also leads to incomplete coverage and structural defect densities in the film [139, 138] which are undesirable for 2DHG transport.

High conductivity 2DHGs with tight density control should then be possible by introducing impurity blocking layers (IBLs). The thermodynamic preference of incorporation [143, 144] dictates that though Si cannot incorporate in metal-rich AlN, it readily incorporates in AlGaN layers by substituting the Ga sites. For a constant dopant flux the Si incorporation in AlGaN shows almost no change with Al% in the crystal till 100% Al content (ie. AlN), is reached [64], where the Si incorporation abruptly drops to zero. Thus ultrathin high Al-composition AlGaN layers inserted in the AlN should effectively suppress the Si up-diffusion from the substrate. Furthermore, high-composition > 90% and thin < $1-2$ nm AlGaN layers will allow the layers to remain fully-strained to the AlN substrate without introducing additional structural defects. The thin layers also prevent parallel conduction channels in the form of 2DEGs due to polarization difference at the AlGaN/AlN interfaces. The small band offsets make the bound states in the quantum well shallow. These thin, high-composition > 90% AlGaN layers IBLs are investigated in this study in comparison to the N-rich nucleation layers mentioned above. The effect of such IBLs on the chemical, structural and transport properties of the UID-GaN/AlN 2DHG heterostructures is next described.

Table 2.2 shows a series of samples that were grown using a Veeco Gen10
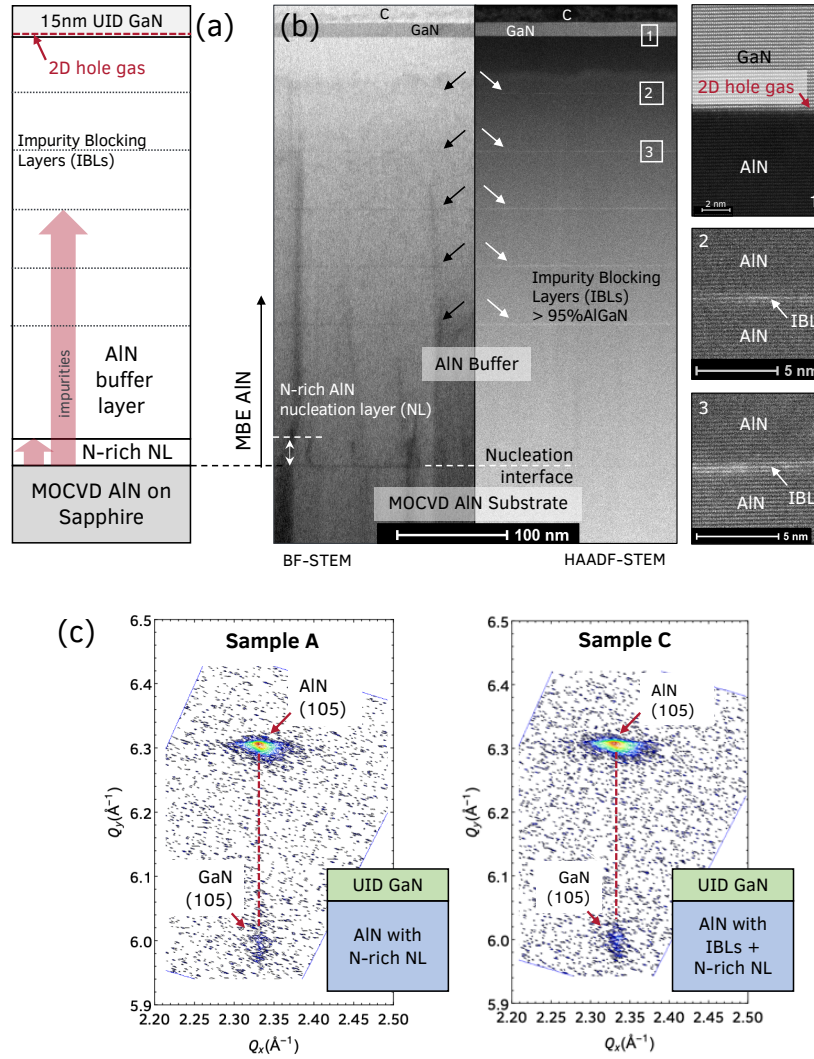
Figure 2.11: (a) Heterostructure details of sample C, with an AlN nucleation layer (NL) grown under N-rich conditions and impurity blocking layers (IBLs) marked in the buffer layer. (b) Scanning transmission electron microscope (STEM) images of the cross-section of a GaN/AlN heterostructure of sample C. The bright-field (BF) image shows the presence of the N-rich NL. The IBLs are visible in both BF and high angle annular dark field (HAADF) image. (c) X-ray diffraction Reciprocal space maps (RSM) around the AlN (105) peak confirms that the GaN layers in sample A and C are fully strained to the AlN buffer layer. *Figure from Chaudhuri et al. [8]*

MBE system under nominally similar conditions. All samples included a ~

420−440 nm AlN buffer layer grown at a substrate temperature $T_{sub} = 780°C$, fol-

lowed by a 15 nm layer of undoped GaN grown at T_{sub} = 750°C. The three samples differed structurally with respect to the type of the AlN buffer layer.These differences are qualitatively highlighted below, and described in Table 2.2:

- In sample A, the first ~30 nm of AlN nucleation layers (NL) was grown under N-rich conditions with Al:N flux ratio ~0.9. The rest of the buffer layer was grown under metal-rich condition with Al:N flux ratio ~1.33, for a total thickness of ~420 nm. No IBLs were introduced in the buffer layer in this sample.

- In sample B, the AlN was grown under Al-rich conditions throughout. Thin IBLs with high-composition Al were incorporated periodically every ~55 nm in the AlN buffer layer. A total ~430 nm thick AlN buffer layer was grown with 8 IBLs.

- In sample C, the AlN buffer layer with ~30 nm of N-rich AlN nucleation layer followed by Al-rich AlN with 5 IBLs separated by ~55 nm was grown, for a total thickness of ~440 nm. The layer structure is shown in **figure 2.11 (a)**.

- A control sample with only AlN with IBLs and no GaN to investigate the background resistivity.

After the ~ 420 – 440 nm AlN buffer layer growth, the substrate was cooled down to T_{sub} = 750°C for the growth of the UID GaN layer. The 2DHG is expected to form at this GaN/AlN interface. The thickness of the UID GaN layers was ~15 nm for all three samples. The MBE growth recipe details are provided in the Appendix A.

Figure 2.11 (b) shows STEM scans of the cross-section of sample C, taken using a bright-field (BF) detector and a High-Angle Annular Dark Field (HAADF) detector. Threading dislocations propagating through the substrate to the surface are visible, a signature of heteroepitaxial AlN growth. The N-rich nucleation layer is visible in the BF scan, and shows contrast due to the slightly higher dislocation density in the layer. Most of these dislocations, originating from the N-rich nucleation interface, do not propagate beyond the N-rich layer. The scans from the HAADF detector, which detect the atomic number Z contrast clearly show the periodic high-composition AlGaN IBL layers located ~ 55 nm apart. The zoomed-in scan of the IBLs shows the Ga incorporation in the AlN over 2-3 monolayers (MLs). The GaN /AlN interface where the 2D hole gas is expected is also shown, which is smooth and abrupt as desired.

The thin GaN layers are expected to be compressively strained to the AlN buffer layer due to the 2.4% in-plane lattice mismatch. X-Ray diffraction reciprocal space maps (RSMs) shown in **figure 2.11 (c)** confirm this. The relative position of the AlN and GaN (105) peaks show that the GaN layers are pseudomorphically strained to AlN buffer layer in both sample A and C. Only the AlN and GaN diffraction peaks are visible with no discernible peak from the AlGaN IBL layers due to their composition and thinness. The RSMs confirm there was no structural effect of the IBLs on the GaN layer, and that the samples are similar structurally and as targeted for generating a 2DHG. Omega rocking curve scans taken around the GaN (002) peak (not shown here) confirm that all three samples have similar screw-type threading dislocation densities of ~ 10^8 cm^{-2}.

Results of room temperature Hall-effect measurements, performed at magnetic field of 0.32 T using soldered corner Indium contacts to the 2DHG, are

summarized in **table 2.2**. The three samples with the undoped GaN epitaxial layer showed a repeatable positive Hall coefficient confirming the presence of mobile holes. The control sample with IBLs only was found to be highly resistive, confirming that the IBLs in the buffer layer do not form parallel conduction channels. Since no p-type acceptor doping is present in the sample, the conduction in samples A, B and C are entirely due to the 2DHG at the GaN/AlN interface. The fact that it indeed is a 2DHG is confirmed by the fact that the density does not freeze out at 77 K, and the mobility increases. Before discussing the hole transport properties further, we report the chemical effect of the IBLs.

Secondary ion mass spectrometry (SIMS) analysis was performed on the three samples to investigate the impurity profiles of the films and the effect of the different buffer layers and IBL designs. The measured concentration profile for Si and O impurities are shown in **figure 2.12**, along with the Ga atomic fractions. The SIMS detection limits are $1-2\times10^{17}$ atoms/cm^3 for Si and O. The three regions of interest from the right side are: (c) the AlN/substrate nucleation interface, (b) the AlN buffer layer with IBLs, and (a) the GaN-AlN interface where the 2DHG is expected. They are plotted separately for ease of comparison.

In sample A, concentration spikes of Si and O are observed at the AlN/substrate nucleation interface. The peak concentrations are $\sim 3\times10^{19}$ cm^{-3} and $\sim 1\times10^{21}$ cm^{-3} respectively. The Si profile tails into the AlN buffer layer for a distance of ~20 nm. No Ga is detected in the AlN buffer layer. This is expected as no IBLs were grown in Sample A. No Si, O peaks are observed in the buffer layer, with the Si and O impurity levels remaining at the detection limit of around $\sim 1\times10^{17}$ cm^{-3} and $\sim 5\times10^{17}$ cm^{-3}. It is noted that the O level starts rising slowly in the top 100 nm of the AlN buffer layer. However, at the
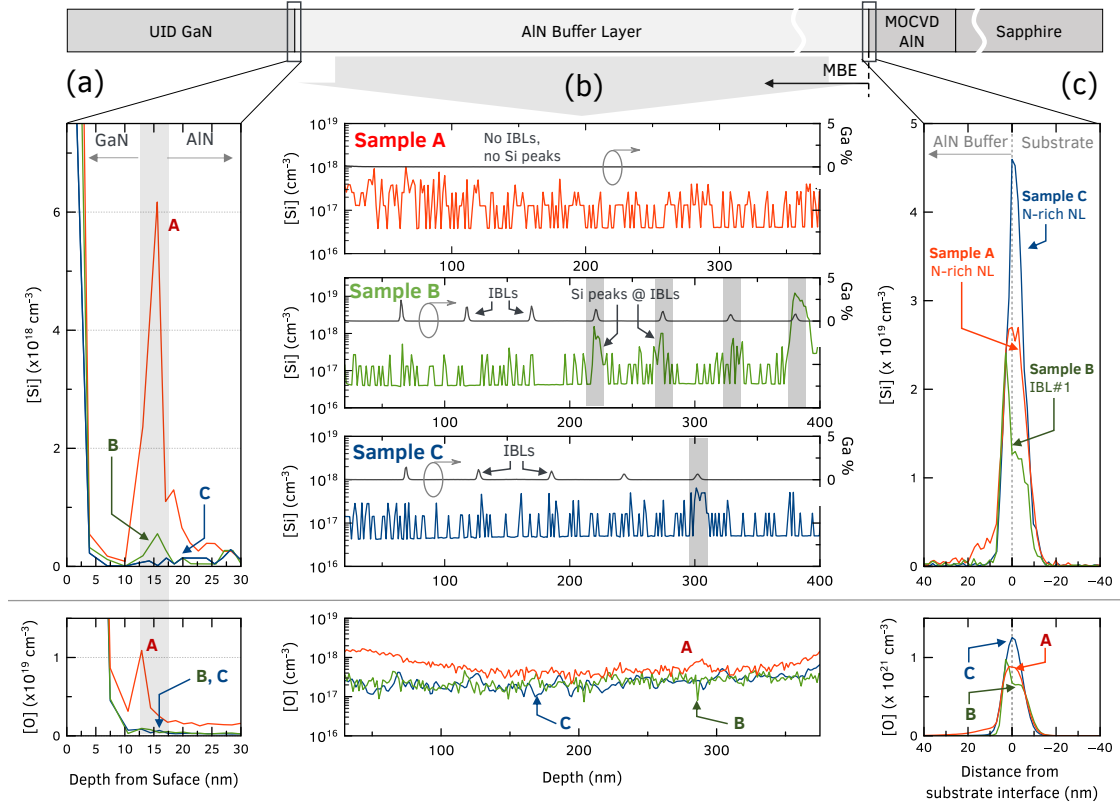
Figure 2.12: Secondary ion mass spectrometry (SIMS) profiles showing the impurity levels and Ga atomic fractions : (a) at the GaN-AlN interface where the 2DHG is expected, (b) in the AlN buffer layer, and (c) at the AlN-substrate nucleation interface, for the three samples A, B and C. The positions of the IBLs are marked by the peaks in the Ga atomic compositions in (b). The Si peaks corresponding to the IBLs in sample B and C are also indicated. The results show that the high-concentration AlGaN IBLs are effective in blocking the impurities from floating up and incorporating in the GaN layer. *Figure from Chaudhuri et al. [8]*

GaN/AlN interface, a clear concentration spike is observed for both Si and O profiles. The peak concentrations are $\sim 6 \times 10^{18}$ cm^{-3} and $\sim 1 \times 10^{19}$ cm^{-3} respectively. This points to the fact that despite using an N-rich NL layer in the AlN, some of the Si and O floated up during the growth of the metal-rich AlN buffer layer and incorporated in the initial layers of the epitaxial GaN layer. The Si spike extends over ~ 3 nm into the GaN layer, where the 2DHG is expected to reside. Clearly, the ~ 30 nm N-rich NL in this sample is not effective enough

to prevent the impurities from floating up during the growth of the AlN buffer layer.

The panel labeled Sample B shows the impurity profile when IBLs are introduced. The SIMS profile shows the incorporation of Ga, each peak corresponding to an IBL. The resulting AlGaN layers have > 95% Al composition, in agreement with the STEM scans in **figure 2.11**. The Si concentration exhibits peaks at the nucleation interface, and subsequent peaks coincide with the position of the IBLs. The Si peak density is $\sim 2 \times 10^{19}$ cm^{-3} for the first IBL at the nucleation interface, $\sim 1 \times 10^{19}$ cm^{-3} for the next and then drops to $\sim 1 \times 10^{18}$ cm^{-3} for the next 3. No Si peak is observed after 5 IBLs, beyond which the Si concentration remains at the detection limit of $\sim 1 \times 10^{17}$ cm^{-3} even at the IBL positions. This confirms that the Si observed at the GaN/AlN interface is not from the growth chamber ambient but is floating up from the substrate surface, as otherwise Si peaks would have occurred at every IBL position and not just the first 5. A small apparent Si spike of $\sim 5 \times 10^{17}$ cm^{-3} in **figure 2.12 (a)** visible at the GaN/AlN interface is around the same magnitude of the Si concentration in the adjacent AlN buffer layer in **figure 2.12 (b)**. However this concentration is an order of magnitude lower than the concentration in sample A. The O concentration profile in the AlN buffer layer does not show any spikes and is at the detection limit of $\sim 2 \times 10^{17}$ cm^{-3}. There is no O peak observed at the GaN/AlN 2DHG interface. This evidence suggests that the IBLs in sample B are far more effective in blocking Si and O compared to the N-rich NL in sample A. Further investigations are underway to determine the difference in the chemical behavior of the blocking of oxygen and silicon impurities.

The SIMS profile of sample C shows the impurity concentrations when both

the the N-rich NL and IBLs are used in the AlN buffer layer. Si and O concentration spikes are observed at the AlN nucleation interface, with peak concentrations of $\sim 5 \times 10^{19}$ cm^{-3} and $\sim 1 \times 10^{21}$ cm^{-3} respectively. The Ga atomic fraction profile in the AlN buffer layer that the IBLs are spaced ~55 nm apart with a concentration of > 95% AlGaN. A small Si peak of $\sim 5 \times 10^{17}$ cm^{-3} is observed only at the first IBL, beyond which the Si profile remains at the detection limit of $\sim 1 \times 10^{17}$ cm^{-3}. The O profile does not show any peaks in the buffer layer and remains at $\sim 2 \times 10^{17}$ cm^{-3}. Importantly no Si and O peaks are observed at the GaN-AlN interface. The impurity levels at the interface are an order lower than that seen in sample A at $\sim 1 \times 10^{17}$ cm^{-3} and $\sim 1 \times 10^{18}$ cm^{-3} for Si and O respectively. These results suggest that the combination of N-rich NL and IBLs used in sample C is most efficient in blocking the Si, O impurities floating up from the substrate from reaching the GaN layer where the 2DHG is located. Indeed this is borne out in the transport properties of the 2DHGs.

The measured 300 K and 77 K Hall-effect data for the three samples A, B and C is presented in **table 2.2**. Temperature-dependent Hall-effect measurements were performed compare the 2DHG transport between samples A and B/C, which have an order of magnitude difference in the impurity levels at the GaN/AlN interface. The samples were measured from 300 K to 20 K, at 1 T magnetic field in a Van der Pauw configuration with soldered Indium corner contacts. The results are shown in **figure 2.13**. Both samples show similar mobile hole densities $\sim 5 \times 10^{13}$ cm^{-2} throughout measured the temperature range. These densities are expected from the difference in polarization at the AlN/GaN heterojunction. The holes do not freeze-out even at 20 K, confirming the 2DHG is highly degenerate and metallic in nature for both samples.
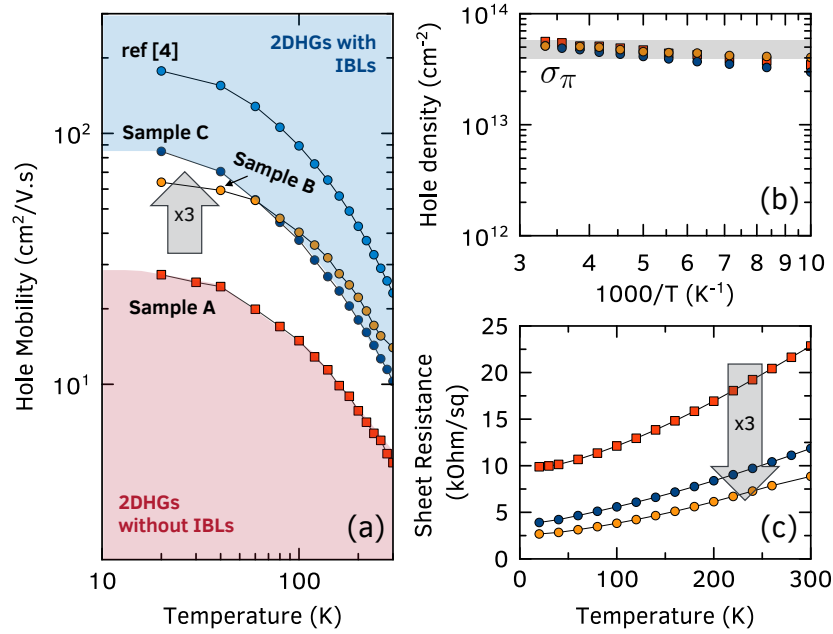
Figure 2.13: Temperature dependent Hall-effect measurement results for sample A, B and C. (a) Comparing the holes mobilites, 3× boost in mobilities is observed in sample B and C compared to sample A throughout the temperature range due to the suppression of impurities at GaN/AlN interface. Data from other samples grown under similar conditions [3] is also included, and shows high hole mobilities upto ~190 cm^2/Vs at 20 K. (b) The 2DHG sheet concentration is approximately the same in all the samples. (c) This results in 3× higher conductivity in sample B and C compared to sample A. *Figure from Chaudhuri et al. [8]*

A significant difference is observed in the measured Hall-effect mobilities. Sample A shows a room temperature mobility of ~ 5 cm^2/Vs, whereas the sample B and C have a 2× higher mobility of ~ 10 – 14 cm^2/Vs. The samples show a similar trend of mobility as a function of temperature. This is explained by the freeze out of acoustic and optical phonons [5], and agrees with previous report [3] of GaN/AlN 2DHG. However, the 2DHG mobility in sample B, C is consistently 2-3× higher that of sample A, with the highest mobilities of 85 cm^2/Vs and 64 cm^2/Vs respectively at 20 K. Other samples under similar growth conditions with IBLs have exhibited even higher mobilities, the highest [3] among

them is also plotted in **figure 2.13** for reference. This boost in mobility of sample B and C results in 3× lower sheet resistivity compared to sample A throughout the measured temperature range, as seen in **figure 2.13 (c)**.

The comparison of SIMS provides clear evidence that the presence of charged donor impurities at the GaN-AlN interface plays an important role in limiting the mobility of the 2DHG in these structures. Quantitatively, the mobility of a 2DHG of density p_s limited by Coulomb scattering from ionized background impurities of uniform 3D concentration N_{imp} is given by [129] :

$$\mu_{\text{imp}} \approx \frac{4(2\pi)^{5/2}\hbar^3(\epsilon_0\epsilon_s)^2}{m_{\text{eff}}^2\, e^3} \cdot \frac{p_s^{3/2}}{N_{\text{imp}}}, \tag{2.6}$$

where $\hbar$ is the reduced Planck's constant, e is the electron charge and ϵ_0 is the vacuum permittivity. $\epsilon_s = 8.9$ is the relative dielectric constant of the GaN channel. This expression considers a simplified single parabolic valence band (VB) with hole effective mass [130] $m_{\text{eff}} = 2.0\ m_0$. The value of the mobility for the GaN 2DHG of density $p_s = 5 \times 10^{13}$ cm^{-2} due to ionized background impurities is plotted as a function of N_{imp} in **figure 2.14(a)**. It reduces from $\mu_{imp} \geq 100$ cm^2/V·s at $N_{imp} \sim 5 \times 10^{18}$cm^{-3} to $\mu_{imp} \sim 5$ cm^2/V·s at $N_{imp} \sim 1.5 \times 10^{20}$cm^{-3}.

The dominant intrinsic scattering mechanism at room temperature for GaN/AlN 2D holes is due to acoustic phonons (AP) [5] through the deformation potential coupling. Using the simplified and calibrated model in equation (2.3), the expected room-temperature AP-limited mobility of the GaN/AlN 2DHG is ~ 60 cm^2/Vs, which is plotted in **figure 2.14 (a)**.

Other scattering mechanisms affecting the 2DHG that are less effective at room temperature are also included in **figure 2.14 (a)**. The room-temperature polar optical phonon (POP) limited mobility is set [5] at 110 cm^2/Vs. An extrinsic scattering mechanism limited mobility, which encompasses the effect of

mechanisms such as interface roughness, dislocations, etc., is set to 200 cm^2/Vs. Since the acoustic and optical phonon scattering modes are frozen out at low temperatures, the extrinsic value of 200 cm^2/Vs corresponds to the highest 10 K Hall mobility measured in GaN/AlN 2DHGs [3]. The resultant total mobility (μ_{Total}) approximated by Matthiessen's rule is plotted as a function of ionized donor concentration in **figure 2.14 (a)**.

In a chemically and structurally pure GaN/AlN heterostructure in the low impurity limit, AP scattering is the dominant scattering mechanism for 2D holes at room temperature. However, it is evident from **figure 2.14 (a)** that there exists a critical background impurity concentration above which the ionized impurity scattering becomes the dominant scattering mechanism, and lowers the 2DHG mobility to below its intrinsic AP-scattering limit. This critical impurity concentration $N_{\text{imp}}^{\text{cr}}$ is obtained by equating equations (2.6) and (2.3):

$$N_{\text{imp}}^{\text{cr}} \approx A' \, T \, \frac{D^2 \, m_{\text{eff}}^{1/3} \, (\epsilon_0 \epsilon_s)^{5/3}}{\rho \, v_s^2} p_s \tag{2.7}$$

where $A' = (120 \, k_B)/(\hbar^{2/3} \, e^{10/3})$ is a material independent constant. For convenient numerical estimates, equation (2.7) is cast in the form :

$$\begin{aligned} N_{\text{imp}}^{\text{cr}} \quad &\approx \quad 5 \times 10^{17} \text{ cm}^{-3} \times \\ &\epsilon_s^{5/3} \left(\frac{D}{1 \text{ eV}}\right)^2 \left(\frac{m_{\text{eff}}}{m_0}\right)^{1/3} \left(\frac{p_s}{10^{13} \text{ cm}^{-2}}\right) \times \\ &\left(\frac{10^3 \text{ kg/m}^3}{\rho}\right)\left(\frac{10^3 \text{ cm/s}}{v_s}\right)^2 , \end{aligned} \tag{2.8}$$

where m_0 is the free-electron mass. Substituting the values for the GaN/AlN 2DHG system, a $N_{\text{imp}}^{\text{cr}} \sim 1.2 \times 10^{19}$ cm^{-3} is obtained. Thus it is expected that when the background impurity density exceeds $\sim 1.2 \times 10^{19}$ cm^{-3}, impurity scattering is dominant and the resultant 2DHG mobility is lower than the intrinsic AP-limited mobility.
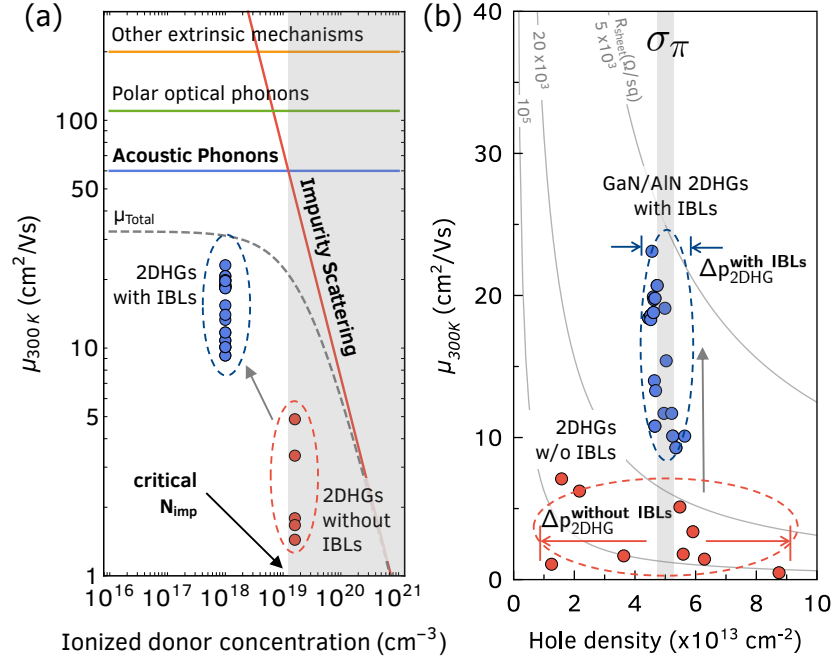
Figure 2.14: (a) Theoretical room temperature (RT) mobility μ_{300K} of a GaN/AlN 2DHG of density $\sim 5\times 10^{13}$ cm^{-2}, as a function of concentration of ionized background impurities N_{imp}. The 2DHG scattering is limited by ionized impurity scattering at impurity concentrations $N_{imp} \geq N_{imp}^{cr} \sim 1.2 \times 10^{19}$ cm^{-3}. The 2DHGs with IBLs ensure that N_{imp}^{cr} and thus have a higher phonon-limited mobility. (b) 300K mobility vs charge density of GaN/AlN 2DHG samples grown with and without the IBLs under similar conditions. A polarization-induced 2DHG density of $\sim 5 \times 10^{13}$ cm^{-2} is expected in all the samples. The samples without the IBLs, exhibit a larger spread in the 2DHG densities and lower mobilities. The samples with IBLs are in agreement to the expected 2DHG density and have higher mobilities, resulting in high-conductivity 2DHGs. *Figure from Chaudhuri et al. [8]*

To compare with this theoretical prediction, the experimentally measured room-temperature Hall-effect mobilities of the GaN/AlN 2DHGs with AlN buffer layers grown without IBLs (similar to sample A) and with IBLs (similar to sample C) are plotted in **figure 2.14 (a)**. They fall in two blocks. The impurity densities at the 2DHG interface are estimated to be 1.6×10^{19} cm^{-3} for the former and 10^{18} cm^{-3} for the latter, following the SIMS results of sample A and C. The experimental data agree with the trend predicted by the model: the 2DHGs

with $N_{\text{imp}} \geq N_{\text{imp}}^{\text{cr}}$ have a lower mobility than those with $N_{\text{imp}} \leq N_{\text{imp}}^{\text{cr}}$, support-ing the hypothesis that impurity scattering plays a dominant role in transport of 2DHGs without IBLs. Furthermore, since equation (2.8) is a function of basic material parameters, it serves as a useful rule-of-thumb for designing and op-timizing heterostructures with 2D carriers not limited to the GaN/AlN 2DHG studied here. The deviation from theory in **figure 2.14 (a)** is attributed to the single parabolic VB assumption for the mobility calculations, which ignores inter-valence band scattering. The low mobility samples could possibly also have impurity concentrations higher than 1.6×10^{19} cm^{-3} leading to the spread in their mobilities.

If the donor impurity concentration is high enough that its integrated sheet concentration in GaN becomes comparable to the mobile hole density of $\sim$ 5×10^{13} cm^{-2}, the donors can compensate the holes resulting in significant de-viation from the expected hole density $\sigma_\pi \sim 5 \times 10^{13}$ cm^{-2}. This will also affect the mobility of the uncompensated holes due to neutral impurity scattering. The strong effect on the hole density is clearly seen in **figure 2.14 (b)**, where the room temperature 2DHG mobilities versus densities are plotted for samples with and without IBLs. The samples without IBLs show a significantly large spread in the 2DHG densities with $\Delta p_s \sim 7 \times 10^{13}$ cm^{-2} and low mobilities. The 2DHG in the samples with IBLs consistently exhibit a higher mobility, and den-sities as expected of $\sim 5 \times 10^{13}$ cm^{-2} in all samples. More importantly, they exhibit tight control over the density which shows a 7× reduction in the spread to $\Delta p_s < 1 \times 10^{13}$ cm^{-2}. The variation in the 2DHG mobilities among these samples with IBLs is believed to be due to other non-dominant extrinsic scatter-ing mechanisms such as interface roughness scattering or dislocation scattering. Varying the extrinsic scattering mechanism limited mobility from 200 cm^2/Vs

to 60 cm^2/Vs is expected to cause a $\sim$ 10 cm^2/Vs variation of mobilities at room temperatures and $\sim$ 100 cm^2/Vs at low temperatures. These are in agreement with the measured mobility data spread observed in **figures 2.13 and 2.14**.

Thus, suppressing the impurities using IBLs not only results in higher mobilities, it also enables tightly controlled 2DHGs densities. An AlN buffer layer with 4 IBLs or a combination of N-rich NL and 1 IBL is efficient enough to block the impurities from affecting the 2DHG. As a further confirmation of the effectiveness of the IBLs, a UID-GaN/AlN 2DHG sample with a thinner $\sim$ 100 nm AlN buffer layer with N-rich NL and only 1 IBL showed a room temperature mobility of $\sim$ 10 cm^2/Vs at density of 4.4$\times$10^{13} cm^{-2}. These optimized GaN/AlN 2DHGs offer the highest room temperature p-type conductivity compared to other single-channel 2DHGs reported in III-nitrides [3].

2.5 Very High density InGaN/AlN 2DHGs

The GaN/AlN high density 2DHGs discussed so far have recently been used as a transistor channel to break the GHz-speed barrier for the first time in a GaN p-channel FET [39] with record high on-currents greater than 0.5 A/mm and f_t/f_{max} of 23/40 GHz. As will be shown in detail in chapter 3, the as-grown 2DHG density in these devices is partially depleted under the gate using a recess etch. However the access resistances are determined by the as-grown 2DHG conductivity and therefore the density. If the 2DHG density is engineered to be higher in the access regions, the resultant lower access resistance should further enhance the on-currents, transconductance and therefore operation speeds of these state-of-art GaN p-channel FETs.

In this section very high 2DHG densities $> 1 \times 10^{14}$ cm^{-2} are demonstrated in carefully designed and grown pseudomorphic InGaN layers on thick, relaxed AlN buffer layers. It is shown that introduction of Indium in the strained GaN channel of a GaN/AlN structure boosts the resulting mobile charge densities, primarily because of the increase in piezoelectric component of polarization in the strained InGaN layer. This work represents the first report of polarization-induced carrier densities greater than 1×10^{14} cm^{-2} at a single III-nitride heterointerface, which is just an order below the sheet atomic density of 10^{15} cm^{-2}. The best hole mobilities in these high-density 2DHGs are found to be $\sim$ 5 cm^2/Vs at 300 K and $\sim$ 15 cm^2/Vs at 10 K. These are lower than $\sim$ 25 cm^2/Vs and $\sim$ 200 cm^2/Vs at 300 K and 10 K respectively seen in GaN/AlN 2DHGs. These lower mobilities are shown to be due to the dominance of alloy disorder scattering at room temperature. By comparing the experimental data to a simple scattering model, the InGaN/AlN 2DHG system allows the direct measurement of the alloy fluctuation potential of 1.0 eV for hole transport in InGaN.

When a metal-polar GaN or InGaN crystal is epitaxially grown on a thick AlN buffer layer, as shown in figure 2.15 (a), a fixed negative sheet charge σ_{π} arises due to the intrinsic polarization field discontinuity (ΔP) at the In-GaN/AlN interface. The polarization in III-nitride semiconductors has two components - the spontaneous polarization P_{SP} and the piezoelectric polarization P_{PZ}. The polarization-induced fixed sheet charge σ_{π} at the InGaN/AlN interface, as a function of In composition x and strain relaxation r in the InGaN layer, is given by [100]:

$$\begin{aligned}
\sigma_\pi(x,r) &= P_{SP}^{InGaN} - P_{SP}^{AlN} - P_{PZ}^{InGaN} \\
&= P_{SP}^{InGaN} - P_{SP}^{AlN} - 2\epsilon_{xx}\left(e_{31} - e_{33}\frac{C_{13}}{C_{33}}\right) \\
&= \Delta P_{SP} - 2\frac{a(r)-a_0}{a_0}\left(e_{31} - e_{33}\frac{C_{13}}{C_{33}}\right),
\end{aligned} \qquad (2.9)$$

where $e_{31/33}$ are the piezoelectric coefficients and $C_{13/33}$ are the elastic con-stants of InGaN. ϵ_{xx} is the isotropic in-plane strain in the InGaN layer, given by $\epsilon_{xx} = (a(r) - a_0)/a_0$ where a_0 is the relaxed in-plane lattice constant of InGaN, and $a(r)$ is the lattice constant of the strained InGaN film on AlN. a_0, $e_{31/33}$, $C_{13/33}$, P_{SP}, P_{PZ} are functions of the indium composition x and are assumed to be linear interpolation of corresponding values for GaN ($x = 0$) and InN ($x = 1$) [1, 2].

An InGaN layer grown on AlN is ideally expected to be compressively strained throughout the composition range as both GaN ($a_0^{GaN} = 3.189\,\text{Å}$) and InN ($a_0^{InN} = 3.553\,\text{Å}$) have larger in-plane lattice constant than AlN ($a_0^{AlN} = 3.112\,\text{Å}$). However, a real crystal tends to relax to release the built-up strain energy. The actual epitaxial strain relationship between InGaN crystal and AlN buffer layer underneath is represented by the relaxation r through the relation $a = r \cdot (a_0 - a_0^{AlN}) + a_0^{AlN}$. The value $r = 0$ represents a pseudomorphic InGaN layer on AlN whereas $r = 1$ represents a fully relaxed InGaN layer on AlN. Therefore the σ_π is a function of the InGaN composition x and film relaxation r.

The simulated charge and energy band profile for a metal-polar 11 nm In-GaN layer on AlN with $x = 0.07$ are shown in **figure 2.15 (b)**. The polarization-induced *negative* fixed charge σ_π at the InGaN/AlN interface is indicated in the charge profile. If the InGaN layer is sufficiently thick [3], then σ_π is partly com-pensated by *mobile holes* which are confined by the valence band offset at the
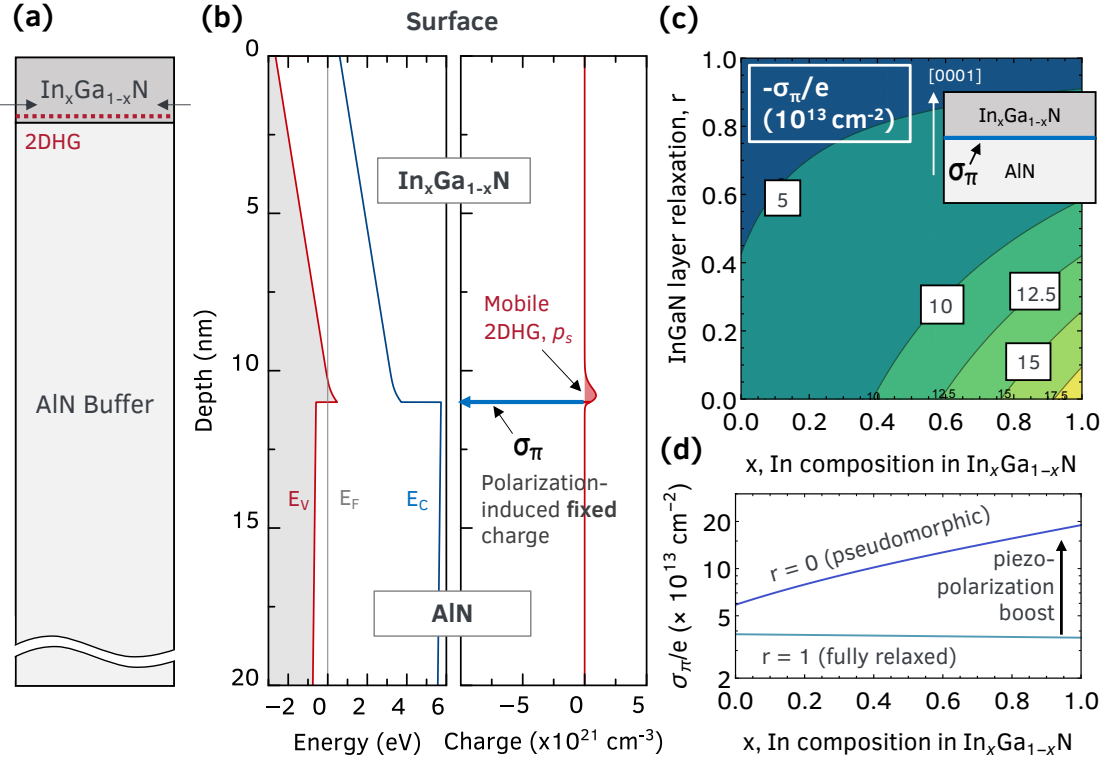
Figure 2.15: (a) Metal-polar undoped InGaN/AlN heterostructure with the expected 2DHG at the interface studied in this work. (b) A simulated band diagram and charge profile for 11 nm $In_{0.07}Ga_{0.93}N$ on AlN buffer layer, showing the negative polarization-induced fixed sheet charge σ_π at the InGaN/AlN interface which is partly compensated by the mobile 2DHG of density p_s. (c) Contour plot of the expected σ_π in this hetereostructure as a function of the InGaN layer relaxation r and In composition x in the InGaN layer. The 1D profiles along the $r = 0$ and $r = 1$ is plotted in (d). An increase in polarization fixed charge is expected on increasing In composition while maintaining pseudomorphic compressive strain in the layer.

InGaN/AlN interface to form a mobile 2D hole gas (2DHG). Within this model, the σ_π therefore represents the maximum achievable 2DHG density p_s in a given InGaN/AlN structure.

The upper limit of sheet density σ_π in metal-polar InGaN/AlN heterostructures is calculated as a function of x and r using equation (2.9) and the known values of elastic and polarization constants[1, 100]. The results are shown as
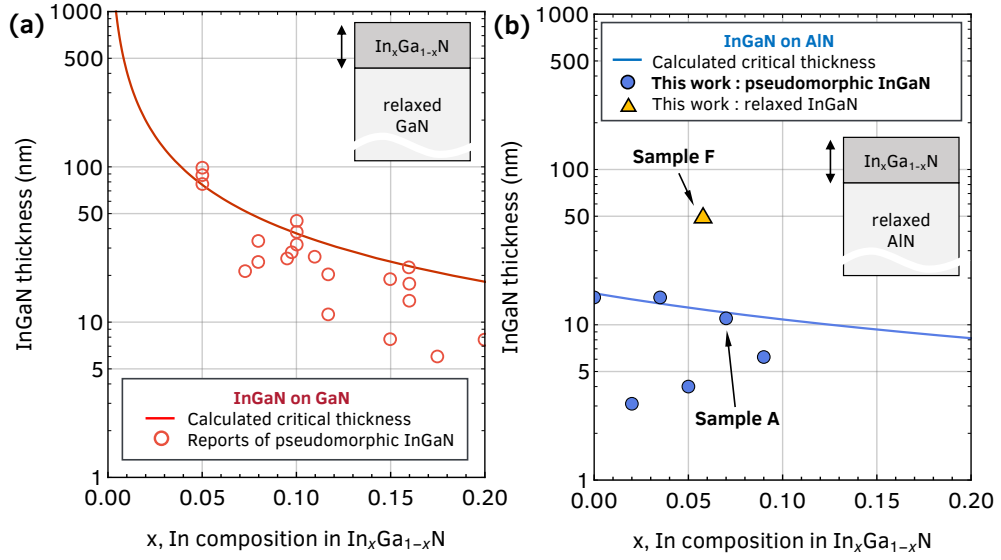
Figure 2.16: (a) Experimental reports of pseudomorphic InGaN layers on GaN [9, 10] compared with the calculated critical coherent thickness [11] of InGaN on GaN to validate the model. (b) Pseudomorphic and relaxed InGaN on AlN samples grown using MBE in this work, and the calculated critical coherent thickness[11] of InGaN on AlN as a function of In composition. The extracted strains agree with the theoretical model. The X-ray diffraction scans of samples A and F are shown in figures 2.17 (c) and (d).

Table 2.3: Structural details of the InGaN/AlN heterostructures studied in this work, with their corresponding 2DHG densities p_s, mobilities μ_p measured via Hall-effect at 300 K and 77 K. Sheet resistance R_s of $> 10^3$ $k\Omega/$sq indicates resistive samples in which the transport could not be extracted using Hall effect measurements. All samples had a ~400 nm thick AlN buffer layer grown on metal-polar AlN on Sapphire template and were unintentionally-doped (UID). The mean values of the Hall-effect results are shown here across multiple measurements on co-loaded samples. All conductive samples exhibited positive Hall-coefficient confirming the presence of mobile holes.

ID	Channel layer	p_s^{300K} 10^{14} cm^{-2}	μ_p^{300K} cm^2/Vs	R_s^{300K} $k\Omega/sq$	p_s^{77K} 10^{14} cm^{-2}	μ_p^{77K} cm^2/Vs	R_s^{77K} $k\Omega/sq$
A	11 nm In$_{0.07}$Ga$_{0.93}$N	1.43	3.6	16.2	0.56	9.84	10.6
B	4 nm In$_{0.05}$Ga$_{0.95}$N	3.15	0.27	73.5	2.36	0.54	49
C	3.1 nm In$_{0.02}$Ga$_{0.98}$N	-	-	$> 10^3$	-	-	$> 10^3$
D	6.2 nm In$_{0.09}$Ga$_{0.91}$N	4.29	0.95	15.3	2.29	2.27	21.34
E	15 nm In$_{0.06}$Ga$_{0.94}$N	1.5	2.2	17.6	0.52	9.5	10.7
F	50 nm In$_{0.06}$Ga$_{0.94}$N	-	-	$> 10^3$	-	-	$> 10^3$
G	13 nm GaN	0.46	23.11	5.9	3.4	105	1.7

a contour plot in **figure 2.15 (c)**. The profiles along $r = 0$ and $r = 1$ are plotted in **figure 2.15 (d)**. At $x = 0$ and $r = 0$, i.e. in a pseudomorphic GaN/AlN structure, $\sigma_\pi \sim 5 \times 10^{13}$ cm^{-2}. This agrees with the experimentally measured 2DHG densities in undoped GaN/AlN interfaces[3]. In a fully relaxed InGaN film ($r = 1$), σ_π decreases with increasing In composition x. This is because InN has a lower spontaneous polarization P_{SP} than GaN. However, the lattice mismatch between InGaN and AlN increases with x, increasing the strain ϵ_{xx} and thereby increasing the P_{PZ} contribution to the σ_π. The net effect is a boost in σ_π from $\sim 5 \times 10^{13}$ cm^{-2} for GaN/AlN to $> 1.5 \times 10^{14}$ cm^{-2} for InN/AlN. Therefore, a pseudomorphically strained InGaN layer on AlN should result in a higher σ_π and consequently higher 2DHG concentrations than those in GaN/AlN structures.

The epitaxial growth of pseudomorphic InGaN layers on AlN is particularly challenging due to different thermal stability and lattice mismatch. InN starts decomposing at $\sim 630°$C, which is below the optimal MBE growth temperature [138, 64] of AlN of $\sim 750 - 1000°$C. This necessitates growth interruption to lower the temperature before InGaN deposition. Additionally, due to the lattice mismatch with respect to the AlN substrate, there exists a finite InGaN coherent critical thickness h_c beyond which it relieves the strain energy by forming misfit dislocations [11, 145] and no longer remains pseudomorphic to AlN. Using the Fischer model [11] of strain relaxation, the critical thickness h_c of InGaN grown on (relaxed) AlN and GaN substrates are calculated as a function of the In composition x. The calculated values are plotted as solid lines in **figures 2.16 (a,b)**. Previous experimental reports of pseudomorphic InGaN grown on GaN [9, 10] agree well with the calculation in **figure 2.16 (a)**, validating the model. For InGaN on AlN heterostructures, the expected h_c decreases with increasing

In composition x - from 15 nm for $x = 0$, to 3 nm for $x = 1$, as shown in **figure 2.16 (b)**. The h_c of 15 nm for GaN/AlN ($x = 0$) concurs with the previous experimental observation [3] of 13 nm pseudomorphic GaN on AlN. According to this model, low-composition $x < 0.1$ InGaN layers thinner than $\sim 15 - 10$ nm should be pseudomorphically strained to the underlying AlN, and with expected charge $\sigma_\pi > 5 \times 10^{13}$ cm^{-2}.

Additionally, for the fixed charges σ_π to be compensated by a mobile 2DHG, the InGaN layer needs to be thicker than a certain critical thickness d_0 beyond which the polarization dipole is neutralized by carriers from the surface states. For example, in an AlN/GaN 2DEG [146], $d_0 \sim 1$ nm. For a GaN/AlN 2DHG, this critical thickness has been experimentally found [3] to be $d_0 \sim 3$ nm.

Thus, considering the above trade-offs, it is expected that $\sim 3 - 15$ nm thick, low-composition $x < 0.1$ undoped InGaN layers grown on AlN should be pseudomorphically strained and yield mobile 2DHGs with densities higher than 5×10^{13} cm^{-2}.

To test this, a series of InGaN on AlN heterostructures were grown using plasma assisted molecular beam epitaxy (PA-MBE) on metal-polar MOCVD-grown AlN on sapphire templates. The growth followed a similar procedure as the GaN/AlN 2DHG growths, and the growth process is summarized in appendix A. After unloading from the MBE system, all the samples were dipped in concentrated HCl solution for ~ 15 mins to remove any excess metal droplets of Ga or In present on the surface before any further characterization. The structures grown and their transport properties are summarized in **table 2.3**. Table **Table 2.3** summarizes the structures of the InGaN/AlN samples, labelled A to G, and their transport properties.
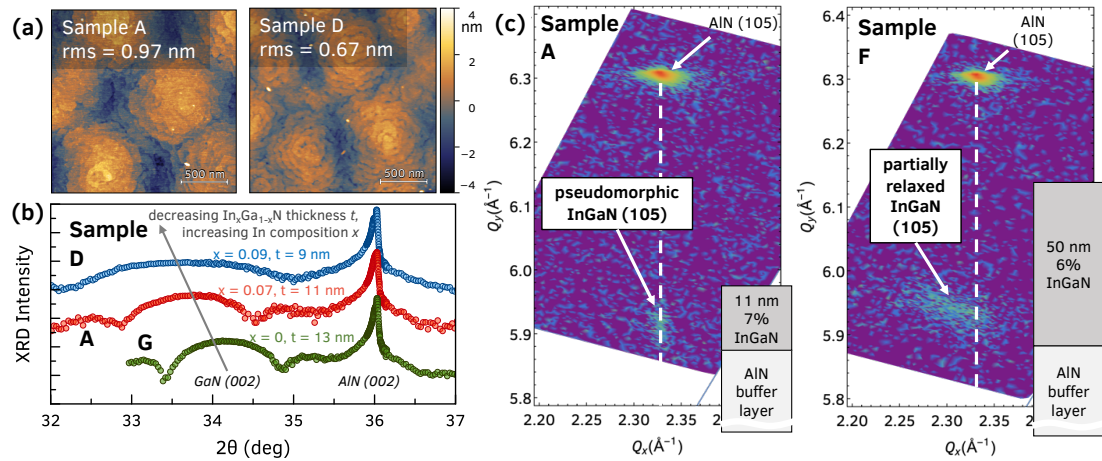
Figure 2.17: (a) Representative AFMs of the surface of InGaN/AlN heterstructures, samples A and D in Table 1. Atomic steps are visible forming spirals around threading dislocations with a screw component. (b) An X-ray diffraction (XRD) symmetric coupled scan along (002) showing the position of the In peak change with the InGaN composition which allows accurate extraction of the thickness and the composition of the layer. (c) XRD reciprocal space map (RSM) of sample A and sample F around the AlN (105) asymmetric peak confirming an 11 nm $In_{0.07}Ga_{0.93}N$ layer is psuedomorphically-strained to the AlN buffer whereas a 50 nm thick $In_{0.06}Ga_{0.94}N$ layer on AlN is relaxed. This agrees well to the calculated curves in figure 2.16 (b) of critical thickness of InGaN/AlN.

Atomic force microscopy (AFM) scans of all samples showed smooth surface morphology with root mean square (rms) roughnesses of < 1 nm. Scans from samples A and B are shown in **figure 2.17 (a)**. Atomic steps were visible forming spiral features, a characteristic of a screw dislocation mediated MBE-growth [147]. The other samples in **Table 2.3** exhibited similar surface morphology. X-ray diffraction (XRD) scans along (002) symmetric peak for selected samples A, B and G are shown in **figure 2.17 (b)**. The InGaN compositions and the layer thicknesses are extracted accurately from the (002) peak position and the fringe spacings respectively. The extracted data for all samples are summarized in **Table 2.3**. XRD reciprocal space mapping (RSM) around asymmetric AlN (105) peak was performed to characterize the strain in the InGaN layers and compare

with the critical thickness predictions. Apart from sample F, the InGaN layers in the other samples were also confirmed to be fully strained to AlN. One of the scans from sample A with a 11 nm of $In_{0.07}Ga_{0.93}N$ layer is shown in **figure 2.17 (c)**. The relative positions of the InGaN and AlN (105) peaks clearly confirm that the InGaN layer is pseudomorphically strained to AlN. The experimental data also agree well to the theoretically predicted critical thickness of InGaN/AlN plotted in **figure 2.16 (b)**. To further validate this model, sample F with a thick ~ 50 nm of $In_{0.06}Ga_{0.94}N$ layer on AlN was also grown under similar conditions and characterized. Since 50 nm is above the predicted critical thickness in **figure 2.16 (b)**, the film is expected to relax. The XRD RSM for sample F, shown in **figure 2.17 (d)**, confirms that it is indeed the case and that the 50 nm InGaN layer has party relaxed and is no longer pseudomorphically strained to the AlN. To the authors' best knowledge, this is the first controlled study of pseudomorphic epitaxial growth of InGaN layers directly on AlN.

Thus, the InGaN/GaN samples A-E have the desired structures in which a high-density 2DHG is expected. Hall-effect measurements were performed on the samples using soldered corner Indium contacts confirm the presence of the 2DHG. First, a control sample with just the epitaxially grown AlN buffer layer without any InGaN grown on top was measured and confirmed to be resistive. Any measured conductivity in the other samples hence should arise from mobile carriers at the undoped InGaN/AlN interface. All the samples except sample C and F showed Hall conductivity with a *positive* Hall coefficient. The results of the Hall-effect measurements are summarized in **Table 2.3**. Sample G, the GaN/AlN sample, shows a 300 K 2DHG density of $\sim 4.5 \times 10^{13}$ cm^{-2} as expected [3]. Among the InGaN/AlN samples, sample C and F are found to be resistive. The polarization-induced 2DHG density is most likely absent

in Sample C as the $In_{0.02}Ga_{0.92}N$ thickness of 3.1 nm is very close to the critical thickness $d_0 \sim$ 3nm to induce the 2DHG. High resistance in sample F could be due to the high density of mistfit dislocations at the InGaN/AlN interface generated by the relaxation of the InGaN layer. Interestingly, the room temperature 2DHG densities for all conductive InGaN/AlN samples are greater than 1×10^{14} cm^{-2}, which is more than 2× the GaN/AlN 2DHG density! The Hall mobilities range around 0.5 - 4 cm^2/Vs at room temperature, and increase to 2 - 10 cm^2/Vs at 77 K. The carriers do not freeze-out at cryogenic temperatures and show an increase in mobilities upon cooling - confirming the presence of high-density 2DHGs in these undoped InGaN/AlN heterostructures. The best measured Hall mobilities and charge densities are 2.6/9.8 cm^2/Vs and 1.47/0.59 × 10^{14} cm^{-2} at 300K/77K respectively for sample A with 11 nm $In_{0.07}Ga_{0.93}N$. These represent the first time that such high 2D charge densities are measured in a single channel III-nitride semiconductor system.

Figure 2.18 (a) compares the experimentally measured 2DHG Hall densities in the InGaN/AlN samples to the expected densities p_s calculated using a self-consistent 1D Schrondinger Poisson solver [55]. The densities are calculated as a function of InGaN thickness for the grown compositions. The GaN/AlN 2DHG density (sample G) agrees with what is expected. A clear discrepancy is observed in the expected and observed InGaN/AlN 2DHG densities. InGaN/AlN heterostructures with thick InGaN and *low In composition of* 2 − 9% are expected to have 2DHG densities in the range of $\sim 6 \times 10^{13}$ cm^{-2}. However we observe high 2DHG densities of $> 1 \times 10^{14}$ cm^{-2} in all the InGaN/AlN samples grown in this work, which is 2× the expected value at these In compositions. The Hall densities are however repeatable across Hall-effect measurements and samples grown on different MBE systems. The reason for this discrepancy is not yet

understood and needs further investigation.

Sample A with 11 nm $In_{0.07}Ga_{0.93}N$ 2DHG was chosen for further investigation of hole transport in this high-density 2DHG system in comparison to the control sample G. **Figure 2.19** shows the temperature-dependent Hall-effect measurement results from 300 K down to 10 K on samples A and G. The InGaN/AlN 2DHG density show a 2× increase compared to the GaN/AlN 2DHG density throughout the temperature range down to 10 K, as seen in **Figure 2.19 (a)**. This also shows the robustness of the 2DHG with temperature. The InGaN/GaN 2DHG mobility is ~3 cm^2/Vs at 300 K and increases with cooling, reaching ~ 15 cm^2/Vs at 10 K, as seen in **Figure 2.19 (b)**. The trend in temperature-dependent mobilities is similar to what is observed in GaN/AlN 2DHGs [3]. The GaN/AlN 2DHGs show mobilites ~ 25/190 cm^2/Vs at 300/10 K. The InGaN/GaN 2DHG mobilities are considerably lower than GaN/AlN 2DHG mobilities, albeit at a higher charge density. Their high charge density however results in a InGaN/GaN 2DHG sheet resistance of ~15/10 kΩ/sq. at 300 K/10 K, which is comparable to the GaN/AlN 2DHGs used in state-of-art p-channel FETs [39, 5]. Hence, even with the lower room temperature hole mobilities, the InGaN/GaN 2DHG is suitable for device applications as source of drain regions to prevent source starvation.

How do we increase the room-temperature moblities of these high-density 2DHGs? To answer this, first the limiting carrier scattering mechanism needs to be understood. In "clean" GaN/AlN 2DHGs, the room temperature mobilities are limited by acoustic phonon (AP) scattering [5]. The acoustic-phonon limited hole mobility $\mu_{AP}(x)$ for a 2DHG in $In_xGa_{1-x}N$/AlN heterostructure with density p_s at temperature T under the single parabolic valence band approximation is
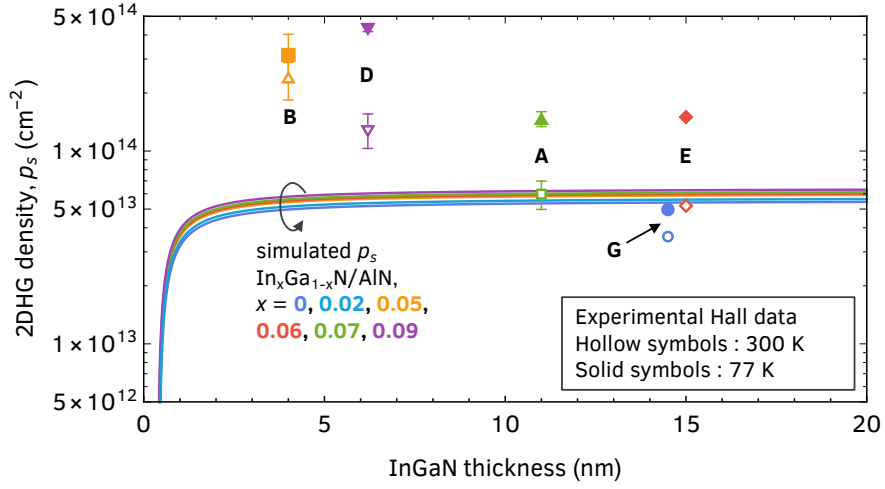
Figure 2.18: The 2DHG densities in the InGaN/AlN structures plotted as a function of InGaN layer thickness, and compared to simulated values.
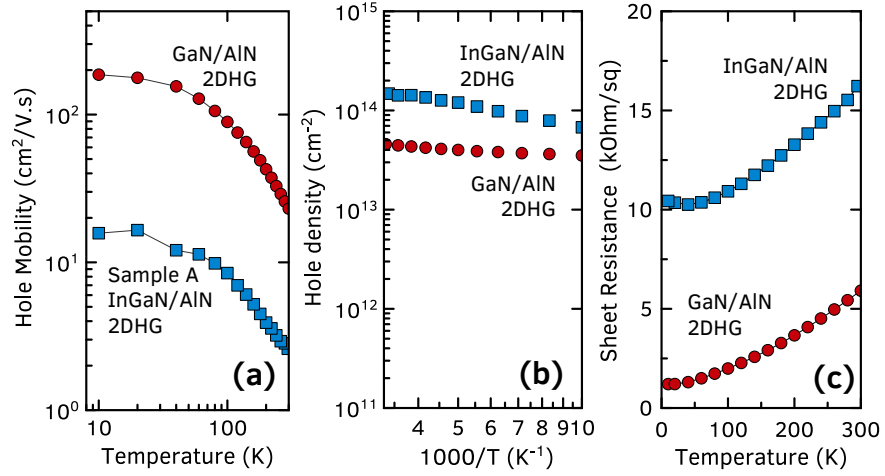
Figure 2.19: Temperature dependent Hall-effect measurement results for an InGaN/AlN 2DHG (sample A) and a GaN/AlN 2DHG (sample G). (a) The InGaN/AlN 2DHG charge density is double that of the GaN/AlN 2DHG throughout the temperature range. (b) The 2DHG mobility however is about $10\times$ lower in the InGaN/AlN 2DHG, with a 300 K (10 K) mobility of ~3 cm^2/Vs (~18 cm^2/Vs). (c) The InGaN/AlN 2DHG room temperature sheet resistance of ~ 15 kΩ/sq is competitive to the other 2DHGs demonstrated in III-nitrides.

given by [129] :

$$\mu_{\text{AP}}(x) \approx \frac{16e\,\rho\,v_s^2\,\hbar^3}{3k_B T\,D_{ac}^2\,m^\star(x)^2\,b(p_s,x)}, \tag{2.10}$$

74

where where e is the electron charge, $\hbar$ is the reduced Planck's constant and k_B is the Boltzmann constant. D_{ac} = 6.2 eV is the acoustic phonon deformation potential [8]. $m^\star(x)$ is effective mass of holes in InGaN of composition x, interpolated between the effective heavy-hole mass of GaN ($2m_0$) and InN ($1.6m_0$), where m_0 is the free electron mass. Note that the $m^\star$ for holes in InGaN is always lower than that of GaN. $b(p_s, x) = \left[\left(33m^\star(x)e^2\, p_s\right) / \left(8\hbar^2\epsilon_0\epsilon_s\right)\right]^{1/3}$ is the variational Fang-Howard wavefunction parameter that quantifies the spatial spread of the 2DHG.

Because of the $\sim 2\times$ higher carrier density p_s, acoustic phonon scattering limited mobility μ_{AP} is expected to be lower in the InGaN/AlN 2DHG system compared to GaN/AlN. Additionally, scattering is also expected from mechanisms specific to alloyed crystal channels. In particular, carriers experience scattering from the disorder they see in the crystal potential, i.e. alloy disorder scattering. Quantitatively, under a single parabolic valence band approximation, the alloy disorder limited mobility μ_{Alloy} of 2D hole carriers in an alloy channel with composition x is given by [148] :

$$\mu_{\text{alloy}} \quad (p_s, x) \approx$$
$$\frac{e\hbar^3}{m^\star(x)^2\ \Omega_0(x)^2\ U_{AL}^2\ x(1-x)} \cdot \frac{16}{3\ b(p_s, x)}, \tag{2.11}$$

where $\Omega_0(x) = \sqrt{3}/8 \cdot a_0(x)\, c_0(x)$ is the effective volume each Ga or In atom occupies in the crystal, where a_0 and c_0 are the interpolated in-plane and out-of-plane lattice constants of InGaN. U_{AL}, the alloy fluctuation potential, is the on-site potential difference if a Ga atom is replaced by an In atom, or vice versa. The value of U_{AL} represents the strength or sensitivity of the alloy scattering, and is typically on the order of the corresponding band offset between the constituents of the alloy. U_{AL} for an alloy is typically extracted by fitting to experimental data.

Effect of alloy disorder scattering on electrons has previously been investigated in III-nitride semiconductors, both for 2D *electrons* in AlGaN [149] and InGaN channels [150], and bulk polarization-doped graded structures [151]. Similar investigations of alloy scattering of holes have not yet been reported. Hole transport has been studied in Mg-doped bulk alloys. In Mg-doped InGaN [152], a decrease in room temperature hole mobility with increasing In concentration upto $x = 0.25$ is observed, mobilites remaining below 10 cm^2/Vs throughout. However, the added presence of impurity scattering and the freezing out of holes at low temperatures in Mg-doped InGaN layers do not allow for an in-depth probe of the alloy disorder scattering. The polarization-induced, undoped In-GaN/AlN 2DHG therefore offers a unique opportunity to study this scattering mechanism.
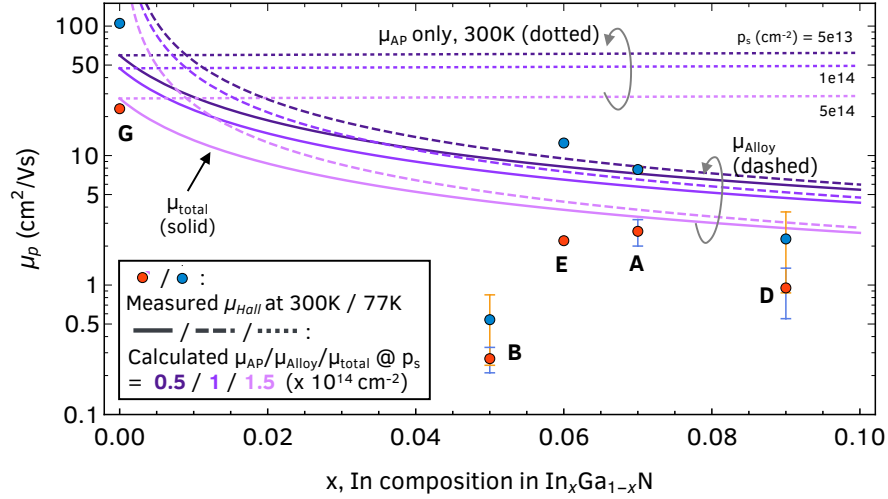
Figure 2.20: The theoretical room-temperature total hole mobility as a function of the InGaN composition, taking into account scattering due to acoustic phonons (AP) and alloy disorder, for different 2DHG densities. Alloy scattering is expected to dominate in InGaN/AlN 2DHGs, limiting the hole mobilities to below the intrinsic limit. The experimental data measured in this work concurs with the theoretical predictions.

Using equations (2.10) and (2.11), μ_{AP} and μ_{Alloy} for In$_x$Ga$_{1-x}$N/AlN 2DHG

at room temperature are calculated as a function of Indium content $x = 0$ to 0.1 for 2DHGs densities of $p_s = (0.5, 1, 1.5) \times 10^{14}$ cm^{-2}. GaN physical constants of density $\rho = 6.15 \times 10^3$ kg/m^3 and sound velocity $v_s = 7963$ m/s are used as an approximation for low-composition InGaN with $x < 0.1$. The total mobility μ_{tot} limited by AP and alloy disorder scattering is then calculated according to Matthiessen's Rule $\mu_{tot}^{-1} = \mu_{Alloy}^{-1} + \mu_{AP}^{-1}$. The results are plotted in **figure 2.20**, along with the measured Hall data of InGaN/AlN 2DHGs from **table 2.3**.

A reasonable agreement is observed between the calculated hole mobilities with $U_{AL} = 1.0$ eV and the experimentally measured Hall mobilities. It is observed that AP scattering does not change significantly within the indium concentration range of $x = 0$ to 0.1. The alloy disorder limited scattering is observed to be the dominant scattering mechanism for 2DHGs in InGaN/AlN with In composition $x > 0.01$. μ_{alloy} is a strong function of x, and decreases down from ~ 50 cm^2/Vs at $x = 0.01$ to ~ 6 cm^2/Vs at $x = 0.1$ for $p_s = 5 \times 10^{13}$ cm^{-2}. The observed deviation from calculated value in sample B is attributed to the InGaN layer being very thin (4 nm) and therefore the 2DHG being very close to other possible remote scattering centers on the surface [153]. The alloy fluctuation potential $U_{AL} = 1.0$ eV for holes in InGaN agrees with the reported valence band offset [154] between InN and GaN $\Delta E_v \sim 1.07$ eV. Interestingly, this potential is lower than the $U_{AL} \sim 2.4$ eV for electrons in InGaN. This is physically expected since the effect of Ga by In cation substitution has a lower effect on the *p-orbital like* valence bands which primarily from the N atoms, than the *s-orbital like* conduction bands. If $\Omega_0(x)$ is considered to be the effective volume Ga or In cation occupies in the unit cell as $\Omega_0(x) = \sqrt{3}/8 \cdot a_0(x) c_0(x)$, then $U_{AL} = 1.9$ eV results in the best fit to the experimental data.

It is clear from the calculated model and supporting experimental data that, unlike the case in Si/SiGe [155], the effect of alloy scattering in these In-GaN/AlN 2DHGs dominate over the effect of decreasing hole effective mass in the alloy. Hence, a path to higher 2DHG mobility through alloying might not be feasible. However carefully engineered in-plane strain [5, 156] could potentially be used to boost the mobility of these InGaN/AlN and decrease their sheet resistances further, as discussed in section 2.7.

The room temperature sheet resistances of these InGaN/AlN 2DHGs are ~ 15 kΩ/sq, which make them candidates for enabling low-resistance p-type regrown contacts to the GaN/AlN 2DHG for device applications. As-grown p++InGaN contact layers to the GaN/AlN 2DHG channel have enabled the lowest p-type contact resistivities [38] in GaN/AlN pFETs [39], as discussed in section 3.3. However, the presence of these p-doped contact layers require complicated fabrication process to monolithically integrate the GaN/AlN pFET with its n-type analog, the AlN/GaN/AlN HEMTs [54]. The demonstration of the In-GaN/AlN 2DHG opens up the possibility of a better alternative in the form of selective-area regrown InGaN contacts. In a GaN/AlN heterostructure, the GaN layer is etched away selectively in photolithographically-defined ohmic/access regions and InGaN is *regrown* in those regions. This should yield high-density InGaN/AlN 2DHGs in the ohmic/access regions which makes a 2D-2D valence band contact to the GaN/AlN 2DHG under the gate. This should lower the p-type contact resistances in these pFETs even further, while maintaining integration possibilities for wide-bandgap CMOS [53, 137]. Details are discussed in chapter 3, 5, 6.

2.6 Conclusions
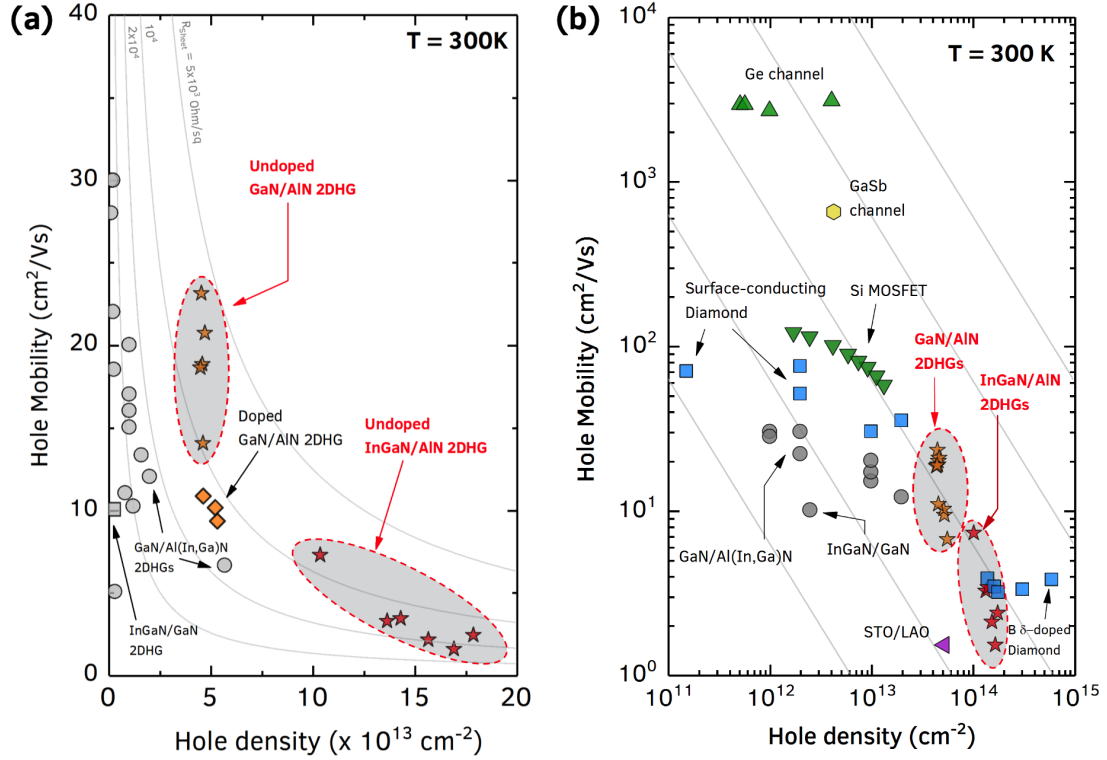
Figure 2.21: Comparison of room-temperature transport properties of 2D hole gases presented in this chapter with prior work. (A) Comparison with previously reported 2DHGs in nitride heterostructures [12, 13, 14, 15, 16, 17, 18, 19]. Unless labelled, the heterostructures have Mg-doping. The doped as well as undoped structures reported in this work have much higher hole densities and decent mobilities, enabling record high p-type conductivity of ~6 kΩ/sq. (B) Comparing across other semiconductor material systems such as oxides $SrTiO_3/LaAlO_3$ [20], surface-conducting diamond [21, 22, 23, 24], strained Ge/SiGe [25, 26, 27], Si inversion channels [28], and GaSb/InGaAs [29], this work has the highest room temperature hole density, and the highest conductivities among wide-bandgap semiconductors (III-nitrides, oxides, diamond).

How do the observed polarization-induced 2D hole gases in the GaN/AlN and InGaN/AlN heterostructures demonstrated in this chapter compare to those reported previously in nitride semiconductors, and in general to hole gases cutting across various semiconductor material systems? This is shown in **figures 2.21 (a,b)**. **Figure 2.21 (a)** shows that the 2DHG densities of $p_s \sim 5 \times 10^{13}$

cm^{-2} measured the undoped and doped GaN/AlN heterostructures are close to the limit of the difference in polarization between AlN and coherently strained GaN. This is the dual of the 2D electron gas, where the corresponding limits are also seen in binary AlN/GaN heterojunctions. The hole densities are much higher than previously reported 2D hole gas densities in nitride semiconductors [12, 13, 14, 15, 16, 17, 18, 19, 126].

In fact, these densities are among the highest among all semiconductor heterostructures, including SrTiO$_3$/LaAlO$_3$ [20], surface-conducting diamond [21, 22, 23, 24], strained Ge/SiGe [25, 26, 27], Si inversion channels [28], and GaSb/InGaAs [29] as shown in **figure 2.21 (b)**. Only B δ-doped diamond has a higher sheet hole density, however the surface nature of the 2DHG makes them unreliable. Introducing In in the strained GaN channel pushes the already high 2DHG density in the channel to $p_s > 1 \times 10^{14}$ cm^{-2}, which is just an order lower than the 2D crystal limit of $\sim 10^{15}$ cm^{-2}.

Compared to other semiconductors, the 2DHG mobilities in the wide-bandgap nitrides are not on the high side because of the high valence band effective mass of both heavy and light holes [157] in GaN due to its large bandgap. Narrower bandgap semiconductors such as Ge/SiGe and GaSb/InGaAs heterojunctions show higher 2D hole gas mobilities due to smaller valence band effective masses. However, narrow bandgaps also mean limited capacity to handle high voltages, limiting them to low power applications. The large bandgap of the III-nitride semiconductors means that the high 2DHG densities can be modulated effectively with a gate, because the semiconductor intrinsically is capable of sustaining much larger electric fields.

These record high (In)GaN/AlN 2DHG densities and high mobilities are

made possible by using a combination of N-rich nucleation layer and IBLs to suppress the degradation of the density control and transport properties of the 2DHG by surface segregation of Si and O impurities. Though this technique was demonstrated for MBE grown structures on AlN on sapphire templates, the same principles apply to MOCVD growths and to AlN films grown on other substrates (e.g. Silicon, SiC, single-crystal bulk AlN etc). These findings are also important for UV photonic devices where p-type layers are grown on the top of Si-doped n-layers. Similar precautions must be taken to avoid undesired compensation of the very low hole densities and reduction in their mobilities. The same issues are also expected to arise if the polarity of the films are flipped, and a 2DEG is generated at the GaN/AlN interface on N-polar AlN buffer layer. With the rising relevance of AlN as the platform for UV photonics and future RF electronics [137, 53], significant interest exists in using 2DEGs and 2DHGs on AlN to make RF p-channel [38, 39] and n-channel transistors [47, 54] and enable wide-bandgap RF CMOS-type devices. Combining the results of this work with recent advancements in homoepitaxial growths of AlN [64, 65] should enable fundamental scientific studies of 2DEGs and 2DHGs in such polar heterostructures and simultaneously enable significant technological advances. Additionally, the large density of holes in InGaN/AlN provide an epitaxial platform for investigation of scientific phenomena by possible integration of other compatible materials [33] such as ferrimagnetic Mn_4N. AlGaN/AlN heterostructures designed using similar principles as presented here could be used for applications which need $p_s < 5 \times 10^{13}$ cm^{-2}.

The discovery of the undoped 2D hole gas in (In)GaN/AlN heterostructures thus offers an attractive, clean, and technologically relevant platform to study the materials science and physics emerging in wide-bandgap and polar

semiconductor heterostructures due to very large built-in electric fields. Strong effects of tunneling and Rashba-induced spin-orbit coupling are expected in these structures. The first unambiguous observation of the elusive polarization-induced 2D hole gas in undoped nitride semiconductor heterostructures thus completes a long search for its existence. Because of the fundamentally different origin of the 2D hole gas in the nitrides in the intrinsic polarization fields from broken inversion symmetry, this form of doping is expected to scale down to the individual unit cells, and not be affected by random dopant fluctuations. Future generations of small transistors can take advantage of, and someday depend on this unique scaling property of polarization-induced doping - now available in both the n-type and p-type recipes.

2.7   Future Directions

Similar to how the discovery of the undoped AlGaN/GaN 2DEG [99] unmasked the physics of polarization in III-nitride semiconductor hterostructures [100], the discovery of the undoped GaN/AlN 2DHG presented in this chapter opens up new scientific questions. It also allows new experimental investigations. This section lays out these open scientific questions for future direction of research.

- **Experimental strategies to improve room-temperature GaN 2DHG mobilities through strain engineering**

  Room temperature mobilities of holes in GaN are limited by acoustic phonon scattering [5, 128]. It has been predicted that the phonon limited hole mobility can be enhanced by applying suitable in-plane tensile strain

in a bulk GaN crystal and pulling the GaN split-off valence band (VB) up [128]. Since the GaN layer in the GaN/AlN 2DHG is already under high compressive strain of 2.4%, this route is not feasible. Instead Bader et al. [5] proposed application of *uniaxial* (1) tensile strain perpendicular to the current flow, or (2) in-plane compressive strain along the current flow direction. Both these configurations should reduce the heavy hole effective mass and hence boost the phonon limited hole mobility. These predictions however have not yet been validated experimentally. Experimental demonstration of this effect will be very valuable for the theoretical understanding of the GaN VB physics. **Figure 2.22** shows the possible experimental setups to test this theoretical prediction.

In-plane, uniaxial strain relaxation is predicted to increase the room temperature hole mobilities in GaN/AlN heterostructure from ~ 25 cm^2/Vs at 2.4% compressive strain to ~ 50 cm^2/Vs in fully relaxed state [5]. A fin structure [156] can be used to experimentally test the effect of strain relaxation on the GaN/AlN 2DHG. The experimental realization is shown in **figure 2.22 (a)**. The etched fin should result in strain release in the shorter dimension. Since a dry etch results in sloped etch profile [158] which might not be efficient in releasing the strain, a combination of wet and dry etch to make vertical profile should be ideal. As-grown Mg-InGaN contact layers (see chapter 3) can be used to contact the 2DHG at the edges of the fin. This experiment can also be used to probe the orientation dependence of the 2DHG mobility by designing suitable masks. Further, by taking advantage of the higher lateral etch rate of AlN compared to GaN in hot phosphoric acid [159], T-shaped fins could enhance the strain relaxation in the GaN layer.
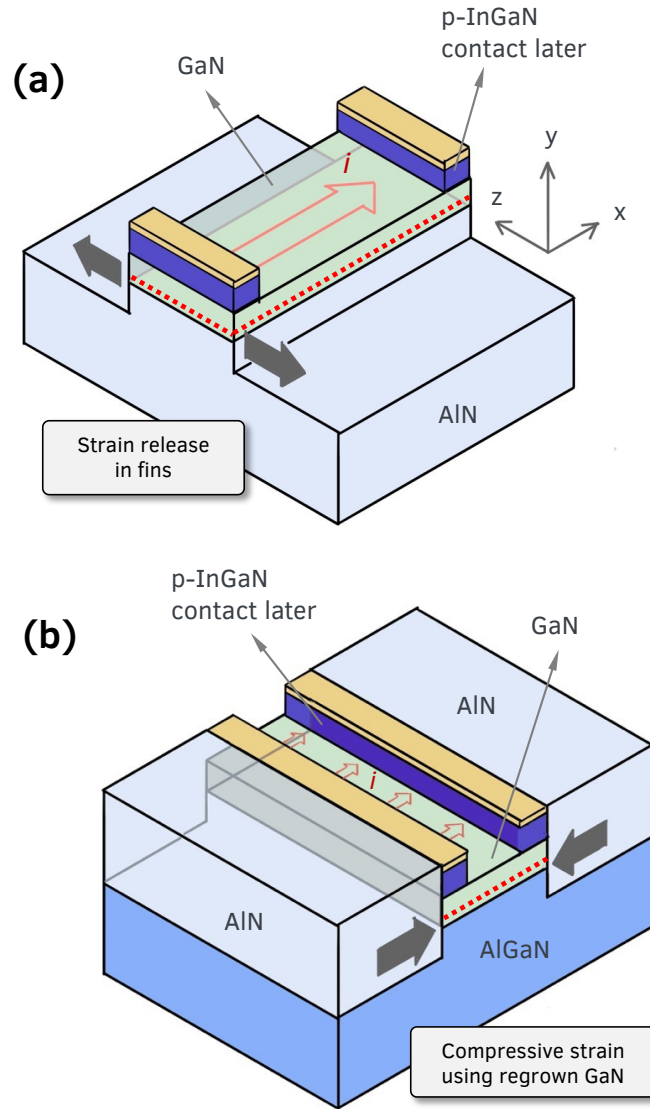
Figure 2.22: Strategies to increase the 2DHG mobility in GaN by applying a uni-axial, in-plane strain. The current flows along x direction, represented by the red hollow arrow. (a) the compressive strain in the pseudomorphic GaN layer on AlN is released by forming narrow fins parallel to the current direction. This is strain relaxation expected to result in a 2× room temperature mobility boost. (b) Compressive strain parallel to the current flow is applied to the pseudomorphic GaN on AlGaN, by regrowing AlN layers in trenches. This should result in 3× boost in hole mobilities. The ohmic contact is made through Mg-InGaN layers. *The schematics are modified and updated from Bader et al. [5]*

Application of a uniaxial, in-plane compressive strain along the carrier

flow in the GaN/AlN 2DHG is expected to increase the room temperature

mobility from $\sim$ 25 cm^2/Vs at 2.4% compressive strain to $\sim$ 75 cm^2/Vs at 4.8% [5]. This can be potentially achieved by selectively etching trenches and regrowing AlInGaN layer with larger lattice constant than GaN. However, when regrown on AlN buffer layer, the regrown AlInGaN layer will *always* be compressively strained. Hence, a better configuration for this experiment will be to use an GaN/AlGaN 2DHG and selectively regrow AlN regions. This is shown in **figure 2.22 (b)**. The 2DHG still remains in GaN and as-grown Mg-InGaN ohmic layers are used to connect to the 2DHG. AlN is then regrown in etched trenches at the ends of the channel region. Since AlN on AlGaN is tensile strained, the AlN regrowth region will apply the compressive strain to the GaN channel. The mobility can be extracted from either a Hall-bar configuration or from the channel conductivity. A controlled experiment with a series of trench, channel thicknesses should reveal the experimental effect of varying the compressive strain along the current direction.

- **Route to higher 2DHG mobilties through lower charge densities**

The room temperature mobility of the GaN/AlN 2DHG is limited by acoustic phonon scattering [5], which is a function of both temperature T and 2DHG density p_s. **Figure 2.23** shows the estimated dependence of the AP- and POP-limited GaN/AlN 2DHG mobility on p_s calculated using equations (2.3) and (2.4). Clearly, another possible route to higher room temperature mobilities is to reduce the 2DHG density.

In an FET structure, the 2DHG p_s is controlled electrostatically by the gate voltage V_G. The dependence can be extracted through a capacitance-voltage measurement. By then measuring the change in channel conductance g_D as function of gate voltage the carrier mobility μ_p can be extracted
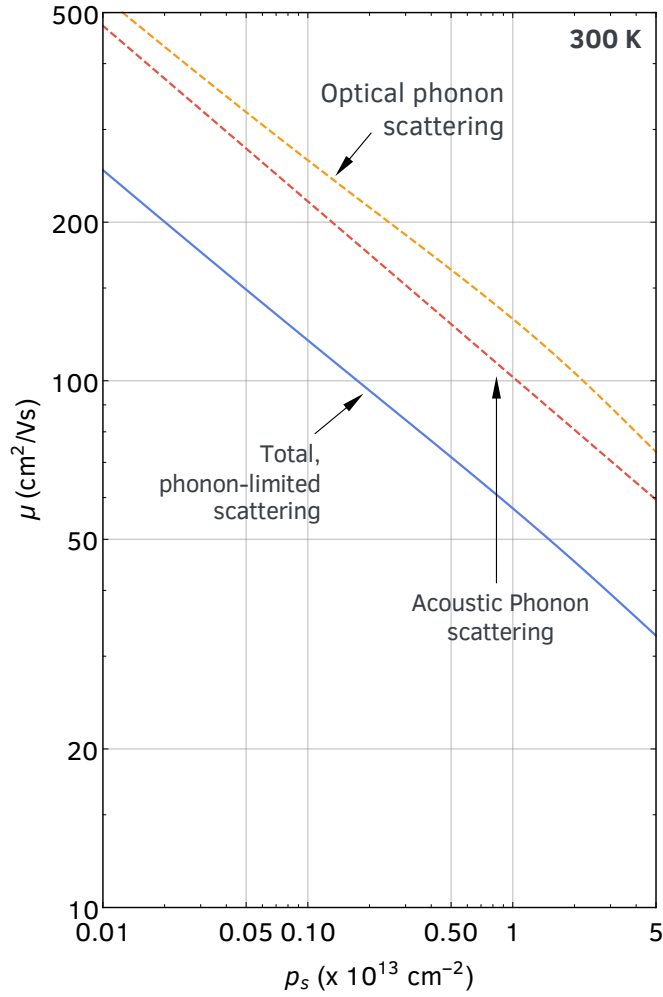
Figure 2.23: Room-temperature, phonon scattering limited mobility of a GaN/AlN 2DHG as a function of 2DHG density, assuming single parabolic valence band [8, 30]. The 2DHG mobility is expected to increase if the density is reduced either electrostatically by applying a gate voltage, or by tuning the polarization-difference at the interface using alloys.

through the relation $g_D(V) = q_e.\mu_p.p_s(V)$, where q_e is the electron charge. The resultant *field effect* (FE) mobility as a function of hole density will be valuable data to probe the hole scattering mechanisms in GaN. This is well studied in GaN 2DEGs [160], and 2DHGs on other semiconductors [161] but the lack of high-conductivity GaN 2DHGs till recently has held back the FE mobility study of holes in GaN. A couple of reports [32, 17]

have extracted *Hall* mobility as function of p_s by varying the polarization-difference across different samples, however a FE mobility is much more valuable for modelling since it is extracted from a single sample, and hence all other variables are held constant. FE mobility is the relevant mobility for electrical conductivity in a transistor channel.

Preliminary FE mobility extracted from an early-generation GaN/AlN pFET [31] is shown in **figure 2.24 (a)**. The data needs to be taken with some caution since the CV curve and the conductance were measured on different structures on the same die. Nevertheless, this serves as a useful starting point. The density dependent Hall mobilities reported by other groups [32, 17] are also plotted for reference.
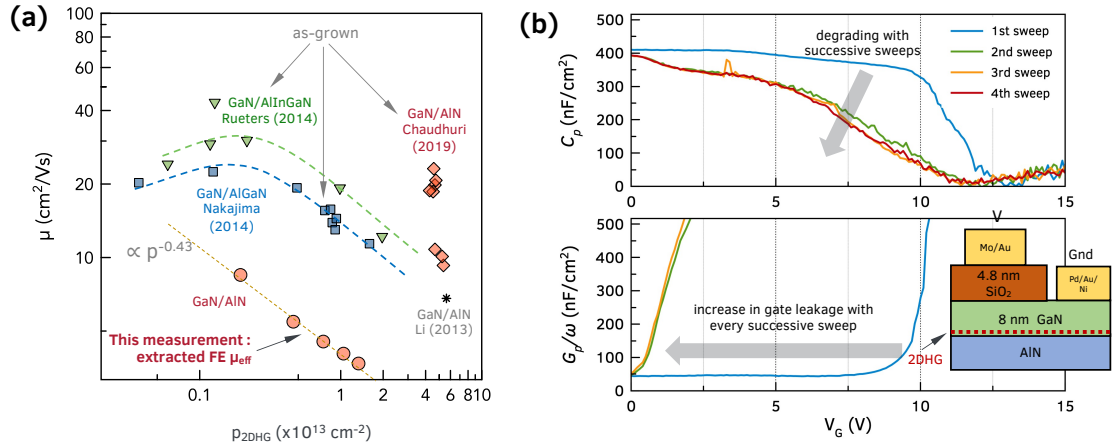
Figure 2.24: (a) Initial results from field effect mobility measurements from a GaN/AlN 2DHG. The data was extracted from a GaN/AlN FET with L_G = 20 μm, reported in Bader et al. [31]. The extracted mobilities are lower than the Hall mobilities, and show an increase with decrease in densities. Also plotted are Hall mobility as a function of density reported by other groups [32, 17]. (b) Capacitance and normalized conductance vs applied gate biases on a p-MIS-HFET (from device in figure 3.12). The capacitance value at 0 bias agrees with the expected value from the gate stack (inset). However severe degradation of the $\sim$ 4 nm SiO_2 gate dielectric device is observed over successive measurements.

Currently, the main challenge preventing reliable extraction of FE mo-

bility is the high gate leakage and device degradation in the state-of-art GaN/AlN 2DHG pFETs. A representative CV measurement for a scaled GaN/AlN p-MIS-HFET is shown in **figure 2.24 (b)**. The first CV sweep looks reasonable with the capacitance value agreeing to the expected gate structure and low leakage (indicated by the normalized conductivity) till the channel pinch-off at ~10 V. Successive voltage sweeps however degrade the device and the gate leakage increases with every sweep. Clearly, p_s in the channel cannot be extracted from these unreliable, unrepeatable CV profiles. The gate leakage are being addressed in the future generations of GaN/AlN pFETs (see section 3.6). Field effect mobility, not just at room temperature, but also for low temperatures, can then be extracted and analyzed.

- Along the same lines, another way to control the 2DHG density is to make use of its polarization-induced origin. This offers epitaxial control on the 2DHG densities by tuning the polarization difference across the interface by **incorporating alloys** in the barrier or channel layer. **Figure 2.25** shows the calculated polarization-induced fixed charge at the metal-polar GaN/AlGaN and AlGaN/AlN interfaces.

Initial growths of AlGaN/AlN 2DHGs have resulted in resistive films. Two samples with 15 nm thick AlGaN films of 25% and 75% Al composition were grown on an AlN buffer with IBLs, along with a control GaN/AlN 2DHG sample. The control sample showed a sheet resistance of $\sim$ 7 kΩ/sq at room temperatures. The AlGaN/AlN samples however were too resistive to be measured by Hall effect with resistances $>$ 10^5 Ω/sq.

Why are the AlGaN/AlN films resistive, whereas InGaN/AlN films (stud-
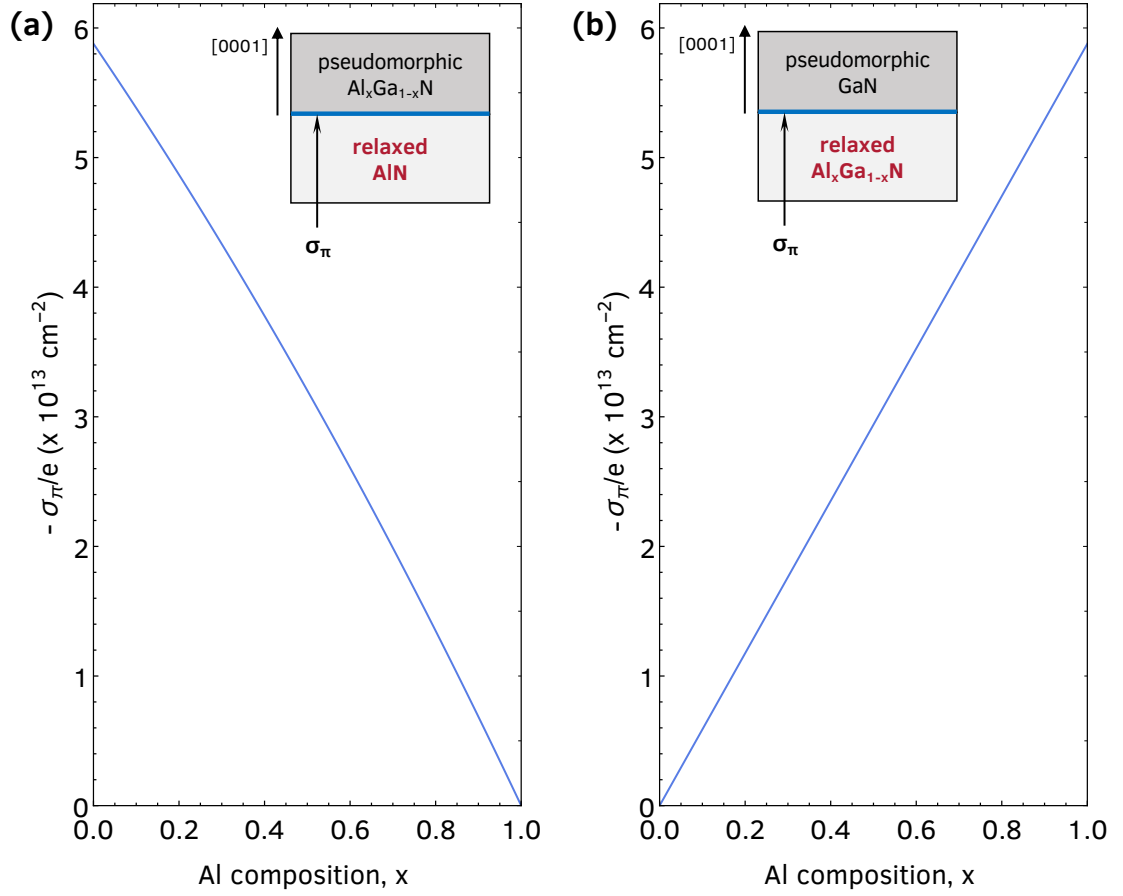
Figure 2.25: Polarization-induced fixed charge density expected at the metal-polar AlGaN/AlN and GaN/AlGaN heterointerfaces as a function of Al composition. The top layer is assumed pseudomorphic to the relaxed buffer layer. It should be possible to tune the 2DHG density by varying the Al composition during epitxial growth.

ied earlier in this chapter) grown under similar conditions, show high conductivity 2DHGs? This discrepancy is explained by taking a closer look at the charge densities and dominating scattering mechanisms.

Similar to the InGaN/AlN 2DHG, the hole mobilities in the AlGaN/AlN 2DHG are expected to be limited by alloy disorder scattering. **Figure 2.26** compares the expected transport of the 2DHG in AlGaN/AlN heterostructure with the 2DHG in InGaN/AlN heterostructure. **Figure 2.26 (a)** shows the alloy disorder limited mobility μ_{Alloy} as a function of alloy composi-
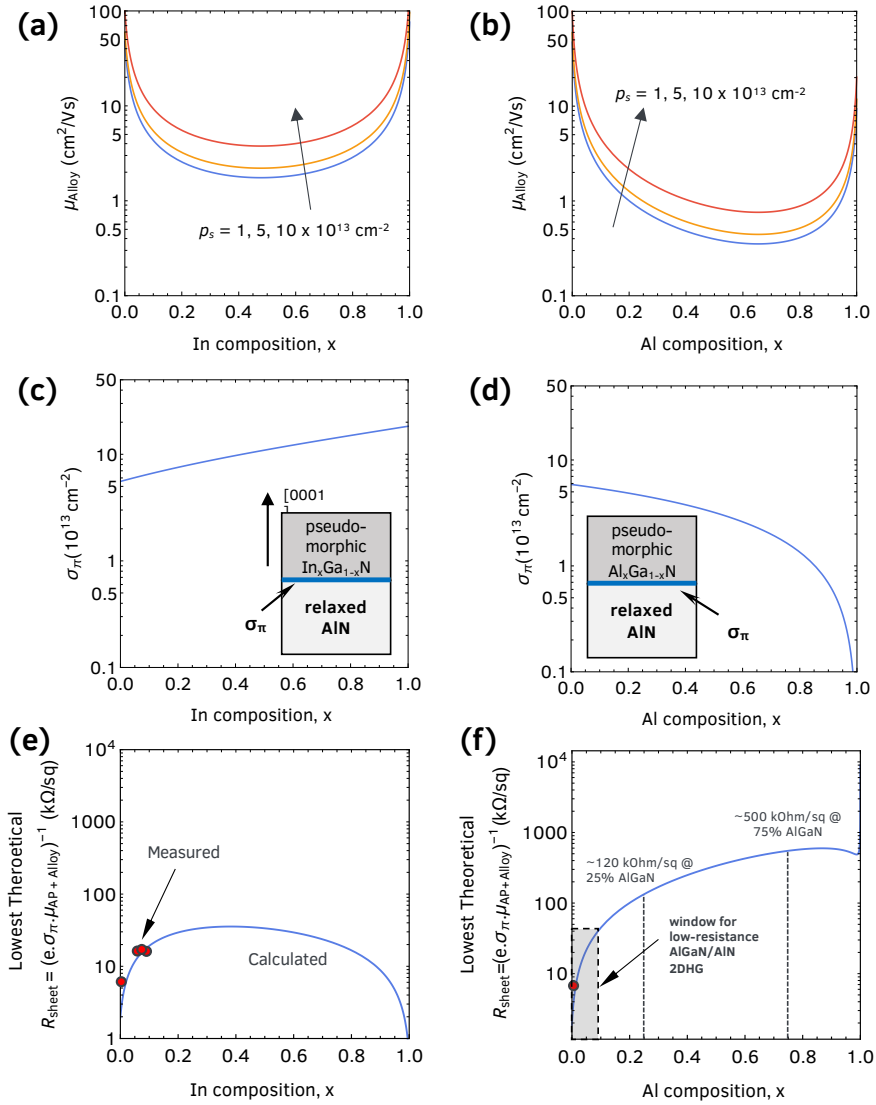
Figure 2.26: Comparison of the expected transport properties of a metal-polar InGaN/AlN 2DHG and AlGaN/AlN 2DHG. Due to low polarization-induced hole densities and high alloy-disorder scattering, the AlGaN/AlN 2DHGs are expected to have high sheet resistances > 100 kΩ/sq at room-temperatures for Al composition > 20%. This model predicts a small-window of Al compositions of 0-10% to obtain conductive AlGaN/AlN 2DHGs.

tion for InGaN/AlN 2DHG, calculated using equation (2.11). The curves for three different 2DHG densities, 1, 5, 10 $\times 10^{13}$ cm^{-2}, are shown. The alloy limited mobility has a characteristic U-shape, with the lowest mobility $\sim$ 1 cm^2/Vs at 50% InGaN. **Figure 2.26 (c)** shows an *increase* in the

polarization-induced charge σ_π with increase in indium composition, assuming a pseudo-morphic InGaN layer. This should correspond to the 2DHG density if a suffienciently thick InGaN layer is grown. **Figure 2.26 (e)** shows the calculated resultant sheet resistance $R_{sheet} = (q_e p_s \mu_p)^{-1}$, where $\mu_p = (\mu_{AP} + \mu_{Alloy})^{-1}$ is room-temperature mobility limited by alloy scattering and acoustic phonon scattering (from equation (2.10)), $p_s = \sigma_\pi$ is the 2DHG density, and e is the electron charge. Thus, R_{sheet} represents the theoretical lowest room-temperature sheet resistance attainable in the InGaN/AlN system. The calculation predicts a $R_{sheet} \sim 10$ kΩ/sq at In compostion $< 10\%$, which agrees well with the experimental data from **table 2.3**.

Along the same lines, the expected alloy disorder limited mobility μ_{Alloy} as a function of alloy composition for AlGaN/AlN 2DHG is shown in **figure 2.26 (b)**. Similar U-shaped curve is is seen, with the lowest mobility < 0.5 cm^2/Vs due to a higher valence band offset between AlN and GaN compared to InN and GaN. σ_π at the AlGaN/AlN interface *decreases* with increase in Al composition, shown in **figure 2.26 (d)**. This results in the expected sheet resistance R_{sheet} to monotonically increase with the Al composition as shown in **figure 2.26 (f)**. The expected sheet resistances of 2DHGs in 25% AlGaN/AlN and 75% AlGaN/AlN are 120 and 500 kΩ/sq respectively. This low 2DHG density combined with the high alloy disorder scattering could be the reason why the AlGaN/AlN films were found to be resistive experimentally. High-composition AlGaN/AlN 2DHGs therefore might not be suitable for transport experiments. But it should be worth growing AlGaN/AlN heterostructure with 0-10% Al composition to validate the model in **figure 2.26 (f)** and investigate the transport

in AlGaN/AlN 2DHGs.

On the other hand, the effect of alloy scattering should be minimal in a GaN/AlGaN 2DHG, since the mobile holes reside in the binary GaN channel. The 2DHGs in these heterostructures are therefore expected to result in higher phonon-limited mobilities at lower densities. A controlled study as a function of AlGaN composition will be very valuable to determine the mobility as function of sheet density. Other groups have reported [32, 17] similar series of growths, as shown in **figure 2.24 (a)**. It will also be interesting to determine whether there exists a trade-off between density and mobility for application in transistors.

- **What is the dominant extrinsic scattering mechanism limiting low temperature mobilities of the undoped 2DHG?**

  Room-temperature mobility of holes in very high purity GaN has been shown to be limited by acoustic phonon (AP) scattering [5]. However the scientific question of which extrinsic scattering mechanism dominates at low temperatures, i.e. when the phonons are frozen out, still remains open. The answer to this question will determine the upper limit of GaN hole mobility. Currently the highest hole mobilities in GaN is ~200 cm^2/Vs, in the undoped GaN/AlN 2DHGs. Because of their thermal activated nature, holes in a Mg-doped GaN layer freeze-out upon cooling and hence no investigations into their low temperature transport has been possible so far. The GaN/AlN 2DHG not only survives down to 10 K, but also becomes more conductive upon cooling - thus making it the perfect platform to study the extrinsic scattering mechanisms in this carrier system. The 2DHG heterostructures studied here have binary semiconductors and have minimal alloy scattering and impurity scattering from

dopants, hence it is conceivable that the extrinsic scattering mechanism is scattering due to charged dislocations [162] or interface roughness scattering [163, 164].

The 2DHGs studied in this chapter are grown on AlN on Sapphire template substrates with dislocation densities $\sim 10^{10}$ cm^{-2}. The recent availability of single-crystal AlN substrates with 6 orders of magnitude lower dislocation densities have made it possible to experimentally observe the effect of dislocations on the 2DHG. Initial results [30] show an increase in low temperature mobilities reaching upto 280 cm^2/Vs at 10 K (more details in appendix B). Carrier screening is also expected to play a role at these high 2D densities.

It is possible that the low temperature 2DHG mobilities could be improved by sharper interfaces. The very high charge densities and the built-in field in the GaN [7] means the 2DHG is "pressed up" against the interface. Therefore a small variation in the roughness of the GaN/AlN interface could cause a large suppression in mobility previous. Theoretical studies performed in N-polar GaN/AlGaN 2DEGs [163] and highly confined 2DEGs [164] should help guide a controlled experimental study.

- One of the advantages of the polarization-induced nature of GaN/AlN 2DHG is the relatively high mobility at low temperatures, which makes it suitable for **magnetotransport experiments**. Analysis of longitudinal and Hall resistances from a suitably designed gated Hall bar at high magnetic fields and low temperatures should be very valuable probe of the GaN valence band. Although observed in other 2DHG systems [165, 166, 167, 168, 169], quantum transport phenomena such as Shubhinikov de Haas (SdH) oscillations have not been observed in GaN 2DHGs

so far. As done for GaN 2DEGs [99], SdH oscillations can be used to better understand the valence band of GaN, for example, enable the first experimental measurement of VB hole effective mass m_{eff} to compare to the spread in theoretical predictions [157].

The low temperature 2DHG mobilities of $\mu_p \sim 200 - 300$ cm^2/Vs means these observing quantum magnetotransport phenomena require access to very high magnetic fields (B) of 33-50 T and above to satisfy the condition $\mu_p.B > 1$ for observation of SdH [129]. Facilities such as National Magnetic Field laboratory (Maglab) offers access to such large magnetic fields, both pulsed and continuous. The dependence of FE mobility of the 2DHG on applied gate voltage might also be helpful, since lower B might be sufficient if 2DHG mobility rises with decrease in 2DHG density.

These experiments are currently limited by ohmic contacts. State-of-art Mg-InGaN contact layers, which show record low contact resistances at room temperatures, become more resistive upon cooling thanks to freeze-out of the thermal-generated carriers (see **figure 3.6**). Even though the channel itself gets more conductive, the contact resistance dominates the measured signal. **Figure 2.27** shows the longitudinal and Hall resistances $R_{xx/xy}$ measured from a Hall bar configuration as a function of temperature. The resistance, initially decreasing with temperature T, rises sharply below 10 K. This unfortunately makes it unsuitable for magneto-transport measurements which are usually performed at $T < 1$ K. Soldered indium contacts to the 2DHG do not show this increase in resistance at low temperatures, as seen in **figure 2.5**. However, the use of these large-area, hand-made indium contacts result in high noise levels during the sensitive magnetotransport measurements of $R_{xx/xy}$. In the future, regrown n++
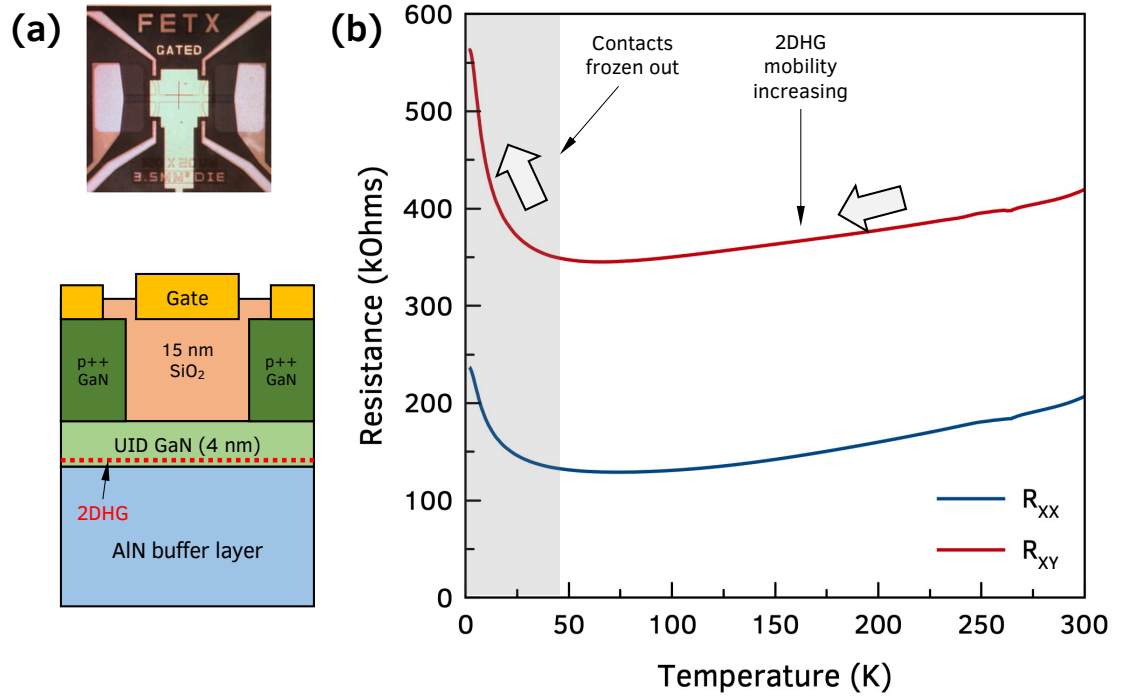
Figure 2.27: (a) Schematic of a gated Hall bar fabricated on a GaN/AlN 2DHG sample. A 15 nm SiO_2 gate dielectric was used to suppress gate leakage. (b) The measured R_{xx} and R_{xy} versus temperature at $B = 0$. The resistances initially decrease with temperature because of the increase in 2DHG mobilites, but then start increasing. This is expected due to the freezing out thermally generated holes in the ohmic contact layers (also see figure 3.6 for supporting data). This increase of resistance at $T < 20$ K is not observed when large-area soldered indium contacts are used instead of ohmic-contact layers, as shown in figure 2.5. The non-zero value of R_{XY} indicates a high mixing between the longitudinal and perpendicular current components, indicative of either non-uniformity of the sample or improper Hall bar design. These issues need to be addressed before the next magnetotransport experiment.

GaN tunnel contacts or metallic sidewall contacts might offer a solution to this bottleneck.

- **What are the velocity limits of 2D Holes in GaN?**

So far the discussion has been about the low field hole transport. However the high (electric) field transport of carriers is also valuable especially for high-speed RF transistors. The intrinsic speed, characterized by the cut-off frequecy f_T, of a pFET with gate length L_G is determined by the hole

transit time and is given by $f_T = L_g/v_s$. v_s here is the average source injection velocity, referred to sometimes as saturation velocity. The saturation *electron* velocity in GaN has been experimentally found to be a function of the charge density [49, 170, 48] (see section 4.4.2). This is because polar optical phonon scattering locks the Fermi level at optical phonon energy of 92 meV [48]. The lack of high-conductivity 2DHG so far means no experimental measurement of the saturation velocity of a GaN 2DHG has been reported yet. A saturation velocity of 6.6 $\times 10^6$ cm/s was extracted using photo-assisted method [171] in low Mg-doped bulk GaN. With the GaN/AlN pFETs breaking speed records in WBG pFETs, the knowledge of the hole velocity limits will be very valuable to extract the speed limits of such pFETs. A density dependent velocity [170] can be extracted by using gated, highly-scaled TLMs with low resistance ohmic contacts. Alternatively, the velocity can also be extracted from a transit time analysis on a series pFETs with different L_g [49, 172]. The main challenges for these experiments are once again, low-resistance ohmic contacts and gate leakage.

- **Why does the (In)GaN/AlN 2DHG density change with temperature?**

  Interestingly, the purely polarization-induced GaN/AlN 2DHGs show a slight decrease in density with reduction in temperature, which remains a mystery and an open scientific question. The theory of polarization dictates a fixed charge density of σ_π ~ -5 $\times 10^{13}$ cm^{-2} at the metal polar GaN/AlN interface, which is then compensated by holes to form the 2DHG. Because no there is no thermal activation of carriers, the carrier density is not expected to change with temperature. This is what is observed in GaN 2DEGs [173].
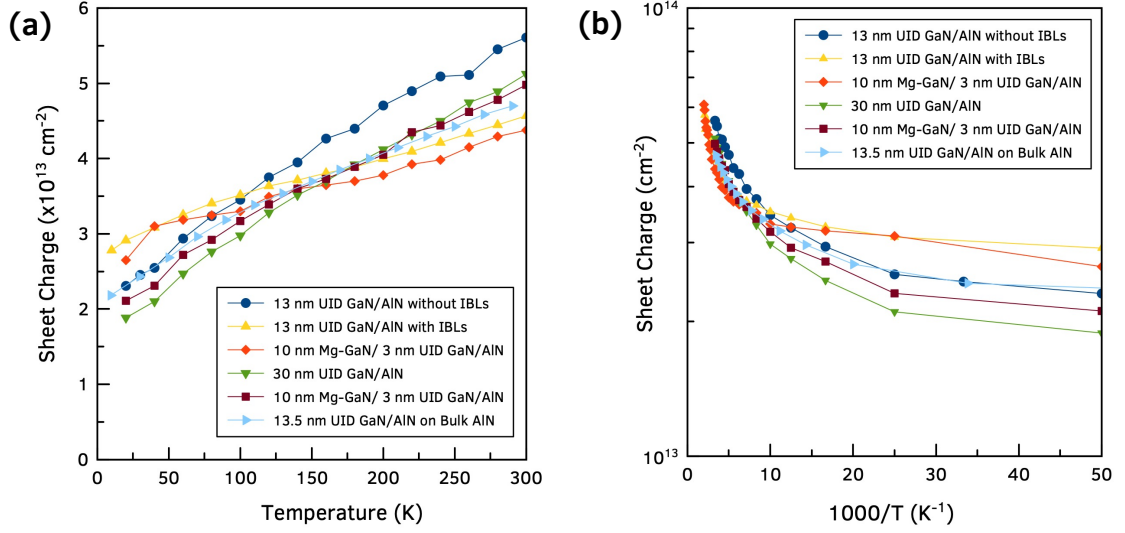
Figure 2.28: GaN/AlN 2DHG charge density as a function of temperature, plotted in a (a) linear scale and (b) log scale. The 2DHG density in these structures decrease almost linearly upon cooling, reaching almost half their densities at room temperature. This behavior is observed in samples with and without IBLs [8], with different ohmic contact scheme, and different substrates [33].

Figure 2.28 shows the measured charge density as a function of temperature across multiple GaN/AlN 2DHG samples. The room temperature 2DHG density of 4-5×10^{13} cm^{-2} agrees with the polarization theory, but interestingly the low temperature 2DHG density reduces to 2-3×10^{13} cm^{-2} at 10 K. This change is almost linear, different from thermally activated holes in Mg-GaN which freeze out exponentially. Interestingly, this behavior is observed across 2DHG samples grown on different substrates [33] (bulk AlN, AlN template), different buffer layer schemes (with and without IBLs in AlN buffer layer), different growth chambers, different UID GaN layer thicknesses and with/without a Mg-doped Ohmic contact layer. This trend is observed not just at temperatures below 300 K, but also at high temperatures upto 500 K (see **figure 2.7**). The origin of this behavior is therefore believed to be fundamental to the Ga(In)N/AlN 2DHG system.

Numerous hypothesis have been tested to explain this observation. The change in piezoelectric polarization component to the polarization difference due to the difference in thermal expansion coefficient does not explain this magnitude of change. Neither does the change in surface barrier height with temperature. One possible explanation is that the measured 2DHG Hall density is due to the parallel conduction of heavy holes (HH) and light holes (LH), and is also a function of their individual mobilities. Due to the difference in temperature dependence of the HH and LH mobilities, the apparent Hall density changes with temperature. Experiments combining temperature dependent CV profile and magnetotransport should help test this hypothesis.

- **What is the origin of the higher than expected 2DHG densities in the InGaN/AlN heterostructures?**

  Low composition (In <10 %) InGaN/AlN 2DHGs have been grown on different wafers and MBE systems and the high densities of $> 10^{14}$ cm^{-2} are found to be robust and repeatable. Even though these 2DHG densities are expected to be higher than those of GaN/AlN 2DHGs, quantitatively the densities are much higher than predicted at the given compositions. According to **figure 2.15 (d)**, 2DHG densities of $> 10^{14}$ cm^{-2} are expected only at very high In compositions of >90 %, and not at <10 % grown in this work. These values cannot be explained by the accepted polarization theory [100, 1] or the recently proposed corrected polarization constants [174] for III-nitride semiconductors. The origin of these large hole densities is therefore an open question which requires further investigation. A controlled study of transport in InGaN/AlN samples with a series of InGaN thickness by keeping the composition constant, or vice versa should

yield valuable insights and help provide the answers.

CHAPTER 3

GHZ-SPEED GAN/ALN P-CHANNEL HETEROJUNCTION FIELD EFFECT TRANSISTORS

3.1 Introduction

AlGaN/GaN HEMTs are used for switching at high voltages or high-power high-frequency signal amplification [101]. However integration with other low voltage section of the circuits is challenging. In most applications, the high-power GaN HEMT switch is driven by low-power silicon complementary metal-oxide-semiconductor (CMOS) control integrated circuits (ICs) [175] at the gate side. From a circuit design perspective, the gate driver circuits do not need to handle high power and hence it makes sense to make use of the mature process technology that silicon CMOS offers. However different materials for different parts of the circuit limits the possibility of integration. The Si gate driver ICs are separate dies and need to be integrated at the package or circuit level, depending on size, using complicated interconnects. This introduces parasitic inductances and large voltage overshoots which limit the GaN HEMT switching speeds [176, 177]. In the bigger picture, this results in reduced efficiency of the switch, resulting in higher power consumption. With the rise of data centers, internet of things (IoT) etc, power conversion and switching is becoming more important by the day and any power loss during conversion is expected to significantly increase carbon footprint.

Monolithically-integrated gate drivers circuits for GaN power switches is thus desired. Having both the high-power and low voltage logic part of the circuit integrated on the same platform will reduce the efficiency loss due to

parasitics, and also shrink the component sizes as an added benefit. CMOS-logic based GaN circuits that can replicate the Si-CMOS gate driver circuitry is ideal. However, unlike Si where both p-channel and n-channel metal-oxide-semiconductor field effect transistor (MOSFET) are very mature technologies, GaN p-channel FET are far behind in terms of performance and development compared to their n-channel counterparts. This is mainly due to the challenges posed by the wide-bandgap property of GaN.

One way to get around the lack of high-performance pFETs is to use alternate circuit topologies such as direct coupled FET logic (DCFL) using just n-channel HEMTs [178, 179]. By combining enhancement-mode and depletion-mode GaN HEMTs, GaN integrated power ICs by industrial groups [180, 181, 182] have been demonstrated and are entering the markets. Even though this is a decent work-around which is also being pursued commercially, DCFL circuits have limitations of low yield, difficult fabrication processes and high temperature sensitivity. The realization of CMOS logic on GaN is expected to overcome these drawbacks, which is currently being held back by the lack of a high-performance GaN pFET.

This chapter demonstrates record performance in p-channel FETs on this AlN platform making use of the newly discovered high-conductivity GaN/AlN 2DHG. First the challenges holding back the GaN pFET performance are discussed, along with a survey of current GaN pFETs and how the community is overcoming or circumventing these challenges. The record p-type high-conductive channels provided by the GaN/AlN 2DHG serves as a perfect platform for p-channel FETs, and are investigated in detail. Record low resistance p-type ohmic contacts are demonstrated with specific contact resistivities down

to low-10^{-5} Ω cm^2 or contact resistance of < 5 Ω.mm. Both these developments from the material side have combined to improve the GaN/AlN pFET performance over the past 6 years and have demonstrated high currents upto 0.5 A/mm and speeds of 23/40 GHz. Thus, better materials supported by state-of-art device fabrication techniques have not only enabled the GaN/AlN pFETs on this AlN-platform, but taken them to territories never thought possible. Efforts and future plans to integrate this pFETs n-type transistors for CMOS demonstration are discussed in detail in chapter 6.

3.2   Current Challenges for GaN pFETs

Figure 3.1 shows the schematic of a field effect transistor (FET) - consisting of a channel controlled by gate and contact regions connecting the channel to the external circuits. The on-resistance R_{on} is determined by the sum of contact resistance R_c, access resistance R_a and channel resistance R_{ch}. A low on-resistance is desired to maintain a low knee voltage V_{knee}. In a normally-on device, the R_a and R_{ch} are determined by the as-grown sheet resistance of the 2D carriers [183]. The R_a and R_c affect the speed of the transistor (extrinsic cut-off frequency f_T) through the parasitic charging time $C_{gs}(R_s + R_d)$, where C_{gs} is the gate-source capacitance and $R_{s/d} = R_a + R_c$ are the source and drain resistances. The parasitic charging time adds to the intrinsic transit time of the carrier across a channel and degrades the f_T. Hence, low contact, access and sheet resistances are desired for maximizing the transistor performance.

Before moving to GaN pFETs, it is worth taking a closer look at GaN n-channel HEMTs to highlight what constitutes a "good transistor". In a GaN

HEMT, a high mobility 2DEG at the Al(Ga)N/GaN interface is used as the channel. The lack of impurities, high quality heterostructures with abrupt interfaces, conduction band effective mass of $0.2m_0$ (m_0 is the free electron mass) result in high 2D electron densities of $\sim 0.5-1\times10^{13}$ cm^{-2} with reasonably high room temperature mobilities of $1200-1800$ cm^2/Vs. The resultant low sheet resistances in the order of $300-200$ Ω/sq. combined with the high breakdown voltages make these HEMTs ideal for high-frequency, high power applications.
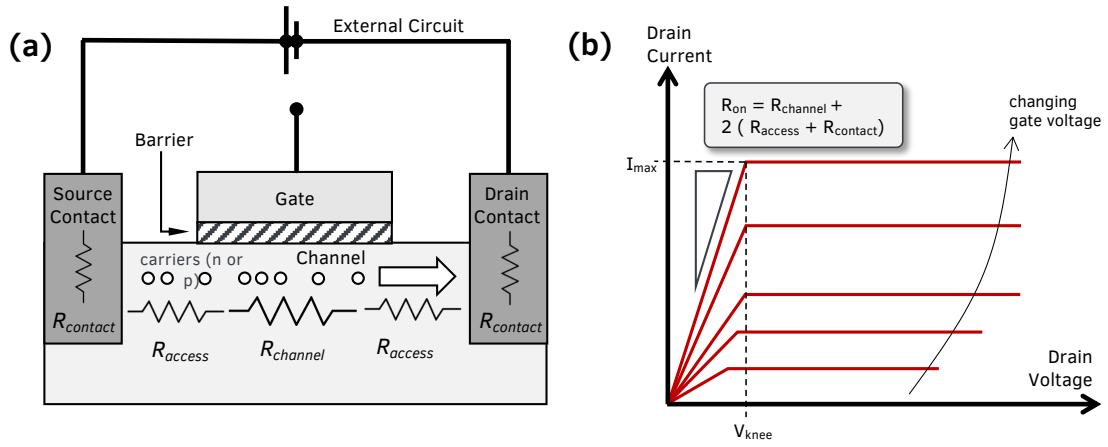
Figure 3.1: (a) Schematic showing a cross-section of a field effect transistor (FET). It consists of a conductive channel, connected to the external circuit through ohmic contacts. The gate capacitively controls the charge density in the channel, and therefore the current flowing through the channel. (b) A cartoon of a FET output characteristics showing the on-resistance R_{on}, the maximum drain current I_{max} and the knee voltage $V_{knee} = I_{max}.R_{on}$. R_{on} and V_{knee} is determined by the resistance components in (a). $V_{knee} \approx 0$ (very low R_{on}) is desired for best performance of the transistor.

Since the 2DEG transistor channel is buried under an insulating barrier, low resistance ohmic contacts are necessary to connect the transistor channel to external circuitry. The lowest contact resistances for GaN HEMTs are achieved through n++ regrown ohmic contacts. State-of-art contact resistances are typically in the order of 0.1 Ω mm (width normalized) and as low as 0.026 Ω mm [178, 158], which is very close to the theoretical limit [184]. These n++GaN re-

gions connect to the 2DEG through the sidewalls in a configuration very similar to n++Si ohmic well in planar Si n-MOSFET technology. High charge concentrations ([Si] > 1×10^{20} cm^{-2}) in the regrown GaN result in very low interface resistances between the two regions. Low-resistance ohmic contacts to AlGaN/GaN 2DEG are also formed by depositing alloyed metal contacts. Optimum alloying conditions yield contact resistances in the order of 0.3-0.6 Ω.mm which dependent on 2DEG density and barrier composition, which is higher than regrown contacts. The regrown ohmic technology has thus been one of the key enabler of ultra-scaled GaN RF HEMTs [54, 178], and are possible due to high levels of Si-type doping for n-type GaN.

Thus, high-conductivity 2DEGs and low resistances ohmic contacts through heavily Si-doped GaN regions are critical for the success of scaled GaN HEMTs for RF applications. Along the same lines, the complementary p-type realization of GaN FET requires a high conductivity 2DHG and a low resistance ohmic contact. However the wide bandgap/deep valence bands of GaN makes it orders of magnitude tougher to achieve these two requirements, and translates to the following challenges :

- Inefficient p-type doping of GaN :
  Magnesium is the common p-type impurity dopant in GaN [98]. However the thermal activation energy of 160 – 200 meV (dependent on Mg concentration) makes it inefficient compared to n-type Si doping (activation energy 15 meV). This results in <4 % of the Mg atoms in the GaN crystal contributing mobile holes of conduction at room temperatures [127]. Additionally, thermodynamics places an upper limit of ~ 10^{21} cm^{-3} on the amount of Mg atoms that can be incorporated into a GaN crystal

[185]. Pushing the Mg concentration more than this limit results in self-compensation [185] and also introduces crystal defects [186], thereby destroying the conductivity. Typical hole concentrations obtained in Mg-doped GaN is therefore limited to $10^{17} - 10^{18}$ cm^{-3}.

- Low hole mobilities :

  In a relaxed GaN crystal, the valence band consists of closely spaced heavy hole (HH) and light hole (LH) band at the Γ point separated by $\sim$ 5 meV. Majority of the mobile holes reside in the HH band with high (in-plane) effective mass of $\sim 1.5 - 2m_0$. It has been shown that the room temperature mobility of bulk of 2D holes are limited by acoustic phonon scattering [128, 5]. This limits room temperature mobility to < 50 cm^2/Vs, $\sim$ 30$\times$ lower than 1800-2000 cm^2/Vs seen in GaN 2DEGs. In fact, experimental room temperature hole mobilities of Mg-GaN is typically lower (5-10 cm^2/Vs) because of the added impurity scattering off Mg dopant atoms.

- Lack of low-resistance ohmic contacts :

  Because of the deep GaN valence bands, no metal exists with suitable workfunciton of > 7.5 eV to form an ideal ohmic contact to the valence band. Usual ohmic schemes for p-type GaN use nickel (Ni), palladium (Pd) or platinum (Pt) based metal stacks on heavily Mg-doped layers to yield typical contact resistances of $> 20 - 100$ Ω mm. Heavy p-type doping is also a bottleneck, which is necessary for low-resistance contact between metal and GaN,.

Motivated by the dream of realizing GaN CMOS operation, numerous groups have bypassed the low-conductivity Mg-doping by using polarization-induced 2DHGs as transistor channels to demonstrate p-type GaN FETs. The

various heterostructures used were briefly discussed in chapter 2. Notable reports from the early 2010s came out of the work at National Institute of Advanced Industrial Science and Technology in Tokyo [12, 133, 32] and RWTH Aachen [16, 17], who used a Mg-doped GaN channel on top of a standard Al(In,Ga)N/GaN HEMT heterostructure to form the 2DHG channel in parallel to the 2DEG. Recent reports (since 2018) include the work at MIT [60], who demonstrated a scaled self-aligned gate process to eliminate the high access resistances. Research group from HKUST demonstrated an enhancement mode GaN pFET by flourine (F)-treatment under the gate [126]. All the groups above successfully demonstrated GaN CMOS logic [58, 59, 60, 61, 13, 62] using their versions of pFET. Further details and discussion on the CMOS realizations are presented in chapter 6. However, these pFETs are still limited by low currents < 100 mA/mm due to the low charge densities in the channel. To overcome this, group at UCSB use a Mg-doped GaN/AlGaN super lattice to form multi channels [187], but they needed complex 2D geometry such as finFETs to electrostatically control the channel. The best numbers on currents are still 2-3 orders of magnitude lower than those seen in GaN n-channel HEMTs ($\sim 1\,A/mm$). Higher on-currents are desired to be able to efficiently integrate with the HEMTs and make use of the advantages a current matched CMOS circuit has to offer.

3.3 Mg-InGaN Ohmic Contacts to GaN/AlN 2DHG

In the last chapter, the undoped GaN/AlN 2DHGs were demonstrated which offer the record high-conductivity hole channels with high charge densities $\sim 5 \times 10^{13}\ cm^{-2}$. These should potentially serve as a good p-type channel for a transistor with low access and channel resistances. However, since the 2DHG

here is buried in an undoped insulating WBG material, the first step towards re-
alizing a device is to form low-resistance ohmic contacts to the external circuits.
In this section, record low-resistance contact to the GaN/AlN 2DHG, down to
few Ω.mm is demonstrated using as-grown Mg-doped InGaN contact layers.

As elaborated in the previous section, ohmic contacts to the valence bands in
p-type GaN faces fundamental limitations mainly because of its wide bandgap
E_g of 3.5 eV - the very property that makes GaN attractive for the high power
applications. The valence bands in GaN lie much deeper in GaN, $q\chi + E_g$ below
the vacuum level, where $q\chi$ = 4.1 eV is the electron affinity of GaN. To form an
ohmic contact, the metal should have high workfunction $q\phi_M > q\chi + Eg$ = 7.5 eV.
Typical metal workfunctions however are in the order of 4-5 eV, which makes
the metal-pGaN contact intrinsically Schottky. The energy band alignment is
shown in inset of **figure 3.2**. The characteristic energy barrier to overcome by
the holes in the valence band $q\phi_B$ for a thermionic emission (TE) is given by
$q\phi_B$ = $(q\chi + Eg) - q\phi_M - \phi_B$ thus represents the Schottky voltage that will be
dropped across the contact. A survey of the commonly used metals in III-nitride
semiconductor processing, along with their characteristic ϕ_B is presented in **fig-
ure 3.2**. Clearly, the most suitable metals for ohmic contacts to p-type GaN are
Pt, Pd, Ni, Au.

One way to circumvent this Schottky barrier is to use a heavily p-doped GaN
next in contact with the metal. This reduces the triangular barrier *width* which
the holes in the valence band see. This depletion width in the semiconductor de-
pends on the doping level. If the barrier is narrow enough, the carriers can tun-
nel through instead of going over, resulting in thermionic field emission (TFE)
or field emission (FE) of carriers at a voltage drop $< \phi_B$. The contact resistance
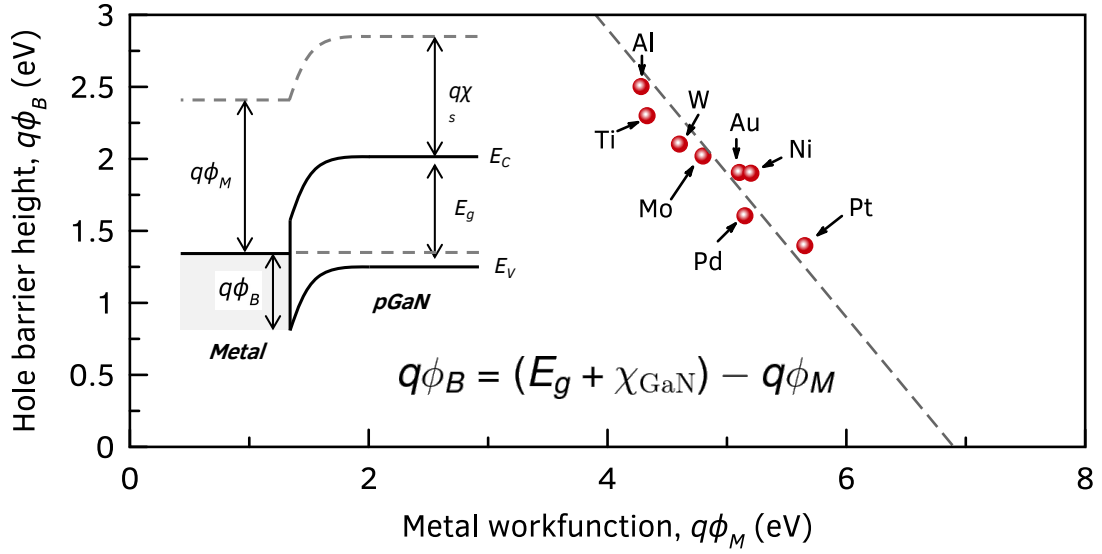
Figure 3.2: Hole barrier height for different metals used for p-type contacts on p-GaN. The inset shows the band alignment at the Schottky contact between the metal and p-GaN [34, 35, 36, 37]

is thereby lowered by increasing the carrier concentration in the semiconductor. In p-type GaN, the high ionization energy of Mg and solubility limits of incorporating Mg limits the hole concentrations to around $10^{17} - 10^{18}$ cm^{-3}.

Due to the two limitations listed above, typical specific contact resistances to p-GaN are in the order $10^{-2} - 10^{-5}$ Ω cm^2 [188, 189, 190], which is still orders higher than that of n-type contacts which show $10^{-6} - 10^{-7}$ Ω cm^2 for regrown ohmic contacts to 2DEGs. The high resistance of p-type ohmic limits not just the GaN p-channel transistors but also efficiency of the mature GaN LED technology [191]. Groups have investigated the effect of alloying the metal stack to reduce the ϕ_B. For example, annealing Ni in oxidizing ambient form NiO at the interface [192], or even use thin Mg-InGaN contact layers between the Mg-GaN and ohmic metal [193]. p-type ohmic contacts remain an major challenge in GaN, and wide bandgap semiconductors in general.

Hence, before making high performance transistors within these limita-

tions, it is important to engineer low-resistance ohmic contacts to the high-conductivity GaN/AlN 2DHG.

What happens if a p-type ohmic metal is deposited on the surface of a un-doped GaN/AlN 2DHG heterostructure? To test this, unalloyed Pd/Pt metals were deposited directly on an as-grown GaN/AlN 2DHG with a 15 nm UID GaN layer, labelled sample A, as shown in **figure 3.3 (a)**. Transfer length method (TLM) test structures [194] were used to extract the resultant contact resistance and sheet resistances. To best interpret the Schottky-like non-linear IVs, the TLM analysis was performed as a function of current. The TLM I-Vs and the extracted resistances are plotted in **figure 3.3 (b, c)**.
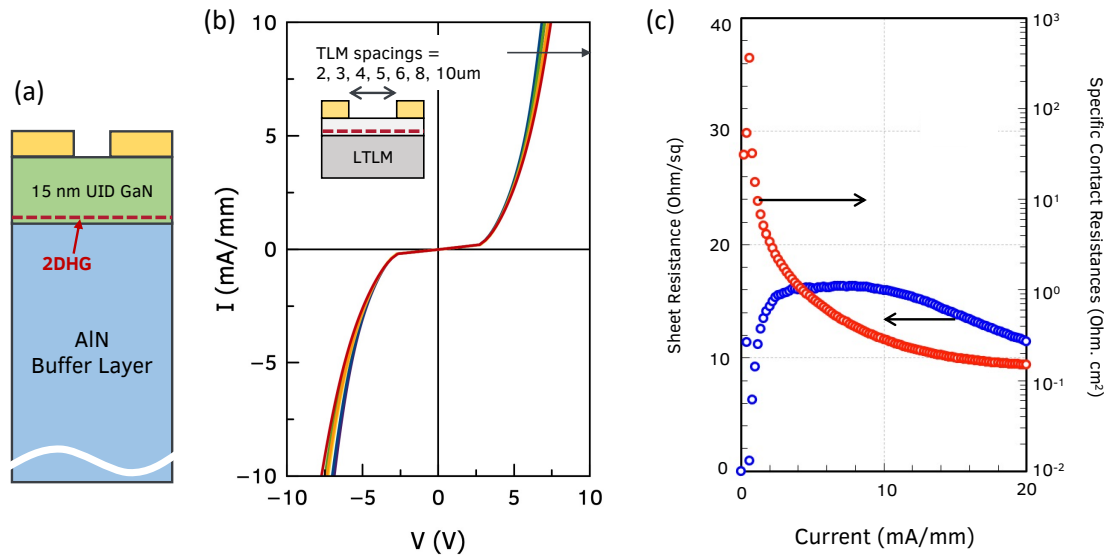
Figure 3.3: Schematic cross-section of ohmic metals deposited directly on an un-doped GaN/AlN 2DHG sample (b) TLM IVs showing non-linear Schottky-like behavior. (c) Extracted sheet and contact resistance from the TLM analysis as a function of excitation currents. This structure shows very high contact resistances of $> 10^{-1}$ $\Omega.cm^2$, which is not ideal for a transistor operation.

The extracted sheet resistance agrees to the as-grown sheet resistance measured via Hall on unprocessed samples. However, very high contact resistance of $> 10^{-1}$ $\Omega\,cm^2$ is extracted. The IV curves show Schottky-like non linear behav-

ior with a turn on voltage of 3-4 V. This high contact resistance is not unexpected as there a large and wide potential barrier for the electrons to overcome because of the undoped layer separating the 2DHG and metal. This is shown in the energy band diagram in **figure 3.4 (b)**. Clearly, this contact scheme of Pd/Pt on UID GaN is not suitable for the final objective of a high performance FET. Alternate contact schemes are desired to drastically reduce the contact resistance.

Table 3.1: Summary of the as-grown samples for ohmic contacts to undoped GaN/AlN 2DHG. All the samples were 15 nm UID GaN on ~450 nm of AlN buffer layer grown under the same growth conditions. Samples B1, B2, B3 had 15 nm ohmic contact layer grown on top of the UID GaN layer. The growth details are provided in appendix A.

Sample ID	Ohmic contact layer	[Mg] (cm^{-3})	as-grown R$_{sheet}$ (kΩ/sq.)	ρ_c @ 10 mA/mm (Ω.cm^2)
A	-	-	10	~10^0
B1	15 nm Mg-GaN	~1×10^{19}	10.79	~2×10^{-2}
B2	15 nm Mg-GaN	~4×10^{19}	12.73	~3×10^{-3}
B3	15 nm Mg-In$_{0.04}$Ga$_{0.96}$N	~1×10^{20}	10.88	~2×10^{-5}

For Mg-doped GaN, incorporation of highly p-type doped layers under the metal have shown to improve the contact resistivity to p-GaN [195]. A similar ohmic scheme is studied to investigate the effect of Mg-doped contact layers to the GaN/AlN 2DHG.

Towards this, a series of 3 GaN/AlN 2DHG samples were grown. The sample structures, labelled B1, B2, B3, are shown in **figure 3.4 (a)**. Each sample was grown using PA-MBE following growth recipes similar to that of the undoped GaN/AlN structure. The details of the growth is provided in appendix A. All samples had a 15 nm of UID GaN layer to generate a 2DHG at the interface, with an additional 15 nm Mg-doped contact layer on top. The samples differed in the level of Mg doping - sample B1 and B2 has Mg-doped GaN layers with [Mg] of 1×10^{19} cm^{-3} and 4×10^{19} cm^{-3} respectively. Sample B3 had a 15 nm

In$_{0.04}$Ga$_{0.96}$N contact layer with [Mg] $\sim 1 \times 10^{20}$ cm^{-3}. Mg-InGaN contact layers have earlier demonstrated low-resistance contacts to Mg-GaN layers for vertical transport in GaN LEDs [196]. The dopant densities were confirmed by SIMS on calibration samples.

Details of the samples are summarized in **table 3.1**. All three samples had similar as-grown sheet resistance of ~10 kΩ/sq as measured by Hall-effect at room temperature. The top Mg-doped layers are not expected to substantially contribute to the Hall measurement since the thermally activated hole density is two orders lower than the 2DHG density. The low sheet resistance is therefore due to the underlying 2DHG at the GaN/AlN interface.
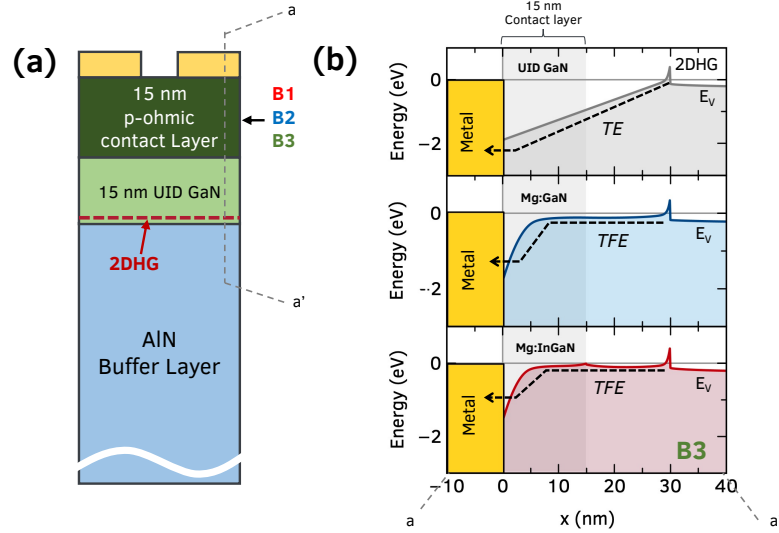
Figure 3.4: (a) Layer diagram of the series of MBE-grown GaN/AlN 2DHG samples B1, B2, B3 with different contact layers. The details of the samples are summarized in table 3.1. (b) Energy band profile of the metal-contact layers, for UID GaN, Mg-GaN and Mg-InGaN contact as the contact layers. The higher doping level results in a narrower barrier width for the holes in the valence band, promoting thermionic field emission (TFE) over thermionic emission (TE), and thereby lowering the contact resistance.

Figure 3.4 (b) shows the expected energy band diagrams for different contact layers, Mg-GaN and Mg-InGaN, on the GaN/AlN 2DHG. These are calculated

using a self-consistent 1D Schrodinger Poisson solver. Also plotted for reference is the band diagram for a GaN/AlN sample with no Mg doping in the top layer (sample A). The control sample shows a wide triangular potential barrier for the holes in the VB quantum well with barrier ~2 eV high. The presence of Mg dopants in the contact layer pulls the Fermi level closer to the valence bands near the ohmic metal. Thus, even though the barrier height is approximately the same, higher doping results in a narrower barrier and is expected to enable low resistance contacts by allowing thermoionic field emission (TFE). If there are trap states near the valence band, then there is an added possibility of trap-assisted tunnelling [195] which should derease the contact resistance further.
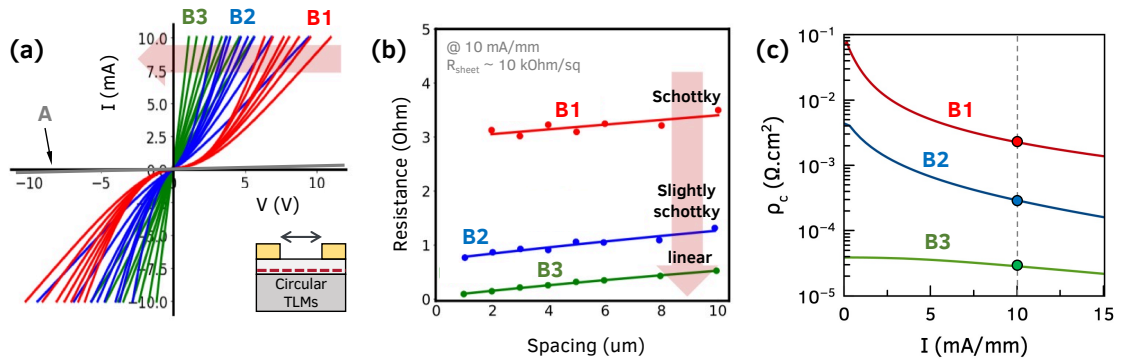
Figure 3.5: (a) IV curves for the three different ohmic contact layers in samples B1, B2 and B3. The I-V curve for sample A (without ohmic contact layer) is shown in grey, which is barely visible at this scale due to the high resistance. (b) The TLM extraction using resistance as function of TLM spacings, extracted at 10 mA/mm. (c) Extracted specific contact resistivities as a function of current. The Mg-InGaN contact layer in sample B3 clearly has the most ohmic behavior and lowest contact resistance among the three. *Figures (a), (b) modified from Bader et al. [38], © 2019 IEEE*

Circular TLMs using unalloyed Pd-based contacts as ohmic metals were measured to characterize the ohmic contacts to the 2DHG. **Figure 3.5** summarizes the results. **Figure 3.5 (a)** shows the IVs from the three samples for nominal TLM spacings of 2, 3, 4, 5, 6, 8, 10 μm. A clear trend in the nature of contacts is visible, with sample B1 showing Schottky-like behavior. Even though the re-

sistance is lower than the undoped sample A from **figure 3.3**, it is not suitable for device purposes. TLM IVs in samples B2 and B3 show more linear behavior, with a visible increase in linearity with increase in the Mg-doping levels. The resistance as a function of TLM spacings is plotted in figure 3.5 (b) extracted at a low current of 10 mA/mm. The slope of the linear fit of of the resistance vs spacing represents R_{sheet}/W, where W is the width of the TLM. Clearly, all three samples have similar slopes which concurs with fact that the as-grown Hall resistances were similar across the samples. Additionally, it confirms that the lateral conduction is dominated by the 2DHG and not the higher-resistance p-doped layers. The y-intercept of the linear fit of the TLM gives $2R_c$, where R_c is the contact resistance. Again, corroborating with the IVs in **figure 3.5 (a)**, a lower R_c is observed in the higher Mg-doped samples. The extracted R_c and specific contact resistivity ρ_c as a function of current for the three samples is plotted in **figure 3.5 (c)**. Mg-InGaN contacts show low $\rho_c \sim 10^{-5}$ Ωcm^2, orders of magnitude lower resistance than the Mg-GaN layers in this controlled experiment. Hence, these are highly suitable for use as ohmic contacts in p-channel GaN/AlN FETs.

Because a lot of scientifically important experiments such as magnetotransport are best performed at ultra-low temperatures, it is valuable to characterize the behaviour of the p-type contacts on cooling. To investigate, TLM measurements on Mg-InGaN capped sample B3 were performed at 200 K and 77 K using a temperature-controlled stage in a probe station. The results are shown in **figure 3.6**. For this experiment, the Mg-InGaN layer was etched away in the regions between the TLM patterns, as shown in inset of **figure 3.6 (b)**, so as to ensure the current conduction between the contacts is through the 2DHG and not the Mg-InGaN layer. TLM extractions were performed at different tempera-
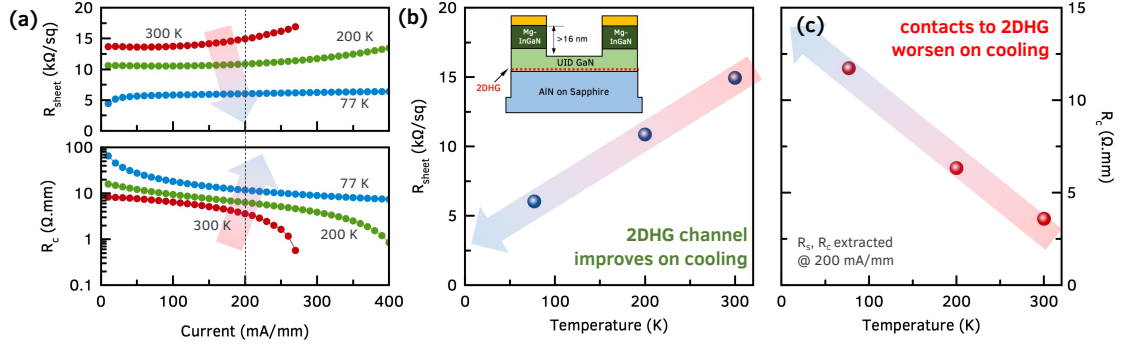
Figure 3.6: Low temperature TLM measurements on Mg-InGaN contacts. (a) Extracted contact and sheet resistances as function of current for Mg-InGaN contacts to the GaN/AlN 2DHG at 300 K, 200 K and 77 K. (b) sheet resistance, and (c) contact resistances extracted at 200 mA/mm. These results show that while the 2DHG resistance decreases upon cooling, the contacts get more resistive.

tures and the contact and sheet resistances were extracted as function of current.

Figure 3.6 (b) shows that the sheet resistance of the 2DHG "channel" extracted at 200 mA/mm *decreases* 3× upon cooling - going from 15 kΩ/sq at 300 K to 5 kΩ/sq at 77 K. This is consistent with the expected increase in 2DHG mobility due to the phonon freezeout at low temperatures (see **figure 2.6**). However, the contact resistance has the opposite dependence on temperature. It *increases* from ∼ 3 Ω mm at 300 K to 12 Ω mm at 77 K - a 4× rise. This is attributed to the freezing out the thermally generated holes in the Mg-InGaN contact layers leading to a wider barrier for the holes. Additionally, this behavior points to the fact the the carriers undergo TFE and not pure FE or trap-assisted tunnelling. Nevertheless, the Mg-InGaN contacts show low resistance at room temperature and are suitable for use in devices that operate at room temperature and higher.

Figure 3.7 compares the results of this work to ohmic contact resistances reported in literature to p-GaN and 2DHGs. Interestingly, not only do the Mg-InGaN contacts shows lower contact resistance than the other Mg-GaN contacts in this study, but these are *among* the best for *any* p-type contacts to GaN re-
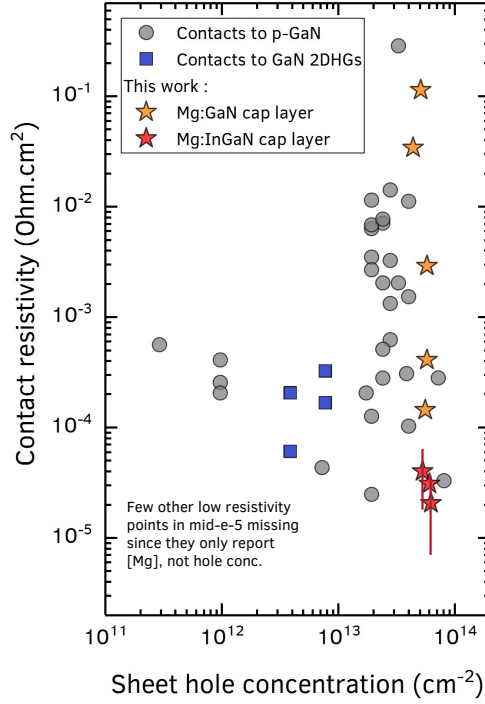
Figure 3.7: Benchmark plot comparing the various ohmic contacts reported to p-GaN in literature. The Mg-InGaN contacts to the GaN/AlN 2DHG presented in this work represent some of the lowest contact resistances across all reports.

ported in literature. However one needs to be slightly careful in this comparison as the reports have different ohmic metal stacks, Ni, Pa etc. Also, there is a potential of misinterpreting and underestimating the non-linear IVs during TLM extraction which is why a fair comparison needs closer look at the extraction methodology as well. Furthermore, a lot of reports of high efficiency LEDs and pFETs do not explicitly mention their the p-type ohmic contact resistances or scheme, so there might be some missing points on the plot. However, the authors are confident that the Mg-InGaN contacts to the GaN/AlN 2DHG are among the lowest among contacts to 2DHGs for GaN pFETs.

Better contact resistances are predicted at higher In concentration InGaN [193], but InGaN pseudomorphic to AlN is very highly strained and growth of high In composition in strained crystals becomes challenging due to composi-

tional pulling effects. These results also indicate this contact scheme might not be the best for performing low temperature magnetotransport measurements even though the GaN/AlN 2DHG survives and in fact gets better at low temperature providing a great opportunity to access the valence bands through SdH oscillations. The very high contact resistances mean that the total voltage measured experimentally will be dominated by the voltage drop across the contacts and not the 2DHG channel. On the brighter side, these ohmic contacts should get better at high temperatures! This makes it attractive high temperature applications especially thanks to the high thermal conductivity of AlN.

3.4   Scaled RF GaN/AlN p-channel FETs

With the a low resistance ohmic contact to the high-conductivity GaN/AlN 2DHG identified, all the components required for demonstrating a high performance pFET on this AlN platform are in place. The past 8 years has seen rapid improvements in the performance of GaN/AlN pFETs, thanks to advancements in the epitaxial materials supported by device fabrication improvements.

The first GaN/AlN pFET was reported in 2013 [19]. The GaN/AlN 2DHG channel had high sheet resistance of 17 kΩ/sq at room temperature. The low channel mobility and high contact resistances meant a very high drain voltage of V_{DS} = 50 V was needed to reach current levels of currents of 100 mA/mm. Even though this is not ideal for a circuit implementation of the device, it nevertheless demonstrated the potential of the GaN/AlN platform to sustain high on-currents and biases.

As seen in chapter 2, the control of compensating impurities during MBE

growth using IBLs improved the sheet resistance of the GaN/AlN 2DHG by 3×. These new and improved GaN/AlN 2DHG were used with a new recessed gate process to demonstrate [31] enhancement-mode GaN/AlN pFETs with on currents upto 10 mA/mm at reasonable V_{DS} of 5 V and 4 orders on-off ratio in long channel devices with gate length L_G = 7 μm. These metrics were achieved with a heavily p++GaN contact layer with contact resistance of 14.89 Ω.mm. Reducing the contact resistance should boost the current in the pFET further. Indeed, a year later, on-currents of upto 100 mA/mm (at V_{DS} = 10 V) were achieved in devices with L_G = 600 nm for the first time in GaN pFETs [38]. This jump was primarily due to improvements in low resistance Mg-InGaN contacts (3× lower R_c) and Schottky recessed gate.

The rapid improvements over the past 3 years have made it clear that the GaN/AlN platform for pFETs are yet to reach their full potential. In this section, we build upon the previous work by scaling down the gate lengths further and consequently pushing the on-currents higher to upto 0.5 A/mm at room temperature, and ~ 1 A/mm at 77 K - reaching current levels similar to GaN n-channel HEMTs. These results make near-current matched complementary circuits possible on this AlN-platform. Additionally, the scaled devices break the GHz barrier for the first time in GaN pFETs with f_T/f_{MAX} upto 23/40 GHz. This never before thought possible performance ushers in new era in wide bandgap (WBG) GaN pFETs and opens up the possibilities of new application spaces for WBG complementary circuits for RF applications.

The device process starts with the epitaxial growth of the GaN/AlN 2DHG. **Figure 3.8** shows the layer structure of the MBE grown sample. A 15 nm Mg-InGaN/15 nm UID GaN/500 nm AlN buffer was grown using plasma assisted
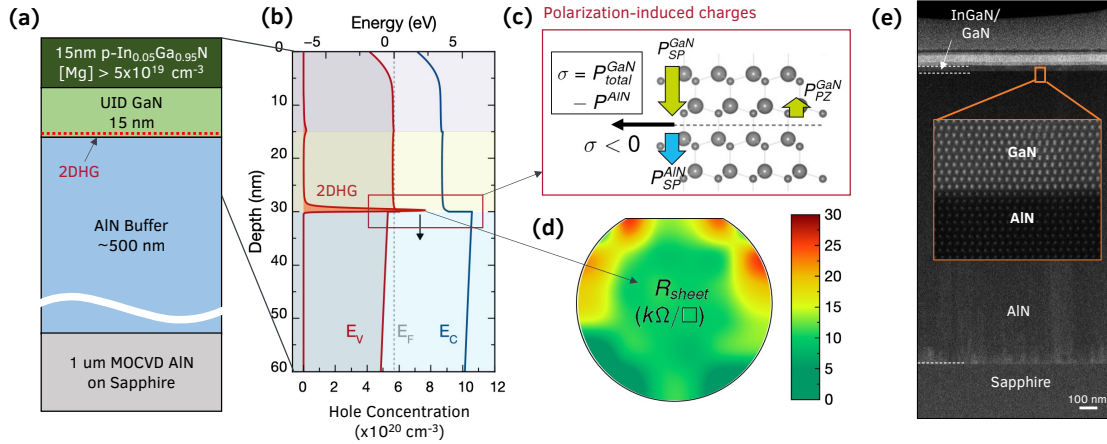
Figure 3.8: (a) Layer structure of the epitaxial film grown by MBE, dashed line indicating where a high-density 2D hole gas (2DHG) is present. (b) Energy band diagram showing the band alignment at the GaN/AlN interface and the 2DHG. (c) Polarization difference at the undoped GaN/AlN interface gives rise to fixed negative sheet charges, which together with a valence band offset between the GaN and AlN, leads to a tightly-confined mobile 2DHG channel. (d) The sheet resistance map shows the uniformity of the 2DHG across the MBE-grown 2 inch wafer, pieces of which were used for fabricating the devices in this work. (e) Cross-sectional STEM scan showing highly uniform epitaxial growth and sharp, abrupt GaN/AlN interface as desired. *Figure modified from Nomoto, Chaudhuri et al. [39], © 2020 IEEE*

molecular beam epitaxy (PAMBE) on 2-inch AlN on sapphire template substrates. The growth details are provided in appendix A. The TEM cross-section of the epitaxial growth confirms sharp abrupt interfaces, as seen in **figure 3.8 (e)**. Uniform sheet resistance of ~ 10 kΩ/sq is measured across the wafer surface using Hall-effect at room temperature.

The fabrication process for the scaled, T-gated GaN/AlN pFET is summarized in **figure 3.9**. After a mesa isolation etch, Pd-based ohmic metals were deposited followed by two critical etches using Cl-based ICP dry etch - (1) global etch to remove the InGaN contact layers except under the ohmic pad, and (2) local recess defined by electron-beam lithography (EBL) which removes the GaN under the gate and defines the gate to 2DHG distance of 8 nm. Mo/Au gates

L_g (nm)	120
W_g (um)	25 x 2
L_{sd} (nm)	680
L_{recess} (nm)	~60
D_{recess} (nm)	~7
$T_{channel}$ (nm)	~8
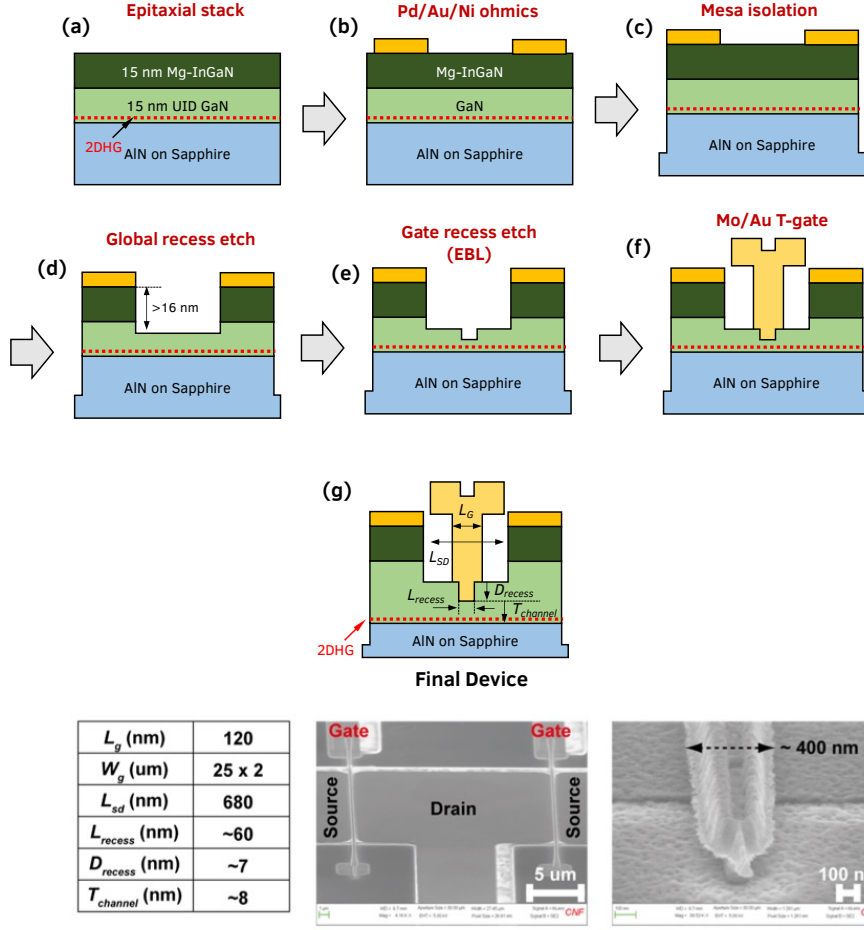
Figure 3.9: Fabrication process for scaled GaN/AlN p-FETs, which consists of (a) MBE grown GaN/AlN heterostructure with the Mg-doped $In_{0.05}Ga_{0.95}N$ layer, (b) non-alloyed Pd/Au/Ni ohmics, (c) Cl_2 -based ICP etching for mesa isolation , (d) first "global" recess etch step for removing Mg-InGaN, (e) second recess etch with electron-beam lithography (EBL) to thin the gate-channel distance and define the channel, and (f) Mo/Au Schottky T-gate. (g) Enlarged cross-sectional schematic of the final device structure with a T-gate of L_G = 120 nm, W_G = 25 μm × 2, and 70° angled-view SEM images of the fabricated p-FETs and T-gate. *Figure modified from Nomoto, Chaudhuri et al. [39], © 2020 IEEE*

were then deposited using electron beam evaporation. The final device cross-section and dimensions are shown in **figure 3.9 (g)**. Gate length L_G were varied from 600 nm to 60 nm.

TLM measurements after the global etch step showed contact resistances of < 5 Ω mm at current levels greater than 100 mA/mm, confirming the robustness
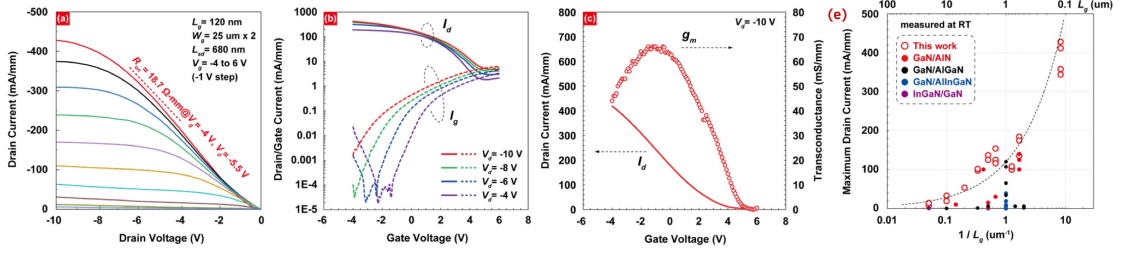
Figure 3.10: Transistor characteristics of the p-channel FETs with L_G = 120 nm, W_G = 25 μm × 2, and L_{SD} = 680 nm. (a) Output I-V curves show current saturation and an on-resistance of 18.6 Ω mm at V_{GS} = -4 V. (b) Log-scale transfer curves show two orders of I_{on}/I_{off} modulation, limited by Schottky gate leakage. (c) The linear-scale transfer curve shows normally-on operation and a peak $g_{m,ext}$ of 66 mS/mm. (d) maximum drain current I_D versus gate length L_G for scaled GaN/AlN p-channel FETs shows the effect of device scaling. *From Nomoto, Chaudhuri et al. [39], © 2020 IEEE*

and repeatability of the Mg-InGaN based ohmic contact scheme to the 2DHG.

Figure 3.10 shows the DC device characteristics of a device with L_G = 120 nm, source drain distance of 680 nm. The gate base length is 60 nm. The output characteristics show a good set of family curves with nice saturation. The maximum saturation on currents reach 428 mA/mm and are repeatable on multiple devices. Transfer characteristics show an on/off ratio of about 2 orders of magnitude and is limited by gate leakage. A reasonable threshold voltage of 4 V and peak transconductance g_m of 66 mS/mm are obtained. **Figure 3.10 (d)** plots the measured max on currents across different devices with varying late lengths. Clearly the currents rise with decreasing gate lengths, obeying the MOSFET scaling principles [197].

Small signal RF characterizations were performed by measuring S parameters from 50 MHz to 40 GHz using microwave probes in air and then dembedding using open structure on the same die. The small-signal characteristics are shown in **figure 3.11**, with an extracted voltage and power gain cut-off frequencies f_T/f_{MAX} of 19.7/23.3 GHz. These represent the highest f_T/f_{MAX} reported in
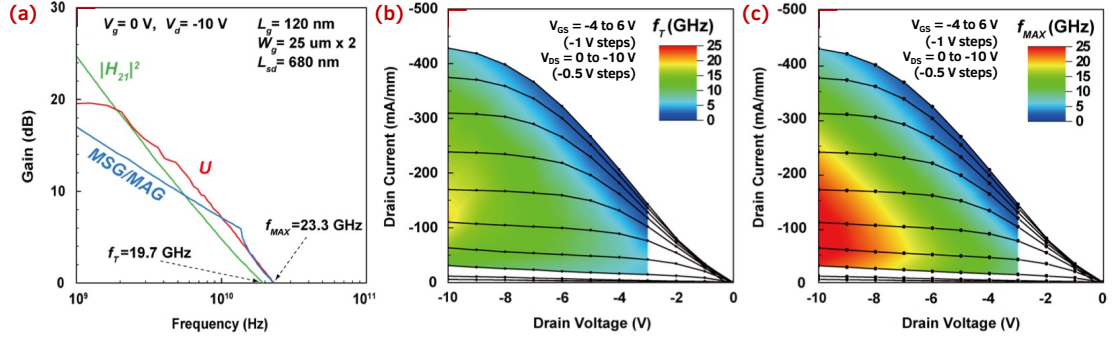
Figure 3.11: Small-signal measurements on the p-channel FETs with $L_G = 120$ nm, $W_G = 25\,\mu m \times 2$, and $L_{SD} = 680$ nm. (a) S-parameter measurement results on the GaN/AlN p-channel FETs showing cut-off frequencies $f_T/f_{MAX} = 19.7/23.3$ GHz. (b) and (c) show the V_{DS} and V_{GS} bias dependence of the f_T and f_{MAX} respectively. The colors indicate frequencies on the contour maps. *From Nomoto, Chaudhuri et al. [39], © 2020 IEEE*

III-nitride based pFETs so far, and are orders of magnitude higher than $f_T = 230$ MHz reported back in 2013 [16] in GaN/AlInGaN pFET.

Even though this generation of device exhibits high on-currents, the on/off ratio is slightly lower than 2 orders and is limited by gate leakage current. Insertion of a thin gate dielectric layer to form a metal-insulator-semiconductor (MIS) gate should help increase the on-off ratio and boost the current through suppression of gate leakage. This is supported by the previous GaN/AlN MIS-HFET results [31] which showed 4 orders on/off ratio in a 7 μm long channel device. Also, on examination of a TEM cross-section image, it was found that T-gates in the scaled GaN/AlN p-FETs had a broken Mo gate head. Fixing the gate head should potentially decrease the gate resistance and therefore help boost the f_{MAX}.

To test these improvements, new round of pFET devices were fabricated using the same device fabrication flow the previous round but with a couple of modifications : (1) the Mo/Au gate metal was deposited using sputtering as
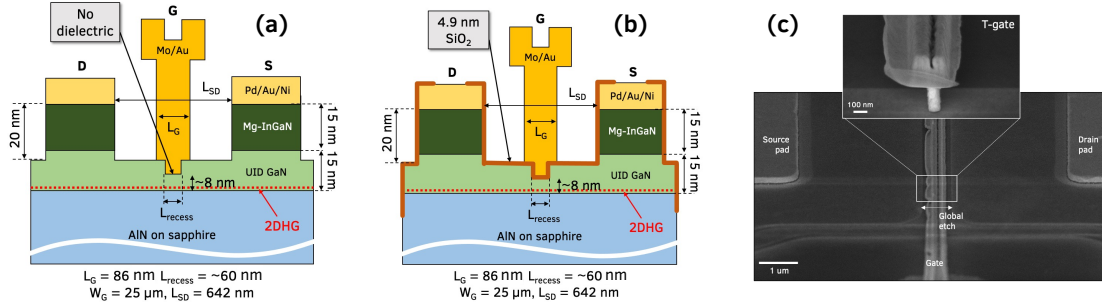
Figure 3.12: Fabricated GaN/AlN pFETs with (a) Schottky-gate and (b) ALD SiO$_2$ under the gate (MIS-gated), with similar device dimensions. The MIS gate is expected to reduce the gate leakage compared to a Schottky gated device. (c) SEM image of the sputtered Mo T-gate head showing an intact gate head, which is expected to reduce the gate resistance and thereby boost the f_{MAX}

opposed to electron-beam evaporation, to obtain a more mechanically stable T-gate head, (2) a thin 4.9 nm SiO$_2$ layer was deposited using atomic layer deposition (ALD) under the gate metal to act as a gate dielectric. The fabricated metal-insulator-semiconductor (MIS)-HFET and a control Schottky gated device are shown in **figure 3.12 (a) and (b)**. Both similar device dimensions of L_G = 86 nm, W_G = 25 μm $\times$ 2, and L_{SD} = 642 nm. An SEM scan of the device is shown in **figure 3.12 (c)**. The new sputtered T-gate are confirmed to be intact as intended.

Figure 3.13 (a) and (b) show the transfer characteristics of the MIS-HFET and the Schottky gated device fabricated. The Schottky gated device showed similar characteristics as the previous round, with a high on current of 430 mA/mm and an on/off ratio of 89. The low on-off ratio is clearly limited by the gate leakage. In comparison, the MIS-HFET shows a clearly suppression of the gate leakage. This results in not only a higher on-off ratio of > 2 orders (140), but also a higher on-current of 501 mA/mm! The output curves for the MIS-HFETs show good transfer characteristics, with a low R$_{on}$ of 16 Ω mm.

The IV characteristics of the Schottky-gated device was also measured at
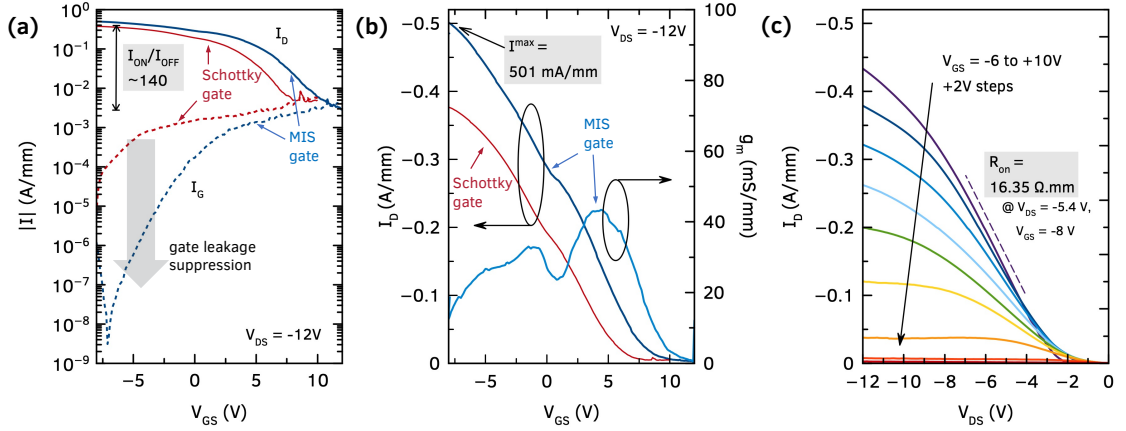
Figure 3.13: DC characteristics comparing the Schottky gated and the MIS-gated p-HFETs (a) shows a suppression of gate leakage in the MIS-gated device, which leads to a higher (>2 orders) of current on-off ratio. (b) the linear transfer curve shows the MIS-gated device reaches on currents upto 501 mA/mm. The family curves show good output characteristics and low R_{on}
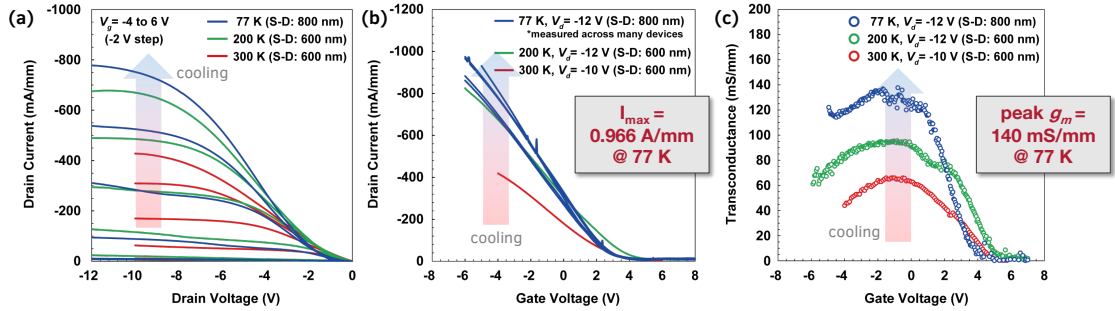
Figure 3.14: Low temperature DC characteristics of the Schottky gated pFET, with (a) family curves, (b) linear output curves and (c) transconductance curves at 300 K, 200 K, and 77 K. The improvement in the mobility of the 2DHG with cooling, leads to a lower channel resistance and therby high on-currents and higher peak g_m. A maximum on current of 0.96 A/mm is recorded, which is the highest on-current ever recorded in GaN pFETs.

temperatures below the room temperature at 200 K and 77 K. The results are shown in **figure 3.14**. As seen in **figure 3.6**, the Mg-InGaN ohmic contact resistance is expected to increase due to freezing out of thermally activated carriers, but the 2DHG sheet resistance is expected to decrease due to freezeout of phonons. In the FET, the high channel mobility dominates and as a result the maximum on currents increases with decrease in temperature. It reaches upto

123

0.966 A/mm at 77 K, which is the highest on-current ever reported in a GaN p-channel FET, and at the same level as GaN HEMTs! This result is not only exciting for applications where the system can be cooled, but also show that the currents can be improved drastically if the room temperature mobilities of the 2DHG is boosted further.
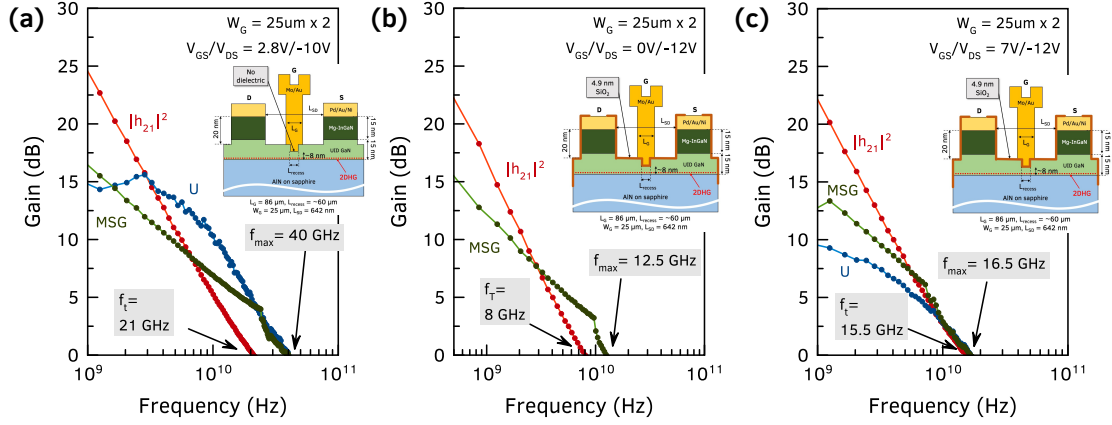
Figure 3.15: Small signal measurements on the p-channel FETs shows cutoff-frequencies of f_T/f_{MAX} of 21/40 GHz in the Schottky gated device, and best f_T/f_{MAX} of 15.5/16.5 GHz in the MIS-gated FET.

Figure 3.15 shows the small signal characteristics of the MIS-HFETs and Schottky-gated FETs. The Schottky-gated FET shows an f_T/f_{MAX} of 21/40 GHz, an increase of 13 GHz in the f_{MAX} compared to the previous generation. This confirms the hypothesis that the new T-gates with sputtering result in lower gate resistances. The best MIS-HFETs showed f_T/f_{MAX} of 15.5/16.5 GHz, which is the first GHz speed MIS-HFETs in GaN. Even though the intrinsic cut-off frequency f_T is expected to be the same in both the devices because of similar lateral gate lengths, the *extrinsic* f_T is understandably lower in the MIS-gated pFETs than the Schottky gated devices, because larger source-channel separation results in a lower g_m which in turn increases the parasitic delays.

124

3.5 Benchmark

Thus, combining the high-conductivity 2DHG, Mg-InGaN low resistance
ohmics, and scaled T-gate fabrication processes, pFETs with both Schottky and
MIS gates have been demonstrated with record high on currents and speeds.
Figure 3.16 (a) compares the on currents and on-off ratio of all GaN pFETs re-
ported till date. A high on current and high on-off ratio is desired in a transistor.
The scaled gate devices in this work show 5× improvement in on-current levels
over the long channel devices previously demonstrated. The GaN/AlN pFETs
show on-currents which are more than an order of magnitude higher than the
rest. With further process improvements to reduce the gate leakage currents,
and source-drain scaling, they should soon be able to match the GaN n-channel
HEMT current levels of >1 A/mm.
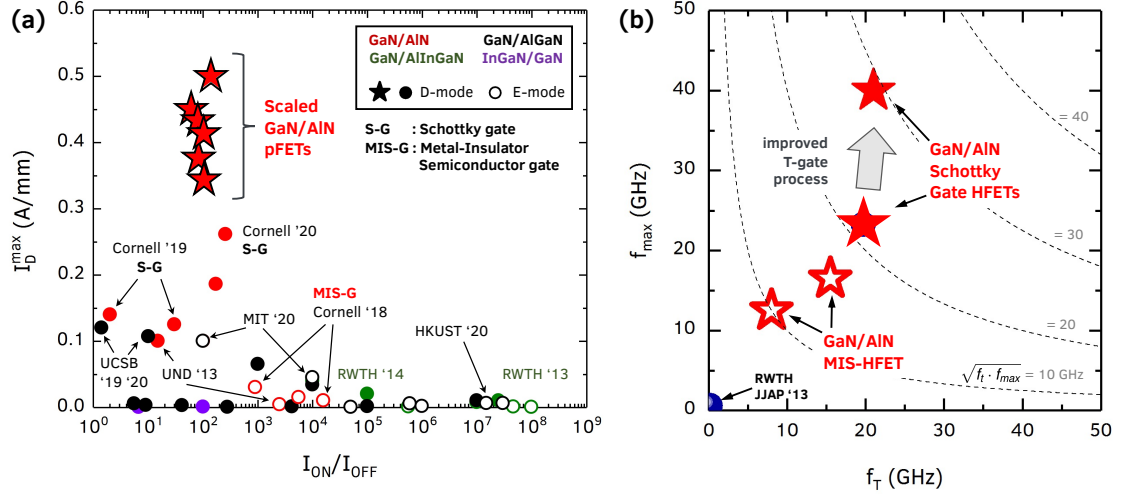
Figure 3.16: (a) Benchmark plot comparing on-currents reported in III-nitride
p-channel FETs in literature. This work represents the new record highest on-
currents, enabled by high-density GaN/AlN 2DHGs. (b) Comparison of the
cut-off frequencies measured in all GaN pFETs, showing the dominance of the
GaN/AlN platform.

Figure 3.16 (b) plots the f_T vs f_{MAX} for all reported GaN pFETs. The domi-

nance of the GaN/AlN pFETs is clear from the fact that apart from the pFETs reported in the work, there is only 1 other GaN pFET on this chart, near the origin with speed in MHz. The highest f_T/f_{MAX} in GaN/AlN pFETs are 21/40 GHz, taking the GaN pFETs to a regime which not so long ago was thought impossible.

The increased drive current and speed of the p-FETs seen here in the AlN/GaN platform, combined with the excellent performance of the n-channel HEMTs on the same AlN-platform [53] is expected to take this wide-bandgap CMOS platform into new application domains in the RF and power electronics arenas.

3.6   Future Directions

The results in this chapter report advancements in the field of GaN p-channel FETs, demonstrating device performance which were thought impossible a few years back. However there is room for improving these pFETs further. Chapter 2 provided directions to improve the 2DHG channel conductivity which should directly translate to an improvement in the pFET performance through reduced access resistances and higher on-currents. This section provides some the future directions from *device design* perspective for pushing the GaN/AlN pFET performance higher :

- **Reduce gate leakage to increase on/off ratio, breakdown**

  A high on-off ratio and a high on current is desired in a pFET. As seen in the figure 3.16 (a), the current state-of-art scaled RF GaN/AlN pFETs

126

show a low drain current on/off ratio ~ 2 order of magnitude, 6 orders lower than the pFETs with the highest on-off ratios [58, 60]. The off state current in these D-mode GaN/AlN pFETs is limited by a high gate leakage current at high positive biases. The introduction of an SiO_2 gate dielectric in a MIS-HFET configuration slightly reduces the gate leakage, but is still slightly above ~ 2 orders of magnitude. Reducing the gate leakage further will increase the on-off ratio and also improve the breakdown voltage of these devices.

It is known that threading dislocations in a crystal provide a potential charge leakage path from the channel to the gate [198, 199]. The current generation of GaN/AlN pFETs were grown on foreign substrates (AlN-on-sapphire templates) with dislocation density of ~ 10^{10} cm^{-2}. This translates to ~50000 leakage paths for a 100 nm long and 50 μm wide gate. Recent availability of high-quality single crystal AlN substrates [200, 201] and advancements in MBE homoepitaxy of AlN [65, 64] have successfully reduced the dislocation density in AlN-based heterostructures by 6 orders of magnitude (more details in appendix B). With approximately 1 leakage path for every 20 100 nm long and 50 μm wide gates, fabricating the GaN/AlN pFET on bulk AlN substrates should help drastically reduce the dislocation-mediated leakage. A comparative study between a parallel processed GaN/AlN pFET on bulk AlN and AlN-on-Sapphire templates will be valuable to pin-point the dominating source of leakage in this device.

Another path to reduce gate leakage, while maintaining g_m, is to introduce a high-K dielectric between the gate metal and the channel. Recent discovery of high dielectric constant of > 20 in MBE-grown epitaxial scan-

dium aluminum nitride (ScAlN) makes it a very attractive candidate for inclusion as an epitaxial high-K dielectric. However, metal-polar ScAlN on GaN is a negative polarization difference interface [202], and hence the thickness of the high-K dielectric needs to be carefully designed so as not to induce a parallel 2DEG in the ScAlN/GaN/AlN structure and screen the 2DHG. A combination of ScAlN + SiO_2 might be a good way to realize the high-K gate dielectric scheme for GaN/AlN pFETs.

- **Source-drain distance scaling**

  Today current-state-of-art GaN pFETs reach record high current levels of 0.5 A/mm thanks to gate length (L_G) scaling. These pFETs, with high-conductivity 2DHG channel and low resistance ohmic contacts, have the potential to achieve even higher current levels and speeds through source-drain separation (L_{SD}) scaling.

  Scaling down the L_{SD} for a given L_G, or the consequent decreased source-gate spacing, results in higher electric field and lower voltage drop in the source-side access region [203] which should result in higher on-currents and hopefully soon reach the GaN HEMT levels of ~1 A/mm.

  Decreasing the L_{SD} should also boost the operating speed of the pFETs [204]. Voltage gain cut-off frequency f_T of an FET (ignoring short channel effects) is given by :

$$f_T \uparrow = \frac{1}{2\pi} \cdot \frac{1}{\frac{C_{gs}+C_{gd}}{g_m^{ext}\uparrow} + C_{gd} \ (R_S \downarrow + R_D \downarrow)}, \tag{3.1}$$

  where, g_m^{ext} is the extrinsic transconductance, $C_{gs/gd}$ are the gate-source and gate-drain capacitances. The arrows indicate the expected trends on L_{SD} scaling. $R_{S/D}$ is the source/drain side access resistances, given by $R_{S/D}$ =

$R_{sh}.L_{SG/GD}/W_G$, where R_{sh} is the sheet resistance of the as-grown 2DHG, W_G is the gate width and $L_{SG/GD}$ is the gate-source or gate-drain distance.

Reduced source side access resistance (R_S) should result in higher extrinsic g_m through $g_m^{ext} = 1/(1 + R_S.g_m^{int})$. This should translate to reduced drain delay (C_{gd}/g_m^{ext}). L_{SD} scaling also reduces the parasitic charging time ($R_D + R_D$).C_{gd}, combining to increase the f_T.
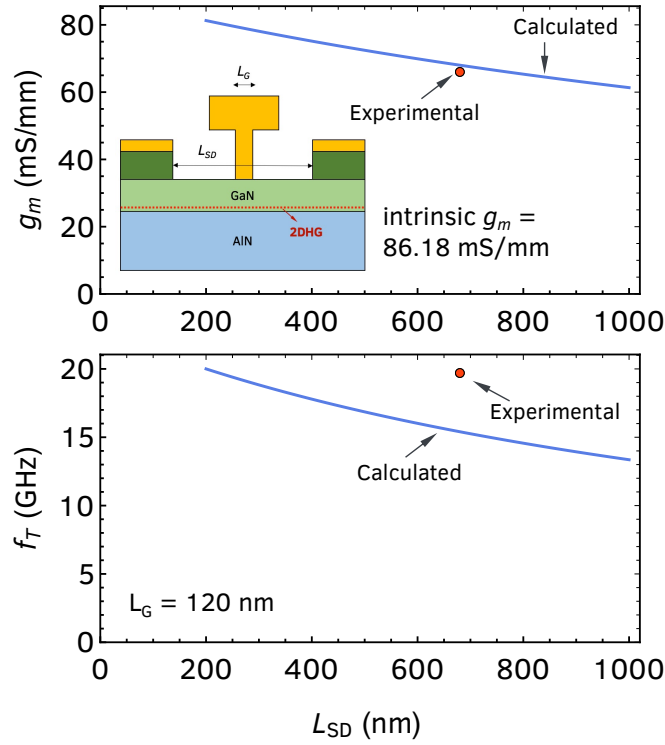
Figure 3.17: Effect of source-drain separation L_{SD} scaling for a given gate length on GaN/AlN pFET transconductance (g_m) and cut-off frequency (f_T). Both g_m and f_T are expected to increase by ∼ 50% on scaling down L_{SD} from 1000 nm to 400 nm. The value of intrinsic g_m used for the calculation is from the small-signal extracted model in scaled GaN/AlN pFETs [39].

Figure 3.17 plots the theoretically expected extrinsic g_m and f_T as a function of L_{SD}, assuming an L_G = 120 nm, R_{sh} of 10 kΩ/sq and a symmetric gate placement between source and drain. The intrinsic g_m = 86.18 mS/mm is extracted from the small-signal model of the GaN/AlN pFET

[39] shown in figure 3.11. Almost 50% increase in the f_T is predicted on scaling down the L_{SD} from 1000 nm to 400 nm.

However, L_{SD} scaling should be accompanied by an asymmetric gate (gate closer to the source than drain) in the future to balance the expected trade-off between f_T and breakdown voltage.

- **Regrown p-type ohmic/tunnel contacts**

  The current state-of-art p-type ohmic contact scheme with the as-grown Mg-InGaN ohmic contact layers makes it necessary for a gate recess etch to remove the Mg-doped layer in the channel region. The pFET fabrication process thus relies heavily on the precise control of this recess etch within 1-2 nm. In the absence of a natural etch stop layer, this is achieved by careful calibration and timing of the ICP dry etch. Nevertheless, this inherently brings with it process variability, lowering the yield. Additionally, the damage from dry etch known to cause n-type defects [205], which can adversely the 2DHG channel.

  An alternative ohmic contact scheme which eliminates the need for gate recess is thus desired, via p-type ohmic regrowth. This should allow the Schottky-gate metal to be placed on the as-grown surface, and the processing to be performed on the ohmic regions away from the channel, maintaining its conductivity. Three possible routes to regrown p-type ohmics are shown in **figure 3.18**.

  The first method, illustrated in **figure 3.18 (a)**, is similar to the MBE n++ regrown GaN contacts to 2DEGs [158]. Part of the as-grown GaN/AlN 2DHG structure is etched away, and then heavily p++ doped GaN or In-GaN regions are selectively regrown in the source and drain regions. If the doping levels are high enough to make it degenerately doped in the con-

tact regions, they form a 3D-2D contact to the 2DHG in the valence band. Recent results from the Mishra group at UCSB confirmed the feasibility of p++ regrown ohmics on finFET structure, and hence would be worth pursuing on the GaN/AlN 2DHG structure.
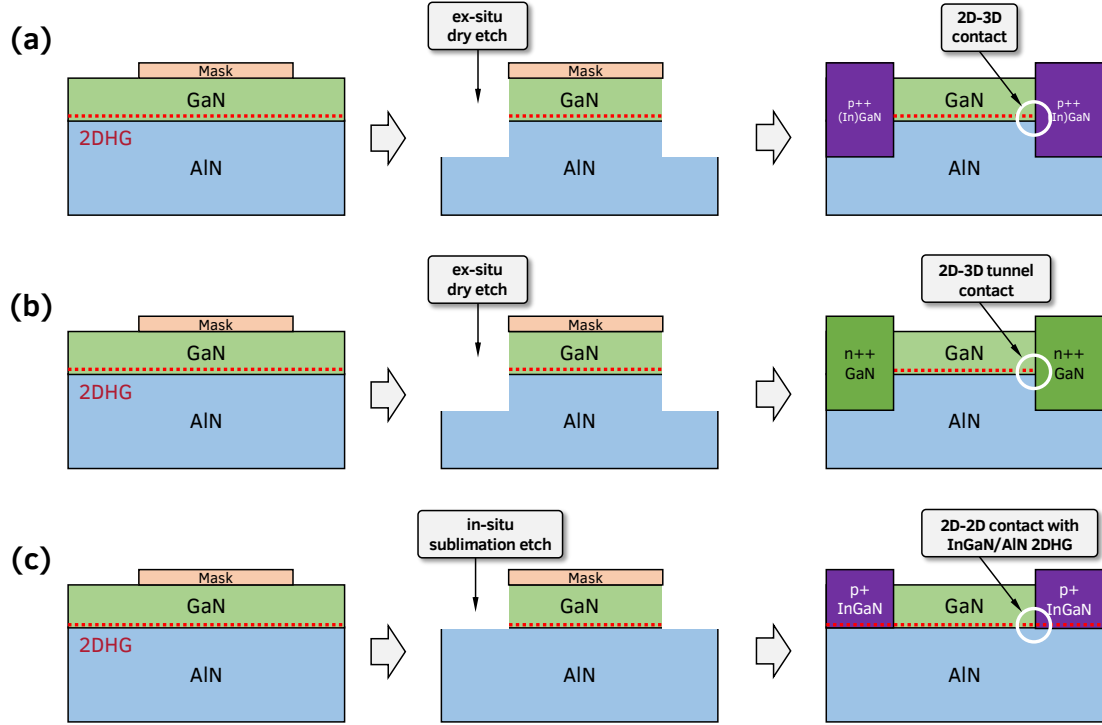
Figure 3.18: Process flow for possible schemes to achieve regrown ohmic contacts to the GaN/AlN 2DHG, using (a) p++InGaN regrowth for 2D-3D contact, (b) n++GaN regrowth for 2D-3D tunnel contacts, and (c) p+InGaN regrown regions on in-situ selective sublimation etched GaN, for 2DHG-2DHG ohmic contacts.

However, in addition to the fundamental challenge of growing degenerately-doped p++GaN, damage during the regrowth etch [205] and contamination from the ambient between the *ex-situ* dry etch and MBE-regrowth steps [206, 207, 208] means the sidewall contact may be high-resistance. Two alternate possibilities are therefore proposed to get around these issues.

MBE n++ regrowth process is very well developed [158]. Regrown n++GaN regions instead of p++(In)GaN could be used to form 2D-3D tunnel contacts to the 2DHG. **Figure 3.18 (b)** illustrates this regrowth scheme. The challange here is that the carriers have to overcome an energy barrier equal to the band gap of GaN for band-to-band tunneling. However, the contamination and defects on the sidewall could potentially assist and enhance the tunnelling process. In addition, this scheme will make integration with HEMTs easier as ohmics for both the HEMT and pFET can be formed by a single regrowth step.

The other alternative takes advantage of two novel components - *in-situ* selective sublimation etch of GaN and the InGaN/AlN 2DHG. The process is shown in figure 3.18 (c). The *in-situ* GaN sublimation etch (discussed in detail in section 6.4) reduces the sidewall contamination from the ambient by performing the etch inside the MBE ultra-high vacuum chamber. AlN acts as a natural etch stop for this technique. Subsequently Mg-InGaN regions are regrown, which forms a InGaN/AlN negative polarization interface in the ohmic regions. This interface is expected to be populated by a high density ($> 10^{14}$ cm^{-2}) 2DHG. This InGaN/AlN 2DHG should makes a 2D-2D contact to the GaN/AlN 2DHG channel under the gate. This is a truly unique p-type ohmic scheme enabled by the technological advancements in this work, and will be scientifically very valuable if realized.

CHAPTER 4

POLARIZATION-INDUCED 2D ELECTRON AND HOLES IN UNDOPED ALN/GAN/ALN HETEROSTRUCTURES

4.1 Introduction

So far in this dissertation, the metal-polar GaN on AlN heterostructure has been studied which generates a 2DHG at the negative polarization interface. These heterostructures have achieved record high p-type conductivity through careful epitaxial growth which enabled record p-type RF FETs in GaN [39].

Although highly technologically relevant on their own, the true technological potential of the these wide bandgap p-type transistors will be achieved by combining with n-channel GaN transistors to form energy-efficient logic or RF complementary circuits [137]. The ubiquitous GaN HEMTs build upon the polarization induced 2DEG grown on GaN buffer layers. With the GaN/AlN pFET already demonstrating record performances, a compatible n-channel transistor on AlN buffer is desired for enabling the true potential of this AlN platform. Furthermore, as will be shown in chapter 5, the AlN buffer provides material advantages over GaN buffer layer for high-power, high-frequency operation of HEMTs [53].

Similar to the GaN/AlN 2DHG channel enabling the pFETs, a 2DEG channel is necessary to make AlN HEMTs. In this chapter, a high-density, polarization-induced 2DEG is obtained on AlN by growing a thin layer of AlN barrier layer on top of the GaN/AlN structure. This leads to a unique 2D electron-hole (E-H) bilayer in an undoped AlN/GaN/AlN heterostructure. Because of the 2

orders higher mobility and conductivity of the 2DEG compared to the 2DHG, the 2DEG dominates the Hall transport measured in this AlN/GaN/AlN heterostructure. Light emission from the recombination of 2DHG and 2DEG in a unique lateral LED geometry confirms the presence of both, and represents the first report of emission from a completely undoped III-nitride semiconductor structure. Next, the transport of the high-density 2DEG on the top interface of the metal polar AlN/GaN/AlN heterostructure is studied in detail, from the perspective of application to RF HEMTs. The room temperature mobilities in these strain GaN channel heterostructures are limited to 700 cm^2/Vs due to a yet-unidentified extrinsic scattering mechanism. However, the high 2DEG densities results in low sheet resistances of $\sim$ 300 Ω/sq, which means the relatively low mobilities do not limit the performance of the resulting AlN HEMTs in the current state-of-art.

4.2   The AlN/GaN/AlN Heterostructure

Figure 4.1 (a) shows a typical metal-polar AlN/GaN/AlN heterostructure. It is similar to the GaN/AlN 2DHG (a thin 30 nm of GaN channel layer grown on thick relaxed AlN buffer layer), but with an additional thin AlN barrier layer of about 4 nm grown on top. Energy band diagram in **figure 4.1 (b)** shows that a 2DEG is expected at the top AlN/GaN interface and a 2DHG at the bottom interface GaN/AlN - the two being separated by the undoped GaN layer of thickness t_{GaN}. This leads to a high intrinsic field of $\sim E_g/q_e.t_{GaN}$ in the GaN channel layer, where E_g is the GaN bandgap, q_e is the electron charge. Because of its polarization-generated nature, the densities of the 2DHG and 2DEG electrostatically depend on the thicknesses of the GaN and AlN layers. These densities can
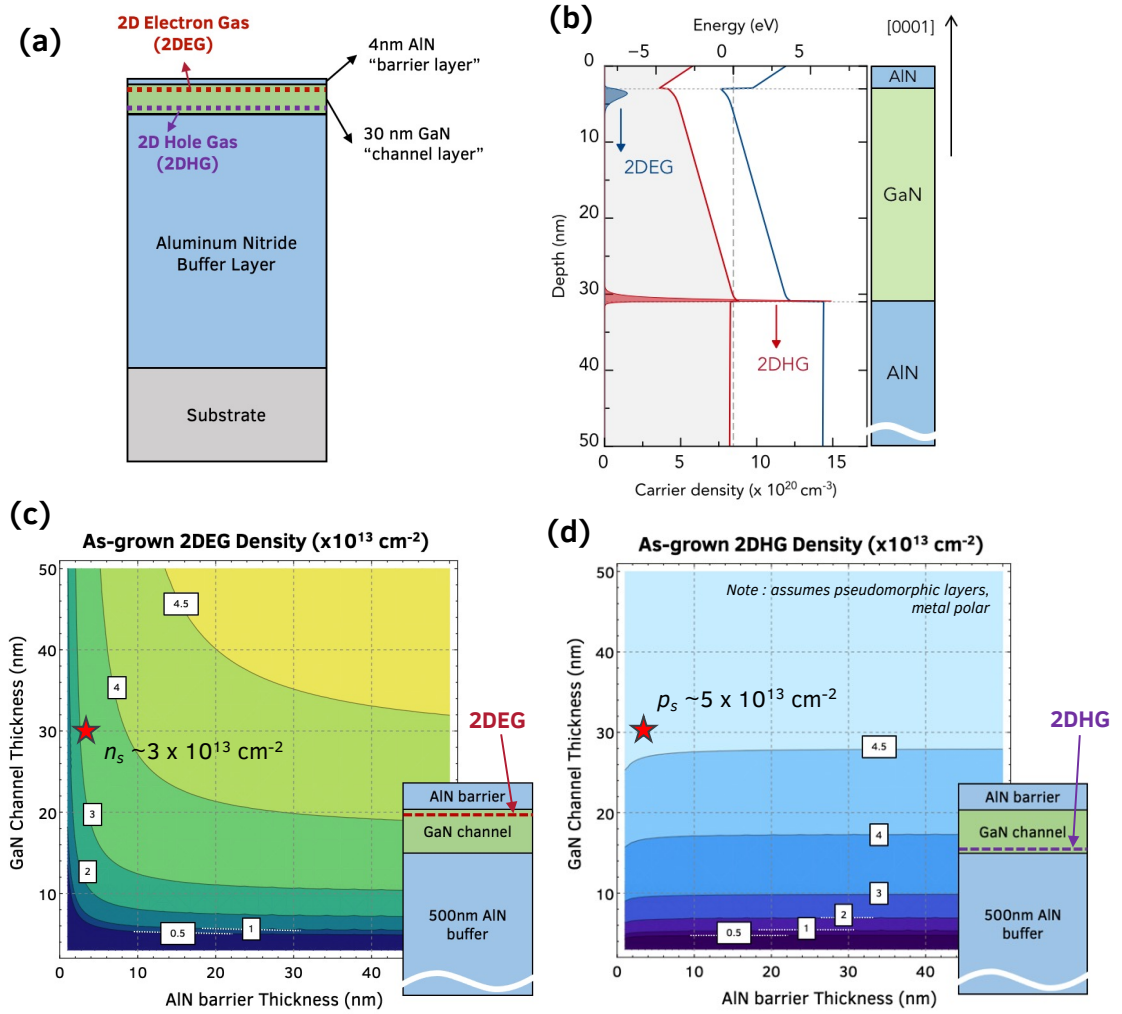
Figure 4.1: (a) Heterostructure details, and (b) energy band diagram showing the expected 2DEG and 2DHG in an AlN/GaN/AlN heterostructure. (c), (d) show the dependence of the 2DEG and 2DHG densities on the GaN channel and AlN barrier layer thicknesses, assuming the layers are pseudomorphic to AlN buffer layers. A 2DEG density of $n_s \sim 3 \times 10^{13}$ cm^{-2} and 2DHG denisty of $p_s \sim 5 \times 10^{13}$ cm^{-2} are expected in a 4 nm AlN/30 nm GaN/AlN structure.

be calculated numerically through 1D Schrodinger-Poisson solver [55] or using simplified analytical equations proposed by Bader [209]. The analytically calculated 2DEG and 2DHG densities in the structure as a function of GaN, AlN layer thicknesses are shown in **figure 4.1 (c,d)**. This calculation assumes the whole heterostructure is pseudomorphic to the AlN buffer layer, ignoring the limitations of growing thick, lattice-mismatched layers. It is found that tunable

2DEG and 2DHG densities upto 5×10^{13} cm^{-2} are accessible without any doping with appropriate heterostructure design. For comparison, the typical 2DEG densities in the AlGaN/GaN HEMTs are in the order of $5-10\times10^{12}$ cm^{-2} - an order lower than the AlN/GaN/AlN 2DEGs. Hence, if realized, these structures are very valuable from a scientific and device standpoint where high density of 2D electron or holes are desired.

AlN/GaN/AlN heterostructures were grown using plasma-assisted MBE on semi-insulating metal-polar MOCVD-grown AlN on Sapphire starting substrates (same substrates used for the 2DHG growths in chapter 2). Multiple samples were grown simultaneously by co-loading 8 mm × 8 mm substrate pieces on a silicon carrier wafer. A ~400 nm thick AlN buffer layer was first grown at a substrate thermocouple temperature of 780°C, at a growth rate of ~420 nm/hr. The subsequent unintentionally-doped (UID) GaN (~30 nm), AlN (4 nm) layers were grown at a reduced substrate temperature of 750°C. Details of the MBE growth are provided in appendix A.

Hall effect measurements were performed at room temperature and 77 K using corner soldered Indium contacts. A negative Hall coefficient sign was observed, which is a signature of mobile electrons in the sample. A electron sheet density of 2.2×10^{13} cm^{-2} was measured at 300 K and 77 K, with corresponding mobilities of 442 cm^2/Vs, and 650 cm^2/Vs. The lack of carrier freeze-out and the increase in 2DEG mobilities confirms that the AlN/GaN/AlN structure has a degenerate 2DEG present.

However, it is still unclear whether the 2DHG is present in these structures. An investigation of the indium contacts tells us why that might be the case. **Figure 4.2 (a)** shows the as-grown 8 mm × 8 mm sample with the soldered Indium
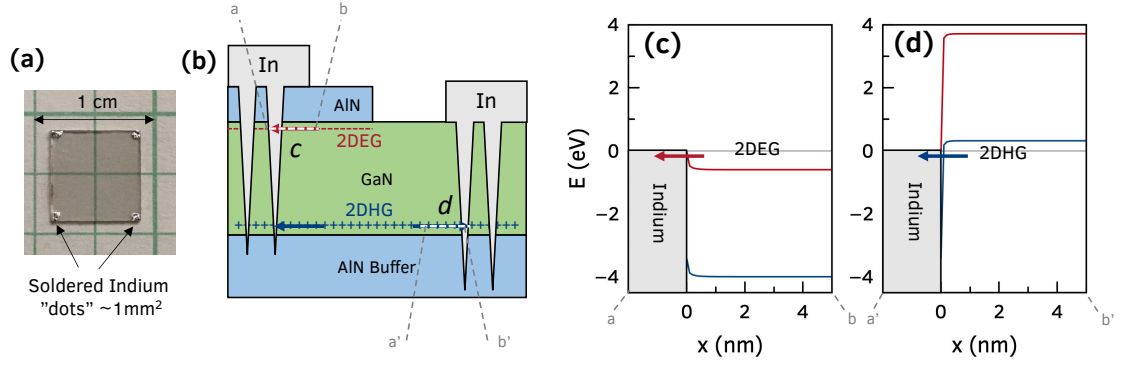
Figure 4.2: (a) Top view of soldered indium contacts on a sample, (b) a cross-section schematic showing how the indium is expected to make contact to both the 2DEG and 2DHG in the heterostruture. (c, d) are the energy band diagrams along the indium-2DEG and indium-2DHG contacts respectively.

contacts at the corners for Hall measurements in a van der Pauw geometry. During the soldering process, the Indium metal is expected to permeate down the threading dislocations, which are perpendicular to the sample surface. The relatively large area (~ 1 mm^2) of the contacts (as compared to a typical transistor ohmic contact pad of 50×50 μm^2) and dislocation density of $\sim 10^9 - 10^{10}$ cm^{-2} aids this phenomenon. The indium metal is thus able to make *direct* contact to the conduction band or valence band of the GaN channel layer. **Figures 4.2 (c, d)** show the band profile of the indium metal making contact to a 2DEG and a 2DHG respectively. Even though the band alignment is Schottky-like for both 2DEG and 2DHG, because of the high charge concentrations the barrier for the carriers is narrow and hence carriers can undergo field emission into the indium metal.

It is clear from **figure 4.2 (b)** that if both 2DEG and 2DHG are present in the structure, then the indium metal will connect to both. Due to lower mobility of ~ 15 cm^2/Vs at RT, the typical 2DHG sheet resistance is on the order of 10 kΩ/sq, where as the sheet resistance of the 2DEG is 500-300 Ω/sq for a 2DEG mobility of $\sim 400 - 600$ cm^2/Vs. In case of parallel conduction, path of least

resistance, i.e. the 2DEG, dominates (see equation (4.1)) transport. This explains the negative Hall coefficient observed in Hall measurements.

However, note that even though indium metal seems to contact both the 2DEG and 2DHG, these contact resistances are not low enough to be "transistor quality". These hand-made contacts have relatively large resistances which are suitable for a Hall-effect and transport measurements where the contact effects are cancelled out or do not dominate, but not in high-performance, scaled transistors.

4.3   The Undoped 2D Electron-Hole Bilayer

The question still remains - is the expected 2DHG present in this MBE-grown AlN/GaN/AlN heterostructure? If it is, then etching away the top AlN barrier from the structure should leave only the 2DHG underneath in the resulting GaN/AlN heterostructure. To test this, two 8 mm × 8 mm, co-loaded, 4 nm AlN/30 nm GaN/AlN heterostructure samples were grown using MBE. ICP dry etch was used to remove the top AlN barrier layer in these samples. **Figure 4.3 (a)** shows the schematic of the two samples, labelled sample A and B. Sample A was covered with photoresist in a cross-pattern. Sample B was not patterned. Sample A and B underwent the same dry etch using a low power BCl_3-based ICP etch to leave ~13 nm GaN on AlN structure. **Figure 4.3 (c)** shows the STEM cross-section across the edge of the pattern on Sample A, confirming that the top AlN layer is removed in the etched regions. The unetched regions in sample A is expected to have both the 2DEG and the 2DHG, whereas the etched regions on sample A, B are expected to have just the 2DHG.
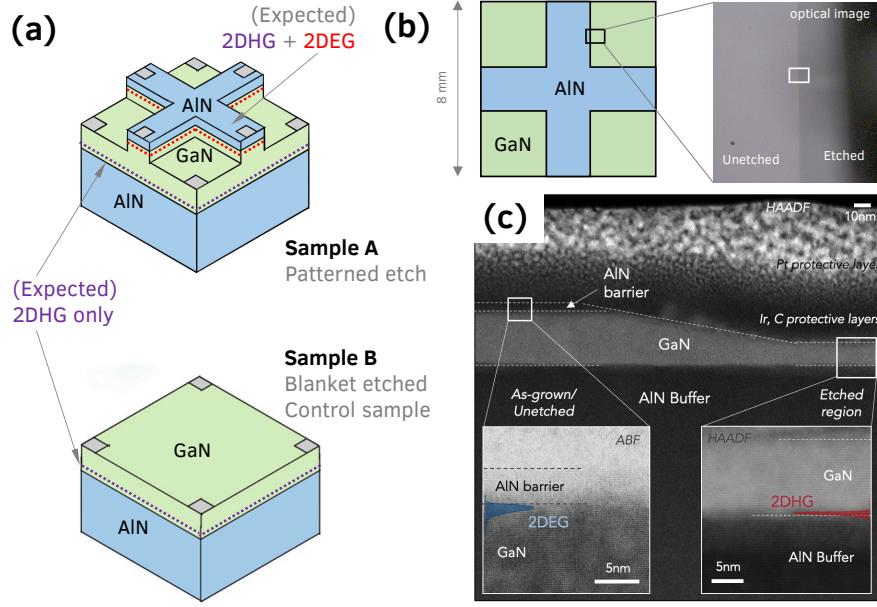
Figure 4.3: (a) Schematics of the AlN/GaN/AlN samples in this study. Sample A underwent a patterned etch to remove the AlN barrier layer, leaving a cross-shaped pattern in the center unetched. Sample B underwent a blanket etch, leaving a GaN/AlN heterostructure after the etch. (b) Optical image of the edge of the pattern in sample A, across which (c) a cross-sectional scanning transmission electron microscope (STEM) scan is taken. The etched and unetched regions are clearly visible in the cross-sectional STEM scan, indicating the interfaces where the polarization-induced 2DEG and 2DHG are expected.

Magnetic-field dependent Hall effect measurements using soldered indium contacts were performed at room temperatures on sample A and B to determine the carrier type. The magnitude of the slope of the Hall resistance R_{xy} versus applied magnetic field B is related to the carrier density through $R_{xy}/B = 1/q_e.n_s$, where q_e is the electron charge. The sign of the slope indicates the sign of the Hall coefficient and identifies the type of majority carriers - a positive slope indicates holes and negative slope indicates electrons.

Both samples A and B showed negative Hall coefficient in the as-grown structures before etching due to the 2DEG at the top interface. Post etching, the measured R_{xy} vs B for samples A and B are plotted in **figure 4.4**. Sample
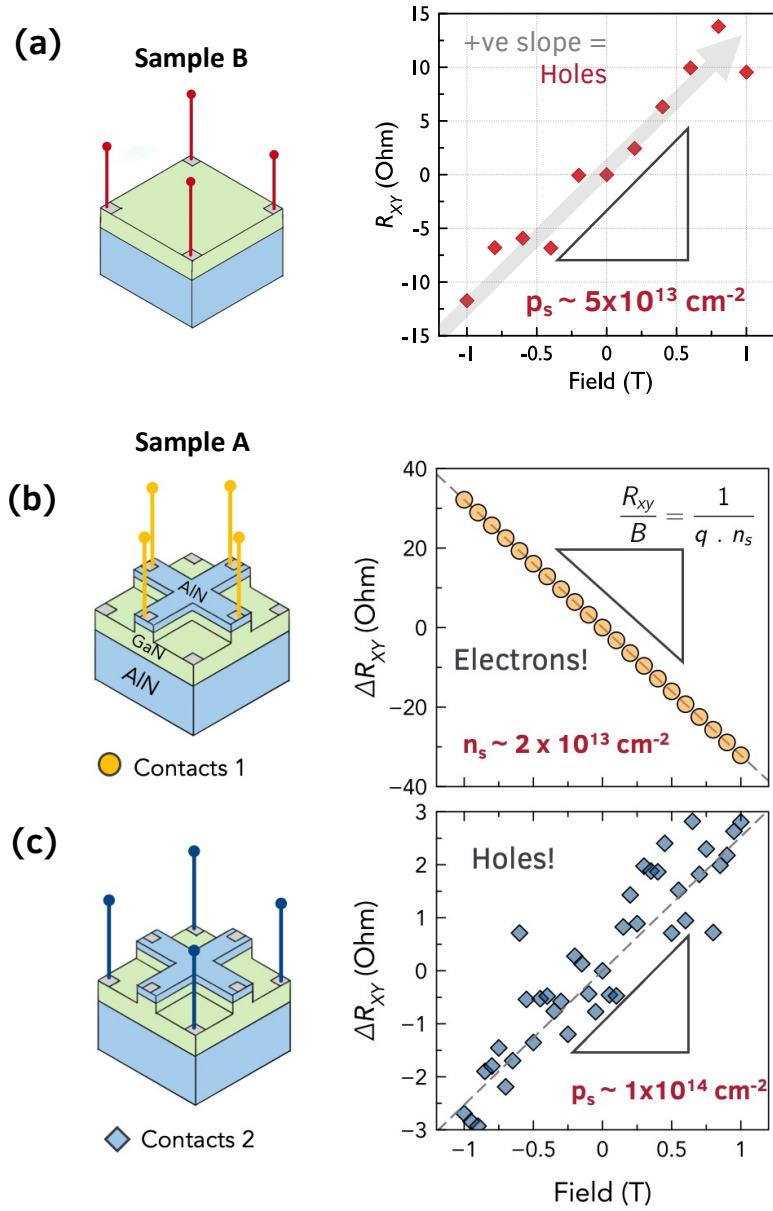
Figure 4.4: Hall resistance R_{XY} versus applied magnetic field B for (a) sample B, showing holes, (b) unetched region of sample A showing electrons, and (c) etched regions of sample A showing holes.

B showed a positive slope corresponding to a hole density of 5×10^{13} cm^{-2} that agrees to the simulated 2DHG density, as well as experimental hole density from an as-grown 13 nm GaN on AlN sample [3]. The switching of Hall sign after the etch confirms that the etched GaN/AlN sample contains a 2DHG. However,

because the top layers have been completely removed in sample B, this result cannot directly comment on whether the 2DHG and 2DEG exist simultaneously in the *same* sample.

The geometry of patterned sample A should be able to distinguish between the 2DEG and 2DHG. Because of the cross-like etch pattern, two sets of indium contacts possible for a 4-contact VdP Hall-effect measurement. Contacts 1 are made on the unetched regions which should contain the 2DEG. The negative slope of R_{xy} vs B, in **figure 4.4 (b)**, confirms that it is indeed the case. Contact 2, on the other hand, are made in the etched corners and should contain only the 2DHG. This is also confirmed by the Hall measurement in **figure 4.4 (c)**. Together with the results on sample B, this conclusively proves the co-existence of purely polarization-induced 2DHG and 2DEG in this undoped AlN/GaN/AlN heterostructures. This represents the first direct electrical proof of its existence.
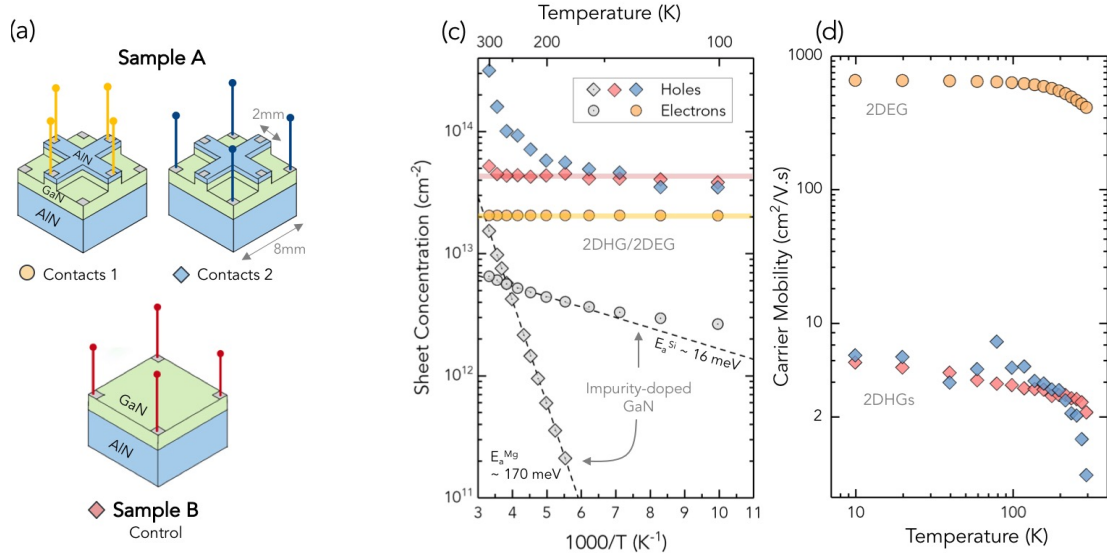
Figure 4.5: Temperature dependent Hall effect measurement results from sample A (both sets of contacts) and sample B, along with Mg- and Si-doped GaN control samples. These results confirm the presence of 2DHG and 2DEG in the AlN/GaN/AlN hetersotructure.

To further characterize the 2DEG-2DHG bilayer, temperature dependent

Hall-effect measurements were performed on samples A and B from room temperature down to 10 K in a magnetic field of 1 T. An excitation current of 10 μA was used. The results are shown in **figure 4.5**. **Figure 4.5 (b)** shows the measured carrier densities as a function of temperature. Also plotted are control samples of Mg-doped p-type GaN ([Mg] $\sim 6 \times 10^{18}$ cm^{-3}) and Si-doped n-type GaN ([Si] $\sim 5 \times 10^{17}$ cm^{-3}) grown on semi-insulating GaN templates. Both the control samples show freeze-out of carriers corresponding to activation energies of 170 meV and 16 meV for the Mg-GaN and Si-GaN respectively, confirming the thermal activation of carriers. On the other hand, the 2DEG in sample A and the 2DHG in the sample B show high charge densities of 2×10^{13} cm^{-2} and 5×10^{13} cm^{-2} respectively. These densities agree to the expected values and do not freeze-out on cooling, confirming their polarization-induced origins. A higher than expected hole density of $> 10^{14}$ cm^2/Vs is measured in sample A via contacts 2 at room temperatures, which exhibit slight freeze-out upon cooling. This is believed to be a artifact of the sample geometry and will be discussed below.

Figure 4.5 (c) shows the temperature dependence of the carrier mobilities in samples A and B. The 2DEG mobility in sample A goes up from 420 cm^2/Vs at 300 K to $\sim$ 700 cm^2/Vs at 10 K upon cooling. Further discussion on the 2DEG mobility provided in section 4.4.1. The temperature trend of the 2DHG mobilities in sample A and B are similar, increasing from 1-2 cm^2/Vs at 300 K to 6 cm^2/Vs at 10 K, due to phonon freeze-out in GaN/AlN 2DHG. However, the 10 K hole mobilties were limited to < 10 cm^2/Vs compared to 200 cm^2/Vs reported in as-grown GaN/AlN structures [3], which might be due to the surface damage from the dry etch [205].

The presence of high density holes and electrons in their respective conduction band (CB) and valence band (VB) quantum wells separated by a semi-conducting GaN layer sets up a vertical diode-like band alignment in the AlN/GaN/AlN heterostructure. It should be possbile to turn this diode "on" by applying a large enough bias ($> E_g^{GaN}/q_e \sim 3.4$ V) vertically. Although a complete understanding of the setup requires a comprehensive numerical 2D electrostatics model, a couple of unique experimental observations point to presence of this vertical diode setup in the AlN/GaN/AlN heterostructures.
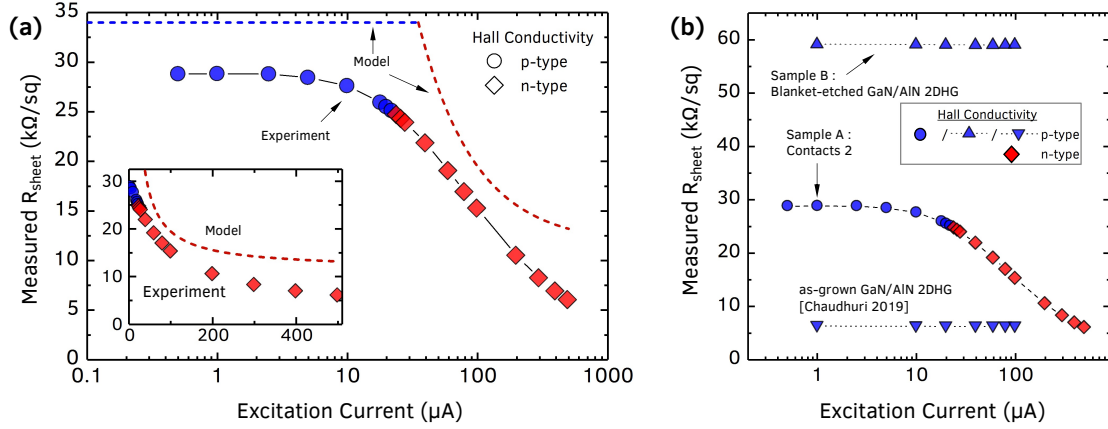
Figure 4.6: (a) The measured sheet resistance of sheet resistance R_{sheet} in the etched area of sample A (contacts 2), as a function of excitation current. A unique decrease in sheet resistance is observed with increase in excitation current. The simple circuit model, shown in figure 4.8, explains this trend. (b) This behavior is not observed in as-grown GaN/AlN 2DHGs [3] or blanket etched GaN/AlN (sample B), where the R_{sheet} has no dependence on the excitation current as expected from a Hall effect measurement.

In a Van der Pauw resistivity measurement, the excitation current is driven across a pair of contacts along one edge of the sample, and the voltage is measured across the other pair of contacts along the other edge. The sheet resistance is then determined through the Van der Pauw formula. The measured sheet resistance, which is the property of the material, is expected to be independent of the excitation current. Figure **figure 4.6 (b)** shows the measured sheet resis-

tance of GaN/AlN 2DHG samples vs excitation current. Both sample B (etched GaN/AlN heterostructure) and an as-grown GaN/AlN 2DHG [3] exhibit constant sheet resistance across the current range, as expected. The polarity of the carriers also remains positive (holes) from the Hall coefficient sign. The same behavior is also seen in as-grown AlN/GaN/AlN 2DEGs, where the resistance and polarities are independent of the excitation current used during measurement.

However, an unusual behavior is observed in the sheet resistance of the 2DHG in the etched areas of sample A (contacts 1 in **figure 4.5**). **Figure 4.6 (a)** shows the measured Van der Pauw sheet resistance as a function of excitation current for contacts 1 on sample A. At low excitation currents $< 10\,\mu$m, the sheet resistance is constant at about 25 kΩ/sq and the carrier polarity obtained from the Hall sign stays positive, as expected from the 2DHG in the region. However on increasing the current beyond 10 μA, the measured sheet resistance starts decreasing. Around the same value, interestingly the Hall coefficient sign also *flips* to negative, now indicating mobile electrons. It remains negative beyond 10 μA while the sheet resistance keeps decreasing down to 5 kΩ/sq at 500 μA. **Figure 4.6 (b)** contrasts this behavior to the the GaN/AlN samples, which show constant resistance vs current as expected. The drop in resistance after a certain "turn-on" current value points to a *current-controlled diode-like behavior*. This is not unreasonable to imagine since sample A contains two high density carrier gases of opposite polarities separated by a GaN layer.

In such a vertical diode like setup, a recombination of the two carrier gases is expected to emit photons if their wavefunctions sufficiently overlap. The energy of the emitted photon should be close to the energy bandgap of the separating
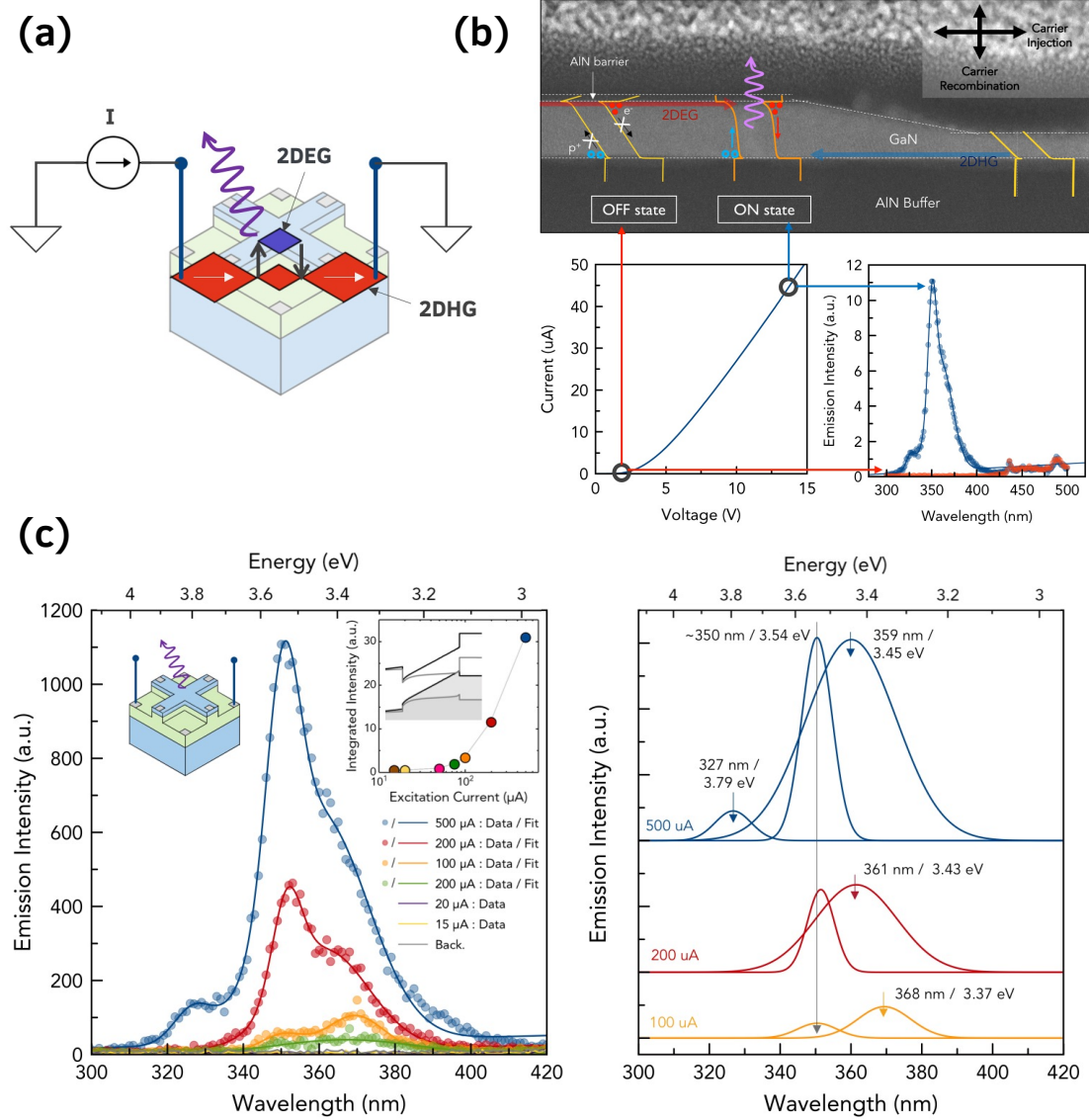
Figure 4.7: (a) Schematic showing the sample geometry and contact scheme for the electro-luminescence (EL) measurement (b) Cross-section STEM showing the energy band diagram of the vertical diode in its OFF state, and turning ON at high currents. (c) The emission spectra as a function of excitation currents, showing clear peaks around 3.4-3.6 eV. No emission is detected below 10 μA.

GaN layer, ie. $\sim E_g^{GaN}$ = $\sim$3.4 eV (364 nm). To study its optical properties, electro-luminisence (EL) measurement was performed on sample A by injecting current through the indium contacts at the opposite etched corners of the sample in a 2 probe setup. This is illustrated in the inset of **figure 4.7 (a)**. The IV charac-

145

teristics in this configuration, shown in **figure 4.7 (b)**, shows a non-ohmic behaviour with an apparent turn-on voltage of ~ 4 V. This can attributed partly to the Schottky-like behaviour of the indium metal contact to the valence of GaN, and partly to a possible diode-like behaviour of the E-H bilayer. The emission spectra measured at different injected current level is shown in **figure 4.7 (c)**. At low currents ($< 50\,\mu$A), no clear emission is observed above the background detection level. On increasing the injection current beyond 50μA, significant photon emission from the sample is measured in 340 nm - 380 nm wavelength range. The emission intensity is observed to increase at higher excitation current with clear peak emerging around the wavelength of 350 nm. Gaussian fits of the measured spectra at the higher current levels are shown in **figure 4.7 (c)**. There are 2 distinct peaks observed at 360 nm and ~ 352 nm, which increase in intensity with increasing current, and a third peak at 327 nm which emerges at 500 μA. This result indicates that the detected photons are emitted as a result recombination of carriers separated in energy of ~ 3.5 eV, further proving the presence of the two carriers in this AlN/GaN/AlN bilayer system. To the author's knowledge, this the first demonstration of electrically-pumped light emission from completely undoped III-nitride semiconductor heterostructure.

The above signatures of the vertical diode, i.e. the sheet resistance drop and light emission beyond a certain turn-on current, are slightly counter intuitive as the current is injected only through 2DHG layer but somehow leads to the recombination of the 2DEG and 2DHG. A natural question that arises is - how do the 2DEG and 2DHG layers interact in this setup? A simple circuit model of the structure can qualitatively explain the observed phenomena and the origin of the diode-like behaviour. The equivalent circuit diagram and model is shown in **figure 4.8 (a)**. The current path through the structure is simplified and each

146
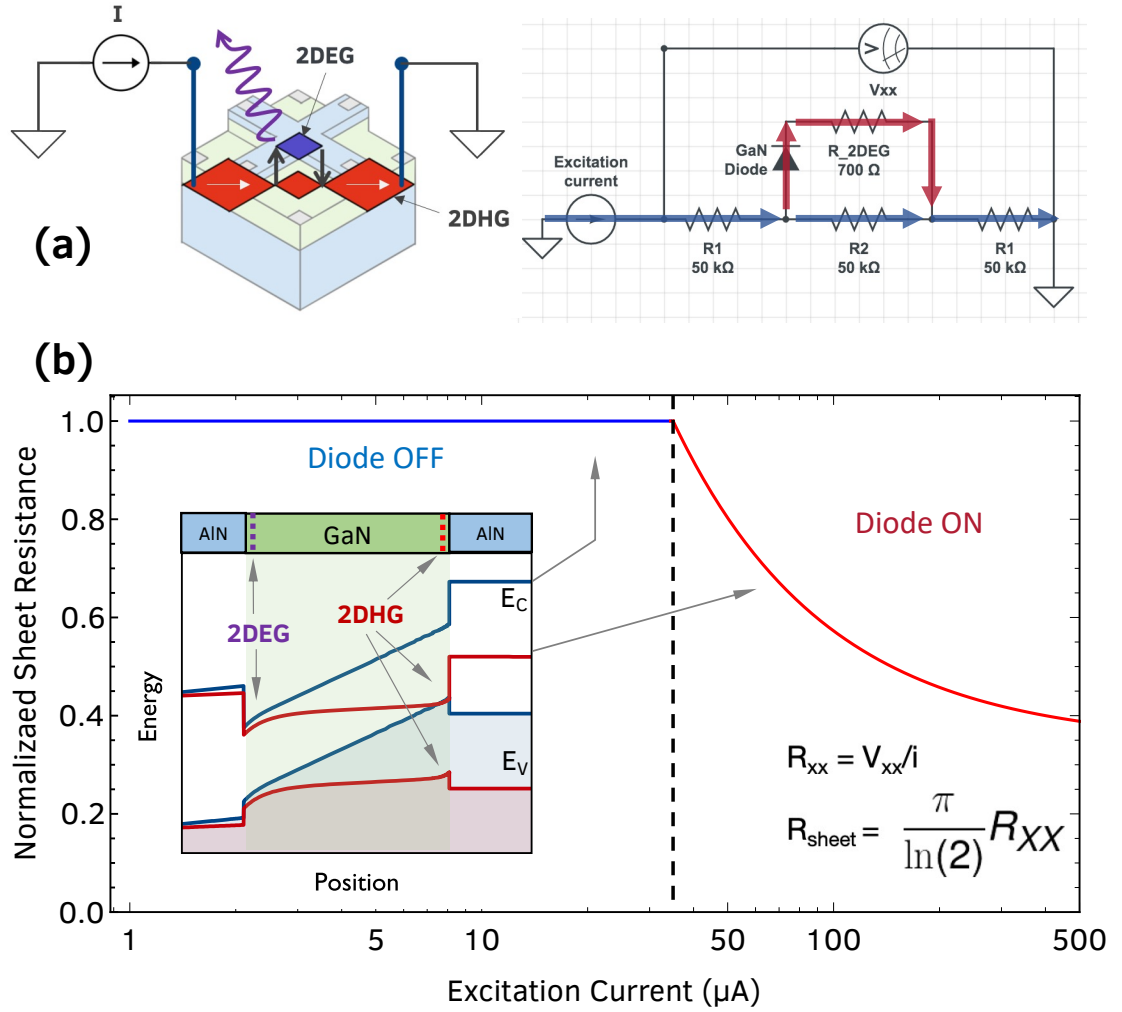
Figure 4.8: (a) Simple circuit model representing a straight line path between the two corner contacts by a network of resistors, and a GaN diode. The GaN diode represents the vertical diode band alignment between the 2DEG and 2DHG as shown in the inset. (b) The trend of resistance vs excitation current according to this model qualitatively agrees to the experimentally observed behavior in figure 4.6.

section of 2DHG and 2DEG are represented by resistors of suitable values estimated by the experimental sheet resistances. A GaN diode with turn-on voltage of 3.5 eV represents the vertical diode in the structure.

When a small current is passed through the 2DHG, the voltage drop across R_1 (the 2DHG) is small remains below the turn-on voltage of the GaN diode.

Hence all the conduction is through the 2DHG by mobile holes. If the injection current is increased, the voltage drop across the GaN diode slowly increases. Once it reaches beyond a certain critical current, the diode turns on. In this situation, because the 2DEG offers a path of lower resistance to the current, and *the current flows through the 2DEG layer bypassing the 2DHG*. The calculated normalized resistance versus injected current in the circuit is plotted in **figure 4.8 (b)**. This shows how the resistance of the current path decreases as a function of the current beyond a certain critical value of $\sim 30\ \mu A$. The current flowing through the 2DEG also partly explains why we observe a flip in the Hall coefficient. The model is plotted alongside experimental data in **figure 4.7**. This simple model agrees reasonably well with the trend seen in the experimental values of the measured sheet resistance measured. Additionally, the diode turn-on explains why the light emission in the EL measurement is observed beyond a certain critical current. It corresponds to the flattening of the GaN energy bands and subsequent overlapping of the 2DEG, 2DHG wavefunctions which result in recombination of electrons and holes.

The above model simplifies a complex 2D electrodynamics problem into a simple circuit and is able to qualitatively explain the observations. However, a more rigorous model and measurements of specially designed device structures is required to explain the phenomena more comprehensively.

Although structures with both 2DHG and 2DEGs have previously been reported in III-nitrides [16, 17, 12], they all contain Mg-doped layers to induce the 2D hole gas, which provide parallel conduction channels in the structures and mask the 2DHG conduction effects. A few groups have attributed the deviation from expected electrical characteristics in HEMTs to the possible presence of a

2DHG [210]. But so far, no direct transport study of an undoped E-H bilayer in III-nitride heterestructure exists, mainly due to the lack of purely polarization-induced holes. This work represents the first electrical and optical proof of the E-H bilayers, and opens up the space for the exploration of rich physics obtained by the interaction between these carriers. Undoped E-H bilayer systems in other material systems such as GaAs [211] have enabled study of rich physical phenomena such as excitonic interactions [212], Coloumbic drag between closely spaced electrons and holes [213], superfluidity [214] etc. The AlN/GaN/AlN E-H bilayer can serve as a platform to study such phenomena which previously has not been possible in the III-nitride semiconductors (more discussion in section 4.5). Additionally, this heterostructure is also a prime candidate to enable high performance wide-bandgap CMOS as it provide channels for both p-type and n-type transistors, with the added material and device advantages of an AlN buffer [137, 53].

4.4   AlN/GaN/AlN 2DEGs for high-power RF HEMTs

In the previous section, polarization-induced 2DEGs were demonstrated on the AlN platform by growing an AlN barrier layer on top of the GaN channel layer to form a 2DEG-2DHG bilayer. The rest of this chapter will focus on the 2DEG at the top GaN/AlN interface and its transport properties, specifically for its use as an n-type transistor channel in high-power RF AlN/GaN/AlN HEMTs. The resulting transistor results are discussed in chapter 5.

2DEGs in III-nitride semiconductors are generated by the polarization difference across epitaxial heterointerfaces. The magnitude of this polarization
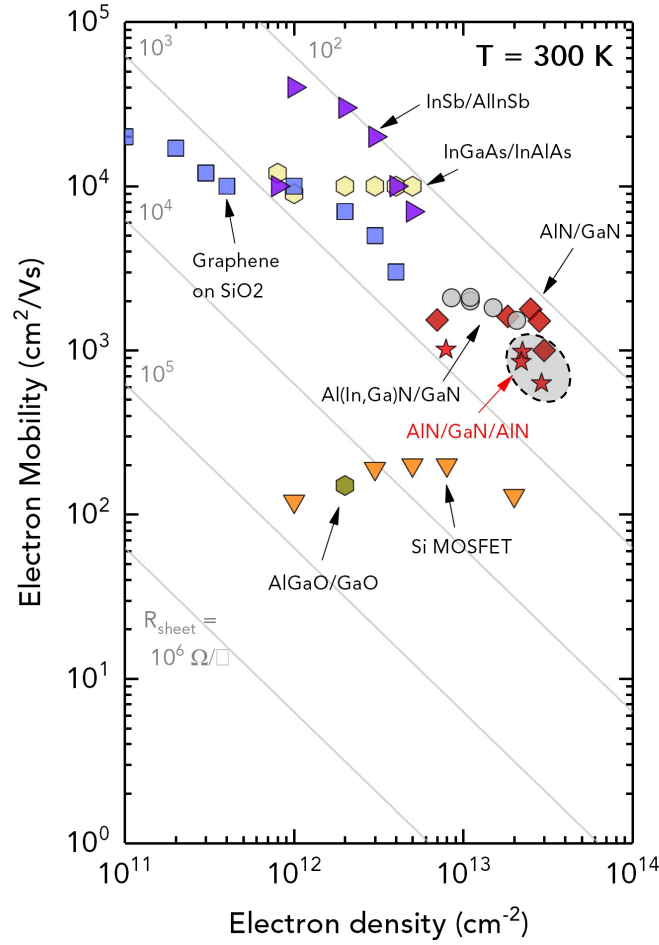
Figure 4.9: Benchmark plot comparing the best room-temperature transport of AlN/GaN/AlN 2DEGs with 2D electron systems across all semiconductor material platforms.

difference electrostatically determines the 2DEG densities in the as-grown heterostructures. In a structurally and chemically pure heterostucture, the 2DEG mobilities are ideally limited by polar optical phonon (POP) scattering [132] at room temperature (RT). This POP scattering increases with the increase in charge densities n_s. Typical AlGaN/GaN 2DEGs of n_s in mid-10^{12} cm^{-2} have exhibit RT mobilities upto ~1800-2000 cm^2/Vs. In InAlN/GaN [123, 215] or AlN/GaN [124, 216] heterostructures, 2DEGs with higher n_s ~ 1×10^{13} cm^{-2} exhibit typical RT mobilities of ~1200 cm^2/Vs.

The all-binary AlN/GaN/AlN heterostructure enables even higher as-grown 2DEG densities than InAlN/GaN and AlN/GaN heterostructures at $n_s \sim 2 - 4 \times 10^{13}$ cm^{-2}. These high 2DEG densities are responsible for low access resistances and high on-currents in scaled RF HEMTs [54, 53]. The high charge densities result in low sheet resistances of ~ 300 Ω/sq. which are comparable to AlGaN/GaN 2DEGs and enable high-performance RF HEMTs. However, if the 2DEG mobility is increased it can potentially improve the transconductance and speeds of the RF HEMTs even further. Hence, there is an increasing interest to understand the 2DEG mobility and the dominating scattering mechanism in these AlN/GaN/AlN structures with strained GaN channels.

Before getting into the details of the transport, it is useful to learn how this 2DEG compares to 2D electrons in other semiconductor materials. **Figure 4.9** compares the room temperature electron mobilities measured in the AlN/GaN/AlN heterostructures in this work against the 2DEGs measured across other semiconductors. The undoped AlN/GaN/AlN allows access to high 2DEG densities of $\sim 2 - 3 \times 10^{13}$ cm^{-2} which are not possible in other material systems, that too without any chemical dopants. These high charge densities translate to some of the highest transistor currents of > 3 A/mm. When combined with the high breakdown voltages owning to the large bandgap of GaN and AlN, this structure is ideal for high-power operation.

The electron density in silicon inversion channels n-MOSFET can reach upto $\sim 1 \times 10^{13}$ cm^{-2} under high gate biases, But the electron mobilities at these densities are still limited to 100-200 cm^2/Vs even after more than 40 years of research into ways to boost the channel mobilities. On the other hand, InGaAs and InSb offer some of the highest room temperature mobilties at room tem-

perature thanks to low electron effective masses, and therefore produce some of the fastest THz-speed transistors, but their electron densities are an order lower compared to the AlN/GaN/AlN 2DEGs. Additionally, Si and InGaAs both have lower breakdown voltages than GaN, and therefore are not suitable for high-power operations.

The 2DEG densities in the AlN/GaN/AlN heterostructures therefore offer an opportunity to study the electron transport in the uncharted territories of $n_s > 3 \times 10^{13}$ cm^{-2}. In the following sub-sections we take a closer look at the transport of these 2DEGs, the current state-of-art and its limitations.

4.4.1 Low-field transport

AlN/GaN/AlN heterostructures with strained 30 nm GaN channel layer and 4 nm AlN barrier layer on top [47] show high 2DEG densities of $\sim 2-3 \times 10^{13}$ cm^{-2} (depending on the GaN cap thickness), which are higher than typical densities of $\sim 5-10 \times 10^{12}$ cm^{-2} seen in AlGaN/GaN HEMTs. How do the mobilities of such high carrier density 2DEGs compare to those in GaN HEMTs?

The room temperature mobility of GaN 2DEG in a chemically and structurally pure crystal is expected to be limited by scattering off polar optical phonons (POP). POP and acoustic phonon (AP) scattering determine the *intrinsic* mobility limit at a given temperature. At low temperatures, the phonons exhibit freeze-out, and the mobility is then limited by *extrinsic* scattering mechanisms in an impure crystal. Common extrinsic scattering mechanisms which affect GaN 2DEGs are interface roughness (IR) scattering, charged dislocation scattering [119].
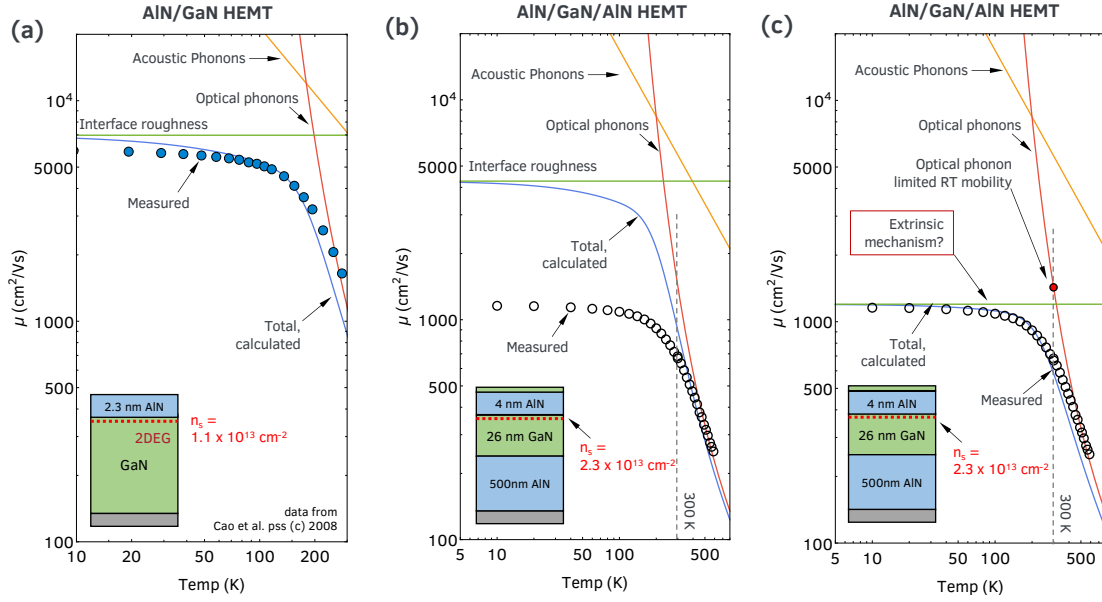
Figure 4.10: Temperature dependent Hall effect mobilities of (a) an AlN/GaN HEMT with 2DEG density of 1.1×10^{13} cm^{-2}, and (b, c) ALN/GaN/AlN HEMTs with 2DEG density of 2.3×10^{13} cm^{-2}. The mobility in the AlN/GaN HEMT is limited by optical phonon scattering at room temperatures and by interface roughness scattering at low temperature. However, the AlN/GaN/AlN 2DEG transport is affected by an unknown extrinsic scattering mechanism at temperatures < 400 K. *High-temperature Hall-effect measurements were peformed by Sophia Handley.*

Figure 4.10 (a) shows the temperature dependent mobility experimentally measured in a AlN/GaN 2DEG [217] of density 1.1×10^{13} cm^{-2}. The 2DEG density remains constants throughout the temperature range. The calculated mobilities due to AP scattering, POP scattering and IR scattering are also plotted. The total mobility due to all scatterers is calculated using Mattheisen's Rule. The total theoretical mobility agrees well with the measured data. The room temperature mobility of this 2DEG is around 1800 cm^2/Vs and is limited by POP scattering. On cooling, the AP and POP freeze-out and the mobility rises and saturates at the IR limited value of $\sim$ 6000 cm^2/Vs at 10 K. Therefore the extrinsic scattering mechanism domintating the low-temperature mobility here is interface roughness scattering. This is expected since there are no intentional

dopants or alloyed layers in the crystal.

To study the temperature-dependence of 2DEGs on AlN, AlN/GaN/AlN heterostructure with a strained 26 nm GaN channel layer and 4 nm AlN barrier layer was grown using PA-MBE on 6H-SiC substrate. The details of growth are presented in detail in appendix A. Temperature-dependent Hall measurements were performed using corner Indium contacts from T = 10 K to 590 K. The results are plotted in **figure 4.10 (b,c)**. The room-temperature mobility of the AlN/GaN/AlN 2DEG is ~ 700 cm^2/Vs, which increases upon cooling and saturates to ~ 1100 cm^2/Vs at 10 K.

The theoretical curves for mobilities due to AP scattering, POP scattering and IR scattering are plotted in **figure 4.10 (b)**. The AP and POP scattering are calculated using equations (2.3) and (2.4), by substituting the GaN valence band constants with corresponding conduction band (CB) constants of electron effective mass m_{eff} = 0.23m_0 (where m_0 is the mass of free electron) and CB deformation potential of 9.1 meV. For an estimated dislocation density of 10^{10} cm^{-2} in these samples, the charged dislocation scattering limited mobility is > 2 × 10^4 cm^2/Vs, which is an order greater than measured values and hence is disregarded in this analysis.

From **figure 4.10 (b)**, the experimental data agrees well with the predicted total mobility at temperatures T > 400 K. However, the data deviates from the prediction at T < 400 K. Even though the trend seems similar to the AlN/GaN 2DEG mobility in **figure 4.10 (a)**, ie. the mobility rises upon cooling and then saturates, the saturation value of ~ 1100 cm^2/Vs is much lower than predicted IR scattering limited value of ~ 5000 cm^2/Vs. This tells that, unlike the AlN/GaN 2DEGs, the dominating extrinsic scattering mechanism is not interface rough-

ness in these AlN/GaN/AlN 2DEGs.

Now lets assume a temperature-independent extrinsic scattering mechanism which limits the mobility to $\mu_{Ext} \sim 1200$ cm^2/Vs. The total calculated mobility, shown in **figure 4.10 (c)**, then agrees very well with the experimental data throughout the temperature range of 10 - 500 K. It is therefore clear that an extrinsic scattering mechanism limits the mobility of these AlN/GaN/AlN 2DEG. The calculations here eliminate IR scattering or dislocation scattering as the dominant extrinsic mechanism. Identifying this extrinsic mechanism is therefore necessary to explain the transport in these 2DEGs, and provide a path to higher mobilities. This remains an open scientific question in the field.
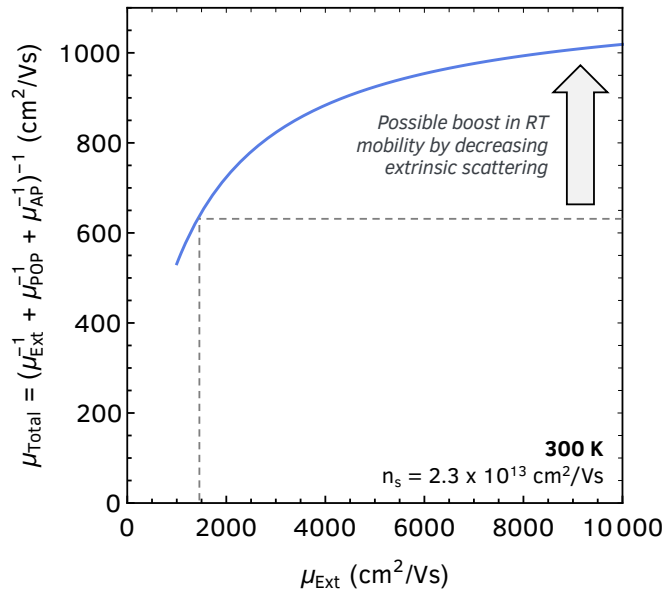
Figure 4.11: Calculated total mobility at room temperature of AlN/GaN/AlN 2DEG (density 2.3×10^{13} cm^{-2}) as a function of the extrinsic scattering mechanism limited mobility μ_{Ext}. Total mobility considers the scattering due to optical μ_{POP} and acoustic phonons μ_{AP} and the unknown extrinsic mechanism. Once the extrinsic scattering mechanism is identified and its effect reduced, the room temperature 2DEG mobility can be increased to the phonon limit of ~1000 cm^2/Vs.

However, within the constraints of this yet-to-be identified extrinsic mechanism, what is the highest room temperature mobility that can be achieved in

this AlN/GaN/AlN 2DEG? To answer this question, the extrinsic mechanism limited mobility μ_{Ext} is varied from 1200 to 10^4 cm^2/Vs, and the resultant total 2DEG mobility ($n_s \sim 2.3 \times 10^{13}$ cm^{-2}) at room temperature is calculated. The result is plotted in **figure 4.11**. The total mobility approaches the POP scattering limited mobility of ~ 1000 cm^{-2}/Vs when the $\mu_{Ext} > 6000$ cm^2/Vs. Thus, if the extrinsic scattering mechanism is identified, and its effect is reduced, the room temperature mobilities in the as-grown AlN/GaN/AlN 2DEG can be boosted to ~ 1000 cm^2/Vs. This corresponds to a reduction in sheet resistance from ~ 390 to ~ 270 Ω/sq. for a 2DEG density of $\sim 2.3 \times 10^{13}$ cm^{-2}, which is highly desired for reducing the access resistances in high-speed RF HEMTs.
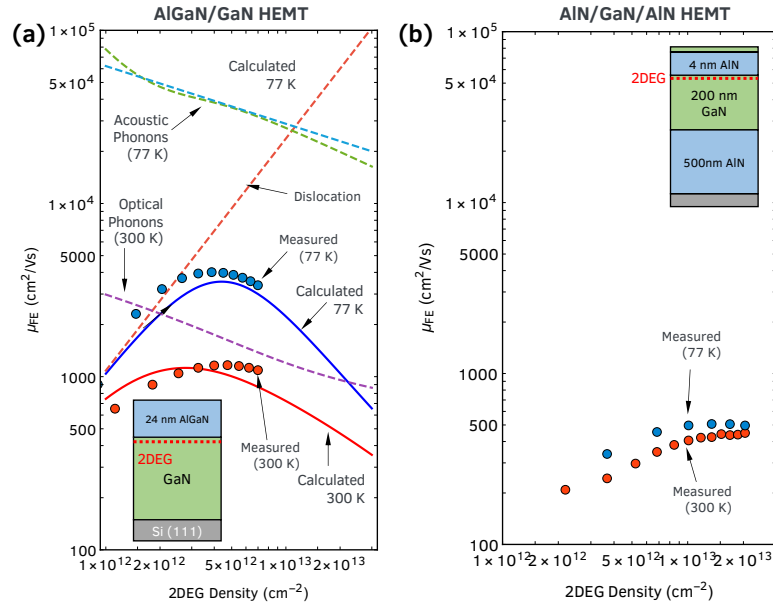
Figure 4.12: Field effect (FE) mobilities as a function of 2DEG densities of an (a) AlGaN/GaN 2DEG and (b) AlN/GaN/AlN 2DEG, measured from output conductance of gate controlled channel in a FATFET ($L_G = 20$ μm).

Phonon limited scattering is expected to decrease with decrease in 2DEG density. Hence, the density dependent mobility study is also critical to identifying the limiting scattering mechanism in a 2DEG system. One way to vary the density is through field-effect, i.e. by applying a voltage through the gate in an

FET. By measuring the corresponding change in channel conductance, the FE mobility can be extracted (see section 2.7).

Field effect (FE) mobilities were extracted for an AlN/GaN/AlN HEMT and a standard GaN HEMT with large gates L_G = 20 μm. The 2DEG density as a function of gate voltage under the gate is obtained from CV profile. The preliminary results from this experiment are shown in **figure 4.12**. **Figure 4.12 (a)** shows the FE mobility as a function of 2DEG density for a control AlGaN/GaN HEMT sample. The mobilities increase with decrease in density, peak and then fall at really low densities. Upon cooling, the mobility increases, as expected from phonon freezeout. Fitted curves for phonon scattering and dislocation scattering are also plotted. Comparison to the theoretical model shows that, in the AlGaN/GaN 2DEG, the room temperature mobilities are limited by POP scattering at high densities, and by dislocation scattering at low charge densities. This concurs with what is expected and reported for these 2DEGs in literature, and validates the experiment and extraction method.

Figure 4.12 (b) shows the preliminary results of FE mobility measurements performed on the AlN/GaN/AlN HEMT sample. This is the same sample which showed output powers of 3 W/mm at 10 GHz [218]. The extracted mobilites behave slightly different compared to the AlGaN/GaN HEMT. The 2DEG mobilities, both at room temperature and 77 K, decrease with decrease in density, and no "peak" is observed. Efforts are currently underway to explain the measured data with appropriate scattering models. Together with the data in **figure 4.10**, this data in **figure 4.12** is valuable in the quest to identify the dominating extrinsic scattering mechanism, and to explain the transport of this 2DEG system.
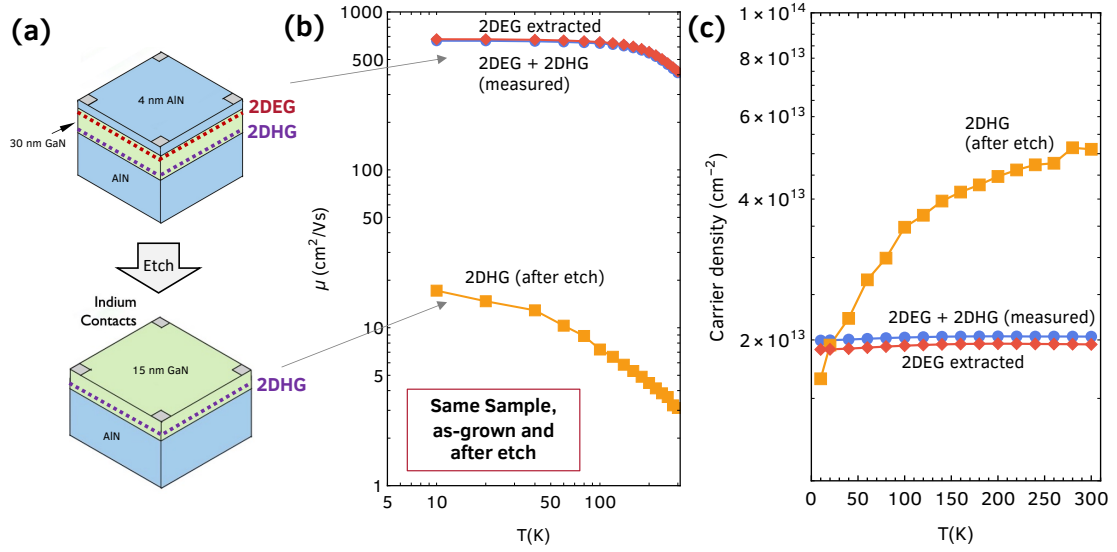
Figure 4.13: (a) Hall-effect measurement was performed on an as-grown AlN/GaN/AlN bilayer sample, which was then etched down to reveal just the 2DHG and Hall-effect measurement was repeated. (b), (c) show the extracted 2DEG, 2DHG mobility and density as a function of temperature assuming parallel conduction in the as-grown sample Hall measurement.

One of the differences between the AlN/GaN HEMT and AlN/GaN/AlN HEMT is the presence of a high-density 2D hole gas at the bottom GaN/AlN interface. A natural question therefore arises that whether the 2DHG underneath is affecting the measured 2DEG Hall mobilities. One way that is possible is via parallel conduction during the Hall measurement leading to spurious results. As discussed earlier, the soldered indium contacts used in this are expected to make contact to both the 2DEG and 2DHG present underneath. If parallel conduction occurs from two channels with hole and electron densities p_s, n_s respectively, and corresponding mobilities μ_p, μ_n, then the *apparent* measured density n_{Hall} and mobility μ_{Hall} are given by :

$$n_{Hall} = \frac{(\sigma_n + \sigma_n)^2}{\sigma_p \mu_p - \sigma_n \mu_n} \tag{4.1}$$

$$\mu_{Hall} = \frac{\sigma_p \mu_p - \sigma_n \mu_n}{(\sigma_n + \sigma_n)} \tag{4.2}$$

where $\sigma_n = q_e n_s \mu_n$ and $\sigma_p = q_e p_s \mu_p$ are the conductivities of the two layers,

q_e is the electron charge. The Hall sign will be negative (apparent electrons) if inequality $\sigma_n \mu_n > \sigma_p \mu_p$ holds, and positive (apparent holes) when vice versa.

For the AlN/GaN/AlN heterostructure, the typical σ_n/σ_p is ~ 33 and μ_n/μ_p is ~ 70, therefore $\sigma_n \mu_n >> \sigma_p \mu_p$ always holds. Using the above expressions, one can extract the "real" 2DEG mobility from the measure "apparent" Hall mobility. **Figure 4.13** shows the extracted mobilities and densities for the bilayer sample B studied in the previous section. It is clear that the $n_{Hall} \sim n_s$ and $\mu_{Hall} \sim \mu_n$ because of the higher conductivity and mobility. Therefore the lower 2DEG mobilities in these AlN/GaN/AlN structures are *not* an artifact of the measurement of a parallel 2DEG and 2DHG.
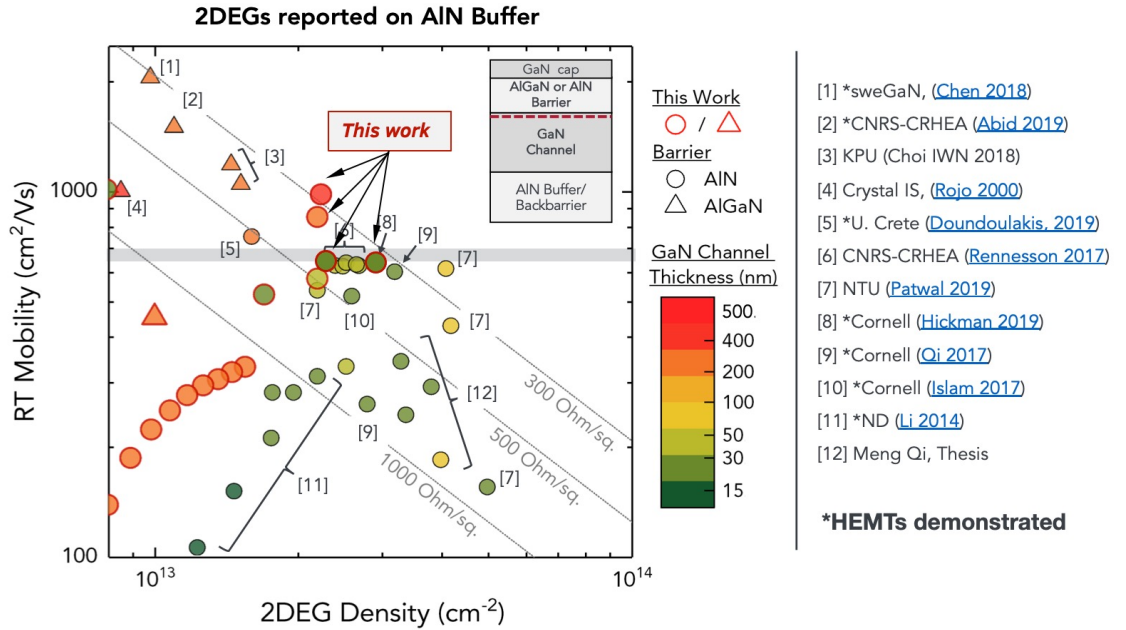
Figure 4.14: Benchmark of all reported 2DEGs in Al(Ga)N/GaN/AlN heterostructures, grown on different substrates (Si, SiC, sapphire) using different epitaxial growth techniques (PAMBE, NH$_3$-MBE, MOCVD) [40, 41, 42, 43, 44, 45, 46].

Are these 2DEG mobilities sensitive to the growth technique or substrate choice? There has been a rising interest of the field in these AlN/GaN/AlN

2DEGs motivated by the promising HEMT results. There have been numerous reports of epitaxial growth of AlN/GaN/AlN and AlGaN/GaN/AlN structures using different epitaxial techniques [40, 41, 42, 43, 44, 45, 46] and on different substrates such as Silicon [40], SiC [54, 45], sapphire [219] and single-crystal AlN [42]. **Figure 4.14** compares the room-temperature transport of all the reported 2DEGs on the AlN platform so far. No clear trend is visible between growth techniques or substrates. However, a trend is observed in terms of the GaN channel layer thickness. Interestingly, the RT mobility measured in these 2DEGs with a strained GaN channel layer thickness $\leq$ 50 nm remains below ~700 cm^2/Vs *across all reports*. The highest mobilities of 1200-2000 cm^2/Vs are all measured in thick, relaxed GaN channel layers (> 200 nm) with AlGaN barriers. These structures and numbers are comparable to the typical numbers in GaN HEMTs, but they loose out on the advantages offered by the relaxed AlN barrier in a pseudomorphic, binary structure. The benchmark data points are replotted as a function of GaN channel layer thickness in **figure 4.15 (a)**, which makes this trend clearer.

To investigate this observed trend of 2DEG mobility with GaN channel thickness in a more controlled manner, a series of AlN/GaN/AlN heterostructures, summarized in **Table 4.1**, were grown on semi-insulating Si-face 6H-SiC substrates using PA-MBE. The epitaxial structure is shown in **figures 4.17 (a,b)** in the representative STEM image. All the samples had a ~ 450 nm AlN buffer layer, a 4 nm AlN top barrier layer, and a ~ 1.5 nm GaN passivation layer. The GaN channel layer thickness t_{QW} was varied from 20 nm to 500 nm between samples. X-ray diffraction (XRD) scans confirmed the targeted thicknesses. Low field Hall-effect measurement results are plotted in **figure 4.15 (b)**. Increasing the channel layer thickness showed an increase in the 2DEG density, which is ex-
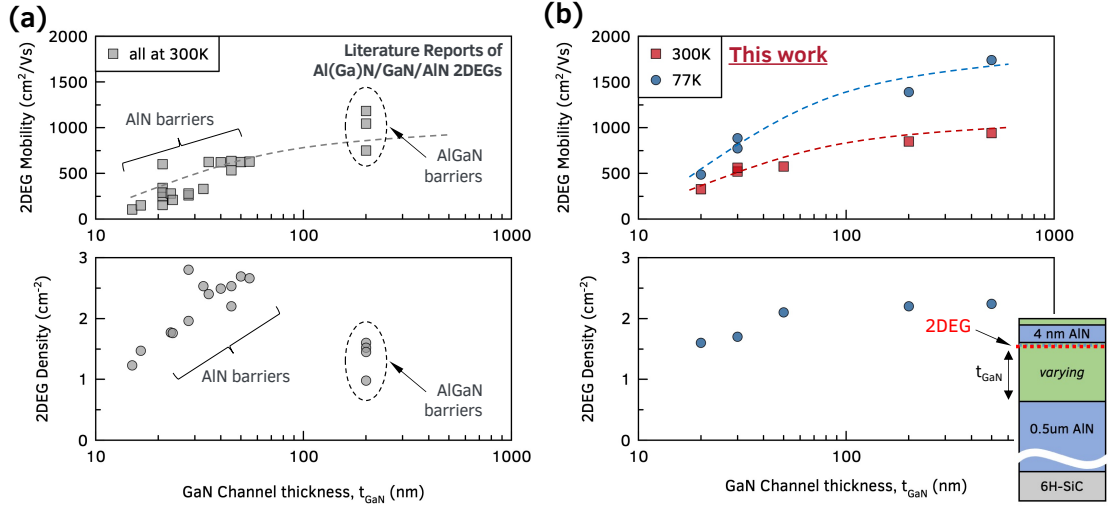
Figure 4.15: Room temperature 2DEG mobilities in Al(Ga)N/GaN/AlN heterostructures as a function of the GaN channel thickness, (a) from literature reports, and (b) from a controlled growth study in this work. A clear trend is observed - thicker GaN channel layer results in higher room-temperature mobilities.

pected electrostatically. Interestingly, both the room temperature and low temperature (77 K) Hall-effect mobilities increase with t_{QW}. A 500 nm channel structure showed higher charge *and* RT mobility (~ 950 cm^2/Vs) compared to a 20 nm channel structure (~ 327 cm^2/Vs). This observation is consistent with the trends observed across the literature reports studying this structure, as shown in **figure 4.15 (a)**, and could help identify the unknown extrinsic mechanism limiting the 2DEG mobilities in this AlN/GaN/AlN heterostructure.

4.4.2   High-field velocities

The intrinsic cut-off frequency f_T of an FET with gate length L_G is determined by the electron transit time $\tau = 1/2\pi f_T = L_G/v_e$, where v_e is the average ensemble velocity of the carriers in the channel. At low electric fields F, this velocity is determined by the carrier mobility μ_n through $v = \mu_n.F$. At high electric fields,
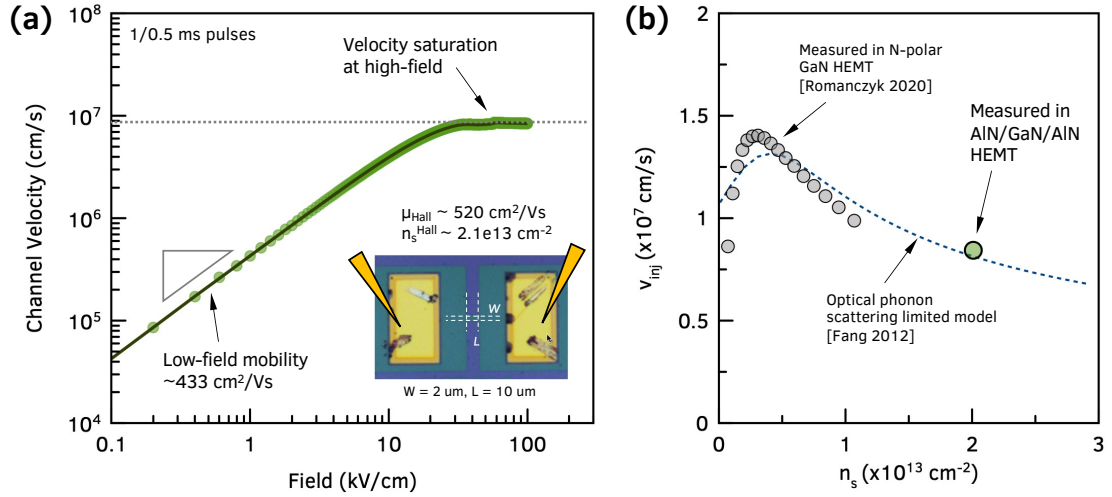
Figure 4.16: (a) The electron channel velocity in an AlN/GaN/AlN heterostructure [47], extracted from a pulsed IV measurement across a constriction of length/width of 10/2 μm, as shown in the inset. (b) The extracted channel velocity of 8.45×10^6 cm/s agrees well with the POP-limited theoretical model of velocity as a function of 2DEG density [48]. Data from Romanczyk et al. [49] is also included for the low-density 2DEG region.

the velocity is expected to saturate. In GaN 2DEGs, this saturation of velocity at room temperature is due to the optical phonon scattering. This POP-limited velocity is predicted to be dependent on the carrier density in the channel [48], with a peak velocity of $\sim 1.4 \times 10^7$ cm/s.

Hence, the channel velocity is an important parameter to determine intrinsic limit of operation of a high-speed FET. **Figure 4.16** shows the first channel velocity measurement in an AlN/GaN/AlN heterostructure. Post-processed room-temperature Hall measurement of an MBE-grown 4 nm AlN/30 nm GaN/AlN heterostructure [47] showed a 2DEG density n_s of 2.1×10^{13} cm^{-2} and mobility of 520 cm^2/Vs.

To measure the velocity-field curve, a voltage V is applied across a TLM-like constriction of length L and width W, and the current I is recorded. The setup is shown in the inset of **figure 4.16 (a)**. The resultant velocity v_e and electric field

F are extracted using :

$$v_e = \frac{I}{e\, n_s W} \tag{4.3}$$

$$F = \frac{V - IR_c}{L}, \tag{4.4}$$

where R_c is the contact resistance of the ohmic pads (should be as low as possible). Pulsed IV measurement with pulse width of 1 ms is performed to avoid self-heating effects at high-biases.

The extracted velocity-field curve is shown in the **figure 4.16 (a)**. As expected, at low electric fields, the velocity is directly proportional to the field. Low-field drift mobility of $\sim 433\ \mathrm{cm}^2/\mathrm{Vs}$ is extracted from the slope of the curve. This is slightly lower than the Hall mobility. The channel velocity saturates at $\sim 8.45 \times 10^7$ cm/s at saturation electric field of ~40 kV/cm.

Is the extracted velocity value reasonable? For a GaN 2DEG, the high-field velocity is expected to be a function of the charge density n_s [48]. **Figure 4.16 (b)** plots the predicted velocity versus charge density at room temperature. It rises at low densities, peaks at around $3 - 4 \times 10^{12}$ cm^{-2} and then falls as $\sim 1/\sqrt{n_s}$. This predicted behavior was recently confirmed experimentally by Romanczyk et al. [49] in N-polar GaN 2DEGs. The measured velocity in the AlN/GaN/AlN 2DEG is plotted in **figure 4.16 (b)**, and agrees well with the theory. It explains why the velocity is lower than the peak velocity of 1.4×10^7 cm/s.

In the future, a density dependent velocity measurement will be very valuable to extract the peak velocity, since that is what determines the operation speed limit of the AlN/GaN/AlN HEMT.

4.4.3 Shubhnikov-de-Haas oscillations

Magnetotransport measurements are a valuable tool to probe 2D carrier transport and the nature of scattering mechanisms. The AlN/GaN/AlN heterostructure poses two hurdles towards magnetotransport investigations of the 2DEG. Firstly, the relatively high density and low mobility 2DEGs in AlN/GaN/AlN require high magnetic fields (> 25 T) to resolve quantum oscillations. But a more severe hurdle is the ability to make electrical contacts to the 2DEG through the ~6.2 eV bandgap AlN barrier layer that would remain ohmic down to cryogenic temperatures and allow such a measurement to be done in the first place.

In the study presented in this section, these hurdles are overcome to obtain the first Shubhnikov-de-Haas (SdH) oscillations in the AlN/GaN/AlN heterostructure. This is achieved by going to high magnetic fields upto 45 T, and by using MBE-regrown n^{++} GaN ohmic contacts to the 2DEG for cryogenic measurements. New phenomena for 2DEGs in nitride semiconductors are revealed as a result. Because even at $n_s \sim 3 \times 10^{13}$ cm^{-2} the heterostructure allows only single subband occupation, a rather large fraction of the Brillouin zone is accessed by magnetotransport of the Fermi surface, extending to 13.8% to the Brillouin Zone edge. This is a far larger k-space of the GaN conduction band than is accessible in 2DEG in the conventional AlGaN/GaN heterostructures. An electron effective mass of $\sim 0.3m_0$ at $n_s \sim 2 - 4 \times 10^{13}$ cm^{-2} is extracted from the SdH at this high conduction-band states. This implies a highly density-dependent effective mass, which would change from $\sim 0.3m_0$ at $n_s \sim 3 \times 10^{13}$ cm^{-2} to $\sim 0.2m_0$ at $n_s \sim 1 \times 10^{12}$ cm^{-2}, the entire range accessible with varying gate voltage. Beats are observed in the SdH oscillations, revealing not multiple subbands, but a large electron spin-splitting, with a characteristic energies of ~60 meV.
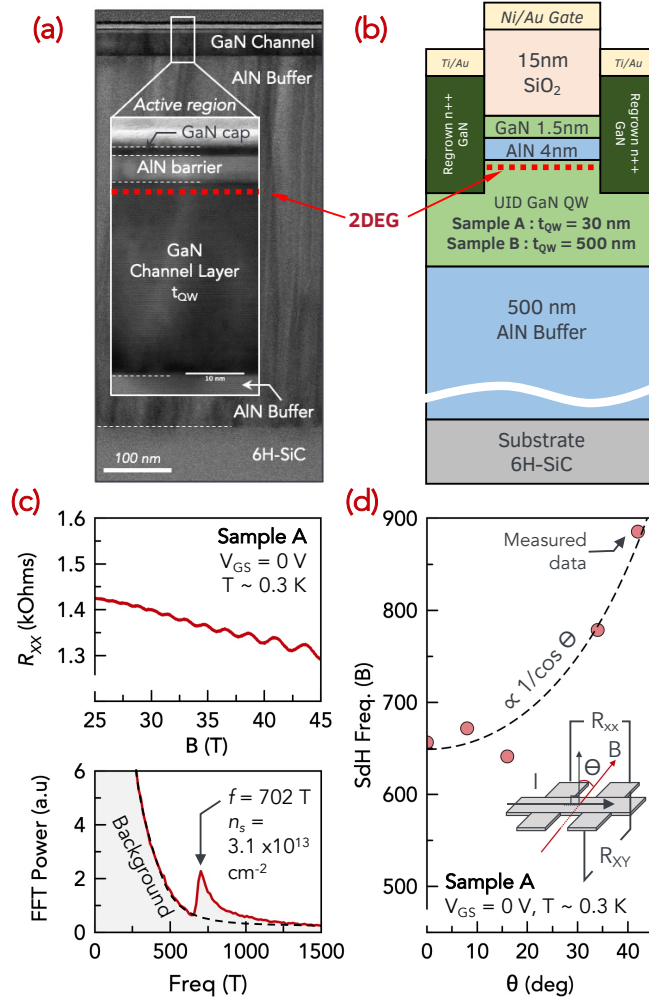
Figure 4.17: (a) Representative STEM of showing the AlN/GaN/AlN heterostructure grown on 6H-SiC with t_{QW} = 30 nm thin GaN channel layer. (b) Schematic cross-section of the fabricated Hall-bar structure used for the magnetotransport measurements, with low resistance MBE-regrown n++GaN ohmic contacts to the 2DEG and SiO$_2$ dielectric under the gate. Samples A and B differ in the thickness of the GaN channel layer. (c) Longitudinal resistance of sample A measured at selected gate voltages in a gated-Hall bar shows clear oscillations at magnetic fields above 25 T. The Fast Fourier transform (FFT) spectrum of the oscillations in $1/B$ shows a clear peak above the background, which confirms the periodic nature of the oscillations in $1/B$ - signature of SdH oscillations. (d) The frequencies of these oscillations vary as $1/\cos\theta$ on rotating the sample with respect to the magnetic field, θ being the angle between the sample and field lines, confirming that the oscillations are from 2D confined electrons.

165
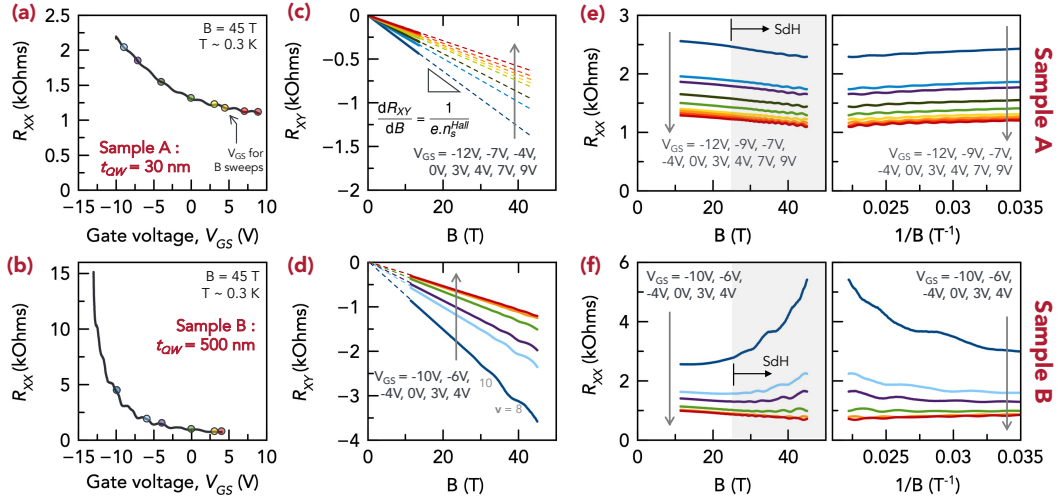
Figure 4.18: (a), (b) Gate voltage V_{GS} sweeps for samples A and B at 45 T showing the oscillations arising from sweeping through the quantized Landau levels, and modulation of 2DEG density resulting in modulation of longitudinal resistance R_{XX}. (c),(d) Hall resistances R_{XY} as a function of magnetic fields B at different V_{GS} for Samples A and B. The dashed lines are linear extrapolated data for extraction of the Hall densities. (e), (f) Longitudinal resistance R_{XX} as a function of B and $1/B$, exhibiting Shubnikov-de-Haas (SdH) oscillations at $B \gtrsim 25$ T. All measurements are performed at temperature T ~ 0.3 K.

Table 4.1: Low-field Hall-effect measurement results of MBE-grown AlN/GaN/AlN samples on 6H-SiC with different GaN channel layer thicknesses. The mobilities show an increasing trend with channel thickness. High-field magneto-transport measurements reported here were performed on samples labelled A and B, with 30 nm and 500 nm GaN channel layers respectively.

GaN layer thickness (t_{QW}) (nm)	Mobility (cm²/Vs)		2DEG Density (10^{13} cm^{-2})		SdH Sample ID
	300 K	77 K	300 K	77 K	
20	327	487	1.6	1.55	
30	520	774	1.70	1.68	
30	562	885	2.8	2.8	A
200	849	1390	2.2	2.2	
500	941	1740	2.24	2.23	B

According to the **table 4.1**, the apparent 2DEG Hall mobilities are lower in an AlN/GaN/AlN heterostructure with a thinner GaN channel layer. However, thinner channel layer is desired in an AlN/GaN/AlN RF HEMT due to

increased reliability, increased vertical scaling and better thermal performance. Therefore, to study the effect of the GaN channel thickness on the channel transport, the samples with t_{QW} = 30 nm and 500 nm from **table 4.1** were chosen for subsequent high-field magnetotransport measurements, henceforth referred to as sample A and B respectively. Because of the AlN backbarrier being 500 nm away from the 2DEG, the sample B electrostatically mimics a conventional AlN/GaN HEMT without a backbarrier.

Depositing metal on the AlN surface to make ohmic contacts to the 2DEG typically results in Schottky contacts of high resistance to the 2DEG even upon annealing, because of the large bandgap AlN barrier layer. Instead, MBE-regrown ohmic contacts are used in this work. To make these, samples A and B underwent recess dry etching in photolithography-defined ohmic regions. The patterned samples were then reintroduced into the MBE chamber and highly n-type doped GaN with [Si]~ 1×10^{20} cm^{-3} were grown to make lateral contacts to the 2DEG. The cross-section schematic in **figure 4.17 (b)** shows MBE-regrown n++GaN and deposited Ti/Au ohmic metal stacks contact scheme to the 2DEG, resulting in low specific contact resistance in 10^{-7} Ω cm^2 at room temperatures [47]. High density mobile electrons with n_{3D} ~ 1×10^{20} cm^{-3} in the degenerately-doped ($E_F \sim E_c$ + 97 meV) n++ GaN regrown ohmic contacts connect to the 2DEG from the edge, and are expected to remain conductive down to sub-Kelvin temperatures; they are the crucial enabler of both scaled RF HEMTs, and the low-temperature magnetotransport measurements in the AlN/GaN/AlN structures studied here.

Gated Hall bar of dimensions 120 μm $\times$ 20 μm were fabricated on samples A and B. 15 nm thick SiO$_2$ dielectric layer was deposited followed by Ni/Au gate

metal gate stack to prevent current leakage through the gates.

Magnetotransport measurements were performed at the National High Magnetic Field Laboratory (NHMFL) Tallahassee FL in the 45 T hybrid magnet setup [220]. The magnetic field B was swept from 11 - 45 T by controlling the resistive magnet. The longitudinal resistance R_{XX} and Hall resistance R_{XY} were measured in a 4-point configuration in the Hall bar geometry using standard low-frequency lock-in techniques at low injection current levels. The gate bias V_{GS} was controlled using an external voltage source. The measurements were performed at a calibrated sample temperature range of 0.3 K - 20 K in a He3 cryostat using a cryogenic temperature controller.

Shubhnikov de-Haas (SdH) quantum oscillations in the longitudinal magnetoresistance are a result of quantization of the 2D electron density of states (DOS) into Landau levels. The oscillatory component of the resistance ΔR_{XX} is given by [221] :

$$
\begin{aligned}
\Delta R_{XX}^{osc} \propto \frac{\chi}{\sinh(\chi)} \cdot e^{-\pi/\mu B} \\
\cdot \left(\frac{q_e B}{2\pi \hbar n_s}\right)^{1/2} \cdot \cos\left(\frac{2\pi^2 \hbar n_s}{q_e B}\right),
\end{aligned}
\tag{4.5}
$$

where $\chi = 2\pi^2 k_B T / \hbar \omega_c$, with k_B the Boltzmann constant, T the absolute temperature, and $\omega_c = q_e B/m^\star$ is the characteristic cyclotron frequency with q_e the electron charge and $m^\star$ the electron effective mass. Scattering-induced broadening of the Landau density of states determines the magnetic field for the onset of SdH oscillations through the relationship $\omega_c \tau_q = \mu.B > 1$, where τ_q is the quantum scattering lifetime and $\mu = q_e \tau_q / m^\star$ is the corresponding mobility. This is different than Hall mobility which is related to the transport or classical lifetime τ_c through $\mu_{\text{Hall}} = q_e \tau_c / m^\star$. However, μ_{Hall} is used to approximate the onset

of SdH oscillations and design an experiment as it is directly measurable. For sample A, with low temperature Hall mobility of ~ 900 cm^2/Vs, onset of SdH oscillations are expected $B > 11$ T. Experimentally, even higher B is required to suppress the effect of the broadening and obtain clean SdH oscillations for accurate analysis.

To test this, the magnetic field B was swept from 11 to 45 T and the R_{XX} was measured for sample A at applied $V_{GS} = 0$ V. The measured raw data is plotted in **figure 4.17 (c)**. Clear oscillations are observed at high magnetic fields above 25 T. On performing a fast Fourier transform (FFT) of the measured R_{XX} signal versus $1/B$, a single oscillation frequency peak is resolved above the background in the FFT spectrum. This confirms that the observed oscillations in R_{XX} are periodic in $1/B$, and are thus indeed SdH oscillations. When sample A was rotated with respect to the magnetic field during the sweeps, the frequency of the R_{XX} oscillations versus $1/B$ varied as $1/\cos\theta$, where θ is the angle between the magnetic field and the normal to the sample surface. This behavior, shown in **figure 4.17 (d)**, is a signature of a 2D Fermi surface that confirms that the oscillations are from 2D confined carriers in the heterostructure. This represents the first observation of quantum oscillations from a 2DEG in an AlN/GaN/AlN heterostructure.

The above measurements were performed at $V_{GS} = 0$ V. With the presence of quantum oscillations confirmed in the AlN/GaN/AlN heterostructures with the current experimental setup, a more in-depth transport study is undertaken by varying the parameters on which the SdH oscillations depend. In the following sections, the gate voltage V_{GS} is used to electrostatically tune the 2DEG densities in the channel. At a given 2DEG density, the temperature damping

term $\chi \sinh(\chi)$ and collision damping term $e^{-\pi/\mu B}$ in equation (4.5) are varied using temperature and magnetic field to extract the electron effective mass $m^{\star}$ and quantum scattering time τ respectively - both for sample A and control sample B. The magnetic field is kept perpendicular to the sample surface in all the subsequent measurements.
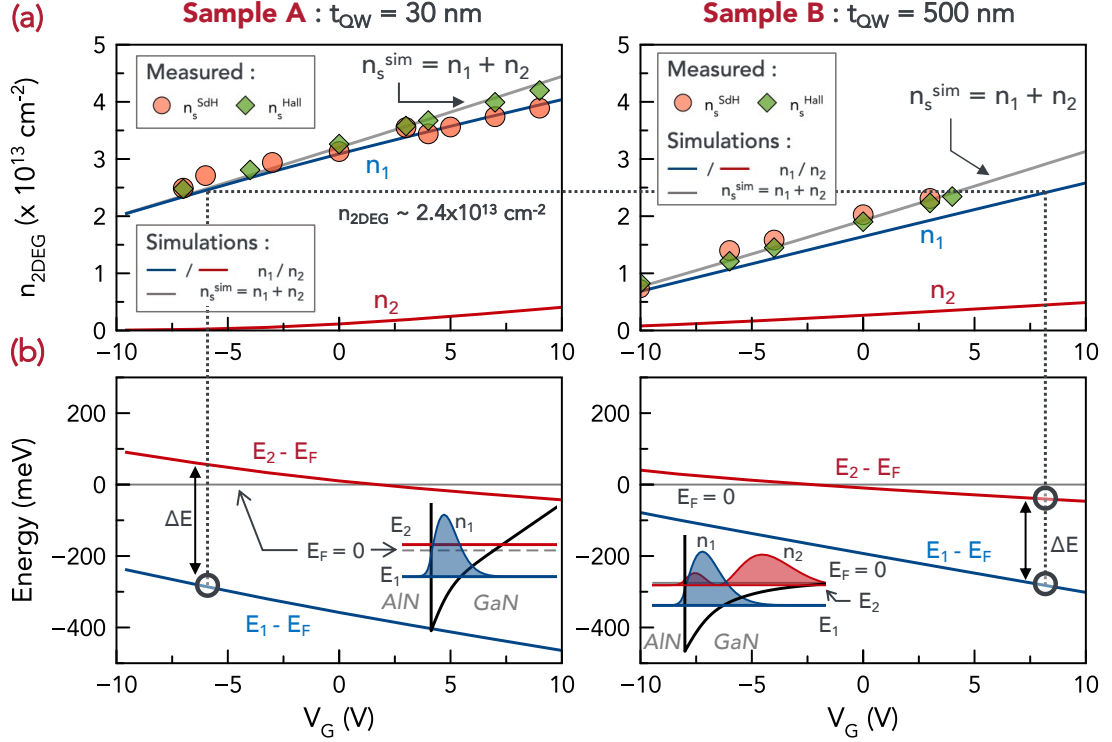
Figure 4.19: (a) The 2DEG density variation with gate voltage V_{GS} as experimentally measured by Hall-effect n_s^{Hall} and from SdH oscillation frequencies n_s^{SdH}. The solid lines for comparison are calculated electrons densities populating the first sub-band n_1, second sub-band n_2, and the total density n_s^{sim}. (b) The relative energies of the first E_1 and second E_2 sub-bands in the triangular quantum well as a function of V_{GS}. Insets contrast the expected conduction band profiles at the AlN/GaN 2DEG interface in samples A and B at total 2DEG density of $n_s^{sim} = 2.4 \times 10^{13} \text{ cm}^{-2}$.

Gate voltage sweeps were performed on sample A and B at ~ 0.3 K at 45 T to test the electrostatic control over the carrier density. The applied voltage bias on the gate V_{GS} should modulate the density of electrons n_s in the 2DEG, and in turn

result in the modulation of R_{XX} through the relation $R_{XX} \propto 1/(q_e n_s v_n)$, where v_n is the electron velocity. **Figures 4.18 (a,b)** show the measured change in R_{XX} with V_{GS} sweep, both in negative and positive directions, for samples A and B respectively. The increase in resistance with decreasing V_{GS} confirms an effective gate control and modulation of the electron channel by the applied bias. Furthermore, when the density of states are quantized into Landau levels at the high B-fields, sweeping the gate voltage moves the Fermi level through these quantized states are results in plateau-like features in the R_{XX} vs V_{GS}. Each plateau corresponds to an integer (i) multiple of the quantized conductance $G_0 = q_e^2/h$. Such features are indeed observed in both **figures 4.18 (a,b)** which confirms the Landau quantization of electron DOS. The corresponding Landau filling factors are..

To extract the gate voltage dependent 2DEG densities, Hall resistances R_{XY} was measured as a function of magnetic field B at various V_{GS}. The data for samples A and B is plotted in **figures 4.18 (c,d)** respectively. The slope $s = dR_{XY}/dB$ of these curves are related to the 2DEG Hall density n_s^{Hall} through the relation $n_s^{\mathrm{Hall}} = 1/q_e \cdot s$. The 2DEG Hall-densities thus extracted from low field R_{XY} for the two samples are plotted in **figure 4.19 (a)**. The range of applied V_{GS} in this experiment is limited by the leakage of charge through the dielectric gate. Within this V_{GS} range, the 2DEG densities in sample A vary from $n_s^{\mathrm{Hall}} \sim 2.5\text{--}4.0\times 10^{13}$ cm^{-2}. The densities in sample B are slightly lower at $n_s^{\mathrm{Hall}} \sim 1 - 2.5 \times 10^{13}$ cm^{-2}. For comparison, a self-consistent 1D Schrodinger-Poisson solver [55] is used to solve for the 2DEG densities as a function of V_{GS} for both the samples. The simulated values n_s^{sim} are plotted in **figure 4.19 (a, b)**. A fair agreement is observed between the simulated n_s^{sim} (grey line) and measured 2DEG Hall-densities n_s^{Hall} in **figure 4.19 (a)**.

The densities n_s^{Hall} extracted from Hall resistance R_{XY} represent the total 2DEG density at a given V_{GS}. Depending on the confining potential profile, these electrons will populate one or more of the quantized enerygy sub-bands of the triangular quatum well. Figure 4.19 (b) shows how the calculated energy levels of the two lowest sub-bands, E_1 and E_2, of the quantum well changes with the gate voltage V_{GS}. E_F is the Fermi level as indicated in the energy band diagram insets. At a given V_{GS}, the sub-bands lying below the E_F will be degenerately populated by electrons. The corresponding electron populations n_1 and n_2 in the first two sub-bands with energies E_1 and E_2 are calculated and plotted as function of V_{GS} in **figure 4.19 (a)**, resulting in a total 2DEG density, $n_s^{\text{sim}} = n_1 + n_2$.

A closer look at the separation between the energy levels, $\Delta E = E_2 - E_1$, highlights the electrostatic difference between samples A and B. At a 2DEG density of $n_s = 2.4 \times 10^{13}$ cm^{-2}, sample B is expected to have both sub-bands populated with electrons with $\Delta E \sim 200$ meV. On the other hand, at the same 2DEG density, sample A is expected to have only the lower sub-band populated due to a larger sub-band separation of $\Delta E \sim 350$ meV. The sub-band splitting is enhanced in sample A compared to sample B at the same n_s because of the higher electrostatic field from the AlN backbarrier resulting in a narrower quantum well. This pushes the second sub-band above the Fermi level. This is illustrated in the simulated conduction band profiles for samples A and B at $n_s = 2.4 \times 10^{13}$ cm^{-2} in the insets of **figure 4.19 (b)**. As a result sample A has only one sub-band occupied all the way up to $n_s = n_1 =\sim 3 \times 10^{13}$ cm^{-2}. Sample B has a weaker effect of the AlN backbarrier 500 nm away, and behaves more like a conventional AlN/GaN heterostructure [124, 216] with all electrons populating the lowest sub-band till $n_s \sim 1 \times 10^{13}$ cm^{-2}.

The period of SdH oscillations $\Delta(1/B)$ is a direct measure of the carrier density n_s using equation (4.5). Presence of multiple electron populations with different Fermi surfaces lead to multiple SdH oscillation periods or frequencies, provided they have an appropriate τ_q to satisfy $\omega_c \tau_q > 1$. Hence, the FFT analysis of the SdH oscillations should enable us to distinguish the electron populations n_1, n_2 in the first two sub-bands, as opposed to the Hall densities n_s^{Hall} which are agnostic to the sub-band occupation and represent the total carrier concentration $n_1 + n_2$.

Towards this, magnetic field sweeps were performed at various applied V_{GS} at T ~ 0.3 K for samples A and B. The measured R_{XX} data is shown as a function of B and $1/B$ in **figures 4.18 (c, d)** respectively. Both the samples exhibit clear SdH oscillations which are confirmed to be periodic in $1/B$ at magnetic fields above ~25 T.

From the R_{XX} data for samples A and B in **figure 4.18 (c, d)**, the SdH periods at different gate voltages V_{GS} are identified from their corresponding Fast Fourier transform (FFT) spectra. $\Delta(1/B)$ is linked to the carrier density n_s^{SdH} through the relation $\Delta(1/B) = e\hbar/m^\star \epsilon_F = e/\pi\hbar \cdot n_s^{SdH}$. The extracted densities n_s^{SdH} are plotted in **figure 4.19 (a)** for both samples.

In sample B, interestingly two peaks corresponding to two dominant, closely spaced oscillation frequencies are observed in the FFT spectra at $V_{GS} > -6$ V, which manifest as a beats in the measured SdH oscillations. These point to the presence of two carrier populations, which are attributed to the breaking of spin degeneracy giving rise to two Fermi surfaces. The total density $n_s = n_\uparrow + n_\downarrow$, where $n_{\uparrow/\downarrow}$ is the electron density with spin up/down, agrees well with the Hall-densities n_sHall and simulated n_s^{sim}, as shown in **figure 4.19**. Further

discussion is presented later in this section. However no sign of second sub-band occupation is observed in sample B in the SdH oscillations, possibly be due to a lower mobility of the carriers in the second sub-band [222].

In sample A, simulation predicts the second sub-band population of $n_2 > 1 \times 10^{12}$ cm^{-2} at $V_{GS} > 0$ V. Experimentally, only a single dominant FFT peak is observed in the FFT spectrum for all V_{GS}. The corresponding extracted densities n_s^{SdH} is plotted in **figure 4.19 (a)**. Interestingly, the SdH density agrees to the calculated first sub-band population n_1. Specifically for $V_{GS} > 3$ V, where the a significant second sub-band population is expected, n_s^{SdH} agrees to expected n_1, and n_s^{Hall} agrees with the calculated $n_s^{sim} = n_1 + n_2$. This means that the SdH oscillations are dominated by the electrons in the first sub-band. A lower mobility of the electrons in the second sub-band [222] might be the reason they do not show SdH oscillations. However, this confirms our simulated prediction of single sub-band population till $n_s \sim 3 \times 10^{13}$ cm^{-2}. This corresponds to a large single 2D Fermi surface with wavevector $k_F = \sqrt{2\pi n_s} \sim 1.37$ nm^{-1}, which extends 13.8% towards the Brillouin Zone edge $\pi/a_{GaN} = 9.8$ nm^{-1}. Thus, the AlN/GaN/AlN heterostructure with thin GaN channels offer a unique system extends the range of the electric quantum limit in semiconductor heterostructures and allows the Fermi surface sample higher regions of the wurtzite GaN conduction band (CB) than was previously accessible.

In equation (4.5), $\chi/\sinh\chi$ is the thermal damping of the SdH oscillations as a result of the thermal broadening of the Landau levels. Raising the sample temperature and carefully tracking the reduction in the SdH oscillation amplitudes allows us to extract the electron effective mass $m^\star$ at the Fermi-surface through the relation $\chi = 2\pi^2 k_B T/\hbar\omega_c$. Because of the enhanced electrostatic confinement
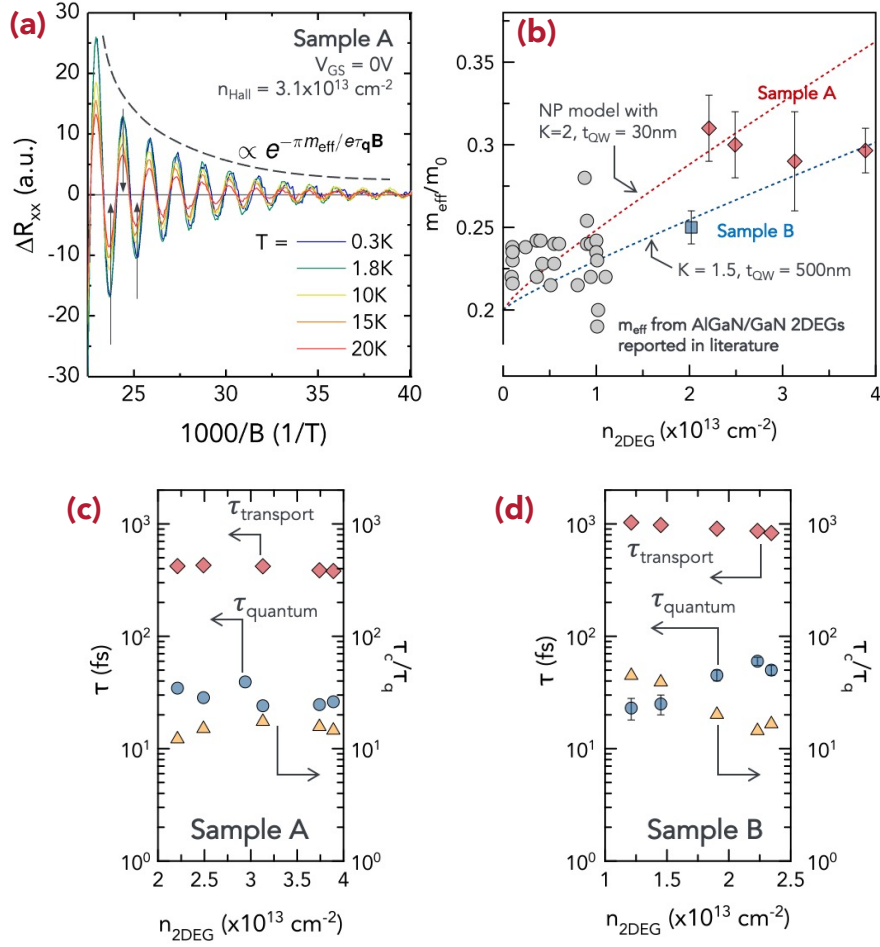
Figure 4.20: (a) Temperature-dependent SdH at $V_G = 0V$ for sample A showing the thermal damping of the oscillations (b) Extracted electron effective mass as a function of 2DEG density from samples A and B, compared to other reports from AlGaN/GaN 2DEGs. (c) Transport ($\tau_{transport}$) and quantum ($\tau_{quantum}$) lifetimes extracted from the damping of SdH oscillations, along with their ratios for (c) sample A and (d) sample B.

of 2DEG carriers, the AlN/GaN/AlN structure offers us a valuable opportunity to probe the wz-GaN CB $m^\star$ than previously reported.

Magnetic field B sweeps were performed at different n_s controlled through V_{GS} at T = 0.3 K, 1.8 K, 10 K, 15 K, and 20 K. The thermal damping of the background subtracted SdH oscillations for sample A at V_{GS} = 0 V is shown in **figure 4.20(a)**. The amplitudes at the first 5 extrema were used to extract
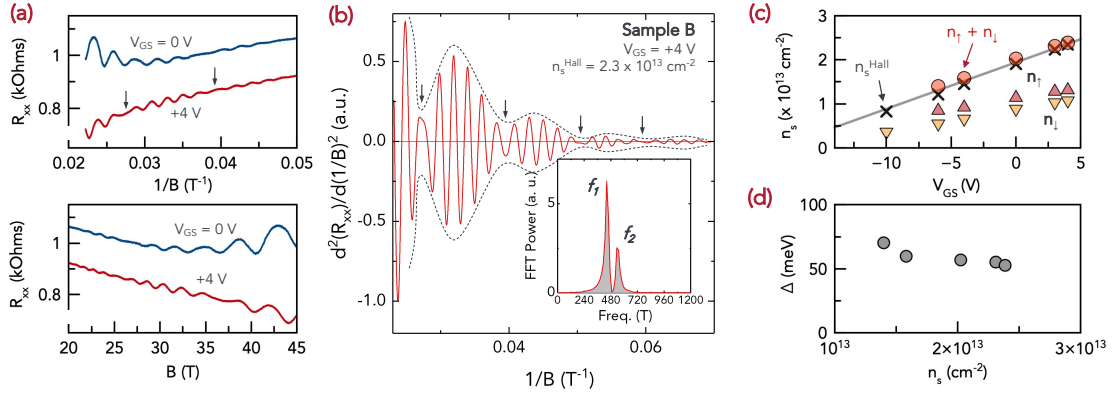
Figure 4.21: (a) Raw data of measured R_{XX} in sample B plotted as a function of B and $1/B$ at two selected gate voltages V_{GS}. Beat like pattern is observed in the SdH oscillations (arrows marking nodes). (b) Second derivative of the SdH oscillations in sample B at V_{GS} = 4 V amplifying the beats in the measured raw data. Inset shows the corresponding FFT spectra, with two closely space peaks attributed to spin-up and spin-down electrons with densities $n_{\uparrow}$ and $n_{\downarrow}$ respectively. Similar double-peaked FFT spectra is observed for $V_{GS} > -6$ V. (c) Gate voltage V_{GS} dependence of the extracted $n_{\uparrow}$ and $n_{\downarrow}$. The total electron density $n_s = n_{\uparrow} + n_{\downarrow}$ agrees well with the measured Hall densities n_s^{Hall}. (d) High zero-field spin splitting energies Δ extracted from the SdH beats in sample B as a function of total charge density.

the $m^{\star}$. **Figure 4.20 (b)** shows the extracted $m^{\star}$ for samples A and B as a function of the 2DEG density. Also plotted are the the previously reported [223, 224, 225, 226, 227, 228, 229, 230, 231, 232, 233, 234, 235, 236, 237] values of GaN electron effective mass, experimentally measured using magnetotrasport in Al(Ga)N/GaN 2DEGs.

The extracted electron effective mass from sample B at a 2DEG density of $\sim 2 \times 10^{13}$ cm^{-2} is $m^{\star} \sim 0.25$ m$_0$, where m$_0$ is the free electron mass. This is consistent with the previously reported values of GaN electron effective mass $m^{\star} \sim 0.19 - 0.23$ m$_0$ measured in Al(Ga)N/GaN 2DEGs with density $\sim 10^{12}$cm^{-2}.

However, for sample A, the extracted effective mass is $m^{\star} \sim 0.3m_0$ for a higher 2DEG density $n_s \sim 2 - 4 \times 10^{13}$ cm^{-2}. This is the first experimental mea-

surement of the electron effective mass in GaN at such high electron densities. The $m^\star$ measured in the AlN/GaN/AlN with 30 nm GaN channel is therefore significantly higher than the previously reported $m^\star \sim 0.20 - 0.23$ for lower AlGaN/GaN 2DEG densities. The higher $m^\star$ is believed to arise from the non-parabolicity of the GaN CB as the Fermi surface moves farther away from the conduction band edge.

The CB non-parabolicity can be captured by deriving the effective mass $m^\star(E)$ for an arbitrary non-parabolic dispersion [238] under Kane's two-band model [239] using :

$$m^\star(E) = m_0^\star (1 + 2\lambda E)$$
$$= m_0^\star \left(1 + 2\frac{K}{E_g} \left(\langle \hat{T} \rangle + E_F \right) \right), \tag{4.6}$$

where $m_0^\star$ is the band-edge electron effective mass, E_g is the GaN energy band-gap. $E = \langle \hat{T} \rangle + E_F$ is the perpendicular-direction average electron energy above the CB minimum, where $\langle \hat{T} \rangle$ is the average confinement energy and $E_F = \hbar^2 \pi n_s / m^\star$ is the Fermi surface energy of the 2DEG. The Kane's two-band approximation considers interaction between electrons in the bottom-most CB and top-most VB. $\lambda = K/E_g$, where K is a free parameter, represents the deviation from parabolic bands. A larger λ means a higher non-parabolicity due to the effect of other CB and VBs outside the two-band model. Thus, K is used [228, 240] to fit equation (4.6) to the experimental data and comment on the non-parabolicity.

Previously in GaN 2DEGs, Knap et al. [228] used $K \sim 1$ to explain the measured GaN $m^\star$ in the range $n_s = 3 - 9 \times 10^{12} \text{cm}^{-2}$. Syed et al. [240] found better agreement to experimental $m^\star$ over a wider density range $n_s \sim 1 - 9 \times 10^{12} \text{ cm}^{-2}$ with $K = 1.9 - 2.5$.

Equation (4.6) is used to fit the extracted $m^{\star}$ data from samples A and B. Using a modified Fang-Howard variational wavefunction with a confining electric field [241] $F_{QW} = (E_g + 4\pi\hbar^2 n_s/m_0^{\star})/t_{QW}$ leads to $\langle \hat{T} \rangle = \hbar^2 b^2/8m_0^{\star}$, where $b^3 = \frac{12m_0^{\star}}{\hbar^2}\left(\frac{11q_e^2 n_s}{32\epsilon_{GaN}} + q_e F_{QW}\right)$. **Figure 4.20 (b)** shows the calculated curve with $m_0^{\star} = 0.2\,m_0$ and $K = 1.5$ agrees reasonably well to the range of data from sample B, whereas a higher $K = 1.5$ is needed to fit the data from sample A. The effect of non-parabolicity is expected to increase as the Fermi level moves further away from the band-edge, and therefore a larger K required to explain sample A is consistent with the higher confinement effects. This result highlights the need for incorporating non-parabolic effective mass in modelling of low-field mobility and device characteristics of AlN/GaN/AlN heterostructures with such high charge densities.

Quantum scattering lifetime τ_q is the lifetime of an electron in a magnetic quantum state under the effect of all scattering events. These quantum scattering events result in smearing of the Landau levels and thus damping SdH oscillations in $1/B$. This smearing characterized by the collision broadening energy Γ, which is linked to the scattering lifetime through $\Gamma = \hbar/(2\tau_q)$. τ_q can therefore be extracted from the damping of SdH oscillations by appropriate fitting of the exponential decay term in equation (4.5).

The quantum scattering times for samples A and B at different charge densities (controlled by V_{GS}) extracted from the corresponding Dingle plots are plotted in **figure 4.20 (c)**. For sample A, $\tau_q \sim 20 - 40$ fs, and $\tau_q \sim 50$ fs for sample B with no discernible trend with the 2DEG density. The classical transport lifetimes τ_c derived from the corresponding low field Hall-effect mobilities are $\tau_c \sim 400$ fs and $\tau_c \sim 900$ fs for samples A and B respectively. Both τ_c and τ_q

were lower for sample A compared to B. The lifetime ratio τ_q/τ_c ratio represents the angular preference of the dominant scattering mechanisms [162, 242]. A ratio $\tau_c/\tau_q \gg 1$ indicates the dominance of long-range Coulombic scattering from charged defects, impurities, or charged dislocations. Since these samples are heteroepitaxially grown on lattice-mismatched 6H-SiC substrates with threading dislocation densities of the order $10^9 - 10^{10}$ cm^{-2} in both the samples, scattering from dislocations is hypothesized to be the dominant mechanism here. Recent demonstrations [64, 65] of high-quality homoepitaxial AlN films on low-dislocation density bulk AlN cystal substrates, with orders of magnitude lower dislocation densities of $10^4 - 10^5$ cm^{-2} should enable valuable investigations into this hypothesis.

Sample B shows interesting beating behavior in the SdH oscillations. **Figure 4.21 (a)** plots the raw data of measured R_{XX} from sample B as a function of B and $1/B$ at two gate voltages V_G = 0V and 4 V. A beating behaviour is observed in both cases. To amplify the beats for easier analysis of the frequency, a second derivative of R_{XX} with respect to $1/B$ for V_{GS} = 4 V is calculated and plotted in **figure 4.21 (b)**. A beating pattern with periodic nodes, and decaying oscillations with $1/B$ is clearly visible. The FFT spectra is shown in the inset, where two closely spaced peaks corresponding to two oscillation frequencies f_1 = B_1 ~ 444 T and f_2 = B_2 ~ 543 T are resolved. Similar beats are present in all SdH oscillations measured at V_G > −6 V. No such beats however were observed in the field sweep R_{XX} measured in sample A.

What is the origin of these beats? According to equation (4.5), two closely-spaced frequencies in an SdH oscillation correspond to two separate "pockets" of carriers with slightly different energies but similar thermal and colli-

sion damping. The possibilities include (1) occupation of two sub-bands of the quantum well, or (2) loss of spin-degeneracy of electrons occupying a single sub-band. In case (1), the extracted electron densities $n_{1,2} = q_e/\pi\hbar \cdot B_{1,2}$ in the first and second sub-bands are $n_1 = 2.15$ and $n_2 = 2.62 \times 10^{13}$ cm^{-2} respectively. The total 2DEG density is $n_s = n_1 + n_2 = 4.76 \times 10^{13}$ cm^{-2}, which is approximately 2× the measured Hall density of 2.34×10^{13} cm^{-2} from **figure 4.19**. This discrepancy is resolved however, if the peaks are interpreted as case (2) - splitting of spin de-generacy. The the calculated spin-up and spin-down electron densities, given by $n_{\uparrow,\downarrow} = q_e B_{\uparrow/\downarrow}/2\pi\hbar$ result in a total density of $n_s = n_\uparrow + n_\downarrow = 1.07 + 1.31 = 2.38 \times 10^{13}$ cm^{-2}, which agrees with the both the Hall-density n_s^{Hall} and simulated carrier density n_s^{sim} at $V_{GS} = 4$ V. Similar extraction of $n_\uparrow$ and $n_\downarrow$ is performed for the SdH measured other V_{GS} and are plotted in **figure 4.21 (c)**.

Zero-field spin-splitting in 2DEGs is attributed to a Rashba-Bychkov like mechanism [243] linear in k arising due to the large electrostatic confining po-tential at the heterointerface. The coupling coefficient α and zero-field spin-split energy Δ are given by

$$\alpha = \frac{\delta n \, \hbar^2}{m^\star} \sqrt{\frac{\pi}{2(n_s - \delta n)}} \quad \text{and} \quad \Delta = 2\alpha k_F, \tag{4.7}$$

where $\delta n = n_\uparrow - n_\downarrow$, $n_s = n_\uparrow + n_\downarrow$ and k_F is the Fermi wavevector. The Δ ex-tracted from sample B at different V_{GS} is plotted as a function of n_s in **figure 4.21 (d)**. Previously reported [244, 245, 246, 226, 247, 248, 249, 250, 251, 252, 253] spin-splitting energies extracted from SdH oscillations in AlGaN/GaN 2DEGs < 1×10^{13} cm^{-2} range from $1 - 13$ meV. The $\Delta \sim 50 - 60$ meV found here is 4× higher than the highest measured spin splitting energy of 13 meV [249] in GaN 2DEGs. The exact mechanism of spin-splitting in GaN 2DEGs is not well understood. Experimentally, there is a disagreement in spin-splitting energies measured using weak anti-localization (WAL) and SdH [245]. Theoretical esti-

mates from the Rashba mechanism [246, 254] and the Dresselhaus mechanism due to bulk inversion asymmetry [255] predict an order of magnitude lower $\Delta < 1$meV than the measured values. The Rashba coupling in AlGaN/GaN 2DEGs is suggested to be the reason behind the recently reported large g^* factor of 7 with in-plane anisotropy [256]. Lo et al.[257] proposed an additional spin-splitting mechanism of coupling between $\Delta_{C1} - \Delta_{C3}$ conduction bands to explain the observation of large Δ. These models also predict an increase in spin-splitting at higher carrier densities [250] due to the increase in electric field in the quantum well. Our measured data aligns with this prediction, and indicates an uncharacteristically high spin-splitting for this material system that requires further exploration.

This study presents the results of the first high magnetic field measurements on AlN/GaN/AlN double heterostructure. A MBE-growth series provides empirical evidence of the decreasing 2DEG Hall-mobilities with decreasing GaN channel layer thickness. The mobilities in the thin GaN channel structures are lower than typical AlGaN/GaN 2DEGs, albeit at 2-3× the charge densities. By using low-resistance regrown n++GaN ohmic contacts and very high magnetic fields up to 45 T at NHMFL, Shubhinokov-de-haas (SdH) oscillations are observed in the magnetotransport measurements. The results are, for most part, what is expected from this 2DEG system. The SdH oscillations provide an experimental proof of the additional electrostatic confinement by the AlN back-barrier in an AlN/GaN/AlN heterostructure with a thin 30 nm GaN channel. This confinement increases the quantum well sub-band energy separation and results in the population of only the lowest sub-band till $n_s \sim 3 \times 10^{13}$ cm^{-2}. This now-confirmed electrostatic confinement is expected to boost the transconductance of a field effect transistor (FET) by pushing the 2DEG channel closer to the

gate even at lower charge densities. This should translate to higher operation speeds of the AlN/GaN/AlN HEMTs compared to similar AlN/GaN HEMTs via more aggressive scaling. Thus, these magnetotransport results hold a technological value in addition to their high scientific value of giving access to a larger part of the Brillion zone of wurtzite GaN than previously accessed.

Electron effective mass of $0.3m_0$ is extracted at 2DEG densities of $n_s \sim 2 - 3 \times 10^{13}$ cm^{-2}. These are the first such measurements at these high densities and are higher than the masses of $0.20 - 0.23m_0$ typically seen in lower density GaN 2DEGs. This is shown to be the effect of non-parabolicity of the wz-GaN CB at the high energy states near the Fermi level. The values of effective masses and CB non-parabolicity presented here should enable accurate modelling of electronic devices which use this AlN/GaN/AlN 2DEG as a conductive channel.

A quantum scattering lifetime of ~ 400 fs is extracted from these 2DEGs. The ratio of the classical to quantum lifetimes is $\gg 1$ throughout the measured density range, which points to the dominance of dislocation scattering in these 2DEGs at low temperatures. Interestingly, clear beats are observed in the SdH oscillations at various gate voltages in one of the AlN/GaN/AlN samples with 500 nm thick GaN channel. A possible interpretation is presented which attributes these beats to the loss of spin degeneracy resulting in formation of two parallel-conducting populations of electrons and therefore two Fermi levels. A zero B-field spin-splitting energies of ~ 60 meV is extracted following this reasoning at a 2DEG density of $1.5 - 2.5 \times 10^{13}$ cm^{-2}. This value is about 4× higher than previously measured spin-splitting energy in AlGaN/GaN 2DEGs. This interpretation may not be complete, but the data is presented to the field

as an open question which needs further investigation. Recent advancement in homoepitaxy of AlN [64, 65] offers a possible path to further study this AlN/GaN/AlN 2DEG in a more structurally pure form. The orders of magnitude lower dislocation densities should enhance the low temperature mobilities, to give access to lower Laundau filling factors, cleaner SdH oscillations at lower magnetic fields.

As shown earlier in this chapter, a complementary polarization-induced 2D hole gas (2DHG) is also expected to be present in these AlN/GaN/AlN heterostructures at the bottom GaN/AlN interface. These 2DHGs have a typical sheet resistance in the order of 10 kΩ/sq at room temperature [3, 63] mainly due to the lower hole mobilities [5]. This is more than 30$\times$ higher the typical sheet resistance of the 2DEG densities of 300 Ω/sq. Because of this, the 2DEG dominates the parallel transport in a measurement where the ohmic contact connects to both the 2DEG and 2DHG, like a soldered indium contact. However, in the magenetotransport experiments presented here, the regrown n++GaN ohmics contact only to the conduction band of the GaN and hence just the 2DEG. Therefore, it is not surprising that no signs of the 2DHG is seen in the measured magnetotransport data.

4.5   Future Directions

The AlN/GaN/AlN heterostructure offers an opportunity to study new fundamental transport phenomena for the first time in III-nitrides because of the presence of high density, highly confined 2DEG and 2DHG in close proximity. This section presents some of the immediate future directions and exciting ex-

periments that can be performed :

- **Individually contacted and gated 2DEG, 2DHG** :

  Individual contacts to the 2DHG and 2DEG in the same AlN/GaN/AlN heterostructure is currently a technological hurdle, overcoming which will highly benefit the design of future devices, integration of p- and n-channel transistors, and scientific transport experiments. Recent scientific studies of closely spaced 2DEG-2DHG bilayers in other semiconductor systems such as GaAs [211], Si [258] were possible only after the crucial advancements of individual ohmic contacts [259] and precise gate control over the densities [260, 261].

  The AlN/GaN/AlN 2DHG-2DEG is in its nascent state having been discovered only 2 years ago. Currently, parallel contacts to the 2DEG and 2DHG is made using large area indium contacts (see **figure 4.2**). MBE-regrown n++GaN ohmic contacts [158] are used to contact the conduction band only. However no contact scheme which can access *only* the buried 2DHG in an AlN/GaN/AlN heterostructure is currently available. The ideal solution for this is a p-type ohmic regrowth regrowth process. However, achieving p-type regrowth is challenging with the current available processes because of the (1) difficulty in obtaining highly doped Mg-GaN, (2) plasma etch damage causing N-vacancies which are n-type [205] and (3) n-type impurities from exposure to the ambient [206, 207, 208]. Ongoing efforts into developing in-situ sublimation etch of GaN a p-type regrowth process shows promise, and might make individual contacts to the 2DHG soon possible (see sections 3.6 and 6.4).

  Regarding the control of the carrier densities in the AlN/GaN/AlN het-
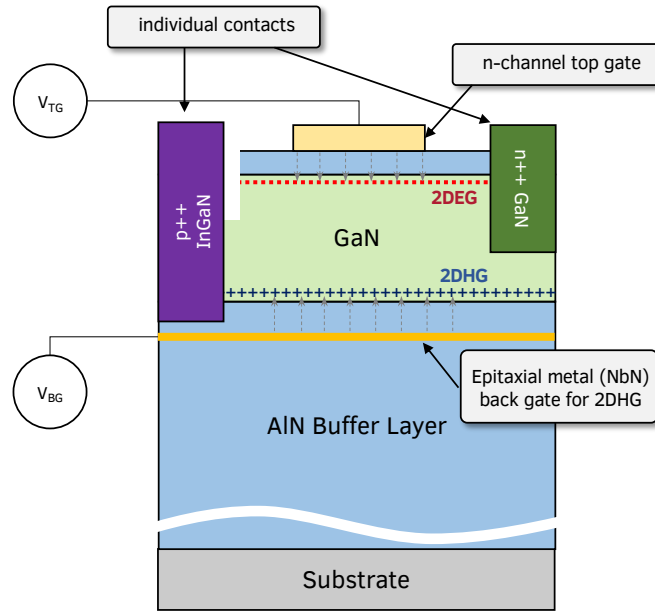
Figure 4.22: Schematic showing an undoped AlN/GaN/AlN bilayer sample, with individually contacted and gated 2DEG and 2DHG. The 2DHG contact is realized using p-type ohmic regrowth, is electrostatically coupled to an epitaxial metal in the AlN buffer layer acting as a back gate.

erostructure, a top gate is electrostatically coupled to the 2DEG, which simultaneously screens the 2DHG. The 2DHG sees the electric field applied from top gate only after the 2DEG is depleted using a negative bias. Therefore, for simultaneous electrostatic control over the 2DEG and 2DHG, a backgate is necessary. A possible dual gate configuration for this structure is shown in **figure 4.22**. Incorporation of epitaxial metal like NbN, TiN [262, 263] in the AlN 5-10 nm below the 2DHG interface in the AlN/GaN/AlN structure should make it possible to control the buried 2DHG density.

- **Coulomb drag and other coupled transport phenomena in bilayers**

  When parallel 2D carriers are present in a crystal, such as in the AlN/GaN/AlN bilayer, the level of electrostatic interaction between the

parallel 2DEG and 2DHG depends on the relative distance between the carriers and the electrostatic screening due to the carrier densities. Intuitively, a carrier, say a electron in the 2DEG, "sees" a hole in the parallel 2DHG only if it is closer to the hole than another electron in the 2DEG layer. This is represented by the following rule-of-thumb - for interacting 2DHG-2DEG bilayer with densities n, the separation between the layers d needs to satisfy $d.k_F < 1$, where $k_F = \sqrt{2\pi n}$ is the 2D Fermi wave-vector.

If $d.k_F \gg 1$, the can be treated as non-interacting, parallel conducting layers for transport. If $d.k_F \approx 1$, weak interaction is possible which manifests in phenomena such as Coulomb drag [264, 265, 258, 266]. If $d.k_F \ll 1$, then strong interaction such exciton condensates [267] or exciton insulators [268] are possible.

Now, for 2DEG/2DHG densities of $n = 3 \times 10^{13}$ cm^{-2}, $k_F^{-1} = 7\,\text{Å}$. This increases to $k_F^{-1} = 2$ nm at $n = 5 \times 10^{12}$ cm^{-2}. Hence to observe any coupled transport phenomena in this system, reducing the carrier density via gating is crucial. It is also necessary to reduce the inter-layer distance while suppressing the leakage between the layers (low threading dislocation densities).

Assuming individual gate control and low-resistance ohmic contacts to weakly-coupled 2DEG and 2DHG, if a current I_1 flows through one carrier gas, there is a momentum transfer to the other carrier layer, manifesting as Coulomb drag. This leads to the separation of charges in the other carrier gas and can be measured as a voltage drop V_2. The Coulomb drag is represented by a drag resistance term $\rho_D = V_2/I_1$. This phenomena has been measured in other bilayer systems such as GaAs [265] and Si [258, 266],
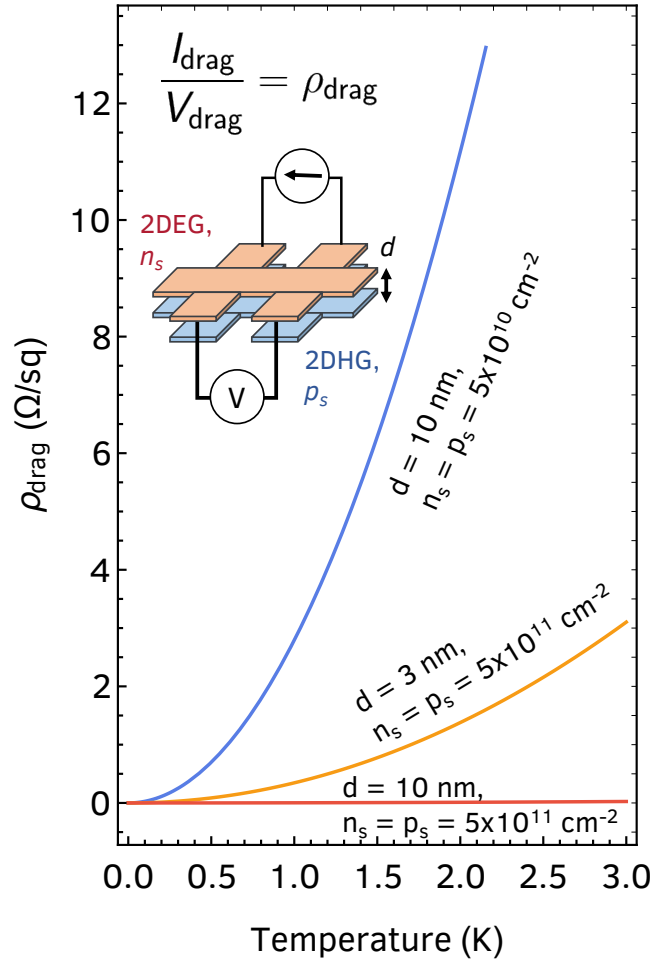
Figure 4.23: Calculated Coulomb drag between a 2DHG and 2DEG of densities p_s and n_s respectively, separated by a perfectly insulating GaN barrier of thickness d. A low density of 5×10^{10} cm^{-2} for d of 10 nm is necessary to observe the effect of Coulomb drag between the carriers.

and is given by [269] :

$$\rho_D = \alpha . \frac{T^2}{d^4 (n.p)^{3/2}},$$ (4.8)

$$\alpha = \frac{1.202 \, \hbar (4\pi\epsilon_{GaN}\epsilon_0)^2 k_B^2}{128\pi e^6}$$

where T is the temperature, $\hbar$ is the reduced Planck's constant, k_B is the Boltzmann constant. α is the material parameter dependent on the GaN dielectric constant ϵ_{GaN}. This drag resistance is independent of mobilities

of the individual carrier gases, since it is a consequence of a single momentum transfer path.

Figure 4.23 shows the calculated Coulomb drag for different 2DHG, 2DEG densities and bilayer separation in a AlN/GaN/AlN heterostructure. At a reasonable separation of 10 nm, a 2DEG-2DHG charge densities of $n/p <= 5 \times 10^{11}$ cm^{-2} is necessary to observe the drag effect. Even though there are still few technical challenges that need to be overcome before realizing weak coupling (individual gates, contacts), the undoped AlN/GaN/AlN system remains the most promising platform to realize weakly coupled 2DEG-2DHG systems in III-nitride semiconductors.

- **Signatures of parallel 2DEG-2DHG bilayers in Magnetotransport**

  Under weak coupling condition ($d.k_F >> 1$), both 2DHG and 2DEG act as non-interacting, independent conduction layers. This leads to parallel conduction if the contacts connect to both the layers simultaneously. Section 4.4.1 already presented the effect of this parallel conduction on Hall mobility, where the 2DEG dominates over the 2DHG.

  However, under high magnetic fields, the parallel conduction shows up in the measured magnetoresistance R_{xx}, Hall coefficient R_H and Hall resistance R_{xy}. Assuming a Hall factor of unity, the magnetic field (B) depen-

dence of the R_{xx}, R_{xy} and the measured Hall density n_{Hall} is given by [270]:

$$R_{XX} = \frac{B^2\left(\mu_n^2\mu_p p_s - \mu_n n_s \mu_p^2\right) + \mu_n n_s + \mu_p p_s}{q_e\left(B^2\mu_n^2\mu_p^2\left(p_s - n_s\right)^2 + \left(\mu_n n_s + \mu_p p_s\right)^2\right)} \qquad (4.9)$$

$$R_H = \frac{\left(p_s - b^2 n_s\right) + (B\mu_n)^2\left(p_s - n_s\right)}{q_e\left((bn_s + p_s)^2 + (B\mu_n)^2\left(p_s - n_s\right)^2\right)} \qquad (4.10)$$

$$R_{XY} = R_H\, B \qquad (4.11)$$

$$n_{Hall} = \frac{1}{q_e\, R_H} \qquad (4.12)$$

where q_e is the electron charge, n_s/p_s are the 2DEG/2DHG densities, μ_n/μ_p are the 2DEG/2DHG mobilities and $\beta = \mu_n/\mu_p$. Figure 4.24 shows the calculated B dependence of the AlN/GaN/AlN structure upto $B = 14$ T (maximum magnetic field currently accessible at Cornell). Three cases are shown :

1. For a control case, in which only the 2DEG conducts with no parallel 2DHG. $n_s = 2 \times 10^{13}$ cm^{-2}; $\mu_n = 1000$ cm^2/Vs. $p_s = 0$

2. Same 2DEG as in (1), but with a parallel 2DHG with $p_s = 5 \times 10^{13}$ cm^{-2}, $\mu_p = 25$ cm^2/Vs. This represents the best *room-temperature* mobility of the GaN/AlN 2DHG [3].

3. Same 2DEG as in (1), but with a higher conductivity parallel 2DHG with $p_s = 3 \times 10^{13}$ cm^{-2}, $\mu_p = 200$ cm^2/Vs. This represents the best *low temperature* mobility of the GaN/AlN 2DHG [3].

As seen in **figure 4.24 (c-f)**, no field dependence is expected in R_H, n_{Hall} or R_{xx} when the conduction is only through the 2DEG (case 1).

In case 2, the presence of a parallel 2DHG causes the measured n_{Hall} slightly greater than the n_{2DEG}. However, no appreciable change with respect to B is observed in the R_H, n_{Hall}. The change in magnitude of R_{xx}

(a) B variable

2DEG

2DHG

R_{XY}

R_{XX}

Uncoupled, parallel 2DEG-2DHG
bilayer with contacts to both

(b)

Case	n_s (10^{13} cm^{-2})	μ_n (cm^2/Vs)	p_s (10^{13} cm^{-2})	μ_p (cm^2/Vs)
I	3	1000	0	-
II	3	1000	5	25
III	3	1000	3	200

(c) R_H (m^2/C)

(d) $n_{Hall} = 1/eR_H$ (10^{13} cm^{-2})

(e) $R_{XY} = B.R_H$ (Ω)

(f) R_{XX} (Ω)

B (T)
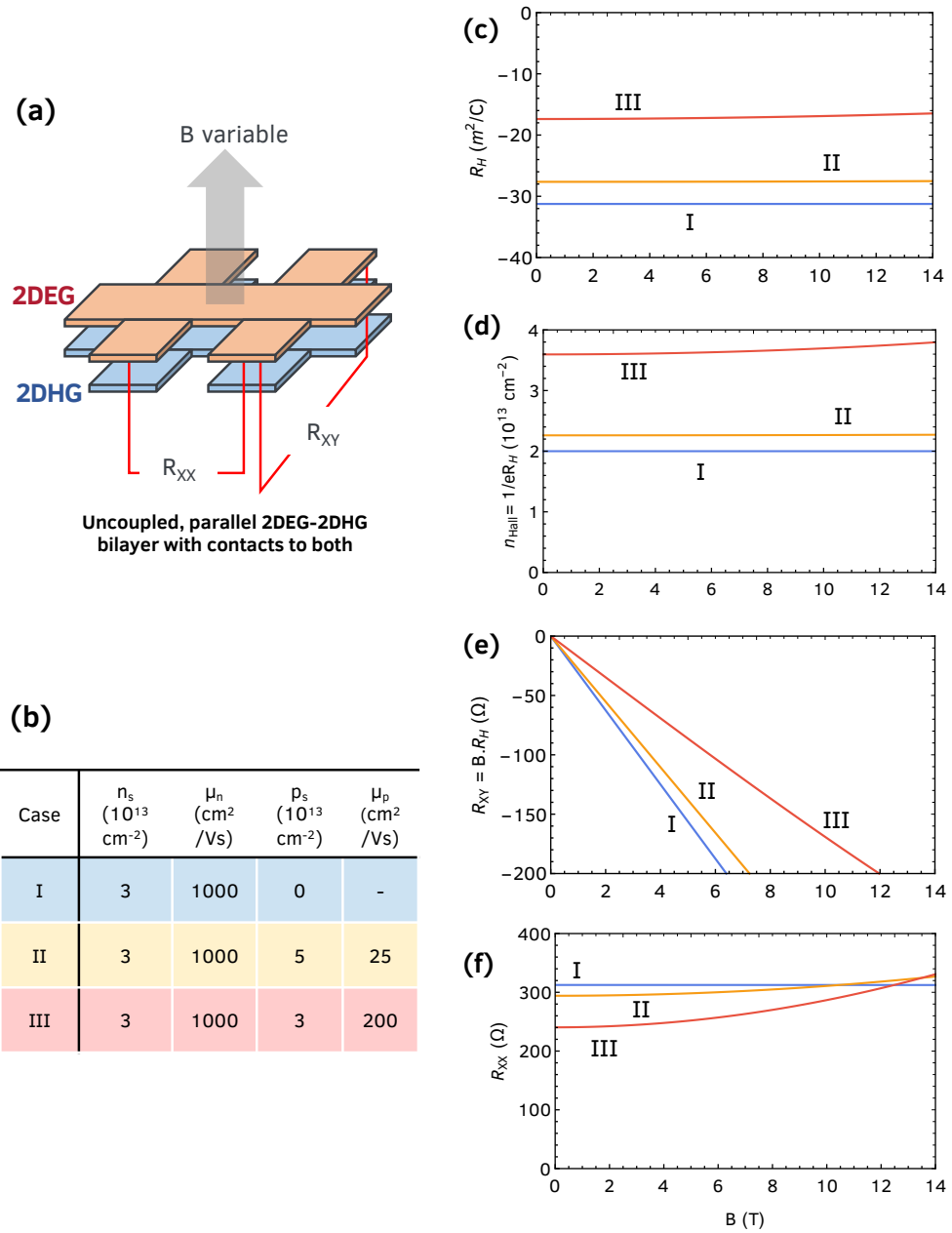
Figure 4.24: (a) Hall bar configuration for measuring the longitudinal resistance R_{XX} and Hall resistance R_{XY} across an uncoupled 2DEG-2DHG bilayer. (b) Table showing the assumed values of 2DEG and 2DHG transport for cases I, II and III. (c - f) Show the expected behaviour of the Hall coefficient (R_H), measured Hall density n_{Hall}, R_{XY} and R_{XX} for cases I-III when the magnetic field is swept from 0 to 14 T. A large change in R_{XX} and field dependence of n_{Hall} is expected for parallel 2DHG-2DHG conduction in case III - which represents the case when the AlN/GaN/AlN sample is at a temperature of < 10 K.

between B = 0 to 14 T is ~ 20 Ω. This is a very small change and might be difficult to detect experimentally.

In case 3, the higher conductivity of the 2DHG has a greater effect on the field-dependent transport. The R_H increases with temperature, leading to an increase in measured n_s with B and non-linearity in R_{XY} vs B. Furthermore, the R_{xx} value changes by~ 100 Ω at 14 T from the zero field value.

Thus, this calculation shows that the magnetic field dependent Hall-effect measurements at low temperature (< 10 K) is expected provide a magnetotransport proof of the presence of parallel 2DHG-2DEG in the AlN/GaN/AlN heterostructures. Low resistance parallel contacts to both the 2DEG and 2DHG in a Hall bar configuration is necessary for this experiment.

- **Tuning the Light emission in 2DEG-2DHG bilayer**

  Section 4.3 presented the observation of light emission from a 2DEG-2DHG bilayer AlN/GaN/AlN heterostructure. On application of a voltage bias under suitable configuration, electrons and holes seperated by the GaN layer recombine and emit photons near the bandgap of GaN.

  Since this observation, 2DHGs have also been observed in InGaN/AlN heterostructures (see section 2.5) with very high hole densities > 10^{14} cm^{-2}. A scientifically interesting experiment will be to repeat the same configuration as shown in **figure 4.7** in an undoped AlN/InGaN/AlN heterostructure with different In composition in the InGaN layer. If the detected emission is indeed from the electron-hole recombination, the emission peak should shift with the change in In composition in the channel. Additionally, if 2DEG and 2DHG are individually gated, then the inten-

sity of the emitted light can also be controlled via a third terminal. This tunability of the emission energy and intensity will make the bilayer LED more technologically and scientifically attractive for applications such as an optical modulator.

- **Examining the Dominant Scattering mechanisms in the AlN/GaN/AlN 2DEG**

The 2DEG in the AlN/GaN/AlN is some of the highest densities seen in any semiconductor system. These uncharted territories therefore bring new questions regarding the 2DEG transport. Results of some of the investigations are presented in this chapter, including high-field magneto-trasport. However, the scientific question of what is the limiting mechanism for 2DEG mobility still remains open - and needs to be answered to fully understand the system and improve the resultant devices.

From **figure 4.10**, an extrinsic mechanism which limits the 2DEG mobility to ~ 1200 cm^2/Vs should be able to explain the 2DEG transport in these structures.

One of the hypotheses is that parallel holes in the 2DEG lead to a low apparent mobility [271]. However a parallel conduction model, presented earlier in this chapter, shows that the 2DEG still dominates. Furthermore, both the 2DEG and 2DHGs are separated by a distance too far to be coupled electrostatically.

The presence of the 2DHG in the structure could have an indirect effect on the scattering of the 2DEG. For example, there exists a high built-in field in the GaN quantum well below/behind the 2DEG which adds to the confining potential. This was confirmed through SdH. This could lead
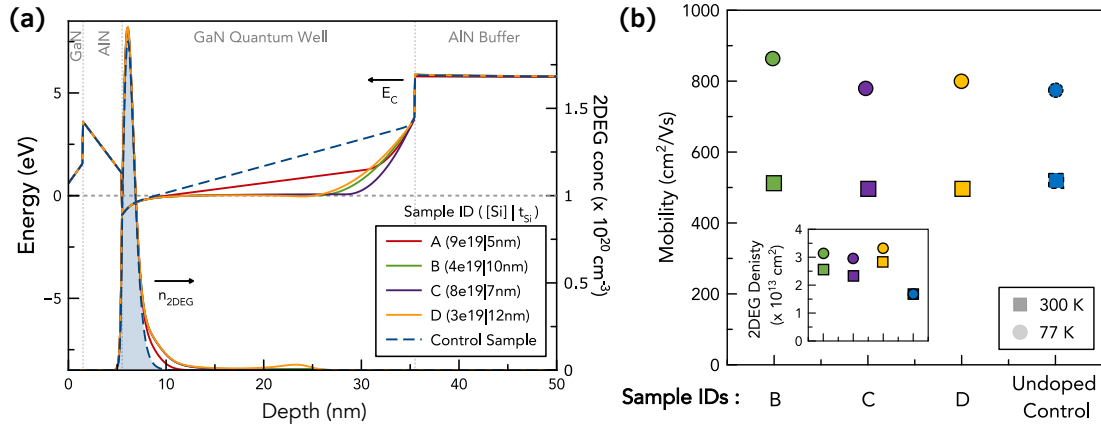
Figure 4.25: Investigations into the effect of Si doping at the GaN/AlN back barrier in an AlN/GaN/AlN HEMT. (a) Shows the energy band profile for samples A, B and C with different Si doping concentrations and doping thicknesses, each one of them effectively compensating the charges to result in no electric field in the GaN channel layer below the 2DEG. (b) The Hall-effect measurement results at room temperature and 77 K for samples A, B, C and D. Even though the Si doping increases the total 2DEG concentration slightly (inset), the 300 K and 77 K mobilities are similar to that from a control heterostructure with no Si doping.

potentially higher scattering from the interface or even enhanced phonon scattering.

Hence a controlled study to eliminate the 2DHG and compare the change in 2DEG mobility should be valuable. Si doping and/or graded AlGaN at the backbarrier GaN/AlN interface should be able to eliminate the 2DHG and examine its effect. Initial studies have been performed with Si delta-doped backbarrier. The results, summarized in **figure 4.25**, show no appreciable change in Hall mobility of the 2DEG. Future studies should use graded AlGaN and doped AlGaN at the GaN/AlN backbarrier interface to test their effect on the 2DEG transport in these AlN/GaN/AlN heterostructures.

CHAPTER 5

ALN/GAN/ALN HIGH ELECTRON MOBILITY TRANSISTORS

5.1 Introduction

In the previous chapter, tunable, high-conductivity 2DEGs were demonstrated in the AlN/GaN/AlN heterostructure. These 2DEGs are used as a channel layer for fabricating n-channel transistors or HEMTs on the AlN platform, which are the focus of this chapter.

Over the past 30 years, GaN-based HEMT has established itself in the high-power, high-frequency application space - thanks to its wide bandgap (3.4 eV), high electron velocities (1.4×10^7 cm/s), and ability to form heterostructures (leading to high carrier mobilities) [101]. In this chapter, we go over the design considerations for a power amplifier and show that AlN HEMTs hold a significant material advantage over GaN HEMTs, mainly thanks to its higher thermal conductivity. The thermal advantage is examined in detail through both modelling and supporting experimental results. A brief review of the state-of-art of AlN/GaN/AlN HEMTs is presented, which have demonstrated output powers upto 2 W/mm at 94 GHz. The output powers in these AlN/GaN/AlN HEMTs are believed to be limited by surface states dispersion. A new *in-situ* passivation technique is demonstrated as a way to overcome this limitation and provide a path to higher output powers. Finally, taking advantage of the electrostatic tunability the AlN/GaN/AlN heterostructure offers, the first enhancement mode operation in AlN MOS-HEMTs is demonstrated by scaling down the GaN channel layer to 3 nm.

194

With the advent of IoT, autonomous vehicles and cloud-based computing, the need for low latency, high data rate communication are ever increasing. The recent release of iPhone 12 made ushered in the 5G era [108] which uses the sub-6 GHz and 30+ GHz frequency bands, the latter of which is better known as millimeter wave (mm-wave). Consequently the demand for high-frequency, high-power components for monolithic microwave integrated circuits (MMIC) is driving the fundamental research into materials which can keep up with the performance demands.
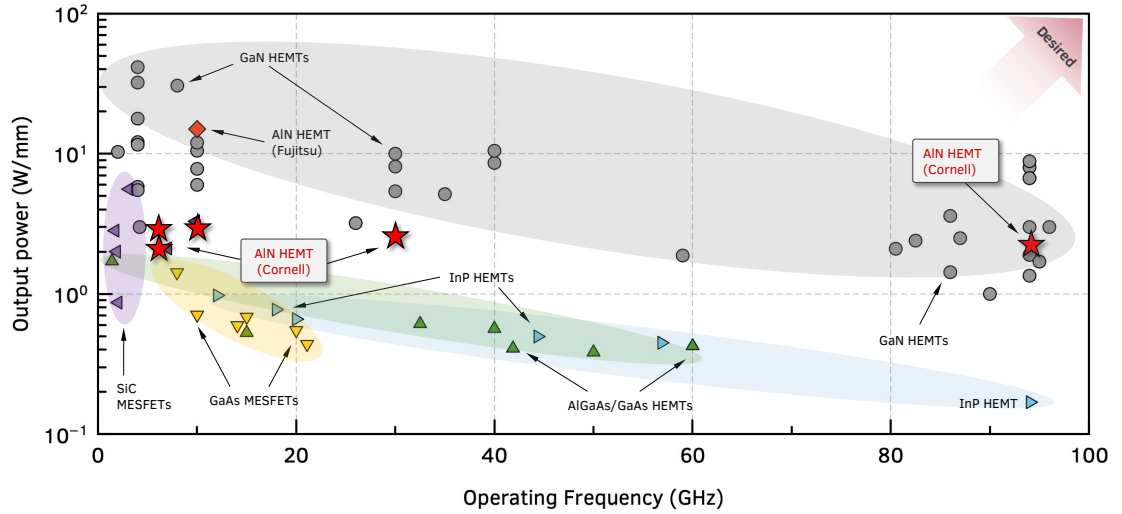
Figure 5.1: Benchmark plot comparing the normalized output powers of amplifiers based on the AlN HEMTs versus other semiconductor transistor technologies. The narrower bandgap material technologies (GaAs, InP) are unable to provide high power due to their inherently low breakdown voltages. SiC provides higher output powers but at lower speeds, and hence are mainly used for high-voltage switching applications. The GaN HEMT-based PAs currently provide the best output power-speed characteristics, as a result of 3 decades of commercial research and development. Within 5 years of its conception at Cornell, the AlN HEMTs have shown great promise, showing output powers of 2 W/mm at 94 GHz which are comparable to the GaN numbers at those frequencies. The output powers are expected to increase with device processing and design improvements.

The major competitors in the mm-wave power amplifiers (PA) arena are gallium arsenide high-electron-mobility transistors (GaAs HEMTs) [272, 273], sil-

icon germanium heterojunction bipolar transistors (SiGe HBTs) [274], and indium phosphide HBTs [275, 276]. Because of their relatively low voltage handling capabilities thanks to their narrow bandgaps (< 1.4 eV), these operate at relatively low power levels (< 1 W/mm) and are not suitable for high-power signal amplification. This is seen in **figure 5.1**, which compares the output powers reported from amplifiers based on different semiconductor device technologies.

Gallium nitride, thanks to its wider bandgap and high saturation velocity, was identified in the 1990s as a suitable candidate for power amplification [101]. A wider bandgap (3.4 eV) results in a higher breakdown voltage, and a high electron mobility and saturation velocity (1.4×10^7 cm/s) of the electrons results in higher intrinsic frequency of operation. Thanks to these suitable material properties and over two decades of scientific and technological development and commercialization, GaN high electron mobility transistor (HEMT) based PAs have demonstrated higher power outputs in the mm-wave frequency range than Si-, GaAs- and InP-based PAs. Current state-of-art GaN PAs have demonstrated exceptional output powers of 40 W/mm and 30 W/mm at 4 and 8 GHz respectively in field-plated metal-polar GaN HEMTs [277, 278], 15 W/mm in X-Band (7-11 GHz) GaN HEMTs on AlN [279] and >8 W/mm at upto 94 GHz using an N-polar GaN HEMTs [280, 281].

Even though GaN HEMTs show high powers at low frequencies, they are still limited to < 10 W/mm at > 100 GHz, as seen in **figure 5.1**. These bands are especially important for future of communication in 6G and beyond. A large discrepancy is observed when the experimentally measured output power densities are compared to the intrinsic material output power limit for GaN RF

HEMTs, especially at lower cutoff frequencies (f_T) [111]. This difference is explained by considering the effect of heat generation and dissipation during the amplifier operation. In a simple picture, a power amplifier (PA) transforms a low-power input AC signal into an amplified higher-power AC output signal, with the difference coming from the applied DC bias power. In a real world device, only a part of this DC power goes into amplifying the output (depending on the amplifier efficiency) - the remaining power is transferred into the surroundings and the semiconductor material itself in the form of heat. This leads to a highly localized rise in temperature on the drain side of the transistor channel, which deteriorates the electronic properties such as mobility, saturation velocity, limiting the maximum output power that can be extracted from the transistor. The heating is also responsible for a thermal stress gradient in the device semiconductor layers which reduces the reliability and lifetime of the transistor.

Therefore, it is important for any high-power RF platform to efficiently conduct the heat away from the active region channel in order to enhance the performance.

5.2 Thermal Advantage of AlN Buffer Layer

Aluminum nitride, with its ultra wide bandgap of 6.2 eV, has an expected critical electric field of 15 MV/cm - 5× that of GaN. Incorporating it in the buffer of an AlN/GaN/AlN HEMT structure should in principle allow the resultant device to handle higher voltages than GaN HEMTs. However, the critical advantage the AlN buffer layer provides is in the form of enhanced thermal management.

197
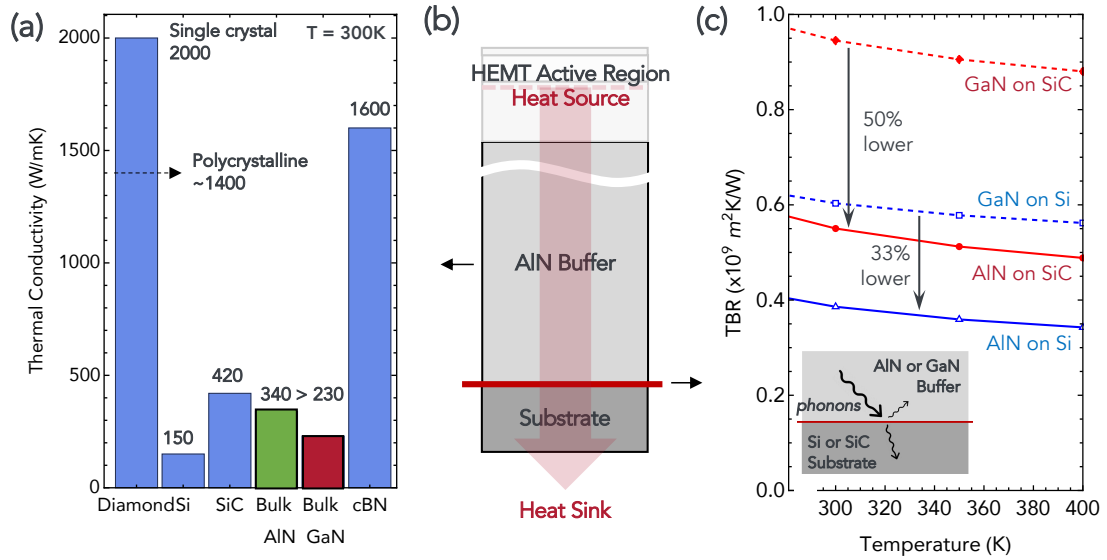
Figure 5.2: (a) Thermal conductivities of some commonly used materials in III-nitride electronics [50, 51]. Ternary and quartery alloys are expected to have lower conductivities than their constituent binary counterparts. (b) Theoretical thermal boundary resistances (TBR) calculated using Density mismatch model (DMM) [52] under Debye approximation. AlN is expected to have a lower TBR compared to GaN buffers on common substrates such as silicon and silicon carbide. A perfect homoepitaxially grown AlN on single crystal AlN substrates will not have any thermal boundary resistance as a boundary is not defined in that case. *Figure from Hickman, Chaudhuri et al. [53]*

In an RF HEMT, the drain side of the gate, where the electric field peaks, acts as a heat source. In the absence of a top heat-conducting layer, the heat primarily conducts through the buffer, into the substrate and to the heat sink at the bottom - as illustrated in **figure 5.2 (b)**. The thermal resistances between the channel and sink therefore play a crucial role in determining the channel temperature and thereby the device performance. The thermal resistances in this setup are in two forms (1) (inverse of) thermal conductivity of the buffer and substrate materials, and (2) thermal boundary resistances between two materials. Both these resistances are manifestations of the fundamental physics of heat transport via phonons and therefore are intrinsic to the semiconductor materials if we consider an ideal crystal material. This allows us compare the AlN platform

(AlN buffer on substrate), with the conventional GaN platform (GaN buffer on substrate) and highlight the advantage which the AlN provides us with respect to the expected thermal performance.

Figure 5.2 (a) compares the experimentally measured thermal conductivity values of common materials in III-nitride devices. Silicon (111) and silicon carbide (SiC) are commonly used substrates for these family of devices. SiC, with a high thermal conductivity of ~420 W/mK is the substrate of choice for effective thermal management in the current state-of-art RF GaN HEMTs. Single-crystal diamond [50] and cubic-boron nitride (c-BN) [51] have the highest thermal conductivities and there are efforts to integrate these as conduction/heat spreading layers in RF HEMTs [282]. In III-nitrides semiconductors, AlN has a higher thermal conductivity of 340 W/m.K compared to 230 W/mK of single-crystal GaN. It is clear from these values that an AlN buffer holds an advantage over a GaN buffer in terms of heat conduction away from the active region.

An additional factor to consider is the thermal boundary resistance (TBR) between the substrate and the buffer layer. TBR is an intrinsic property of an interface where it acts as a resistance to heat flow and leads to a rise in temperature. In a microscopic picture, according to the diffusive mismatch model (DMM) [52], the TBR at a perfect interface between two ideal materials arises due to the difference in phonon density of available states for a heat carrying phonon to scatter into when moving from one material to the other. The calculated TBR between AlN and GaN buffer layers and commonly used Si(111) and SiC substrates are shown in **figure 5.2 (c)**. The Debye density of states approximation has been used. This model predicts that an AlN buffer should have a lower TBR compared to GaN buffer on both SiC and Si substrates, by $\sim$ 50%

and ~ 33% respectively. Experimental measurement of TBRs for these structures have yielded values a couple of orders higher which is attributed to the non-ideal crystal structure near the nucleation interface. This is especially true in case of GaN, where AlN nucleation layers and/or stress-management layers with lower crystal quality result in high TBRs. AlN, with a lower lattice mismatch, can be directly grown on SiC with a better crystal quality and thus lower a TBR. Recent availability of high quality single-crystal substrates have opened up the possibility of homoepitaxial growth of GaN and AlN on bulk GaN and bulk-AlN substrates respectively, in which TBR will be completely eliminated [64, 65]. Even in this case, comparing to GaN on GaN, AlN on bulk AlN holds a thermal advantage due to higher thermal conductivity.

Thus an AlN buffer should theoretically lead to a better thermal management in RF HEMT when compared to a GaN buffer grown heteroepitaxially on Si, SiC or homoepitaxially on bulk substrates. This should translate to a performance boost high power operation of AlN buffer devices. However it must be noted that the values are for near-perfect crystals, and the actual epitaxial crystal quality determines the value of thermal resistances encountered in a real device. Hence the translation of these expected device performance boosts depend heavily on the quality of the material grown.

Thermal characterizations were performed, in collaboration with Prof Martin Kuball's laboratory in University of Bristol, to validate the above theoretical predictions for MBE-grown AlN films used in our AlN HEMTs. Transient thermoreflectance (TTR) was carried out on a sample consisting of a ~600 nm thick MBE-grown AlN on a 370 μm thick 6H-SiC substrate. The structural details of the epitaxial film is shown in **figure 5.3**. The sample had a very low screw dis-
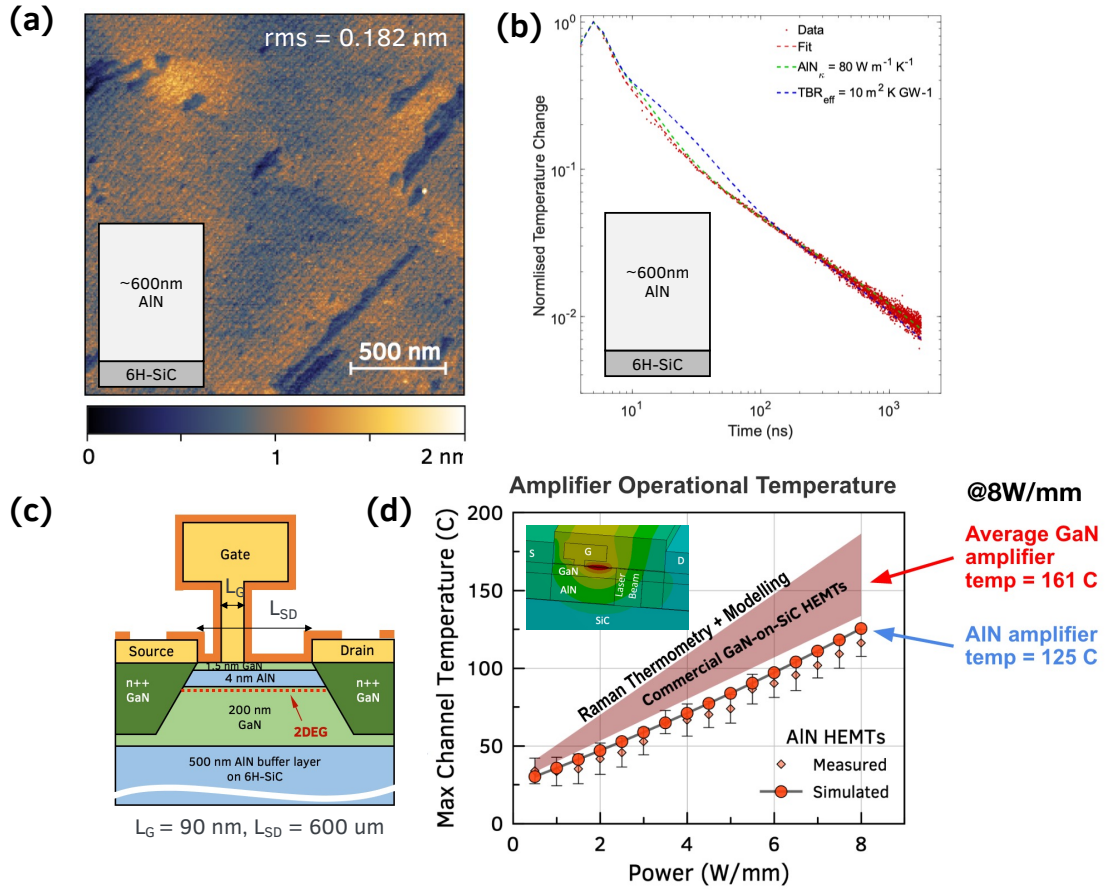
Figure 5.3: (a) AFM scan of the surface showing low dislocation density in a MBE-grown 500 nm AlN on SiC. (b) Transient thermoreflectance (TTR) measurement results, with extracted AlN isotropic thermal conductivity of $\kappa > 80$ W/mK and AlN/SiC TBR of < 10 m²K/GW (d) Channel temperature of AlN HEMT, cross-section in (c), measured using Raman thermometery. AlN HEMTs show atleast 20% reduction in channel temperature compared to GaN HEMTs of similar dimensions at 8 W/mm power outputs. *These measurements were performed at Bristol University in Prof. Kuball's lab.*

location density of 10^6 cm^{-2}, evident from the sharp X-ray rocking curve peak and surface morphology. The TTR measurement results and fitted parameters are shown in figure 5.3. SiC substrate in-plane and out-of-plane thermal conductivities of κ_{IP} 463 +130/-100 W/m.K and κ_{OP} 253 +75/-55 W/m.K, extracted from a bare substrate, is used as a fitting parameter. The thinness of the AlN epi-layer limits the sensitivity of TTR measurement. A best estimate AlN (isotropic)

thermal conductivity of $\kappa > 80$ W/m.K and AlN/SiC TBR of < 10 m^{2}K/GW were extracted, which agrees well with literature reports [283].

Raman thermometry was used to measure the channel temperature of an AlN/GaN/AlN HEMT grown and fabricated on a similar AlN on SiC buffer layer as in figure **figure 5.3 (a)**. The device cross-section is shown in **figure 5.3 (c)**, and the measured channel temperature in **figure 5.3 (d)**. An ANSYS simulation of the HEMT was performed to simulate the channel temperature using the thermal parameters of AlN, SiC extracted by TTR. The agreement between the measured and simulated channel temperature as a function of output power validates the results. To quantify the effect of the AlN buffer layer, the same ANSYS simulation was performed with one change - the AlN was replaced by a GaN buffer layer. The resulting channel temperature as a function of output power is shown in **figure 5.3 (d)**. The spread in the values is to take into consideration the variation in the reported thermal conductivities of epitaxial GaN layers and GaN/SiC TBRs [284]. The results show that for the same device dimensions, an MBE-AlN buffer layer results in a $\sim$ 23 % lower channel temperature compared to a GaN buffer layer of same thickness, when operated at 8 W/mm output power. As a corollary, for the same maximum operating temperature (same mean time to failure), the AlN HEMT can output higher powers. This cooler channel temperature is a result of the combination of both higher thermal conductivity of AlN vs GaN, and lower TBR of AlN/SiC vs GaN/SiC.

5.3   MBE-grown AlN buffer layers on SiC for RF HEMTs

Due to the lack of native substrates until recently, epitaxial growth of III-nitride semiconductor optoelectronics and electronic devices are mostly performed on foreign substrates. These include sapphire, silicon carbide (SiC), silicon. The selection of substrate is mainly driven by the cost, availability and the specific needs of the final device application (for example, high thermal conductivity for RF PAs, UV transperency for UV LEDs).

Silicon carbide has been the substrate of choice for RF GaN applications primarily due to its high resistivity and high thermal conductivity (~ 420 W/m.K). The latter is especially important for high-frequency power amplifiers, where the channel temperature limits the output powers, and hence thermal management is of highest importance. High purity semi-insulating SiC (both poly-types 6H or 4H) wafers up to 4-inch are commercially available from US-based vendors such as CREE, II-VI Advanced Materials, with 6-inch wafers in development and slated to be available by 2025.

6H-SiC substrates offer an additional advantage for epitaxial growth of AlN layers due to its small in-plane lattice mismatch of < 1 %. This is the reason AlN nucleation layers are used for growing thick GaN buffer layers in RF GaN HEMTs. It therefore offers a great substrate platform for investigating AlN/GaN/AlN HEMTs, as > 0.5 μm thick AlN buffer layers can be grown directly on the SiC substrate without any other nucleation layer or strain compensating layer. Of course, the ideal substrate to realize the AlN HEMTs is a single crystal bulk AlN. Recent availability of high quality single crystal bulk AlN substrates [285] have led to exploration of new homoepitaxial AlN growth

techniques [64, 65] (see appendix B). But extremely high cost, limited availability and small wafer sizes restrict their current usage to scientific exploration only.
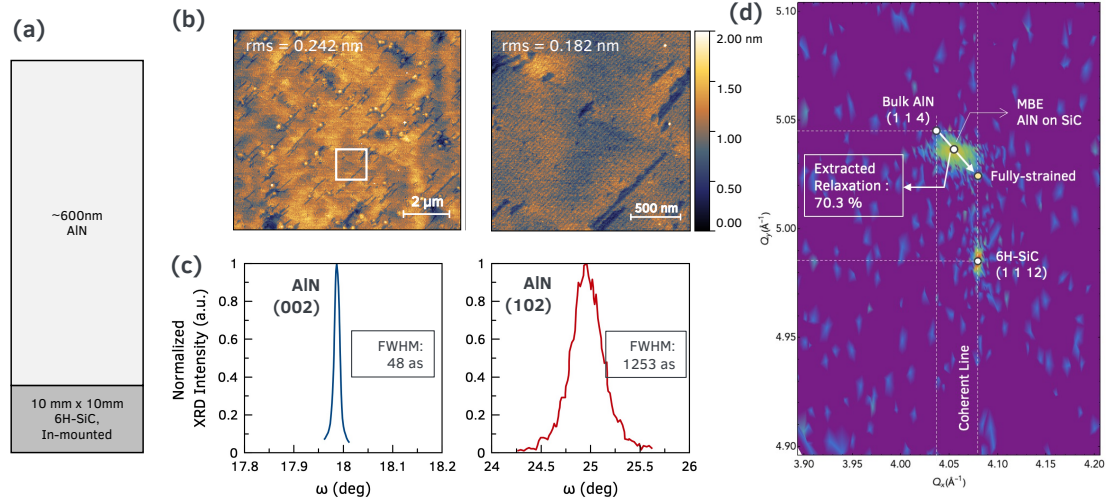
Figure 5.4: (a) Layer structure of high quality AlN "buffer layer" grown on 6H-SiC (b) surface morphology shown in atomic force microscopy scans, showing smooth, parallel features with low density of spiral features. (c) XRD rocking curves showing the low screw type threading dislocation density. (d) Reciprocal space map around the AlN (1 1 4) peak shows the AlN layer partially relaxes by forming edge type dislocations, which is confirmed by the AlN (102) FWHM in (c).

Figure 5.4 shows a ~600 nm AlN layer grown using PA-MBE on 6H-SiC wafers. The wafers were obtained from II-VI Advanced Materials with additional CMP surface treatment performed at NovaSiC [286]. The growth was performed in metal-rich growth conditions, with an initial Ga pre-deposition to promote layer-by-layer growth [287]. Growth details are provided in the appendix A. **Figure 5.4 (b)** shows the atomic force microscopy scans of the AlN surface. Clear parallel terraces are observed indicating layer by layer growth. This surface morphology is in fact similar to very high-quality homoepitaxial AlN growths performed on single-crystal AlN substrates [64] and is surprising for a heteroepitaxial growth. Very few spirals are visible on the larger 10×10

μm^2 scan, signifying a low screw dislocation density. This is supported by the XRD rocking curve (RC) along AlN (002) symmetric peak, which shows a full width half max (FWHM) of 48 arcsec. This corresponds to a very low screw-type dislocation density [288] of $\sim 10^6$ cm^{-2}. The reciprocal space map around AlN (114) peak is shows a 70% relaxation in the AlN layer with respect to the SiC susbtrate. This relaxation is believed to give rise to edge-type dislocations, the density of which is estimated to be $\sim 10^9$ cm^{-2} from the FWHM of the XRD-RC along the AlN (102) peak.

The ability to grow thick, high-quality AlN buffer layers is critical to all the electronic devices on the AlN platform. The quality of crystal growth determines both their thermal and electrical performances. These high quality AlN on SiC buffer layers are used for AlN/GaN/AlN HEMT heterostructures reported in this dissertation. These AlN buffer layers enable uniform growth of 2DEG across a 3-inch wafer area, with smooth surface morphologies and uniform sheet resistance, as shown in **figure 5.5**. These uniform, reliable growths are crucial first step of any new device development process. The details of the active layer growth and detailed MBE growth conditions are provided in appendix A for reference.

5.4   State-of-art AlN/GaN/AlN HEMTs

The AlN platform [53] for mm-wave integrated circuits (MMIC) offers the possibility of integrating both active components such as p- and n-channel transistors (for PAs and low-noise amplifiers) and passive components such as bulk acoustic wave (BAW) filters [289] and SiC substrate integrated waveguides (SIW)
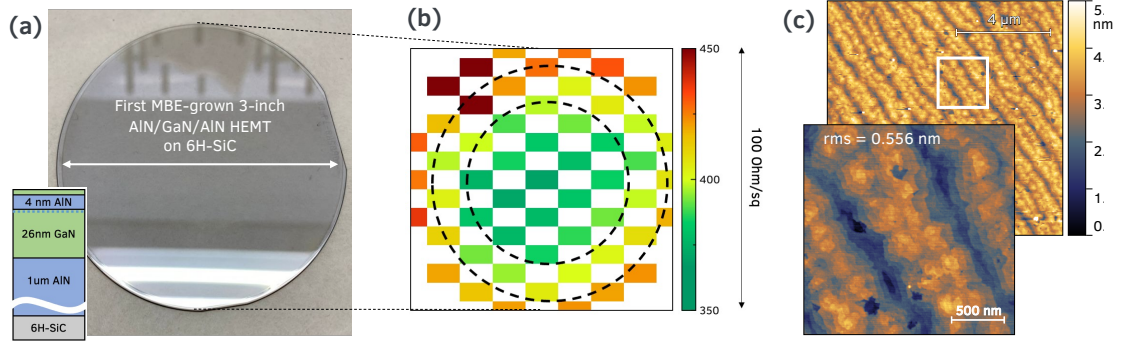
Figure 5.5: (a) Growth of AlN/GaN/AlN HEMT structure on a 3-inch SiC wafer. The layer structure is shown in the inset (b) Contactless sheet resistance mapping (performed by Dr. Shinohara at Teledyne Technologies) shows the presence of the 2DEG across the surface of the wafer. (c) Smooth surface morphology with rms roughness ~ 0.5 nm, which is desired for device fabrication.

[57]. The workhorse of this platform is the scaled AlN/GaN/AlN high electron mobility transistors (HEMTs) grown on thick AlN buffer layers which can act as both PAs and LNAs. These AlN HEMTs promise mm-wave signal amplification at power levels higher than those measured currently in GaN HEMT based PAs. The high thermal conductivity (340 W/m.K), high breakdown field [47, 290] of AlN and larger polarization and band offset with respect to GaN are expected to boost the performance of AlN HEMTs. This has led to a rising interest of the community in these AlN-buffer based HEMT heterostructures. There have been numerous reports of epitaxial growth of AlN/GaN/AlN and AlGaN/GaN/AlN structures using different techniques and substrates [40, 41, 42, 43, 44, 45, 46]. These heterostructures have been used to demonstrate AlN-based HEMTs for RF amplification [279, 47, 42, 44, 46] and high-power switching [290, 291].

In particular, recent AlN HEMTs on SiC [279, 218, 54] have made giant strides towards fulfilling the promise of high output powers at mm-wave frequencies. The current state-of-art AlN/GaN/AlN HEMT [54] is presented in
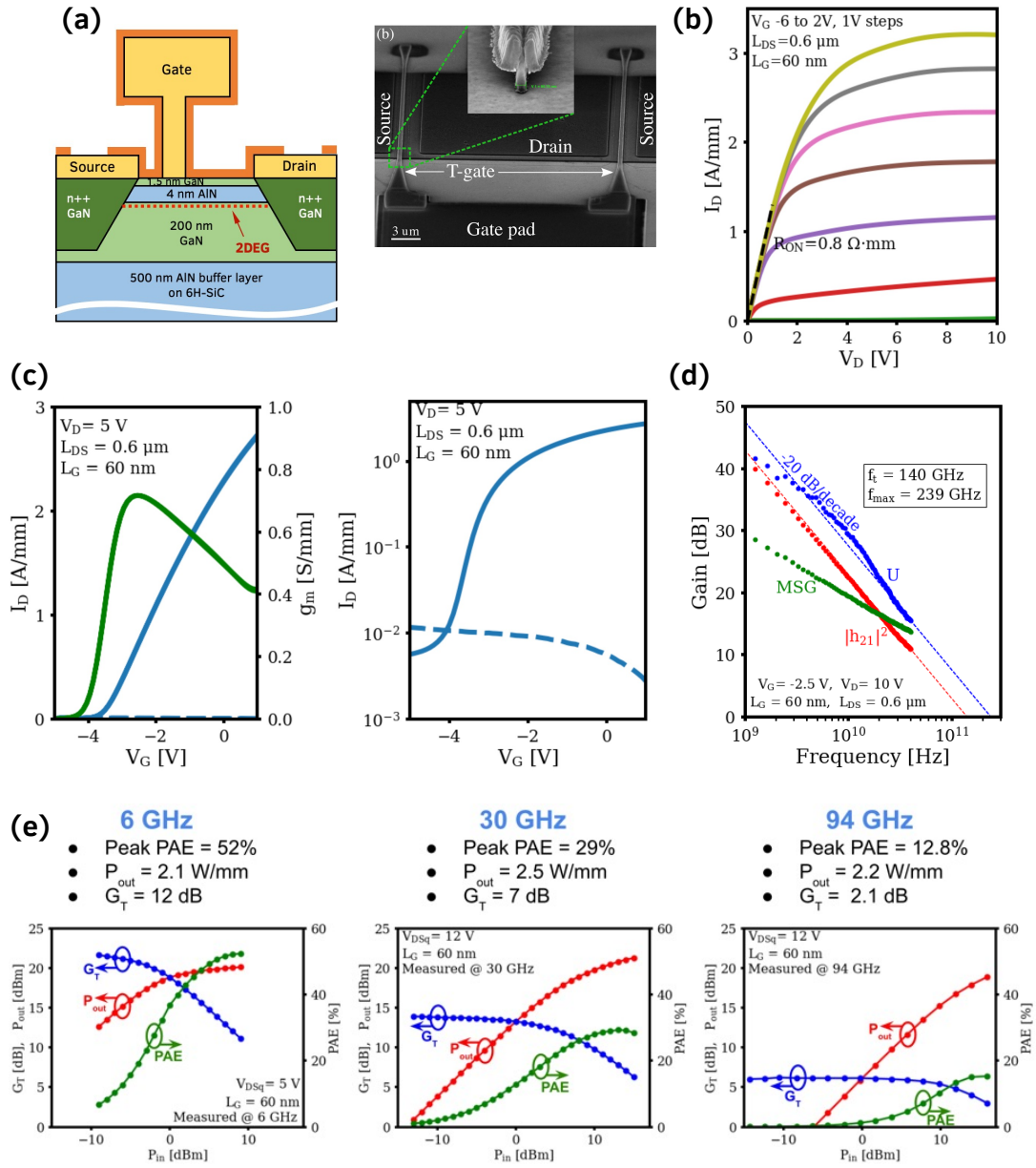
Figure 5.6: (a) Cross-section of a state-of-art AlN/GaN/AlN HEMT, with 200 nm GaN channel and ex-situ SiN passivation layer. A top-side SEM shows the 60 nm long T-gate. (b) Output characteristics, (c) Transfer characteristics, and (c) small-signal measurement results show high on-currents and high speeds on operation. (d) load-pull power sweeps of a 2×25 μm device biased in Class AB operation, at 6 GHz, 30 GHz and 94 GHz. *Figures by Austin Hickman. Load-pull measurements were performed at AFRL and UCSB by Neil Moser and Matt Guidry respectively.*

figure 5.6. **Figure 5.6 (a)** shows the cross-section of the device, with MBE regrown ohmic contact regions, along with an SEM of the L_G = 60 nm long T-gate. The output characteristics of the AlN HEMT in **figure 5.6 (b)** shows high on-currents of >3 A/mm, which is among the highest reported in any transistor. The transfer characteristics in **figure 5.6 (c)** show a peak transconductance g_m ~ 0.7 S/mm, and approximately 3 orders of magnitude of current on-off ratio. Small-signal measurement in **figure 5.6 (d)** shows cut-off frequencies of f_T/f_{MAX} = 140/239 GHz.

These high cut-off frequencies, high on-currents and high-breakdown voltages [47] make high-power, high-frequency signal amplification possible in these devices. The large-signal measurement results are shown in **figure 5.6 (e)**. The state-of-art scaled, T-gated AlN/GaN/AlN HEMTs on SiC demonstrate output powers of 2.1, 3.1, 2.5 and 2.2 W/mm at 6, 10, 30, 94 GHz respectively without field plates [218, 54]. Additionally, AlGaN/GaN/AlN HEMTs on single crystal AlN substrates have recently demonstrated phenomenal 15 W/mm in the X-band [279], further demonstrating the potential of this platform for high-power amplification. The large signal performance of these AlN-based HEMTs are compared against other semiconductor transistor technologies in **figure 5.1**. Although these results are remarkable for a device technology early in its development stage, it can be seen that they are still below the state-of-art GaN HEMTs' output powers of upto 8 W/mm at 94 GHz [281, 292, 293].

It has been found [54] that the dispersion from surface states is what limits the capability of the current generation of AlN HEMTs to truly achieve its potential. In the next section, a possible solution to control the DC-RF dispersion in AlN/GaN/AlN HEMTs by using a new *in-situ* crystalline AlN passivation
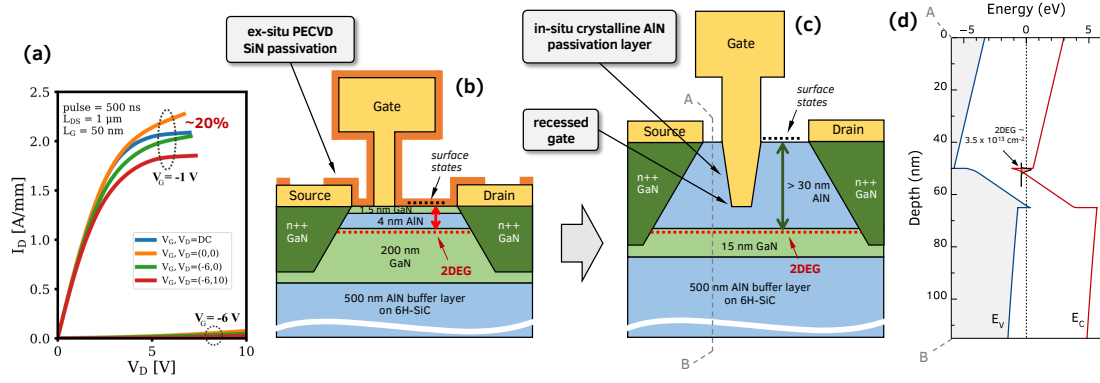
Figure 5.7: (a) Pulsed I_D-V_D measurement results for the the current state-of-art AlN/GaN/AlN RF HEMTs [54], showing a ~ 20% DC-RF dispersion due to surface states. (b) Schematic of the state-of-art AlN/GaN/AlN RF HEMTs with ex-situ SiN passivation. The surface states on the as-grown surface is present ~ 6 nm away from the 2DEG, and is not effectively supressed using the PECVD SiN. (c) Schematic of the proposed AlN/GaN/AlN HEMT with in-situ crystalline AlN passivation layer. A > 30 nm AlN top layer acts both as a barrier for the 2DEG and makes sure the surface states are far from the 2DEG channel. A recessed gate is required to keep the gate close to the channel and maintain the transconductance and speeds. (d) A self-consistent 1D Schrodinger Poisson band simulation [55] of an as-grown AlN/GaN/AlN structure with 50 nm of AlN passivation layer and 15 nm GaN channel layer. A 2DEG of density ~ 3.5×10^{13} cm^{-2} is expected at the top AlN/GaN interface.

scheme is studied.

5.5 *in-situ* AlN passivation for reduced dispersion

Figure 5.7 (b) shows the cross-section of the current state-of-art AlN/GaN/AlN RF HEMTs [54]. Positively charged surface donor states are expected to be present on the as-grown heterostructure surface which is ~ 6 nm away from the 2D electron gas (2DEG) channel. If these surface states are not controlled or passivated, they capture electrons from the transistor channel and cause current collapse and DC-RF dispersion under large signal operation [294, 183]. The typ-

ical way to counter this effect is to deposit silicon nitride (SiN) to passivate the surface states after the HEMT fabrication [295, 296]. For the AlN HEMT in **figure 5.7 (b)**, ex-situ SiN passivation layer was deposited using PECVD as the last step in the HEMT fabrication process. Pulsed $I_D - V_D$ measurement results of these devices are shown in **figure 5.7 (a)**. The device demonstrated an on-current dispersion of ~20% and ~1 V knee voltage walkout for quiescent gate/drain biases of -6/10 V. This dispersion translates to soft gain compression in large-signal measurement results [54] at high input powers. Clearly, the ex-situ SiN passivation is not completely successful in suppressing the RF dispersion from the surface states in these devices. A more effective passivation of these surface states is hence desired to unlock the true potential of the AlN/GaN/AlN HEMTs and exceed power outputs of the state-of-art GaN HEMTs [280, 281].

In this section, we demonstrate a solution to control the DC-RF dispersion by using an in-situ crystalline AlN passivation scheme for AlN/GaN/AlN HEMTs. The proposed scheme is shown in **figure 5.7 (c)**. Instead of a thin, ~ 5 nm AlN barrier, a thick, > 30 nm AlN layer is grown on top of a compressively strained GaN channel. In addition to acting as the electrostatic barrier layer for the 2DEG, this AlN layer takes the as-grown surface far from the 2DEG channel and hence reduces carrier trapping. We show experimentally that the GaN channel layer should be pseudomorphically strained to the AlN buffer layer for this scheme to work. A thin < 15 nm GaN channel layer maintains the in-plane compressive strain > 2% and consequently allows the growth of 30+ nm thick crack-free AlN passivation layer on top. A low sheet resistance 2DEG is demonstrated over a quarter of 4-inch wafer. Demonstration devices are fabricated using a new recessed-gate AlN HEMT process. Pulsed $I_D - V_D$ measurements on these devices show a reduced DC-RF dispersion of $2 - 6\%$, the best

device showing a 10× reduction compared to the ~ 20% dispersion seen in ex-situ SiN-passivated AlN HEMTs. These results confirm the efficacy of this new in-situ passivation technique to help increase the high-power RF performance of next-generation AlN HEMTs.

The metal-polar AlN/GaN/AlN HEMT heterostructure consists of a top AlN barrier layer, a thin GaN channel layer and a > 0.5 μm thick AlN buffer layer epitaxialy grown on a resistive 6H silicon carbide (SiC) substrate. The relatively low lattice mismatch of < 1% AlN with respect to SiC enables the heteroepitaxial growth of 0.5-1.0 μm thick, crack-free AlN buffer layers on SiC. Additionally the high thermal conductivity of SiC makes it a suitable substrate for mm-wave AlN HEMT PAs. **Figure 5.7 (d)** shows the energy band diagram of the as-grown heterostructure, calculated using a self-consistent 1D Schrodinger-Poisson solver [55]. A 2DEG channel is induced at the top GaN/AlN interface [209] without the need of impurity doping due to the positive polarization difference. The 2DEG density in the as-grown heterostructure electrostatically depends on the thicknesses of the GaN channel layer and AlN barrier layer [297]. In general, beyond the certain critical GaN channel thickness of ~ 3 nm, thicker GaN or AlN layers result in higher 2DEG densities. The high polarization difference between AlN and GaN results in 2DEG densities of $2-3\times10^{13}$ cm^{-2} in an as-grown 4 nm AlN/200 nm GaN/500 nm AlN heterostructure with room temperature mobilities of ~ 720 cm^2/Vs. When processed into scaled RF HEMTs [54], the high 2DEG density translates to low access resistances and high on-currents of > 3 A/mm, high extrinsic transconductance of 0.8 S/mm and high speeds with f_T/f_{MAX} of 123/233 GHz.

Making the AlN top barrier layer thicker > 30 nm in the AlN/GaN/AlN

211

structure should move the surface states away from the 2DEG channel. The thicker AlN barrier layer is also expected to increase the as-grown 2DEG density compared to a 4 nm AlN barrier layer. This should further reduce the access resistance in the final HEMTs - an additional advantage of the proposed in-situ AlN passivation layer. However, incorporating this proposed AlN passivation scheme into the AlN HEMT process poses the following challenges. From the epitaxial growth perspective, a 2.4% lattice mismatch between GaN and AlN crystals makes it challenging to grow thick AlN layers on relaxed GaN without cracking. Careful control of the layer strains is necessary to overcome this. From the transistor perspective, the gate needs to be close to the 2DEG in order to maintain electrostatic control over the channel. Therefore, this passivation technique makes it necessary to incorporate a recess-gate geometry. The optimum design of the in-situ crystalline AlN passivated AlN/GaN/AlN HEMT is shown in **figure 5.7 (c)**.

The following sections tackle the challenges listed above. First, the growth of thick AlN barrier layers is demonstrated by ensuring almost pseudomorphically-strained GaN channel layers. Next, the resultant 2DEG transport is characterized and a well-controlled recess etch process is demonstrated which preserves the 2DEG. Finally, the results of the fabricated in-situ passivated AlN/GaN/AlN HEMT are presented, that demonstrate the successful reduction of the DC-to-RF dispersion.

GaN Channel Strain in AlN/GaN/AlN Heterostructures

The in-plane lattice constant of a relaxed wurtzite AlN crystal a_0^{AlN} = 3.112 Å is smaller than that of GaN a_0^{GaN} = 3.189 Å. The resulting ~2.4 % in-plane lattice mismatch makes the epitaxial growth of thick AlN barrier layers on relaxed GaN challenging. Consider the case of AlN/GaN HEMT heterostructures, where the AlN barrier layer is under tensile strain on *relaxed* GaN buffer layers. There exists a critical coherent thickness t_{cr} below which the AlN layer remains strained to GaN. Using the Blanc's estimate [298] of $t_{cr} \sim b_e/2f$, where b_e = 0.3189 nm is the Burgers vector length in strained AlN and f = 0.024 is the lattice mismatch between AlN and relaxed GaN, results in a critical thickness of ~ 6.5 nm. Beyond this thickness, the tensile-strained AlN layer relaxes and releases the strain energy in the form of cracks along hexagonal planes. This has been observed experimentally in AlN/GaN HEMT structures [173], where structures with AlN barriers > 7 nm showed hexagonal cracks on the surface in atomic force microscopy (AFM) scans. These cracks lead to a suppression of the 2DEG mobility and are undesired in a device heterostructure.

Now consider the AlN/GaN/AlN HEMT structure which is grown on relaxed AlN buffer layers. If the GaN channel layer is *compressively strained* to the AlN buffer layer (i.e. the GaN lattice constant is closer to that of AlN compared to its relaxed state), a smaller lattice mismatch f between the top AlN barrier layer and the GaN channel is obtained. f decreases with increase in in-plane compressive strain ϵ_{xx}^{GaN} in the GaN layer. Consequently, the coherent critical thickness t_{cr} of the AlN barrier layer is expected to increase with ϵ_{xx}^{GaN} through the relation $t_{cr}(\epsilon_{xx}^{GaN}) \sim b_e/2 \ f(\epsilon_{xx}^{GaN})$, where t_{cr} amd f are functions of ϵ_{xx}^{GaN}.

The calculated critical thickness of the top AlN barrier layer in an
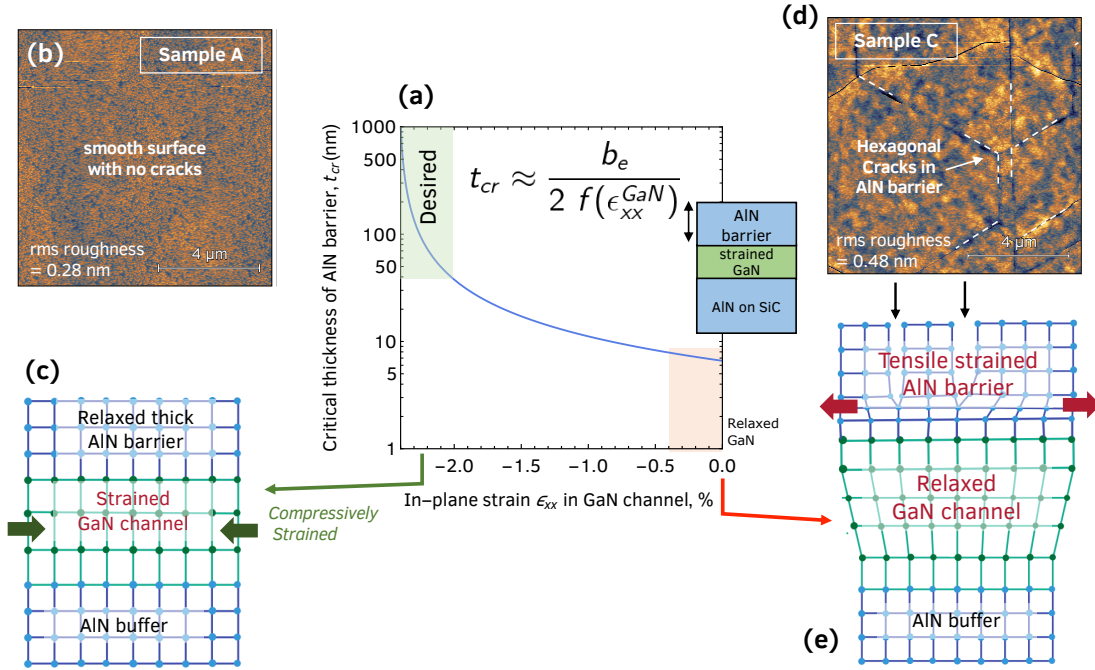
Figure 5.8: (a) The calculated dependence of the critical coherent thickness of the AlN passivation/barrier layer on the compressive strain of GaN layer in the AlN/GaN/AlN structure. A higher GaN compressive strain results in larger AlN critical thickness. A GaN channel layer almost pseudomorphic to AlN with > 2% compressive-strain is desired to grow thick > 30 nm AlN barrier layers which will act as in-situ passivation. (b) and (d) show the atomic force microscopy (AFM) scans of the surface of AlN/GaN/AlN samples A and C with 15 nm and 200 nm of GaN channel layers respectively. Hexagonal cracks are observed on the surface of sample C, which form to relieve the tensile strain in the AlN barrier, as illustrated in (e). Sample A however shows smooth surface with no cracks as the whole structure is pseudomorphic to AlN as shown in (c).

AlN/GaN/AlN HEMT structure is plotted in **figure 5.8 (a)**. When the GaN channel is completely relaxed, the critical thickness of AlN is $t_{cr}(\epsilon_{xx}^{GaN} = 0) \sim 6.5$ nm. This is similar to the AlN/GaN HEMT structure [173]. The cartoon in **figure 5.8 (e)** represents the situation when an AlN layer thicker than $t_{cr}(\epsilon_{xx}^{GaN} = 0)$ is grown on a relaxed GaN channel layer. The AlN barrier layer relaxes to relieve the strain and forms cracks. On the other extreme, in an AlN/GaN/AlN HEMT, the whole structure can also be pseudomorphic to the AlN buffer, which means

the ϵ_{xx}^{GaN} = -2.4%. Under such conditions, the AlN barrier layer is no longer under any tensile strain, and the critical thickness of the relaxed layer thus approaches infinity. The cartoon in **figure 5.8 (c)** illustrates this desired condition. Growth conditions can lead the crystal to be in a state between the above two extremes, where the GaN layer starts to partially relax and the top AlN layer builds up some tensile strain. Therefore, the strain in the GaN layer ϵ_{xx}^{GaN} is the critical parameter for enabling the growth of thick AlN layers for our proposed in-situ passivation scheme. From **figure 5.8 (a)**, it is clear that a compressive strain of $> 2\%$ in the GaN layer is desired to grow crack-free in-situ AlN passivation layers thicker than 30 nm.

Table 5.1: Summary of the AlN/GaN/AlN heterostructure studied in this work with their corresponding structural and 2DEG transport properties. The strain in GaN channel layers ϵ_{xx}^{GaN} were extracted from the X-ray diffraction reciprocal space maps detailed in figures 5.9 and 5.10. Hall-effect measurements were used to determine the 2DEG density n_s, room temperature mobility μ_n and the sheet resistance R_{sheet}. The high sheet resistance in sample C, due to the crystal cracking, makes is difficult to reliably determine the 2DEG mobility and charge densities.

Sample ID	Heterostructure $t_{AlN}/t_{GaN}/t_{AlN}$	ϵ_{xx}^{GaN}	Surface Morphology	300K n_s ($\times10^{13}$ cm^{-2})	300K μ_n (cm^2/Vs)	300K R_{sheet} (Ω/sq)
A	100/15/500	-1.97 %	Smooth with no cracks	4.24	297	495.2
B	100/30/500	-1.78 %	No cracks in as-grown structure, but optically visible cracks during device processing	4.86	316	406
C	100/200/500	-0.6 %	Cracks in as-grown structure, visible in AFM	-	-	2.51×10^5
D	50/15/500 Quarter 4" wafer	-1.97 %	Smooth, no cracks	3.57	358	428

The compressive strain in the GaN layer, ϵ_{xx}^{GaN}, in turn depends on its thickness t_{GaN}. The exact relation between the strain and thickness of an epitaxial layer depends on the growth technique, growth modes, growth temperature, starting substrate etc. Hence, to experimentally determine the relationship between t_{GaN} and ϵ_{xx}^{GaN} in our heterostructures, a series of 100 nm AlN barrier/GaN/500 nm AlN heterostructures were grown using plasma-assisted
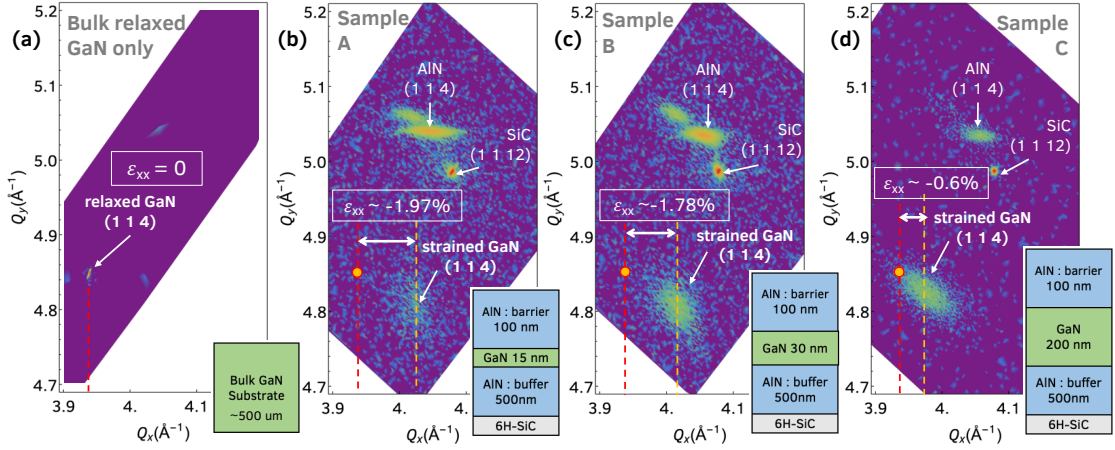
Figure 5.9: (a) X-ray diffraction reciprocal space map (RSM) of a control bulk GaN substrate showing the (114) reciprocal reference space point of a relaxed GaN layer. (b), (c), (d) show the RSM for a series of AlN/GaN/AlN samples with GaN layer thicknesses of 15 nm, 30 nm, 200 nm. The in-plane compressive strain in the GaN layers, extracted with respect to the relaxed GaN (114) point, decreases with increase in the GaN layer thickness.

molecular beam epitaxy (PA-MBE) on 6H-SiC substrates. Only the GaN layer thickness t_{GaN} was varied between these samples. Details of the epitaxial growths are provided in the appendix A.

Reciprocal space mapping (RSM) using X-ray diffraction were performed on these AlN/GaN/AlN heterostructures around the SiC (1 1 12)/GaN (1 1 4) peaks to extract the in-plane lattice spacings of the GaN layer. Reciprocal space maps for AlN/GaN/AlN samples with t_{GaN} = 15, 30, 200 nm are shown in **figure 5.9**. The samples, labelled A, B and C respectively, are summarized in **table 5.1**. RSM scan was also performed on single crystal bulk GaN substrate for calibration. The extracted in-plane spacing of a_0^{GaN} = 3.189 Å from the bulk GaN sample agrees with the relaxed GaN lattice constant value. From the RSMs from the AlN/GaN/AlN structures, it is clear that the in-plane lattice constants of the GaN layers are smaller than a_0^{GaN}, confirming the compressive strain. Using a_0^{GaN} as the reference, the strain in the GaN layers ϵ_{xx}^{GaN} of different thicknesses are ex-
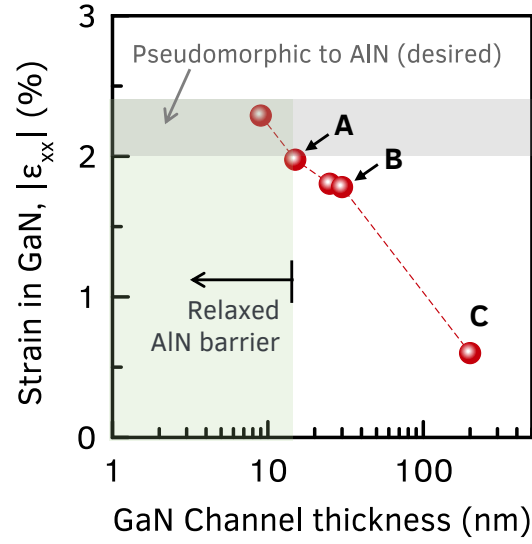
Figure 5.10: Experimental dependence of the in-plane compressive strain in the GaN layer as a function of its thickness in an MBE-grown AlN/GaN/AlN heterostructure grown on 6H-SiC. The strains are extracted from X-ray diffraction reciprocal space maps shown in figure 5.9. The results show a GaN channel thickness of < 15 nm results in the > 2% compressive strain desired for growing > 30 nm thick AlN passivation layers. The finite lattice constant difference between the strained GaN channel and fully relaxed AlN is a result of a slight elastic relaxation, which is not expected to generate extra dislocations.

tracted from their in-plane lattice spacings. The extracted strains ϵ_{xx}^{GaN} are listed in **table 5.1** and plotted in **figure 5.10** as a function of t_{GaN}. Data from other AlN/GaN/AlN samples with t_{GaN} = 9, 22 nm are also included. It clearly seen that a thinner GaN layer is more compressively strained to AlN as expected. Comparing the data in **figures 5.8 and 5.10**, we infer that a GaN channel layer thinner than 15 nm is required in an AlN/GaN/AlN struture to maintain a > 2% compressive strain and thereby grow the desired in-situ crack-free AlN passivation layer of > 30 nm. The finite lattice constant difference between the strained GaN channel and fully relaxed AlN is a result of a slight elastic relaxation, which is not expected to generate extra dislocations between the two.

The difference in the strains in the AlN/GaN/AlN samples with different

t_{GaN} are also directly evident from the corresponding surface morphology. **Figure 5.8 (a) and (c)** shows the 10 μm $\times$ 10 μm atomic force microscopy (AFM) scans of the surface of AlN/GaN/AlN samples A and C. Both these samples have a 100 nm AlN barrier grown on top of the GaN layer. Sample A, with ~ 2% compressively-strained 15 nm GaN channel layer shows a very smooth surface with sub-nm root-mean-square roughness of 0.28 nm. On the other hand, sample C, with an almost relaxed (ϵ_{xx}^{GaN} ~ 0.5%) 200 nm GaN channel layer, exhibits clear hexagonal cracks on the as-grown AlN surface. These are similar to those seen in AlN/GaN HEMT structures [173], and signify the top AlN layer has relieved its high tensile strain by cracking. These cracks lead to the sample being highly resistive, with 3 orders higher sheet resistance compared to sample A and B. It is also worth pointing out that even though sample B, with 30 nm GaN channel, did not show cracks on the as-grown surface, hexagonal cracks developed during the device fabrication process which were visible under optical microscope. This further provides the experimental evidence that a thin, < 15 nm GaN channel layer is needed in the AlN/GaN/AlN structure to grow a thick in-situ passivation AlN layer with desired structural properties.

2DEG Transport in in-situ passivated AlN/GaN/AlN Heterostructures

In addition to the structural properties, optimal 2DEG transport is necessary for the HEMT. The as-grown 2DEG sheet resistance determines the access resistances in the recessed-gate AlN HEMT shown in **figure 5.7 (c)**. A low sheet resistance is thus desired. It is found that, for a given AlN passivation layer

thickness, a thinner GaN layer results in higher sheet resistance due to both lower charge density and lower mobilities.

In an AlN/GaN/AlN structure, the 2DEG density n_s depends electrostatically both on the AlN barrier layer and the GaN channel layer. Specifically, for a given AlN barrier layer thickness in an AlN/GaN/AlN heterostructure, a thinner GaN layer results in a lower 2DEG density [46] (see figure 5.14). The measured room temperature 2DEG densities for samples A, B and C in this study are listed in **table 5.1**. Sample C was found to be too resistive with sheet resistance of $> 10^5$ Ω/sq., and therefore the 2DEG density mobility could not be reliably determined through Hall measurements. This due to the cracks in the AlN barrier layer, further emphasizing the need for strained GaN layers. The lower 2DEG density in sample A, with 15 nm GaN channel layer, compared to sample B, with 30 nm GaN channel layer, confirm the expected trend of lower n_s in thinner GaN channels for the same AlN thicknesses.

Simultaneously, a thinner GaN channel layer in the AlN/GaN/AlN structure has been found to result in a lower 2DEG room-temperature mobility μ_n. This experimental trend is supported independently both by data from controlled studies in our group as well as literature reports [290, 40, 41, 42, 45] of AlN/GaN/AlN heterostructure growths, as shown in figure 4.15. Interestingly, this trend is independent of the epitaxial growth method (eg. MOCVD vs MBE) and the starting substrates (Si, SiC, Sapphire, Bulk AlN). The probable causes are the dislocation densities, proximity to the bottom interface, higher confinement field in the well etc. The exact reason however is not clear at this moment, and is being actively investigated in the community. More discussion on the 2DEG mobilities in this structure is provided in section 4.4.1.

Thus, for thinner GaN channel layers, a combination of lower 2DEG densities n_s with the lower mobilities μ_n results in higher 2DEG sheet resistance through $R_{sheet} = 1/q_e\mu_n n_s$. Hence, even though the thinnest possible GaN channel layer is desired structurally, the thicker the channel the better for the 2DEG transport. As a trade-off, a 15 nm GaN channel layer thickness is chosen for fabricating and testing in-situ passivated HEMTs. According to the experimental evidence, this is the thickest GaN channel that allows growth of thick AlN passivation layer ($\epsilon_{xx}^{GaN} \sim 2\%$), while maintaining a "transistor-worthy" 2DEG sheet resistance for the device.

With the optimum heterostructure now determined, a quarter-of-4-inch wafer of in-situ passivated AlN/GaN/AlN HEMT structure was grown for fabricating devices. The sample, labelled D, had a 50 nm AlN passivation layer/15 nm GaN channel layer/500 nm AlN buffer layer on a 6H-SiC substrate. **Figure 5.11 (a)** shows the sheet resistance map of the as-grown wafer. The wafer shows presence of the 2DEG across the whole wafer surface and good uniformity with a sheet resistance of $\sim$ 450 Ω/sq. at room temperature.

To test the effect of the passivation layer on the transport of the 2DEG, temperature-dependent Hall effect measurements were performed on the AlN/GaN/AlN HEMT structure with and without the thick AlN passivation layer. A 10 mm $\times$ 10 mm piece diced from the quarter wafer D and a 4 nm AlN/30 nm GaN/500 nm AlN heterostructure sample were measured from 300 K down to 10 K. The 4 nm "thin-barrier" heterostructure is representative of the structure used in the current state-of-art RF AlN HEMTs [47] without in-situ passivation. The results of the temperature dependent Hall measurements are presented in **figure 5.11 (b), (c), (d)**.
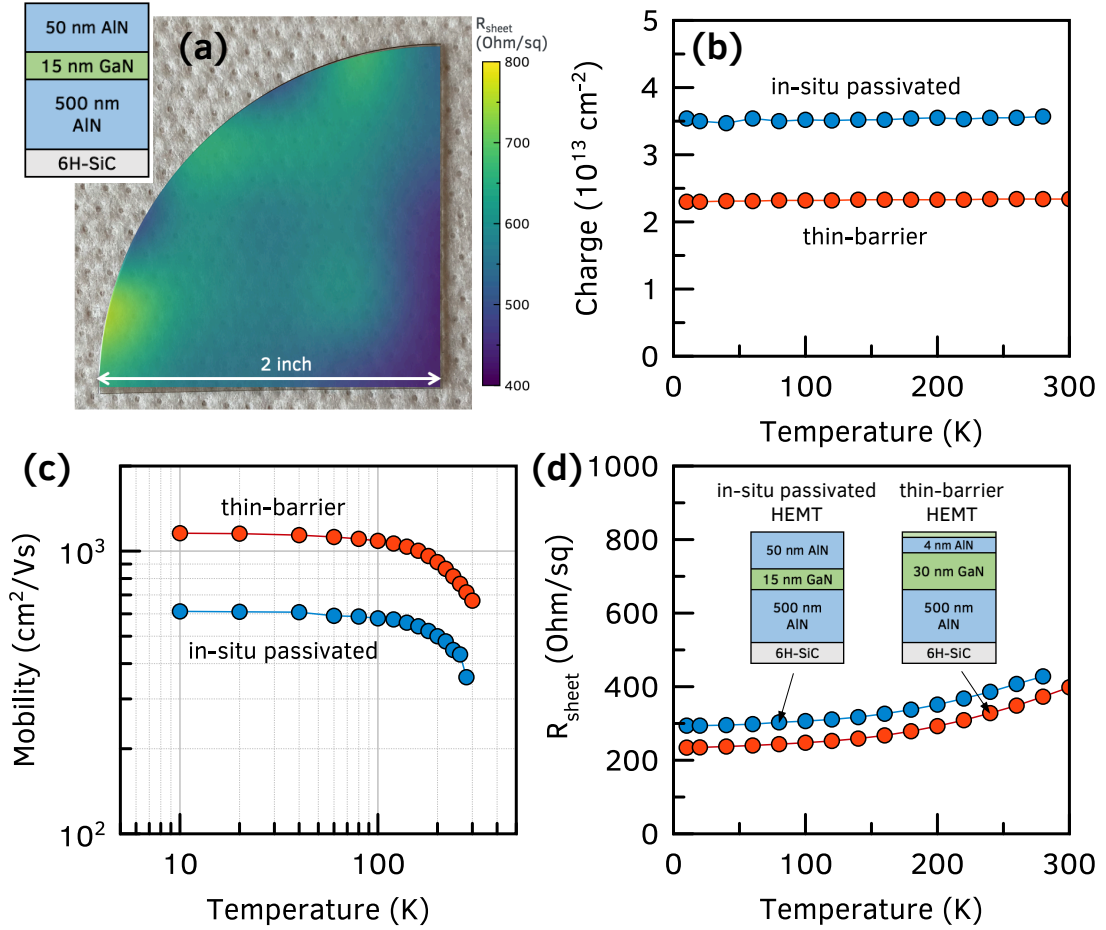
Figure 5.11: (a) Sheet resistance map of an in-situ passivated 50 nm AlN/15 nm GaN/500 nm AlN heterostructure, sample D, grown on a quarter-of-4 inch SiC wafer. The 2DEG is present across the whole wafer. (b), (c) and (d) present the results of temperature dependent Hall-effect measurements comparison between an in-situ passivated and a thin-barrier AlN/GaN/AlN structure. The in-situ passivated sample shows higher charge and lower mobility compared to the thin-barrier structure. However both show almost similar sheet resistance, confirming the suitability for transistor fabrication.

From the charge densities plot in **figure 5.11 (b)**, the in-situ passivated structure shows a higher 2DEG density of 3.5×10^{13} cm^{-2} compared to 2.2×10^{13} cm^{-2} for the thin-barrier structure, both of which agree to simulated densities. They do not freeze out on cooling, as expected from polarization-induced 2DEGs. **Figure 5.11 (c)** shows the temperature dependence of the 2DEG mobilities. The mobilities for the thin-barrier structure are $\sim$ 650 and 1100 cm^2/Vs at 300 K and 10 K. These values comparable to mobilities reported previously [40, 41, 42, 45, 46] in these AlN/GaN/AlN heterostructures. On the other hand, the 2DEG mobilities in the in-situ passivated AlN/GaN/AlN heterostructure are $\sim$ 350 and 600 cm^2/Vs at 300 K and 10 K. It is $\sim$ 2× lower than the thin barrier sample throughout the measured temperature range, albeit at a $\sim$ 1.5× higher charge density. This trend of lower 300 K mobility at higher densities is expected since optical phonon scattering, which is the dominant electron scattering mechanism at room temperature in III-nitride semiconductors, increases with 2DEG density [132]. However the exact cause of the lower mobility is under investigation, especially at low temperatures. The trade-off between charge density and mobility results in a comparable sheet resistance of $\sim$ 400 and $\sim$ 250 at 300 K and 10 K in both the structures, as shown in **figure 5.11 (d)**. Therefore, moving from a thin-barrier to in-situ AlN passivated structure is not expected to drastically affect the access resistances of the AlN/GaN/AlN HEMTs.

A thick 50 nm AlN passivation layer in the as-grown sample D heterostructure necessitates a recess etch in the HEMT channel region, i.e. the region right under the gate in **figure 5.7 (c)**. This is to ensure that the gate metal is placed close to the 2DEG channel to maintain high gate-channel capacitance and transconductance. In the thin-barrier devices without in-situ passivation, the gate metal is deposited directly on the as-grown heterostructure surface.

Hence it is also important to characterize the post-etch 2DEG transport since this will determine the HEMT channel performance.

To do so, in-situ passivated samples B (100 nm AlN/30 nm GaN/500 nm AlN) and a diced 10 mm × 10 mm piece from wafer D (50 nm AlN/15 nm GaN/500 nm AlN) were chosen for a blanket etch test. The top AlN layer in these AlN/GaN/AlN samples were etched away in short ~ 5 nm steps using a low-power BCl_3-based inductive-coupled plasma (ICP) dry etches. This simulates the etch which the 2DEG in the channel region sees during the recess etch process in the final HEMT fabrication. Hall effect measurements were performed after each successive etch to characterize the 2DEG. **Figure 5.12** shows the measured 2DEG density, mobilities and sheet resistance as a function of the remaining top AlN barrier layer thickness in the two samples. From **figure 5.12 (a)**, the measured 2DEG densities in both samples B and D agree with the densities expected from a self-consistent 1D Schrodinger-Poisson simulation of their respective layer structures. The 2DEG density slowly decreases as the AlN barrier gets thinner, completely disappearing at a critical thickness of ~ 3 nm. Correspondingly, the 2DEG mobilities, both at 300 K and 77 K, maintain their as grown value till an AlN thickness of ~ 20 nm and then start to decrease, as shown in **figure 5.12 (b), (c)**. As the AlN layer gets thinner, the sheet resistance, plotted in **figure 5.12 (d), (e)**, exhibits orders of magnitude jump from ~ 400 Ω/sq in the as-grown structures to ~ 1 MΩ/sq at a thickness of < 3 nm. A good electrostatic control over the 2DEG densities is thus demonstrated with the etch process, with important information of the 2DEG resistance as a function of recess depth thickness. These information are very valuable for the AlN HEMT device design and modelling. They provide the option to design both enhancement (E)-mode and depletion (D)-mode AlN HEMTs depending on the gate
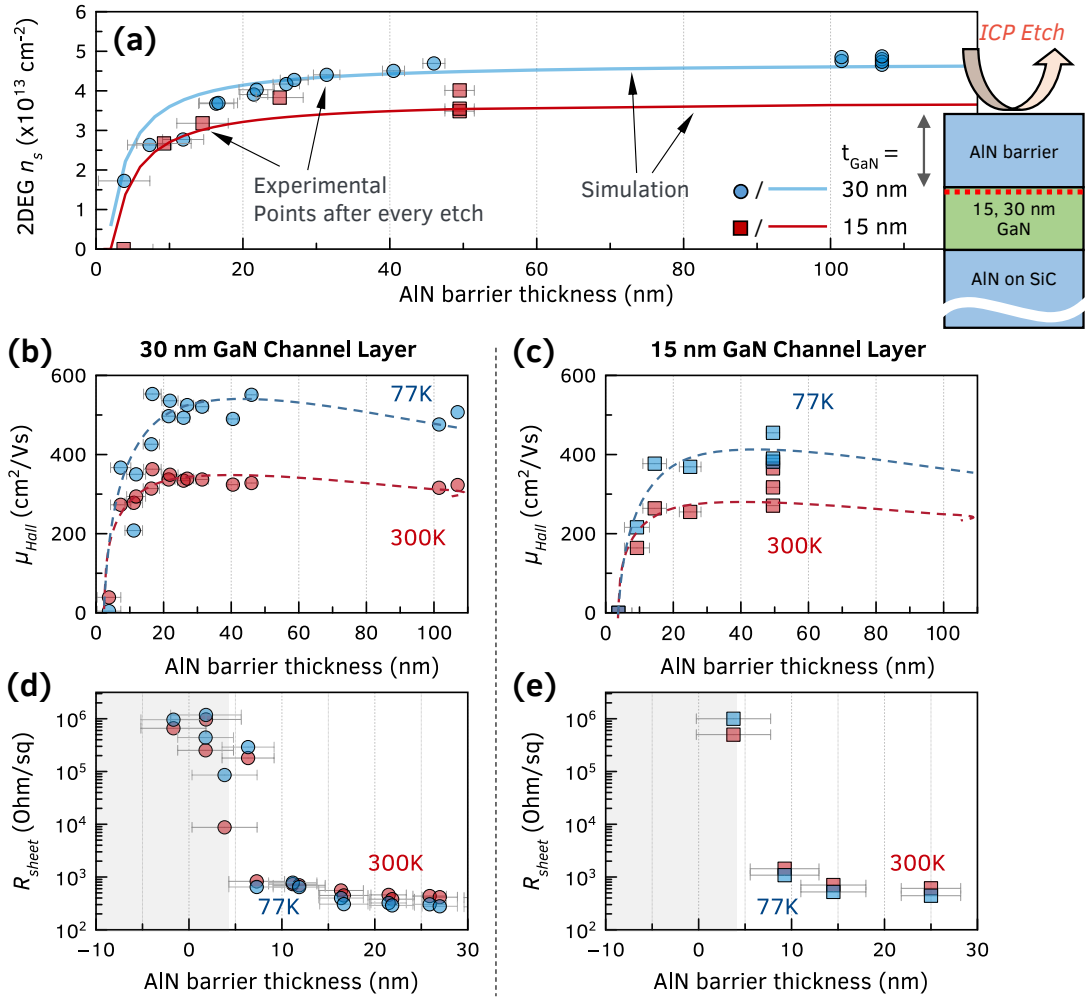
Figure 5.12: 2DEG transport in in-situ passivated AlN/GaN/AlN samples B and D as a function of remaining AlN barrier/passivation layer thickness to characterize the effect of the gate recess etch on the channel. Hall-effect measurements are performed after each step to remove the top passivation layer in short steps using low-power ICP dry blanket etches. (a) A good agreement to the measured and expected 2DEG charge density as a function of AlN thickness is observed, confirming good charge control of the channel. (b), (c) present the 2DEG mobility as a function of barrier thickness, which remain constant at large thicknesses but drop below remaining AlN barrier thickness of ~ 10 nm. (d), (e) show the sheet resistance remains ~400 Ω/sq as the remaining AlN barrier thickness decreases to ~ 3 nm, after which the sample becomes resistive.

recess depth. Furthermore, these results demonstrate that the low-power recess etch process is ready to be incorporated into the transistor fabrication process.

Reduced Dispersion in AlN/GaN/AlN HEMTs

To test the in-situ crystalline AlN passivation scheme, scaled recessed-gate RF HEMTs were fabricated on 10 mm × 10 mm diced pieces of the quarter wafer D. The in-situ passivated AlN/GaN/AlN HEMT process started with the MBE-regrown ohmic contacts. The as-grown heterostructure was patterned using a SiO_2/Chromium mask and dry etched using a inductively-coupled plasma (ICP) etch to expose the 2DEG sidewall. The sample was then reintroduced into the MBE chamber where a n++GaN with [Si] ∼ 1×10^{20} cm^{-2} was grown to form the ohmic contacts. Devices were isolated using a ion-implantation, followed by deposition of Ti/Au ohmic metal. A 2-step lithography was used to form the recessed T-gates. An SiO_2/Chromium/ZEP520 mask was deposited and patterned using electron beam lithography (EBL) to define the gate stem length. The AlN passivation/barrier layer was etched to the desired depth using the low-power ICP etch. A second PMGI SF9/ZEP520a mask was deposited and patterned using EBL, which defined the gate head dimensions. The Ni/Au metal was then deposited via e-beam evaporation and followed by lift-off to form the gates. A relatively shallow recess etch was used in these demonstration HEMTs. Resultant gate-to-channel distance is ∼ 15 nm. Also, instead of a T-gate, the gate head was placed directly on the AlN surface. The device geometry and dimensions are shown in the inset of **figure 5.13**.

The DC characteristics of the fabricated HEMTs devices are shown in **figure**

(a) $|I|$ (A/mm) vs V_{GS} (V)

V_{DS} = 5 V
L_G/L_{SD} = 230/700 nm

I_D

I_G

(b) I_D (A/mm) / g_m (S/mm) vs V_{GS} (V)

V_{DS} = 5 V
L_G/L_{SD} = 230/700 nm

L_{SD} = 700/1000 nm

Source Gate Drain

n++ GaN   50 nm AlN   n++ GaN

15 nm L_G = 230/70 nm

15 nm GaN

2DEG

(c) I_D (A/mm) vs V_{DS} (V)

L_G/L_{SD} = 230/700 nm
pulse 500 ns
V_{GS} = 4 V to -4 V, steps of -1 V

~2%

V_G, V_D=
-4, 8
-4, 0
0, 0
DC

(d) I_D (A/mm) vs V_{DS} (V)

L_G/L_{SD} = 70/1000 nm
pulse 500 ns
V_{GS} = 4 V to -4 V,
steps of -1 V

~6%

V_G, V_D=
-4, 8
-4, 0
0, 0
DC
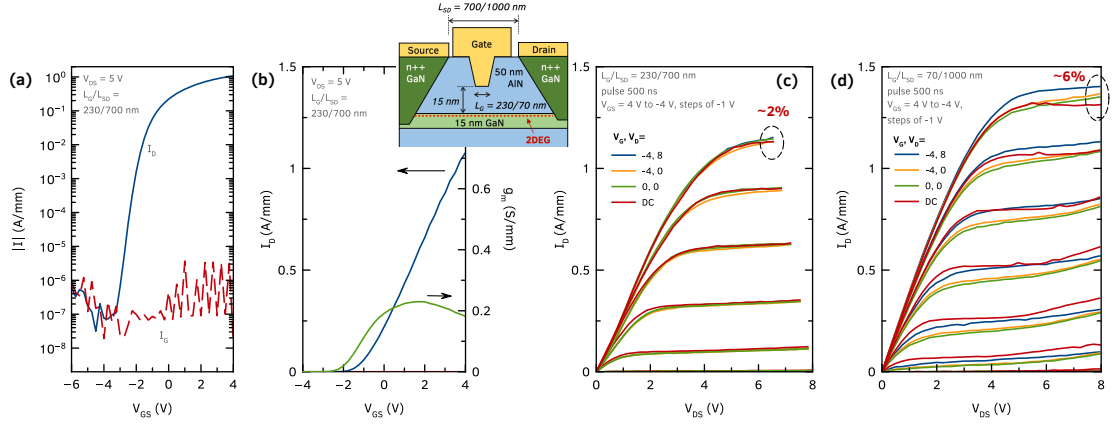
Figure 5.13: (a), (b) DC characteristics of a scaled, in-situ passivated AlN/GaN/AlN HEMT with a recessed gate length L_G = 230 nm and gate-channel distance of 15 nm. The device shows good transfer characteristics with on/off ratio of 7 orders and a maximum on-current of > 1 A/mm. (c), (d) Pulsed I_D-V_D measurement results from two representative in-situ passivated AlN/GaN/AlN HEMTs with different gate dimensions. The low DC-RF dispersion of ~ 2% and ~ 6% across multiple devices confirm the efficacy of this in-situ crystalline AlN passivation scheme compared to the ex-situ PECVD SiN (shown in in figure 5.7 (a)) for AlN/GaN/AlN HEMTs.

5.13 (a), (b). A maximum on-current of ~ 1 A/mm and high I_{on}/I_{off} ratio of ~ 7 orders is measured in the device with a gate length L_G = 230 nm. The impressive 7 orders I_{on}/I_{off} ratio is higher than the 2-4 orders typically observed in ex-situ SiN passivated AlN HEMTs [54]. The peak g_m is ~ 0.2 S/mm, which is understandably lower than ~ 0.8 S/mm measured in ex-situ passivated AlN HEMTs [54], due to a larger gate-channel distance and a lower 2DEG mobility in the 15 nm channel. This translates to relatively low cut-off frequencies of f_T/f_{MAX} = 51/75 GHz for a device with L_G = 180 nm. However, these results confirm that the new self-aligned recessed-gate HEMT process works and is suitable for device fabrication.

To characterize the DC-RF dispersion in the devices, pulsed I_D-V_D measurements were performed using 500 ns pulse width and 0.05% duty cycle. The

results from two in-situ passivated AlN HEMTs with gate lengths L_G = 230 nm and 70 nm are shown in **figure 5.13 (c) and (d)**. The HEMTs show an on-current dispersion of ~2% and ~6% and knee voltage walkout of < 0.2 V at quiescent gate/drain biases of -4/8 V. These are drastically lower than 20% measured in the state-of-art ex-situ SiN passivated AlN HEMTs [54], shown in **figure 5.7 (a)**, albeit at slightly different bias and current level. However, the low dispersion results across multiple devices serve as an experimental confirmation that the in-situ crystalline AlN passivation technique is indeed effective in reducing the RF dispersion in these AlN/GaN/AlN HEMTs. Interestingly, both the devices show signs of *negative* dispersion - with the DC I_D lower than the pulsed I_D under quiescent gate/drain bias of -4/8 V. This is beneficial to the large-signal performance of a HEMT and the reason for this behavior is currently under investigation. Future devices with scaled T-gates and deeper recess etches, conceptualized in **figure 5.7 (c)**, should show better small signal characteristics and translate the advantage of the lower DC-RF dispersion to the large signal performance.

In summary, this work presents in-situ crystalline AlN as a potential passivation technique for III-nitride RF HEMTs. The efficacy of this passivation scheme is demonstrated on AlN/GaN/AlN RF HEMTs. Through a theoretical model and a series of epitaxial growths, it is found that a < 15 nm GaN channel layer is necessary for growing 30+ nm thick AlN passivation layers in these heterostructures. Large area growths of the optimized in-situ passivated AlN/GaN/AlN HEMT structures are performed on quarter-of-4 inch SiC wafer. A sheet resistance of ~ 450 Ω/sq and 2DEG density of 3.5×10^{13} cm^{-2} is measured across the wafer at room temperature, which is suitable for HEMT fabrication. The 2DEG is also shown to survive the low-power ICP etch for forming the re-

cess gates. Pulsed I_D-V_D measurements on the fabricated scaled recess-gate RF HEMTs show a much reduced RF dispersion down to $\sim 2 - 6\%$, which is almost an order of magnitude lower compared to the dispersion in previously reported ex-situ SiN passivated AlN/GaN/AlN HEMTs.

Since the RF dispersion from the surface states limits the RF power outputs of the current state-of-art AlN/GaN/AlN HEMTs, it is expected that the new passivation scheme and the recess-gate HEMT fabrication process developed as part of this work should push the output powers even higher. The next generation of in-situ passivated AlN HEMTs with aggressive scaled T-gates should be able soon confirm this.

To the authors' best knowledge, this represents the first demonstration of in-situ passivation of HEMTs using thick *crystalline* AlN layers which also act as a barrier layer for the 2DEG. Previously, in-situ *amorphous* AlN has been used to demonstrate passivation of MBE-grown GaN HEMTs [299]. However, these layers require a low-temperature MBE growth condition at $> 200°$ C below the growth temperature of the rest of the heterostructure. The crystalline AlN passivation layer in this work are grown as part of the HEMT structure growth and does not need separate growth calibrations. Even though the metal-polar AlN/GaN/AlN HEMT is used as a demonstration in this work, this passivation technique is not limited to this structure and can be applied to other III-nitride heterostructures as well by appropriately controlling the strains in the layers. Since the findings of this work are not affected by the polarity, this passivation technique should also be beneficial to heterostructures grown on N-polar AlN such as N-polar GaN/AlN HEMTs.

5.6   Enhancement-mode AlN/GaN/AlN MOS-HEMTs with ultra-thin 3 nm GaN channels

Wide bandgap (WBG) enhancement-mode (E-mode) or normally-off n-channel and p-channel transistors are highly desirable for enabling energy-efficient high-voltage complementary (CMOS) circuits, both for logic and RF applications [137]. As presented in the previous chapters, best-in-class GaN/AlN p-channel FETs have recently been realized, thanks to the discovery high-conductivity undoped GaN/AlN 2DHGs [3]. The recessed gates in these pFETs offer the option of either E-mode or D-mode operation depending on the recess etch depth. The D-mode GaN/AlN pFETs have very recently demonstrated record high currents >0.5 A/mm in scaled devices with L_G ~ 80 nm and broken the GHz speed barrier with f_T/f_{MAX} = 23/40 GHz. On the E-mode side, 1.5 μm long p-channel GaN/AlN MIS-HFETs have shown [209] on-currents of 30 mA/mm. The current in the E-mode pFETs can be improved further by scaling the gate lengths, as done in the D-mode pFETs.

The availability of high-performance p-type FETs and the material advantages of the AlN buffer layer (higher thermal conductivity, wider bandgap) have propelled the AlN platform as leading contender for realizing wide bandgap RF complementary circuits [137]. On this AlN platform, D-mode AlN/GaN/AlN HEMTs have demonstrated high-power RF amplification with output powers of 3.3/2.2 W/mm at 10/94 GHz respectively [54, 218]. These normally-on devices have typical threshold voltages around −5 V. The missing component for realizing CMOS logic operation on the AlN platform is the E-mode, normally-off n-channel FET.

In this section, the first demonstration of enhancement-mode operation AlN/GaN/AlN metal-oxide-semiconductor (MOS) HEMTs is presented. Normally-off operation is achieved by lowering the GaN channel layer thickness down to 3 nm, as opposed to p-GaN gate, recess gating or ion implantation typically done in the normally-off GaN HEMTs. This approach ensures that the resulting devices are epitaxially compatible with previously demonstrated E-mode GaN/AlN pFETs. The as-grown structure is shown to contain a 2DHG which is depleted on application of positive gate bias, before the accumulation of a 2DEG - the III-nitride analog of silicon-on-insulator n-MOSFETs operation. Long channel self-aligned MOS-HEMTs with gate lengths L_G = 6, 12 μm are fabricated, which show on currents upto 100 mA/mm, very high on-off ratio of 9 orders of magnitude and good output characteristics. The devices obey $1/L_G$ scaling, making them really promising for future RF and CMOS-logic applications on the AlN platform.

Because of its wide bandgap and high conductivity 2DEGs, GaN HEMTs find applications in both high-frequency power amplifiers as well as high-power switches. Normally-off operation is especially desired in power electronics, since they enable safer operation and simpler gate driver circuitry. However, the inherent presence of the polarization-induced 2DEG in an as-grown Al(Ga)N/GaN HEMT structure makes specific processing steps necessary to achieve normally-off operation. This is done by modifying the energy band alignments underneath the gate - by either using gate recess [300], p-GaN gates [301] or by modifying the surface using ion implantation [302]. Additionally, few companies have realized normally-off operation by combining a normally-on, high-power GaN HEMT with a normally-off, low-voltage silicon MOSFET in a cascode configuration [303]. This provides a stable positive threshold and

avoids complicated HEMT fabrication, but introduces packaging challenges and switching speed limits due to parasitics.
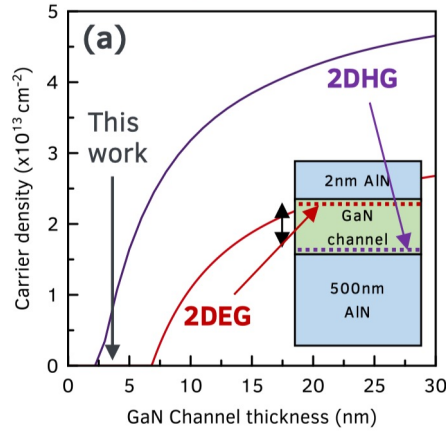
Figure 5.14: 1D-Poisson simulation showing the control of the as-grown 2DEG, 2DHG densities in the AlN/GaN/AlN heterostructure by adjusting the GaN channel thickness. A heterostructure with 2 nm AlN barrier/3 nm GaN channel layer is not expected to have any 2DEG in the as-grown structure.

The electrostatics of the AlN/GaN/AlN HEMTs on AlN platform offers an new way to achieve normally-off n-channel operation by scaling down the GaN channel layer thickness. The AlN/GaN/AlN double heterostructure has opposite signs of polarization induced fixed sheet charges at the two opposite heterointerfaces of the GaN quantum well channel. This gives rise to a 2D electron (2DEG) at one interface, and a 2D hole gas (2DHG) at the other interface in an as-grown heterostructure. The densities of the 2DEG and 2DHG depend on the AlN barrier layer and GaN channel layer thicknesses. **Figure 4.1** shows the calculated 2DEG and 2DHG densities in a metal-polar AlN/GaN/AlN heterostructure as a function of the AlN and GaN thickness. Consider a structure with the AlN barrier layer thickness fixed at 2 nm. **Figure 5.14** shows the variation of the 2D electron and hole gas densities in this structure with the GaN channel layer thickness. Clearly, there exists a critical GaN thickness of ~7 nm below which no 2DEG is expected in the as-grown heterostucture. Sim-

ilarly, the critical thickness for the existence of a 2DHG is around 2 nm. An AlN/GaN/AlN heterostructure with a GaN layer thickness between 2 and 7 nm is therefore expected to have a 2DHG but not a 2DEG in the as-grown structure.

An AlN/GaN/AlN heterostructure with a 2 nm AlN barrier and 3 nm GaN channel is studied in this work. **Figure 5.15 (a)** shows the energy band diagram of the heterostructure with and without an applied positive bias. A 2DHG is expected to be present when no bias is applied (as-grown). On applying a positive bias to the gate on the surface, the bands are pulled down, depleting the 2DHG. Once the applied bias is greater than a certain threshold voltage, the 2DHG is completely depleted and a 2DEG starts accumulating at the top GaN/AlN interface. According to the simulation, even though the as-grown structure has a 2DHG, this structure should show enhancement-mode operation of an n-channel FET upon suitable device fabrication. Interestingly, unlike the previous AlN/GaN/AlN heterostructures studied in this dissertation where a 2DEG and a 2DHG were present in parallel, this structure is expected to be able to switch between a 2DHG and a 2DEG by gate voltage - in an undoped heterostructure.

The undoped metal-polar 2 nm AlN/3 nm GaN channel layer/500 nm AlN buffer layer heterostructure was grown using plasma-assisted MBE on 6H-SiC substrates. The details have been provided in the appendix A. A hole density of 2.6×10^{13} cm^{-2} and mobility of 5.8 cm^2/Vs were obtained by room temperature Hall effect measurement on the as-grown sample. The sheet resistance of ~40 kΩ/sq is reasonable for a GaN 2DHG. Atomic force microscopy and photo-luminescence measurements were performed to confirm the quality of the growth, the results shown in **figure 5.15 (b)**. Under excitation by a 325 nm
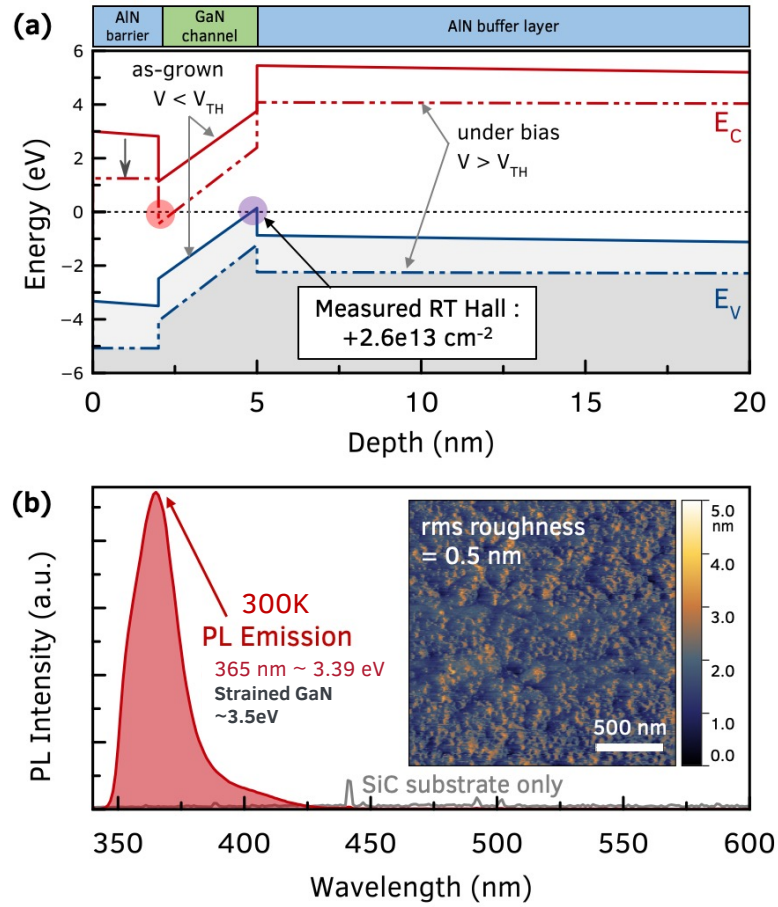
Figure 5.15: (a) Layer structure and band diagram of the sample used in this work, showing an expected 2DHG in as-grown structure and 2DEG induced by applying positive gate bias. (c) Photoluminescence and AFM scans (inset) of the MBE-grown heterostructure, confirming high-quality epitaxial growth and presence of a thin GaN quantum well.

He-Cd laser, a sharp photoluminescence peak was observed at 3.39 eV at room temperature, which is indicative of high quality crystal GaN layer. The slight red shift in the PL compared to a compressively strained GaN bandgap of 3.5 eV is believed to be due to the quantum confinement in the thin GaN well. A smooth surface top surface in the AFM scan with sub-nm rms roughness further confirms high quality epitaxial growths, and that the sample is ready to be fabricated into a transistor.
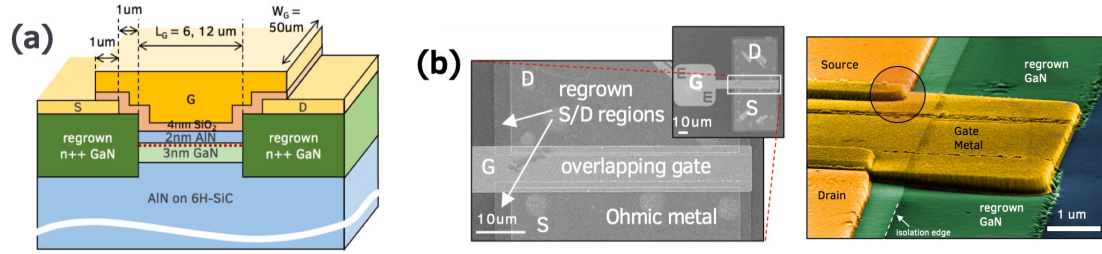
Figure 5.16: (a) Schematic cross-section of the long channel AlN MOS-HEMT with regrown source drain contacts and self-aligned, overlapping gates. (b) SEM images of the fabricated devices, showing the overlapping regions of the gate.

The schematic of the fabricated long-channel MOS-HEMTs with overlapping gates is shown in **figure 5.16 (a)**. The device geometry is similar to that of a Si n-MOSFET. First, the source and drain regions were formed by MBE-regrowth. Dry etch was performed to define the ohmic regions, and then reintroduced into the MBE chamber to grow n++ GaN with [Si]~ 10^{20} cm^{-3}. The devices were isolated using ion-implantation. A ~3.8 nm SiO$_2$ was deposited as the dielectric layer under the gate using atomic layer deposition (ALD). The channel/gate length L_G, defined as the distance between the edges of the regrown ohmic regions, was varied from 3 to 12 μm with a further 2 μm overlap with the source/drain regions. Top and angled view of scanning electron microscopy (SEM) scans of the final fabricated devices are shown in **figure 5.16 (b)**, with the gate overlapped regions clearly visible.

Capacitance-voltage measurements were performed to characterize the MOS-capacitors and determine whether a electron channel is indeed induced. The source and drain contacts were shorted to ground, and a 1 MHz AC voltage signal was applied at the gate around a bias voltage V_G sweep from -2 to 3 V. The resultant CV profiles obtained from two devices with L_G = 6 and 12 μm are shown in **figure 5.17 (a)**. A non-zero capacitance C_{OFF} is observed at V_G = -2
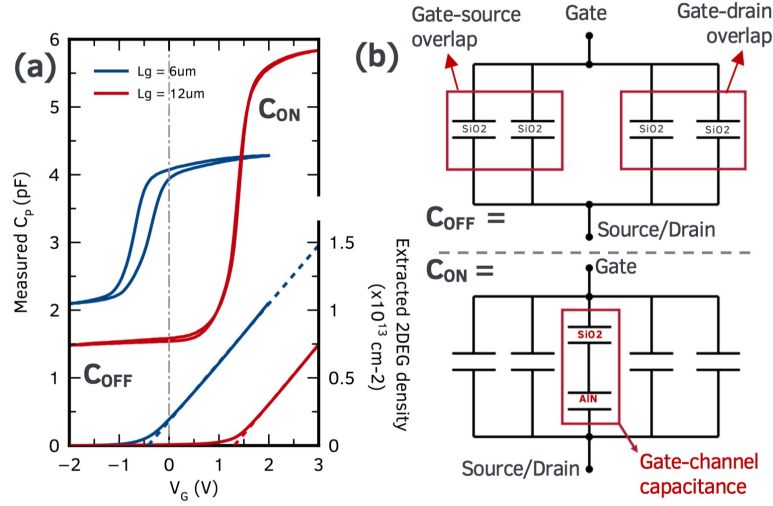
Figure 5.17: (a) CV curves of showing channel turn-on and extracted 2DEG densities in channel. (b) The equivalent CV model shows a large gate-S/D overlap capacitance dominating the $C_{OFF} > 0$.

V in both the devices. This is expected due to the overlap capacitances at the gate/source and gate/drain overlap regions, as shown in the equivalent capacitance network in **figure 5.17 (b)**. Note that no capacitance is expected from the channel region even though there is a 2DHG since the n++GaN regions do not connect to the valence bands. On sweeping to $V_G > 0$, a sharp increase in the measured capacitance C is observed in both the devices reaching a value of C_{ON}. This rise in the capacitance confirms the electron accumulation and formation of a 2DEG channel. $C_{ON} - C_{OFF}$ corresponds to the gate-channel capacitance C_{GS} which agrees with the theoretical value of 7.6×10^{-7} F/cm^2 for a gate and 2DEG seperated by 2 nm AlN barrier layer and 3.8 nm SiO$_2$ dielectric. The 2DEG density n_s in the channel as a function of voltage is then extracted using $q_e \, n_s = \int_{-2}^{3} dV(C(V) - C_{OFF})$, where q_e is the electron charge. The result is plotted in **figure 5.17 (a)**. Because of the high C_{GS}, a high 2DEG density of 0.7 - 1 $\times 10^{13}$ cm^{-2} is achieved at a moderate gate bias of 3 V. The difference in turn-on voltage in the two devices is believed to be an effect of interface traps at the SiO$_2$-AlN

interface. This is also evident in the hysteresis in the CV curve of the $L_G = 6\ \mu$m device. However the CV profile is conclusive evidence that an undoped sample which showed 2DHG conduction as grown, switches to 2DEG conduction upon application of gate bias, and represents the first such observation.
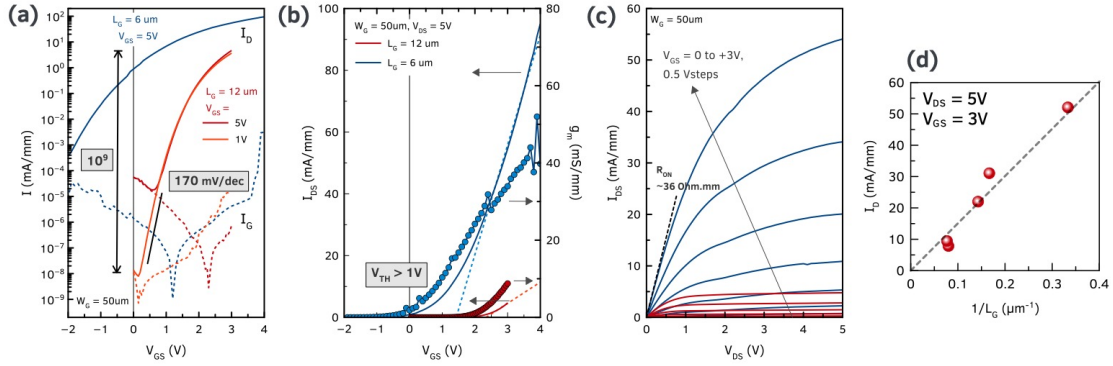
Figure 5.18: (a), (b) Transfer characteristics and (c) family curves of two representative MOS-HEMTs with L_G = 6 and 12 μm. The results confirm enhancement-mode operation with threshold voltage $V_{TH} > 0$, on-off ratios of up to 9 orders of magnitude and on currents upto 100 mA/mm. (d) For devices with similar V_{TH}, the on-currents exhibit $1/L_G$ gate length dependence.

With the formation of the channel established, the DC characteristics of the MOS-HEMTs were measured. The results for the L_G = 6 and 12 μm devices are plotted in **figure 5.18**. They exhibit on-off ratios as high as 10^9, which is the highest on-off ratio among reported in AlN/GaN/AlN HEMTs [47, 54]. A sub-threshold slope of ~170 mV/dec is measured. Importantly, both the devices showed enhancement-mode operation as desired and expected, with threshold voltages V_{TH} of +1 and +2 V. The family curves for these long channel devices show good transistor behavior with current saturation at drain voltages of ~ 5 V. The 6 μm long channel device exhibits on-currents upto 100 mA/mm. For devices with similar V_{TH}, the maximum on currents exhibit $1/L_G$ scaling, which means higher on-currents can potentially be accessed by further scaling down the gate lengths.
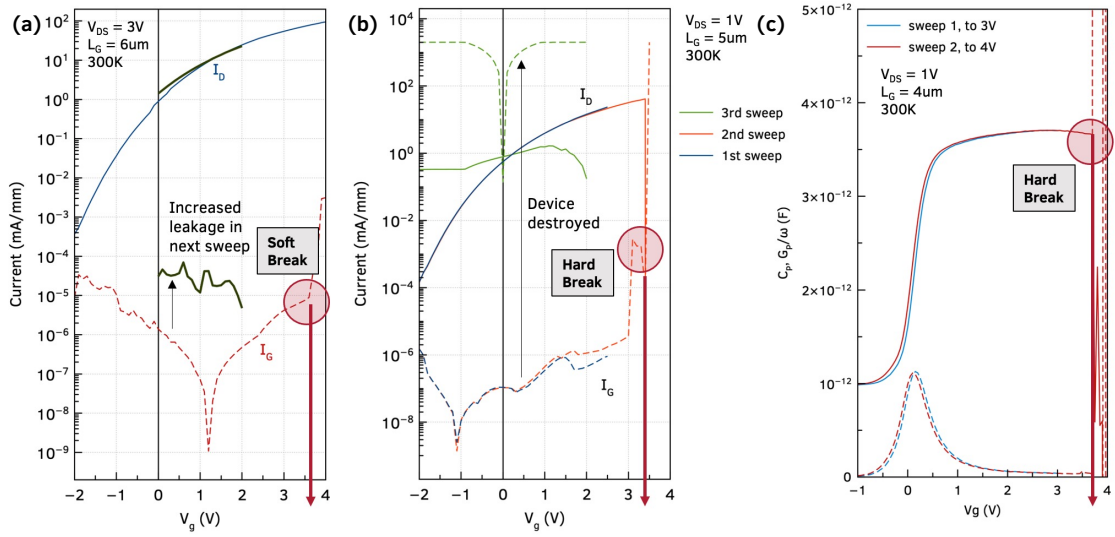
Figure 5.19: Observed breakdown when the gate voltage is swept to ~3.7 V in three devices with different L_G.

Even in the 6 μm device, the current is not completely saturated and is still rising at V_{GS} = 4 V, as visible from **figure 5.18 (a) and (b)**. Applying higher V_{GS} should push the on-currents higher. However, the gate-source overlap regions limit the gate bias accessible for device operation. **Figure 5.19** shows the output curves and CV profile of three devices with different gate lengths of 4, 5, 6 μm. All of them exhibit a breakdown at a V_{GS} ~ 3.7 V. This is attributed to the gate-source overlap capacitor which has a 3.8 nm SiO_2. 3.7 V corresponds to a field of 10 MV/nm in the SiO_2 layer, which is close to the expected critical field of silicon dioxide. This limits the range of gate biases accessible in these proof-of-principle devices to approximately ±3.7 V and prevents the on-currents from reaching its maximum saturation value. Future devices should be able to solve this limitation by decreasing the capacitance in the overlap regions.

The first demonstration of an enhancement-mode AlN/GaN/AlN MOS-HEMTs is thus achieved in 3 nm GaN "delta" quantum well channel heterostructures. **Figure 5.20** compares its output and transfer characteristics with
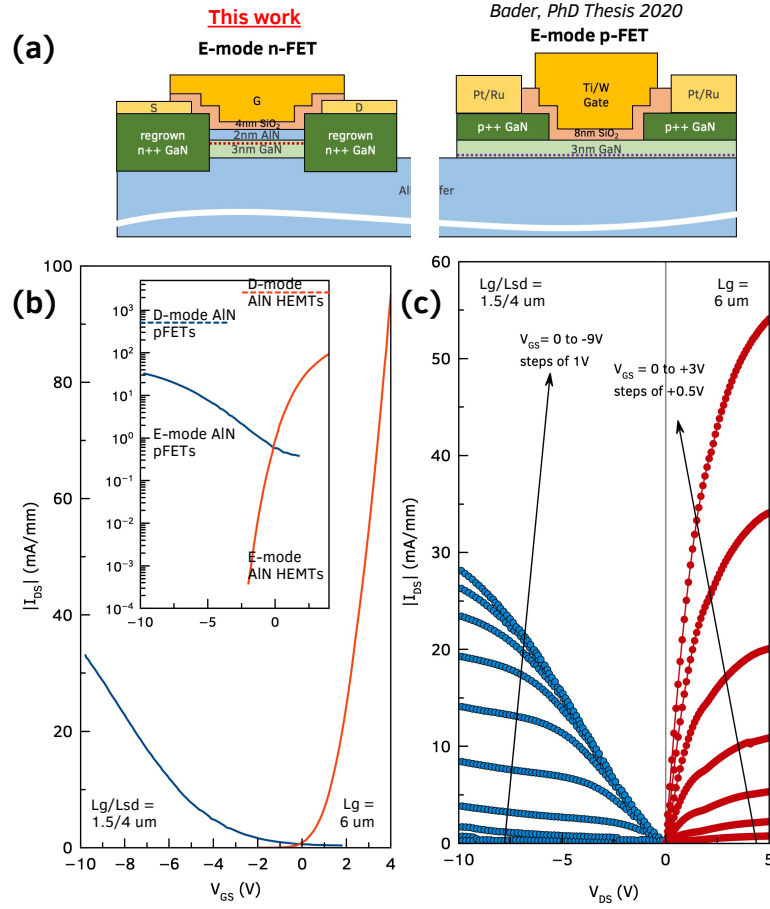
Figure 5.20: E-mode n-channel MOS-HFET results plotted with previously demonstrated E-mode GaN/AlN p-channel FET demonstrating the compatibility for complementary operation. The typical current levels for best D-mode FETs on this platform are marked for reference

a previously demonstrated long channel E-mode GaN/AlN pFET [209]. Note that both the n- and p-channel devices use a similar undoped 3 nm GaN channel, making them perfect candidates for integration. Both low voltage and RF complementary circuits are now possible via suitable device process flow (see section 6.3). Hence this work takes the AlN platform closer to realization of WBG CMOS. Previously unseen applied voltage-controlled switching between a polarization-induced 2DEG and a 2DHG presents a unique playground to create new devices. Ambipolar devices on GaN are now possible if p- and n- type

contact to the same channel are realized. A better SiO_2 deposition process to reduce the AlN-SiO_2 interface should lead to more consistent threshold voltages across devices in the future, especially with the lack of a gate recess step. Frequency dependent capacitance voltage measurements should help to quantitatively track the improvement in the interface trap densities with different SiO_2 deposition conditions. Channel length scaling, and reducing the capacitance in the gate-S/D overlap regions should allow these E-mode AlN MOS-HEMTs reach their true potential by maximizing the on-currents and breakdown voltage and consequently the power handling capabilities.

5.7   Future Directions

The AlN/GaN/AlN RF HEMTs, still in its early stage of development, has made great progress over the past 4 years to compete with GaN-HEMT based PAs. This shows the immense promise of the platform, and is expected to exceed the GaN HEMT PA performance especially at 100+ GHz. Towards that, future directions are listed below which should improve the performance of the current-state-of-art :

- **ScAlN as high-K dielectric and etch stop layer**

   To access higher powers and high breakdown voltages in of AlN HEMTs it is necessary to suppress the gate leakage current which limits the off-state. Gate to drain Fowler-Nordheim tunneling plays a critical role in determining the breakdown characteristics in lateral III-nitride FETs. To reduce this tunnelling, a high-K dielectric is desired for the scaled AlN HEMTs, similar to how high-K dielectric HFO was critical in Si CMOS

239

technology scaling [304]. A higher K allows a thicker dielectric layer under the gate without compromise of reduction the gate capacitance.

ScAlN has garnered interest thanks to its high piezoelectricity and ferro-electricity properties [305, 306, 307, 308]. Recent investigations into MBE epitaxial growth of ScAlN films have led to discovery of high dielectric constant of ~ 21 at Sc concentrations of 25%. This is almost 2.5× the di-electric constants of GaN, AlN. Since these are epitaxial films grown in the same MBE system as the HEMTs, this makes the ScAlN very attractive for integration into the in-situ AlN passivated AlN HEMT structure as a high-K dielectric and etch stop layer.
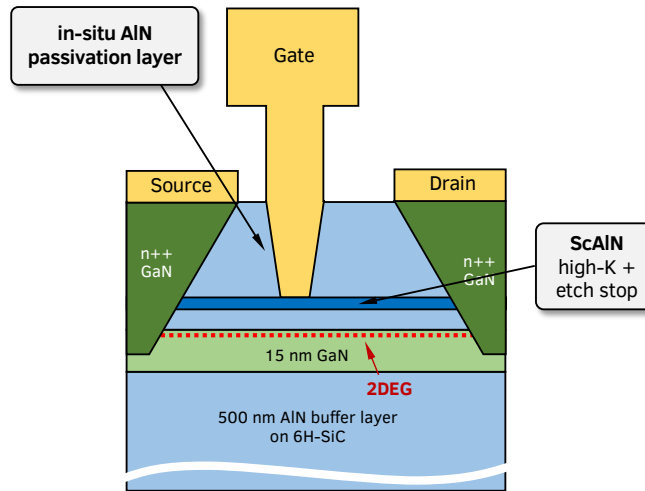
Figure 5.21: Cross-section of a in-situ AlN passivated HEMT with an ScAlN high-K dielectric with also acts as an etch stop layer for the gate recess.

The proposed device cross-section is shown in **figure 5.21**. Instead of a thick, 30+ nm AlN barrier layer, a ScAlN layer is incorporated 5-10 nm away from the 2DEG channel. Recent MBE-grown ScAlN/AlN/GaN HEMTs structures have shown 2DEG densities of 1×10^{13} cm^{-2} with RT mo-bilities of 1000 cm^2/Vs, so no adverse effect on the transport of the 2DEG channel is expected on the incoporation of the ScAlN layer. The thick AlN

layer on top of ScAlN then acts as the in-situ passivation layer.

The ScAlN layer provides an additional advantage of acting as a natural etch stop layer during the HEMT gate recess process, thanks to the 10:1 etch selectivity of ScAlN with respect to AlN [309]. This bypasses the reliance on a carefully timed dry etch process and ensures that the device characteristics are more repeatable. The gate metal is placed on the ScAlN layer, so the ScAlN layer then acts as the gate dielectric. This should reduce the gate leakage and hence increase the breakdown voltage of the HEMT, which when combined with the high on-currents of the HEMTs, should be able to operate at higher powers.

- **in-situ passivation using amorphous AlN**

  The output powers of the current generation of AlN HEMTs are believed to be limited by DC-RF dispersion from the surface states [54]. Section 5.5 presented a possible solution in the form of in-situ crystalline AlN passivation. This required modification to the HEMT fabrication process, including a critical timed etch step to define the gate recess depth. In the absence of a natural etch stop layer in the gate stack, the etch depth determined by the plasma calibration, chemistry and precise timing, all of which can potentially vary between runs and lead to inconsistent device characteristics.

  One of the alternative to circumvent this limitation is to use an in-situ *amorphous* AlN instead of crystalline AlN as a passivation layer. MBE-grown amorphous passivation layers have previously been demonstrated [299] using low temperature growth regimes, and were found to be effective in reducing the DC-RF dispersion from the surface states in GaN HEMTs. The lower growth temperatures for the amorphous AlN (T_{sub} <

250°C) can be incorporated into the HEMT MBE growth recipe by cooling the sample after growth.

An AlN HEMT with this passivation scheme will have a ~ 4 nm of crystalline AlN barrier layer, followed by an amorphous AlN passivatiob layer. Since the etch rates of amorphous AlN and crystalline AlN are expected to be different, recess etch should be more controllable than the in-situ crystalline AlN passivation. Furthermore, a thinner crystalline AlN barrier layer should maintain the 2DEG mobility at > 650 cm^2/Vs, as opposed to ~ 350 cm^2/Vs measured in post-recess etched crystalline AlN passivated HEMT at similar charge densities of $2 - 3 \times 10^{13}$ cm^{-2}.

- **AlGaN channel AlN HEMTs for higher breakdown**

  AlGaN channel HEMTs on GaN have been used for pushing the breakdown voltages higher for power switching applications [310]. The incorporation of AlGaN channels on AlN HEMT should also lead to a boost in the breakdown voltage of these devices thanks to the wider bandgap channel. For the same reason, the AlN/AlGaN/AlN heterostructure should also be suitable for Schottky barrier diodes (SBDs).

  However the channel 2DEG mobility is expected to be lower because of the alloy disorder scattering in the AlGaN channel. Initial series of MBE growths of 15 nm AlN/24 nm AlGaN/AlN HEMTs on SiC substrates [311] have demonstrated good charge control via AlGaN composition tuning, with densities varying from 3×10^{13} cm^{-2} in 10% AlGaN channel to ~ 1.5×10^{13} cm^{-2} in 58% AlGaN. It was also observed that the room temperature mobilities of > 25% AlGaN channel HEMTs are limited by alloy disorder scatting to below 50 cm^2/Vs. However, a 10% AlGaN channel showed a decent phonon-limited 300 K mobility of 250 cm^2/Vs, promis-

ing for transistor operation.

- **Backgate for AlN HEMT using 2DHG**

  The presence of the 2DHG under the 2DEG in an AlN/GaN/AlN het-
  erostructure presents an opportunity of applying a backgate bias, similar
  to body biasing in silicon-on-insulator (SOI) devices [312]. **Figure 5.22
  (a)** shows the configuration for using the 2DHG as a backgate for AlN
  HEMTs. A backgate bias in this configuration will provide electrostatic
  control over the top-gate threshold voltage (V_{TH}) of the AlN HEMT. This
  can be used to compensate for the V_{TH} variation from processing or to
  switch between E-mode and D-mode operation in the same device [313].
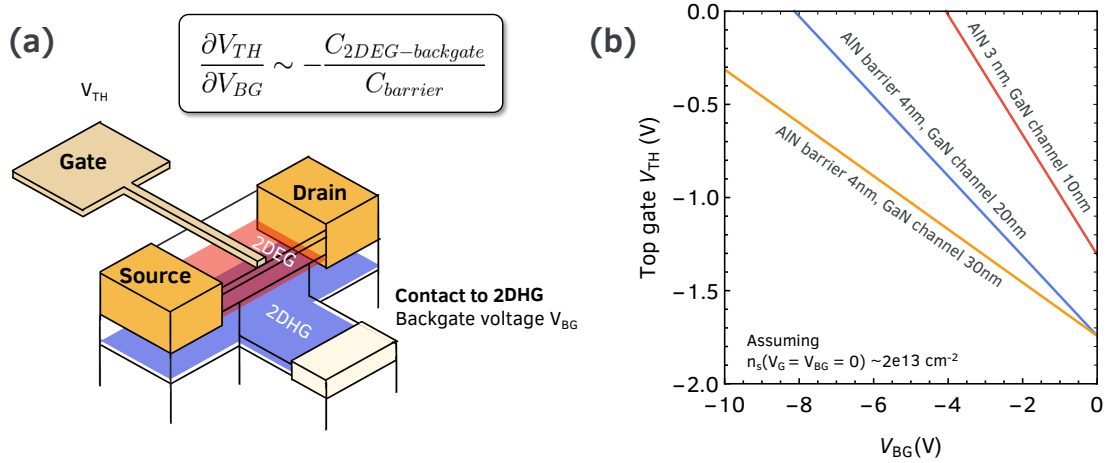
Figure 5.22: Body-biasing in AlN HEMTs using the 2DHG as a backgate. (a) shows a schematic of such a realizion, which will require a contact to the 2DHG at the back. (b) Expected dependence of the AlN HEMT threshold voltage on the applied backbias on the 2DHG, for different AlN barrier layer and GaN channel layer thicknesses.

Assuming the individual access to the 2DHG through a suitable ohmic contact that does not connect to the 2DEG, the 2DHG can be considered as a buried metallic layer, which can be connected to an external bias. In this configuration, the 2DEG channel is electrostatically coupled to both

the top gate and the bottom (2DHG) gate, represented by parallel plate capacitances C_{barr} and $C_{2DEG-backgate}$ respectively. The relative variation in the HEMT threshold voltage with respect to the applied backgate voltage V_{BG} applied to the 2DHG is given by $\partial V_{th}/\partial V_{BG} \propto -C_{2DEG-backgate}/C_{barr}$, which is in turn determined by the gate-2DEG distance and the 2DEG-2DHG separation. **Figure 5.22 (b)** shows the predicted variation of the threshold voltage for an AlN/GaN/AlN HEMT with different AlN barrier and GaN channel thicknesses. Experimental demonstration will require development of individual ohmic contacts to the 2DEG and 2DHG first.

CHAPTER 6

INTEGRATED RF ELECTRONICS ON THE ALN PLATFORM

6.1 Introduction

This dissertation has so far used the physical understanding of the 2D carriers on AlN material to demonstrate actives device in the form of RF transistors of both flavors - the AlN/GaN/AlN HEMT [218] and GaN/AlN pFET [39]. This presents the opportunity of integrating these two record-performance devices monolithically [137] towards achieving complementary circuits which operate at speeds faster than the previous demonstrations of complementary operation in GaN [13, 62, 61, 58, 60]. In fact, the mechanical properties of AlN platform enable this integration to go beyond just the active devices and include *all* of the RF front end elements such as power amplifiers (PAs), low noise amplifiers (LNAs), RF filters, RF antennas and waveguides to carry the RF signals between them.

Figure 6.1 compares the conductivities of the 2DEGs and 2DHGs presented in this work against similar 2D hole and electron channels in other semiconductor platforms. Ideally, a high-conductivity channel (low R_{ON}) and wide energy bandgap E_g (high operating voltage) are desired for high-power applications such as PAs. On the n-side, InP HEMTs with InGaAs channels offer the highest conductivities thanks to very high electron mobilities. However the narrow channel bandgap of < 1 eV makes them unsuitable for high power applications. Focusing on the wide bandgap materials (E_g > 3 eV), the AlN/GaN 2DEGs [173] exhibit the highest conductivities at a channel bandgap of 3.4 eV. The AlN/GaN/AlN 2DEGs studied in this work have slightly lower conductiv-
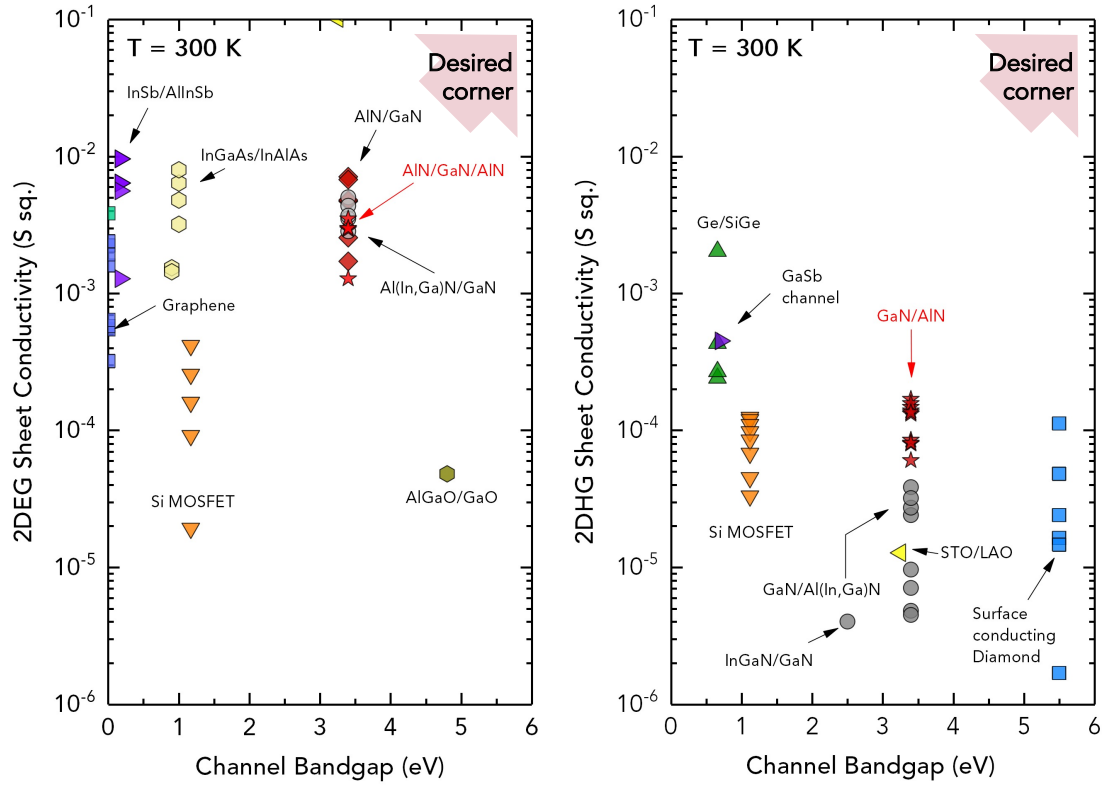
Figure 6.1: Benchmark comparing the hole and electron channel conductivities across semiconductor material systems as a function of the energy bandgap which, under suitable device design, determines ability of the device to withstand high voltages. The AlN platform offers some of the highest conductivities in a wide bandgap semiconductor.

ities than the best AlN/GaN 2DEGs, however they are more than suitable for making competitive high-power RF HEMTs.

On the p-side, the GaN/AlN 2DHG clearly has the highest reported conductivity reported among the 2D carriers in widebandgap semiconductors. Again narrow gap materials such as strained Ge [26] win purely in terms of hole mobilities due to their lower hole effective mass but cannot sustain high electric fields. A wide bandgap is simultaneously necessary to modulate the high charge densities in the channel. Clearly, the 2DEGs and 2DHGs on the AlN platform offer the highest conductivity channels for wide bandgap semiconductors. Therefore,

purely from the fundamental material limits perspective, circuits integrating these 2DEGs and 2DHGs should be highly suitable for high-power applications. For example, energy-efficient complementary logic circuits for high-power applications such as power converters and switches [102].
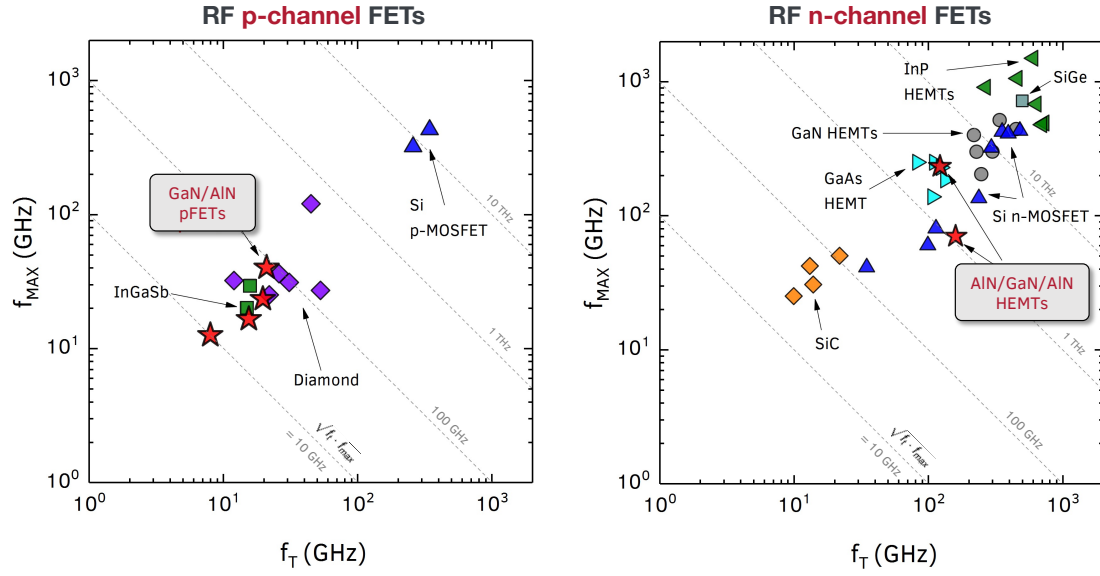
Figure 6.2: Benchmark comparing the speeds of p-channel and n-channel FETs across all semiconductor systems. The AlN platform devices, GaN/AlN pFET and AlN/GaN/AlN HEMT, are the only wide bandgap devices on both charts - a truly exclusive advantage!

A further advantage in high-speed operation emerges on comparing the AlN-platform FETs to transistors based on other semiconductor materials. **Figure 6.2** plots the voltage gain and power gain cut-off frequencies f_T and f_{MAX} of n-channel and p-channel RF transistors reported in literature. The mature Si p-MOSFET technology have achieved highest speeds of ~400 GHz [314, 315], as seen in **figure 6.2 (a)**. Among wide bandgap semiconductors, the highest speeds of operation have been demonstrated by pFETs on diamond with f_T/f_{MAX} of around 50/120 GHz [316]. However, in these devices the critical electric field is not determined by the diamond bandgap since the 2D hole channel is formed on the surface and not in the bulk [317], which somewhat negates the advan-

tage of a wide bandgap platform. Interestingly, the GaN/AlN pFETs presented in chapter 3 represent the *only* III-nitride semiconductor FETs on this chart exhibiting best f_T / f_{MAX} ~ 40 GHz.

Among the n-channel RF FETs, again the highest speeds of operation is achieved by the narrow bandgap SiGe and InP HEMTs [318, 319], thanks to their high room temperature electron mobilities. InP HEMTs [320, 321, 322] have in fact demonstrated the first amplification at terahertz speeds using a solid state device, while the state-of-art Si n-MOSFETs technology today exceed 400 GHz [314]. Among widebandgaps, the conventional GaN HEMTs show speeds comparable to Si MOSFETs at 400 GHz [323, 324, 325], owing to heavy investment and technological development spanning the last two decades. In comparison, the relatively "new kid on the block" AlN/GaN/AlN HEMT on the AlN-platform shows speeds upto 250 GHz [47]. Although this is not as high as the state-of-art GaN HEMTs, the numbers are improving and is already high enough to show large-signal amplification at frequencies upto 94 GHz [218].

From the benchmark charts in **figure 6.2**, it is seen that diamond and SiC provide high-power RF amplification capability in p-channel and n-channel respectively. However, the AlN-platform FETs are the only wide bandgap platform to provide *both* n-channel and p-channel FETs capable of operating at GHz speeds.

Thus, the AlN-platform FETs are not only attractive for complementary logic, but also for *complementary RF circuits*. This opportunity for integration of RF electronics is unique to the AlN-platform and is the reason why AlN is the leading candidate for future of RF electronics.

Additionally, this integration opportunity in theory exists beyond the active devices, to passive RF devices such as filters, SiC waveguides and antennas [53]. Since 2020, efforts in the Jena-Xing Group into realizing these AlN-based passive components have yielded world record RF passives such as epitaxial AlN bulk acoustic waveguide (BAWs) operating at 10 GHz [56] and SiC-based substrate integrated waveguides (SIWs) [57] operating at D-band. These passive devices utilize the same MBE-grown epitaxial AlN films on 6H-SiC which are used to make the AlN FETs, thereby providing evidence of the feasibility of all-AlN monolithic RF front end. Such monolithic integration, which will drastically reduce circuit size, increase speed of operations (through reduced parasitics) and reduce costs, is impossible in the current state-of-art since RF components LNAs, PAs, filters are all made of different materials integrated on the package level. This vision of the all-AlN monolithic integrated RF front end is presented in **figure 6.3**.

With all the individual components of this vision now experimentally demonstrated and available, this chapter presents the next steps in integrating RF active and passive components on the AlN platform. First, the recent work in the field in integrating GaN nFETs and pFETs for CMOS logic is presented in order to calibrate the reader to the challenges of such integration and what the AlN platform is up against. Using the learnings from GaN CMOS, few novel epitaxial and process design concepts are proposed for monolithic integration of the AlN-based complementary FETs. One common feature across the designs is the need for selective area etch and regrowth. An ex-situ etch introduces contaminants in the crystal from the ambient which are especially harmful for p-type devices. To overcome this challenge, in-situ thermal etch of GaN is demonstrated in the next section, and is believed to be a significant
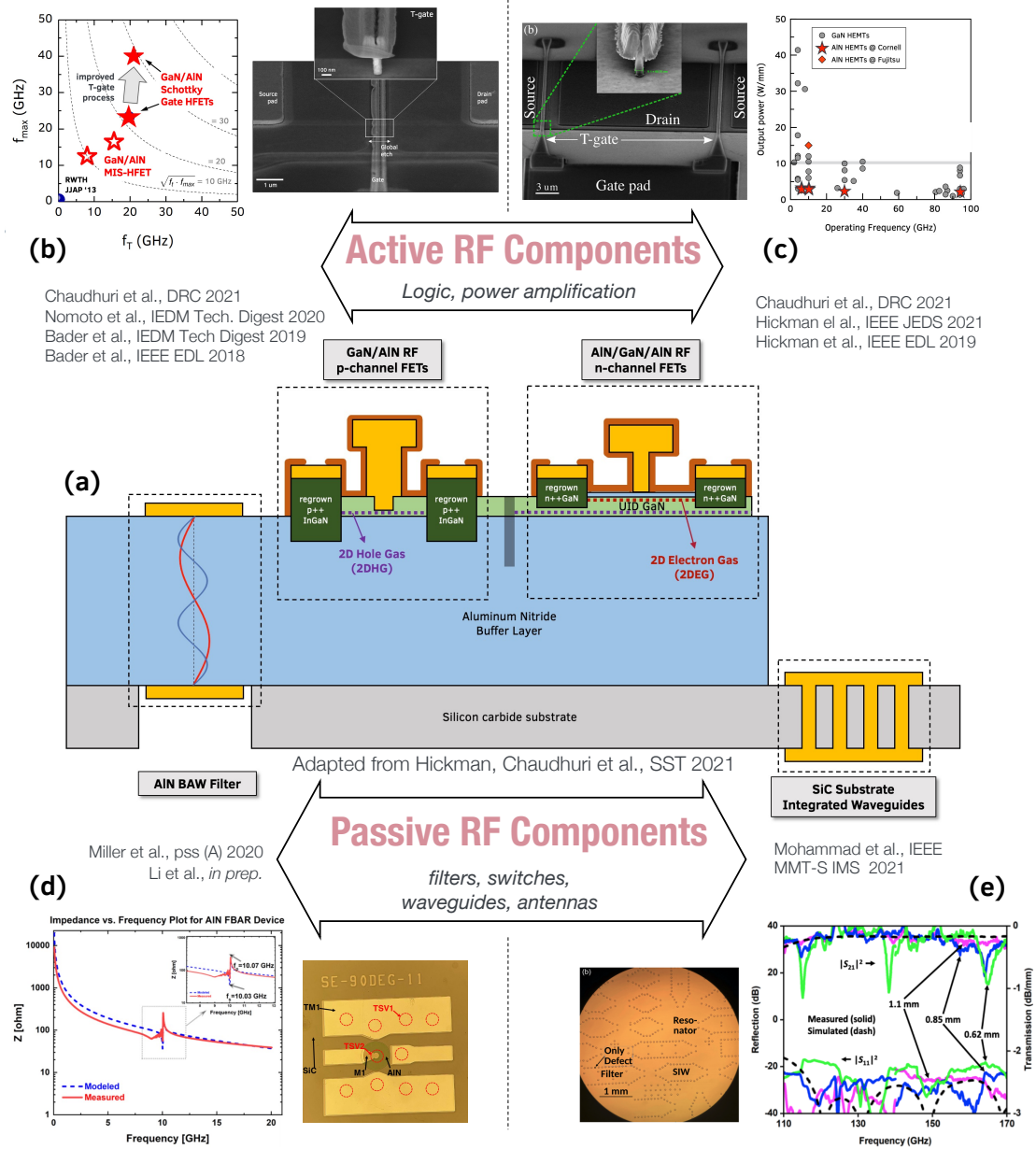
Figure 6.3: The envisioned AlN platform, with integrated active devices (n- and p-channel RF transistors) and passive devices (bulk acoustic waveguide (BAW) filters and substrate integrated waveguides (SIW) all monolithically compatible to enable integrated RF electronics for next-generation of communication systems. *Figures modified from Hickman et al. [53], Zhao et al. [56] and Asadi et al. [57].*

processing step in realizing the monolithic complementary operation on AlN.

Summaries of the recent results of the passive RF components on AlN platform

is provided, which will be critical to bring out the true potential of the AlN RF electronics platform.

6.2   Survey of GaN-based CMOS-logic Realizations

With the focus of this chapter on monolithic integration of discrete electronic devices in III-nitride semiconductors, it is helpful to take a brief look at the other similar efforts in the field to understand the technical challenges expected. The last 5 years have seen a number of demonstrations of GaN-based complementary circuits [102] driven by the research in GaN pFETs [32, 16, 60, 17]. These efforts aim to achieve CMOS-like logic [59] to enable integrated gate driver circuitry for energy efficient GaN high-power switches [102]. Prospects of GaN CMOS and comparison with other wide bandgap platforms are detailed in Bader et al. [137].

With the GaN HEMT well established in the commercial space since over 2 decades, the performance of the GaN pFETs is what limits the GaN CMOS realizations. The material properties lead to low-conductivity p-type channels and high-resistance VB contacts compared to the n-type analog GaN HEMTs. Several groups have demonstrated GaN pFETs using different techniques [187, 126, 32, 16, 60, 17] to overcome these limitations (discussed in detail in Chapter 3). Among these, few groups from RWTH Achen [62], HRL [13], AIST [61], MIT [60] and HKUST [58, 59] have gone on to monolithically integrate their pFETs with epitaxially-compatible GaN HEMTs and have demonstrated simple complementary logic operation on GaN.

In addition to the fundamental scientific challenges posed by GaN pFETs,

the integration process serves up additional technological challenges. First is the low on-currents of GaN pFET (typically in ~10-100 mA/mm) compared to GaN HEMTs (typically ~1 Am/m). Hence different pFET and HEMT gate widths, W_p and W_p respectively, are necessary to compensate for this mismatch. Typical value of W_n/W_p used is 1/10 [61, 58, 60].

Secondly, co-fabrication of devices places constraints since certain processes such as regrowth etch in one region can potentially damage the other. To get around this, careful design of the epitaxial stack and process flow is necessary. **Figure 6.4** illustrates the strategies adopted so far for realizing monolithic complementary GaN circuits. All the schemes are based on metal-polar HEMT heterostructures on GaN buffer layers grown on Si/SiC/Sapphire substrates. The Al(In)GaN/GaN interface provides the polarization-induced 2DEG channel for the HEMT. For complementary logic circuit application, normally-off or E-mode operation necessary to reduce steady-state losses. This is achieved by either using a p-GaN gate [60, 58] and/or a gate recess etch [61, 13, 62].

For inducing a p-channel in the GaN HEMT structure, a GaN layer is needed on top of the Al(In)GaN barrier layer to induce a 2DHG using polarization. Furthermore, Mg-doped p-GaN contact layers are necessary for making an ohmic contact to the 2DHG. This results in a parallel 2DHG on top of the 2DEG which needs to be selectively "adjusted" during the pFET-HEMT integration. Strategies include growth of the n-type HEMT stack, followed by selective etch to remove the 2DEG and regrowth of the p-type stack from GaN buffer up [13]. Or alternatively, growth of the full n- and p-type epitaxial stack and selective removal of the 2DHG top layers to leave just the 2DEG for the HEMTs [60, 58, 61]. In the latter scheme, couple of groups have smartly made use of the p-GaN
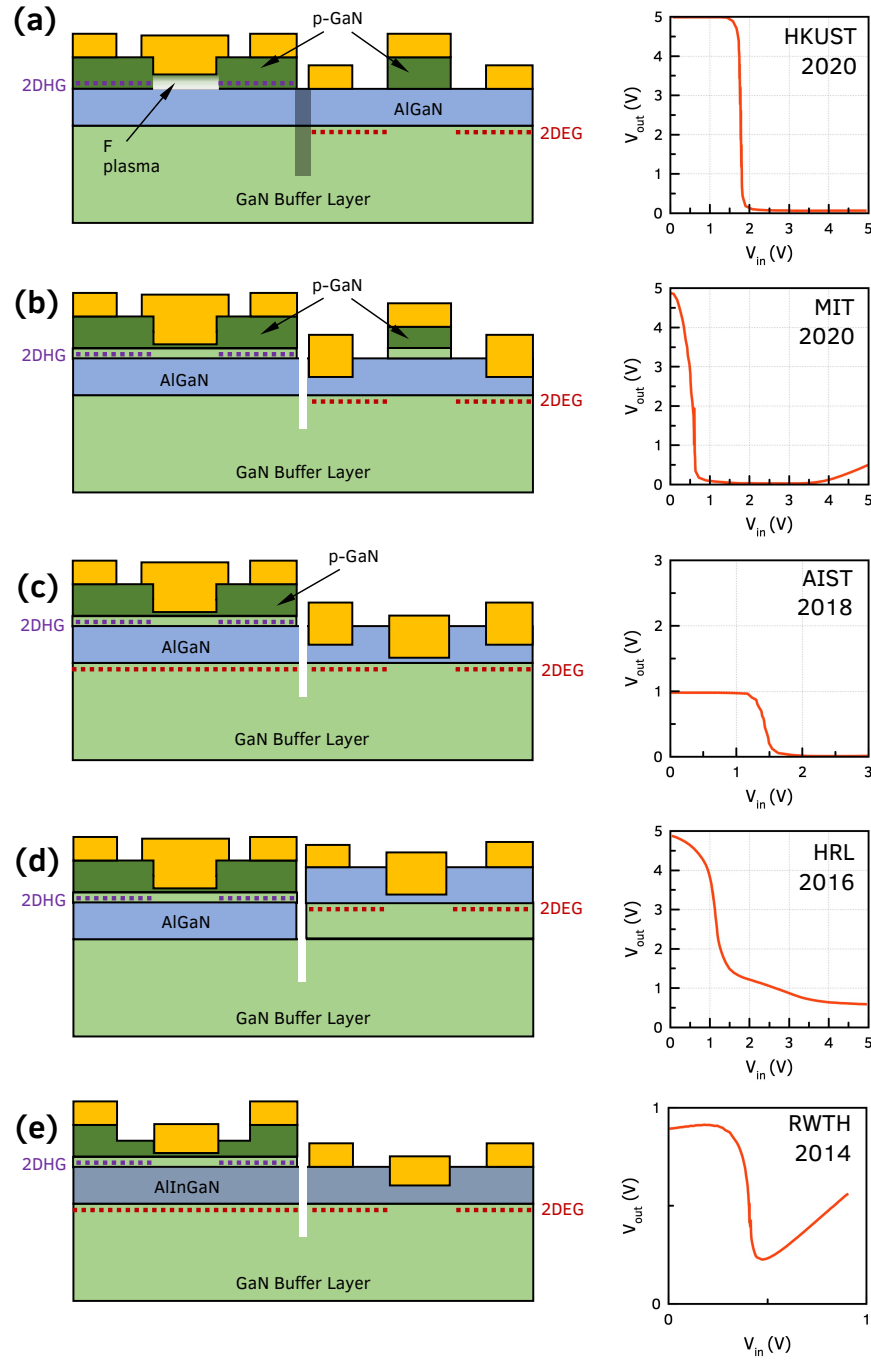
Figure 6.4: Schematics of GaN CMOS-logic realizations by groups from (a) HKUST [58, 59] (b) MIT [60], (c) AIST [61], (d) HRL [13] and (e) RWTH Achen [62], with their coressponding logic inverter characteristics for comparison.

ohmic contact layer in the epitaxial stack to enable E-mode operation in HEMTs [60, 58]. This regrowth-free technique has shown real promise with inverter

253

rail-to-rail operation at V_{DD} of 5 V, as seen in the I-V characteristics of figure 6.4 (a). A full variety of logic gates such as NOT, NAND, NOR [59] have also been recently demonstrated on GaN.

The GaN platform has the advantage of an already mature HEMT technology in terms of epitaxial growth and fabrication processes. The GaN CMOS-integration effort builds on this knowledge. On the other hand, AlN-based electronics is a much newer technology where *both* the n- and p-channel FETs are relatively new. Still rapid progress has been seen over the past 4 years, with individual devices already performing at par with, and sometimes better than, their GaN counterparts. Integrating these individual components will hopefully result in the sum being greater than its parts, and will very soon exceed performance of the GaN complementary circuits, especially in the RF domain.

6.3 AlN-based CMOS Realizations

This section provides selected ideas of epitaxial and fabrication process flow towards monolithically integrating AlN-based n- and p-channel FETs, in the hope that it will guide the future efforts to realize them. This list does not claim to be exhaustive, but rather represent those ideas which are most feasible given the current state-of-art and the author's learnings over the past 4 years.

Based on the devices discussed in the previous chapters and the AlN-platform concept in **figure 6.3**, the most natural and logical monolithic realization of the AlN-based CMOS is shown in **figure 6.5**.

In this realization, first an undoped AlN/GaN/AlN epitaxial structure is
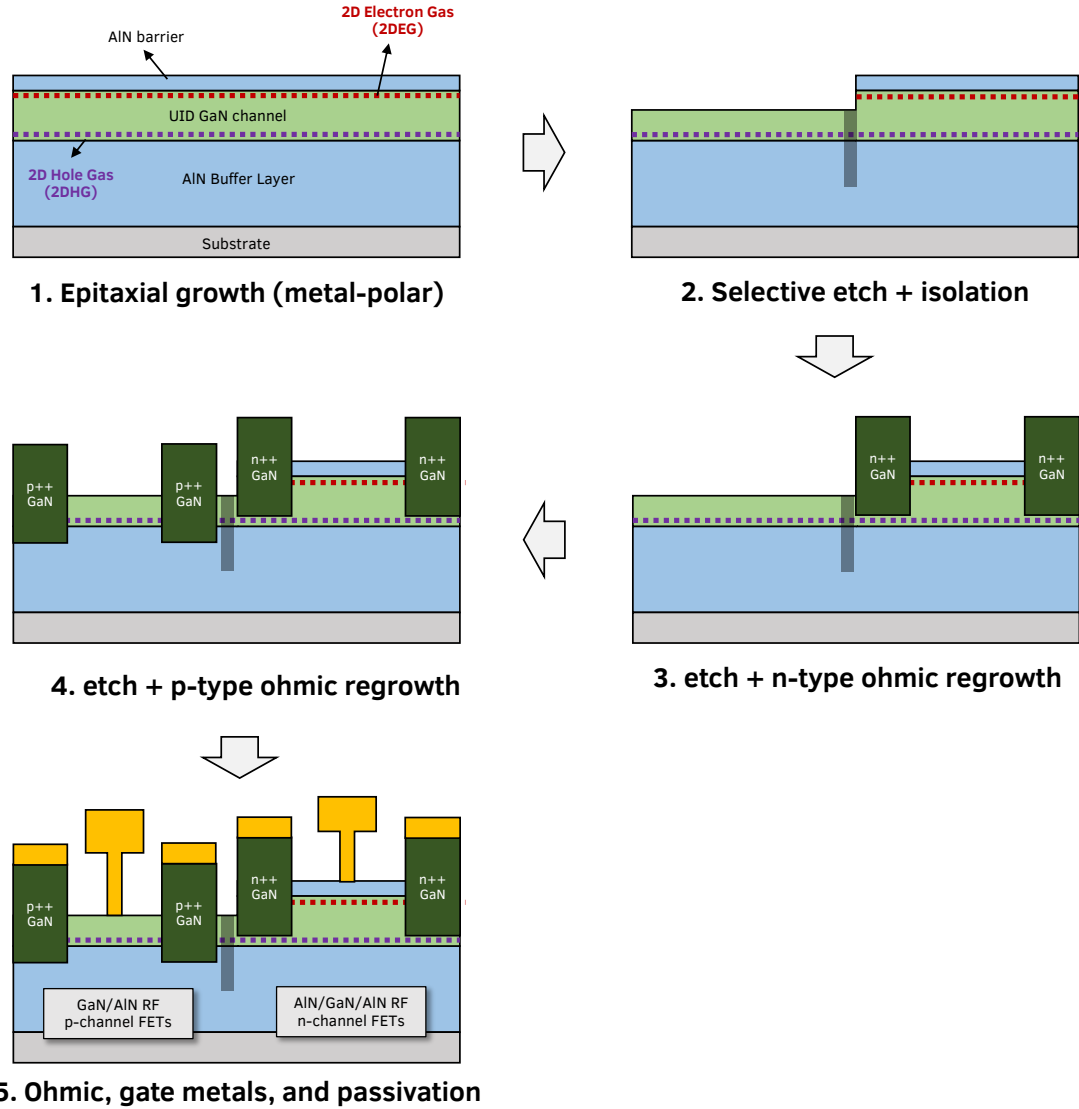
Figure 6.5: Proposed process flow for integrating AlN pFET and HEMT on the AlN/GaN/AlN heterostructure using n and p type regrown ohmic contacts.

grown on the substrate. The sample should have a 2DEG-2DHG bilayer across the entire as-grown surface. Next, using suitable lithography, selective area etch is performed to remove the AlN barrier layer from some parts of the sample. As experimentally shown in chapter 4, this leaves only the 2DHG in the etched area of the sample. Isolation is performed by either ion-implantation or mesa etch. This is followed by two successive ohmic regrowths for the n- and p-type ohmic

contacts to the 2DEG and the 2DHG by selectively etching and regrowing n++ and p++ GaN in etched regions. Finally gate and ohmic metals are put down, with the desired patterned interconnects, and passivation layer is deposited to form laterally-separated pFET and HEMT on AlN-platform.

The main technological hurdle in realizing this integration scheme is the un-availability of p-type regrown ohmic contacts to the 2DHG, unlike the n++ GaN regrowth which is well developed [158]. P-type ohmic regrowth is challenging mainly due to (1) fundamental limits to the carrier density/conductivity of the p++ regrown regions, and (2) impurities from exposure to the ambient [206, 207, 208] and damage from the dry etch [205] at the regrowth interface are both n-type, which lead to improper contact between the VB of the regrown GaN and the 2DHG. The second challenge can be tackled by using an in-situ sublimation etch which is discussed in the next section. However, it is still a work in progress and until p-type regrown ohmic contacts are ready, Mg-InGaN p-type ohmic contact layer needs to be incorporated in the initial as-grown epi-taxial heterostructure.

Along this line, an alternate realization is to grow the 2DHG heterostruc-ture first and then *regrow* the HEMT heterostructure. This is illustrated in **figure 6.6**. The as-grown epitaxial stack consists of p-InGaN/UID GaN/AlN which will serve as the material for pFET. Then part of the sample is masked and se-lectively etch down all the way into the AlN buffer. The sample is then rein-troduced into the chamber where an AlN/GaN/AlN stack is regrown to form the 2DEG. Thus, part of the sample has a 2DEG-2DHG bilayer and the other part just has a 2DHG. These two regions then undergo the transistor fabrication and form the monolithic HEMT and pFET. This scheme avoids the need of a p-

1. Epitaxial growth (metal-polar)

2. Selective etch

3. n-type heterostructure regrowth

4. etch + n-type ohmic regrowth

5. Ohmic, gate metals, and passivation
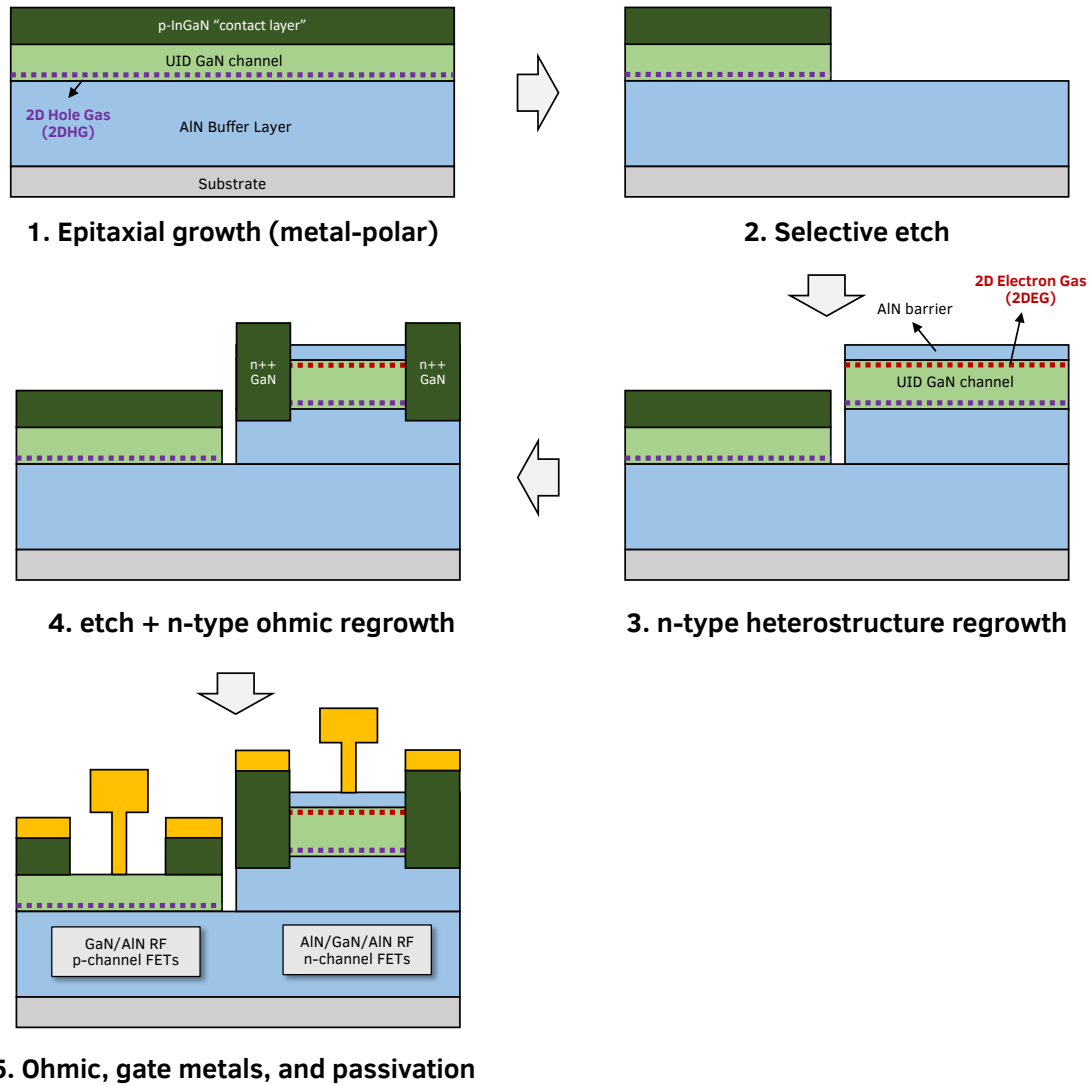
Figure 6.6: Proposed process flow for pFET and HEMT integration on AlN by growing a p-type stack for the pFET, selectively etching away the active region and regrowing the n-type stack for the HEMT.

type regrowth, but still needs an n-type ohmic regrowth, resulting in two MBE regrowths in total. The author believes this scheme to be the most achievable given the current state-of-art and will hopefully be realized experimentally very soon.

Beyond the two discussed above, a couple more novel schemes to integrate AlN-based CMOS have emerged thanks to the very recent developments in the

field. They are listed below. Even though these schemes need bit more epitaxial growth development before being realized, each of them present certain unique advantages which make them scientifically and technologically interesting.
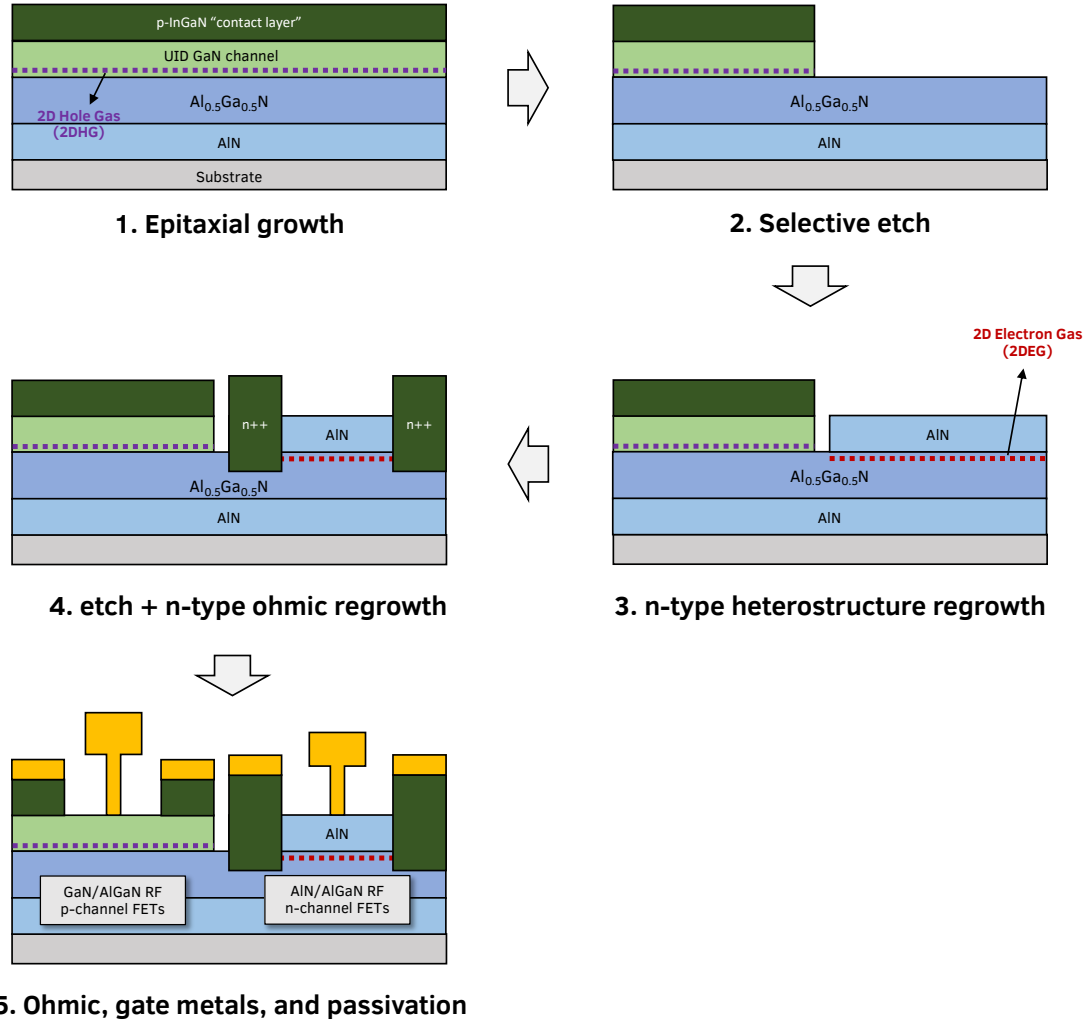
Figure 6.7: Proposed process flow for AlN-based RF CMOS by using an GaN/AlGaN 2DHG and an AlN/AlGaN 2DEG as channels for the pFET and HEMT on AlN. This configuration avoids parallel 2DEG or 2DHG channels in any part of the sample.

- The recent observations of 2DHGs in metal-polar GaN/AlGaN heterostructures [326] and 2DEGs in AlN/AlGaN heterostructures [327, 311] on AlN buffer layers provide a opportunity to combine the two. The pos-

sible scheme is shown in **figure 6.7**. The main advantage of this configuration is the avoidance of a parallel 2DEG-2DHG anywhere on the sample. Of course, to realize this under the constraints of lack of p-type regrown contacts, a p-InGaN/GaN/AlGaN stack needs to be grown first incorporating the p-ohmic contact layer. The InGaN/GaN layers are then selectively etched away part of the sample, either using an ex-situ dry etch or in-situ sublimation etch. Then the AlN/AlGaN 2DEG stack is regrown on top of the buffer layer to form the n-type regions. The two regions are then used to fabricate the HEMTs and pFETs. A second regrowth is required to make the ohmic contacts to the 2DEG. Since the electron channel is high-composition AlGaN, n++ GaN might not be sufficient to connect to the conduction bands and graded AlGaN ohmic regions might be necessary.

- Because of the flipped polarities, an *N-polar* GaN/AlN structure is expected to induce a 2DEG. 2DEG density of ∼ 5×10^{13} cm^{-2} and electron mobility of ∼ 200 cm^2/Vs has recently been observed in our group in an N-polar GaN/AlN structure grown on N-face of single-crystal bulk AlN substrates. Additionally, metal-polar GaN/AlN 2DHGs with high low temperature mobilities have also been obtained on single-crystal AlN substrates [30] (see appendix B). These two observations, plus the availability of high-quality single-crystal AlN [200, 201] provide another very novel configuration to realize an AlN CMOS. This is illustrated in **figure 6.8**. Essentially, GaN/AlN epitaxy is performed on *both* sides of the single-crystal substrate - with one side yielding a 2DEG and the other a 2DHG. An N-polar GaN/AlN HEMT should not require a ohmic regrowth, hence this process will need just one "regrowth" in total. Through substrate vias (TSVs) can be fabricated to interconnect the n- and p-FETs. However, the

1. Epitaxial growth (metal-polar)

2. Flip and re-introduce

4. Ohmic, gate metals, and passivation

3. Regrow N-polar GaN/AlN 2DEG
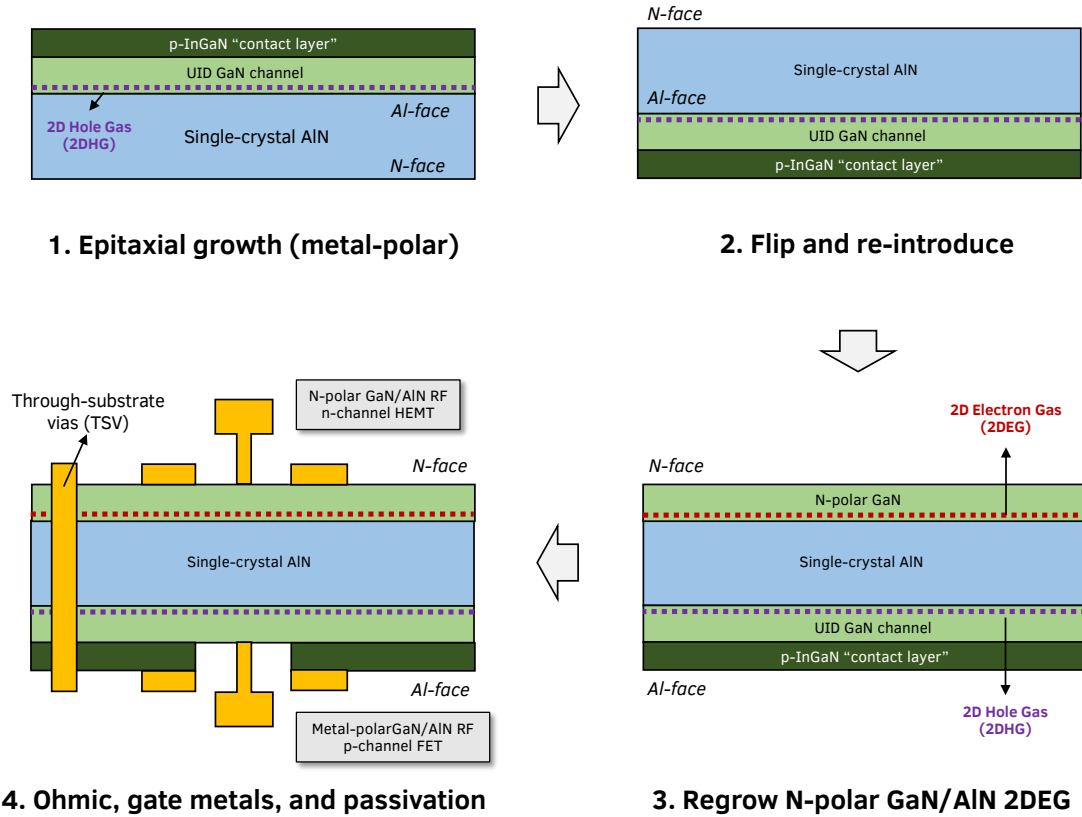
Figure 6.8: A unique realization of AlN CMOS by combining a metal-polar GaN/AlN pFET and nitrogen-polar GaN/AlN HEMT on two sides of a single crystal AlN substrate. This will also necessitate through-substrate vias (TSVs) to connect the two devices.

complexity of the structure results in a number of process constraints since epitaxial growth needs to be performed on one side, unloaded, flipped and then performed on the other side. The typical ex-situ and in-situ cleaning processes [64, 65] for MBE-growth on bulk AlN substrates during the second growth can potentially damage the initial epitaxial layers. This realization also limits the choice of substrate. It needs to be single crystal bulk AlN, which has a limited availability and costlier than SiC, Si or Sapphire. Furthermore, N-surface CMP polishing of single-crystal AlN substrates is not as well developed as Al-side mainly due to the higher reactivity of the N-face. However, rapid progress is being made in this field, and should

soon enable this AlN CMOS configuration.

6.4   *in-situ* Sublimation Etch of GaN

The AlN CMOS realization conceptualized in the last section relies on atleast
one step of selective area etch and regrowth. The MBE regrowth technique [158]
has helped achieve some of the lowest n-type contact resistances to 2DEGs and
proven to be critical for enabling high-power RF HEMTs. A typical MBE re-
growth process consist of the following steps :

1. Putting down a suitable etch mask, patterned using photolithography or
   electron beam lithography depending on the feature size.

2. Etching away the III-nitride material to the desired depth, typically us-
   ing a ICP plasma dry etch. A low-power plasma is used to minimize the
   damage to the crystal and its electronic properties from the physical ion
   bombardment.

3. (Re)introduction of the patterned sample into the MBE chamber and re-
   growth of desired epilayers. For example, highly degenerately doped
   n++GaN is grown for n-type ohmic contacts.

The etched surface of the sample is exposed to the ambient, even if only for a
short while, between steps 2 and 3. This introduces impurities such as Si, O, C at
the etched sidewall regrowth interface [206, 207, 208] which are n-type dopants
in GaN. These impurities concentrations are on the order of $10^{17} - 10^{19}$ cm^{-3},
extending $50 - 100$ nm across the interface[206, 207, 208]. Since the impurities
are n-type, they do not have a large effect on the n-type regrown contacts if a

suitable wet chemical cleaning using HCl or piranha is performed right before loading into the MBE chamber [158, 47]. However, these impurities pose a real problem for *p-type* regrown contacts as they form a energy barrier for the holes between the VB of the regrown layer and the 2DHG. An impurity concentration as-low-as-possible is therefore desired at the regrowth interface to enable a p-type ohmic regrowth process.

In this section an in-situ regrowth etch using thermal sublimation of GaN is proposed. Using this instead of ex-situ plasma-based dry etch in step 2 avoids the exposure of the sample to ambient between steps 2 and 3. The sample instead remains in ultra-high vacuum MBE chamber throughout and hence avoids contamination of the regrowth interface. The feasibility of the technique to etch a GaN/AlN 2DHG structure is demonstrated. A blanket etch and a patterned etch of the GaN is demonstrated by heating the sample to upto 1200°C. Through a comparative study, SiO_2 is found to be the more suitable ex-situ deposited dielectric mask for this etch as opposed to SiN.

The thermal decomposition of a GaN film in an epitaxial growth chamber under the ultra high vacuum of $< 10^{-8}$ Torr and temperatures above 800°C has been studied and reported previously [328]. This process is a thermodynamic competitor to the process of epitaxial growth and hence GaN film growths are performed at temperatures below 800°C in an MBE growth chamber. However, this process of decomposition can be used for in-situ nanofabrication processes. It has been used to fabricate GaN nanowires [329] and mesoporous GaN [330]. Near-vertical etch profiles with good selectivity was obtained with in-situ deposited SiN mask.

It has also been reported that the presence of Al in the GaN layer decrease

the thermal decomposition rate by orders of magnitude [328]. A controlled study found that the rate of thermal decomposition at 1000°C dropped from ~ 1 μm/min in GaN to ~ 10.1 nm/min at 5% AlGaN. This means a buried AlGaN or AlN layer can potentially act as an etch stop for thermal decompostion etch of GaN. Although this study was performed in an MOCVD chamber at a chamber pressure of 76 Torr, this trend is expected to apply even to the ultra-high vacuum chamber of MBE.

Building on these two observations, an in-situ regrowth etch is conceptualized for (In)GaN/AlN 2DHG structures. Using a compatible ex-situ deposited mask, the aim is to selectively etch and remove the GaN layer (or InGaN layer) in the unmasked region and stop the etch on the AlN buffer layer interface.

First, to test and determine the GaN sublimation etch conditions, an MBE-grown 15 nm UID GaN on AlN 2DHG sample *without* any mask was prepared. The target was a blanket etch removal of the GaN layer across the surface to leave just the AlN buffer layer. The in-situ sublimation etch experiments were performed in a Veeco Gen10 MBE system, with a background chamber pressure of $< 10^{-9}$ Torr during the experiment. No gas flow or source shutters were open during the experiment. The GaN/AlN sample was ultrasonicated in acetone, methanol and propanol for 15 min each, following which it was mounted in a molybdenum faceplate. The sample was then outgassed at 200°C for 7 hours and 500°C for 2 hours before introducing into the MBE growth chamber. The substrate was heated using the radiative CAR heater at a ramp rate was 30°C/min and monitored using the thermocouple reading. The growth surface was continuously monitored using RHEED with no CAR rotation.

The substrate temperature as a function of time during the in-situ etch pro-
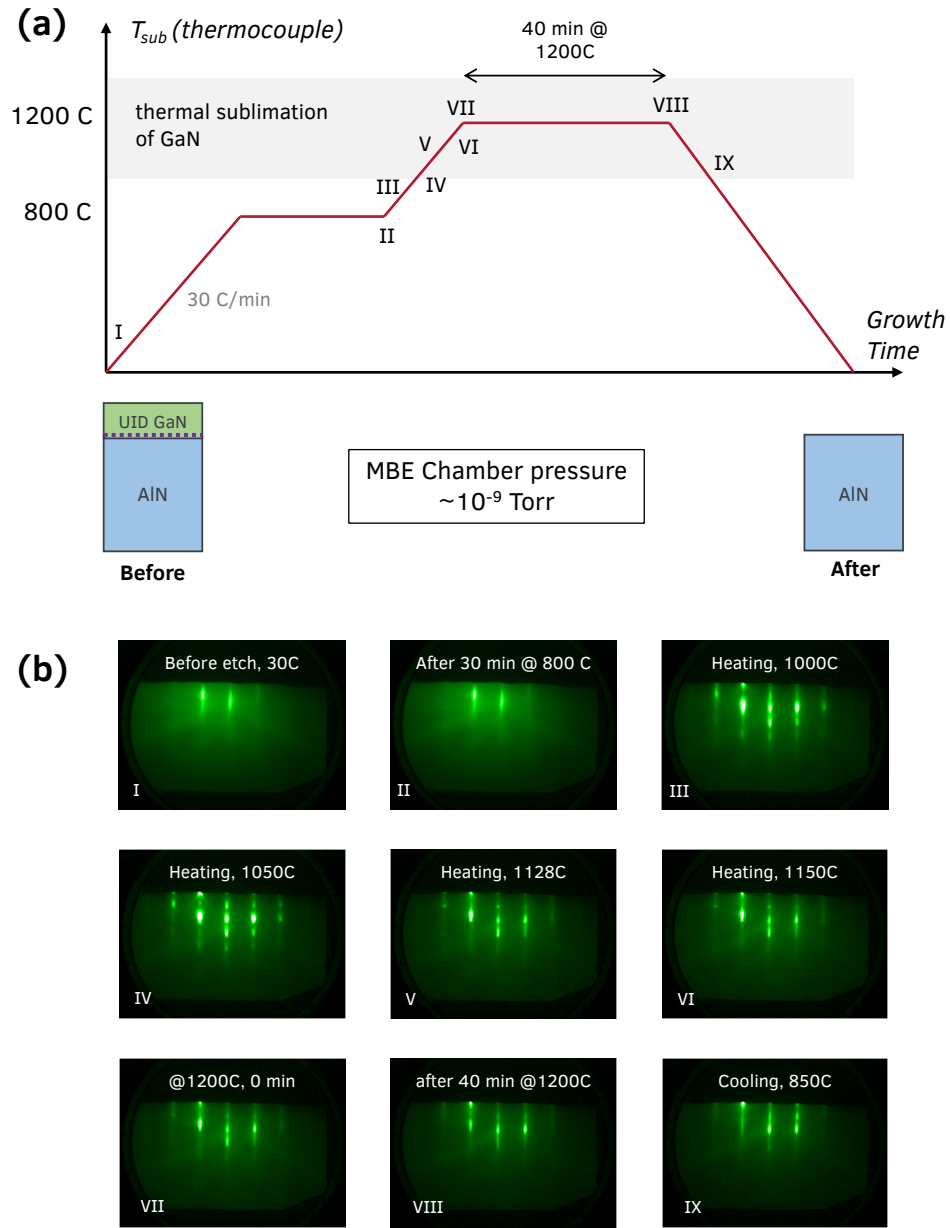
Figure 6.9: (a) Timing diagram illustrating the recipe used for the in-situ thermal etch of GaN in a Gen10 MBE growth chamber at a background pressure of $\sim 10^{-9}$ Torr. The thermal decomposition of GaN occurs at substrate temperature $> 1050°C$. (b) The RHEED pattern recorded at various times/temperatures during the in-situ etch process. A clear change in pattern from streaky to spotty to again streaky is observed - a signature of the roughening of GaN surface due to thermal decomposition and eventual smoothening out when all GaN is decomposed.

cess is illustrated in the **figure 6.9**. The process began by heating the substrate from ~30°C to 800°C. The substrate was left at the 800°C for ~20 min for further outgassing. The corresponding RHEED pattern from the sample surface is shown in **figure 6.9 (b)**. The initial surface of the GaN/AlN structure is smooth indicated by a streaky RHEED. No significant changes were observed during the outgassing at 800°C and the RHEED pattern remained streaky. The sample temperature was then set to 1200°C at 30°C/min. The RHEED pattern started to change around 1000°C, with spots starting to appear along the RHEED streaks. The RHEED became very spotty at 1050°C, which indicates a very rough surface with 3D island-like formations likely due to the ongoing GaN decomposition. As the temperature increased further, the RHEED pattern started "smoothening" out till the streaky RHEED was recovered. This is attributed to almost all the GaN being completely decomposed and the AlN layer now exposed. The final RHEED pattern from the AlN surface was streaky, indicating smooth surface. To ensure complete etching, the sample was held at 1200°C for 40 mins. This step can potentially be made shorter if required as RHEED stayed streaky since the AlN is not expected to decompose. After 40 mins, the sample was cooled down and unloaded from the MBE chamber.

X-ray diffraction and atomic force microscopy (AFM) were performed to confirm whether the in-situ sublimation etch process did indeed remove the GaN layer completely from the GaN/AlN structure. The results are showed in **figure 6.10**. AFM scans of the surface show a difference in surface morphology before and after the etch, seen in **figure 6.10 (a)**, corroborating with the removal of the top GaN layer. An increase in surface root mean square (rms) roughness was observed, going 1.37 nm from 0.6 nm across a 2 μm × 2 μm scan. Although this is not ideal, interface roughness scattering is not expected to dominate the
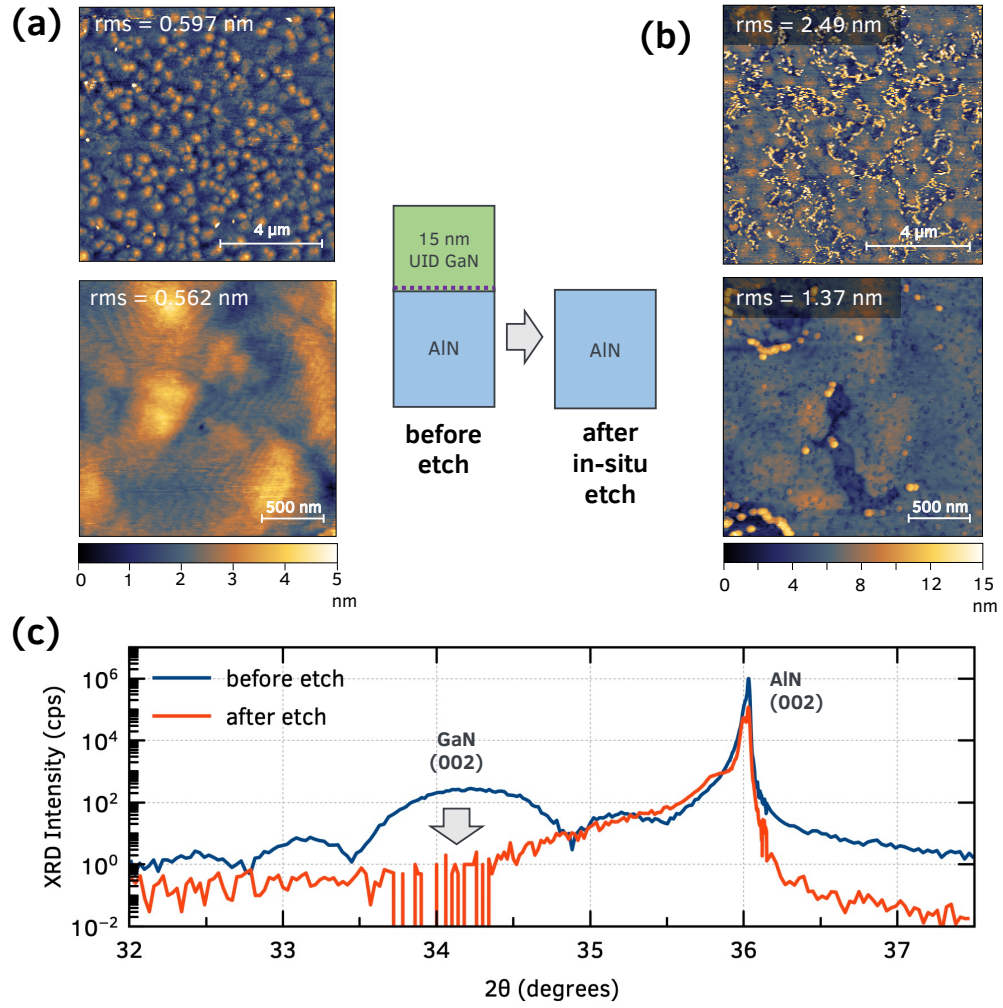
Figure 6.10: Structural characterizations before and after the in-situ GaN *blanket* etch of a 15 nm GaN/AlN heterstructure. (a, b) Show atomic force microscopy (AFM) scans before and after the etch. (c) X-ray diffraction scan confirms that the GaN is completely removed by the etch.

2D carrier transport at room temperatures. Furthermore, the surface can be smoothed during the subsequent crystal regrowth to ensure smoother interface for the 2D carriers.

Figure 6.10 (b) shows the XRD scan along (002) for the sample before and after the sublimation etch. The GaN (002) peak is no longer visible after the etch, again confirming the removal of the top GaN layer by the in-situ etch. The

slightly asymmetric AlN (002) peak in the XRD after etch is believed to be due to the presence of AlGaN IBLs in the AlN buffer layer.

Now that the in-situ GaN etch is confirmed, the next step is to demonstrate selective area etching with suitable patterned mask so that the masked region remains unetched and the exposed GaN regions are etched. Previous reports of in-situ sublimation etch of GaN have only used in-situ deposited SiN masks, hence a controlled study is necessary to test the compatibility of ex-situ deposited masks with this etch process. Both ex-situ silicon nitride (SiN) [158] and SiO_2 [207] have been previously used as masks for selective-area GaN regrowths. Since the sublimation etch goes to temperatures upto 1200°C which is higher than typical MBE regrowth temperatures (< 800°C), it also necessary to characterize the difference in physical and chemical behavior of the dielectric mask used for a patterned etch.

A controlled study was performed to investigate this. Two 8 mm × 8 mm pieces were prepared from the same 15 nm UID GaN on AlN 2DHG wafer, labelled sample A and B. Sample A had 257 nm of SiO_2 deposited using atomic layer deposition (ALD) and sample B had 207 nm of SiN deposited using plasma-enhanced chemical vapor deposition (PECVD). The dielectric on both samples were patterned using photolithography. They then underwent the in-situ GaN etch with a recipe identical to that in **figure 6.9 (a)**. The RHEED beam was adjusting to obtain the RHEED pattern from the exposed GaN surface, and the sample was not rotated during the etch.

The RHEED evolution during the etch for the two samples are shown in **figures 6.11**. For sample A, with SiO_2 mask, the RHEED pattern behaved as expected. This is shown in **figure 6.11 (a)**, where the RHEED pattern went
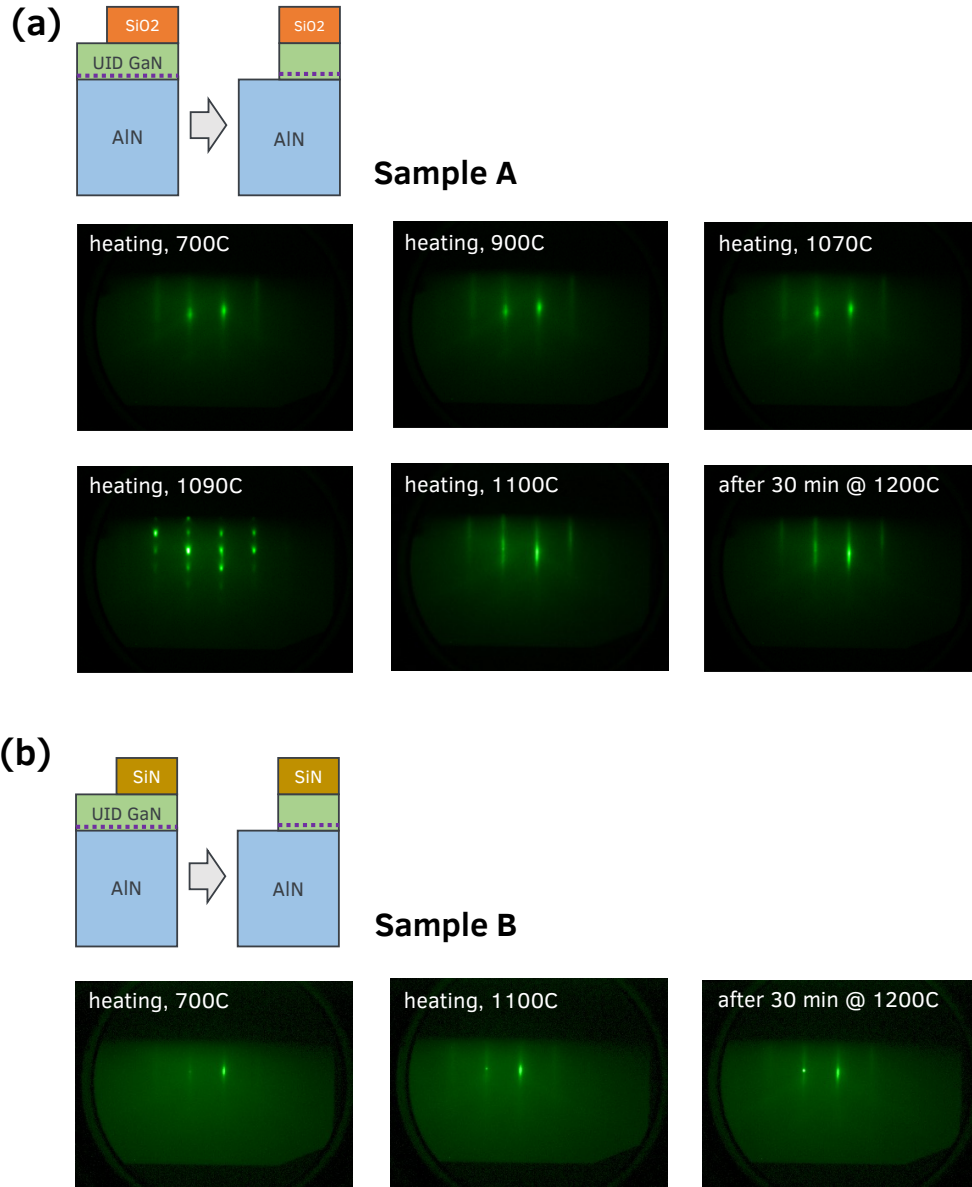
Figure 6.11: Comparison of RHEED evolution during the in-situ *selective-area sublimation* of GaN with (a) patterned SiO_2 mask and (b) patterned SiN mask.

from streaky to spotty to streaky concurring with the observations of the blanket etch sample in **figure 6.9 (b)**. However, sample B with with SiN mask behaved weirdly, as shown in **figure 6.11 (b)**. Almost no discernible change was observed in the RHEED pattern during the etch process. The RHEED remained smooth even at 1200°C, indicating a slightly different behavior compared to sample A.
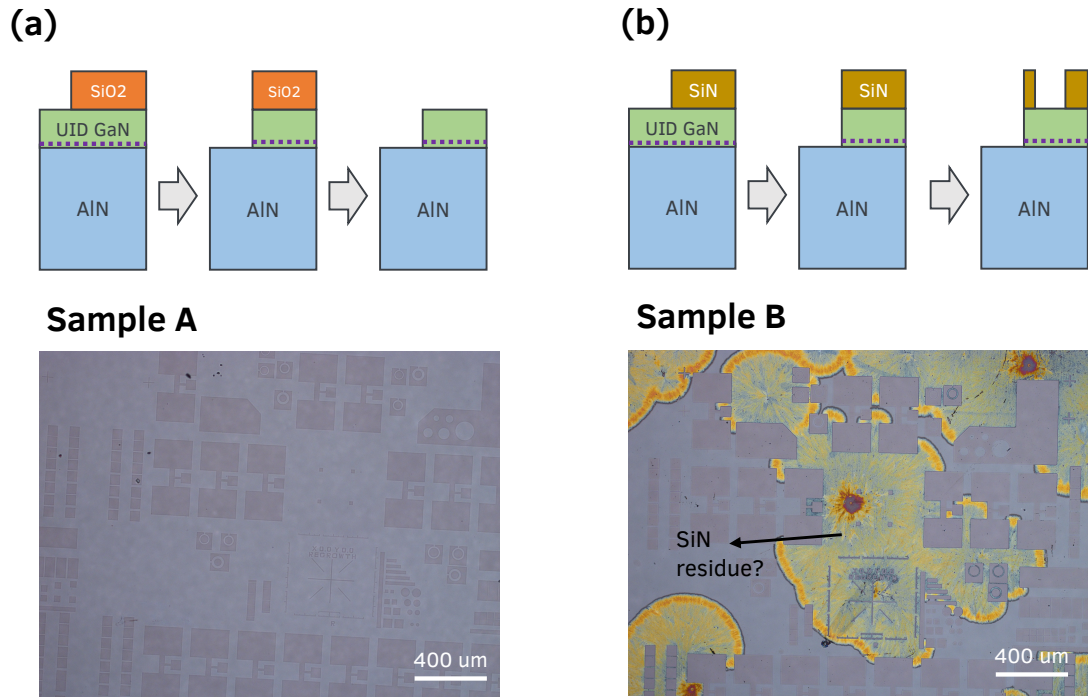
Figure 6.12: Comparison of optical images of surfaces of sample A and B after the in-situ etch and BOE dip to remove the mask. The SiN residue could not be removed from the surface even after leaving it overnight in HF.

Both samples A and B were unloaded from the growth chamber and dipped in buffered oxide etch (BOE) to remove the dielectric mask. The optical microscope images after the BOE clean is shown in **figure 6.12**. Sample A looks optically clean with no residue of SiO_2 mask visible. Whereas on sample B, SiN residue observed. This residue is spread out non-uniformly over the sample surface. This residue could not be removed even after leaving it in HF overnight, which is weird since as-deposited PECVD SiN has a high etch rate in BOE. This observation indicates a change in PECVD SiN structural or chemical properties due to the high vacuum, high temperature anneal during the in-situ etch. It worth noting that *in-situ* MBE deposited SiN mask has been used previously as a thermal etch mask, and demonstrated high thermal stability [329]. Hence, these observations could be pointing to a difference in the thermal stabil-

269

ity of the PECVD-deposited SiN (densities or stoichiometry during the anneal [331]) and/or effect of exposure to the ambient (oxidation). Further investigation should reveal the origin of these observations.
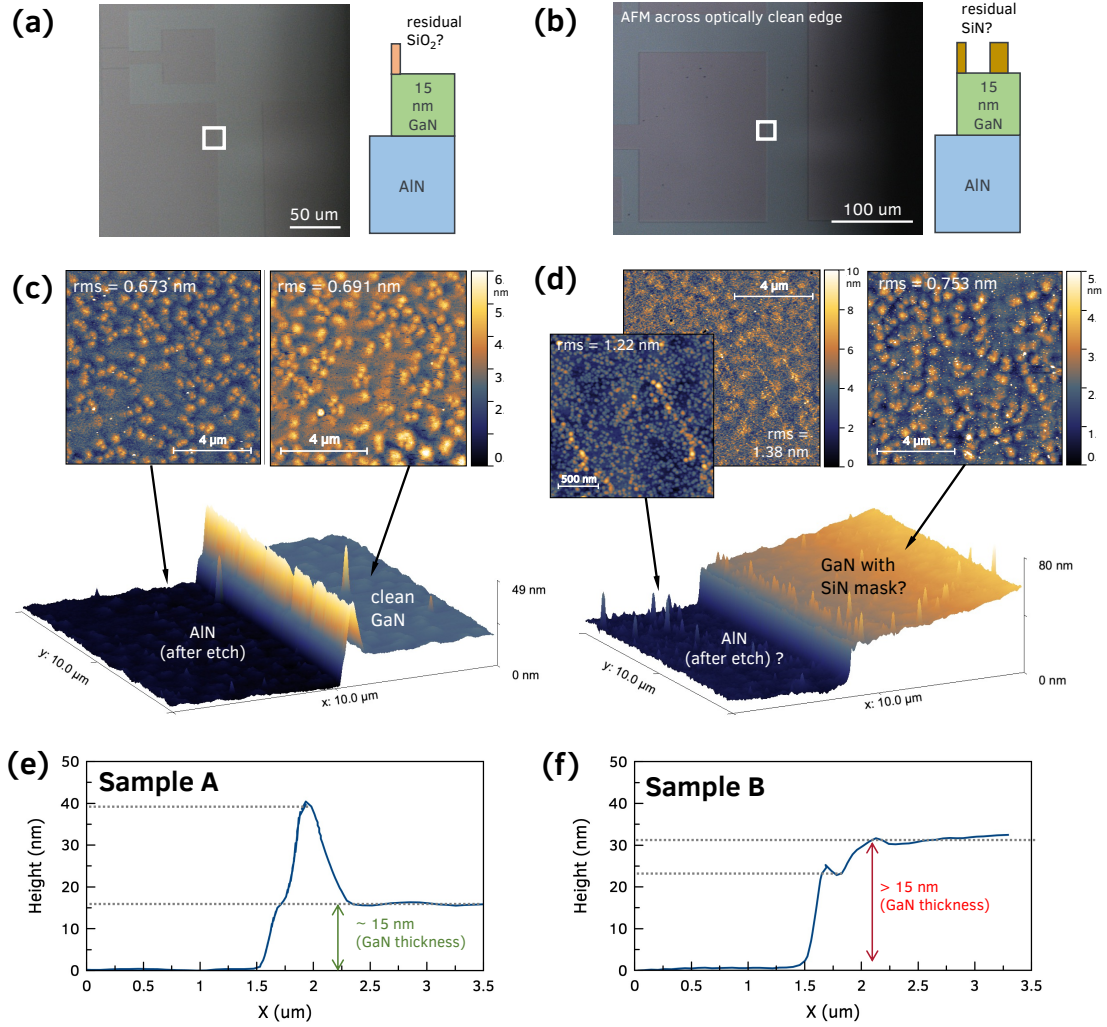
Figure 6.13: Atomic force microscopy scans across a patterned step edge for samples A and B. (a, b) Optically clean parts of the sample were chosen to probe the edge profile. (c,d) show the AFMs scans on the etched and unetched regions of the samples. Sample B showed roughening of the etched surface. (e-f) are the etch profiles across the step edge. The step height in sample A is consistent with the ~ 15 nm of GaN being etched away, but there is a bunny ear like feature on the edge.

Atomic force microscopy (AFM) scans near the edge of a were performed to characterize the etch profile. For sample B, a relatively optically clean are with

no visible SiN residue was chosen for the AFM scans. The results are shown in **figure 6.13**.

Sample A, with the SiO_2 mask, showed smooth morphology with rms roughness of ~ 0.6 nm very close to pre-etch as-grown surface in both the etched and masked region. The etch profile shows a step height of ~15 nm, confirming that the UID GaN layer was removed and the etch stopped at the AlN buffer layer. Interestingly, a "bunny ear" like feature observed on the step edge which rises ~25 nm. The origin of this feature is not clear at the moment, and needs to be solved with process such as planarization to incorporate into the fabrication process.

In Sample B, the surface on the etched side was slightly rougher at rms of 1.38 nm compared to the pre-etch surface rms of 0.6 nm over the same area. Interestingly, even though the RHEED did not show any change during the in-situ etch, the AFM profile shows a clear step edge. No bunny ear like feature was observed as in sample A. The measured step height is around 30 nm, which indicates that there is still residual SiN present on the unetched area. Because of this, it is unclear whether the step profile is due to the GaN etch or patterned SiN. Chemical analysis of the sample in the future should be able to answer these questions.

In summary, this short study demonstrates the feasibility of in-situ thermal sublimation etch of GaN for regrowths. This can be used to regrow both epitaxial stack or ohmic contacts. From the differences in behavior observed in the SiN and SiO_2 masks, SiO_2 mask is found to be more suitable for this technique compared to PECVD deposited SiN. This is the first such controlled study to compare the effect of dielectric mask on in-situ thermal etch of GaN. Initial at-

tempts to regrow a 2DHG after in-situ sublimation etches have proven to be unsuccessful so far with all the resulting films resistive. Further chemical investigations in the form of SIMS profiles across the regrowth interfaces are necessary to understand the reason why.

6.5   Passive RF devices on AlN Platform

The previous sections focused on the monolithic integration of the n-type and p-type transistors for complementary circuits, to be used for gate driver logic circuits to drive high-power switches, PAs and LNAs. Even though these active devices are the heart of the RF front-end circuits, the passive components such as filters, waveguides and antennas, which operate at suitable frequencies, are equally essential. Towards this, there has been a dedicated effort in the Jena-Xing group to develop passive RF components on the AlN platform. Overcoming the micro-fabrication challenges have yielded initial results that already show record performances within a year of conception.

This section presents the summary of these recent advancements in RF passive components on AlN. Highlights include epitaxial AlN thin-film bulk acoustic resonators (FBARs) with 10 GHz operating frequency [56] and SiC substrate integrated waveguides (SIWs) and SIW-based filters for D-band operation (110-170 GHz) with record low insertion losses [57]. These are fabricated on the same epitaxial MBE-AlN on SiC material that is used in the RF HEMTs for PAs, maintaining epitaxial compatibility for future integration.

Only short summaries of these works are presented here to update the reader with the latest developments in the AlN platform beyond the transistors, and

to highlight the repertoire of RF devices now available on the AlN platform. Interested reader are encouraged to go through the references [57, 56] for detailed discussions.

6.5.1 Epitaxial AlN Bulk Acoustic Waveguide Resonators

With the rise of 5G, internet of things (IoT) [332, 333], the commercial operating frequencies of RF circuitry are slowly entering into the mm-wave regime (30+ GHz). Filters are an essential part of the RF front end, especially on the receiver side where they discern or "filter" the required information-carrying signal frequency among all the other signals received by the antenna. For example, in a cell phone, each communication frequency band needs its own filter to avoid cross-talk and congestion.

CMOS-compatible filters are micro electro-mechanical (MEMS) devices utilizing a piezoelectric material. These filters are acoustic resonators with a given resonant determined by its geometry. The coupling between electromagnetic waves and acoustic waves is used to filter the signal at this resonant frequency and reject all other frequencies. AlN is a popular choice for these MEMS filters thanks to its excellent piezoelectric and acoustic properties and CMOS-BOEL compatibility [113]. Surface acoustic waveguides (SAWs), which utilize surface wave modes, are used for applications below 2 GHz [334]. Bulk acoustic waveguides (BAWs) and FBARs are most suitable for the sub-6 GHz frequency bands. Scaling current BAW technologies to higher frequencies is fundamentally challenging and provides a unique opportunity for the epitaxial AlN platform.

The bulk acoustic waveguid (BAW) consists of the piezoelectric material AlN

between metal electrodes to form an acoustic cavity. The acoustic waves reflect off the metal electrodes and form standing waves like an accordion. The resonant frequency f_0 is determined by the thickness t of the AlN through $f_0 = v_s/2t$, where v_s is the speed of sound in AlN. For sub-6 GHz frequencies, the AlN needs to be few microns thick while maintaining the crystal quality, specifically in the c-axis orientation. The AlN crystal quality is quantified by the sharpness of the AlN (002) X-ray diffraction peak. A narrower FWHM results in higher electromechanical coupling coefficient (k_t^2) [335] and hence a more efficient, lower-loss filter. For micron-scale BAWs, AlN films are directly deposited on metal electrodes or Si using reactive ion (RI) sputtering, yielding decent crystal quality and high throughput, and is therefore used commercially. Typical $k_t^2 \sim 0.08$ for sputtered AlN with (002) FWHMs of 4000-8000 arcsecs are used in sub-6 GHz sputtered AlN BAWs [335].

To access higher frequencies, scaling down the AlN piezoelectric material is essential. A 400 nm thin AlN film is needed for resonance at 10 GHz. This scaling down is a fundamental challenge for RI sputtering growth. In sputtering, the crystal nucleates with highly disordered columns, which then slowly coalesce as the AlN film gets thicker [336]. Therefore sputtered AlN films the FWHM is inversely proportional to the film thickness, and hence lower k_t^2. Therefore, the technical challenge is to obtain thin, sub-micron AlN layers with high crystal quality to access 10+ GHz operation frequencies.

Epitaxial AlN offers a viable solution. The fundamental growth kinetics of epitaxy means the crystal has *higher* quality when it is thinner - the opposite trend when compared to sputtering. Growing on a low lattice mismatch substrate like SiC means the dislocations can be kept to minimum even at relatively
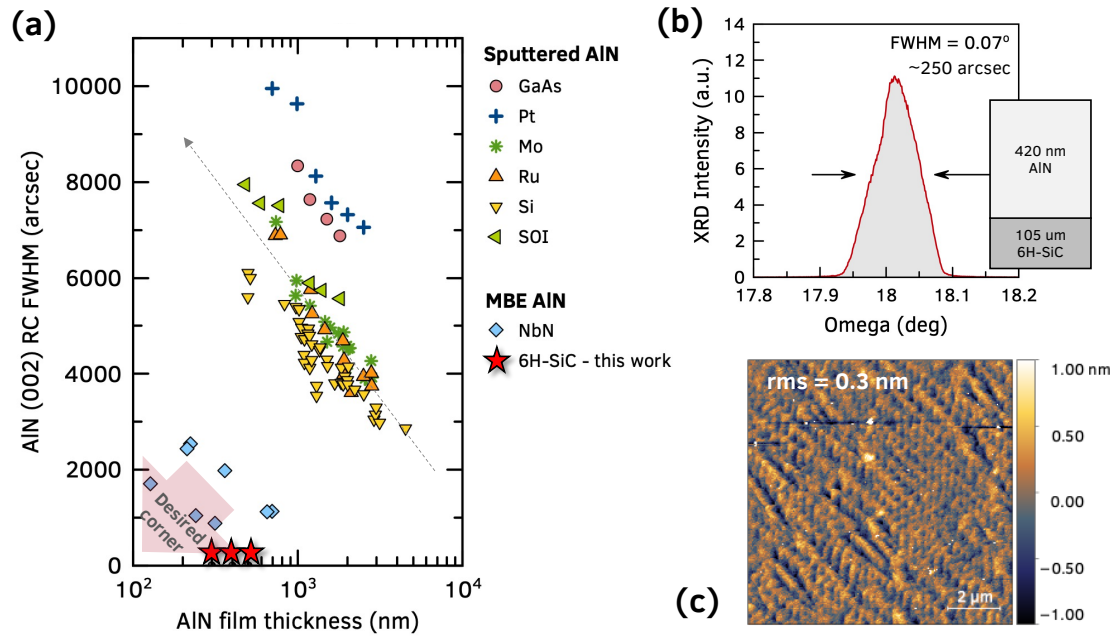
Figure 6.14: (a) Benchmark comparing the AlN (002) XRD rocking curve FWHM of sputtered AlN and MBE-AlN as a function of AlN film thickness. The crystal quality of AlN (signified by smaller FWHM) decreases as sputtered AlN films get thinner. At sub-micron thicknesses, the MBE-AlN shows 20× lower FWHM, desired for FBARs with resonant frequencies at 10+ GHz. (b) Representative XRD RC of an MBE-grown 430 nm AlN on 100 μm thin SiC substrate. (c) Surface AFM scan showing a smooth AlN surface. This sample was used to fabricate the FBAR device shown in figure 6.15.

thicker films upto a micron [287]. **Figure 6.14 (a)** compares the FWHMs of MBE-grown AlN films on 6H-SiC versus sputtered films as function of thickness. The details of the MBE growth is provided in appendix A. Clearly, the MBE-grown AlN are orders of magnitude better than sputtered films at sub-micron thickness and hence is suited to be used to making BAWs.

To explore this, ~ 420 nm of AlN was grown on the Si-face of a full 3-inch 6H-SiC wafer using PA-MBE. Since the BAW resonators needs the epitaxial AlN to be released from the substrate, these SiC substrate wafers were specially thinned down to 100 μm for etching from the back, C-face side. **Figure 6.14 (b)** shows the XRD omega rocking curve scan along AlN (002) peak. The FWHM was 0.07°

or ~ 250 arcsec. This is orders of magnitude lower than measured in thicker sputtered AlN. Atomic force microscopy (AFM) scans in **figure 6.14 (c)** shows a smooth final surface with rms roughness 0.3 nm. XRD also confirms that the film is 90% relaxed, which is desired as any residual stress in the epitaxial AlN film can potentially warp it when suspended.
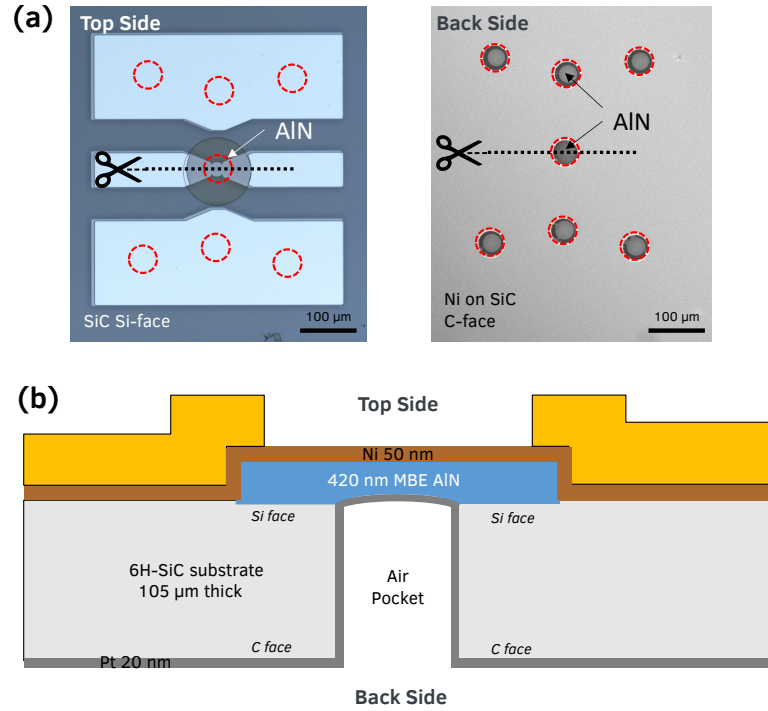
Figure 6.15: (a) Top and bottom side scanning electron microscope (SEM) images of epitaxial AlN based FBARs. (b) Cross-section of the FBAR, showing the suspended AlN resonator layer between Ni and Pt electrodes. *This work is reported in Zhao et al. [56]*

Figure 6.15 (a) shows the top and bottom view of the final FBAR fabricated with a newly developed process. The key step is the through SiC etch from the backside which stops at the epitaxial AlN and releases. 50 nm Ni and 20 nm Pt form the top and bottom electrodes, as shown in the device cross-section in **figure 6.15 (b)**. The resultant FBARs showed a resonant frequency of 10 GHz, with a quality factor Q of 251 and $k_t^2 = 1\%$. This represents the first report of FBAR at this high frequency using MBE grown AlN films [56]. Further improvement in

the Q is expected in the future with more refinements to the fabrication process, especially the etch.

To push to higher frequencies above 10 GHz, thinning down the AlN layer as well as the metal electrodes further is necessary. At those scales the performance bottleneck will be the higher electrode resistance (due to thinner metal layers). Epitaxial metal electrodes such as NbN/AlN/NbN might provide a opportunity [289] to push the performance limits of this new filter technology, made possible by epitaxial AlN platform.

6.5.2 SiC Substrate Integrated Waveguides (SIW)

Integration of discrete RF components such as filters, amplifiers on the AlN platform also requires interconnects to carry RF signals between these components. Current mm-wave integrated circuits (MMIC) technology uses microstrip lines or co-planar waveguides (CPW)s [337], where the RF signal is confined as electron-magnetic (EM) wave modes in adjacent metal lines. This configuration, although suited for low frequencies, results in high loss from air resulting in limited power handling capability at frequencies above 100 GHz. Since the AlN-based PAs and LNAs are aiming for D-band operation, new waveguide solutions are desired to ensure the signal is carried with high efficiency.

As a solution, substrate integrated waveguides (SIWs), in which the EM signal is confined through the cross-section of a high dielectric constant substrate by forming a network of through-substrate-visas (TSVs), offer higher much power carrying capability at these high frequencies. This has been demonstrated previously at the chip level for mm-wave operation [338]. At D-band

frequencies, monolithic integration of the SIWs have become possible with active devices on the same substrate since the TSV separation is on the order of < 1 mm in high dielectric substrates such as Si, AlN, SiC etc.
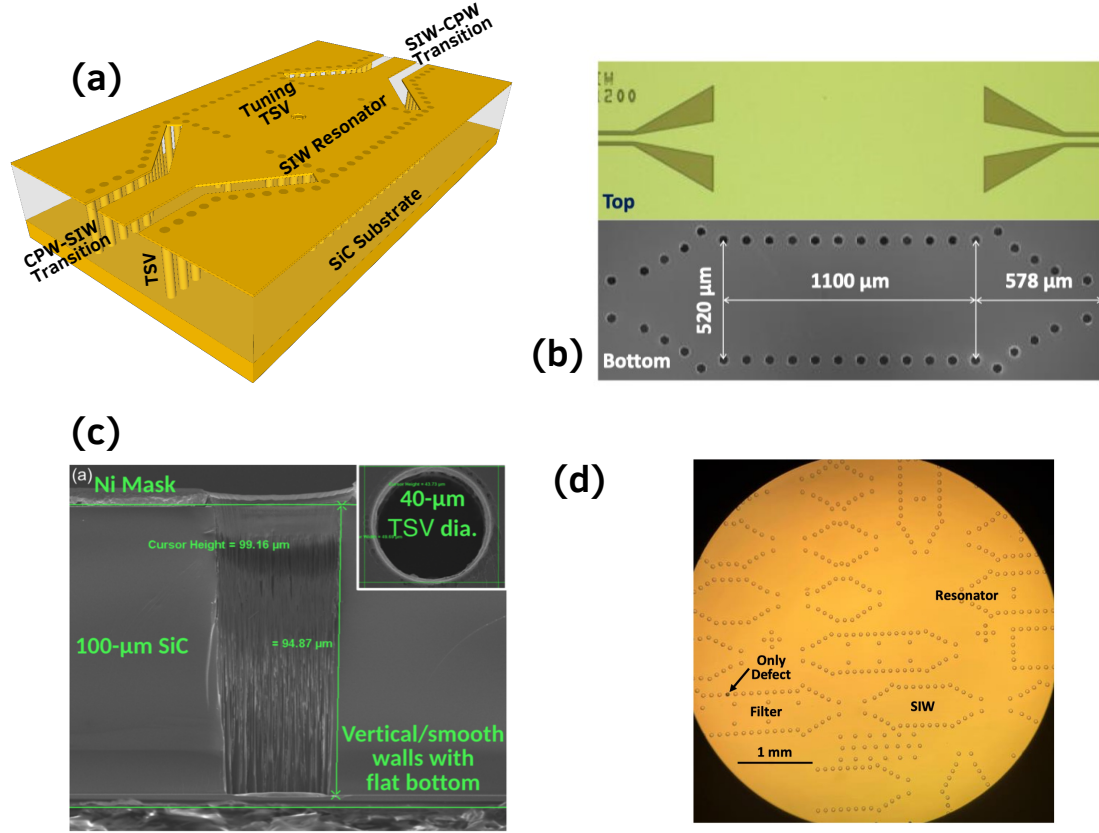
Figure 6.16: SiC substrate integrated waveguides (SIW) using through-substrate vias (TSVs). (a) shows the design of an SIW resonator. (b) SEM scans of the top and bottom surfaces of a 1100 μm long SIW. (c) Cross-section of the TSV, demonstrating the etch process control. (d) Large area optical image of the SIW structures showing uniformity of the etch across the wafer. *Figures from Asadi, Li et al. [57]*

Recent efforts in Jena-Xing Group have yielded D-band SIWs realized on 100 μm thin 6H-SiC substrates with low insertion loss of 0.22 dB/mm. **Figure 6.16 (a)** shows the design of a SIW resonator flanked by two CPW-SIW transitions. Achieving this required careful fabrication and control over through SiC etching to form the TSVs. **Figure 6.16 (b)** shows the top and bottom view of D-band SiC

SIW between CPW-SIW transitions. **Figure 6.16 (c)** shows the cross-sectional SEM image of one of the TSVs, highlighting the vertical etch profile with horizontal flat bottom. Additionally, this SiC SIW technology can be extended to design RF filters [57] and edge emitting antennas [57] as well, as shown in the optical image in **figure 6.16 (d)**. 3-pole filters operating at 135 GHz have been demonstrated with low 1 dB insertion loss [57]. These early results within a year of conception, fabricated on the same material platform on which the active devices and resonators are made, make it an ideal candidate to integrate with the AlN n-channel HEMTs and p-channel FETs for enabling the next-gen efficient RF electronics on AlN-on-SiC platform [53].

APPENDIX A

MOLECULAR BEAM EPITAXIAL GROWTHS

A.1 PA-MBE growth of GaN/AlN 2DHGs

This section details the plasma assisted molecular beam epitaxial (PA-MBE)
growth of (In)GaN/AlN 2D hole gas structures, which are studied in chapters 2
and 3. Results of short investigations in determining the growth conditions for
optimal 2DHG transport active layer and large area growths of the 2DHG on
full 2-inch wafers are also provided.

A.1.1 Detailed Growth Recipe

The GaN/AlN 2DHG heterostructures studied in this dissertation are grown
in a Veeco Gen10 plasma assisted molecular beam epitaxy (PA-MBE) system,
with standard effusion sources for Ga, Al and an RF plasma source for N. 8
mm × 8 mm diced pieces of metal-polar MOCVD-grown AlN on sapphire tem-
plates from DOWA are used as starting substrates. The substrates are ultrason-
icated in acetone, methanol and iso-propanol for 15 minutes each and mounted
on lapped 3-inch Si wafers using molten indium. They are then out-gassed at
200°C for 7 hours and 500°C for 2 hours under vacuum before introducing into
the MBE growth chamber. For the active nitrogen flux during growth, the RF
plasma power is 400 W and the N gas flow rate is set at 2 sccm, corresponding
to a calibrated N-limited growth rate of 0.52 μm/hour. Magnesium and sili-
con dopant cells are kept cold throughout the growth. Reflection high energy

electron diffraction (RHEED) is used for in-situ monitoring of the growth. The growth chamber pressure is $\sim 2.01 \times 10^{-5}$ Torr during the growth.
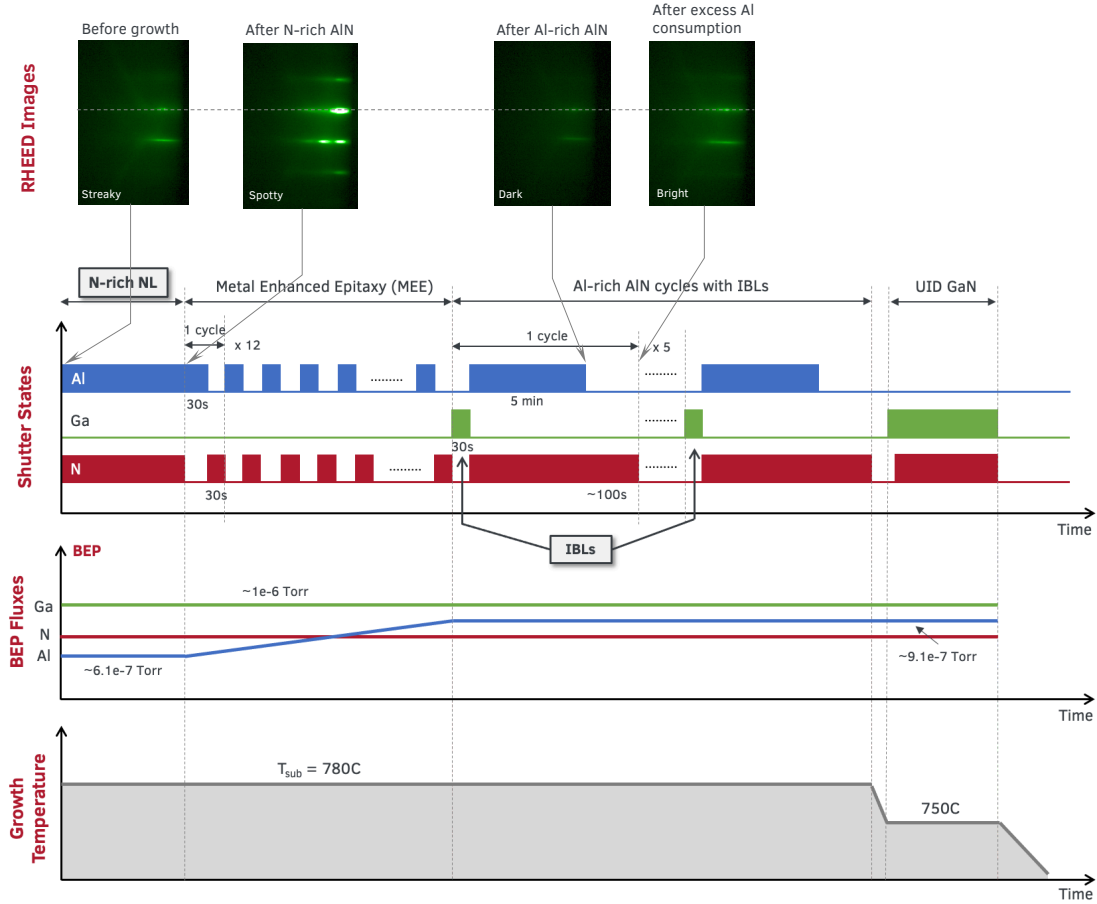
Figure A.1: (a) Timing diagram for MBE growth of an undoped, GaN/AlN 2DHG structure, with both N-rich nucleation of AlN and IBLs in the buffer. Characteristic RHEED pattern evolution at various stages of the growth is also shown. *Figure from Chaudhuri et al. [8]*

The growth recipe for the undoped GaN/AlN 2DHG is illustrated in the timing diagram in **figure A.1**. The sample is heated to $T_{sub} = 780°C$ for AlN buffer growth. The first ~30 nm of AlN, the nucleation layer (NL), is grown under N-rich conditions by opening both Al and N shutter simultaneously at Al BEP of $\sim 6.1 \times 10^{-7}$ Torr, corresponding to an Al:N flux ratio ~0.9. The Al cell temperature is then ramped up at 3°C/min to a final BEP flux of $\sim 9.1 \times 10^{-7}$ (Al:N

flux ratio ~1.33). While the cell temperature ramped up, migration enhanced epitaxy (MEE) cycles are performed to smoothen out the growth surface. The Al shutter and N shutter are alternatively opened for 30 s each. As the Al flux slowly ramped up, the monitored RHEED pattern goes from spotty, indicating a rough surface as expected from a N-rich AlN growth [138], to streaky, indicating a smooth surface with a coalesced film.

The rest of the AlN buffer layer is grown in metal-rich conditions in a 3-step cycle consisting of (1) Ga pre-deposition, (2) Al-rich AlN growth and (3) N anneal. Ga BEP flux of ~ 1×10^{-6} Torr is initially deposited on the surface for ~30 s while N and Al shutter remains closed. Both the Al and N shutter are then opened simultaneously to grow AlN under metal rich conditions. After 5 min of AlN growth, the Al shutter is closed and the excess Al metal on the surface is consumed by the incident N flux [63]. The pre-deposited Ga has a dual role here - to act as a surfactant for the subsequent AlN growth [287] and to form the high-composition AlGaN IBLs. A small amount of this pre-deposited Ga metal incorporates into the initial layers of the AlN crystal to form high-composition > 90 – 95% AlGaN, due to non-idealities of the growth conditions - N leak from around the shutter when it is closed and instantaneous variance in Al and N fluxes when the shutter is opened. Reports have also shown that a small amount of Ga is incorporated into AlN crystal when used a surfactant for AlN growth [339]. The AlGaN composition and thickness is controlled by the Ga BEP flux, deposition time and substrate temperature during the AlN growth, which were optimized separately. Since Al desorption rate from AlN growth surface is low at $T_{sub} = 780°C$, the accumulated Al metal is periodically consumed after 5 mins of AlN growth by closing the the Al shutter and keeping the N shutter open. The consumption of Al is monitored by tracking the saturation of the RHEED

pattern intensity [63]. This technique of consumption of excess Al on the surface also ensures a sharp, abrupt AlN-GaN interface [63], minimizing the interface roughness scattering of the 2D carriers.

The substrate is then cooled down to T_{sub} = 750°C for the UID-GaN growth. The Ga shutter is opened for 10 s at a Ga BEP flux of ~ 1×10^{-6} Torr before the N shutter waiss opened to wet the growth surface, following which the N shutter is also opened to grow the 15 nm thick UID-GaN channel. The GaN grown at high Ga flux is not an issue here since the total growth duration of the 15 nm thick GaN layer is low. However, the Ga cell temperature should be lowered to reduce the BEP flux in case a thicker GaN layer is being grown to reduce the accumulation of excess Ga metal droplets on the final surface.

Figure A.1 also includes representative RHEED patterns from the AlN crystal surface from the same orientation at different stages of the growth. The RHEED intensity profile during the nucleation process is plotted in **figure A.2**. The RHEED pattern starts off streaky before growth, signifying a smooth starting AlN template surface. The RHEED pattern turns spotty and bright after the N-rich AlN nucleation, indicating the roughening and incomplete coverage of the AlN surface, expected from a N-rich AlN growth [138]. During the MEE cycles, the RHEED slowly turns dark and streaky. The decreasing N consumption time during the MEE cycles indicates the increasing Al flux, as more N is required to consume the 30 s of Al flux. Once the Al:N > 1, the RHEED no longer saturates during the N part of the MEE cycle. Also shown is a comparison of the RHEED pattern after 5 min of Al-rich AlN growth and after the subsequent consumption of excess Al by nitrogen. The RHEED pattern remains the same, but the streaks become brighter and saturate, indicating the absence of Al metal
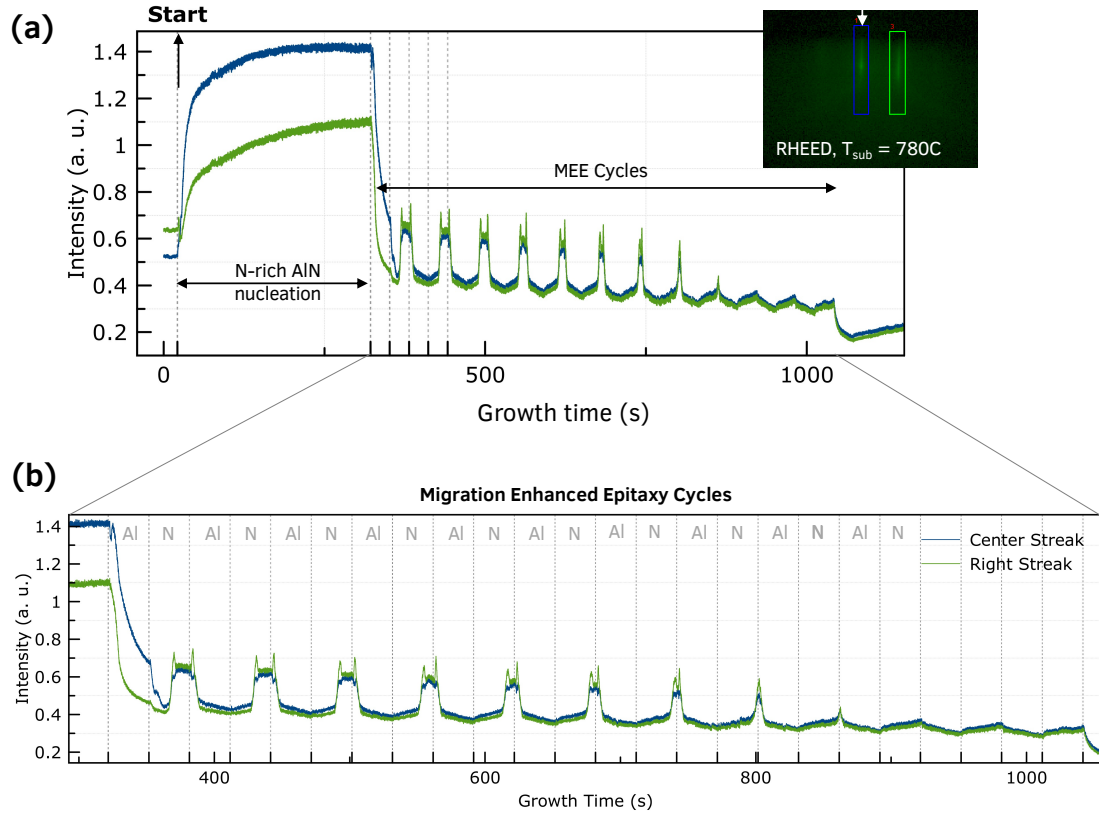
Figure A.2: (a) RHEED intensity of the specular beam tracked during the AlN nucleation growth shown in figure A.1. The RHEED gets very bright during the intial AlN growth under N-rich condition, indicating a rough and metal free growth surface. Once the MEE cycles begin, the RHEED starts getting streakier and dimmer, indicating the smoother surface. (b) zooms into the RHEED behavior during MEE. The N consumption time decreases as the Al flux increase, indicating the growth slowly moving from N-rich to Al-rich regime.

on the surface [63].

A.1.2 Variations in the 2DHG active region

Compared to MBE growth of GaN, optimal MBE growth of InGaN requires a different growth conditions in terms of lower substrate temperature and lower Ga fluxes. Hence, slight modifications are required in the above growth recipe to incorporate the InGaN layers in the active region. They are as follows :

- **InGaN channel for InGaN/AlN 2DHGs** :

  After the growth of AlN buffer layer with the IBLs, the substrate is cooled down to T_{sub} = 655°C for the growth of the InGaN layer during a ~ 2.5 min growth interruption. Different InGaN layer thicknesses and compositions are obtained varying the Ga (Φ_{Ga}) and In (Φ_{In}) fluxes with respect to active N flux (Φ_N) and shutter open times. The relative flux conditions of Φ_{Ga} + $\Phi_{In} > \Phi_N$, $\Phi_{Ga} < \Phi_N$ were maintained to ensure N-limited InGaN MBE growth conditions [340].

- **Mg-InGaN ohmic contact to GaN/AlN 2DHGs** :

  The sample growth proceeds as described for the undoped GaN/AlN 2DHG . After 15 nm of UID GaN layer is grown at the substrate temperature T_{sub} = 750°C in metal rich conditions ($\Phi_{Ga} > \Phi_N$), the shutters are closed and the plasma is killed.

  During this growth interrupt, the following is done carefully : (1) desorb excess Ga on the surface by annealing the sample at 750°C and monitoring the RHEED intensity, which should get brighter as the Ga desorbs. (2) Start cooling down the substrate to the InGaN growth temperature of T_{sub} = 655°C. This interrupt is crucial, since the top GaN surface, if exposed to 750°C for too long after all the Ga has desorbed, will start roughening. (3) Cool the Ga cell temperature to reduce the Ga BEP flux to ensure $\Phi_{Ga} < \Phi_N$ at the lower T_{sub}. The last step is crucial to ensure growth of InGaN with targeted composition.

  Then the plasma is struck, and the InGaN layer of the required concentration and thickness is grown by controlling the shutters.

A.1.3   Growth condition optimization studies

In this section, we investigate and demonstrate (1) GaN/AlN heterointerface growth conditions for improved 2DHG transport, leading to (2) controlled 2DHG growths on large areas—quarter of a 2-inch wafer and eventually a full 2-inch wafer [63].

Optimizing the GaN/AlN Interface

A series of samples with ~13 nm UID GaN/AlN were grown at various substrate temperatures and metal-fluxes. The growths were first performed on 8 mm × 8 mm pieces of the starting substrate, mounted at the center of a 3-inch Si lapped wafer to prevent unintentional variation in fluxes from the measured beam equivalent pressure (BEP) before each growth. The samples were rotated at 20 rotations per minute (rpm) during growth.

By keeping the growth conditions of the AlN layer constant, we observed that Ga flux used for the growth of the top UID GaN layer had no perceivable effect on the 2DHG conductivity - as long as the Ga:N flux ratio was >1. Even for metal-rich conditions that lead to the formation of Ga-droplets, the 2DHG conductivity was not affected and the Ga droplets that remained on the surface after growth could be cleaned off by soaking in HCl.

On the other hand, clear trends were observed when the growth conditions of the AlN buffer layer was varied while keeping the GaN layer growth conditions the same. Since significant Al desorption from the growth surface is not expected at the typical growth temperature range of ~650°C - 790°C for Indium-mounted substrates [341], Al-rich AlN growth results in accumulation of excess
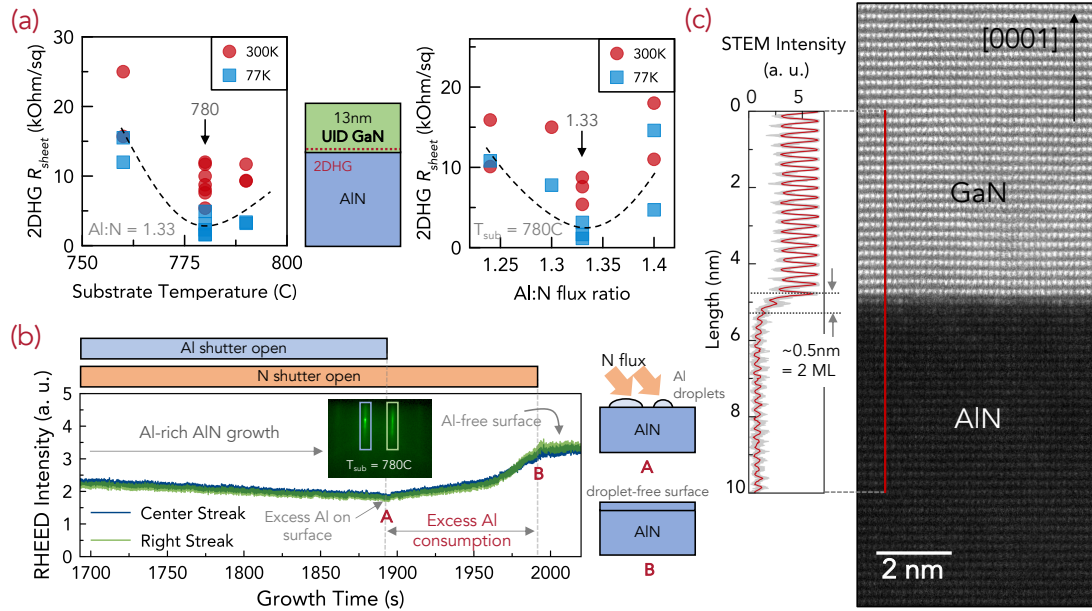
Figure A.3: MBE growth of smooth GaN/AlN interface for high-conductivity 2DHGs. (a) Variation in the sheet resistance of the 2DHG structure with AlN buffer grown at different substrate temperatures and Al:N flux ratios. For all samples, the growth condition for the 13 nm UID GaN on top was kept the same. A resistance minimum is observed for both the variables pointing to an optimum growth condition (dashed lines provided as a guide to the eye). (b) RHEED intensity versus growth time, showing the dimming RHEED as excess Al accumulates on the surface during Al-rich AlN growth. The excess Al droplets are then consumed be keeping just the N-shutter open after the AlN growth. The RHEED intensity brightens and intensity saturates once the excess Al is consumed by N (c) High-angle Annular dark field (HAADF) STEM along the [$\bar{1}$00] zone axis and corresponding line profile of the measured STEM intensity across the GaN/AlN interface. Profiles along 20 lattice lines (grey) are averaged (red), showing clear intensity difference from the Al and Ga atoms and the measured heterointerface is ~1-2 ML in thickness. *Figure from Chaudhuri et al. [63]*

Al metal on the growth surface, causing the resultant RHEED pattern to darken as growth progresses. This is shown in figure **A.3 (b)**. Al droplets on the AlN surface are undesired as they inhibit the formation of an abrupt GaN/AlN interface. To consume these Al droplets, the N shutter is kept open after a period of AlN growth while monitoring the RHEED brightness. The RHEED intensity slowly increases and saturates, indicating that all of the excess Al droplets

have been consumed to form AlN. This cycle of AlN growth followed by Al-consumption is repeated to grow the entire AlN buffer. A similar technique has previously been reported for low-temperature MBE growth of AlN by monitoring laser reflectometry signal [341]. Qualitatively, the amount of excess Al - which is determined by the Al:N flux ratio - can affect the AlN surface morphology. A low density of droplets might lead to incomplete coverage of the surface by AlN, whereas it might not be possible to consume a very high density of Al droplets uniformly. There should then exist an optimum Al:N flux for the smoothest AlN buffer surface, and consequently the sharpest GaN/AlN interface. This should be reflected in the 2DHG transport. **Figure A.3 (a)** shows that it is indeed the case - the 2DHG sheet resistance at both 77 K and 300K show clear statistical minima when plotted versus Al:N flux ratio and also the substrate temperature, with the best transport seen at T_{sub} = 780°C and Al:N flux ratio of 1.33. The hole densities in all samples measured are consistent with the expected polarization-induced charge of ~5×10^{13}, and the optimized low sheet resistance is a result of the improved mobilities.

The lowest 2DHG sheet resistances measured were ~6 kΩ/sq at 300 K and ~2 kΩ/sq at 77 K. These are some of the highest conductivity hole channels reported so far in III-nitrides. Temperature-dependent transport of these 2DHGs [3] show that the conductivity further increases as the temperature is lowered, down to sheet resistance of ~1 kΩ/sq at 10 K. The room temperature transport of the GaN/AlN 2DHG is dominated by acoustic phonons (AP) scattering [128, 5]. At the low temperatures of 77 K, phonons freeze-out and extrinsic scattering mechanisms such as due to interface roughness (IR) dominate. The AlN/GaN interface roughness has previously been shown to be important for the transport of 2D electron gas (2DEG) [342], especially at high charge densities. Similarly,

IR scattering likely plays a significant role in the transport at 77 K of the high-density 2DHGs at the GaN/AlN interface. The consumption of excess Al after Al-rich AlN growth at the optimum Al flux (Al:N ~1.33) and substrate temperature (780°C) are expected to result in high quality heterointerface, decreasing the IR scattering and thereby minimizing the 77 K sheet resistances in figure A.3(a).

An atomic-scale image of a GaN/AlN sample grown under optimal conditions was obtained by imaging the interface cross-section in a scanning transmission electron microscope (STEM). **Figure A.3 (c)** shows the high-angle annular dark field (HAADF) STEM image of the GaN/AlN lattice at the interface where the 2DHG is expected. The STEM intensity profile across the interface is plotted. The intensity profile was measured along 20 different lattice lines in the [0001] direction and averaged to highlight the variations. A clear contrast in STEM intensity between Ga and Al atoms is seen due to difference in their atomic numbers. A transition of ~0.5 nm between the Ga and Al atom layer indicates that under the optimized growth condition for 2DHG transport, the GaN/AlN interface is sharp to the order of ~1-2 ML.

Large area growths

The optimum growth conditions for the high conductivity GaN/AlN 2DHG were used for growths on larger area substrates. The structures used for these growths are differ from the UID GaN on AlN studied in the previous section by addition of a Mg-doped cap layer of (In)GaN on top of the UID GaN layer, which is desired for low resistance ohmic contacts to the 2DHG in a p-channel

transistor (see section 3.3).

Table A.1 summarizes the results of the large area growths. The heterostructure layer details of the wafers and the 300K sheet resistance maps are shown in **figure A.4**. Wafers B and C have a ~ 4% InGaN cap on top of the undoped GaN channel layer, with targeted Mg-doping densities of ~1×10^{19} cm^{-3} and ~5×10^{19} cm^{-3} respectively. The 2DHG sheet densities for each wafer were measured to be approximately uniform across the surface, with varying hole mobilities resulting in the sheet resistance distribution. Since the three wafers A, B and C have different heterostructures, the *uniformity* of the sheet resistances is compared and not their absolute values. The uniformity metrics as (1) Yield = Diced square pieces with a 2DHG / Total # of diced square pieces from the wafer, and (2) Standard deviation of the sheet resistances as a percentage of the mean. A high yield and a low standard deviation is desirable.

Table A.1: Wafer details for large area growths of GaN/AlN 2DHG structures and corresponding uniformity metrics. *considers only the inner 85% area of the full-wafer C

Wafer	Size	Yield	Mean R_{sh} (kΩ/sq.)	Std. Dev.
A	Quarter of 2″	30%	21	15.7%
B	Quarter of 2″	87.5%	10.5	15.8%
C	Full 2″ wafer	100%	13.3	35.8%
			11.4*	20.7%*

Wafer A was grown on a quarter of a 2-inch substrate wafer using the same growth conditions as described in section A.1.3 - the sample was In-mounted on the center of a 3-inch lapped Si wafer, and rotated at 20 rpm (3 sec/rotation). As seen in **figure A.4**, 2DHGs were present in only 4 out of 13 pieces, resulting in a low yield of 30% - indicating a non-uniform growth. The growth rate used for
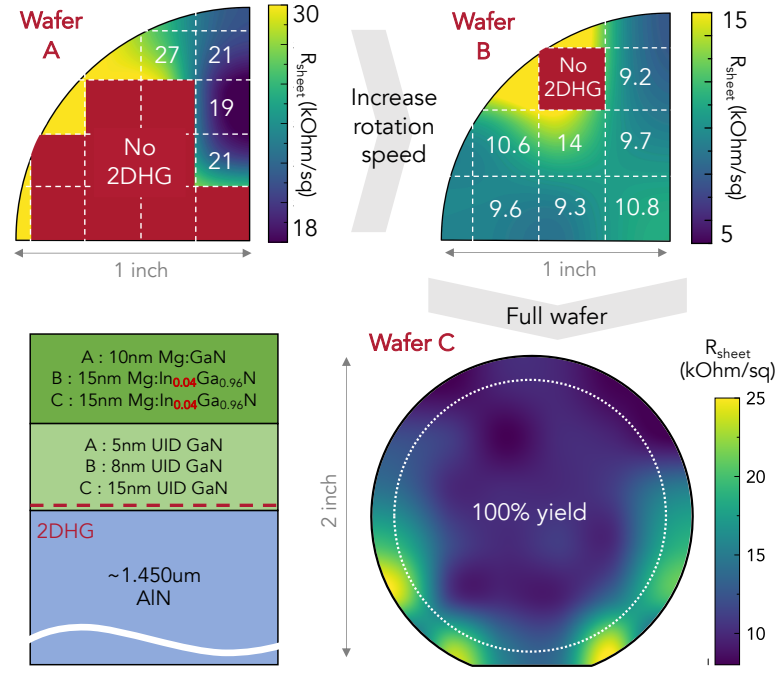
Figure A.4: Sheet resistance maps (300 K) of the 2DHG wafers grown using MBE, along with the corresponding heterostructure details. Wafer A was rotated at 20 rpm; wafers B, C were rotated at 30 rpm during growth. The red regions on the maps indicate areas where no 2DHG was measured (high-resistance, $R_{sh} > 1$ MΩ/sq). The dashed circle inside the full wafer C indicate the area with high-uniform transport. *Figure from Chaudhuri et al. [63]*

this growth was 520 nm/hr or ~1.7 s/ML. Thus, at a rotation speed of 20 rpm, the effective growth rate is ~2 ML per rotation which could be a possible cause of non-uniformity.

To tackle this, wafer B was grown at an increased rotation speed of 30 rpm corresponding to effective growth rate of ~1 ML per rotation, keeping the rest of the growth conditions identically. An increase in the uniformity was observed, with only one piece without a 2DHG, pushing the yield up to 87.5%. Following this result, a third sample - a full 2-inch wafer C, was grown under the same conditions as wafer B. 2DHG conductivity was observed across the whole wafer - a yield of 100%. The lack of carrier freeze-out and increase in their conductiv-

ity at 77 K confirmed that the conductivity was due to a 2DHG. Though the standard deviation of sheet resistance is higher for the entire wafer C compared to wafers A/B, if we consider only the inner ~85% of the wafer surface (dotted circle in **figure A.4**), the standard deviation decreases to 20.7%. This points to a high uniformity in the central part of wafer C. Further study is necessary to understand nominally-higher 2DHG sheet resistances than the small pieces grown under the similar conditions.

A.2 PA-MBE growth of AlN/GaN/AlN 2DEGs

This section presents the detailed growth recipe of the AlN/GaN/AlN bilayer heterostructures, the transport and device applications of which were discussed in chapter 5 and 4. The AlN on SiC MBE-growth recipe is also used to grow the wafers for the epitaxial AlN BAW in chapter 6.

The AlN/GaN/AlN heterostructures are grown in a Veeco Gen10 plasma assisted molecular beam epitaxy (PA-MBE) system, with standard effusion sources for Ga, Al and an RF plasma source for N. High-resistivity, Prime Grade 6H-SiC wafers from II-VI Advanced Materials are used as starting substrates. Before growth, these wafers are sent for CMP polishing on the Si-face to Nova-SiC [286] to enhance the epitaxial starting surface for step-flow growth. The SiC substrates are diced into 10 mmm × 10 mm pieces. Before loading into the MBE system, the substrates are ultrasonicated in acetone, methanol and iso-propanol for 15 minutes each and mounted on lapped 3-inch Si wafers using molten indium, Si face up. They are then outgassed at 200°C for 7 hours and 500°C for 2 hours under vacuum before introducing into the MBE growth chamber. For

the active nitrogen flux during growth, the RF plasma power is kept at 400 W and the N gas flow rate is set at 2 sccm, corresponding to a calibrated N-limited growth rate of 0.52 μm/hour. Magnesium and silicon dopant cells are kept cold throughout the growth. Reflection high energy electron diffraction (RHEED) is used for in-situ monitoring of the growth. The growth chamber pressure is $\sim 2.01 \times 10^{-5}$ Torr during the growth.

A.2.1   in-situ Cleaning of 6H-SiC

Before strating the growth, it is necessary to clean the SiC surface to get rid of the contaminants using Ga polishing technique. The process is shown in **figure A.5**. The SiC substrate is heated up to 780°C with the background chamber pressure at $< 10^{-7}$ Torr. The Ga cell temperature is raised to corresponding to BEP flux of $\sim 4.5 \times 10^{-7}$ Torr. For the polishing, the Ga shutter is first opened for 30 s to deposit Ga on the SiC surface and then closed to allow for the Ga atoms to desorb from the surface. This is then repeated for 10 to 12 cycles.

The surface is monitored using RHEED along the [$\bar{1}$100] azimuth. The RHEED pattern during the first cleaning cycle is shown in **figure A.5**. The intensity of the specular beam is tracked during the successive cleaning cycles. Two changes are observed - (1) the RHEED intensity of the Ga absorption-desorption process slowly starts showing a 2-step behavior, (2) the (1/3, 1/3) beams in the RHEED pattern appear, corresponding to a ($\sqrt{3} \times \sqrt{3}$)R30° reconstruction [343]. The reconstruction is sign of the O atoms being removed from the SiC surface through the chemical reaction $SiO_2 + 2Ga \rightarrow SiO \uparrow + Ga_2O \uparrow$ and leaving a clean surface of SiC to start the growth. The substrate is cooled to 750°C after
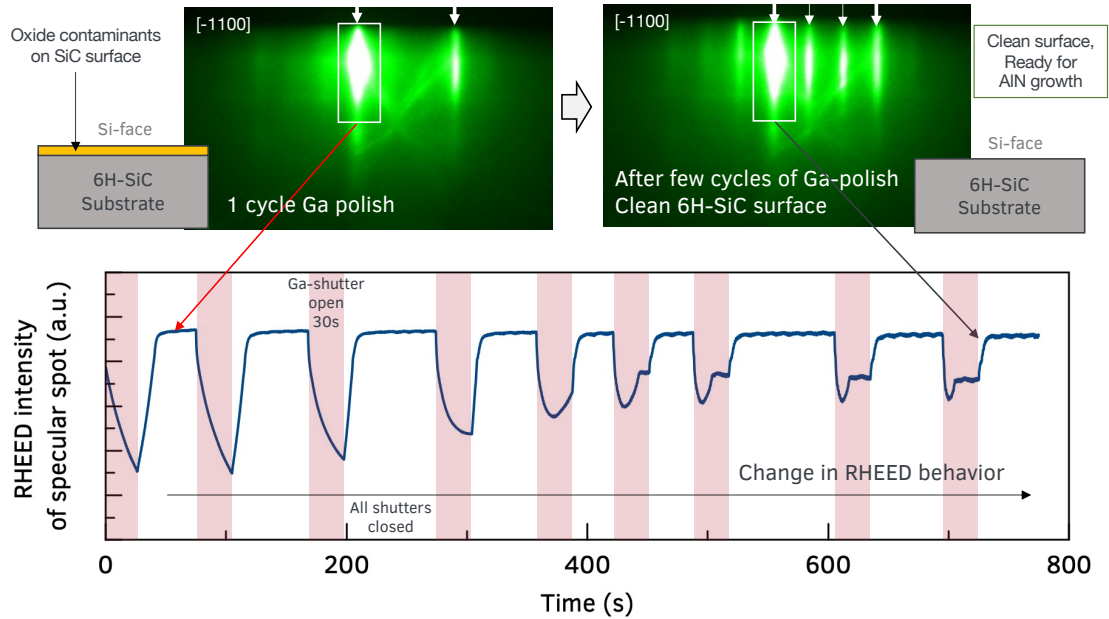
Figure A.5: in-situ cleaning of Si-face of 6H-SiC substrate using Ga desorption. Ga metal is incident on the SiC surface for 30 sec and then allowed to desorb. The intensity of the specular RHEED beam tracked over mulitple cycles. A change in RHEED intensity behavior is observed after 10-12 cycles, which corresponds to appearance of a ($\sqrt{3} \times \sqrt{3}$)R30° reconstruction in the RHEED pattern. This indicates a clean 6H-SiC starting surface.

the cleaning.

N flow is then started and the RF plasma is struck. An interesting phenomenon is observed during the plasma stabilization on the Gen10. The stabilization typically takes about 10 mins before start of the growth. During this time, the (1/3, 1/3) beam in the RHEED slowly disappears within the first 2 mins. **Figure A.6** shows the evolution of the RHEED profile over time. The origin of this behavior is still unclear. Oxygen contamination is unlikely since the oxygen level is very low in the MBE chamber (confirmed through RGA). One possibility for this observation is that the active nitrogen species leaking from the shutter deposits on the SiC surface and modifies the surface reconstruction. Nevertheless, the substrate is now ready for heterostructure growth.
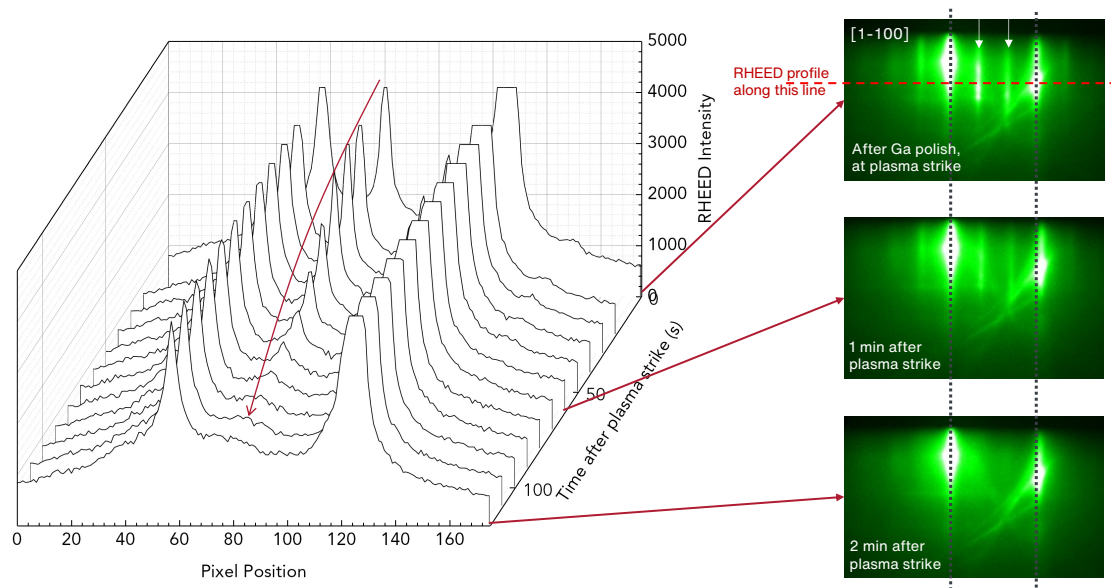
Figure A.6: The (1/3, 1/3) beams in the $(\sqrt{3} \times \sqrt{3})R30°$ reconstructed RHEED from a clean SiC surface slowly vanishes after the plasma is struck (but N shutter is still closed). The reason for this observed behavior is still unclear.

A.2.2 Detailed Growth Recipe
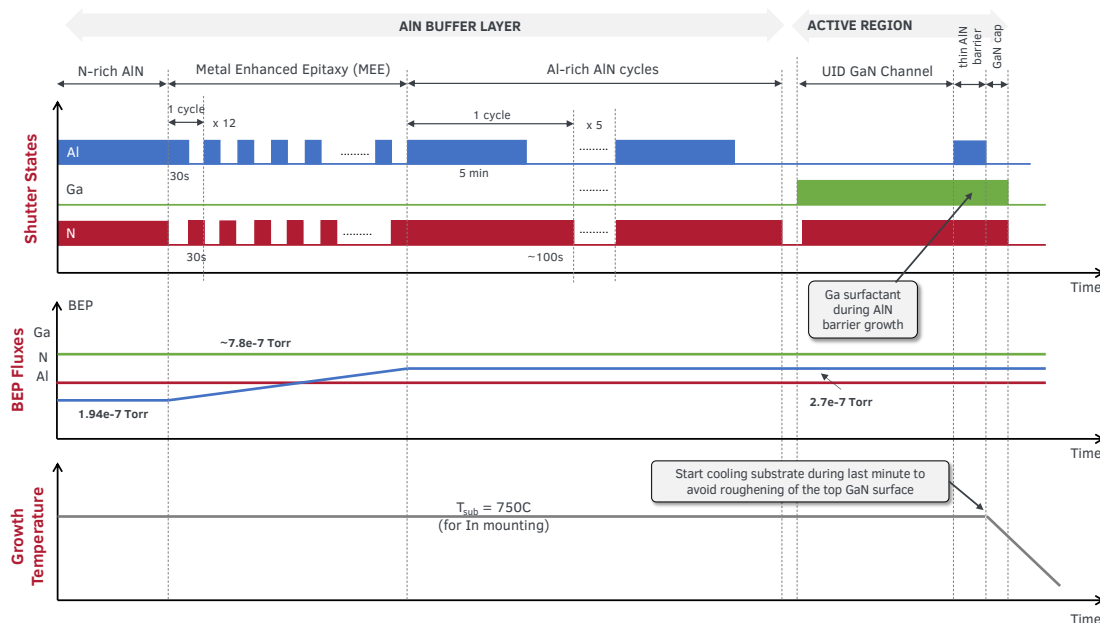
Figure A.7: Timing diagram for MBE growth of an undoped, AlN/GaN/AlN 2DHG structure, with thin AlN barrier layer of < 10 nm.

The growth recipe for the AlN/GaN/AlN HEMT structure with a *thin AlN*

barrier (< 10 nm) and GaN passivation layer, is illustrated in the timing diagram in **figure A.7**. The sample is kept at T_{sub} = 750°C throughout the epi-stack growth. The first ~50 nm of AlN is grown under N-rich conditions by opening both Al and N shutter simultaneously at Al BEP of ~ 6.1×10^{-7} Torr, corresponding to an Al:N flux ratio ~0.9. The Al cell temperature was then ramped up at 3°C/min to a final BEP flux of ~ 2.7×10^{-7} Torr (Al:N flux ratio ~1.1). While the cell temperature ramped up, migration enhanced epitaxy (MEE) cycles are performed to smoothen out the growth surface by alternatively opening and closing the Al and N shutters for 30 s each. The N-rich nucleation layer blocks the Si up diffusion from the SiC surface and it from incorporating in the Ga channel [141, 142].

Once the Al cell is at the targeted cell temperature corresponding to BEP flux of ~ 2.7×10^{-7}, the rest of the buffer is grown under metal-rich AlN condition by opening both the Al and N shutters simultaneously. Since Al desorption rate from AlN growth surface is negligible at T_{sub} = 750°C, the accumulated Al metal is periodically consumed after 5 mins of AlN growth by closing the the Al shutter and keeping the N shutter open. The consumption of Al is monitored by tracking the saturation of the RHEED pattern intensity [63]. A total of ~ 550 nm thick AlN buffer was grown in this manner. This technique of consumption of excess Al on the surface also ensures a sharp, abrupt AlN-GaN interface [63].

After the buffer growth, the Ga shutter is opened for 10 s at a Ga BEP flux of ~ 7.8×10^{-7} Torr before the N shutter is opened to wet the growth surface, following which the N shutter is also opened to grow the UID-GaN channel. After the required thickness of GaN, the Al shutter is opened *while keeping the Ga shutter open* to grow the AlN barrier. The Ga does not incorporate in the barrier

but acts as surfactant during the AlN growth, thanks to the thermodynamic preference of N to form AlN over GaN in the presence of both species. The Al shutter is then closed to grow the GaN passivation layer, after which all shutters are closed and the plasma is killed. Care is taken to avoid keeping the sample at high temperature ≥ 750 C and/or with N shutter open since it will result in the roughening of the GaN surface. However that is not a concern if the top layer is AlN.

A few additional notes regarding the MBE growth are as follows :

- The AlN/GaN/AlN HEMT stack uses a N-rich AlN nucleation layer on SiC to stop the contamination of Si. However, for applications where the chemical properties of the crystal are not that important and/or the Si riding is tolerable, the N-rich layer not necessary. Instead metal rich AlN nucleation with Ga surfactant results in a better crystal quality. It has been reported that Ga acts as a surfactant for promoting step flow growth mode of AlN on 6H-SiC with suitable starting surface [287]. **Figure A.8 (a)** shows the timing diagram of this technique. About 10 s of Ga flux at $\sim 6.2 \times 10^{-7}$ Torr is incident on the clean SiC surface before opening the N and Al shutter simultaneously. This Ga "pre-deposition" leads to marked difference in the final crystal quality and surface of the AlN crystal. **Figure A.8 (b,c,d)** compares two samples with 600 nm of AlN grown on SiC under same growth conditions except for one difference. One was grown with the Ga pre-dep step before nucleation and the other without. Even though both the surfaces are very smooth in an atomic force microscope (AFM) scan, a marked difference in the morphology is observed. In the sample without Ga pre-dep, spiral features are visible, which are signs of

screw dislocations [147]. These spirals are completely lacking in the AFM of the sample with Ga pre-dep indicating a low screw dislocation density in the crystal. This is corroborated by X-ray diffraction rocking curve scan along AlN (002). The sample with Ga pre-dep shows an order of magnitude lower FWHM, corresponding to estimated 3 orders reduction in screw dislocation density from $\sim 10^9$ cm^{-2} to $\sim 10^6$ cm^{-2}.

The Ga pre-dep is a critical step, which requires low N leakage when shutter closed [344], low N plasma stabilization time [344] and optimal Ga flux [345]. This technique is especially promising for applications such as the epitaxial AlN for BAW, where the Si floating on the AlN growth front is not of particular concern.

- The above growth recipe for AlN/GaN/AlN HEMTs does not include any impurity blocking layers (IBLs) [8] in AlN buffer layer. This is because the N-rich AlN layer has been shown to be effective in stopping the Si up diffusion in PA-MBE AlN on SiC [142, 141]. Additionally even if some Si, O do float up from the substrate, they are expected to incorporate at the GaN/AlN lower interface which is >20-30 nm away from the 2DEG at the AlN/GaN top interface (depending on the GaN channel thickness) and should not influence the transport of the 2DEGs. Hence IBLs are typically not required for the HEMTs.

  However, for applications which make use of both the 2DEG and 2DHG in the AlN/GaN/AlN heterostructure - for example, light emission from bilayer, 2DHG as a backgate etc., the 2DHG transport properties are also equally valuable. In those cases it is recommended to include the IBLs in the AlN buffer layer. The buffer growth will then follow the same steps as shown in **figure A.1**.
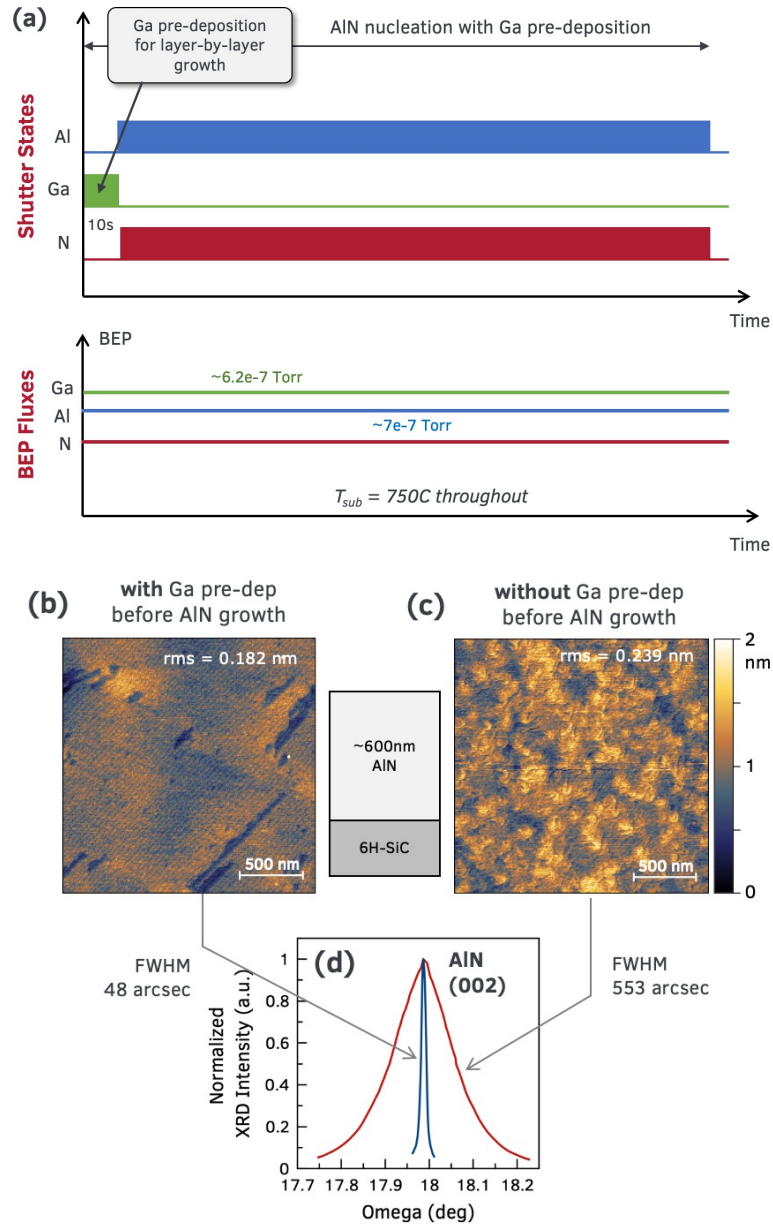
Figure A.8: (a) Timing diagram showing the metal-rich nucleation of AlN on SiC using Ga as a surfactant. The Ga metal is deposited before opening the Al and N shutters, to promote layer-by-layer growth. (b) Compares the quality of 600 nm AlN film grown under metal-rich conditions with and without the Ga pre-dep step. The sample with Ga showed orders lower screw dislocation density, evidenced from the lack of spirals in the surface AFM and (002) AlN FWHM of 48 arcsec.

- In the above recipe, the substrate temperature T_{sub} corresponds to the thermocouple temperature T_{tc} of an SiC piece mounted on Si wafer with In-

dium, not the surface temperature. Thus the T_{tc} needs to be adjusted if the mounting method is modified, for example, when using faceplates.
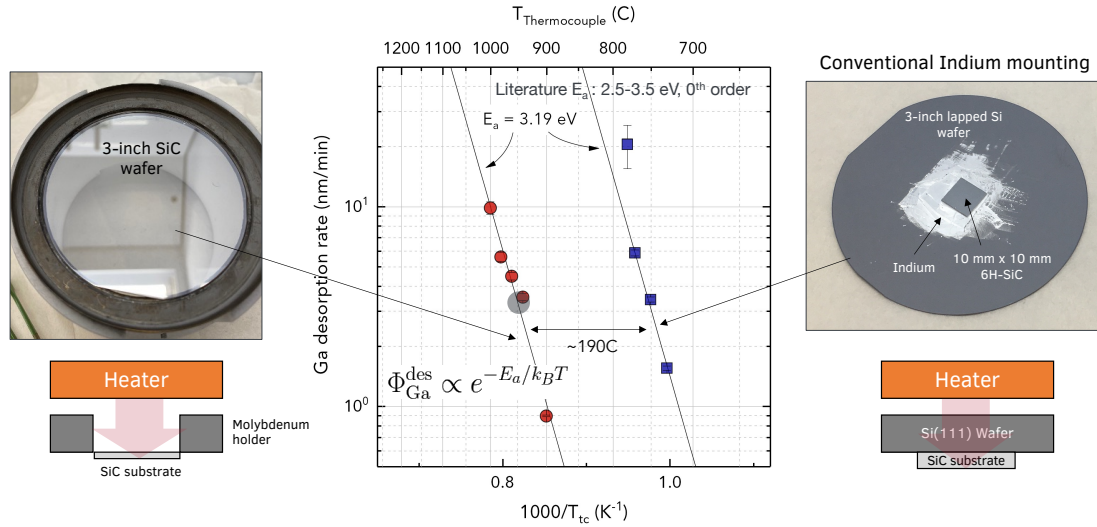
Figure A.9: Comparison of the surface temperature of a SiC substrate wafer with and without Indium mounting using Ga desorption time. The surface temperature on the faceplate mounted wafer is ~190°C cooler than indium-mounted wafer at the same thermocouple temperature.

As an example, for the full 3-inch wafer HEMT growths, the SiC substrate wafer is directly loaded onto the 3-inch molybdenum block in the MBE chamber without any backside metal coating. SiC is transparent to IR radiation because of which, at the same T_{tc}, the actual surface temperature of the SiC full wafer is lower compared to an indium-mounted SiC substrate piece. The temperature offset between different mounting schemes is be quantified by comparing the desorption times of a fixed known Ga flux. **Figure A.9** plots the Ga desorption time as a function of the T_{tc} for the similar SiC substrate wafer with and without indium mounted. The indium mounted SiC surface is about 190°C hotter than the faceplate mounted SiC wafer at the same T_{tc}. Hence applying an offset to the substrate temperatures used in the recipe above is necessary in this case while keeping the rest of the growth conditions same.

A.2.3   *in-situ* AlN passivated AlN/GaN/AlN HEMTs
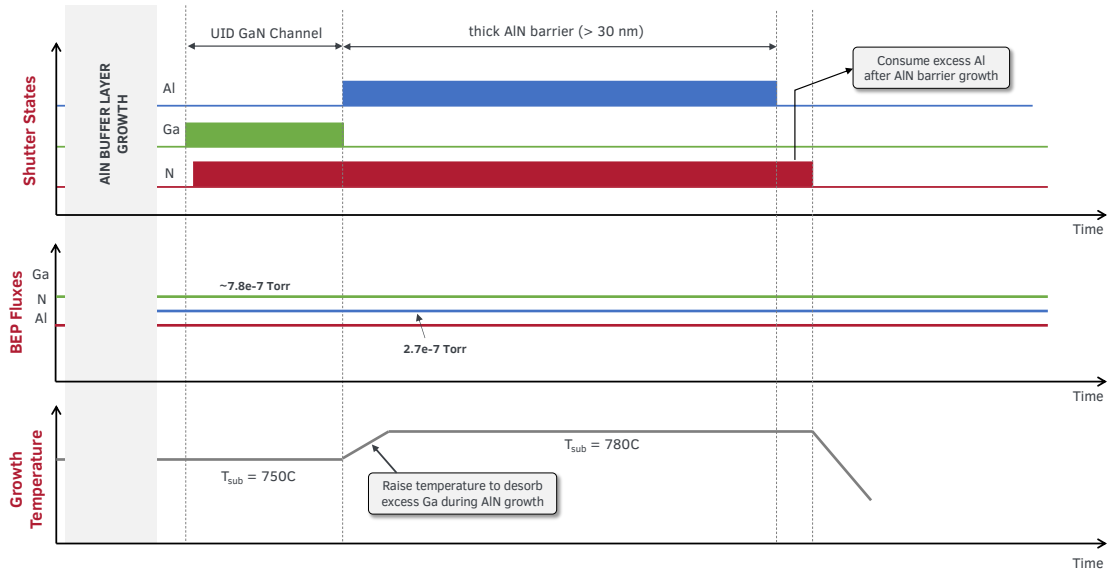
Figure A.10: Timing diagram for the modified active region recipe for an in-situ passivated AlN HEMT with thick AlN barrier layer. The nucleation and buffer layers' growth is same as shown in figure A.7.

The growth recipe in **figure A.7** is suitable for AlN/gaN/AlN HEMT structure with thin (~ 5-10 nm) top AlN barriers. Certain modifications need to be incorporated to grow the in-situ passivated HEMT structures with thick, > 30 nm top AlN barrier. The modified recipe is shown in the timing diagram in **figure A.10**. After the AlN buffer layer and GaN channel layer growth, the Al shutter is opened and Ga shutter is closed, while keeping the N shutter open throughout. During the AlN growth, the substrate temperature is raised to 770°C. This enhances the desorption rate of the excess Ga metal on the surface which has accumulated during the GaN channel layer growth. Since the AlN top layer growth is > 6 min long, all the Ga is desorbed by the time the AlN layer growth finishes. After that, the Al shutter is closed and N kept open to consume the excess Al on the surface. This is tracked by the RHEED intensity, which increases and saturates once all the Al is consumed. Finally, all shutters are closed, RF

plasma is killed and the sample is cooled down to finish the growth.

APPENDIX B

BULK ALN PLATFORM

Unlike Si, III-nitride semiconductors currently lack low-cost, large-diameter, high-quality native substrates for homoepitaxial growth. Right since the 1990s, the community has gotten get around this by developing growth techniques on foreign substrates like SiC, Sapphire, Si. The choice of substrate is dictated by the application and cost-performance ratio. Driven by the potential performance gains in vertical transistors lasers and (visible) LEDs, there is an ongoing effort in the field to develop high-quality native substrates. HVPE grown bulk GaN substrates have recently become commercially available and have enabled high performance vertical diodes as well as transport studies [4, 346, 347, 348].

Similarly, physical vapor transport (PVT) grown bulk AlN substrates are now available in up to 2-inch diameter wafers sizes [285]. These are mainly driven by UV LEDs and laser development, and were instrumental in the demonstration of the first UV-C Laser [349]. Other electronic devices are also being investigated on the bulk AlN substrates [310, 279] with promising performance gains thanks to the ultra low dislocation densities of 10^4 cm^{-2}. As of now, the cost of these substrates are very high, limiting their use in high-performance applications and scientific investigations. But with further research and development they are poised to get cheaper and see mainstream adoption soon.

This chapter aims to serve as a motivation for studies of electronic devices beyond vertical transistors and LEDs on these bulk AlN substrates. Bulk AlN is the native substrate for the AlN-platform transistors discussed in this dissertation, and is the structurally purest realization of these heterostructures. This chapter summarizes the potential gain in performance expected for the AlN-

platform lateral transistors on bulk AlN substrate.

Results of some of the recent studies at the Jena-Xing Group in growing these heterostructures on bulk AlN are also presented, which are enabled by new advancements in MBE homoepitaxy of AlN [65, 64].

B.1 Single-crystal AlN substrates for transistors

Single crystal bulk AlN substrates provide a number of potential advantages to a lateral transistor thanks to its low dislocation densities of $10^4 - 10^5$ cm^{-2} and high thermal conductivities of ~ 340 W/m.K. **Figure B.1 (a)** summarizes the advantages of an AlN/GaN/AlN RF HEMT on bulk AlN vs on conventional substrate such as SiC and Si. These advantages are equally applicable for p-channel GaN/AlN FETs too. These can be broadly classified as follows :

- **Higher breakdown voltages through reduced gate leakage** :

    High breakdown voltage is desired in an RF HEMT to maximize the voltage handling capability. In a typical lateral III-nitride semiconductor FET, the breakdown is limited by the leakage of carriers from the channel to the gate instead of the channel semiconductor critical field. This leakage is either by Fowler-Nordheim tunnelling, or through charged threading dislocations which act as leakage paths. Typically heteroepitaxial AlN HEMTs on SiC or Si have dislocation densities in the order of than $10^9 - 10^{10}$ cm^{-2} due to the lattice mismatch. For a 100 nm long and 50 μm wide gate, this corresponds to ~ 50000 leakage paths. In a high-quality bulk AlN, the dislocation density is 6 orders lower at $10^4 - 10^5$ cm^{-2} which results in 1 leakage path in every 20 transistors instead. Hence a lower dislocation

(a)

(b)
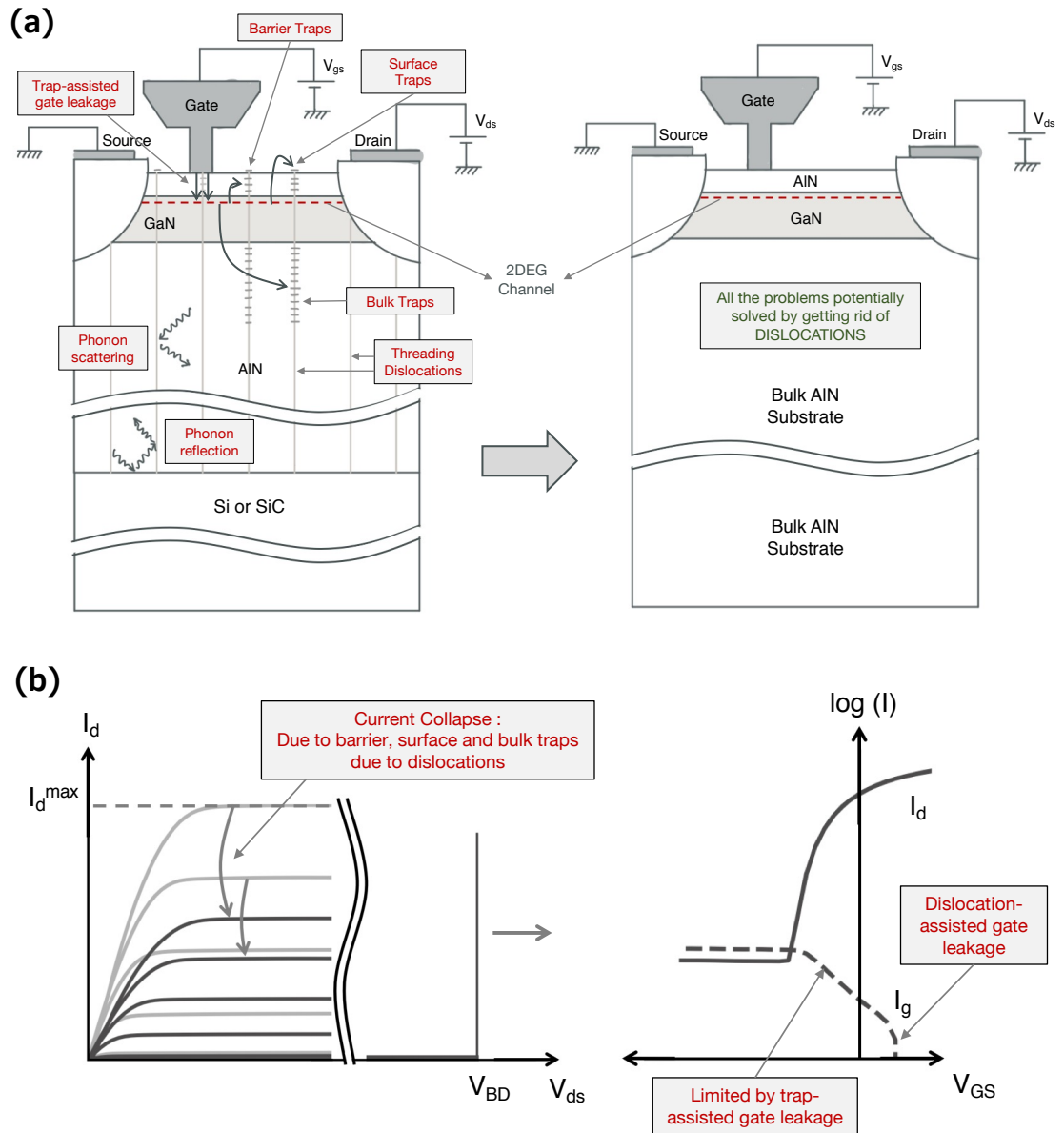
Figure B.1: Advantages of a low-dislocation single crystal AlN substrate for AlN-based HEMTs. (a) cartoon showing how the bulk AlN substrate eliminates the dislocation related traps, phonon scattering in the bulk and thermal boundary resistance at the buffer-substrate interface. (b) These result in lower current collapse amd suppression of gate leakage current. These advantages equally apply for p-channel transistors on bulk AlN as well.

mediated gate leakage is expected, which should translate to higher on-off ratios and higher breakdown field, closer to the material limits.

- **Higher currents through reduced current collapse :**

Under high operation biases, the charges from the transistor channel are trapped in surface traps, bulk traps, buffer traps present near the active region. Since these traps respond slowly to the applied RF signal, they do not contribute to current flow at high frequencies and cause a current collapse. This is observed as a reduction in current knee and increase in R_{ON} during pulsed measurements under high quiescent bias conditions. In an AlN HEMT on SiC or Si, these traps are introduced by the threading dislocations. If each threading dislocation contributes one deep-level bulk trap per unit cell, then a dislocation density of 10^{10} cm^{-2} gives trap density of $\sim 10^{18}$ cm^{-3}. By moving to bulk AlN substrates, the bulk traps density also reduces by 6 orders to around $\sim 10^{12}$ cm^{-3}. This should translate to fewer charge being trapped, lower current collapse, and low device degradation.

Combined with higher breakdown voltages, this increases the theoretical maximum output power of the transistor.

- **Higher reliability through better thermal performance :**

The output powers from GaN HEMTs are not limited by the material, but by their thermal performance instead [111]. It is understood that thermal management is the key to achieving higher powers in high-frequency HEMTs. The AlN platform provides an advantage over GaN HEMTs in this regard because of higher thermal conductivity of the buffer layer (see section 5.2) and lower thermal boundary resistances on Si and SiC substrates, and has been experimentally shown to result in cooler channel temperatures than GaN HEMTs. Use of Bulk AlN substrates is expected to further improve the thermal performance.

A transistor operating as an amplifier converts the power delivered by the DC bias P_{DC} to amplify the input AC signal. Depending on the power

(a)

Wide-die approx. – line heat source

1 W

50 um

Epi-stack

Substrate

1 um

Cylindrical Flow

Thermal Boundary Resistance

50 um

Cylindrical Flow

Heat Sink

Temperature profile

(b)

		Top layer = AlN				Top Layer = GaN			
Substrate =		SiC	Si	Diamond	Bulk AlN	SiC	Si	Diamond	Bulk GaN
Thermal Conductivities of (W/mK)	Top Layer	340	340	340	340	160	160	160	230
	Substrate	420	150	2000	340	420	150	2000	230
Thermal Boundary Resistance (x 10^{-9} m^{2}K/W)		5.1	1.7	16	0	3.6	30	12	0

(c)   **(d)**

Figure B.2: (a) Simple model representing a heat disspation by a HEMT as a wire disspating 1 W of power into the 1 μm thick buffer layer on a 50 μm thinned substrate. Because of the dimensions, the heat flow can be assumed to be cylindrical. (b) The values of thermal conductivities and boundary resistances used in this model, representing the best reported values in the literature. (c) Calculated rise in temperature as a function of depth for AlN and GaN buffer layers on different substrates (Si, SiC, native). AlN-on-AlN shows the lowest surface temperature rise, thanks to the absence of thermal bounary resistance.

added efficiency *PAE* of the transistor, part of the input power is dissipated as heat into the crystal $P_{diss} = P_{DC}(1 - PAE)$. In the absence of topside heat sink, this heat is carried by phonons vertically downwards from

the active region on the surface to the heat sink under the substrate. Unimpeded flow of heat is desired to avoid the rise in channel temperature. The presence of crystal imperfections (dislocations) increases the phonon scattering in this path, thereby contributing to rise in the channel temperature. Thus, lower dislocations in the bulk AlN has an advantage in this regard.

Furthermore, the AlN-substrate interface acts as a thermal resistor in the phonon flow path because of the mismatch in phonon density of states [52]. This is quantified as thermal boundary resistance or TBR. It causes a rise in temperature at the interface due to phonon reflections. In the case of homoepitaxial AlN on bulk AlN substrate, there is no buffer-substrate interface, and hence no TBR.

This thermal advantage in an FET can be quantified using a simple heat flow model, show in **figure B.2**. The drain side of the HEMT dissipating heat is represented as a line heat source of width W_G = 50 μm under a wide die approximation. It is dissipates P_{diss} = 1 W as heat into a t_{buffer} = 1 μm thick AlN or GaN buffer layer, which is on a t_{sub} = 50 μm thick substrate. The setup is shown in **figure B.2 (a)**. Because t_{sub} ~ W_G, the temperature rise due to the heat conduction away from the channel can be approximated as a cylindrical heat flow model [350].

According to Fourier's cylindrical heat flow model, the temperature difference ΔT along two points r_1 and r_2 distance away from the heat source is given by :

$$\Delta T = \frac{P_{diss}}{2\pi W_G \kappa_{th}}.Ln\left(\frac{r_1}{r_2}\right),$$
(B.1)

where κ_{th} is the thermal conductivity of the material through which the heat is flowing.

The buffer layer-substrate interface also acts as a resistor, characterized by its TBR R_{BR}. The temperature difference at the interface is then given by :

$$\Delta T_{TBR} = \frac{P_{diss}}{2\pi W_G t_{\text{buffer}}} R_{BR}.$$ (B.2)

Figures B.2 (c), (d) show the calculated temperature profile along the line perpendicular to the surface for AlN and GaN buffers layers respectively on different substrates. The highest reported experimental thermal conductivities and lowest experimental TBRs for the respective materials, listed in **table B.2 (b)**, are used to represent the best case scenarios. The model clearly shows that AlN buffer layer on bulk AlN susbtrate results in the lowest surface temperature. It beats AlN on diamond thanks to the absence of TBR, and GaN on bulk GaN thanks to higher thermal conductivity.

Although this model ignores the effect of dislocations and, more importantly, lateral heat spread, it still highlights the importance of TBR in determining the surface temperature during high power operation. A cooler surface should results in higher power outputs in AlN HEMTs on bulk AlN, compared to GaN and AlN HEMTs on other substrates.

B.2 Early results

Motivated by the above advantages of high-quality bulk AlN substrates and its recent availability [285], numerous efforts in the field to explore their effect on electronic lateral device performance. Recently GaN HEMTs growth on bulk AlN from Fujitsu [279] have demonstrated power outputs up 15 W/mm in X-
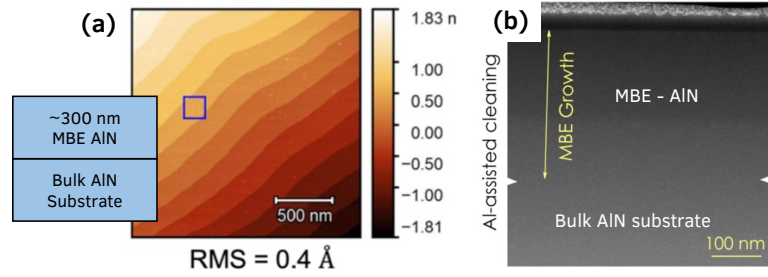
Figure B.3: (a) Representative atomic force microscopy (AFM) scan of a 300 nm homoepitaxial AlN film grown using MBE shows very smooth surface with atomic steps and no sprial features. (b) The cross-sectional TEM showing the lack of an observable boundary between the MBE grown film and substrate - a sign of true homoepitaxy! *Figures from Lee et al. [64] and Cho et al. [65]*

band. Khachariya et al. from NCSU recently showcased [310] very high breakdown fields >9 MV/cm in AlGaN HEMTs on bulk AlN substrates.

In the Jena-Xing Group, there is ongoing effort to realize AlN-based transistors on these bulk AlN substrates. Recently, Lee et al. [64] and Cho et al. [65] developed ex-situ and in-situ cleaning steps critical to for growing high-quality homoepitaxial AlN using on bulk AlN substrates using PA-MBE. The representative structural characteristics of these films are shown in **figure B.3**. Atomic force microscopy (AFM) scan of the surface shows smooth, atomic terraces with no spiral hillocks, signifying step-flow growth mode and low dislocations. In the cross-sectional TEM image, no boundary is visible between the substrate and epitaxial AlN layer, confirming ideal homoepitaxy.

Building on these growth advancements, GaN/AlN 2DHGs [30] and AlN/GaN/AlN 2DEGs [66] have been also been grown recently using MBE on bulk AlN substrates in the Jena-Xing Group. **Figure B.4** compares the Hall transport of these 2D carriers grown on bulk AlN vs grown on foreign substrates (SiC/AlN templates) [3, 47]. At room temperature, the 2DEG, 2DHG mobilities on bulk AlN are to those measured on SiC or templates. But low temperature
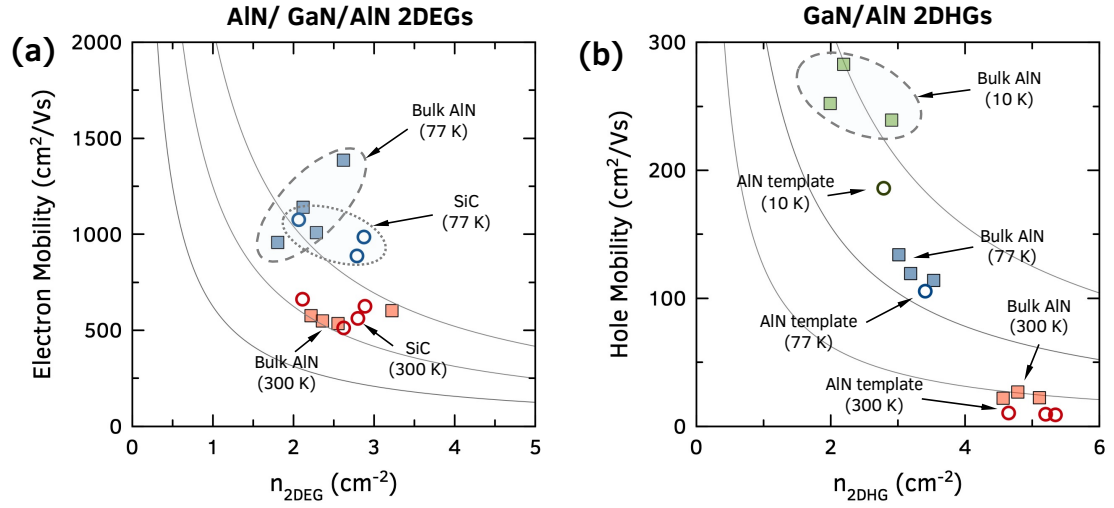
Figure B.4: Comparison of (a) 2DEGs and (b) 2DHGs on bulk AlN substrates and foreign substrates (AlN on sapphire template, SiC). While the room temperature mobilities are comparable, the low temperature mobilities of the 2DEGs/2DHGs on bulk AlN show significant improvement over those on template/SiC. This could be due to the reduced dislocation scattering and/or interface roughness scattering thanks to the low threading dislocation densities in the bulk AlN substrates. *The bulk AlN 2DEG data is from Encomendero et al. [66] and 2DHG data is from Zhang et al. [30]*

mobilities at 10 K are higher on the bulk AlN platform for both the 2DEG and 2DHG. This suggests a reduced scattering from an extrinsic mechanism, most likely dislocation scattering.

These 2DEGs, 2DHGs are currently being made into transistor channels for demonstrating GaN/AlN pFETs and AlN/GaN/AlN HEMTs on bulk AlN. A comparative study between these and the ones on SiC/template substrates will be valuable comparison and hopefully experimentally validate the theoretical predictions listed in the previous section.

Although foreign substrates like sapphire, Si and SiC will dominate the III-nitride semiconductor market in the near future by offering a balance between cost and performance, single crystal AlN substrate will definitely find niche ap-

plications (SATCOM, defense) to cater where the higher performance is desired over cost. But more excitingly, the substrates will tremendously help scientific investigations by offering structural and chemically pure epitaxial crystals for transport experiments.

BIBLIOGRAPHY

[1] F. Bernardini, V. Fiorentini, and D. Vanderbilt, "Spontaneous polarization and piezoelectric constants of III-V nitrides," *Physical Review B - Condensed Matter and Materials Physics*, vol. 56, pp. R10024–R10027, 10 1997.

[2] I. Vurgaftman and J. R. Meyer, "Band parameters for nitrogen-containing semiconductors," *Journal of Applied Physics*, vol. 94, no. 6, pp. 3675–3696, 2003.

[3] R. Chaudhuri, S. J. Bader, Z. Chen, D. A. Muller, Huili, Xing, and D. Jena, "A polarization-induced 2D hole gas in undoped gallium nitride quantum wells," *Science*, vol. 365, no. 6460, pp. 1454–1457, 2019.

[4] M. Horita, S. Takashima, R. Tanaka, H. Matsuyama, K. Ueno, M. Edo, T. Takahashi, M. Shimizu, and J. Suda, "Hall-effect measurements of metalorganic vapor-phase epitaxy-grown p-type homoepitaxial GaN layers with various Mg concentrations," *Japanese Journal of Applied Physics*, vol. 56, p. 031001, 3 2017.

[5] S. J. Bader, R. Chaudhuri, M. F. Schubert, H. W. Then, H. G. Xing, and D. Jena, "Wurtzite phonons and the mobility of a GaN/AlN 2D hole gas," *Applied Physics Letters*, vol. 114, no. 25, 2019.

[6] D. E. Aspnes and A. A. Studna, "Schottky-barrier electroreflectance: Application to GaAs," *Physical Review B*, vol. 7, no. 10, pp. 4605–4625, 1973.

[7] L. Janicki, R. Chaudhuri, S. J. Bader, H. G. Xing, D. Jena, and R. Kudrawiec, "Electric Fields and Surface Fermi Level in Undoped GaN/AlN Two-Dimensional Hole Gas Heterostructures," *Physica Status Solidi - Rapid Research Letters*, vol. 15, 4 2021.

[8] R. Chaudhuri, Z. Chen, D. Muller, H. G. Xing, and D. Jena, "High conductivity Polarization-induced 2D hole gases in Undoped GaN/AlN Heterojunctions enabled by Impurity Blocking Layers," *Journal of Applied Physics*, vol. 130, no. 025703, 2021.

[9] T. Takeuchi, H. Takeuchi, S. Sota, H. Sakai, H. Amano, and I. Akasaki, "Optical properties of strained AlGaN and GaInN on GaN," *Japanese Journal of Applied Physics, Part 2: Letters*, vol. 36, p. L177, 2 1997.

[10] M. Leyer, J. Stellmach, C. Meissner, M. Pristovsek, and M. Kneissl, "The critical thickness of InGaN on (0 0 0 1)GaN," *Journal of Crystal Growth*, vol. 310, no. 23, pp. 4913–4915, 2008.

[11] A. Fischer, H. Kiihne, and H. Richter, "New Approach in Equilibrium Theory for Strained Layer Relaxation," *Physical Review Letters*, vol. 73, no. 20, pp. 2712–2715, 1994.

[12] A. Nakajima, Y. Sumida, M. H. Dhyani, H. Kawai, and E. M. S. Narayanan, "High density two-dimensional hole gas induced by negative polarization at GaN/AlGaN heterointerface," *Applied Physics Express*, vol. 3, no. 12, 2010.

[13] R. Chu, Y. Cao, C. Mary, R. Li, and D. Zehnder, "An Experimental Demonstration of GaN CMOS Technology," *IEEE Electron Device Letters*, vol. 37, no. 3, pp. 269–271, 2016.

[14] T. Zimmermann, M. Neuburger, M. Kunze, I. Daumiller, A. Denisenko, A. Dadgar, A. Krost, and E. Kohn, "P-channel InGaN-HFET structure based on polarization doping," *IEEE Electron Device Letters*, vol. 25, no. 7, pp. 450–452, 2004.

[15] K. Zhang, M. Sumiya, M. Liao, Y. Koide, and L. Sang, "P-Channel InGaN/GaN heterostructure metal-oxide-semiconductor field effect transistor based on polarization-induced two-dimensional hole gas," *Scientific Reports*, vol. 6, no. January, p. 23683, 2016.

[16] H. Hahn, B. Reuters, A. Pooth, B. Hollander, M. Heuken, H. Kalisch, and A. Vescan, "P-channel enhancement and depletion mode GaN-based HFETs with quaternary backbarriers," *IEEE Transactions on Electron Devices*, vol. 60, no. 10, pp. 3005–3011, 2013.

[17] B. Reuters, H. Hahn, A. Pooth, B. Holländer, U. Breuer, M. Heuken, H. Kalisch, and A. Vescan, "Fabrication of p-channel heterostructure field effect transistors with polarization-induced two-dimensional hole gases at metal-polar GaN/AlInGaN interfaces," *Journal of Physics D: Applied Physics*, vol. 47, no. 17, 2014.

[18] M. Shatalov, G. Simin, J. Zhang, V. Adivarahan, A. Koudymov, R. Pachipulusu, and M. A. Khan, "GaN / AlGaN p-Channel inverted heterostructure JFET," *IEEE Electron Device Letters*, vol. 23, no. 8, pp. 452–454, 2002.

[19] G. Li, R. Wang, B. Song, J. Verma, Y. Cao, S. Ganguly, A. Verma, J. Guo, H. G. Xing, and D. Jena, "Polarization-induced GaN-on-insulator E/D Mode heterostructure FETs," *IEEE Electron Device Letters*, vol. 34, no. 7, pp. 852–854, 2013.

[20] H. Lee, N. Campbell, J. Lee, T. J. Asel, T. R. Paudel, H. Zhou, J. W. Lee, B. Noesges, J. Seo, B. Park, L. J. Brillson, S. H. Oh, E. Y. Tsymbal, M. S. Rzchowski, and C. B. Eom, "Direct observation of a two-dimensional hole gas at oxide interfaces," *Nature Materials*, vol. 17, no. 3, pp. 231–236, 2018.

[21] A. A. Yamaguchi, Y. Mochizuki, H. Sunakawa, and A. Usui, "Determination of valence band splitting parameters in GaN," *Journal of Applied Physics*, vol. 83, p. 4542, 1998.

[22] M. Kasu and N. Kobayashi, "High hole mobility (1300 cm^2/Vs) at room temperature in hydrogen-terminated (001) diamond," *Applied Physics Letters*, vol. 80, pp. 3961–3963, 5 2002.

[23] H. J. Looi, R. B. Jackman, and J. S. Foord, "High carrier mobility in polycrystalline thin film diamond," *Applied Physics Letters*, vol. 72, p. 353, 6 1998.

[24] K. Hayashi, S. Yamanaka, H. Watanabe, T. Sekiguchi, H. Okushi, and K. Kajimura, "Investigation of the effect of hydrogen on electrical and optical properties in chemical vapor deposited on homoepitaxial diamond films," *Journal of Applied Physics*, vol. 81, pp. 744–753, 1 1997.

[25] M. Myronov, T. Irisawa, O. A. Mironov, S. Koh, Y. Shiraki, T. E. Whall, and E. H. Parker, "Extremely high room-temperature two-dimensional hole gas mobility in Ge/Si$_{0.33}$Ge$_{0.67}$/Si (001) p-type modulation-doped heterostructures," *Applied Physics Letters*, vol. 80, pp. 3117–3119, 4 2002.

[26] M. Myronov, K. Sawano, Y. Shiraki, T. Mouri, and K. M. Itoh, "Observation of two-dimensional hole gas with mobility and carrier density exceeding those of two-dimensional electron gas at room temperature in the SiGe heterostructures," *Applied Physics Letters*, vol. 91, p. 082108, 8 2007.

[27] R. J. H. Morris, T. J. Grasby, R. Hammond, M. Myronov, O. A. Mironov, D. R. Leadley, T. E. Whall, E. H. C. Parker, M. T. Currie, C. W. Leitz, and E. A. Fitzgerald, "High conductance Ge p-channel heterostructures realized by hybrid epitaxial growth," *Semiconductor Science and Technology*, vol. 19, pp. L106–L109, 10 2004.

[28] M. Kaneko, I. Narita, and S. Matsumoto, "The Study on Hole Mobility in the Inversion Layer of P-Channel MOSFET," *IEEE Electron Device Letters*, vol. 6, no. 11, pp. 575–577, 1985.

[29] S. H. Shin, Y. H. Park, H. C. Koo, Y. H. Song, and J. D. Song, "GaSb/InGaAs 2-dimensional hole gas grown on InP substrate for III-V CMOS applications," *Current Applied Physics*, vol. 17, pp. 1005–1008, 7 2017.

[30] Z. Zhang, J. Encomendero, R. Chaudhuri, Y. Cho, V. Protasenko, K. Nomoto, K. Lee, M. Toita, H. G. Xing, and D. Jena, "Polarization-induced 2D hole gases in pseudomorphic undoped GaN/AlN heterostructures on single-crystal AlN substrates," *in review*, 2021.

[31] S. J. Bader, R. Chaudhuri, K. Nomoto, A. Hickman, Z. Chen, H. W. Then, D. A. Muller, H. G. Xing, and D. Jena, "Gate-recessed E-mode p-channel HFET with high on-current based on GaN/AlN 2D hole gas," *IEEE Electron Device Letters*, vol. 39, no. 12, pp. 1848–1851, 2018.

[32] A. Nakajima, P. Liu, M. Ogura, T. Makino, K. Kakushima, S. I. Nishizawa, H. Ohashi, S. Yamasaki, and H. Iwai, "Generation and transportation mechanisms for two-dimensional hole gases in GaN/AlGaN/GaN double heterostructures," *Journal of Applied Physics*, vol. 115, no. 15, 2014.

[33] Z. Zhang, Y. Cho, M. Gong, S. T. Ho, J. Singhal, J. Encomendero, X. Li, H. Lee, H. G. Xing, and D. Jena, "Epitaxial Ferrimagnetic Mn4N Thin Films on GaN by Molecular Beam Epitaxy," *IEEE Transactions on Magnetics*, 2021.

[34] B. Ofuonye, J. Lee, M. Yan, C. Sun, J.-M. Zuo, and I. Adesida, "Electrical and microstructural properties of thermally annealed Ni/Au and Ni/Pt/Au Schottky contacts on AlGaN/GaN heterostructures," *Semiconductor Science and Technology*, vol. 29, p. 095005, 7 2014.

[35] K. A. Rickert, A. B. Ellis, J. K. Kim, J.-L. Lee, F. J. Himpsel, F. Dwikusuma, and T. F. Kuech, "X-ray photoemission determination of the Schottky barrier height of metal contacts to n–GaN and p–GaN," *Journal of Applied Physics*, vol. 92, p. 6671, 11 2002.

[36] H. B. Michaelson, "The work function of the elements and its periodicity," *Journal of Applied Physics*, vol. 48, p. 4729, 8 2008.

[37] Y. Liu, S. Kijima, E. Sugimata, M. Masahara, K. Endo, T. Matsukawa, K. Ishii, K. Sakamoto, T. Sekigawa, H. Yamauchi, Y. Takanashi, and E. Suzuki, "Investigation of the TiN gate electrode with tunable work function and its application for FinFET fabrication," *IEEE Transactions on Nanotechnology*, vol. 5, pp. 723–728, 11 2006.

[38] S. J. Bader, R. Chaudhuri, A. Hickman, K. Nomoto, S. Bharadwaj, H. W. Then, H. G. Xing, and D. Jena, "GaN/AlN Schottky-gate p-channel HFETs with InGaN contacts and 100 mA/mm on-current," *Technical Digest - International Electron Devices Meeting, IEDM*, pp. 1–4, 2019.

[39] K. Nomoto, R. Chaudhuri, S. J. Bader, L. Li, A. Hickman, S. Huang, H. Lee, T. Maeda, H. W. Then, M. Radosavljevic, P. Fischer, A. Molnar, J. C. M. Hwang, H. G. Xing, and D. Jena, "GaN/AlN p-channel HFETs with $I_{max} >$ 420 mA/mm and ~20 GHz f_T/f_{max}," *Technical Digest - International Electron Devices Meeting, IEDM*, 2020.

[40] S. Rennesson, M. Leroux, M. Al Khalfioui, M. Nemoz, S. Chenot, J. Massies, L. Largeau, E. Dogmus, M. Zegaoui, F. Medjdoub, and F. Semond, "Ultrathin AlN-Based HEMTs Grown on Silicon Substrate by NH_3-MBE," *Physica Status Solidi (A) Applications and Materials Science*, vol. 215, pp. 1–4, 5 2018.

[41] S. Patwal, M. Agrawal, K. Radhakrishnan, T. L. A. Seah, and N. Dharmarasu, "Enhancement of 2D Electron Gas Mobility in an AlN/GaN/AlN Double-Heterojunction High-Electron-Mobility Transistor by Epilayer Stress Engineering," *Physica Status Solidi (A) Applications and Materials Science*, vol. 1900818, pp. 3–9, 2019.

[42] M. Qi, G. Li, S. Ganguly, P. Zhao, X. Yan, J. Verma, B. Song, M. Zhu, K. Nomoto, H. Xing, and D. Jena, "Strained GaN quantum-well FETs on single crystal bulk AlN substrates," *Applied Physics Letters*, vol. 110, no. 6, pp. 6–10, 2017.

[43] J. T. Chen, J. Bergsten, J. Lu, E. Janzén, M. Thorsell, L. Hultman, N. Rorsman, and O. Kordina, "A GaN-SiC hybrid material for high-frequency and power electronics," *Applied Physics Letters*, vol. 113, no. 4, 2018.

[44] U. Choi, D. Jung, K. Lee, T. Kwak, T. Jang, Y. Nam, B. So, and O. Nam, "The Effect of AlN Buffer Layer on AlGaN/GaN/AlN Double-Heterostructure High-Electron-Mobility Transistor," *Physica Status Solidi (A) Applications and Materials Science*, vol. 217, no. 7, pp. 1–8, 2020.

[45] S. M. Islam, M. Qi, B. Song, K. Nomoto, V. Protasenko, J. Wang, S. Rou-vimov, P. Fay, H. G. Xing, and D. Jena, "First demonstration of strained AlN/GaN/AlN quantum well FETs on SiC," *Device Research Conference - Conference Digest, DRC*, no. 10, pp. 5–6, 2016.

[46] G. Li, B. Song, S. Ganguly, M. Zhu, R. Wang, X. Yan, J. Verma, V. Pro-tasenko, H. Grace Xing, and D. Jena, "Two-dimensional electron gases in strained quantum wells for AlN/GaN/AlN double heterostructure field-effect transistors on AlN," *Applied Physics Letters*, vol. 104, no. 19, pp. 1–5, 2014.

[47] A. Hickman, R. Chaudhuri, S. J. Bader, K. Nomoto, K. Lee, H. G. Xing, and D. Jena, "High Breakdown Voltage in RF AlN/GaN/AlN Quantum Well HEMTs," *IEEE Electron Device Letters*, vol. 40, no. 8, pp. 1293–1296, 2019.

[48] T. Fang, R. Wang, G. Li, H. Xing, S. Rajan, and D. Jena, "Effect of Optical Phonon Scattering on the Performance of GaN Transistors," *IEEE Electron Device Letters*, vol. 33, no. 5, p. 709, 2012.

[49] B. Romanczyk, M. Guidry, X. Zheng, H. Li, E. Ahmadi, S. Keller, and U. K. Mishra, "Bias-Dependent Electron Velocity Extracted From N-Polar GaN Deep Recess HEMTs," *IEEE Transactions on Electron Devices*, pp. 1–5, 2020.

[50] C. Y. Ho, R. W. Powell, and P. E. Liley, "Thermal Conductivity of the Ele-ments," *Journal of Physical and Chemical Reference Data*, vol. 1, pp. 279–421, 4 1972.

[51] K. Chen, B. Song, N. K. Ravichandran, Q. Zheng, X. Chen, H. Lee, H. Sun, S. Li, G. A. G. U. Gamage, F. Tian, Z. Ding, Q. Song, A. Rai, H. Wu, P. Koirala, A. J. Schmidt, K. Watanabe, B. Lv, Z. Ren, L. Shi, D. G. Cahill, T. Taniguchi, D. Broido, and G. Chen, "Ultrahigh thermal conductivity in isotope-enriched cubic boron nitride," *Science*, vol. 367, pp. 555–559, 1 2020.

[52] E. T. Swartz and R. O. Pohl, "Thermal boundary resistance," *Reviews of Modern Physics*, vol. 61, no. 3, pp. 605–668, 1989.

[53] A. L. Hickman, R. Chaudhuri, S. J. Bader, K. Nomoto, L. Li, J. C. M. Hwang, H. Grace Xing, and D. Jena, "Next generation electronics on the ultrawide-bandgap aluminum nitride platform," *Semiconductor Sci-ence and Technology*, vol. 36, p. 044001, 4 2021.

[54] A. Hickman, R. Chaudhuri, L. Li, K. Nomoto, S. J. Bader, J. C. M. Hwang, H. G. Xing, and D. Jena, "First RF Power Operation of AlN/GaN/AlN HEMTs With >3 A/mm and 3 W/mm at 10 GHz," *IEEE Journal of the Electron Devices Society*, vol. 9, pp. 121–124, 12 2021.

[55] S. Birner, T. Zibold, T. Andlauer, T. Kubis, M. Sabathil, A. Trellakis, and P. Vogl, "nextnano: General purpose 3-D simulations," *IEEE Transactions on Electron Devices*, vol. 54, pp. 2137–2142, 9 2007.

[56] W. Zhao, M. J. Asadi, L. Li, R. Chaudhuri, K. Nomoto, H. G. Xing, J. Hwang, and D. Jena, "Demonstration of 10 GHz Epi-BAW Resonators on the MBE AlN on SiC HEMT Platform," *in preparation*, 2021.

[57] M. J. Asadi, L. Li, W. Zhao, K. Nomoto, P. Fay, H. G. Xing, D. Jena, and J. C. Hwang, "SiC substrate-integrated waveguides for high-power mono-lithic integrated circuits above 110 GHz," in *IEEE MTT-S International Microwave Symposium*, 2021.

[58] Z. Zheng, W. Song, L. Zhang, S. Yang, J. Wei, and K. J. Chen, "Monolith-ically Integrated GaN Ring Oscillator Based on High-Performance Complementary Logic Inverters," *IEEE Electron Device Letters*, vol. 42, no. 1, pp. 26–29, 2020.

[59] Z. Zheng, L. Zhang, W. Song, S. Feng, H. Xu, J. Sun, S. Yang, T. Chen, J. Wei, and K. J. Chen, "Gallium nitride-based complementary logic inte-grated circuits," *Nature Electronics*, vol. 4, pp. 595–603, 8 2021.

[60] N. Chowdhury, Q. Xie, M. Yuan, K. Cheng, H. W. Then, and T. Palacios, "Regrowth-Free GaN-Based Complementary Logic on a Si Substrate," *IEEE Electron Device Letters*, vol. 41, pp. 820–823, 6 2020.

[61] A. Nakajima, S. Kubota, K. Tsutsui, K. Kakushima, H. Wakabayashi, H. Iwai, S.-i. Nishizawa, and H. Ohashi, "GaN-based complementary metal–oxide–semiconductor inverter with normally off Pch and Nch MOSFETs fabricated using polarisation-induced holes and electron chan-nels," *IET Power Electronics*, vol. 11, no. 4, pp. 689–694, 2018.

[62] H. Hahn, B. Reuters, S. Kotzea, G. Lukens, S. Geipel, H. Kalisch, and A. Vescan, "First monolithic integration of GaN-based enhancement mode n-channel and p-channel heterostructure field effect transistors," *Device Research Conference - Conference Digest, DRC*, vol. 60, no. 10, pp. 259–260, 2014.

[63] R. Chaudhuri, S. J. Bader, Z. Chen, D. Muller, H. G. Xing, and D. Jena, "MBE Growth of Large-Area GaN/AlN 2-dimensional Hole Gas Heterostructures," *Physica Status Solidi (B) Basic Research*, vol. 1900567, pp. 1–5, 2020.

[64] K. Lee, Y. Cho, L. J. Schowalter, M. Toita, H. G. Xing, and D. Jena, "Surface control and MBE growth diagram for homoepitaxy on single-crystal AlN substrates," *Applied Physics Letters*, vol. 116, no. 26, 2020.

[65] Y. Cho, C. S. Chang, K. Lee, M. Gong, K. Nomoto, M. Toita, L. J. Schowalter, D. A. Muller, D. Jena, and H. G. Xing, "Molecular beam homoepitaxy on bulk AlN enabled by aluminum-assisted surface cleaning," *Applied Physics Letters*, vol. 116, p. 172106, 4 2020.

[66] J. Encomendero, Z. Zhang, K. Lee, R. Chaudhuri, A. Hickman, M. Toita, D. Jena, and H. G. Xing, "Complementary 2D Electron and Hole Gases on Single-crystal AlN Substrates," in *63rd Electronic Materials Conference (EMC) (presented)*, 2021.

[67] NASA, "Voyager - The Golden Record." *https://voyager.jpl.nasa.gov/golden-record/*, accessed 2021-08-30.

[68] J. Gertner, *The Idea Factory: Bell Labs and the great age of American innovation.* Penguin, 2012.

[69] J. Neal and J. Bledoe, *Fire In The Belly: Building A World-leading High-tech Company From Scratch In Tumultuous Times.* Down Home Pr, 2005.

[70] J. W. Orton, *The Story of Semiconductors.* Oxford University Press, 2008.

[71] J. Orton and T. Foxon, *Molecular beam epitaxy: a short history.* Oxford University Press USA, 2015.

[72] C. E. Shannon, "A Mathematical Theory of Communication," *Bell System Technical Journal*, vol. 27, no. 3, 1948.

[73] K. Lifshitz, *Makers of the Telegraph Samuel Morse, Ezra Cornell and Joseph Henry.* McFarland, Incorporated, Publishers, 2017.

[74] J. C. Bose, "Detector for electrical disturbances." *U.S. Patent 755840*, 1901.

[75] F. Braun, "On Current Conduction Through Metallic Sulfides," *Semiconductor Devices: Pioneering Papers*, pp. 377–380, 3 1991.

[76] R. Buderi, *The invention that changed the world: How a small group of radar pioneers won the second world war and launched a technical revolution.* Touchstone, New York, 1996.

[77] V. Bush, *Science, the endless frontier.* Princeton University Press, 2020.

[78] "The Origin of Semiconductor Research at Purdue." *https://www.physics.purdue.edu/about/history/semi_conductor_research.html*, accessed 2021-08-30.

[79] L. Edgar, "Method and apparatus for controlling electric currents." *U.S. Patent 1745175*, 1930.

[80] J. Bardeen and W. H. Brattain, "The Transistor, A Semi-Conductor Triode," *Physical Review*, vol. 74, p. 230, 7 1948.

[81] W. Shockley, M. Sparks, and G. K. Teal, "p-n Junction Transistors," *Physical Review*, vol. 83, p. 151, 7 1951.

[82] M. Riordan, "The silicon dioxide solution," *IEEE Spectrum*, vol. 44, pp. 51–56, 12 2007.

[83] J. Hoerni, "Planar silicon diodes and transistors," in *1960 International Electron Devices Meeting*, IRE, 1960.

[84] J. Andrus and W. L. Bond, "Photoengraving in transistor fabrication," *Transistor technology*, vol. 3, pp. 151–162, 1958.

[85] J. S. Kilby, "Invention of the Integrated Circuit," *IEEE Transactions on Electron Devices*, vol. 23, no. 7, pp. 648–654, 1976.

[86] R. N. Noyce, "Semiconductor Device-and-Lead Structure, Reprint of U.S. Patent 2,981,877 (Issued April 25, 1961. Filed July 30, 1959)," *IEEE Solid-State Circuits Newsletter*, vol. 12, pp. 34–40, 2 2009.

[87] D. Kahng, "Silicon-silicon dioxide field induced surface devices," in *The Solid State Device Research Conf.*, (Pittsburgh PA), 1960.

[88] F. M. Wanlass and C. T. Sah, "Nanowatt Logic Using Field-Effect Metal-Oxide Semiconductor Triodes," *Semiconductor Devices: Pioneering Papers*, pp. 637–638, 3 1991.

[89] M. Bohr, "A 30 Year Retrospective on Dennard's MOSFET Scaling Paper," *IEEE Solid-State Circuits Newsletter*, vol. 12, pp. 11–13, 2 2009.

[90] R. R. Schaller, "Moore's law: past, present, and future," *IEEE Spectrum*, vol. 34, pp. 52–55, 6 1997.

[91] K. F. Schuegraf, C. C. Kin, and C. Hu, "Ultra-thin silicon dioxide leakage current and scaling limit," *Digest of Technical Papers - Symposium on VLSI Technology*, vol. 1992-June, pp. 18–19, 1992.

[92] I. L. Markov, "Limits on fundamental limits to computation," *Nature*, vol. 512, pp. 147–154, 8 2014.

[93] H. M. Manasevit and W. I. Simpson, "The Use of Metal-Organics in the Preparation of Semiconductor Materials: I . Epitaxial Gallium- V Compounds," *Journal of The Electrochemical Society*, vol. 116, p. 1725, 12 1969.

[94] A. Y. Cho and J. R. Arthur, "Molecular beam epitaxy," *Progress in Solid State Chemistry*, vol. 10, pp. 157–191, 1 1975.

[95] U. Ruddenklau, "mmWave Semiconductor Industry Technologies," *ETSI White Paper No. 15*, 2018.

[96] B. J. Baliga, "Power Semiconductor Device Figure of Merit for High-Frequency Applications," *IEEE Electron Device Letters*, vol. 10, no. 10, pp. 455–457, 1989.

[97] E. Johnson, "Physical limitations on frequency and power parameters of transistors," in *IRE International Convention Record*, Institute of Electrical and Electronics Engineers, 1985.

[98] S. Nakamura, "Nobel Lecture: Background story of the invention of efficient blue InGaN light emitting diodes," *Reviews of Modern Physics*, vol. 87, pp. 1139–1151, 10 2015.

[99] M. A. Khan, J. N. Kuznia, J. M. Van Hove, N. Pan, and J. Carter, "Observation of a two-dimensional electron gas in low pressure metalor-

ganic chemical vapor deposited GaN-Al$_x$Ga$_{1-x}$N heterojunctions," *Applied Physics Letters*, vol. 60, no. 24, pp. 3027–3029, 1992.

[100] O. Ambacher, J. Smart, J. R. Shealy, N. G. Weimann, K. Chu, M. Murphy, W. J. Schaff, L. F. Eastman, R. Dimitrov, L. Wittmer, M. Stutzmann, W. Rieger, and J. Hilsenbeck, "Two-dimensional electron gases induced by spontaneous and piezoelectric polarization charges in N-and Ga-face AlGaN/GaN heterostructures," *Journal of Applied Physics*, vol. 85, no. 6, pp. 3222–3233, 1999.

[101] U. Mishra, Shen Likun, T. Kazior, and Yi-Feng Wu, "GaN-based RF power devices and amplifiers," *Proceedings of the IEEE*, vol. 96, pp. 287–305, 2 2008.

[102] H. Amano, Y. Baines, E. Beam, M. Borga, T. Bouchet, P. R. Chalker, M. Charles, K. J. Chen, N. Chowdhury, R. Chu, C. De Santi, M. M. De Souza, S. Decoutere, L. Di Cioccio, B. Eckardt, T. Egawa, P. Fay, J. J. Freedsman, L. Guido, O. Häberlen, G. Haynes, T. Heckel, D. Hemakumara, P. Houston, J. Hu, M. Hua, Q. Huang, A. Huang, S. Jiang, H. Kawai, D. Kinzer, M. Kuball, A. Kumar, K. B. Lee, X. Li, D. Marcon, M. März, R. McCarthy, G. Meneghesso, M. Meneghini, E. Morvan, A. Nakajima, E. M. S. Narayanan, S. Oliver, T. Palacios, D. Piedra, M. Plissonnier, R. Reddy, M. Sun, I. Thayne, A. Torres, N. Trivellin, V. Unni, M. J. Uren, M. Van Hove, D. J. Wallis, J. Wang, J. Xie, S. Yagi, S. Yang, C. Youtsey, R. Yu, E. Zanoni, S. Zeltner, and Y. Zhang, "The 2018 GaN power electronics roadmap," *Journal of Physics D: Applied Physics*, vol. 51, p. 163001, 4 2018.

[103] S. Chen, S. Nayak, C. Campbell, and E. Reese, "High Efficiency 5W/10W 32 - 38GHz Power Amplifier MMICs Utilizing Advanced 0.15μm GaN HEMT Technology," *Technical Digest - IEEE Compound Semiconductor Integrated Circuit Symposium, CSIC*, vol. 2016-November, 11 2016.

[104] D. Schwantuschke, B. J. Godejohann, P. Bruckner, A. Tessmann, and R. Quay, "Mm-Wave operation of AlN/GaN-devices and MMICs at V-& W-band," *MIKON 2018 - 22nd International Microwave and Radar Conference*, pp. 238–241, 7 2018.

[105] Y. Niida, Y. Kamada, T. Ohki, S. Ozaki, K. Makiyama, Y. Minoura, N. Okamoto, M. Sato, K. Joshin, and K. Watanabe, "3.6 W/mm high power density W-band InAlGaN/GaN HEMT MMIC power amplifier," *PAWR 2016 - Proceedings of the 2016 IEEE Topical Conference on Power Amplifiers for Wireless and Radio Applications*, pp. 24–26, 3 2016.

[106] R. Ma, K. H. Teo, S. Shinjo, K. Yamanaka, and P. M. Asbeck, "A GaN PA for 4G LTE-Advanced and 5G: Meeting the Telecommunication Needs of Various Vertical Sectors Including Automobiles, Robotics, Health Care, Factory Automation, Agriculture, Education, and More," *IEEE Microwave Magazine*, vol. 18, pp. 77–85, 11 2017.

[107] K. Yuk, G. R. Branner, and C. Cui, "Future directions for GaN in 5G and satellite communications," *Midwest Symposium on Circuits and Systems*, vol. 2017-August, pp. 803–806, 9 2017.

[108] N. Y. Times, "The Apple 5G iPhone Explained: What You Need to Know." *https://www.nytimes.com/2020/10/13/technology/what-you-need-to-know-about-5g-smartphones.html*, accessed 2021-08-30.

[109] W. Saad, M. Bennis, and M. Chen, "A Vision of 6G Wireless Systems: Applications, Trends, Technologies, and Open Research Problems," *IEEE Network*, vol. 34, pp. 134–142, 5 2020.

[110] Z. Zhang, Y. Xiao, Z. Ma, M. Xiao, Z. Ding, X. Lei, G. K. Karagiannidis, and P. Fan, "6G Wireless Networks: Vision, Requirements, Architecture, and Key Technologies," *IEEE Vehicular Technology Magazine*, vol. 14, pp. 28–41, 9 2019.

[111] R. L. Coffie, "High Power High Frequency Transistors: A Material's Perspective," in *High-Frequency GaN Electronic Devices*, pp. 5–41, Springer International Publishing, 2020.

[112] "JUMP Mission - SRC." *https://www.src.org/program/jump/about/mission/*, accessed 2021-08-30.

[113] G. Piazza, V. Felmetsger, P. Muralt, R. H. Olsson III, and R. Ruby, "Piezoelectric aluminum nitride thin films for microelectromechanical systems," *MRS Bulletin*, vol. 37, pp. 1051–1061, 11 2012.

[114] S. Judaprawira, W. I. Wang, P. C. Chao, C. E. Wood, D. W. Woodard, and L. F. Eastman, "Modulation-doped MBE GaAs/n-Al$_x$Ga$_{1-x}$As MESFETs," *IEEE Electron Device Letters*, vol. 2, no. 1, pp. 14–15, 1981.

[115] L. F. Eastman and U. K. Mishra, "The toughest transistor yet," *IEEE Spectrum*, vol. 39, pp. 28–33, 5 2002.

[116] H. P. Maruska and W. C. Rhines, "A modern perspective on the history of

semiconductor nitride blue light sources," *Solid-State Electronics*, vol. 111, pp. 32–41, 9 2015.

[117] J. Cho, J. H. Park, J. K. Kim, and E. F. Schubert, "White light-emitting diodes: History, progress, and future," *Laser & Photonics Reviews*, vol. 11, p. 1600147, 3 2017.

[118] S. Pimputkar, J. S. Speck, S. P. Denbaars, and S. Nakamura, "Prospects for LED lighting," *Nature Photonics*, vol. 3, pp. 180–182, 4 2009.

[119] C. Wood and D. Jena, eds., *Polarization effects in semiconductors: From ab initio theory to device applications*. Boston, MA: Springer US, 2008.

[120] J. P. Ibbetson, P. T. Fini, K. D. Ness, S. P. DenBaars, J. S. Speck, and U. K. Mishra, "Polarization effects, surface states, and the source of electrons in AlGaN/GaN heterostructure field effect transistors," *Applied Physics Letters*, vol. 77, no. 2, pp. 250–252, 2000.

[121] G. Koley and M. G. Spencer, "On the origin of the two-dimensional electron gas at the AlGaN/GaN heterostructure interface," *Applied Physics Letters*, vol. 86, no. 4, pp. 15–18, 2005.

[122] M. J. Manfra, L. N. Pfeiffer, K. W. West, R. De Picciotto, and K. W. Baldwin, "High mobility two-dimensional hole system in GaAs/AlGaAs quantum wells grown on (100) GaAs substrates," *Applied Physics Letters*, vol. 86, no. 16, pp. 1–3, 2005.

[123] Y. L. Fang, Z. H. Feng, J. Y. Yin, Z. R. Zhang, Y. J. Lv, S. B. Dun, B. Liu, C. M. Li, and S. J. Cai, "Ultrathin InAlN/GaN heterostructures with high electron mobility," *Physica Status Solidi (B) Basic Research*, vol. 252, no. 5, pp. 1006–1010, 2015.

[124] Y. Cao, K. Wang, A. Orlov, H. Xing, and D. Jena, "Very low sheet resistance and Shubnikov-de-Haas oscillations in two-dimensional electron gases at ultrathin binary AlN/GaN heterojunctions," *Applied Physics Letters*, vol. 92, no. 15, pp. 15–17, 2008.

[125] S. Hasenöhrl, P. Chauhan, E. Dobročka, R. Stoklas, L. Vančo, M. Veselý, F. Bouazzaoui, M. P. Chauvat, P. Ruterana, and J. Kuzmík, "Generation of hole gas in non-inverted InAl(Ga)N/GaN heterostructures," *Applied Physics Express*, vol. 12, p. 014001, 1 2019.

[126] Z. Zheng, W. Song, L. Zhang, S. Yang, J. Wei, and K. J. Chen, "High I_{ON} and I_{ON}/I_{OFF} Ratio Enhancement-Mode Buried p-Channel GaN MOSFETs on p-GaN Gate Power HEMT Platform," *IEEE Electron Device Letters*, vol. 41, pp. 26–29, 1 2020.

[127] P. Kozodoy, H. Xing, S. P. DenBaars, U. K. Mishra, A. Saxler, R. Perrin, S. Elhamri, and W. C. Mitchel, "Heavy doping effects in Mg-doped GaN," *Journal of Applied Physics*, vol. 87, no. 4, pp. 1832–1835, 2000.

[128] S. Poncé, D. Jena, and F. Giustino, "Route to high hole mobility in GaN via reversal of crystal-field splitting," *Physical Review Letters*, vol. 123, p. 096602, 8 2019.

[129] J. H. Davies, *The Physics of Low-dimensional Semiconductors*. Cambridge University Press, 1997.

[130] J. S. Im, A. Moritz, F. Steuber, V. Härle, F. Scholz, and A. Hangleiter, "Radiative carrier lifetime, momentum matrix element, and hole effective mass in GaN," *Applied Physics Letters*, vol. 70, pp. 631–633, 2 1997.

[131] T. Ohtoshi, A. Niwa, and T. Kuroda, "Dependence of optical gain on crystal orientation in wurtzite-GaN strained quantum-well lasers," *Journal of Applied Physics*, vol. 82, p. 1518, 1997.

[132] B. L. Gelmont, M. Shur, and M. Stroscio, "Polar optical-phonon scattering in three- and two-dimensional electron gases," *Journal of Applied Physics*, vol. 77, no. 2, pp. 657–660, 1995.

[133] A. Nakajima, P. Liu, M. Ogura, T. Makino, S. I. Nishizawa, S. Yamasaki, H. Ohashi, K. Kakushima, and H. Iwai, "Temperature-independent two-dimensional hole gas confined at GaN/AlGaN heterointerface," *Applied Physics Express*, vol. 6, no. 9, 2013.

[134] G. Li, Y. Cao, H. G. Xing, and D. Jena, "High mobility two-dimensional electron gases in nitride heterostructures with high Al composition AlGaN alloy barriers," *Applied Physics Letters*, vol. 97, p. 222110, 11 2010.

[135] K. Köhler, S. Müller, R. Aidam, P. Waltereit, W. Pletschen, L. Kirste, H. P. Menner, W. Bronner, A. Leuther, R. Quay, M. Mikulla, O. Ambacher, R. Granzner, F. Schwierz, C. Buchheim, and R. Goldhahn, "Influence of the surface potential on electrical properties of $Al_xGa_{1-x}N$/GaN heterostructures with different Al-content: Effect of growth method," *Journal of Applied Physics*, vol. 107, p. 053711, 3 2010.

[136] H. Shen and M. Dutta, "Franz-Keldysh oscillations in modulation spectroscopy," *Journal of Applied Physics*, vol. 78, no. 4, pp. 2151–2176, 1995.

[137] S. J. Bader, H. Lee, R. Chaudhuri, S. Huang, A. Hickman, A. Molnar, H. G. Xing, D. Jena, H. W. Then, N. Chowdhury, and T. Palacios, "Prospects for Wide Bandgap and Ultrawide Bandgap CMOS Devices," *IEEE Transactions on Electron Devices*, pp. 1–11, 8 2020.

[138] G. Koblmueller, R. Averbeck, L. Geelhaar, H. Riechert, W. Hösler, and P. Pongratz, "Growth diagram and morphologies of AlN thin films grown by molecular beam epitaxy," *Journal of Applied Physics*, vol. 93, no. 12, pp. 9591–9596, 2003.

[139] B. Heying, R. Averbeck, L. F. Chen, E. Haus, H. Riechert, and J. S. Speck, "Control of GaN surface morphologies using plasma-assisted molecular beam epitaxy," *Journal of Applied Physics*, vol. 88, pp. 1855–1860, 8 2000.

[140] W. E. Hoke, A. Torabi, J. J. Mosca, and T. D. Kennedy, "Thermodynamic analysis of cation incorporation during molecular beam epitaxy of nitride films using metal-rich growth conditions," *Journal of Vacuum Science & Technology B: Microelectronics and Nanometer Structures*, vol. 25, no. 3, p. 978, 2007.

[141] W. E. Hoke, A. Torabi, J. J. Mosca, R. B. Hallock, and T. D. Kennedy, "Rapid silicon outdiffusion from SiC substrates during molecular-beam epitaxial growth of AlGaN/GaN/AlN transistor structures," *Journal of Applied Physics*, vol. 98, no. 8, pp. 1–5, 2005.

[142] C. Poblenz, P. Waltereit, S. Rajan, U. K. Mishra, J. S. Speck, P. Chin, I. Smorchkova, and B. Heying, "Effect of AlN nucleation layer growth conditions on buffer leakage in AlGaN/GaN high electron mobility transistors grown by molecular beam epitaxy (MBE)," *Journal of Vacuum Science & Technology B: Microelectronics and Nanometer Structures*, vol. 23, no. 4, p. 1562, 2005.

[143] E. Iliopoulos and T. D. Moustakas, "Growth kinetics of AlGaN films by plasma-assisted molecular-beam epitaxy," *Applied Physics Letters*, vol. 81, no. 2, pp. 295–297, 2002.

[144] T. Böttcher, S. Einfeldt, V. Kirchner, S. Figge, H. Heinke, D. Hommel, H. Selke, and P. L. Ryder, "Incorporation of indium during molecular beam epitaxy of InGaN," *Applied Physics Letters*, vol. 73, no. 22, pp. 3232–3234, 1998.

[145] J. W. Matthews and A. E. Blakeslee, "Defects in epitaxial multilayers: I. Misfit dislocations," *Journal of Crystal Growth*, vol. 27, pp. 118–125, 1974.

[146] Yu Cao, *Study of AlN/GaN HEMTs : MBE Growth, Transport properties and Device Issues*. PhD thesis, University of Notre Dame, 2010.

[147] B. Heying, E. J. Tarsa, C. R. Elsass, P. Fini, S. P. DenBaars, and J. S. Speck, "Dislocation mediated surface morphology of GaN," *Journal of Applied Physics*, vol. 85, no. 9, pp. 6470–6476, 1999.

[148] G. Bastard, *Wave Mechanics Applied to Semiconductor Heterostructures*. Wiley-Interscience, 1988.

[149] M. Miyoshi, S. Fujita, and T. Egawa, "Numerical and experimental analyses of two-dimensional electron mobility in Al(In,Ga)N/AlGaN heterostructures," *Applied Physics Express*, vol. 8, p. 051003, 5 2015.

[150] P. Sohi, J. F. Carlin, and N. Grandjean, "Alloy disorder limited mobility of InGaN two-dimensional electron gas," *Applied Physics Letters*, vol. 112, no. 26, 2018.

[151] J. Simon, A. Wang, H. Xing, S. Rajan, and D. Jena, "Carrier transport and confinement in polarization-induced three-dimensional electron slabs: Importance of alloy scattering in AlGaN," *Applied Physics Letters*, vol. 88, pp. 1–3, 1 2006.

[152] S. J. Chang, C. H. Chen, P. C. Chang, Y. K. Su, P. C. Chen, Y. D. Jhou, H. Hung, S. M. Wang, and B. R. Huang, "Nitride-Based LEDs with p-InGaN Capping Layer," *IEEE Transactions on Electron Devices*, vol. 50, pp. 2567–2570, 12 2003.

[153] Y. Cao, H. Xing, and D. Jena, "Polarization-mediated remote surface roughness scattering in ultrathin barrier GaN high-electron mobility transistors," *Applied Physics Letters*, vol. 97, p. 222116, 2010.

[154] K. Wang, C. Lian, N. Su, D. Jena, and J. Timler, "Conduction band offset at the InNGaN heterojunction," *Applied Physics Letters*, vol. 91, p. 232117, 12 2007.

[155] M. J. J. Kearney and A. I. I. Horrell, "The effect of alloy scattering on the mobility of holes in a SiGe quantum well," *Semiconductor Science and Technology*, vol. 13, p. 174, 1998.

[156] C. Gupta, Y. Tsukada, B. Romanczyk, S. S. Pasayat, D. A. James, E. Ahmadi, S. Keller, and U. K. Mishra, "First demonstration of improvement in hole conductivity in c-plane III-Nitrides through application of uniaxial strain," *Japanese Journal of Applied Physics*, vol. 58, p. 030908, 3 2019.

[157] B. Santic, "On the hole effective mass and the free hole statistics in wurtzite GaN," *Semiconductor Science and Technology*, vol. 18, no. 4, pp. 219–224, 2003.

[158] J. Guo, G. Li, F. Faria, Y. Cao, R. Wang, J. Verma, X. Gao, S. Guo, E. Beam, A. Ketterson, M. Schuette, P. Saunier, M. Wistey, D. Jena, and H. Xing, "MBE-regrown ohmics in InAlN HEMTs with a regrowth interface resistance of 0.05 Ω.mm," *IEEE Electron Device Letters*, vol. 33, pp. 525–527, 4 2012.

[159] C. Chapin, K. Dowling, X. Xu, and D. G. Senesky, "Development of Thin Film Release of GaN using AlN and Abstract AlGaN Buffer Layers for MEMS Applications." *https://snfexfab.stanford.edu/sites/g/files/sbiybj8726/f/sections/diplayfiles/cc_kd_mocvd_hemt_paper_final_snfwiki2.pdf*, Stanford University, 2015.

[160] X. Z. Dang, P. M. Asbeck, E. T. Yu, G. J. Sullivan, M. Y. Chen, B. T. McDermott, K. S. Boutros, and J. M. Redwing, "Measurement of drift mobility in AlGaN/GaN heterostructure field-effect transistor," *Applied Physics Letters*, vol. 74, p. 3890, 6 1999.

[161] R. Peterson, M. Malakoutian, X. Xu, C. Chapin, S. Chowdhury, and D. G. Senesky, "Analysis of mobility-limiting mechanisms of the two-dimensional hole gas on hydrogen-terminated diamond," *Physical Review B*, vol. 102, p. 075303, 8 2020.

[162] D. Jena and U. K. Mishra, "Quantum and classical scattering times due to charged dislocations in an impure electron gas," *Physical Review B*, vol. 66, p. 241307, 12 2002.

[163] U. Singisetti, M. Hoi Wong, and U. K. Mishra, "Interface roughness scattering in ultra-thin N-polar GaN quantum well channels," *Applied Physics Letters*, vol. 101, no. 1, pp. 1–5, 2012.

[164] R. K. Jana and D. Jena, "Stark-effect scattering in rough quantum wells," *Applied Physics Letters*, vol. 99, no. 1, pp. 1–4, 2011.

[165] K. Shibata, M. Karalic, C. Mittag, T. Tschirky, C. Reichl, H. Ito, K. Hashimoto, T. Tomimatsu, Y. Hirayama, W. Wegscheider, T. Ihn, and K. Ensslin, "Electric-field-induced two-dimensional hole gas in undoped GaSb quantum wells," *Applied Physics Letters*, vol. 114, no. 23, p. 232102, 2019.

[166] E. Piatti, D. Romanin, D. Daghero, and R. S. Gonnelli, "Two-dimensional hole transport in ion-gated diamond surfaces: A brief review (Review article)," *Low Temperature Physics*, vol. 45, p. 1143, 11 2019.

[167] A. Nainani, T. Irisawa, B. R. Bennett, J. Brad Boos, M. G. Ancona, and K. C. Saraswat, "Study of Shubnikov–de Haas oscillations and measurement of hole effective mass in compressively strained $In_xGa_{1−x}Sb$ quantum wells," *Solid-State Electronics*, vol. 62, pp. 138–141, 8 2011.

[168] B. Grbić, R. Leturcq, T. Ihn, K. Ensslin, D. Reuter, and A. D. Wieck, "Strong spin-orbit interactions and weak antilocalization in carbon-doped p -type GaAs $Al_xGa_{1−x}As$ heterostructures," *Physical Review B - Condensed Matter and Materials Physics*, vol. 77, 3 2008.

[169] Y. Sasama, K. Komatsu, S. Moriyama, M. Imura, S. Sugiura, T. Terashima, S. Uji, K. Watanabe, T. Taniguchi, T. Uchihashi, and Y. Takahide, "Quantum oscillations in diamond field-effect transistors with a h -BN gate dielectric," *Physical Review Materials*, vol. 3, 12 2019.

[170] S. Bajaj, O. F. Shoron, P. S. Park, S. Krishnamoorthy, F. Akyol, T. H. Hung, S. Reza, E. M. Chumbes, J. Khurgin, and S. Rajan, "Density-dependent electron transport and precise modeling of GaN high electron mobility transistors," *Applied Physics Letters*, vol. 107, no. 15, pp. 1–5, 2015.

[171] D. Ji, B. Ercan, and S. Chowdhury, "Experimental Determination of Velocity-Field Characteristic of Holes in GaN," *IEEE Electron Device Letters*, vol. 41, pp. 23–25, 1 2020.

[172] B. Sensale-Rodriguez, J. Guo, R. Wang, J. Verma, G. Li, T. Fang, E. Beam, A. Ketterson, M. Schuette, P. Saunier, X. Gao, S. Guo, G. Snider, P. Fay, D. Jena, and H. G. Xing, "Time delay analysis in high speed gate-recessed E-mode InAlN HEMTs," *Solid-State Electronics*, vol. 80, pp. 67–71, 2013.

[173] Y. Cao and D. Jena, "High-mobility window for two-dimensional electron gases at ultrathin AlN/GaN heterojunctions," *Applied Physics Letters*, vol. 90, no. 18, pp. 23–25, 2007.

[174] C. E. Dreyer, A. Janotti, C. G. Van de Walle, and D. Vanderbilt, "Correct implementation of polarization constants in wurtzite materials and impact on III-nitrides," *Physical Review X*, vol. 6, no. 2, pp. 1–11, 2016.

[175] T. Erlbacher, *Lateral Power Transistors in Integrated Circuits*. Cham: Springer International Publishing, 2014.

[176] B. Hughes, J. Lazar, S. Hulsey, M. Musni, D. Zehnder, A. Garrido, R. Khanna, R. Chu, S. Khalil, and K. Boutros, "Normally-off GaN-on-Si multi-chip module boost converter with 96% efficiency and low gate and drain overshoot," *Conference Proceedings - IEEE Applied Power Electronics Conference and Exposition - APEC*, pp. 484–487, 2014.

[177] F. Luo, Z. Chen, L. Xue, P. Mattavelli, D. Boroyevich, and B. Hughes, "Design considerations for GaN HEMT multichip halfbridge module for high-frequency power converters," *Conference Proceedings - IEEE Applied Power Electronics Conference and Exposition - APEC*, pp. 537–544, 2014.

[178] K. Shinohara, D. C. Regan, Y. Tang, A. L. Corrion, D. F. Brown, J. C. Wong, J. F. Robinson, H. H. Fung, A. Schmitz, T. C. Oh, S. J. Kim, P. S. Chen, R. G. Nagele, A. D. Margomenos, and M. Micovic, "Scaling of GaN HEMTs and Schottky diodes for submillimeter-wave MMIC applications," *IEEE Transactions on Electron Devices*, vol. 60, no. 10, pp. 2982–2996, 2013.

[179] M. L. Schuette, A. Ketterson, B. Song, E. Beam, T. M. Chou, M. Pilla, H. Q. Tserng, X. Gao, S. Guo, P. J. Fay, H. G. Xing, and P. Saunier, "Gate-recessed integrated E/D GaN HEMT technology with $f_T / f_{max} > 300$ GHz," *IEEE Electron Device Letters*, vol. 34, no. 6, pp. 741–743, 2013.

[180] S. Moench, R. Reiner, P. Waltereit, S. Muller, R. Quay, O. Ambacher, and I. Kallfass, "A 600V p-GaN Gate HEMT with Intrinsic Freewheeling Schottky-Diode in a GaN Power IC with Bootstrapped Driver and Sensors," *Proceedings of the International Symposium on Power Semiconductor Devices and ICs*, pp. 254–257, 9 2020.

[181] D. Kinzer and S. Oliver, "Monolithic HV GaN Power ICs: Performance and application," *IEEE Power Electronics Magazine*, vol. 3, pp. 14–21, 9 2016.

[182] M. Giandalia, J. Zhang, and T. Ribarich, "650 V AllGaN™ power IC for power supply applications," *WiPDA 2016 - 4th IEEE Workshop on Wide Bandgap Power Devices and Applications*, pp. 220–222, 12 2016.

[183] K. Shinohara, "III-Nitride millimeter wave transistors," in *Semiconductors and Semimetals*, vol. 102, pp. 141–184, Elsevier Inc., 1 ed., 2019.

[184] P. M. Solomon, A. Palevski, T. F. Kuech, and M. A. Tischler, "Low resistance ohmic contacts to two-dimensional electron-gas structures by selective MOVPE," *Technical Digest - International Electron Devices Meeting*, pp. 405–408, 1989.

[185] C. G. Van de Walle, C. Stampfl, and J. Neugebauer, "Theory of doping and defects in III–V nitrides," *Journal of Crystal Growth*, vol. 189-190, pp. 505–510, 1998.

[186] E. Monroy, T. Andreev, P. Holliger, E. Bellet-Amalric, T. Shibata, M. Tanaka, and B. Daudin, "Modification of GaN(0001) growth kinetics by Mg doping," *Applied Physics Letters*, vol. 84, no. 14, pp. 2554–2556, 2004.

[187] A. Raj, A. Krishna, N. Hatui, C. Gupta, R. Jang, S. Keller, and U. K. Mishra, "Demonstration of a GaN/AlGaN Superlattice-Based p-Channel FinFET with High ON-Current," *IEEE Electron Device Letters*, vol. 41, pp. 220–223, 2 2020.

[188] J. O. Song, K. K. Kim, S. J. Park, and T. Y. Seong, "Highly low resistance and transparent Ni/ZnO ohmic contacts to p-type GaN," *Applied Physics Letters*, vol. 83, pp. 479–481, 7 2003.

[189] H. W. Jang and J.-L. Lee, "Mechanism for ohmic contact formation of Ni/Ag contacts on p-type GaN," *Applied Physics Letters*, vol. 85, p. 5920, 12 2004.

[190] H. K. Cho, T. Hossain, J. W. Bae, and I. Adesida, "Characterization of Pd/Ni/Au ohmic contacts on p-GaN," *Solid-State Electronics*, vol. 49, pp. 774–778, 5 2005.

[191] J. O. Song, J. S. Ha, and T. Y. Seong, "Ohmic-contact technology for GaN-based light-emitting diodes: Role of p-type contact," *IEEE Transactions on Electron Devices*, vol. 57, pp. 42–59, 1 2010.

[192] S. H. Lim, T. Y. Ra, and W. Y. Kim, "Interface observation in Au/Ni/p-GaN studied by HREM and energy-filtering TEM," *Journal of Electron Microscopy*, vol. 52, no. 5, pp. 459–464, 2003.

[193] K. Kumakura, T. Makimoto, and N. Kobayashi, "Low-resistance nonal-

loyed ohmic contact to p-type GaN using strained InGaN contact layer," *Applied Physics Letters*, vol. 79, no. 16, pp. 2588–2590, 2001.

[194] D. K. Schroder, *Semiconductor Material and Device Characterization*. Hoboken, NJ, USA: John Wiley & Sons, Inc., 2005.

[195] H. Okumura, D. Martin, and N. Grandjean, "Low p-type contact resistance by field-emission tunneling in highly Mg-doped GaN," *Applied Physics Letters*, vol. 109, 2016.

[196] K. Lee, S. Bharadwaj, V. Protasenko, H. G. Xing, and D. Jena, "Efficient InGaN p-Contacts for deep-UV Light Emitting Diodes," *Device Research Conference - Conference Digest, DRC*, no. 607, pp. 171–172, 2019.

[197] R. H. Dennard, F. H. Gaensslen, H. N. Yu, V. L. Rideout, E. Bassous, and A. R. Leblanc, "Design of Ion-Implanted MOSFET's With Very Small Physical Dimensions," *IEEE Journal of Solid-State Circuits*, vol. 9, no. 5, pp. 256–268, 1974.

[198] S. W. Kaun, M. H. Wong, S. Dasgupta, S. Choi, R. Chung, U. K. Mishra, and J. S. Speck, "Effects of Threading Dislocation Density on the Gate Leakage of AlGaN/GaN Heterostructures for High Electron Mobility Transistors," *Applied Physics Express*, vol. 4, p. 024101, 1 2011.

[199] J. J. M. Law, E. T. Yu, G. Koblmüller, F. Wu, and J. S. Speck, "Low defect-mediated reverse-bias leakage in (0001) GaN via high-temperature molecular beam epitaxy," *Applied Physics Letters*, vol. 96, p. 102111, 3 2010.

[200] R. T. Bondokov, S. G. Mueller, K. E. Morgan, G. A. Slack, S. Schujman, M. C. Wood, J. A. Smart, and L. J. Schowalter, "Large-area AlN substrates for electronic applications: An industrial perspective," *Journal of Crystal Growth*, vol. 310, pp. 4020–4026, 8 2008.

[201] Y. Kumagai, Y. Kubota, T. Nagashima, T. Kinoshita, R. Dalmau, R. Schlesser, B. Moody, J. Xie, H. Murakami, A. Koukitu, and Z. Sitar, "Preparation of a Freestanding AlN Substrate from a Thick AlN Layer Grown by Hydride Vapor Phase Epitaxy on a Bulk AlN Substrate Prepared by Physical Vapor Transport," *Applied Physics Express*, vol. 5, p. 055504, 5 2012.

[202] O. Ambacher, B. Christian, M. Yassine, M. Baeumler, S. Leone, and R. Quay, "Polarization induced interface and electron sheet charges

of pseudomorphic ScAlN/GaN, GaAlN/GaN, InAlN/GaN, and In-AlN/InN heterostructures," *Journal of Applied Physics*, vol. 129, p. 204501, 5 2021.

[203] S. Russo and A. Di Carlo, "Influence of the source-gate distance on the AlGaN/GaN HEMT performance," *IEEE Transactions on Electron Devices*, vol. 54, pp. 1071–1075, 5 2007.

[204] P. Tasker and B. Hughes, "Importance of source and drain resistance to the maximum fT of millimeter-wave MODFETs," *IEEE Electron Device Letters*, vol. 10, pp. 291–293, 7 1989.

[205] M. Kato, K. Mikamo, M. Ichimura, M. Kanechika, O. Ishiguro, and T. Kachi, "Characterization of plasma etching damage on p-type GaN using Schottky diodes," *Journal of Applied Physics*, vol. 103, p. 093701, 5 2008.

[206] M. Monavarian, G. Pickrell, A. A. Aragon, I. Stricklin, M. H. Crawford, A. A. Allerman, K. C. Celio, F. Leonard, A. A. Talin, A. M. Armstrong, and D. Feezell, "High-Voltage Regrown Non polar *m*-Plane Vertical p-n Diodes: A Step Toward Future Selective-Area-Doped Power Switches," *IEEE Electron Device Letters*, vol. 40, pp. 387–390, 3 2019.

[207] M. Xiao, Z. Du, J. Xie, E. Beam, X. Yan, K. Cheng, H. Wang, Y. Cao, and Y. Zhang, "Lateral p-GaN/2DEG junction diodes by selective-area p-GaN trench-filling-regrowth in AlGaN/GaN," *Applied Physics Letters*, vol. 116, p. 053503, 2 2020.

[208] K. Fu, H. Fu, H. Liu, S. R. Alugubelli, T.-H. Yang, X. Huang, H. Chen, I. Baranowski, J. Montes, F. A. Ponce, and Y. Zhao, "Investigation of GaN-on-GaN vertical p-n diode with regrown p-GaN by metalorganic chemical vapor deposition," *Applied Physics Letters*, vol. 113, p. 233502, 12 2018.

[209] Samuel James Bader, *GaN-on-AlN as a Platform for High-Voltage Complementary Electronics*. PhD thesis, Cornell University, 2020.

[210] J. Sun, G. Longobardi, F. Udrea, C. Zhu, G. Camuso, S. Yang, R. Garg, M. Imam, and A. Charles, "Substantiation of buried two dimensional hole gas (2DHG) existence in GaN-on-Si epitaxial heterostructure," *Applied Physics Letters*, vol. 110, p. 163506, 4 2017.

[211] J. A. Seamons, D. R. Tibbetts, J. L. Reno, and M. P. Lilly, "Undoped electron-hole bilayers in a GaAs/AlGaAs double quantum well," *Applied Physics Letters*, vol. 90, no. 5, p. 52103, 2007.

[212] M. H. Szymanska and P. B. Littlewood, "Excitonic binding in coupled quantum wells," *Physical Review B*, vol. 67, p. 193305, 5 2003.

[213] W.-K. Tse and S. Das Sarma, "Coulomb drag and spin drag in the presence of spin-orbit coupling," *Physical Review B*, vol. 75, p. 045333, 1 2007.

[214] D. Neilson, A. Perali, and A. R. Hamilton, "Excitonic superfluidity and screening in electron-hole bilayer systems," *Physical Review B - Condensed Matter and Materials Physics*, vol. 89, no. 6, 2014.

[215] H. Cheng, C. Kurdak, J. H. Leach, M. Wu, and H. Morko, "Two-subband conduction in a gated high density InAlN/AlN/GaN heterostructure," *Applied Physics Letters*, vol. 97, p. 112113, 9 2010.

[216] L. Yang, X. Wang, T. Wang, J. Wang, W. Zhang, P. Quach, P. Wang, F. Liu, D. Li, L. Chen, S. Liu, J. Wei, X. Yang, F. Xu, N. Tang, W. Tan, J. Zhang, W. Ge, X. Wu, C. Zhang, and B. Shen, "Three Subband Occupation of the Two-Dimensional Electron Gas in Ultrathin Barrier AlN/GaN Heterostructures," *Advanced Functional Materials*, vol. 30, 11 2020.

[217] Y. Cao, K. Wang, and D. Jena, "Electron transport properties of low sheet-resistance two-dimensional electron gases in ultrathin AlN/GaN heterojunctions grown by MBE," *Physica Status Solidi (C) Current Topics in Solid State Physics*, vol. 5, 5 2008.

[218] A. Hickman, R. Chaudhuri, N. Moser, M. Elliott, K. Nomoto, L. Li, J. C. M. Hwang, H. Grace Xing, and D. Jena, "Large Signal Response of AlN/GaN/AlN HEMTs at 30 GHz," in *2021 Device Research Conference (DRC)*, pp. 1–2, IEEE, 6 2021.

[219] G. Li, R. Wang, J. Guo, J. Verma, Z. Hu, Y. Yue, F. Faria, Y. Cao, M. Kelly, T. Kosel, H. Xing, and D. Jena, "Ultrathin body GaN-on-insulator quantum well FETs with regrown ohmic contacts," *IEEE Electron Device Letters*, vol. 33, no. 5, pp. 661–663, 2012.

[220] J. R. Miller, "The NHMFL 45-T hybrid magnet system: Past, present, and future," *IEEE Transactions on Applied Superconductivity*, vol. 13, pp. 1385–1390, 2003.

[221] R. Kubo, H. Hasegawa, and N. Hashitsume, "Quantum Theory of Galvanomagnetic Effect. I. Basic Considerations," *Journal of the Physical Society of Japan*, vol. 14, pp. 56–74, 12 1959.

[222] H. L. Stromer, A. C. Gossard, and W. Wiegmann, "Observation of Inter-subband Scattering in a 2-Dimensional Electron System," *Solid State Communications*, vol. 41, no. 10, pp. 707–709, 1982.

[223] A. M. Kurakin, S. A. Vitusevich, S. V. Danylyuk, H. Hardtdegen, N. Klein, Z. Bougrioua, A. V. Naumov, and A. E. Belyaev, "Quantum confinement effect on the effective mass in two-dimensional electron gas of Al-GaN/GaN heterostructures," *Journal of Applied Physics*, vol. 105, no. 7, 2009.

[224] Y. J. Wang, R. Kaplan, H. K. Ng, K. Doverspike, D. K. Gaskill, T. Ikedo, I. Akasaki, and H. Amono, "Magneto-optical studies of GaN and GaN/AlxGa1-xN: Donor Zeeman spectroscopy and two dimensional electron gas cyclotron resonance," *Journal of Applied Physics*, vol. 79, pp. 8007–8010, 5 1996.

[225] S. Syed, J. B. Heroux, Y. J. Wang, M. J. Manfra, R. J. Molnar, and H. L. Stormer, "Nonparabolicity of the conduction band of wurtzite GaN," *Applied Physics Letters*, vol. 83, pp. 4553–4555, 12 2003.

[226] K. S. Cho, T. Y. Huang, H. S. Wang, M. G. Lin, T. M. Chen, C. T. Liang, Y. F. Chen, and I. Lo, "Zero-field spin splitting in modulation-doped $Al_xGa_{1-x}N$/GaN two-dimensional electron systems," *Applied Physics Letters*, vol. 86, pp. 1–3, 5 2005.

[227] W. Knap, H. Alause, J. M. Bluet, J. Camassel, J. Young, M. Asif Khan, Q. Chen, S. Huant, and M. Shur, "The cyclotron resonance effective mass of two-dimensional electrons confined at the GaN /AlGaN interface," *Solid State Communications*, vol. 99, pp. 195–199, 7 1996.

[228] W. Knap, S. Contreras, H. Alause, C. Skierbiszewski, J. Camassel, M. Dyakonov, J. L. Robert, J. Yang, Q. Chen, M. Asif Khan, M. L. Sadowski, S. Huant, F. H. Yang, M. Goiran, J. Leotin, and M. S. Shur, "Cyclotron resonance and quantum Hall effect studies of the two-dimensional electron gas confined at the GaN/AlGaN interface," *Applied Physics Letters*, vol. 70, no. 16, pp. 2123–2125, 1997.

[229] T. Lin, H. Chen, M. Tsai, Y. Chen, and F. Fang, "Two-dimensional electron gas and persistent photoconductivity in AlGaN/GaN heterostructures," *Physical Review B - Condensed Matter and Materials Physics*, vol. 58, no. 20, pp. 13793–13798, 1998.

[230] S. Elhamri, R. S. Newrock, D. B. Mast, M. Ahoujja, W. C. Mitchel, J. M.

Redwing, M. A. Tischler, and J. S. Flynn, "Al0.15Ga0.85N/GaN heterostructures: Effective mass and scattering times," *Physical Review B*, vol. 57, no. 3, p. 57, 1998.

[231] T. Wang, J. Bai, S. Sakai, Y. Ohno, and H. Ohno, "Magnetotransport studies of AlGaN/GaN heterostructures grown on sapphire substrates: Effective mass and scattering time," *Applied Physics Letters*, vol. 76, no. 19, pp. 2737–2739, 2000.

[232] A. Saxler, P. Debray, R. Perrin, S. Elhamri, W. C. Mitchel, C. R. Elsass, I. P. Smorchkova, B. Heying, E. Haus, P. Fini, J. P. Ibbetson, S. Keller, P. M. Petroff, S. P. DenBaars, U. K. Mishra, and J. S. Speck, "Characterization of an AlGaN/GaN two-dimensional electron gas structure," *Journal of Applied Physics*, vol. 87, pp. 369–374, 1 2000.

[233] A. F. Braña, C. Diaz-Paniagua, F. Batallan, J. A. Garrido, E. Muñoz, and F. Omnes, "Scattering times in AlGaN/GaN two-dimensional electron gas from magnetoresistance measurements," *Journal of Applied Physics*, vol. 88, pp. 932–937, 7 2000.

[234] D. R. Hang, C. T. Liang, C. F. Huang, Y. H. Chang, Y. F. Chen, H. X. Jiang, and J. Y. Lin, "Effective mass of two-dimensional electron gas in an $Al_{0.2}Ga_{0.8}N$/GaN heterojunction," *Applied Physics Letters*, vol. 79, no. 1, pp. 66–68, 2001.

[235] Z. F. Li, W. Lu, S. C. Shen, S. Holland, C. M. Hu, D. Heitmann, B. Shen, Y. D. Zheng, T. Someya, and Y. Arakawa, "Cyclotron resonance and magnetotransport measurements in $Al_xGa_{1-x}N$/GaN heterostructures for x=0.15-0.30," *Applied Physics Letters*, vol. 80, pp. 431–433, 1 2002.

[236] S. Syed, M. J. Manfra, Y. J. Wang, H. L. Stormer, and R. J. Molnar, "Large splitting of the cyclotron-resonance line in AlGaN/GaN heterostructures," *Physical Review B*, vol. 67, p. 241304, 6 2003.

[237] L. W. Wong, S. J. Cai, R. Li, K. Wang, H. W. Jiang, and M. Chen, "Magnetotransport study on the two-dimensional electron gas in AlGaN/GaN heterostructures," *Applied Physics Letters*, vol. 73, pp. 1391–1393, 9 1998.

[238] W. Zawadzki, "Electron transport phenomena in small-gap semiconductors," *Advances in Physics*, vol. 23, pp. 435–522, 1 1974.

[239] E. . Kane, "Band Structure of Indium Antimonide," *Journal of Physics and Chemistry of Solids*, vol. 1, pp. 249–261, 1957.

[240] S. Syed, J. B. Heroux, Y. J. Wang, M. J. Manfra, R. J. Molnar, and H. L. Stormer, "Nonparabolicity of the conduction band of wurtzite GaN," *Applied Physics Letters*, vol. 83, no. 22, pp. 4553–4555, 2003.

[241] Y. Cao, "Epitaxial growth of III-nitride electronic devices," in *Semiconductors and Semimetals*, vol. 102, pp. 41–113, Elsevier Inc., 1 ed., 2019.

[242] S. Das Sarma and F. Stern, "Single-particle relaxation time versus scattering time in an impure electron gas," *Physical Review B*, vol. 32, no. 12, pp. 8442–8444, 1985.

[243] Y. A. Bychkov and E. I. Rashba, "Oscillatory effects and the magnetic susceptibility of carriers in inversion layers," *Journal of Physics C: Solid State Physics*, vol. 17, no. 33, pp. 6039–6045, 1984.

[244] D. Spirito, L. Di Gaspare, G. Frucci, F. Evangelisti, A. Di Gaspare, A. Notargiacomo, E. Giovine, S. Roddaro, and F. Beltram, "Magnetotransport investigation of conducting channels and spin splitting in high-density AlGaN/AlN/GaN two-dimensional electron gas," *Physical Review B - Condensed Matter and Materials Physics*, vol. 83, no. 15, pp. 1–6, 2011.

[245] D. Spirito, L. Di Gaspare, F. Evangelisti, A. Di Gaspare, E. Giovine, and A. Notargiacomo, "Weak antilocalization and spin-orbit interaction in a two-dimensional electron gas," *Physical Review B - Condensed Matter and Materials Physics*, vol. 85, no. 23, pp. 1–5, 2012.

[246] I. Lo, J. K. Tsai, W. J. Yao, P. C. Ho, L. W. Tu, T. C. Chang, S. Elhamri, W. C. Mitchel, K. Y. Hsieh, J. H. Huang, H. L. Huang, and W. C. Tsai, "Spin splitting in modulation-doped (formula presented) heterostructures," *Physical Review B - Condensed Matter and Materials Physics*, vol. 65, no. 16, pp. 1–4, 2002.

[247] H. Tang, J. B. Webb, P. Coleridge, J. A. Bardwell, C. H. Ko, Y. K. Su, and S. J. Chang, "Scattering lifetimes due to interface roughness with large lateral correlation length in (formula presented) two-dimensional electron gas," *Physical Review B - Condensed Matter and Materials Physics*, vol. 66, no. 24, pp. 1–7, 2002.

[248] N. Tang, B. Shen, K. Han, F. C. Lu, F. J. Xu, Z. X. Qin, and G. Y. Zhang, "Zero-field spin splitting in AlxGa1-xN/GaN heterostructures with various Al compositions," *Applied Physics Letters*, vol. 93, no. 17, pp. 10–13, 2008.

[249] S. B. Lisesivdin, N. Balkan, O. Makarovsky, A. Patan, A. Yildiz, M. D. Caliskan, M. Kasap, S. Ozcelik, and E. Ozbay, "Large zero-field spin splitting in AlGaN/AlN/GaN/AlN heterostructures," *Journal of Applied Physics*, vol. 105, no. 9, 2009.

[250] I. Lo, M. H. Gau, J. K. Tsai, Y. L. Chen, Z. J. Chang, W. T. Wang, J. C. Chiang, T. Aggerstam, and S. Lourdudoss, "Anomalous k-dependent spin splitting in wurtzite AlGaN/GaN heterostructures," *Physical Review B*, vol. 75, p. 245307, 6 2007.

[251] K. Tsubaki, N. Maeda, T. Saitoh, and N. Kobayashi, "Spin splitting in modulation-doped AlGaN/GaN two-dimensional electron gas," *Applied Physics Letters*, vol. 80, pp. 3126–3128, 4 2002.

[252] W. Z. Zhou, T. Lin, L. Y. Shang, L. Sun, K. H. Gao, Y. M. Zhou, G. Yu, N. Tang, K. Han, B. Shen, S. L. Guo, Y. S. Gui, and J. H. Chu, "Weak antilocalization and beating pattern in high electron mobility $Al_xGa_{1-x}N$/GaN two-dimensional electron gas with strong Rashba spin-orbit coupling," *Journal of Applied Physics*, vol. 104, p. 053703, 9 2008.

[253] N. Thillosen, S. Cabañas, N. Kaluza, V. A. Guzenko, H. Hardtdegen, and T. Schäpers, "Weak antilocalization in gate-controlled Alx Ga1-x N GaN two-dimensional electron gases," *Physical Review B - Condensed Matter and Materials Physics*, vol. 73, p. 241311, 6 2006.

[254] I. Litvinov, "Electron spin splitting in polarization-doped group-III nitrides," *Physical Review B - Condensed Matter and Materials Physics*, vol. 68, no. 15, pp. 1–6, 2003.

[255] L. C. Lew Yan Voon, M. Willatzen, M. Cardona, and N. E. Christensen, "Terms linear in k in the band structure of wurtzite-type semiconductors," *Physical Review B*, vol. 53, pp. 10703–10714, 4 1996.

[256] F. Lu, N. Tang, W. Ge, F. Xu, W. Wang, W. Li, and B. Shen, " The in-plane anisotropy of the effective *g* factors in $Al_{0.25}Ga_{0.75}N$/GaN based quantum point contacts with narrow channels ," *Applied Physics Letters*, vol. 116, p. 182101, 5 2020.

[257] I. Lo, W. T. Wang, M. H. Gau, S. F. Tsay, and J. C. Chiang, "Wurtzite structure effects on spin splitting in GaN/AlN quantum wells," *Physical Review B - Condensed Matter and Materials Physics*, vol. 72, no. 24, pp. 1–5, 2005.

[258] M. Prunnila, S. J. Laakso, J. M. Kivioja, and J. Ahopelto, "Electrons and holes in Si quantum well: A room-temperature transport and drag resistance study," *Applied Physics Letters*, vol. 93, p. 112113, 9 2008.

[259] J. P. Eisenstein, L. N. Pfeiffer, and K. W. West, "Independently contacted two-dimensional electron systems in double quantum wells," *Applied Physics Letters*, vol. 57, p. 2324, 8 1998.

[260] A. F. Croxall, K. D. Gupta, C. A. Nicoll, M. Thangaraj, I. Farrer, D. A. Ritchie, and M. Pepper, "Patterned backgating using single-sided mask aligners: Application to density-matched electron-hole bilayers," *Journal of Applied Physics*, vol. 104, p. 113715, 12 2008.

[261] E. H. Linfield, G. A. C. Jones, D. A. Ritchie, and J. H. Thompson, "The fabrication of a back-gated high electron mobility transistor-a novel approach using MBE regrowth on an in situ ion beam patterned epilayer," *Semiconductor Science and Technology*, vol. 8, p. 415, 3 1993.

[262] C. Richardson, A. Alexander, C. Weddle, C. Richardson, A. Alexander, and C. Weddle, "MBE grown AlN-TiN heterostructures for superconducting quantum circuits," *APS*, vol. 2019, p. V35.006, 2019.

[263] R. Yan, G. Khalsa, S. Vishwanath, Y. Han, J. Wright, S. Rouvimov, D. S. Katzer, N. Nepal, B. P. Downey, D. A. Muller, H. G. Xing, D. J. Meyer, and D. Jena, "GaN/NbN epitaxial semiconductor/superconductor heterostructures," *Nature*, vol. 555, pp. 183–189, 3 2018.

[264] J. A. Seamons, C. P. Morath, J. L. Reno, and M. P. Lilly, "Coulomb Drag in the Exciton Regime in Electron-Hole Bilayers," *Physical Review Letters*, vol. 102, p. 026804, 1 2009.

[265] J. A. Keogh, K. D. Gupta, H. E. Beere, D. A. Ritchie, and M. Pepper, "Fabrication of closely spaced, independently contacted electron-hole bilayers in GaAs-AlGaAs heterostructures," *Applied Physics Letters*, vol. 87, p. 202104, 11 2005.

[266] K. Takashina, K. Nishiguchi, Y. Ono, A. Fujiwara, T. Fujisawa, Y. Hirayama, and K. Muraki, "Electrons and holes in a 40 nm thick silicon slab at cryogenic temperatures," *Applied Physics Letters*, vol. 94, p. 142104, 4 2009.

[267] J. M. Blatt, K. W. Böer, and W. Brandt, "Bose-Einstein Condensation of Excitons," *Physical Review*, vol. 126, p. 1691, 6 1962.

[268] G. Bastard, E. E. Mendez, L. L. Chang, and L. Esaki, "Exciton binding energy in quantum wells," *Physical Review B*, vol. 26, p. 1974, 8 1982.

[269] A.-P. Jauho and H. Smith, "Coulomb drag between parallel two-dimensional electron systems," *Physical Review B*, vol. 47, p. 4420, 2 1993.

[270] C. Hamaguchi, *Basic Semiconductor Physics*. Berlin, Heidelberg: Springer Berlin Heidelberg, 2010.

[271] H. Condori Quispe, S. M. Islam, S. Bader, A. Chanana, K. Lee, R. Chaudhuri, A. Nahata, H. G. Xing, D. Jena, and B. Sensale-Rodriguez, "Terahertz spectroscopy of an electron-hole bilayer system in AlN/GaN/AlN quantum wells," *Applied Physics Letters*, vol. 111, no. 7, 2017.

[272] D. C. Streit, K. L. Tan, R. M. Dia, J. K. Liu, A. C. Han, J. R. Velebir, S. K. Wane, T. Q. Trinh, P. M. D. Chow, P. H. Liu, and H. C. Yen, "High-Gain W-Band Pseudomorphic InGaAs Power HEMT's," *IEEE Electron Device Letters*, vol. 12, no. 4, pp. 149–150, 1991.

[273] R. Lai, M. Wojtowicz, C. H. Chen, M. Biedenbender, H. C. Yen, D. C. Streit, K. L. Tan, and P. H. Liu, "High-Power 0.15-μm V-band Pseudomorphic InGaAs-AlGaAs-GaAs HEMT," *IEEE Microwave and Guided Wave Letters*, vol. 3, no. 10, pp. 363–365, 1993.

[274] U. R. Pfeiffer, S. K. Reynolds, and B. A. Floyd, "A 77 GHz SiGe power amplifier for potential applications in automotive radar systems," *IEEE Radio Frequency Integrated Circuits Symposium, RFIC, Digest of Technical Papers*, pp. 91–94, 2004.

[275] R. Grundbacher, R. Lai, M. Nishimoto, T. P. Chin, Y. C. Chen, M. Barsky, T. Block, and D. Streit, "Pseudomorphic InP HEMT's with dry-etched source vias having 190 mW output power and 40% PAE at V-band," *IEEE Electron Device Letters*, vol. 20, pp. 517–519, 10 1999.

[276] D. L. Ingram, Y. C. Chen, J. Kraus, B. Brunner, B. Allen, H. C. Yen, and K. F. Lau, "427 mW, 20% compact W-band InP HEMT MMIC power amplifier," *IEEE Radio Frequency Integrated Circuits Symposium, RFIC, Digest of Technical Papers*, pp. 95–98, 1999.

[277] Y. F. Wu, A. Saxler, M. Moore, R. P. Smith, S. Sheppard, P. M. Chavarkar, T. Wisleder, U. K. Mishra, and P. Parikh, "30-W/mm GaN HEMTs by Field Plate Optimization," *IEEE Electron Device Letters*, vol. 25, pp. 117–119, 3 2004.

[278] Y. F. Wu, M. Moore, A. Saxler, T. Wisleder, and P. Parikh, "40-W/mm Double Field-plated GaN HEMTs," *Device Research Conference - Conference Digest, DRC*, pp. 151–152, 2 2007.

[279] S. Ozaki, J. Yaita, A. Yamada, Y. Kumazaki, Y. Minoura, T. Ohki, N. Okamoto, N. Nakamura, and J. Kotani, "First demonstration of X-band AlGaN/GaN high electron mobility transistors using free-standing AlN substrate over 15 W mm-1output power density," *Applied Physics Express*, vol. 14, p. 041004, 4 2021.

[280] B. Romanczyk, S. Wienecke, M. Guidry, H. Li, E. Ahmadi, X. Zheng, S. Keller, and U. K. Mishra, "Demonstration of constant 8 W/mm power density at 10, 30, and 94 GHz in state-of-the-art millimeter-wave N-polar GaN MISHEMTs," *IEEE Transactions on Electron Devices*, vol. 65, pp. 45–50, 1 2018.

[281] B. Romanczyk, U. K. Mishra, X. Zheng, M. Guidry, H. Li, N. Hatui, C. Wurm, A. Krishna, E. Ahmadi, and S. Keller, "W-Band Power Performance of SiN-Passivated N-Polar GaN Deep Recess HEMTs," *IEEE Electron Device Letters*, vol. 41, pp. 349–352, 3 2020.

[282] S. Mandal, C. Yuan, F. Massabuau, J. W. Pomeroy, J. Cuenca, H. Bland, E. Thomas, D. Wallis, T. Batten, D. Morgan, R. Oliver, M. Kuball, and O. A. Williams, "Thick, Adherent Diamond Films on AlN with Low Thermal Barrier Resistance," *ACS Applied Materials and Interfaces*, vol. 11, no. 43, pp. 40826–40834, 2019.

[283] Z. Su, J. P. Freedman, J. H. Leach, E. A. Preble, R. F. Davis, and J. A. Malen, "The impact of film thickness and substrate surface roughness on the thermal resistance of aluminum nitride nucleation layers," *Journal of Applied Physics*, vol. 113, p. 213502, 2013.

[284] A. Manoi, J. W. Pomeroy, N. Killat, and M. Kuball, "Benchmarking of thermal boundary resistance in AlGaN/GaN HEMTs on SiC substrates: Implications of the nucleation layer microstructure," *IEEE Electron Device Letters*, vol. 31, no. 12, pp. 1395–1397, 2010.

[285] H. Inc., "HexaTech Launches Deep-UV Transparent 2-Inch Diameter Aluminum Nitride Substrates." *https://www.hexatechinc.com/news-events.html*, accessed 2021-08-30.

[286] NOVASiC, "State of the art wafering and polishing services." *https://www.novasic.com/*, accessed 2021-08-30.

[287] H. Okumura, T. Kimoto, and J. Suda, "Enhancement of initial layer-by-layer growth and reduction of threading dislocation density by optimized Ga pre-irradiation in molecular-beam epitaxy of 2H-AlN on 6H-SiC (0001)," *Physica Status Solidi (C) Current Topics in Solid State Physics*, vol. 7, no. 7-8, pp. 2094–2096, 2010.

[288] J. E. Ayers, "The measurement of threading dislocation densities in semiconductor crystals by X-ray diffraction," *Journal of Crystal Growth*, vol. 135, no. 1-2, pp. 71–77, 1994.

[289] J. Miller, J. Wright, H. G. Xing, and D. Jena, "All-Epitaxial Bulk Acoustic Wave Resonators," *Physica Status Solidi (A) Applications and Materials Science*, vol. 217, p. 1900786, 4 2020.

[290] I. Abid, R. Kabouche, C. Bougerol, J. Pernot, C. Masante, R. Comyn, Y. Cordier, and F. Medjdoub, "High lateral breakdown voltage in thin channel AlGaN/GaN high electron mobility transistors on AlN/Sapphire Templates," *Micromachines*, vol. 10, 10 2019.

[291] I. Abid, R. Kabouche, F. Medjdoub, S. Besendorfer, E. Meissner, J. Derluyn, S. Degroote, M. Germain, and H. Miyake, "Remarkable Breakdown Voltage on AlN/AlGaN/AlN double heterostructure," *Proceedings of the International Symposium on Power Semiconductor Devices and ICs*, pp. 310–312, 9 2020.

[292] K. Makiyama, S. Ozaki, T. Ohki, N. Okamoto, Y. Minoura, Y. Niida, Y. Kamada, K. Joshin, K. Watanabe, and Y. Miyamoto, "Collapse-free high power InAlGaN/GaN-HEMT with 3 W/mm at 96 GHz," *Technical Digest - International Electron Devices Meeting, IEDM*, pp. 1–9, 2 2015.

[293] K. Harrouche, R. Kabouche, E. Okada, and F. Medjdoub, "High Performance and Highly Robust AlN/GaN HEMTs for Millimeter-Wave Operation," *IEEE Journal of the Electron Devices Society*, vol. 7, pp. 1145–1150, 2019.

[294] B. M. Green, K. K. Chu, E. M. Chumbes, J. A. Smart, J. R. Shealy, and L. F. Eastman, "Effect of surface passivation on the microwave characteristics of undoped AlGaN/GaN HEMT's," *IEEE Electron Device Letters*, vol. 21, pp. 268–270, 6 2000.

[295] A. Vertiatchikh, L. Eastman, W. Schaff, and T. Prunty, "Effect of surface passivation of AlGaN/GaN heterostructure field-effect transistor," *Electronics Letters*, vol. 38, p. 388, 4 2002.

[296] R. Vetury, N. Q. Zhang, S. Keller, and U. K. Misha, "The impact of surface states on the DC and RF characteristics of AlGaN/GaN HFETs," *IEEE Transactions on Electron Devices*, vol. 48, no. 3, pp. 560–566, 2001.

[297] R. Chaudhuri, A. Hickman, J. Encomendero, J. Singhal, H. G. Xing, and D. Jena, "E-Mode AlN/GaN/AlN MOS-HFETs with 3 nm GaN Quantum Well Channels," *Device Research Conference (DRC) (presented)*, 2021.

[298] J. Singh, *Physics of Semiconductors and Their Heterostructures*. McGraw-Hill, New York, 1992.

[299] F. A. Faria, K. Nomoto, Z. Hu, S. Rouvimov, H. Xing, and D. Jena, "Low temperature AlN growth by MBE and its application in HEMTs," *Journal of Crystal Growth*, vol. 425, pp. 133–137, 7 2015.

[300] W. Saito, Y. Takada, M. Kuraguchi, K. Tsuda, and I. Omura, "Recessed-gate structure approach toward normally off high-voltage AlGaN/GaN HEMT for power electronics applications," *IEEE Transactions on Electron Devices*, vol. 53, pp. 356–362, 2 2006.

[301] Y. Uemoto, M. Hikita, H. Ueno, H. Matsuo, H. Ishida, M. Yanagihara, T. Ueda, T. Tanaka, and D. Ueda, "Gate injection transistor (GIT) - A normally-off AlGaN/GaN power transistor using conductivity modulation," *IEEE Transactions on Electron Devices*, vol. 54, pp. 3393–3399, 12 2007.

[302] Y. Cai, Y. Zhou, K. M. Lau, and K. J. Chen, "Control of threshold voltage of AlGaN/GaN HEMTs by fluoride-based plasma treatment: From depletion mode to enhancement mode," *IEEE Transactions on Electron Devices*, vol. 53, pp. 2207–2214, 9 2006.

[303] E. A. Jones, F. F. Wang, and D. Costinett, "Review of Commercial GaN Power Devices and GaN-Based Converter Design Challenges," *IEEE Journal of Emerging and Selected Topics in Power Electronics*, vol. 4, pp. 707–719, 9 2016.

[304] S. Migita, Y. Watanabe, H. Ota, H. Ito, Y. Kamimuta, T. Nabatame, and A. Toriumi, "Design and demonstration of very high-k (k~50) HfO2 for ultra-scaled Si CMOS," *Digest of Technical Papers - Symposium on VLSI Technology*, pp. 152–153, 2008.

[305] M. Moreira, J. Bjurström, I. Katardjev, and V. Yantchev, "Aluminum scandium nitride thin-film bulk acoustic resonators for wide band applications," *Vacuum*, vol. 86, pp. 23–26, 7 2011.

[306] J. Casamento, V. Gund, H. Lee, K. Nomoto, T. Maeda, B. Davaji, M. J. Asadi, J. Wright, Y.-T. Shao, D. A. Muller, A. Lal, Huili, Xing, and D. Jena, "Ferroelectricity in Polar ScAlN/GaN Epitaxial Semiconductor Heterostructures," *https://arxiv.org/abs/2105.10114v1*, 2021.

[307] M. Akiyama, K. Kano, and A. Teshigahara, "Influence of growth temperature and scandium concentration on piezoelectric response of scandium aluminum nitride alloy thin films," *Applied Physics Letters*, vol. 95, no. 16, 2009.

[308] M. Pirro, B. Herrera, M. Assylbekova, G. Giribaldi, L. Colombo, and M. Rinaldi, "Characterization of Dielectric and Piezoelectric Properties of Ferroelectric AlScN Thin Films," *Proceedings of the IEEE International Conference on Micro Electro Mechanical Systems (MEMS)*, pp. 646–649, 1 2021.

[309] M. T. Hardy, B. P. Downey, D. J. Meyer, N. Nepal, D. F. Storm, and D. S. Katzer, "Epitaxial ScAlN Etch-Stop Layers Grown by Molecular Beam Epitaxy for Selective Etching of AlN and GaN," *IEEE Transactions on Semiconductor Manufacturing*, vol. 30, pp. 475–479, 11 2017.

[310] D. Khachariya, S. Mita, P. Reddy, S. Dangi, P. Bagheri, M. H. Breckenridge, R. Sengupta, E. Kohn, Z. Sitar, R. Collazo, and S. Pavlidis, "$Al_{0.85}Ga_{0.15}N/Al_{0.6}Ga_{0.4}N$ High Electron Mobility Transistors on Native AlN Substrates with >9 MV/cm Mesa Breakdown Fields," *Device Research Conference 2021 - Conference Digest*, pp. 1–2, 7 2021.

[311] J. Singhal, R. Chaudhuri, A. Hickman, H. G. Xing, and D. Jena, "Properties of 2DEGs in AlN/AlGaN/AlN Double-Heterostructures," *Lester Eastman Conference on High Performance Devices (presented)*, 2021.

[312] H. K. Lim, S. Member, and J. G. Fossum, "Threshold Voltage of Thin-Film Silicon-on-Insulator (SOI) MOSFET's," *IEEE Transactions on Electron Devices*, vol. 30, no. 10, pp. 1244–1251, 1983.

[313] T. Hoshii, A. Nakajima, S.-i. Nishizawa, H. Ohashi, K. Kakushima, H. Wakabayashi, and K. Tsutsui, "Analysis of back-gate effect on threshold voltage of p-channel GaN MOSFETs on polarization-junction substrates," *Japanese Journal of Applied Physics*, vol. 58, p. 061006, 5 2019.

[314] S. Lee, B. Jagannathan, S. Narasimha, A. Chou, N. Zamdmer, J. Johnson, R. Williams, L. Wagner, J. Kim, J. O. Plouchart, J. Pekarik, S. Springer, and G. Freeman, "Record RF performance of 45-nm SOI CMOS technology,"

Technical Digest - International Electron Devices Meeting, IEDM, pp. 255–258, 2007.

[315] J. O. Plouchart, "Applications of SOI technologies to communication," *Technical Digest - IEEE Compound Semiconductor Integrated Circuit Symposium, CSIC*, 2011.

[316] K. Ueda, M. Kasu, Y. Yamauchi, T. Makimoto, M. Schwitters, D. J. Twitchen, G. A. Scarsbrook, and S. E. Coe, "Diamond FET using high-quality polycrystalline diamond with f_T of 45 GHz and f_{max} of 120 GHz," *IEEE Electron Device Letters*, vol. 27, pp. 570–572, 7 2006.

[317] N. Donato, N. Rouger, J. Pernot, G. Longobardi, and F. Udrea, "Diamond power devices: state of the art, modelling, figures of merit and future perspective," *Journal of Physics D: Applied Physics*, vol. 53, p. 093001, 12 2019.

[318] B. Heinemann, H. Rucker, R. Barth, F. Barwolf, J. Drews, G. G. Fischer, A. Fox, O. Fursenko, T. Grabolla, F. Herzel, J. Katzer, J. Korn, A. Kruger, P. Kulse, T. Lenke, M. Lisker, S. Marschmeyer, A. Scheit, D. Schmidt, J. Schmidt, M. A. Schubert, A. Trusch, C. Wipf, and D. Wolansky, "SiGe HBT with f_t/f_{max} of 505 GHz/720 GHz," *Technical Digest - International Electron Devices Meeting, IEDM*, pp. 1–3, 1 2017.

[319] J. Ajayan, D. Nirmal, R. Mathew, D. Kurian, P. Mohankumar, L. Arivazhagan, and D. Ajitha, "A critical review of design and fabrication challenges in InP HEMTs for future terahertz frequency applications," *Materials Science in Semiconductor Processing*, vol. 128, p. 105753, 6 2021.

[320] X. Mei, W. Yoshida, M. Lange, J. Lee, J. Zhou, P. H. Liu, K. Leong, A. Zamora, J. Padilla, S. Sarkozy, R. Lai, and W. R. Deal, "First Demonstration of Amplification at 1 THz Using 25-nm InP High Electron Mobility Transistor Process," *IEEE Electron Device Letters*, vol. 36, pp. 327–329, 4 2015.

[321] E.-Y. Chang, C.-I. Kuo, H.-T. Hsu, C.-Y. Chiang, and Y. Miyamoto, "InAs Thin-Channel High-Electron-Mobility Transistors with Very High Current-Gain Cutoff Frequency for Emerging Submillimeter-Wave Applications," *Applied Physics Express*, vol. 6, p. 034001, 2 2013.

[322] H. B. Jo, S. W. Yun, J. G. Kim, D. Y. Yun, I. G. Lee, D. H. Kim, T. W. Kim, S. K. Kim, J. Yun, T. Kim, T. Tsutsumi, H. Sugiyama, and H. Matsuzaki, "L_g

= 19 nm $In_{0.8}Ga_{0.2}As$ composite-channel HEMTs with f_T = 738 GHz and f_{max} = 492 GHz," *Technical Digest - International Electron Devices Meeting, IEDM*, pp. 1–8, 12 2020.

[323] K. Shinohara, A. Corrion, D. Regan, I. Milosavljevic, D. Brown, S. Burnham, P. J. Willadsen, C. Butler, A. Schmitz, D. Wheeler, A. Fung, and M. Micovic, "220 GHz f_T and 400 GHz f_{max} in 40-nm GaN DH-HEMTs with re-grown ohmic," *Technical Digest - International Electron Devices Meeting, IEDM*, 2010.

[324] K. Shinohara, D. Regan, A. Corrion, D. Brown, Y. Tang, J. Wong, G. Candia, A. Schmitz, H. Fung, S. Kim, and M. Micovic, "Self-aligned-gate GaN-HEMTs with heavily-doped n+-GaN ohmic contacts to 2DEG," *Technical Digest - International Electron Devices Meeting, IEDM*, 2012.

[325] Y. Tang, K. Shinohara, D. Regan, A. Corrion, D. Brown, J. Wong, A. Schmitz, H. Fung, S. Kim, and M. Micovic, "Ultrahigh-speed GaN high-electron-mobility transistors with fT/fmax of 454/444 GHz," *IEEE Electron Device Letters*, vol. 36, pp. 549–551, 6 2015.

[326] C. Beckmann, J. Weiben, H. Kalisch, and A. Vescan, "Two-Dimensional Hole Gases Induced by Spontaneous and Piezoelectric Polarization in Ga-Face GaN-on-AlGaN," *63rd Electronic Materials Conference (EMC) (presented)*, 2021.

[327] I. Abid, J. Mehta, Y. Cordier, J. Derluyn, S. Degroote, H. Miyake, and F. Medjdoub, "AlGaN Channel High Electron Mobility Transistors with Regrown Ohmic Contacts," *Electronics*, vol. 10, p. 635, 3 2021.

[328] M. Arita, S. Kako, S. Iwamoto, and Y. Arakawa, "Fabrication of AlGaN Two-Dimensional Photonic Crystal Nanocavities by Selective Thermal Decomposition of GaN," *Applied Physics Express*, vol. 5, p. 126502, 12 2012.

[329] B. Damilano, S. Vézian, J. Brault, B. Alloing, and J. Massies, "Selective Area Sublimation: A Simple Top-down Route for GaN-Based Nanowire Fabrication," *Nano Letters*, vol. 16, pp. 1863–1868, 3 2016.

[330] B. Damilano, S. Vézian, and J. Massies, "Mesoporous GaN Made by Selective Area Sublimation for Efficient Light Emission on Si Substrate," *Physica Status Solidi (B) Basic Research*, vol. 255, p. 1700392, 5 2018.

[331] D. S. Katzer, D. J. Meyer, D. F. Storm, J. A. Mittereder, V. M. Bermudez, S. F. Cheng, G. G. Jernigan, and S. C. Binari, "Ultra-high vacuum deposition

347

and characterization of silicon nitride thin films," *Journal of Vacuum Science & Technology B, Nanotechnology and Microelectronics: Materials, Processing, Measurement, and Phenomena*, vol. 30, p. 02B129, 3 2012.

[332] Y. Yoshino, "Piezoelectric thin films and their applications for electronics," *Journal of Applied Physics*, vol. 105, p. 061623, 3 2009.

[333] G. Chen and M. Rinaldi, "Aluminum Nitride Combined Overtone Resonators for the 5G High Frequency Bands," *Journal of Microelectromechanical Systems*, vol. 29, pp. 148–159, 4 2020.

[334] M. Clement, L. Vergara, J. Sangrador, E. Iborra, and A. Sanz-Hervás, "SAW characteristics of AlN films sputtered on silicon substrates," *Ultrasonics*, vol. 42, pp. 403–407, 4 2004.

[335] K.-y. Hashimoto, *RF Bulk Acoustic Wave Filters for Communications*. Artech House, 2009.

[336] V. V. Felmetsger, P. N. Laptev, and R. J. Graham, "Deposition of ultrathin AlN films for high frequency electroacoustic devices," *Journal of Vacuum Science & Technology A: Vacuum, Surfaces, and Films*, vol. 29, p. 021014, 2 2011.

[337] R. W. Jackson, "Considerations in the Use of Coplanar Waveguide for Millimeter-Wave Integrated Circuits," *IEEE Transactions on Microwave Theory and Techniques*, vol. 34, no. 12, pp. 1450–1456, 1986.

[338] M. Bozzi, L. Perregrini, and C. Tomassoni, "A Review of Compact Substrate Integrated Waveguide (SIW) Interconnects and Components," *2019 IEEE 23rd Workshop on Signal and Power Integrity, SPI 2019 - Proceedings*, 6 2019.

[339] I. O. Mayboroda, A. A. Knizhnik, Y. V. Grishchenko, I. S. Ezubchenko, M. L. Zanaveskin, O. A. Kondratev, M. Y. Presniakov, B. V. Potapkin, and V. A. Ilyin, "Growth of AlGaN under the conditions of significant gallium evaporation: Phase separation and enhanced lateral growth," *Journal of Applied Physics*, vol. 122, no. 10, 2017.

[340] C. Adelmann, R. Langer, G. Feuillet, and B. Daudin, "Indium incorporation during the growth of InGaN by molecular-beam epitaxy studied by reflection high-energy electron diffraction intensity oscillations," *Applied Physics Letters*, vol. 75, no. 22, pp. 3518–3520, 1999.

[341] V. N. Jmerik, A. M. Mizerov, D. V. Nechaev, P. A. Aseev, A. A. Sitnikova, S. I. Troshkov, P. S. Kop'Ev, and S. V. Ivanov, "Growth of thick AlN epilayers with droplet-free and atomically smooth surface by plasma-assisted molecular beam epitaxy using laser reflectometry monitoring," *Journal of Crystal Growth*, vol. 354, no. 1, pp. 188–192, 2012.

[342] Y. Cao, K. Wang, G. Li, T. Kosel, H. Xing, and D. Jena, "MBE growth of high conductivity single and multiple AlN/GaN heterojunctions," *Journal of Crystal Growth*, vol. 323, no. 1, pp. 529–533, 2011.

[343] L. X. Zheng, M. H. Xie, and S. Y. Tong, "Adsorption and desorption kinetics of gallium atoms on 6H-SiC (0001) Surfaces," *Physical Review B - Condensed Matter and Materials Physics*, vol. 61, p. 4890, 2 2000.

[344] H. Okumura, T. Kimoto, and J. Suda, "Reduction of threading dislocation density in 2H-AlN grown on 6H-SiC(0001) by minimizing unintentional active-nitrogen exposure before growth," *Applied Physics Express*, vol. 4, no. 2, 2011.

[345] H. Okumura, T. Kimoto, and J. Suda, "Enhancement of initial layer-by-layer growth and reduction of threading dislocation density by optimized Ga pre-irradiation in molecular-beam epitaxy of 2H-AlN on 6H-SiC (0001)," *Physica Status Solidi (C) Current Topics in Solid State Physics*, vol. 2096, no. 7, pp. 2094–2096, 2010.

[346] K. Nomoto, B. Song, Z. Hu, M. Zhu, M. Qi, N. Kaneda, T. Mishima, S. Member, T. Nakamura, D. Jena, and H. Grace Xing, "1.7 kV and 0.55 mΩ.cm^2 GaN p-n Diodes on Bulk GaN Substrates With Avalanche Capability," *IEEE Electron Device Letters*, vol. 37, no. 2, 2016.

[347] S. A. Crooker, M. Lee, R. D. Mcdonald, J. L. Doorn, I. Zimmermann, Y. Lai, L. E. Winter, Y. Ren, Y.-J. Cho, B. J. Ramshaw, H. G. Xing, and D. Jena, "GaN/AlGaN 2DEGs in the quantum regime: Magneto-transport and photoluminescence to 60 tesla," *Applied Physics Letters*, vol. 117, p. 262105, 2020.

[348] Y. Cho, J. Encomendero, S.-T. Ho, H. G. Xing, and D. Jena, "N-polar GaN/AlN resonant tunneling diodes," *Applied Physics Letters*, vol. 117, p. 143501, 2020.

[349] Z. Zhang, M. Kushimoto, T. Sakai, N. Sugiyama, L. J. Schowalter, C. Sasaoka, and H. Amano, "A 271.8 nm deep-ultraviolet laser diode for

room temperature operation," *Applied Physics Express*, vol. 12, p. 124003, 11 2019.

[350] M. J. Rodwell, M. Le, and B. Brar, "InP bipolar ICs: Scaling roadmaps, frequency limits, manufacturable technologies," *Proceedings of the IEEE*, vol. 96, no. 2, pp. 271–286, 2008.